Hashemite Kingdom of Jordan

Jordan Journal of Biological Sciences

An International Peer-Reviewed Scientific Journal

Financed by the Scientific Research and Innovation Support Fund

This title is indexed in Scopus

http://jjbs.hu.edu.jo/

المجلة الأردنية للعلوم الحياتية
Jordan Journal of Biological Sciences (JJBS)
http://jjbs.hu.edu.jo

Jordan Journal of Biological Sciences (JJBS) (ISSN: 1995–6673 (Print); 2307-7166 (Online)): An International Peer- Reviewed Open Access Research Journal financed by the Scientific Research and Innovation Support Fund, Ministry of Higher Education and Scientific Research, Jordan and published quarterly by the Deanship of Scientific Research , The Hashemite University, Jordan.

Submission Address
Professor Wedyan, Mohammed A.
The Hashemite Universit y
P.O. Box 330127, Zarqa, 13115, Jordan
Phone: +962-5-3903333 ext.4147
E-Mail: jjbs@hu.edu.jo

المجلة الاردنية للعلوم الحياتية
Jordan Journal of Biological Sciences (JJBS)
http://jjbs.hu.edu.jo

International Advisory Board (Arranged alphabetically)

Instructions to Authors

Scopes

Study areas include cell biology, genomics, microbiology, immunology, molecular biology, biochemistry, embryology, immunogenetics, cell and tissue culture, molecular ecology, genetic engineering and biological engineering, bioremediation and biodegradation, bioinformatics, biotechnology regulations, gene therapy, organismal biology, microbial and environmental biotechnology, marine sciences. The JJBS welcomes the submission of manuscript that meets the general criteria of significance and academic excellence. All articles published in JJBS are peer-reviewed. Papers will be published approximately one to two months after acceptance.

Type of Papers

The journal publishes high-quality original scientific papers, short communications, correspondence and case studies. Review articles are usually by invitation only. However, Review articles of current interest and high standard will be considered.

Submission of Manuscript

Manuscript, or the essence of their content, must be previously unpublished and should not be under simultaneous consideration by another journal. The authors should also declare if any similar work has been submitted to or published by another journal. They should also declare that it has not been submitted/ published elsewhere in the same form, in English or in any other language, without the written consent of the Publisher. The authors should also declare that the paper is the original work of the author(s) and not copied (in whole or in part) from any other work. All papers will be automatically checked for duplicate publication and plagiarism. If detected, appropriate action will be taken in accordance with International Ethical Guideline. By virtue of the submitted manuscript, the corresponding author acknowledges that all the co-authors have seen and approved the final version of the manuscript. The corresponding author should provide all co-authors with information regarding the manuscript, and obtain their approval before submitting any revisions. Electronic submission of manuscripts is strongly recommended, provided that the text, tables and figures are included in a single Microsoft Word file. Submit manuscript as e-mail attachment to the Editorial Office at: JJBS@hu.edu.jo. After submission, a manuscript number will be communicated to the corresponding author within 48 hours.

Peer-review Process

It is requested to submit, with the manuscript, the names, addresses and e-mail addresses of at least 4 potential reviewers. It is the sole right of the editor to decide whether or not the suggested reviewers to be used. The reviewers' comments will be sent to authors within 6-8 weeks after submission.
Manuscripts and figures for review will not be returned to authors whether the editorial decision is to accept, revise, or reject. All Case Reports and Short Communication must include at least one table and/ or one figure.

Preparation of Manuscript

The manuscript should be written in English with simple lay out. The text should be prepared in single column format. Bold face, italics, subscripts, superscripts etc. can be used. Pages should be numbered consecutively, beginning with the title page and continuing through the last page of typewritten material.

The text can be divided into numbered sections with brief headings. Starting from introduction with section 1. Subsections should be numbered (for example 2.1 (then 2.1.1, 2.1.2, 2.2, etc.), up to three levels. Manuscripts in general should be organized in the following manner:

Title Page

The title page should contain a brief title, correct first name, middle initial and family name of each author and name and address of the department(s) and institution(s) from where the research was carried out for each author. The title should be without any abbreviations and it should enlighten the contents of the paper. All affiliations should be provided with a lower-case superscript number just after the author's name and in front of the appropriate address.
The name of the corresponding author should be indicated along with telephone and fax numbers (with country and area code) along with full postal address and e-mail address.

Abstract

The abstract should be concise and informative. It should not exceed **350 words** in length for full manuscript and Review article and **150 words** in case of Case Report and/ or Short Communication. It should briefly describe the purpose of the work, techniques and methods used, major findings with important data and conclusions. No references should be cited in this part. Generally non-standard abbreviations should not be used, if necessary they should be clearly defined in the abstract, at first use.

Keywords

Immediately after the abstract, **about 4-8 keywords** should be given. Use of abbreviations should be avoided, only standard abbreviations, well known in the established area may be used, if appropriate. These keywords will be used for indexing.

Abbreviations

Non-standard abbreviations should be listed and full form of each abbreviation should be given in parentheses at first use in the text.

Introduction

Provide a factual background, clearly defined problem, proposed solution, a brief literature survey and the scope and justification of the work done.

Materials and Methods

Give adequate information to allow the experiment to be reproduced. Already published methods should be mentioned with references. Significant modifications of published methods and new methods should be described in detail. Capitalize trade names and include the manufacturer's name and address. Subheading should be used.

Results

Results should be clearly described in a concise manner. Results for different parameters should be described under subheadings or in separate paragraph. Results should be explained, but largely without referring to the literature. Table or figure numbers should be mentioned in parentheses for better understanding.

Discussion

The discussion should not repeat the results, but provide detailed interpretation of data. This should interpret the significance of the findings of the work. Citations should be given in support of the findings. The results and discussion part can also be described as separate, if appropriate. The Results and Discussion sections can include subheadings, and when appropriate, both sections can be combined

Conclusions

This should briefly state the major findings of the study.

Acknowledgment

A brief acknowledgment section may be given after the conclusion section just before the references. The acknowledgment of people who provided assistance in manuscript preparation, funding for research, etc. should be listed in this section.

Tables and Figures

Tables and figures should be presented as per their appearance in the text. It is suggested that the discussion about the tables and figures should appear in the text before the appearance of the respective tables and figures. No tables or figures should be given without discussion or reference inside the text.

Tables should be explanatory enough to be understandable without any text reference. Double spacing should be maintained throughout the table, including table headings and footnotes. Table headings should be placed above the table. Footnotes should be placed below the table with superscript lowercase letters. Each table should be on a separate page, numbered consecutively in Arabic numerals.

Each figure should have a caption. The caption should be concise and typed separately, not on the figure area. Figures should be self-explanatory. Information presented in the figure should not be repeated in the table. All symbols and abbreviations used in the illustrations should be defined clearly. Figure legends should be given below the figures.

References

References should be listed alphabetically at the end of the manuscript. Every reference referred in the text must be also present in the reference list and vice versa. In the text, a reference identified by means of an author's name should be followed by the year of publication in parentheses (e.g.(Brown,2009)). For two authors, both authors' names followed by the year of publication (e.g.(Nelson and Brown, 2007)). When there are more than two authors, only the first author's name followed by "*et al*." and the year of publication (e.g. (Abu-Elteen *et al*., 2010)). When two or more works of an author has been published during the same year, the reference should be identified by the letters "a", "b", "c", etc., placed after the year of publication. This should be followed both in the text and reference list. e.g., Hilly, (2002a, 2002b); Hilly, and Nelson, (2004). Articles in preparation or submitted for publication, unpublished observations, personal communications, etc. should not be included in the reference list but should only be mentioned in the article text (e.g., Shtyawy,A., University of Jordan, personal communication). Journal titles should be abbreviated according to the system adopted in Biological Abstract and Index Medicus, if not included in Biological Abstract or Index Medicus journal title should be given in full. The author is responsible for the sccuracy and completeness of the references and for their correct textual citation. Failure to do so may result in the paper being withdraw from the evaluation process. Example of correct reference form is given as follows:-

Reference to a journal publication:

Bloch BK. 2002. Econazole nitrate in the treatment of *Candida vaginitis*. *S Afr Med J.* , **58**:314-323.

Ogunseitan OA and Ndoye IL. 2006. Protein method for investigating mercuric reductase gene expression in aquatic environments. *Appl Environ Microbiol.*, **64**: 695-702.

Hilly MO, Adams MN and Nelson SC. 2009. Potential fly-ash utilization in agriculture. *Progress in Natural Sci.*, **19**: 1173-1186.

Reference to a book:

Brown WY and White SR.1985. **The Elements of Style**, third ed. MacMillan, New York.

Reference to a chapter in an edited book:

Mettam GR and Adams LB. 2010. How to prepare an electronic version of your article. In: Jones BS and Smith RZ (Eds.), **Introduction to the Electronic Age**. Kluwer Academic Publishers, Netherlands, pp. 281–304.

Conferences and Meetings:

Embabi NS. 1990. Environmental aspects of distribution of mangrove in the United Arab Emirates. Proceedings of the First ASWAS Conference. University of the United Arab Emirates. Al-Ain, United Arab Emirates.

Theses and Dissertations:

El-Labadi SN. 2002. Intestinal digenetic trematodes of some marine fishes from the Gulf of Aqaba. MSc dissertation, The Hashemite University, Zarqa, Jordan.

Nomenclature and Units

Internationally accepted rules and the international system of units (SI) should be used. If other units are mentioned, please give their equivalent in SI.

For biological nomenclature, the conventions of the *International Code of Botanical Nomenclature, the International Code of Nomenclature of Bacteria,* and the *International Code of Zoological Nomenclature* should be followed.

Scientific names of all biological creatures (crops, plants, insects, birds, mammals, etc.) should be mentioned in parentheses at first use of their English term.

Chemical nomenclature, as laid down in the *International Union of Pure and Applied Chemistry* and the official recommendations of the *IUPAC-IUB Combined Commission on Biochemical Nomenclature* should be followed. All biocides and other organic compounds must be identified by their Geneva names when first used in the text. Active ingredients of all formulations should be likewise identified.

Math formulae

All equations referred to in the text should be numbered serially at the right-hand side in parentheses. Meaning of all symbols should be given immediately after the equation at first use. Instead of root signs fractional powers should be used. Subscripts and superscripts should be presented clearly. Variables should be presented in italics. Greek letters and non-Roman symbols should be described in the margin at their first use.

To avoid any misunderstanding zero (0) and the letter O, and one (1) and the letter l should be clearly differentiated. For simple fractions use of the solidus (/) instead of a horizontal line is recommended. Levels of statistical significance such as: $^{*}P < 0.05$, $^{**}P < 0.01$ and $^{***}P < 0.001$ do not require any further explanation.

Copyright

Submission of a manuscript clearly indicates that: the study has not been published before or is not under consideration for publication elsewhere (except as an abstract or as part of a published lecture or academic thesis); its publication is permitted by all authors and after accepted for publication it will not be submitted for publication anywhere else, in English or in any other language, without the written approval of the copyright-holder. The journal may consider manuscripts that are translations of articles originally published in another language. In this case, the consent of the journal in which the article was originally published must be obtained and the fact that the article has already been published must be made clear on submission and stated in the abstract. It is compulsory for the authors to ensure that no material submitted as part of a manuscript infringes existing copyrights, or the rights of a third party.

Ethical Consent

All manuscripts reporting the results of experimental investigation involving human subjects should include a statement confirming that each subject or subject's guardian obtains an informed consent, after the approval of the experimental protocol by a local human ethics committee or IRB. When reporting experiments on animals, authors should indicate whether the institutional and national guide for the care and use of laboratory animals was followed.

Plagiarism

The JJBS hold no responsibility for plagiarism. If a published paper is found later to be extensively plagiarized and is found to be a duplicate or redundant publication, a note of retraction will be published, and copies of the correspondence will be sent to the authors' head of institute.

Galley Proofs

The Editorial Office will send proofs of the manuscript to the corresponding author as an e-mail attachment for final proof reading and it will be the responsibility of the corresponding author to return the galley proof materials appropriately corrected within the stipulated time. Authors will be asked to check any typographical or minor clerical errors in the manuscript at this stage. No other major alteration in the manuscript is allowed. After publication authors can freely access the full text of the article as well as can download and print the PDF file.

Publication Charges

There are no page charges for publication in Jordan Journal of Biological Sciences, except for color illustrations,

Reprints

Ten (10) reprints are provided to corresponding author free of charge within two weeks after the printed journal date. For orders of more reprints, a reprint order form and prices will be sent with article proofs, which should be returned directly to the Editor for processing.

Disclaimer

Articles, communication, or editorials published by JJBS represent the sole opinions of the authors. The publisher shoulders no responsibility or liability what so ever for the use or misuse of the information published by JJBS.

Indexing

JJBS is indexed and abstracted by:

DOAJ (Directory of Open Access Journals)	CABI
Google Scholar	EBSCO
Journal Seek	CAS (Chemical Abstract Service)
HINARI	ETH- Citations
Index Copernicus	Open J-Gat
NDL Japanese Periodicals Index	SCImago
SCIRUS	Clarivate Analytics (Zoological Abstract)
OAJSE	Scopus
ISC (Islamic World Science Citation Center)	AGORA (United Nation's FAO database)
Directory of Research Journal Indexing (DRJI)	SHERPA/RoMEO (UK)
Ulrich's	

المجلة الأردنية للعلوم الحياتية
Jordan Journal of Biological Sciences (JJBS)
ISSN 1995- 6673 (Print), 2307- 7166 (Online)
http://jjbs.hu.edu.jo

The Hashemite University

Deanship of Scientific Research

TRANSFER OF COPYRIGHT AGREEMENT

Journal publishers and authors share a common interest in the protection of copyright: authors principally because they want their creative works to be protected from plagiarism and other unlawful uses, publishers because they need to protect their work and investment in the production, marketing and distribution of the published version of the article. In order to do so effectively, publishers request a formal written transfer of copyright from the author(s) for each article published. Publishers and authors are also concerned that the integrity of the official record of publication of an article (once refereed and published) be maintained, and in order to protect that reference value and validation process, we ask that authors recognize that distribution (including through the Internet/WWW or other on-line means) of the authoritative version of the article as published is best administered by the Publisher.

To avoid any delay in the publication of your article, please read the terms of this agreement, sign in the space provided and return the complete form to us at the address below as quickly as possible.

Article entitled:----------

Corresponding author: ----------

To be published in the journal: Jordan Journal of Biological Sciences (JJBS)

I hereby assign to the Hashemite University the copyright in the manuscript identified above and any supplemental tables, illustrations or other information submitted therewith (the "article") in all forms and media (whether now known or hereafter developed), throughout the world, in all languages, for the full term of copyright and all extensions and renewals thereof, effective when and if the article is accepted for publication. This transfer includes the right to adapt the presentation of the article for use in conjunction with computer systems and programs, including reproduction or publication in machine-readable form and incorporation in electronic retrieval systems.
Authors retain or are hereby granted (without the need to obtain further permission) rights to use the article for traditional scholarship communications, for teaching, and for distribution within their institution.

☐ **I am the sole author of the manuscript**

☐ **I am signing on behalf of all co-authors of the manuscript**

☐ **The article is a 'work made for hire' and I am signing as an authorized representative of the employing company/institution**

Please mark one or more of the above boxes (as appropriate) and then sign and date the document in black ink.

Signed:_____ **Name printed:** _____
Title and Company (if employer representative) : _____
Date: _____

Data Protection: By submitting this form you are consenting that the personal information provided herein may be used by the Hashemite University and its affiliated institutions worldwide to contact you concerning the publishing of your article.

Please return the completed and signed original of this form by mail or fax, or a scanned copy of the signed original by e-mail, retaining a copy for your files, to:

Hashemite University
Jordan Journal of Biological Sciences
Zarqa 13115 Jordan
Fax: +962 5 3903338
Email: jjbs@hu.edu.jo

Editorial Preface

Jordan Journal of Biological Sciences (JJBS) is a refereed, quarterly international journal financed by the Scientific Research and Innovation Support Fund, Ministry of Higher Education and Scientific Research in cooperation with the Hashemite University, Jordan. JJBS celebrated its 12th commencement this past January, 2020. JJBS was founded in 2008 to create a peer-reviewed journal that publishes high-quality research articles, reviews and short communications on novel and innovative aspects of a wide variety of biological sciences such as cell biology, developmental biology, structural biology, microbiology, entomology, molecular biology, biochemistry, medical biotechnology, biodiversity, ecology, marine biology, plant and animal biology, plant and animal physiology, genomics and bioinformatics.

We have watched the growth and success of JJBS over the years. JJBS has published 14 volumes, 60 issues and 800 articles. JJBS has been indexed by SCOPUS, CABI's Full-Text Repository, EBSCO, Clarivate Analytics- Zoological Record and recently has been included in the UGC India approved journals. JJBS Cite Score has improved from 0.7 in 2019 to 1.4 in 2021 (Last updated on 6 March, 2022) and with Scimago Institution Ranking (SJR) 0.22 (Q3) in 2021.

A group of highly valuable scholars have agreed to serve on the editorial board and this places JJBS in a position of most authoritative on biological sciences. I am honored to have six eminent associate editors from various countries. I am also delighted with our group of international advisory board members coming from 15 countries worldwide for their continuous support of JJBS. With our editorial board's cumulative experience in various fields of biological sciences, this journal brings a substantial representation of biological sciences in different disciplines. Without the service and dedication of our editorial; associate editorial and international advisory board members, JJBS would have never existed.

In the coming year, we hope that JJBS will be indexed in Clarivate Analytics and MEDLINE (the U.S. National Library of Medicine database) and others. As you read throughout this volume of JJBS, I would like to remind you that the success of our journal depends on the number of quality articles submitted for review. Accordingly, I would like to request your participation and colleagues by submitting quality manuscripts for review. One of the great benefits we can provide to our prospective authors, regardless of acceptance of their manuscripts or not, is the feedback of our review process. JJBS provides authors with high quality, helpful reviews to improve their manuscripts.

Finally, JJBS would not have succeeded without the collaboration of authors and referees. Their work is greatly appreciated. Furthermore, my thanks are also extended to The Hashemite University and the Scientific Research and Innovation Support Fund, Ministry of Higher Education and Scientific Research for their continuous financial and administrative support to JJBS.

Professor Wedyan ,Mohammed A.
March, 2024

JJBS

Volume 18, Number 3, September 2025
ISSN 1995-6673

Jordan Journal of Biological Sciences

CONTENTS

Original Articles

JJBS

Volume 18, Number 3,September 2025
ISSN 1995-6673
Pages 383 – 392

Jordan Journal of Biological Sciences

Serotonin Gene Polymorphisms Association with Immune Response, Intestinal Inflammation, and Anxiety Behaviour in Rats Exposed to Sodium Arsenite

Halla Abdul-Hadi Chabuk[1,*] ,Zahraa Isam Jameel [2], Wathiq Mohammed [3]

[1] Department of Biology, College of Science, University of Babylon, Babil, Iraq; [2] Department of Biology, College of Science, University of Al-Qasim Green, Al-Qasim, Babil,Iraq; [3] Department of Biology, College of Science, University of Babylon, Babil, Iraq.

Received: August 3, 2024; Revised: December 25, 2024; Accepted: January 15, 2025

Abstract

Sodium arsenite (SA) is one of the major environmental toxicants and one of the causes of colitis. The potential impact of genetic variation in the serotonin gene exon on behaviours, such as anxiety and immune responses, was explored to investigate the development of intestinal mucosal inflammation, which causes colon pathophysiology in rats exposed to SA. Three groups of 10 rats were employed to achieve our experiment goal: Group 1 served as the control group, Group 2 was administered SA at a dose of 5 mg/kg, and Group 3 were administered SA at a dose of 30 mg/kg for 60 days. Gene expressions for serotonin, cytokine profiles, oxidative stress, and anxious behaviour were estimated. Results indicated a significant increase ($p < 0.05$) in the serotonin, pro-inflammatory cytokines, and oxidative stress (reactive oxygen species, hydrogen peroxide, and nitric oxide) levels and caspase-1 activity in rats exposed to SA, while the level of IL-10 showed a significant decrease in these rats compared with the control group. Rats that had been exposed to SA showed anxiety-like behaviours when subjected to open field testing, as opposed to those in the control group. PCR-single-strand conformation polymorphism (SSCP) analysis showed a multitude of single nucleotide polymorphisms (SNPs) and haplotypes within the serotonin exon area. These genetic variations were correlated with alterations in the serotonin gene polymorphism, which are usually responsible for colitis development. This study demonstrates that genetic variants in the serotonin gene exon are associated with elevated colonic serotonin levels, which subsequently resulted in increased pro-inflammatory cytokines, elevated oxidative stress, increased Caspase-1 activity, decreased anti-inflammatory cytokines, and anxiety-like behaviors in rats exposed to sodium arsenite.

Keywords: Anxiety behaviour, Intestinal Inflammation, Serotonin gene, Sodium arsenite, Open field test, Oxidative stress

1. Introduction

Inorganic sodium arsenite (SA) is one of the important environmental toxicants worldwide. One major cause for human intoxication caused by this element is the consumption of polluted drinking water, which often contains high levels of inorganic arsenic, particularly in groundwater used as drinking water (Bhowmick *et al*., 2018). SA, a form of arsenic, is quickly absorbed by the gastrointestinal system and tends to accumulate in various body fluids and tissues. Arsenite toxicity usually induces changes in various bodily markers and behaviours; several researchers have confirmed that exposure to elevated SA levels in drinking water causes detrimental effects on human health (Prakash and Verma, 2021). These effects encompass a range of physiological disorders, including oxidative stress, gastrointestinal disorders, and immune dysfunction (Jing *et al.,* 2012; Acharyya *et al.,* 2015; Campbell and Colgan, 2019). Gastrointestinal reactive oxygen species (ROS) can be generated from endogenous sources, such as the mitochondrial respiratory system, or through the involvement of the intestinal microbiome (Maraldi *et al*., 2021).

Arsenic toxicity in the gastrointestinal tract causes damage to the epithelial mucosa, especially to enterochromaffin cells (EC), leading to symptoms such as ulcerative colitis, nausea, abdominal pain, and irritable bowel syndrome (Prakash and Verma, 2021). Endocrine enterochromaffin cells are distributed throughout the gut mucosa and are responsible for the secretion of serotonin; the gastrointestinal tract produces, stores, and releases approximately 95% of the body's serotonin. A lack of serotonin is related to a high incidence of gastrointestinal diseases, and it is also involved in processes such as absorption and assimilation, as well as influences mucus and fluid secretion and ion transport within the gastrointestinal system (Hatamnejad *et al*., 2022). Given arsenic's impact on the gastrointestinal tract, its influence on enterochromaffin cells and serotonin regulation is particularly relevant for understanding gut-related disorders. Serotonin (5-HT), an intestinal serotonin, plays a decisive role in regulating different gastrointestinal functions, including gut motility, sensation, increased peristalsis and immune response regulation (Prakash and

* Corresponding author. e-mail:sci.halah.a.hadi@uobabylon.edu.iq.

Verma, 2021). Furthermore, pancreatic enzyme secretion is under the regulatory influence of intestinal serotonin. The impact of 5-HT is accomplished through epithelial 5-HTR2 receptors close to the intestinal mucosa (Banskota *et al*., 2019).

Recent reports also suggest that serotonin has immunomodulatory capabilities that can impact the severity and development of inflammation within the intestines, especially in inflammatory bowel diseases (Coates *et al*., 2017; Ala, 2022). Changes in the serotonin amount secreted by the EC stimulate the nervous system and induce both pathophysiological and physiological responses, such as irritable bowel syndrome (IBS), which has been associated with an imbalance of intestinal microbiota, abnormal intestinal motility, mucosal inflammation, and psychosocial factors (Kendig and Grider, 2015; Esteban-Zubero *et al*., 2017). Moreover, several studies have found that serotonin plays a chief role in activating immune cells to generate proinflammatory cytokines. These findings confirmed that the severity of heavy metals toxic-induced colitis connected with deficiency of IL-10 is raised when combined with serotonin which promotes impacts of serotonin reuptake transporters deficiency. Therefore, serotonin is considered a critical signalling molecule in the colitis pathogenesis (Kwon *et al*., 2019).

Some reports showed that arsenic plays a role in inducing injurious impacts on the immune system of both humans and lab animals; arsenic causes immune suppression and alters the activation and proliferation of macrophages and Th1/Th2 lymphocytes and secretion of cytokines IL-2, IL-10, IL-5, IL-4, IFN-γ and TNF-α (Dangleben *et al*., 2013). Ferrario *et al*. (2016) demonstrated that lymphocytes in individuals exposed to arsenic-contaminated water showed a lower proliferation rate than those of individuals unexposed in the same regions. Moreover, the researchers found that arsenic levels positively correlated with oxidative stresses such as malondialdehyde (MDA), and negatively correlated with superoxide dismutase (SOD) and vitamin E levels in the serum, indicating that chronic exposure stimulates lymphocyte oxidative harm (Dangleben *et al*., 2016 ; Ferrario *et al*., 2016).

Sodium arsenite has genotoxic, carcinogenic, and mutagenic impacts (Ozturk *et al*., 2022). It can also trigger epigenetic disorders via mRNA dysregulations and alterations in histone modifications and global methylation. Moreover, arsenic affects the oxidation processes of proteins and enzymes and, therefore, impacts DNA by producing cross-links between proteins and DNA. Heavy metals' genotoxic ability originates from their capacity to produce reactive oxygen species (ROS), which hinders DNA repair capacity. Due to their high affinity for the sulfhydryl group, these metals can cause negative effects such as genotoxic impacts and mutations in organisms, ultimately leading to the inactivation of essential enzymes. This damages the repair systems by either reducing the expression of DNA repair enzymes or inhibiting ligation (Litwin *et al*., 2013).

Bjørklund *et al.* (2020) mentioned the occurrence of behavioural changes, such as anxiety and memory impairments, resulting from heavy metal poisoning. The open field tests are a widely used ethological estimation tool to evaluate rat anxiety-like behaviour. During this experimental procedure, rodents can freely navigate an unobstructed enclosure enclosed by vertical barriers. In this scenario, rodents demonstrate a propensity to avoid the central areas of the arena and instead choose to stay in the peripheral sections (Kuniishi *et al.,* 2017). This study focuses on investigating the possibility that changes in the level and gene polymorphism of serotonin in the intestine play a significant role in behavioural disorders and immune response activation; this inflammation of the intestinal mucosa contributes to the pathophysiology of colitis and irritable bowel syndrome (IBS) in rats exposed to sodium arsenite.

2. Material and methods

2.1. Ethical approval

The study protocol received approval from the Department of Biology, College of Sciences, University of Babylon (Protocol No. 1312/10-3-2023). The experiments were conducted in adherence to approved guidelines and ethical standards outlined by the National Committee for Research Ethics in Science and Technology (NETNT).

2.2. Experimental animals

This experiment used 30 male Wistar rats (weighing 250 ± 10 g). The rats were obtained from the animal facility at the College of Science, University of Thi Qar. The rats were kept under standard conditions of humidity (50 ± 10%) and temperature (24 °C ± 2) with a 12/12 h dark-light cycle, provided in food and water.

2.3. Experimental design

The rats were randomly divided into three groups; each group contained ten rats. In Group 1, the control group, the rats were administered 1.0 mL of distilled water orally via gavage for 60 days. In Group 2, the sodium arsenite group (SA 5 mg), the rats were administered a low dose (5 mg/kg) of $NaAsO_2$ orally via gavage for 60 days. In Group 3, the sodium arsenite group (SA 30 mg), the rats were administered a low dose (30 mg/kg) of $NaAsO_2$ orally via gavage for 60 days.

2.4. Preparation of sodium arsenite ($NaAsO_2$)

SA was acquired from the laboratory of the Department of Chemistry at the College of Science, University of Babylon, Iraq. Aqueous solutions of low and high doses of SA were prepared by mixing 5 and 30 mg/kg of SA with distilled water, respectively. Animals in groups 2, 3 were orally fed daily with 1.0 ml of either the low or high dose of the SA aqueous solution, respectively. The aqueous extract of sodium arsenate (stock) was stored at room temperature because it is classified as a stable solution. The predetermined lethal dose (LD50) of SA is about 41 mg/kg (Bashir *et al*., 2006).

2.5. Tissue samples

Approximately 50–100 mg of intestinal tissues, specifically from the colon, was rinsed using a phosphate-buffered saline (PBS) solution. The pH range of the PBS was 7.0 to 7.4, and its concentration was 0.01 M. The rinse stage aimed to cleanse with phosphate-buffered saline (PBS) to eliminate residual blood, followed by immediately freezing in liquid nitrogen for further usage. The tissue sample was homogenised in a phosphate-buffered saline (PBS) solution using a glass homogeniser

(Model USCG-P150N, China). The homogenates were centrifuged at 5000 g at a temperature of 4°C for 10 minutes. The resulting supernatants were preserved immediately by freezing them until they could be analysed for serotonin, cytokines, and reactive oxygen species (ROS).

2.6. Biochemical parameters

Estimation of serotonin, cytokine profiles, and Caspase-1 activity

Serotonin levels, pro-inflammatory cytokines (interferon INF-γ, tumour necrosis factor-alpha TNF-α, IL-1β, and IL-12 levels), anti-inflammatory cytokine (IL-10) levels, and caspase-1 activity were measured in intestinal tissue supernatant by using special kits of the enzyme-linked immunosorbent assay (ELISA).

2.7. Estimation of oxidative stress markers (µmol/g)

Reactive oxygen species

According to the manufacturer's instructions, reactive oxygen species (ROS) levels were measured in colonic tissue supernatant using the fluorescence method of the ELISA kit principle (MyBioSource company, United States) at excitation wavelengths 500 nm and emission wavelengths 525 nm.

2.7.1. Hydrogen peroxide and nitric oxide levels

According to the manufacturer's instructions, hydrogen peroxide (H_2O_2) and nitric oxide (NO) levels were measured in colonic tissue supernatant using a colorimetric assay ELISA kit (Elabscience, China). The NO and H_2O_2 levels can be calculated by measuring the OD values at 550 nm and 405 nm, respectively.

2.8. Behavioural study

The open field test

The open field test is a method used to assess locomotor activity, exploratory behaviour, and anxiety levels. The open field comprises a rectangular enclosure measuring 70 × 70 cm, including walls 30 cm in height. Thick paper was placed on the enclosure's floor, upon which lines were drawn to partition the floor into sixteen individual squares. Isolated, dimly illuminated room was used to conduct the research. During the experiment, a rat was placed separately in one of the box's four corners and given 10 minutes to investigate the equipment. Following the conclusion of the experimental trials, the rat was reintroduced to its designated housing enclosure. At the same time, the open field apparatus underwent a thorough cleansing procedure employing a 70% ethyl alcohol solution to ensure optimal sanitation before further testing sessions. Exploratory behaviours and anxiety levels were assessed by measuring the frequency of entrances to the middle square and the time spent in this area. An elevated occurrence of these behaviours implies heightened locomotor activity and exploratory tendencies, as well as a reduced fear level (Habib *et al*., 2015; CHabuk *et al*., 2019). The behavioural parameters were recorded on video and automatically analysed using the software SMARTV3.0.06 (Panlab, Spain).

2.9. Genomic DNA extraction

A DNA Mini Kit (Favorgen, Taiwan) was used to extract genomic DNA from 1.5 mL tissue samples. The purity of the isolated genomic DNA was confirmed to be at a 260: 280 ratio using a nanodrop spectrophotometric method. The established standard procedures determined the integrity of the recovered genomic DNA using agarose gel electrophoresis.

PCR experiment

Gene-specific primers (forward 5-TCTGCCCGATTTTCAAAG-3; reverse 5-GTGAGAGACTCCAAGCTGAAA-3) were used to amplify distinct fragments within the rs8154473 region, including the third exon of the SLC6A4 gene of the rat[21]. The polymerase chain reaction (PCR) experiment was performed using a lyophilised PCR Accu Power Pre Mix (Promega Co., USA), with a final volume of 20 mL for the amplified fragment (initial denaturation 95°C for 5 min, 62°C annealing, and 72°C extension). Following the completion of the PCR test, electrophoresis on agarose gels verified that the resulting PCR products exhibited the anticipated size of 548 base pairs. Per the specified protocols, all PCR products were submitted to a Sanger dideoxy-sequencing facility (Macrogen Inc., South Korea) to verify the electrophoretic genotypes acquired for all samples. BioEdit Suite, version 7.0, correlated the observed variance with the relevant DNA sequences.

2.10. . Statistical analysis

The results were presented as the mean value accompanied by the standard error (SE). The statistical analysis was conducted using a one-way analysis of variance (ANOVA) and the Duncan post-hoc and correlation tests after data were tested for normality and homogeneity of variances. The software SPSS version 25 was employed for this analysis, under the significance value of $P < 0.05$.

3. Results

3.1. Colonic serotonin levels

Figure 1 depicts the serotonin levels in the colons of rats subjected to different doses of SA (5 and 30 mg/kg) over 60 days. Rats that were administered SA demonstrated a statistically significant ($P < 0.05$) elevation in serotonin levels within the colon, as observed in the 5- and 30-mg/kg dosage groups compared to the control group. However, a statistically significant rise ($P < 0.05$) in serotonin levels was seen in rats belonging to Group 3 compared to those in Group 2.

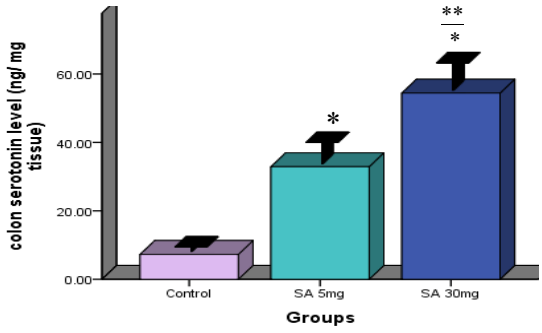

Figure 1. Levels of Serotonin in the colon tissue of rats exposed to SA for 60 days. Each data represents mean±SE from ten rats. *P < 0.05 compared with control group, **P < 0.05 compared with SA group 3

3.2. Colonic Cytokines profile

The changes in the pro-inflammatory cytokines (TNF-α, IL-1β, IL-12), anti-inflammatory cytokine (IL-10) levels, and caspase-1 activity in the colon tissue of laboratory animals are shown in Table 1. There was a significant increase ($P < 0.05$) in the levels of pro-inflammatory cytokines and caspase-1 activity in groups exposed to SA (5 and 30 mg/kg) for 60 days compared to the control group. Meanwhile, the levels of IL-10 significantly decreased ($P < 0.05$) in rats that received SA compared to those of the control group using a one-way ANOVA with the Duncan post-hoc test.

Table 1. Levels of cytokines profiles and caspase-1 activity in the colon tissue from rats exposed to SA for 60 days (n=10 per group).

Parameters \ Groups	Control group mean±SE	SA 5mg group mean±SE	SA 30mg group mean±SE
IFN- γ (pg/mg tissue)	94.28 ± 2.14	96.7± 3.62	99.29 ± 5.07
TNF-α (pg/mg tissue)	32.87 ±1.46	132.57 ± 4.24*	171.71± 3.03*#
IL-12 (pg/mg tissue)	61.12 ± 3.64	252.41 ± 6.63*	305.62± 8.212*#
IL-1β (pg/mg tissue)	4.19 ± 0.44	81.91 ± 3.08*	157.59 ± 2.33*#
caspase-1 (pg/mg tissue)	5.51 ± 0.45	15.97 ± 0.76*	33.13 ± 2.57*#
IL-10 (pg/mg tissue)	7.80 ± 0.73	4.36 ± 0.55*	3.76 ± 0.49*

* The means are statistically significant compared with the control group at $P < 0.05$.

The means are statistically significant compared with the SA group (5gm/kg) at $P < 0.05$.

3.3. Oxidative stress markers

Table 2 presents the levels of oxidative stress detected in the colon tissue across various experimental groups. The experimental findings demonstrate significant elevations ($P < 0.05$) in the concentrations of ROS, H2O2, and NO in the rats subjected to treatment with SA (5 and 30 mg/kg) in comparison to those of the control group using a one-way ANOVA with the Duncan post-hoc test.

Table 2. Presents the levels of oxidative stress markers in colonic tissue of rats exposed to SA for 60 days (n=10 per group).

Parameters \ Groups	Control group mean±SE	SA 5mg group mean±SE	SA 30mg group mean±SE
ROS µmol/ g tissue	2.29±0.39	24.59 ±1.83*	56.29±4.59*#
H_2O_2 mmol /mg tissue	77.28±2.96	133.23±3.32*	219.74±5.547*#
NO µmol/g tissue	1.68±0.33	11.89±1.54*	39.48±2.94*#

* The means are statistically significant compared with the control group at $P < 0.05$.

The means are statistically significant compared with the SA group (5gm/kg) at $P < 0.05$.

3.4. Correlation between colonic Serotonin with cytokines profile and oxidative stress

The Spearman correlation coefficient suggests a highly significant positive correlation at the 0.01 level between serotonin and pro-inflammatory cytokines (IL-1β, IL-12, and TNF-α), caspase-1 activity, and oxidative stress parameters. There was a negative correlation at the 0.01 level between serotonin, IL-10, and interferon INF-γ, which showed no significant correlation with serotonin. The correlations between the parameters were analysis by Pearson's test.

Table 3. Correlation coefficients for colonic serotonin with cytokines profile and oxidative stress.

		IFN	TNF-α	IL-12	IL-1β	caspase-1	IL-10	ROS	NO	H_2O_2
Serotonin levels	Pearson Correlation	0.244	0.875**	0.862**	0.921**	0.858**	- 0.767**	0.825**	0.903**	0.791**
	Sig. (2-tailed)	0.194	0.000	0.000	0.000	0.000	0.000	0.000	0.000	0.000

** Correlation is significant at the 0.01 level (2-tailed).

3.5. The open field test

This test assesses the locomotion, exploration, and anxiety of rats exposed to SA for 60 days by analysing latency time (sec.), ambulation (peripheral and central squares), and the amount of time spent in each area (Table 4). The time that rats spent in the centre squares can be used to assess changes in anxiety-like behaviour; the more anxious rats spent remarkably less time in the central area and more time near the walls. The results show a significant increase ($p < 0.05$) in mean latency time (sec.) and the time spent in the peripheral square (sec.) of the rats treated with SA compared to the control group. The total mean ambulation number (square, peripheral, and central) and amount of time spent in the central square (sec.) of SA-treated rats showed a significant decrease with a significant increase in latency time compared to those of the control group, indicating anxiety-like behaviour.

Table 4: Exposure of rats to SA for 60 days led to locomotors reduction and anxiety behavior, measured by open-fled tests for 10 min. (n=10 per group).

Groups / parameters test	Control group mean±SD	SA 5mg group mean±SD	SA 30mg group mean±SD
latency time(sec.)	69.86 ± 18.54	185.62 ± 16.19*	281.83 ± 10.42*#
Ambulation	51.99 ±5.94	14.10 ± 3.90*	9.00 ± 1.41*#
Time spent in the central square(sec.)	243.37± 12.55	75.38 ± 8.08*	57.18± 8.79*#
Time spent in the Peripheral square(sec.)	379.22± 60.93	525.58 ± 8.11*	542.65± 6.98*

* The means are statistically significant compared with the control group at $P < 0.05$.
# The means are statistically significant compared with the SA group (5gm/kg) at $P < 0.05$.

3.6. Genetic polymorphisms of 5HTT

First, the genomic DNA (Fig. 2) was isolated from the tissue samples so that the target region of the third exon of the SLC6A4 gene in rats could be amplified.

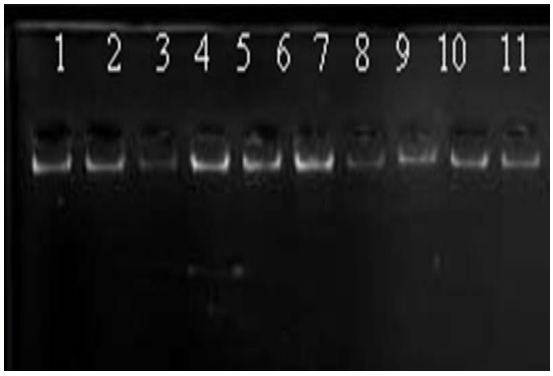

Figure 2. shows the electrophoretic pattern of genomic DNA derived from tissue samples. Lane 1 to lane 11 corresponds to the genomic DNA derived from tissue samples, which were subjected to electrophoresis under the following conditions: 1% agarose gel was used, and 75 volts with 20 milliamperes were applied for 1 hour. Each well contained 10 microlitres of the DNA sample, which was subsequently stained with ethidium bromide.

The process of SLC6A4 genotyping involved amplifying the genomic DNA using primers specifically designed for this purpose. This amplification was carried out using a thermocycler device, following the ideal conditions for this procedure. The findings indicate the detection of a solitary band (548 bp) representing the target sequence of the SLC6A4 gene on the agarose gel (Fig. 2).

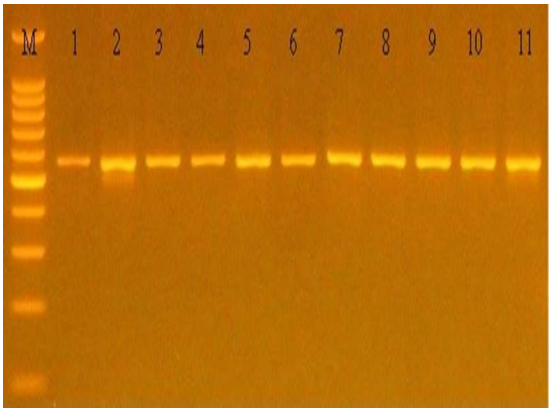

Figure 3. shows that agarose gel electrophoresis was conducted to analyse the patterns of the amplified products (SLC6A4). The DNA size marker, denoted as M, was used for reference. Lanes 1–11 exhibited amplified products that appeared as a single band with a size of 548 bp. The experimental parameters for electrophoresis were established as follows: The agarose gel used in this experiment had a concentration of 1%. Following electrophoresis, the gel was stained with ethidium bromide.

The sequencing results (Fig. 3) show the presence of three SNPs determined in the third exon of the SLC6A4 gene depending on Primer 3 plus reference sequences: XM_017597042.2 (https://www.ncbi.nlm.nih.gov/nuccore/XM_017597042.2). These SNPs were T\C 270, G\T 272, and G\T 525, located at exon 3 according to the reference sequence (ID: XM_017597042.2). Three sequences from 30 sequence isolates were deposited in GenBank at the DNA Data Bank Japan (DDBJ) database (LC777458, LC777459, LC777460).

The results demonstrate a significant association ($p < 0.05$) between DNA polymorphisms according to the three SNPs determined in the third exon of the SLC6A4 gene with treatment compared with the control groups in the table below.

Figure 4. Sequences alignment ID: XM_017597042.2 results for a rat in the third exon of SLC6A4 gene depending on Primer3 [plus] reference sequences: XM_017597042.2 by Bio Edit program version 7.2.5.

Table 5. Mutations distribution in the third exon of SLC6A4 gene

	SNP1(T\C)	SNP 2(G\T)	SNP 3 (T\G)	The chi-square	P- Value
Group 1	8	0	2		
Group2	5	5	0	10.53	0.03*
Group3	6	1	3		
Colum total	10	10	10		

*P ≤ 0.05

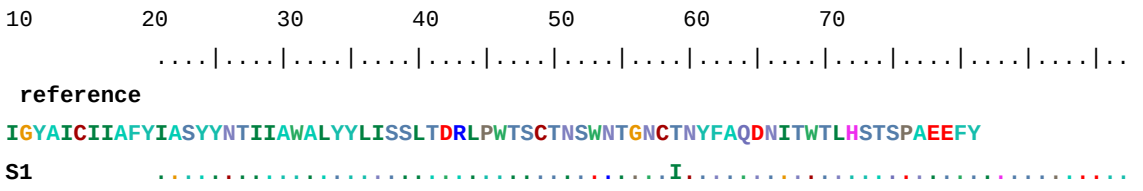

Figure 5. Protein sequence alignment of the genotyped sample with their corresponding reference sequences of the 72 amino acids SLC6A4 gene. The symbol "ref." refers to the NCBI referring sequence. The "S" refers to the genotyped sample. This SNP caused an amino acid substitution of serine to Isoleucine in position 39.

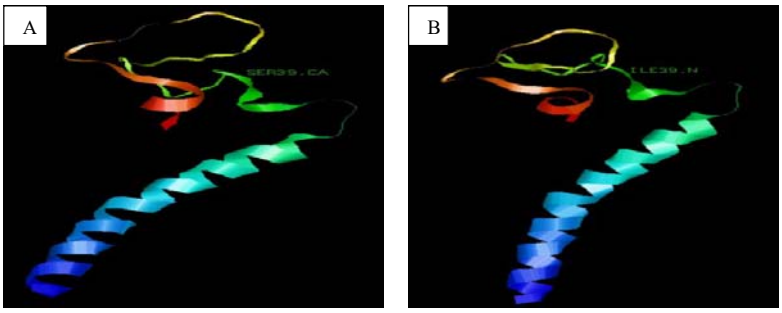

Figure 6. Substitution of serine to Isoleucine in position 39 of SLC6A4 gene (A normal 3D of secondary structure ribbon model, B abnormal 3D of secondary structure ribbon model

4. Discussion

Ingesting contaminated food and water or contacting consumer-infected goods can put people in considerable danger of SA poisoning (Lu *et al*., 2023). In the present study, chronic administration of SA showed a significant rise in the levels of serotonin and pro-inflammatory cytokines (such as IL-12, IL-8, IL-6, and TNFα), probably due to damage in the intestinal epithelium tissues induced by SA, which usually causes a mucosal inflammation accompanied with changes in the number of enterochromaffin cells and the levels of secreted serotonin in the gastrointestinal tract (Acharyya *et al*., 2015). Elevated serotonin levels trigger the immune system by generating different kinds of pro-inflammatory cytokines. These cytokines can cross the blood-brain barrier and send signals to the brain, which responds by altering various behavioural acts. Intestinal serotonin acts as a signal that regulates immune responses and behaviour (Waclawiková and Aidy, 2018). AS causes a block of serotonin receptors resulting in raised severity of colitis; in opposition, serotonin receptor agonists result in an anti-inflammatory impact (Vijayakaran *et al*., 2014). Recently, reports showed that activation of serotonin receptors causes blockade of oxidative stress and pro-inflammatory markers in rats. This indicates that activation of serotonin receptors may appear an efficient and new approach to developing potent therapeutics for inflammatory diseases like inflammatory bowel diseases (Quintero-Villegas and Valdés-Ferrer, 2020). Oxidative stress is one of the main mechanisms underlying SA-induced cell damage. Therefore, one of the possible therapeutic strategies, which may follow to eliminate or reduce the SA toxicity in vivo, is by employing varıous antioxidants. Based on recent studies, nanoselenium treatment during SA intoxication can alleviate the harmful ımpacts of both toxic elements on rodent tissues and cells. Co-administration of nano selenium with SA prohibited apoptosis induction, DNA damage, lipid peroxidation, decline of SA accumulation, serotonın system defect and anxiety-like behaviours (Samad *et al*., 2022).

Recently, there is evidence that the gut microbiota effects are not restricted to the intestine but may include all physiological functions of the organism, such as brain functions, inflammation response and regulation of behaviour. Specifically, when the structures of the gut microbiota are changed by exposure to chemical compounds such as heavy metals or drugs, gut cells respond to these alterations, and thus send signals to the central nervous system by releasing neurotransmitters, hormones and neuropeptides (Baldissarelli *et al*., 2021).

Attention to the gut-brain axis (GBA) has grown with our developed understanding of this axis importance in the pathophysiology of several common clinical disorders including neurodegenerative diseases and behaviour defects. The gastrointestinal tract and brain are important sensory organs accountable for detecting, transporting, and responding to external and internal environmental signals (González Delgado et al., 2022). This can happen through a two-way system called the gut-brain axis (GBA), which involves the production of neurotransmitters such as serotonin. Immune cells in both the brain and intestines consistently respond to environmental agents, leading to changes in immune activity that signal the body's current physiological state (Banskota *et al*., 2019). Recent research reveals that the gut-brain axis regulates inflammatory cytokines, inflammatory nociception and immune homeostasis (Rutsch *et al*., 2020).

According to Keil *et al*. (2011), it has been demonstrated that 95% of orally administered SA which absorbed in the intestine enters the bloodstream, resulting in systemic toxicity and increasing oxidative stress by elevating the levels of the created ROS. Hence, this result indicates that SA administration through drinking water may cause pathological damage to colon cells, as concluded by Chiocchett *et al.* (2018), who demonstrated that exposure to inorganic arsenic induces changes in the

immune system and serotonin levels in the gut, with the severity of these effects contingent upon dosage and duration of exposure. Therefore, it can be postulated that pro-inflammatory cytokines have the capacity to exhibit either an inflammatory or protective function, contingent upon the specific immunological condition of the individual. The acute exposure to arsenic has been found to contribute in the injury of the gut epithelium tissue, as well as increased serotonin levels, pro-inflammatory cytokines, and oxidative stress. Continuous exposure to inorganic substances can lead to an immune-toxic impact (Acharyya *et al*., 2015).

The intestinal epithelium tissue forms a selective permeability barrier that effectively inhibits any harmful substances from passing through it and causing infections. Therefore, any damage would decrease the efficiency of this barrier, leading to a non-specific and unregulated increase of the intestinal permeability, which mostly facilitates the entry of hazardous materials or microbes that probably interact with the immune system components located in the lamina propria (Chiocchetti *et al*., 2018). The commencement of an inflammatory process is associated with a disruption in the integrity of the intestinal barriers, which will elevate the serotonin levels and develop persistent inflammatory conditions (Ferrario *et al*., 2016). These interactions normally stimulate an immunological response; for instance, the expression of tight junction proteins, namely occludin, claudin-5, and zonula occludens-1, is reduced by pro-inflammatory cytokines within the tight junctions. Reduction in protein expression will decrease the integrity and structure of the epithelium cells and ultimately increase permeability (Zhao *et al*., 2023). Inflammation serves as a key mechanism to remove the damaged tissues or start the healing process. Interleukin-1β (IL-1β) and interleukin-18 (IL-18) are cytokines that play a crucial role in promoting inflammation (Waclawiková and Aidy, 2018). These cytokines, as multi-protein complexes found within cells, are processed by inflammasomes; particularly, nucleotide-binding domain leucine-rich repeat (NLR) proteins NLRP3 and NLRC4 in macrophages induce and activate caspase-1. The activated NLRP3 will lead to the proteolytic cleavage of IL-1β and IL-18 precursors, which induce apoptosis of the inflammatory cells (Bauernfeind *et al*., 2011; Ahn *et al*., 2016).

The open field tests were employed to assess the anxiety levels in animals and examine the potential neurobehavioral deficit resulting from exposure to SA. The test outlined in the study has been widely used to detect anxiety-like behaviours in rats (Knight *et al*., 2021). The results revealed that rats exposed to SA exhibited reduced locomotor activity in an open field environment, mirroring the findings of Firdaus *et al*. (2018) study, which suggested that arsenite exposure may have a suppressive effect on both balance and motor activity in rats. Furthermore, cytokine receptors in the brain for IL-1β and TNF-α will be activated by cerebral NF-κB signalling pathways. This activation will lead to the production of secondary cytokines, which have been associated with anxiety and mood disorders. Taken together, these pathways reveal multiple brain signalling pathways that may be activated by chemicals produced during gastrointestinal inflammation, which in turn may trigger glaring alterations in brain functioning that underlie the development of anxiety and a decline in locomotor activity (Waclawiková and Aidy, 2018).

The SLC6A4 gene encodes a protein known as the serotonin transporter, which facilitates the reuptake of serotonin molecules from the synaptic cleft into the presynaptic neurons. The impact of polymorphisms in the SLC6A4 gene on the rate of serotonin reuptake and its function in different disorders has been revealed in studies conducted by Taylor (2013), and Rao et al. (2017). Another study conducted by O'Mahony *et al*. (2015) demonstrated that serotonin (5-HT) functions as a neurotransmitter that has an impact on both immune responses and the communication between the intestines and the brain. A decrease in the copy number variation of the intestinal SLC6A4 transporter can lead to an accumulation of serotonin (5-HT) in the intestines (Dell'Osso *et al*., 2013; Nguyen *et al*., 2014; Catena-Duman and Canli, 2015), which might increase stimulation of the intestinal mucosa and ultimately result in the occurrence of diarrhoea (Sjaarda *et al*., 2017). Depressive symptoms and higher pro-inflammatory cytokine levels are associated with a specific genetic susceptibility that the present study has identified. This vulnerability involves the serotonin transporter gene. This study found that serotonin plays a significant role in the pathophysiology of depression and modulates neural-immune interactions; furthermore, the findings support the concept that shared pathophysiological pathways connect inflammation and depression.

Numerous investigations have demonstrated that the manifestation of a genetic variant in the serotonin transport gene (SLC6A4) in rodents leads to deficits in behaviour (Lam et al., 2018; Veenstra-Vander Weele *et al*., 2012). The investigation of genetic abnormalities associated with 5-HT in individuals with deviant attitudes suggested a potential association with Slc6a4, the gene responsible for encoding SERT. Carneiro *et al.* (2008) conducted a comprehensive investigation of individuals afflicted with diverse disorders, revealing significant associations with SERT across the entire genome. Apart from the present study, an investigation was conducted on uncommon mutations in the Slc6a4 gene. The observed alterations led to the occurrence of a gain-of-function mutation and an increase in SERT activity, as reported by Muller. et al. (2015). The SERT Ala56 mutation, along with the other polymorphisms documented in this study, induces a hyper-functional SERT protein that exhibits enhanced efficiency in the reuptake of 5-HT (Sutcliffe *et al*., 2005).

Arsenic toxicity impacts various systems and pathways involved in learning, memory, locomotion, decision-making, and emotion, according to research in mouse models. Future studies should concentrate on developing therapies to alleviate the neurological effects of arsenic poisoning by delving further into the underlying mechanisms of action, such as epigenetics. To determine the actual effect of arsenic on the central nervous system, more data on health and exposure during the intrauterine period would be useful.

5. Conclusion

This study indicates that variants within the serotonin gene exon correlated with elevated colonic serotonin

levels, which subsequently led to: first, increased pro-inflammatory cytokine (IL-1β, TNF-α, and IL-12) levels; second, elevated oxidative stress (ROS, H2O2, and NO) levels in the colon tissues of rats exposed to sodium arsenite; and finally, increased activity of the caspase-1 enzyme and anxiety behaviour with decreased levels of the anti-inflammatory cytokine IL-10.

Acknowledgment

The authors express gratitude to the University of Babylon/College of Science for the resources provided for this study.

Authors' Contribution Statement

This manuscript was carried out in cooperation between all authors. H.AH.CH. designed the experiment, collected tissue and blood samples from rats, and conducted behavioural and physiological tests. Z.I.J. designed the genetic study. W.M. and H.AH.CH. were responsible for the writing, editing, and data analysis of the manuscript. All authors read and approved the final manuscript.

References

Abrahams BS and Geschwind DH. 2008. Advances in autism genetics: on the threshold of a new neurobiology. *Nat Rev Genet*., 9: 341–55. doi: 10.1038/nrg2346.

Acharyya N, Sajed Ali S, Deb B, Chattopadhyay S and Maiti S. 2015. Green tea (Camellia sinensis) alleviates arsenic-induced damages to DNA and intestinal tissues in rat and in situ intestinal loop by reinforcing antioxidant system. *Environ Toxicol*., 30(9): 1033-1044. https://doi.org/10.1002/tox.21977.

Ahn H, Kang SG, Yoon SI, Kim PH, Kim D and Lee GS. 2018. Poly-gamma-glutamic acid from Bacillus subtilis upregulates pro-inflammatory cytokines while inhibiting NLRP3, NLRC4 and AIM2 inflammasome activation. *Cellu Mol Immunol*., 15(2): 111-119. https://doi.org/10.1038/cmi.2016.13.

Ala M. 2022. Tryptophan metabolites modulate inflammatory bowel disease and colorectal cancer by affecting the immune system. *Int Rev Immunol*., 41(3): 326-345. https://doi.org/10.1080/08830185.2021.1954638,

Baldissarelli LA, Capiotti KM, Bogo MR, Ghisleni G and Bonan CD. 2012. Arsenic alters behavioral parameters and brain ectonucleotidases activities in zebrafish (Danio rerio). *Comparative Biochemistry and Physiology Part C: Toxicol Pharmacol.*, *155*(4),566-572. https://doi.org/10.1016/j.cbpc.2012.01.006

Banskota S, Ghia JE and Khan WI. 2019. Serotonin in the gut: Blessing or a curse. *Biochimie*., 161: 56-64. https://doi.org/10.1016/j.biochi.2018.06.008.

Bashir S, Sharma Y, Irshad M, Gupta SD and Dogra TD. 2006. Arsenic-induced cell death in liver and brain of experimental rats. *Basic Clin. Pharmacol. & Toxicol*., 98(1): 38-43. https://doi.org/10.1111/j.1742-7843.2006.pto_170.x,

Bauernfeind F, Bartok E, Rieger A, Franchi L, Núñez G and Hornung V. 2011. Cutting edge: reactive oxygen species inhibitors block priming, but not activation, of the NLRP3 inflammasome. *J Immunol.,* 187(2): 613-617. doi: 10.1016/j.lfs.2016.11.031.

Belay H, Burton Ch L, Lovic V and Meaney MJ, Sokolowski M and Fleming AS. 2011. Early Adversity and Serotonin Transporter Genotype Interact With Hippocampal Glucocorticoid Receptor mRNA Expression, Corticosterone, and Behavior in Adult Male Rats., *Behav Neurosci*., 125(2): 150–160. DOI: 10.1037/a0022891,

Bhowmick S, Pramanik S, Singh P, Mondal P, Chatterjee D and Nriagu J. 2018. Arsenic in groundwater of West Bengal, India: a review of human health risks and assessment of possible intervention options. *Sci. Total Environ*., 612: 148-169. https://doi.org/10.1016/j.scitotenv.2017.08.216.

Bjørklund G, Oliinyk P, Lysiuk R, Rahaman MS, Antonyak H, Lozynska I, Lenchyk L and Peana M. 2020. Arsenic intoxication: general aspects and chelating agents. *Arch Toxicol*., 94:1879–1897. https://doi.org/10.1007/s00204-020-02739-w,

Campbell EL and Colgan SP. 2019. Control and dysregulation of redox signalling in the gastrointestinal tract. *Nat Rev Gastroenterol Hepatol*., 16(2): 106–120. doi: 10.1038/s41575-018-0079-5.

Carneiro AM, Cook E H, Murphy DL and Blakely RD. 2008. Interactions between integrin alphaIIbbeta3 and the serotonin transporter regulate serotonin transport and platelet aggregation in mice and humans. *J Clin Invest*., 118: 1544–1552. doi:10.1172/JCI33374.

Catena-Dell'Osso M, Rotella F, Dell'Osso A, Fagiolini A and Marazziti D. 2013. Inflammation, Serotonin and major depression. *Curr Drug Targets*., 14(5): 571- 577. doi:10.2174/13894501113149990154.

Chiocchetti GM, Vélez D and Devesa V. 2018. Effect of subchronic exposure to inorganic arsenic on the structure and function of the intestinal epithelium. *Toxicol Lett.,* 286: 80-88. https://doi.org/10.1016/j.toxlet.2018.01.011.

CHabuk H AH, Al-Saadi, H KZ and Al-Harbi HJ. 2019. Physiological and Behavioral Changes of Male Rats Following Social Isolation Stress During Early-Adolescence and Fluoxetine Exposure. *Indian J Public Health.*, *10*(10), 3727.

Coates MD, Tekin I, Vrana KE and Mawe GM. 2017. the many potential roles of intestinal Serotonin (5-hydroxytryptamine, 5-HT) signalling in inflammatory bowel disease. *Aliment Pharmacol Ther*., 46(6):569-580. https://doi.org/10.1111/apt.14226.

Dangleben NL, Skibola CF and Smith MT. 2013. Arsenic immunotoxicity: a review. *Environ Health*., 12: 1-15.

Duman EA and Canli T. 2015. Influence of life stress, 5-HTTLPR genotype, and SLC6A4 methylation on gene expression and stress response in healthy Caucasian males. *Biol Mood Anxiety Disord*., 5: 2-7. doi:10.1186/s13587-015-0017-x.

Esteban-Zubero E, López-Pingarrón L, Alatorre-Jiménez MA, Ochoa-Moneo P, Buisac-Ramon C, Rivas-Jimenez M, Castán-Ruiz S, Antoñanzas-Lombarte Á, Tan D, Joaquín García J and Reiter R J. 2017. Melatonin's role as a co-adjuvant treatment in colonic diseases: A review. *Life Sci*., 170: 72-81.doi: 10.1016/j.lfs.2016.11.031.

Ferrario D, Gribaldo L, Hartung T. 2016. Arsenic exposure and immunotoxicity: a review including the possible influence of age and sex. *Curr Environ Health Rep*., 3: 1-12. DOI 10.1007/s40572-016-0082-3.

Firdaus F, Zafeer MF, Ahmad M and Afzal M. 2018. Anxiolytic and anti-inflammatory role of thymoquinone in arsenic-induced hippocampal toxicity in Wistar rats. *Heliyon*., 4(6):1-22. https://doi.org/10.1016/j.heliyon.2018.e00650.

González Delgado S, Garza-Veloz I, Trejo-Vazquez F, and Martinez-Fierro M L. 2022. Interplay between serotonin, immune response, and intestinal dysbiosis in inflammatory bowel disease. *Int J Mol Sci.*, *23*(24), 15632. https://doi.org/10.3390/ijms232415632

Habib M, Shaker S, El-Gayar N and Aboul-Fotouh S. 2015. The Effects of Antidepressants ―Fluoxetine and Imipramine‖ on Vascular Abnormalities and Toll-Like Receptor-4 Expression in Diabetic and Non-Diabetic Rats Exposed to Chronic Stress. *PLoS ONE.*, 10(3): 1-25. https://doi.org/10.1371/journal.pone.0120559.

Hatamnejad MR, 2022. Baradaran Ghavami S, Shirvani M, Asghari Ahmadabad M, Shahrokh S, Farmani M et al. Selective serotonin reuptake inhibitors and inflammatory bowel disease; Beneficial or malpractice. *Front Immunol.,* 13:980189. https://doi.org/10.3389/fimmu.2022.980189.

Jing J, Zheng G, Liu M, Shen X, Zhao F, Wang J, Zhang J, Huang G, Dai P, Chen Y, Chen J and Luo W. 2012, Changes in the synaptic structure of hippocampal neurons and spatial memory impairment in a rat model caused by chronic arsenite exposure. *Neurotoxicology.*, 33(5): 1230-1238. https://doi.org/10.1016/j.neuro.2012.07.003.

Keil DE, Berger-Ritchie J and McMillin GA. 2011. Testing for toxic elements: a focus on arsenic, cadmium, lead, and mercury. *Lab Med.*, 42(12):735-742. https://doi.org/10.1309/LMYKGU05BEPE7IAW.

Kendig DM and Grider JR. 2015. Serotonin and colonic motility. *Neuro Gastroenterol Motil.*, 27: 899e905. doi:10.1111/nmo.12617.

Knight P, Chellian R, Wilson R, Behnood-Rod A, Panunzio S and Bruijnzeel A W. 2021. Sex differences in the elevated plus-maze and large open field tests in adult Wistar rats. *Pharmacol Biochem Behav.*, 204:173168. doi: 10.1016/j.pbb.2021.173168.

Kuniishi H, Ichisaka S, Yamamoto M, Ikubo N, Matsuda S, Futora E, Harada R, Ishihara K and Hata Y. 2017. Early deprivation increases high-leaning behaviour, a novel anxiety-like behaviour, in the open field test in rats. *Neurosci. Res*., 123:27-35. https://doi.org/10.1016/j.neures.2017.04.012.

Kwon YH, Wang H, Denou E, Ghia JE, Rossi L, Fontes ME and Khan, W. I. 2019. Modulation of gut microbiota composition by serotonin signaling influences intestinal immune response and susceptibility to colitis. *Cell Mol Gastroenterol Hepatol.*, *7*(4): 709-728. https://doi.org/10.1016/j.jcmgh.2019.01.004

Lam D, Ancelin ML, Ritchie K, Freak-Poli R, Saffery R and Ryan J. 2018. Genotype-dependent associations between serotonin transporter gene (SLC6A4) DNA methylation and late-life depression. *BMC Psychiatry.*, 18: 282., doi:10.1186/s12888-018-1850-4.

Litwin I, Bocer T, Dziadkowiec D and Wysocki R. 2013. Oxidative stress and replication-independent DNA breakage induced by arsenic in Saccharomyces cerevisiae. *PLoS Genet.*, 9(7):e1003640. https://doi.org/10.1371/journal.pgen.1003640.

Lu Z, Wang F, Xia Y, Cheng S, Zhang J, Qin X and Chen C. 2023. Involvement of gut-brain communication in arsenite-induced neurobehavioral impairments in adult male mice. *Ecotoxicol Environ Saf.*, 249:114370. https://doi.org/10.1016/j.ecoenv.2022.114370.

Maraldi T, Angeloni C, Prata C and Hrelia S. 2021. NADPH oxidases: redox regulators of stem cell fate and function. *Antioxidants.*, 10(6): 973. 47. https://doi.org/10.3390/antiox10060973.

Muller CL, Anacker AMJ and Veenstra-Vander Weele J. 2015. The serotonin system in autism spectrum disorder: From biomarker to animal models. *Neuroscience.*, 321: 24–41, 2016. doi:10.1016/j.neuroscience..11. 010.

Nguyen NT, Nakahama T, Le DH, Van Son L, Chu HH and Kishimoto T. 2014. Aryl hydrocarbon receptor and kynurenine: recent advances in autoimmune disease research. *Front Immunol.*, 5: 551.doi:10.3389/fimmu.2014.00551.

O'Mahony S, Clarke G, Borre Y, Dinan T and Cryan J. 2015. Serotonin, tryptophan metabolism and the brain-gut-microbiome axis. *Behav Brain Res.*, 277: 32- 48. doi:10.1016/j.bbr.2014.07.027.

Ozturk M, Metin M, Altay V, Bhat RA, Ejaz M, Gul A et al. 2022. Arsenic and human health: genotoxicity, epigenomic effects, and cancer signalling. *Biol Trace Elem Res.*, 1-14. https://doi.org/10.1007/s12011-021-02719-w.

Prakash S and Verma AK, 2021. Arsenic: Its Toxicity and Impact on Human Health. *Int J Biol Innov.,* 3(1): 38-47.Doi: https://doi.org/10.46505/IJBI.2021.3102.

Quintero-Villegas A and Valdés-Ferrer S I. 2020. Role of 5-HT 7 receptors in the immune system in health and disease. *Mol Med*, *26*, 1-8. https://doi.org/10.1186/s10020-019-0126-x

Rao S, Leung CST, Lam MH, Wing YK, Waye MMY and Tsui SKW. 2017. Resequencing three candidate genes discovers seven potentially deleterious variants of susceptibility to major depressive disorder and suicide attempts in Chinese. *Gene.*, 603:34-41. https://doi.org/10.1016/j.gene.2016.12.006.

Rutsch A, Kantsjö, JB and Ronchi F. 2020. The gut-brain axis: how microbiota and host inflammasome influence brain physiology and pathology. *Front Immunol.*, *11*, 604179. https://doi.org/10.3389/fimmu.2020.604179

Samad N, Rao T, Rehman MHU, Bhatti SA and Imran I. 2022. Inhibitory effects of selenium on arsenic-induced anxiety-/depression-like behavior and memory impairment. *Biol Trace Elem. Res.*, 200: 1-10. https://doi.org/10.1007/s12011-021-02679-1.

Sjaarda CP, Hecht P, McNaughton AJ, Zhou A, Hudson ML, Will MJ and Liu X. 2017. The interplay between maternal Slc6a4 mutation and prenatal stress: a possible mechanism for autistic behaviour development. *Sci Rep.*, 7: 8735. doi:10.1038/s41598-017-07405-3.

Sutcliffe JS, Delahanty RJ, Prasad HC, McCauley JL, Han Q, Jiang L, Li C, Folstein SE and Blakely RD. 2005. Allelic heterogeneity at the serotonin transporter locus (SLC6A4) confers susceptibility to autism and rigid-compulsive behaviours. *Am J Hum Genet.*, 77: 265–279, doi:10.1086/ 432648.

Taylor S. 2013. Molecular genetics of obsessive–compulsive disorder: a comprehensive meta-analysis of genetic association studies. *Mol Psychiatry.*, 18:799-805. https://doi.org/10.1016/j.heliyon.2018.e00650.

Veenstra-Vander Weele J, Muller CL, Iwamoto H, Sauer JE, Owens WA, Shah CR, Jessen T and Blakely RD. 2012. Autism gene variant causes hyperserotonemia, serotonin receptor hypersensitivity, social impairment and repetitive behaviour. *Proc Natl Acad Sci U S A.*, 109:5469–74. https://doi.org/10.1073/pnas.1112345109.

Vijayakaran K, Kesavan M, Kannan K, Sankar P, Tandan SK and Sarkar SN. 2014. Arsenic decreases antinociceptive activity of paracetamol: Possible involvement of serotonergic and endocannabinoid receptors. *Environ Toxicol Pharmacol.*, *38*(2), 397-405. https://doi.org/10.1016/j.etap.2014.07.001

Waclawiková B and Aidy SEl. 2018. Role of microbiota and tryptophan metabolites in the remote effect of intestinal inflammation on brain and depression. *Pharmaceuticals.*, 11(3): 63. doi:10.3390/ph11030063.

Zhao Q, Hao Y, Yang X, Mao J, Tian F, Gao Y, Tian X , Yan X and Qiu Y. 2023. Mitigation of Maternal Fecal Microbiota Transplantation on Neurobehavioral Deficits of Offspring Rats Prenatally Exposed to Arsenic: Role of Microbiota-gut-brain Axis. *J Hazard. Mater.*, 131816. https://doi.org/10.1016/j.jhazmat.2023.131816

JJBS

Volume 18, Number 3,September 2025
ISSN 1995-6673
Pages 393 – 402

Jordan Journal of Biological Sciences

Red Ginger (*Zingiber officinale* var. rubrum) Nanoparticles Induce Senescence and Apoptosis in MCF-7 Cells through Downregulation of *BCL2* and Upregulation of *TP53* and *CASP3* Genes

Didik Priyandoko[1], Lusiana Darsono[2], Dwi Davidson Rihibiha[3], Wahyu Widowati[2,*], Ainun Nisa[1], Fadhilah Haifa Zahiroh[4], Hanna Sari Widya Kusuma[4], Dhanar Septyawan Hadiprasetyo[4,5].

[1]*Biology Study Program, Faculty of Mathematics and Science Education, Universitas Pendidikan Indonesia, Bandung, Indonesia;* [2]*Faculty of Medicine, Maranatha Christian University, Bandung, Indonesia;* [3]*Medical Laboratory Technology Study Program, Universitas Jenderal Achmad Yani, Cimahi, Indonesia;* [4]*Aretha Medika Utama, Biomolecular and Biomedical Research Center, Bandung, Indonesia;* [5]*Faculty of Pharmacy, Universitas Jenderal Achmad Yani, Cimahi, Indonesia.*

Received: August 24, 2024; Revised: January 3, 2025; Accepted: January 15, 2025

Abstract

Globally, breast cancer remains a common and serious health concern, with different incidence rates worldwide. Potential directions in cancer treatment include red ginger components and the efficient drug delivery provided by nanoemulsion technology. To assess the potential of red ginger extract nanoemulsion (RGE-NE) as a treatment for breast cancer, this study evaluated RGE-NE on the MCF-7 cell line. Flow cytometry was used to analyze the cell cycle and apoptosis. Using qRT-PCR, the expression of genes linked to apoptosis, including *TP53*, *CASP3*, and *BCL2*, was examined. Using Senescence Associated-β-Galactosidase labeling, the MCF-7 cell senescence detection experiment was carried out. In MCF-7 cells, RGE-NE boosted necrosis, cell death, and apoptosis while decreasing the amount of surviving cells. RGE-NE was shown to upregulate *TP53* and *CASP3* expression while downregulating *BCL2* gene expression at a dose of 200 µg/mL. Additionally, the percentage of cells in the G0/G1 phase dropped and the proportion of cells in the S phase, which indicates cell cycle arrest, increased after receiving RGE-NE treatment. Moreover, MCF-7 cells experienced senescence at exposure to 800 µg/mL of RGE-NE. According to these results, RGE-NE may have anti-breast cancer properties by causing MCF-7 cells to undergo cell cycle arrest, senescence, and apoptosis.

Keywords: Anti-breast cancer, Cytotoxicity, Nanoparticles, *Zingiber officinale* var. rubrum.

1. Introduction

Cancer remains a significant global public health concern (Mahdavifar *et al*., 2016). According to Savitri *et al*. (2023), the most common type of cancer that affects women is breast cancer. Breast cancer is the second most common cancer, affecting 2.1 million individuals (11.6%) and causing 626,679 deaths (6.6%). In Indonesia, the reported incidence of breast cancer was 16.7% (Lim *et al*., 2022). Breast cancer is a complex disease involving various biological processes in its development and progression (Ji *et al*., 2019). One of the key protective mechanisms employed by cells is cell cycle arrest, which allows for DNA repair before proceeding with cell proliferation. The letters M (mitosis), G1 (gap 1), S (DNA synthesis), and G2 (gap 2) stand for different cell cycle phases. The cell cycle includes several checkpoints that guarantee accurate chromosome replication and serve as a crucial defense against tumorigenesis (Thu *et al*, 2018). In cases of severe DNA damage, alternative signal pathways come into play to either induce cell senescence, aiming to prevent the development of malignancies (Lo *et al*., 2015). According to Marvalim *et al*. (2023), Tumor Protein 53 (*TP53)* is an essential transcription factor that controls several biological processes, including as apoptosis, cell cycle arrest, and cellular senescence. One of the most important steps in stopping malignant growth is apoptosis (Rahman *et al*., 2021). According to Cui *et al*. (2007), mitochondrial membrane permeability is regulated by B-cell CLL/lymphoma 2 (*BCL2*), which impacts cytochrome c release and activates Caspase 9 *(CASP9)* and *CASP3*, controlling the process of apoptosis. Caspases, which are cysteine proteases specific to aspartate, destroy hundreds of cellular proteins, including important structural elements, to facilitate cell destruction during apoptosis (Valente *et al*., 2013).

Various types of chemotherapy have been unsuccessful due to side effects, drug resistance, and the selective targeting of certain drugs (Nindrea *et al*., 2023). Currently, researchers are focused on developing medications that use natural ingredients to address these issues. These

* Corresponding author. e-mail: wahyu_w60@yahoo.com, wahyu.widowati@maranatha.edu.

substances may have a multiplicity of benefits, reduce adverse reactions, and be useful in treating different kinds of cancer (Aung *et al*., 2017). There are various studies that report on natural compounds that have anticancer effects and modulate the immune system (Subramaniam *et al.,* 2019). Ginger is a widely used natural spice available in both powdered and fresh root forms. It comprises various bioactive compounds, including gingerol, resin, zingerone, volatile oil, paradol and vitamins A and C. These compounds endow ginger with a range of pharmacological properties, such as antimicrobial, antiviral, antioxidant, antihypertensive, gastroprotective, cardioprotective, antidiabetic, anticancer, and immunomodulatory effects (El-Borm *et al*., 2023). Recent research has brought considerable focus to ginger due to its potential anti-cancer characteristics, particularly in its capacity to combat several malignancies, including colorectal, prostate, breast, and cervical cancers (Mao *et al*., 2019). Numerous compounds in ginger, such as vanilloids (e.g., 6-gingerol and 6-paradol), shogaol, zingerone, and galanal A and B, are recognized for their anticancer properties. These elements play therapeutic roles in disease control by altering a variety of biological functions (Rahmani *et al*., 2014). However, red ginger contains higher concentrations of vanilloid compounds compared to regular ginger (Zhang *et al*., 2022). Traditional medicine uses red ginger extensively, particularly in China, Malaysia, and Indonesia (Suciyati *et al*., 2017). Red ginger rhizome extract's active ingredients include 6-shogaol, which can impede the development of breast and colon cancer cells (Tan *et al*., 2013), and 6-gingerol, which can cause the LNCaP human prostate cancer cell line to undergo apoptosis (Kim *et al*., 2011). However, the therapeutic potential of these compounds is limited by poor solubility and bioavailability, which can be overcome by nanotechnology-based delivery systems such as nanoemulsions. Nanotechnology has evolved into one of the quickest, inventive, and adaptive technologies in modern science and cancer therapy (Chaturvedi *et al*., 2023). Nanoemulsion is a widely applied nanodrug delivery system for bioactive compounds and nutraceuticals (Amalraj *et al*., 2019). Nanoemulsion have the capability to encapsulate inadequately water-soluble drugs, enhancing their solubility, bioavailability, and targeted delivery to cancer cells (Sánchez-López *et al*., 2019). Encapsulating plant extracts is essential for protecting bioactive compounds from degradation (Noore *et al*., 2021). MCF-7 cells were chosen in this research because these cells retain several ideal properties specific to the breast epithelium. These characteristics include the capability to metabolize estrogen, specifically estradiol, through estrogen receptors located within the cell cytoplasm (Camarillo *et al*., 2014). In vitro tests were used in this work to investigate the anticancer properties of red ginger extract nanoemulsions (RGE-NE) on the MCF-7 breast cancer cell type. *BCL2*, *TP53*, and *CASP3* gene quantification, senescence, cell cycles, and apoptosis assessment are among the methods used to assess the RGE-NE potential.

2. Materials and Methods

2.1. Red ginger extract nanoemulsion preparation

The materials were red ginger extract (RGE) with ethanol 70% as the solvent, obtained from PT FAST, Depok, Indonesia (No. Batch 001.07.25.ERJM.01). RGE (15 mL) was added to 100 mL ddH_2O and mixed with a solvent consisting of propylene glycol, 70% ethanol, and 10% DMSO (60 mL). 1% chitosan (40 mL) (Phy Edumedia) was added to the extract solution and stirred using a magnetic stirrer (1500 rpm). Na-TPP 0.4% was added at 1 drop per 3 seconds as much as 20 mL and stirred at 300 rpm. After that, stirred for 15 minutes using a magnetic stirrer (Widowati *et al*., 2023). Nanoparticles were confirmed successfully after the formation of turbidity and sediment. The pellet from this process was a red ginger extract, while the supernatant was RGE-NE. The size of nanoparticles was analyzed by Particle Size Analyzer (PSA) (Beckman Coulter LS 13 320). The results of PSA showed that the RGE-NE had a diameter of less than 1000 nm, which was 773 nm. Thus, that the production of red ginger nanoparticles was successful and can be continued with further testing.

2.2. MCF-7 Cell Line Cell Culture

The ATCC HTB-22 human breast cancer MCF-7 cell line was provided from PT Aretha Medika Utama, Bandung, Indonesia. Using the protocol from Widowati *et al*. (2018), the media used to culture MCF-7 cells was high-glucose DMEM (Biowest, L0103-500) with all necessary components. The cell suspension was seeded into the T25 flask (SPL, 70025). MCF-7 cells were cultivated with 5% CO_2 at 37°C in an incubator (Thermo IH3543). The cells cultivated in the T25 flask were observed using an inverted microscope (Olympus, CKX41-F32FL) until they reached around 70–80% confluence (Widowati *et al*., 2018).

2.3. Apoptosis Assay

Flow cytometry was performed to assess the live cell populations, apoptotic, and necrotic using the Apoptosis Kit (Elabscience, E-CK-A211), as directed by the manufacturer. Six-well plates with five million cells each were incubated for twenty-four hours, different doses of RGE-NE (200, 400, and 800 µg/mL) were applied. After five minutes of centrifugation (1600 rpm), the growing media was discarded and the cells were recovered. After the cell pellet has been resuspended in 500 µL of FACS buffer, an additional centrifugation was carried out. Before analysis, after resuspended in 500 µL of Annexin binding solution, the final pellet, stained with FITC and propidium iodide (PI), and incubated for one hour (Girsang *et al*., 2023; Widowati *et al*., 2018; Widowati *et al*., 2019).

2.4. Cell Cycle Analysis

To analyze the cell cycle, the procedure outlined in the instructions for the Cell Cycle Assay Kit (Red Fluorescence) (Elabscience, E-CK-A351) was followed. Following plating, MCF-7 cells were subjected to doses of 200, 400, and 800 µg/mL of RGE-NE at a density of 5×10^5 cells per well. The control and treated cells were allowed to incubate for one hour after the addition of cold 70% ethanol to prevent cell clumping. Samples were mixed with 100 µL of RNase A after the cells were washed with

PBS. Thirty minutes were spent incubating the cells in a water bath at 37°C after staining them with 50 µg/mL of PI solution. The MacSQuant Analyzer 10 (Miltenyi Biotec) was then used to perform a flow cytometry analysis (Kalamegam *et al*., 2018).

2.5. Senescence Assay

The analysis of senescent cells was conducted using the Senescence Cells Histochemical Staining Kit (Sigma, CS0030). After plating on 6-well plates, the cells were exposed to 200, 400, or 800 µg/mL of RGE-NE for a whole day. The cell was rinsed with 1x PBS solution. After that, it was fixed using a 1x fixation buffer for 7 minutes, followed by another wash using a 1x PBS solution. Following the addition of the staining mixture to each well, the cells were incubated overnight at 37ºC without CO_2. The outcomes of cell staining can be seen through a light microscope (Priyandoko *et al*., 2019).

2.6. Quantification of CASP3, TP53, BCL2 Gene Expression

RNA was extracted and purified from the samples using TRI Reagent (R2050-1-200, Zymo Research) and the Direct-zol RNA Miniprep Plus kit (R2073, Zymo Research) following the manufacturer's protocol. The RNA concentration was then measured using a microdrop plate, with absorbance readings taken at 260/280 nm using a MultiskanTM GO Thermo Scientific spectrophotometer (Model 51119300), as shown in Table 1. A three-step PCR procedure was used for cDNA synthesis using the SensiFAST cDNA Synthesis Kit (BIO-65054, Meridian Bioscience): reverse transcription at 46°C for twenty minutes, priming at 25°C for five minutes, then inactivating the reverse transcriptase at 95°C for one minute (Prasetyo *et al*., 2019; Girsang *et al*., 2023).

Table 1. RNA purity of MCF-7 cells treated with RGE-NE.

No.	Sample	Concentration (ng/µL)	Purity (λ260/ λ280 nm)
1	I	603.36	1.997
2	II	549.68	2.089
3	III	792.08	2.022
4	IV	639.92	2.017
5	V	755.20	2.024

* I: untreated breast cancer cells; II: breast cancer cells+DMSO 1%; III: breast cancer cells+200 µg/mL RGE-NE; IV: breast cancer cells+400 µg/mL RGE-NE; V: breast cancer cells+800 µg/mL RGE-NE.

Real-time qPCR was used to examine constitutively expressed β-Actin genes and the expression of *TP53*, *CASP3*, and *BCL2* genes (Table 2). Widowati *et al.* (2020) employed *β-Actin*, a housekeeping regulatory gene, as an internal control. Using the temperature, time, and RT-qPCR cycle settings listed in Table 3, the AriaMx Real-time PCR System (Agilent, G8830A) was used to amplify the PCR.

Table 2. Primers that are utilized in RT-qPCR.

Genes	Primer		References
Human *CASP3*	F	5'-AGAACTGGACTGTGGCATTGAG -3'	NM_032991.3
	R	5'-GCTTGTCGGCATACTGTTTCAG -3'	
Human *TP53*	F	5'-AGAGTCTATAGGCCCACCCC-3'	NM_000546.6
	R	5'-GCTCGACGCTAGGATCTGAC-3'	
Human *BCL2*	F	5'-GGTCATGTGTGTGGAGAGCG-3'	NM_000657.3
	R	5'-GGTGCCGGTTCAGGTACTCA	
Human *β-Actin*	F	5'-TCTGGCACCACACCTTCTACAATG-3'	NM_001101.5
	R	5'-AGCACAGCCTGGATAGCAACG-3'	

* R: Reverse primer; F: Forward primer

Table 3. Temperature, time, and RT-qPCR cycle settings.

Genes	Temperature; Time; Cycle					
	Predenaturation	Denaturation	Annealing	Pre-elongation	Elongation	~
CASP3	95°C; 5'	95°C; 30"; 40 cycles	58°C; 50"; 40 cycles	72ºC; 50"	72º C; 5'	4ºC
TP53	95°C; 5'	95°C; 30"; 40 cycles	58°C; 50"; 40 cycles	72ºC; 50"	72º C; 5'	4ºC
BCL2	95°C; 5'	95°C; 30"; 40 cycles	58°C; 50"; 40 cycles	72ºC; 50"	72º C; 5'	4ºC
β-Actin	95°C; 5'	95°C; 30"; 40 cycles	58°C; 50"; 40 cycles	72ºC; 50"	72º C; 5'	4ºC

2.7. Statistical Analysis

SPSS software (version 20.0; SPSS Inc., USA) was used to perform the statistical analysis. The data was analyzed using One-Way ANOVA. The Tukey HSD post-hoc test was utilized for data that met the homogeneity and normality criteria, whereas the Dunnett's T3 post-hoc test was employed for not homogeneous and normally distributed data. A threshold of $P < 0.05$ was set for significance. Using GraphPad Prism (version 8.0.244), histograms displaying the mean ± standard deviation were produced.

3. Results

3.1. RGE-NE Impact on MCF-7 Cells Apoptosis

Using flow cytometry, the amount of apoptosis in MCF-7 cells treated with RGE-NE was assessed. The relative distribution of necrotic, viable, early apoptotic, and late apoptotic cells is shown. The comparison of each therapy on viable cells, necrotic cells, late apoptosis, and early apoptosis is displayed in Figures 1 and 2. RGE-NE treatment caused necrosis and apoptosis, as well as a reduction in viable cells. The degree of apoptosis rose as the nanoemulsion concentration increased.

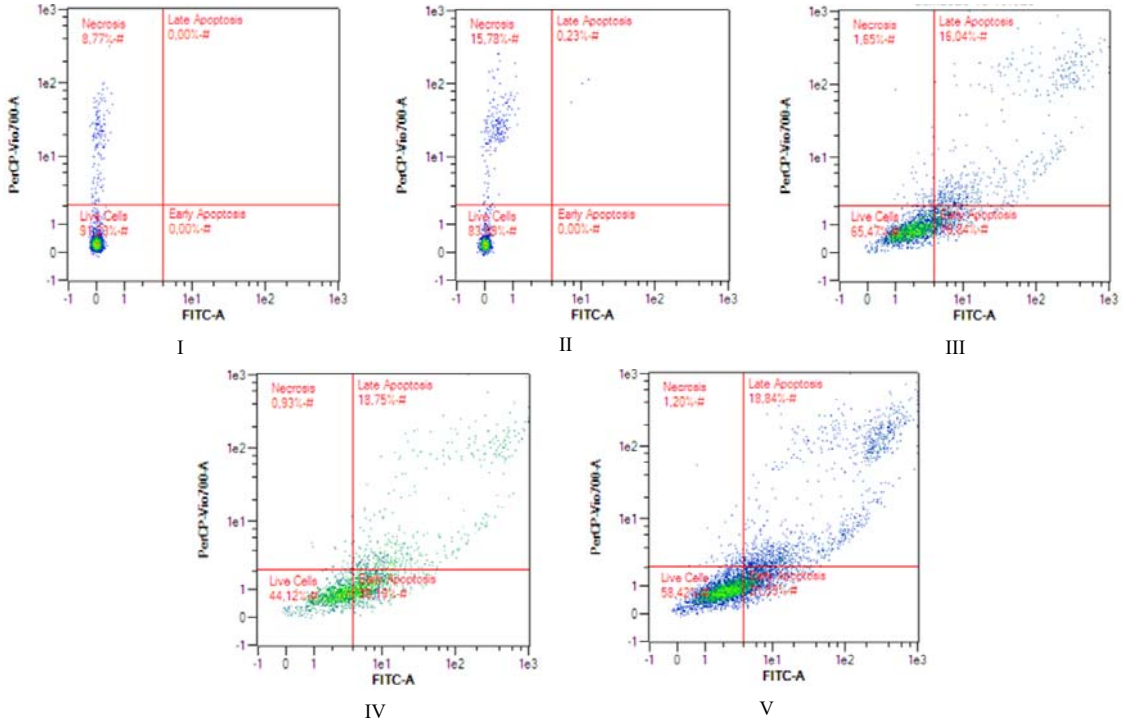

Figure 1. Dot plots showing different RGE-NE concentrations in relation to breast cancer cells' apoptosis

* I: untreated breast cancer cells; II: breast cancer cells+DMSO 1%; III: breast cancer cells+200 µg/mL RGE-NE; IV: breast cancer cells+400 µg/mL RGE-NE; V: breast cancer cells+800 µg/mL RGE-NE.

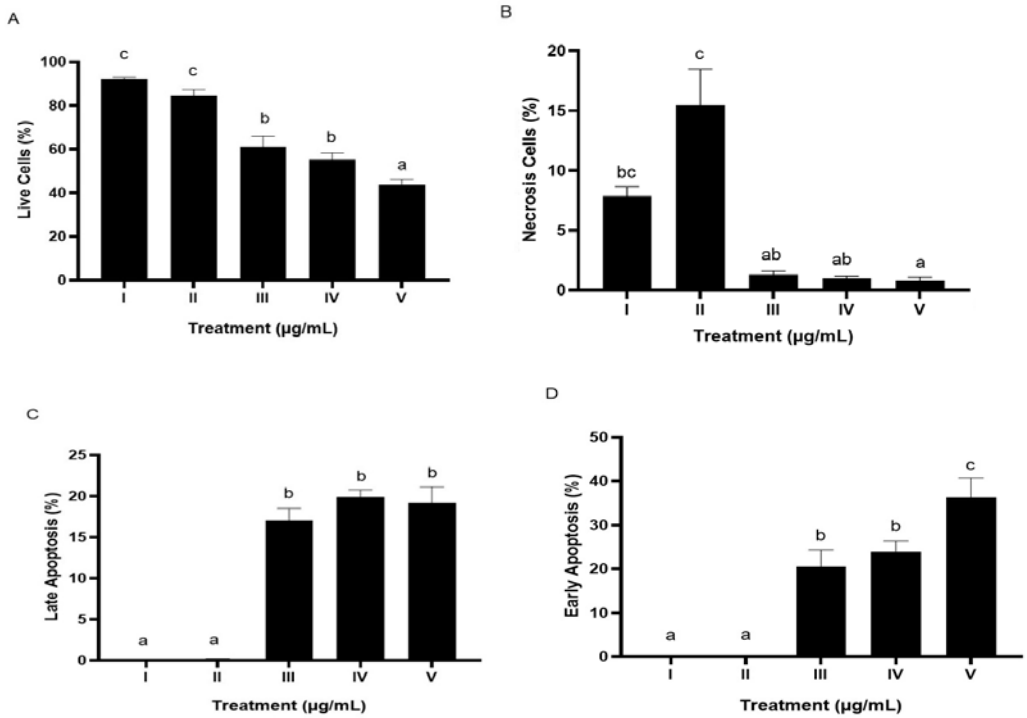

Figure 2. Effect of various concentration of RGE-NE toward apoptosis in breast cancer cells

***(A)** live cells, **(B)** necrosis cells, **(C)** late apoptosis, and **(D)** early apoptosis.

* I: untreated breast cancer cells; II: breast cancer cells+DMSO 1%; III: breast cancer cells+200 µg/mL RGE-NE; IV: breast cancer cells+400 µg/mL RGE-NE; V: breast cancer cells+800 µg/mL RGE-NE.

* Data are presented as mean ± SD from three independent replicates. Different letters indicate significant differences ($p<0.05$, Tukey's HSD): live cells (A), necrotic cells (B), late apoptosis (C), and early apoptosis (D).

3.2. Effect of RGE-NE on the Apoptosis Gene Expression in MCF-7 Cells

Gene expression was investigated using RT-PCR in order to evaluate the apoptosis-related gene expression that RGE-NE produced in MCF-7 cells. Proapoptotic genes like *TP53* and *CASP3* as well as antiapoptotic genes like *BCL2* were assessed in this study. Figure 3 illustrates that in MCF-7 cells, RGE-NE at 200 µg/mL (group III) exhibited the highest expression of *TP53* and *CASP3* and the lowest expression of the *BCL2* gene. Comparing RGE-NE at 200 µg/mL concentration (group III) to the negative control (group I), it can dramatically boost *TP53* and *CASP3* gene expression and decrease *BCL2* gene expression.

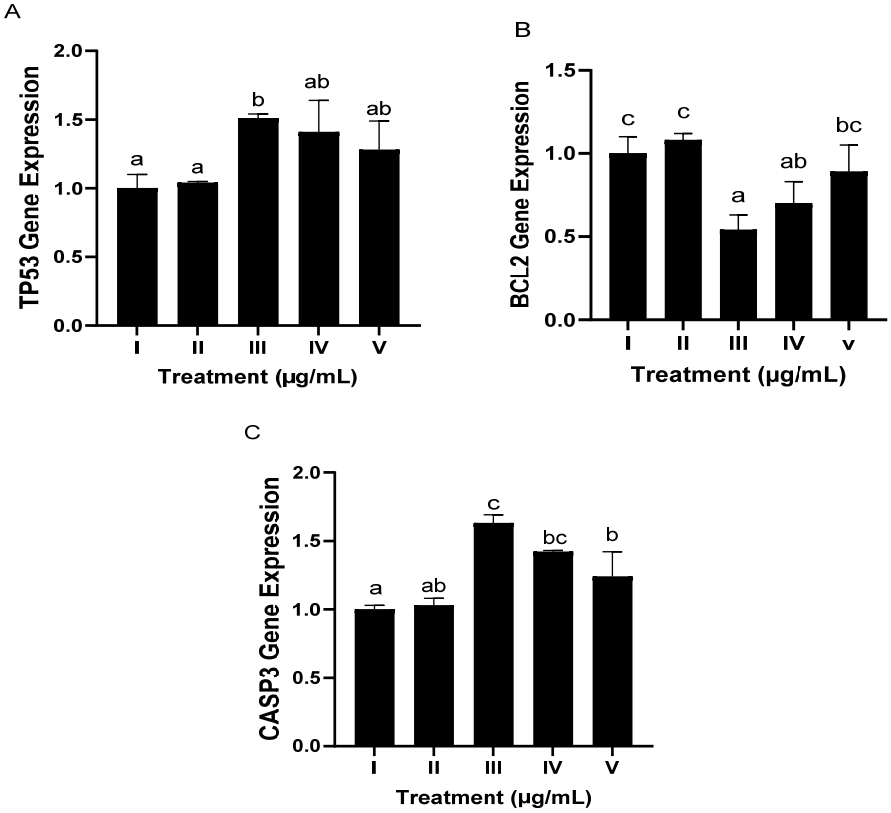

Figure 3. Effect of various concentrations of RGE-NE toward *TP53*, *BCL2*, and *CASP3* genes expression in breast cancer cells

* **(A)** *TP53*, **(B)** *BCL2*, **(C)** *CASP3* genes expression in breast cancer cells

*I: untreated breast cancer cells; II: breast cancer cells+DMSO 1%; III: breast cancer cells+200 µg/mL RGE-NE; IV: breast cancer cells+400 µg/mL RGE-NE; V: breast cancer cells+800 µg/mL RGE-NE.

* Data are presented as mean ± SD from three independent replicates Different letters indicate significant differences ($p<0.05$, Tukey's HSD test) for *TP53* (ab, abc, bc), *BCL2* (a, ab, bc, c), and *CASP3* (ab, abc, b, c).

3.3. Effect of RGE-NE on the MCF-7 Cell Cycle

Flow cytometry was employed to examine how RGE-NE affects cell cycle distribution and to determine if alterations in cell cycle distribution are associated with the observed reduction in cell viability. PI fluorescent dye was used to determine DNA content and analyze cell cycle distribution. Every therapy in the G2/M, S, and G0/G1 stages is compared in Table 4. As concentration rose, the proportion of cell cycle distribution increased in the S phase and reduced in the G0/G1 phase. RGE-NE at 800 µg/mL demonstrated the biggest reduction in the G0/G1 phase (90.30±2.90%) of the cell cycle. Furthermore, it showed the largest rise in the G2/M phase (1.86±1.55%) and S phase (7.27±1.67%) cell counts. Consequently, MCF-7 cells were arrested in the S phase rather than the G0/G1 phase upon treatment with RGE-NE. This finding suggests that the S phase, where fewer cells progress through the cycle, is the site of cell cycle arrest or delay.

Table 4. Effect of various concentrations of RGE-NE toward cell cycles in breast cancer cells

Sample	Cell Cycle		
	G0/G1 phase (%)	S phase (%)	G2/M phase (%)
I	91.43±0.54	4.83±0.70	0.64±0.35
II	92.49±1.23	6.02±0.98	0.42±0.14
III	92.04±1.34	6.09±1.10	0.60±0.14
IV	91.87±0.56	6.64±0.75	0.69±0.26
V	90.30±2.90	7.27±1.67	1.86±1.55

*I: untreated breast cancer cells; II: breast cancer cells+DMSO 1%; III: breast cancer cells+200 µg/mL RGE-NE; IV: breast cancer cells+400 µg/mL RGE-NE; V: breast cancer cells+800 µg/mL RGE-NE.

3.4. RGE-NE at Various Concentrations' Impact on MCF-7 Cell Senescence

In this study, we used the senescence-associated β-galactosidase (SA-β-gal) staining to identify cells undergoing senescence in MCF-7 cell culture. Beta-galactosidase activity is one of the characteristic signs of cells that have reached the senescence stage. As a result, senescent cells were identified by blue staining. The senescence morphology of MCF-7 cells treated with RGE-NE can be observed in Figure 5. In addition to visual observation, we performed quantitative analysis to measure the percentage of cells showing beta-galactosidase activity. The senescence staining measurements indicated a notable impact of RGE-NE treatment on MCF-7 breast cancer cells in comparison to the negative control (group I) (Figure 6). The induction of senescence increased as the concentration rose, reaching its maximum at 800 µg/mL (group V) RGE-NE. These findings suggest that RGE-NE can cause MCF-7 breast cancer cells to undergo senescence.

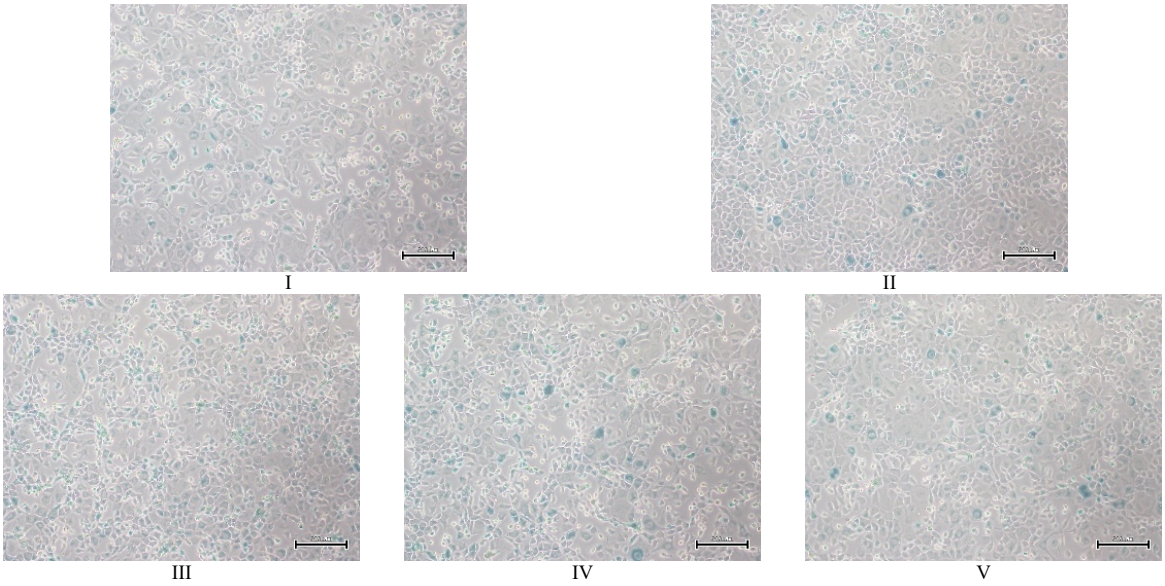

Figure 4. Effect of various concentration of RGE-NE toward senescence morphology in breast cancer cells. The magnification used was 40x. *I: untreated breast cancer cells; II: breast cancer cells+DMSO 1%; III: breast cancer cells+200 µg/mL RGE-NE; IV: breast cancer cells+400 µg/mL RGE-NE; V: breast cancer cells+800 µg/mL RGE-NE.

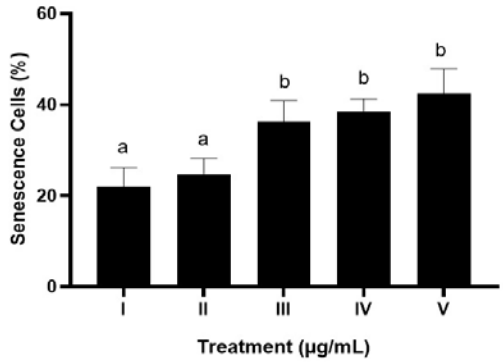

Figure 5. Effect of various concentration of RGE-NE toward senescence in breast cancer cells

*I: untreated breast cancer cells; II: breast cancer cells+DMSO 1%; III: breast cancer cells+200 µg/mL RGE-NE; IV: breast cancer cells+400 µg/mL RGE-NE; V: breast cancer cells+800 µg/mL RGE-NE.

* Data are presented as mean ± SD from three independent replicates. Different letters (a, b) indicate significant differences between treatments ($p<0.05$) according to Tukey's HSD post hoc test.

4. Discussion

This study demonstrated that red ginger extract nanoemulsions (RGE-NE) exerts anticancer effects on MCF-7 cells by inducing apoptosis, disrupting the cell cycle, and promoting senescence, highlighting its therapeutic potential against breast cancer. Bioactive substances with anticancer properties, including flavonoids, gingerol, and shogaol, are found in red ginger (*Z. officinale* var. *rubrum*) (Semwal *et al*., 2015). Some pungent vanilloids are primarily responsible for the anticancer properties of red ginger (Zhang *et al*., 2022). Red ginger's predominant vanilloids, 6-gingerol and 6-shogaol, contribute to its piquant flavor (Semwal *et al*., 2015). Strong anti-cancer activities of ginger have previously been confirmed for 6-shogaol and 6-gingerol (Panyajai *et al*., 2022; Ghasemzadeh *et al*., 2015). 6-Shogaol prevented the growth of tumors and specifically caused the death of leukemia cells in the model of U937 xenograft mice, according to Lee *et al*., (2008). Adding 6-gingerol inhibits the human breast cancer cell line from reproducing MDA-MB-231. The extract from the rhizome of red ginger, according to Ghasemzadeh *et al*. (2015), exhibited anticancer effects on the HeLa cancer cell line

without harming normal cells. The use of nanoemulsions to deliver bioactive compounds from red ginger extract has shown promising results in enhancing their anticancer effects and modulating biological processes, including apoptosis, cell cycle, and senescence cells.

Nanoemulsions, which are emulsions on a nanoscale, enhance the delivery of active compounds, and they have proven to be useful in enhancing the apoptotic and antiproliferative impacts of ginger extracts across different cancer models (Panyajai *et al*., 2022; Alharbi *et al*., 2023). This study's results align with the overall advancement in research exploring ginger and its nano-based formulations for cancer treatment. Multiple research experiments have validated ginger's anti-tumor characteristics. The utilization of nano-based treatments, like nanoemulsions, has shown promise in enhancing the anticancer effects of ginger and its bioactive constituents (Chen *et al*., 2023). Among the various stabilizing and delivery agents, chitosan has attracted particular attention due to its biocompatibility and ability to improve nanoparticle stability and drug delivery efficiency. Over the years, because of its possible use in biomedicine, chitosan has been extensively studied, especially in relation to the creation and application of medication delivery systems (GuarÍn-González *et al.,* 2022). Chitosan is biodegradable polysaccharide that has been widely used as coating material for various type of nanoparticles due to its biodegradable, biocompatible and non-toxic properties, in addition to its capacity to improve penetration (Nallamuthu *et al.*, 2015). Additionally, the bioactivity of chitosan includes anti-inflammatory, blood anti-coagulant, antibacterial, and antioxidant activities, further contributing to its versatility and effectiveness in biomedical applications (Hassan *et al.,* 2021). In addition, mechanical properties of nanoemulsion are enhanced by the addition of chitosan. The enhancement is attributed to increased stability and electrostatic interaction within the emulsion. Chitosan insertion also facilitates controlled release (Diedrich *et al*., 2023).

RGE-NE appears to exert its anticancer effects primarily by influencing cell death mechanisms. Lack of cell death characterizes cancer (Kadam *et al*., 2016), whereas in normal physiology, apoptosis is essential for growth, development, senescence, and ultimate demise (Yuan *et al*., 2022). Each cell in the body carries a latent mechanism that triggers its own self-destruction through apoptosis (Shahouzehi *et al.,* 2023). Apoptosis has been defined as an active, programmed mechanism of self-cell dismantling that prevents inflammation, whereas necrosis is portrayed as passive, involuntary cell death triggered by external disturbances, leading to the unregulated release of inflammatory cell components (Fink *et al*., 2005). Flow cytometry analysis revealed that RGE-NE induced both apoptosis and necrosis in MCF-7 cells in a dose-dependent manner (Figures 1 and 2). Ginger extracts at varying concentrations induced dose-dependent apoptosis in the HT 29 and HCT 116 colon cancer cell lines, according to research done by Abdullah *et al* (2010). According to studies, 6-shogaol promotes apoptotic pathways, which in turn prevents lung, colon, and osteosarcoma from growing. Pro-apoptotic protein expression increases as a result, while anti-apoptotic protein expression decreases (Nguyen *et al*., 2019).

Cancer cells often evade apoptosis by disrupting apoptotic triggers or inhibiting caspase function. Two major mechanisms include the suppression of pro-apoptotic proteins such as BAX and BAK, and the overexpression of the anti-apoptotic protein BCL2. Although BCL2 itself is not classified as an oncogene, its dysregulation or mutation can increase the risk of tumor initiation and progression (Pfeffer *et al*., 2018). According to Perri *et al.* (2016), mutant *TP53* also hinder the development of cancer by interfering with processes that improve DNA repair, stop the cell cycle, and trigger apoptosis in response to oncogenic stimuli. Based on the results, RGE-NE can decrease *BCL2* gene expression while increasing *TP53* and *CASP3* expression (Figure 3). Apoptosis-related genes, such as *BCL2*, are activated by *TP53*, which also initiates caspase activation through signaling complexes that cause apoptosomes to form in the mitochondria or cell death at the cell membrane (Wiman *et al*., 2006; Pashaei-Asl *et al*., 2017). Consequently, by removing *BCL2* and turning on *CASP3*, *TP53* may promote apoptosis. Using Real-Time PCR, Pashaei-Asl *et al*. (2017) examined how ginger affected the expression of the *BCL2* and *TP53* genes in ovarian cancer cells (SKOV-3). The findings demonstrated that adding ginger extract to ovarian cancer cell lines reduced the expression of the *TP53* and *BCL2* genes. Ginger can boost the expression of *CASP9* mRNA in Caspase family members as well as *CASP3* and BAX proteins, according to in vitro cell research conducted by Luo *et al*. (2023). We also looked at the mechanism via which RGE-NE influences the development of MCF-7 cells. The G1, S, and G2 interphases and mitosis (M) comprise the cell cycle. In the G1 phase, cells divide, assemble proteins for DNA synthesis, and create RNA. Numerous signals, such as stress, metabolic, and environmental stimuli, take place during the G1 phase and affect the cell's developmental pathway. The ability of the cells to differentiate, self-renew, or even perish is controlled by these signals. DNA replication usually occurs during the S phase. Decreased gene expression activity is another characteristic of the S phase. In the meantime, the G2 phase is when new proteins are synthesized and cells prepares for division. The M stage is characterized by nuclear and cytoplasmic divisions. A cell uses its cytoplasm to split into two daughter cells during the process known as mitosis (Moghaddam *et al*., 2017; Wang, 2021).

The data presented (Table 4) shows that as the concentration of RGE-NE increases, less cells are in the G0/G1 phase, which may indicate that RGE-NE is causing cells to leave this phase early or is keeping them from staying in it. This premature movement out of G0/G1 could indicate that the cells are being forced into an abnormal state, where they are unable to properly complete their growth and preparation for DNA replication. After RGE-NE treatment, the percentage of S phase cells significantly increased, suggesting that RGE-NE creates a bottleneck at this stage, which causes an accumulation of S phase cells as a result of inefficient DNA replication. This "arrest" or delay in the S phase is a hallmark of a disruption in the DNA replication process, which is often targeted by anti-cancer therapies to prevent cancer cells from multiplying. In line with this observation, MCF-7 cells treated to RGE-NE had a marked increase in the S phase and a decrease in the

G0/G1 phase cell percentage, signifying the beginning of the S phase cell cycle arrest brought on by fewer cell division cycles, as shown in Figure 4. This result aligns with the observations of Bernard *et al*. (2017), who found comparable effects in MDA-MB-231 cells treated with (10)-gingerol. According to their research, the beginning of S phase arrest was indicated by a rise in S phase cells and a decrease in G1 phase cells.

Moreover, the data (Table 4) shows a modest increase in cells in the G2/M phase with higher RGE-NE concentrations, indicating that some cells are being arrested or delayed in the final stages before cell division. This effect might suggest that RGE-NE causes cells to either pause before entering mitosis due to DNA damage or insufficient preparation for division, or it could directly impair the mitotic machinery, thereby preventing cell division. Studies where MDA-MB-231 and MCF-7 breast cancer cells treated with 6-shogaol underwent different cell cycle arrests in the G2/M phase have shown similar cell cycle disturbances (Ray *et al*., 2015). Both monolayer and stem cell-like spheroid cultures demonstrated this arrest, with 6-shogaol further obstructing the stem cell renewal route. A decrease in levels of Cdk1, Cdc24c, and Cyclin B, which are crucial for M/G2 phase progression, was observed as cells accumulated in this phase. The downregulation of Cyclin B notably suppressed cell proliferation, especially in MCF-7 and HeLa cell lines. Furthermore, T47D breast cancer cells were shown to perish when their cell cycle was suppressed in the G1/G0, S, and M/G2 phases. This collective evidence suggests that RGE-NE, like other anti-cancer agents, may exert its effects by disrupting the normal cell cycle, thereby inhibiting cancer cell proliferation, and potentially inducing cell death.

When cells in cell culture undergo cell cycle arrest, they are often overstimulated by serums, nutrients, oncogenes, and other factors, which results in senescence. As a pro-senescent state in cancer characterized by an overactive mTOR-centric network, cell cycle arrest frequently leads to senescence in cancer (Blagosklonny, 2011). Cell cycle arrest just permits the emergence of this situation. The findings of this research validate that RGE-NE has the capability to trigger senescence in MCF-7 cells (Figure 6). Blue-stained cells signify β-galactosidase positive cells. As illustrated in Figure 5, MCF-7 cells treated with RGE-NE showed a higher number of blue-colored cells compared to untreated controls. Previous research has identified ginger and its components as having potential benefits in addressing cellular aging. Research by Moaddel *et al*. (2022) identified extract of ginger, specifically gingerenone A, as a promising natural senolytic compound, which exhibits high selectivity to promote senescent cell death (Moaddel *et al*., 2022). Another study on ginger extracts containing 6-gingerol and 6-shogaol showed their potential to prevent myoblast cell senescence due to their antioxidant properties (Sahardi *et al*., 2020). Furthermore, studies by Kaewtunjai *et al*. (2018) demonstrated that in A549 lung cancer cells, ginger extract promoted telomere length reduction and the beginning of cellular senescence.

5. Conclusion

In summary, RGE-NE showed potential as an anticancer agent in MCF-7 breast cancer cells by specifically enhancing the activity of the *CASP3* and *TP53* genes while reducing the activity of the *BCL2* gene, as well as by inducing apoptosis and necrosis and modifying the expression of apoptosis-related genes. Additionally, RGE-NE affected the cell cycle by causing MCF-7 cells to enter the S phase, suppressing the G0/G1 phase, and promoting cell senescence. These results demonstrate that RGE-NE may interact with important systems such as apoptosis, cell cycle regulation, and cellular senescence to cure breast cancer. However, there are limitations that must be acknowledged, namely that this study only focused on in vitro analysis, and the findings may not be fully applicable to the in vivo system due to the complexity of the tumor microenvironment. Future studies incorporating animal models and detailed toxicological assessments are recommended to validate the findings and advance the application of RGE-NE in clinical settings.

Acknowledgement

We express our gratitude to the Minister of Education, Culture, Research, and Technology of the Republic of Indonesia (Competitive National Research-Fundamental Research 2023) for providing funding for this study (grant number 051/PG/PG.02.00.PL/2023). We also acknowledge the invaluable support provided by Aretha Medika Utama, Biomolecular and Biomedical Research Center, Indonesia. We express our gratitude to the following individuals from Aretha Medika Utama: Annisa Firdaus Sutendi, Nindia Salsabila Mia Dewi, Faradhina Salfa Nindya, Adilah Hafizha Nur Sabrina, and Vini Ayuni. Additionally, we appreciate the assistance with the preparation of red ginger (*Zingiber officinale* var. rubrum) extract provided by PT Fathonah Amanah Shidiq Tabligh (FAST), Depok, Indonesia.

References

Abdullah S, Abidin SAZ, Murad NA, Makpol S, Ngah WZW, and Yusof YAM. 2010. Ginger extract (*Zingiber officinale*) triggers apoptosis and G0/G1 cells arrest in HCT 116 and HT 29 colon cancer cell lines. *Afr J Biochem Res.*, **4(4):** 134-42.

Alharbi DS, Albalawi SF, Alghrid ST, Alhwity BS, Qushawy M, Mortagi Y, and Elsherbiny N. 2023. Ginger oil nanoemulsion formulation augments its antiproliferative effect in ehrlich solid tumor model. *Foods.*, **12(22):** 4139.

Amalraj A, Jude S, Sukumaran NP, and Gopi S. 2019. Nanomaterials in nutraceutical and phytonutrient industries. In Industrial applications of nanomaterials, Elsevier, pp. 441-474.

Aung TN, Qu Z, Kortschak RD, and Adelson DL. 2017. Understanding the Effectiveness of Natural Compound Mixtures in Cancer through Their Molecular Mode of Action. *Int J Mol Sci.,* **18 (3)**: 656.

Bernard MM, McConnery JR, and Hoskin DW. 2017. (10)-Gingerol, a major phenolic constituent of ginger root, induces cell cycle arrest and apoptosis in triple-negative breast cancer cells. *Exp Mol Pathol*., **102(2):** 370-376.

Blagosklonny MV. 2011. Cell cycle arrest is not senescence. *Aging (Albany NY)*. **3:** 94-101.

Camarillo IG, Xiao F, Madhivanan S, Salameh T, Nichols M, Reece LM, Leary JF, Otto KJ, Natarajan A, Ramesh A, and Sundararajan R. 2014. In*:* Electroporation-based therapies for cancer: from basics to clinical applications*.* Cambridge: Elsevier, p. 55–102.

Chaturvedi VK, Sharma B, Tripathi AD, Yadav DP, Singh KRB, Singh J, and Singh RP. 2023. Biosynthesized nanoparticles: a novel approach for cancer therapeutics. *Front Med Technol*., **5**: 1236107.

Chen GQ, Nan Y, Huang SC, Ning N, Du YH, Lu DD, Yang YT, Meng FD, and Yuan L. 2023. Research progress of ginger in the treatment of gastrointestinal tumors. *World J Gastrointest Oncol.*, **15 (11):** 1835-1851.

Cui Q, Yu JH, Wu JN, Tashiro SI, Onodera S, Minami M, and Ikejima T. 2007. P53-mediated cell cycle arrest and apoptosis through a caspase-3-independent, but caspase-9-dependent pathway in oridonin-treated MCF-7 human breast cancer cells. *Acta Pharmacol Sin*., **28(7):** 1057-1066.

Diedrich C, Zittlau IC, Khalil NM, Leontowich AFG, Freitas RAd, Badea I, and Mainardes RM. 2023. Optimized Chitosan-Based Nanoemulsion Improves Luteolin Release. *Pharmaceutics*., **15 (6):** 1-18.

El-Borm HT, Gobara MS, and Badawy GM. 2023. Therapeutic Potential of Ginger Extract on the Embryotoxicity and Nephrotoxicity Induced by Labetalol in Rat Fetuses. *Jordan J Biol Sci*., **16(1)**: 93-103.

Fink SL, and Cookson BT. 2005. Apoptosis, pyroptosis, and necrosis: mechanistic description of dead and dying eukaryotic cells. *Infect Immun*., **73(4):** 1907-1916.

Ghasemzadeh A, Jaafar HZ, and Rahmat A. 2015. Optimization protocol for the extraction of 6-gingerol and 6-shogaol from *Zingiber officinale* var. rubrum Theilade and improving antioxidant and anticancer activity using response surface methodology. *BMC Complement Altern Med*., **15;** 1-10.

Girsang E, Lister IN, Ginting CN, Widowati W, Arumwardana S, Marthania M, and Rizal R 2023. Chlorogenic acid in preventing and curing ultraviolet-induced damage in human skin fibroblast as an antiaging cell model. *Pharmaciana*., **13:** 159-165.

GuarÍn-González YA, and Cárdenas-Triviño G. 2022. New Chitosan-based chemo pharmaceutical delivery systems for tumor cancer treatment: Short-review. *J Chil Chem Soc.,* **67(1):** 5425-5432.

Hassan ME, Shehata HA, Fahmy A, Badr M, Tamer TM, and Omer AM. 2021. Development of biodegradable poly (vinyl alcohol)/chitosan cross linked membranes for antibacterial wound dressing applications. *Jordan J Biol Sci.,* **14(1)**: 1-6.

Ji X, Lu Y, Tian H, Meng X, Wei M, and Cho WC. 2019. Chemoresistance mechanisms of breast cancer and their countermeasures. *Biomed Pharmacother.,* **114:** 1-9.

Kadam CY, and Abhang SA. 2016. Apoptosis markers in breast cancer therapy. *Adv Clin Chem*., **74:** 143-193.

Kaewtunjai N, Wongpoomchai R, Imsumran A, Pompimon W, Athipornchai A, Suksamrarn A, Lee TR, and Tuntiwechapikul W. 2018. Ginger extract promotes telomere shortening and cellular senescence in A549 lung cancer cells*. ACS Omega*. **3(12):** 18572-18581.

Kalamegam G, Sait KH, Ahmed F, Kadam R, Pushparaj PN, Anfinan N, Rasool M, Jamal MS, Abu-Elmagd M, and Al-Qahtani M. 2018. Human Wharton's jelly stem cell (hWJSC) extracts inhibit ovarian cancer cell lines OVCAR3 and SKOV3 in vitro by inducing cell cycle arrest and apoptosis. *Front Oncol.,* **8:** 1-18.

Kim HW, Oh DH, Jung C, Kwon DD, and Lim YC. 2011. Apoptotic effects of 6-gingerol in LNCaP human prostate cancer cells. *Soonchunhyang Med Sci*., **17(2):** 75-79.

Lee HS, Seo EY, Kang NE, and Kim WK. 2008. (6)-Gingerol inhibits metastasis of MDA-MB-231 human breast cancer cells. *J Nutr Biochem.,* **19(5):** 313-319.

Lim YX, Lim ZL, Ho PJ, and Li J. 2022. Breast cancer in Asia: incidence, mortality, early detection, mammography programs, and risk-based screening initiatives. *Cancers*. **14(17):** 1-21.

Lo A, Serravallo M, and Jagdeo J. 2015. Epigenetic Mechanisms of Sirtuins in Dermatology. **Epigenetics and Dermatology.** Academic Press, Oxford, pp. 137-175.

Luo L, Chen Y, Ma Q, Huang Y, Hong T, Shu K, and Liu Z. 2023. Exploring the mechanism of an active ingredient of ginger, dihydrocapsaicin, on triple negative breast cancer based on network pharmacology and in vitro experiments. *Oncol Lett.,* **25(5):** 1-4.

Mahdavifar N, Pakzad R, Ghoncheh M, Pakzad I, Moudi A, and Salehiniya H. 2016. Spatial analysis of breast cancer incidence in Iran. *Asian Pac J Cancer Prev*., **17(S3):** 59-64.

Mao QQ, Xu XY, Cao SY, Gan RY, Corke H, Beta T, and Li HB. 2019. Bioactive compounds and bioactivities of ginger (*Zingiber officinale* Roscoe). *Foods*., **8(6):** 1-21.

Marvalim C, Datta A, and Lee SC. 2023. Role of p53 in breast cancer progression: An insight into p53 targeted therapy. *Theranostics*., **13(4):** 1421-1442.

Moaddel R, Rossi M, Rodriguez S, Munk R, Khadeer M, and Abdelmohsen K, Gorospe M, Ferrucci L. 2022. Identification of gingerenone A as a novel senolytic compound. *PLoS One*., **17(3):** 1-10.

Moghaddam AB, Moniri M, Azizi S, Abdul Rahim R, Bin Ariff A, Navaderi M, and Mohamad R. Eco-friendly formulated zinc oxide nanoparticles: induction of cell cycle arrest and apoptosis in the MCF-7 cancer cell line. *Genes*., **8(10):** 1-15.

Nallamuthu I, Devi A, and Khanum F. 2015. Chlorogenic acid loaded chitosan nanoparticles with sustained release property, retained antioxidant activity and enhanced bioavailability. *Asian J Pharm Sci.,* **10(3):** 203-211.

Nguyen ST, Vo PH, Nguyen TD, Do NM, Le BH, Dinh DT, Truong KD, and Van PP. 2019. Ethanol extract of Ginger *Zingiber officinale* Roscoe by Soxhlet method induces apoptosis in human hepatocellular carcinoma cell line. *Biomed Res Ther*., **6(11):** 3433-3442.

Nindrea RD, Dwiprahasto I, Lazuardi L, and Aryandono T. 2023. Development of a breast cancer risk screening tool for women in Indonesia. *Clin Epidemiol Glob Health*., **24:** 1-6.

Noore S, Rastogi NK, O'Donnell C, and Tiwari B. 2021. Novel Bioactive Extraction and Nano-Encapsulation. *Encyclopedia*., **1(3):** 632-664.

Panyajai P, Chueahongthong F, Viriyaadhammaa N, Nirachonkul W, Tima S, Chiampanichayakul S, Anuchapreeda S, and Okonogi S. 2022. Anticancer activity of *Zingiber ottensii* essential oil and its nanoformulations. *PLoS One*., **17(1):** 1-15.

Pashaei-Asl R, Pashaei-Asl F, Gharabaghi PM, Khodadadi K, Ebrahimi M, Ebrahimie E, and Pashaiasl M. 2017. The inhibitory effect of ginger extract on ovarian cancer cell line; application of systems biology. *Adv Pharm Bull*., **7(2):** 241-249.

Perri F, Pisconti S, and Scarpati GD. 2016. P53 mutations and cancer: a tight linkage. *Ann Transl Med.,* **4(24):** 1-4.

Pfeffer CM, and Singh AT. 2018. Apoptosis: a target for anticancer therapy. *Int J Mol Sci.* **19(2):** 1-10.

Prasetyo A, Sidharta BR, Hartini YS, and Mursyanti E. 2019. Toxicity of bioactive compound from endophytic fungi isolated from red ginger (*Zingiber officinale* var. rubrum) utilizing brine shrimp lethality assay. *Biogenesis (J Biol Sci)*., **7(1):** 30-37.

Priyandoko D, Widowati W, and Gunawan KY. 2019. Ethanolic Extract of Moringa's leaves (*Moringa oleifera*) Induce Senescence on Adenocarcinomic Alveolar Basal Epithelial Cells (A549 Cell-lines). *Proceeding of ICOHETECH*., 156-159.

Rahman MA, Hannan MA, Dash R, Rahman MDH, Islam R, Uddin MJ, Sohag AAM, Rahman MH, and Rhim H. Phytochemicals as a Complement to Cancer Chemotherapy: Pharmacological Modulation of the Autophagy-Apoptosis Pathway. *Front Pharmacol*., **12:** 1-20.

Rahmani AH, and Aly SM. Active ingredients of ginger as potential candidates in the prevention and treatment of diseases via modulation of biological activities. *Int J Physiol Pathophysiol Pharmacol*., **6(2):** 125-136.

Ray A, Vasudevan S, and Sengupta S. 2015. 6-Shogaol inhibits breast cancer cells and stem cell-like spheroids by modulation of Notch signaling pathway and induction of autophagic cell death. *PLoS One*., **10(9):** 1-22.

Sahardi NF, Jaafar F, Nordin MF, and Makpol S. 2020. Research Article *Zingiber officinale* Roscoe Prevents Cellular Senescence of Myoblasts in Culture and Promotes Muscle Regeneration. *Evid Based Complement Alternat Med*., **2020(1):** 1-13.

Shahouzehi B, Masoumi-Ardakani Y, Fallah H, and Aminizadeh S. 2023. Concomitant Administration of L-carnitine and Performing HighIntensity Interval Training Effects on the Genes Involved in Mitochondrial Fusion and Apoptosis in Rat Liver. *Jordan J Biol Sci.,* **16(1)**: 21-26.

Sánchez-López E, Guerra M, Dias-Ferreira J, Lopez-Machado A, Ettcheto M, and Cano A, Espina M, Camins A, Garcia ML, Souto EB. 2019. Current applications of nanoemulsions in cancer therapeutics. *Nanomaterials*., **9(6):** 1-29.

Savitri AD, Hidayati HB, Veterini L, Widyaswari MS, Muhammad AR, Fairus A, Zulfikar MQB, Astri M, Ramasima NA, Anggreani DP, Nainatika RSA, and Juliana J. 2023. An In-Silico Study on Allicin Compound in Garlic (*Allium sativum*) as A Potential Inhibitor of Human Epidermal Growth Factor Receptor (Her)-2 Positive Breast Cancer. *Jordan J Biol Sci*., **16(1)**: 7-12.

Semwal RB, Semwal DK, Combrinck S, and Viljoen AM. 2015. Gingerols and shogaols: Important nutraceutical principles from ginger. *Phytochemistry*. **117:** 554-568.

Subramaniam S, Selvaduray KR, and Radhakrishnan AK. Bioactive compounds: natural defense against cancer?. *Biomolecules*., **9(12):** 1-15.

Suciyati SW, and Adnyana IK. 2017. Red ginger (*Zingiber officinale* Roscoe var rubrum): A review. *Pharmacologyonline*., **2(8):** 60-65.

Tan BS, Kang O, Mai CW, Tiong KH, Khoo AS, Pichika MR, Bradshaw TD, and Leong CO. 2013. 6-Shogaol inhibits breast and colon cancer cell proliferation through activation of peroxisomal proliferator activated receptor γ (PPARγ). *Cancer Lett*., **336(1):** 127-139.

Thu KL, Soria-Bretones I, Mak TW, and Cescon DW. 2018. Targeting the cell cycle in breast cancer: towards the next phase. *Cell Cycle*., **17(15):** 1871-1885.

Valente LJ, and Strasser A. 2013. Distinct target genes and effector processes appear to be critical for p53-activated responses to acute DNA damage versus p53-mediated tumour suppression. *BioDiscovery*., **8:** 1-16.

Wang Z. 2021. Regulation of Cell Cycle Progression by Growth Factor-Induced Cell Signaling. *Cells*., **10(12):** 1-23.

Widowati W, Darsono L, Lucianus J, Setiabudi E, Obeng S, Stefani S, Wahyudianingsih R, Tandibua KR, Gunawan R, Wijayanti CR, Novianto A, Kusuma HSW, and Rizal R. 2023. Butterfly pea flower (*Clitoria ternatea* L.) extract displayed antidiabetic effect through antioxidant, anti-inflammatory, lower hepatic GSK-3β, and pancreatic glycogen on Diabetes Mellitus and dyslipidemia rat. *J King Saud Univ Sci*., **35(4):** 1-10.

Widowati W, Darsono L, Suherman J, Afifah E, Rizal R, Arinta Y, Mozef T, and Suciati T. 2020. Regulation of Adipogenesis and Key Adipogenic Gene Expression by Mangosteen Pericarp Extract and Xanthones In 3t3-L1 Cells. *Biotropia*., **27(1):** 14-21.

Widowati W, Jasaputra DK, Onggowidjaja P, Sumitro SB, Widodo MA, Afifah E, Rihibiha DD, Rizal R, Amalia A, Kusuma HS, and Murti H. 2019. Effects of Conditioned Medium of Co-Culture IL-2 Induced NK Cells and Human Wharton's Jelly Mesenchymal Stem Cells (hWJMSCs) on Apoptotic Gene Expression in a Breast Cancer Cell Line (MCF-7). *J Math Fundam Sci.,* **51(3):** 205-224.

Widowati W, Jasaputra DK, Sumitro SB, Widodo MA, Afifah E, Rizal R, Rihibiha DD, Kusuma HSW, Murti H, Bachtiar I, and Faried A. 2018. Direct and Indirect Effect of TNFα and IFNγ Toward Apoptosis in Breast Cancer Cells. *Mol Cell Biomed Sci*., **2(2):** 60-69.

Wiman KG. 2006. Strategies for therapeutic targeting of the p53 pathway in cancer. *Cell Death Differ.,* **13(6):** 921-926.

Yuan L, Cai Y, Zhang L, Liu S, Li P, and Li X. 2022. Promoting apoptosis, a promising way to treat breast cancer with natural products: A comprehensive review. *Front Pharmacol*., **12:** 1-45.

Zhang S, Kou X, Zhao H, Mak KK, Balijepalli MK, and Pichika MR. 2022. Zingiber officinale var. rubrum: Red ginger's medicinal uses. *Molecules*., **27(3):** 1-31.

JJBS

Volume 18, Number 3,September 2025
ISSN 1995-6673
Pages 403 – 410

Jordan Journal of Biological Sciences

Molecular Docking and Molecular Dynamics Simulation of *Kaempferia galanga* Bioactive Compounds as Cancer Immunotherapy against PD-L1 Through Inhibition of RAS, JAK, ERK Protein

Wira Eka Putra[1,*] , Diana Widiastuti[2], Arief Hidayatullah[3], Muhammad Fikri Heikal[4], Sustiprijatno[5]

[1]*Biotechnology Study Program, Department of Applied Sciences, Faculty of Mathematics and Natural Sciences, Universitas Negeri Malang, East Java, Indonesia;* [2]*Department of Chemistry, Faculty of Mathematics and Natural Science, Universitas Pakuan, West Java, Indonesia;* [3]*United Nations Development Programme Indonesia, Health Governance Initiative, Eijkman-RSCM Building, Jakarta, Indonesia;* [4]*Department of Biology, Faculty of Mathematics and Natural Sciences, Universitas Negeri Malang, East Java, Indonesia;* [5]*Research Center for Applied Botany, National Research and Innovation Agency, West Java, Indonesia.*

Received: October 11, 2024; Revised: January 10, 2024; Accepted: January 20, 2025

Abstract

Cancer remains the world's biggest health issue which kills nearly one in six people worldwide. Several modalities have been proposed, including the conventional and recently developed approach including cancer-immunotherapy. The main challenge of the therapy is to develop effective and safer treatments with minimal side effects. Therefore, the discovery of new drugs to complement and enhance current therapies is urgently needed. In the present study, we aimed to evaluate *Kaempferia galanga* bioactive compounds as potential cancer immunotherapy agents targeting PD-L1 by inhibiting RAS, JAK, ERK proteins through molecular docking and molecular dynamics simulation. *In silico* study was performed including the ligands and target proteins preparation, drug likeness and toxicity screening, molecular docking, molecular dynamic simulation, and biological activity prediction. Inhibiting the expression of PD-L1 through blocking the activation of several target proteins such as RAS, JAK, and ERK could be a promising strategy against cancer. *In silico* study demonstrated that sandaracopimaradiene has favorable binding affinity scores compared to other bioactive compounds against the target proteins, ERK. Molecular dynamics simulation also demonstrated the stable pattern of sandaracopimaradiene on some parameters which indicate that this compound effectively bound to the target proteins. The findings indicate that sandaracopimaradiene is a compound comparable to the anticancer control drug, ruxolitinib. Finally, the biological activity prediction also strengthens the role of sandaracopimaradiene against cancer development.

Keywords: Cancer-immunotherapy, *Kaempferia galanga*, natural products, PD-L1, molecular dynamics simulation.

1. 1. Introduction

Cancer is still the major public health problem worldwide. Unfortunately, cancer is causing a high rate of death, accounting almost for one in six deaths globally (Bray *et al*., 2024; Dunn 2023; Sung *et al*., 2021). The risk factors of certain cancers might vary, but some common factors that increase the occurrence of cancer include smoking, alcohol intake, obesity, chemicals, and lack of physical exercise. These factors then promote the genetics alteration and instability which further causes cancer initiation (Marino *et al*., 2024; Lazarus *et al*., 2022; Łukasiewicz *et al*., 2021). Cancer is a complex disease which covers not only the tumor, but also the environment surrounding the tumor. Treating cancer is challenging and demonstrates rapid developments. Conventional treatments including surgery, chemotherapy, and radiotherapy have been proposed. Recently, to optimize the treatment, some advanced cancer therapies including cancer immunotherapy demonstrated promising patient outcomes (Debela *et al*., 2021; Bondhopadhyay *et al*., 2020).

Modulating the immune system to fight the cancer is the main principle of cancer immunotherapy. The modulation of the immune system could be approached by strengthening the immune cells or improving the immune function to recognize and inhibit the action of the cancer. One of the most targeted molecules for cancer immunotherapy is PD1/PD-L1 axis (Tan *et al*., 2020). PD1/PD-L1 interaction plays a pivotal role for cancer to evade from the immune system destruction. Thus, by blocking this axis or reducing the expression of the checkpoint molecules could prevent the cancer progression, and at the same time enhance the function of immune cells (Esfahani *et al*., 2020). Clinical study demonstrated that PD1/PD-L1 blockade in patient with breast cancer could improve the objective response rates (Liu *et al*., 2021; Koh, 2021). Although PD-1/PD-L1 blockade has demonstrated promising outcomes, several studies have also reported side effects and the development

* Corresponding author. e-mail: wira.putra.fmipa@um.ac.id.

of drug resistance during therapy (Reynolds *et al*., 2021; Andrews *et al*., 2019). Therefore, finding new agent for PD1/PD-L1 blockade which more effective and has minimum unwanted effects is urgently needed.

It has been widely demonstrated that plants-derived natural products showed significant effect in treating multiple types of diseases, including cancer (Putra et al., 2023; Shrihastini et al., 2021; Putra and Rifa'i, 2019). *Kaempferia galanga* is a traditional medicinal plant known for its therapeutic properties, including anti-inflammatory and immunomodulatory activities. It originates from India and is widely distributed across several Southeast Asian countries, including Indonesia, Malaysia, Myanmar, and Thailand. Traditionally, *K. galanga* has been used for ameliorating some diseases such as cold, cough, toothache rheumatism, and hypertension (Wang *et al*., 2021; Kumar, 2020; Srivastava *et al*., 2019). Importantly, K. galanga is rich in functional bioactive compounds, including hexadecanoic acid, oleic acid, 2-propenoic acid, octadecanoic acid, glycidyl stearate, sandaracopimaradiene, nonoxynol-2, and phthalic acid (Ali *et al*., 2018). Interestingly, a study confirmed that *K. galanga* extracts have anti-cancer effects on breast cancer by inhibition of a breast cancer resistance protein (Elshamy *et al*., 2019). Another study demonstrated that *K. galanga* extract could inhibit metastasis by suppressing the MMP9 protein expression which was responsible in metastasis. Interestingly, *K. galanga* extract also inhibits the migration of breast cancer cell lines (Ahlina *et al*., 2020). However, the study of *K. galanga* bioactive compounds as cancer immunotherapy is based on limited data. Therefore, in the present study, we aimed to evaluate the activity of K. galanga bioactive compounds in inhibiting several proteins, including RAS, JAK, and ERK, which are responsible for PD-L1 expression, using in silico approaches. The in silico approach facilitates the screening of compounds according to their drug-likeness and less toxic properties. This approach also enables the selection of drugs by assessing their binding affinity and stability via molecular docking and dynamics simulation.

2. Materials and Methods

2.1. Drug likeness and toxicity prediction

Several major *K. galanga* bioactive compounds including hexadecanoic acid (CID. 985), oleic acid (CID. 445639), 2-propenoic acid (CID. 6581), octadecanoic acid (CID. 5281), glycidyl stearate (CID. 62642), sandaracopimaradiene (CID. 443469), nonoxynol-2 (CID. 24773), phthalic acid (CID. 1017) were computationally evaluated (Ali *et al*., 2018). SwissADME webserver (http://www.swissadme.ch/) was used to evaluate the drug-likeness (Daina et al., 2017). Additionally, ProTox 3.0. webserver (https://tox.charite.de/protox3/) was used to predict the toxicity level and the probability of the compounds to induce toxicity (Banerjee et al., 2024).

2.2. Ligand structure preparation

All chemicals structure of *K. galanga* bioactive compounds were retrieved from PubChem database (https://pubchem.ncbi.nlm.nih.gov/). Tipifarnib (CID. 159324), Ruxolitinib (CID. 25126798), and GDC-0994 (CID. 154702204) were used as control for RAS, JAK, and ERK inhibitor, respectively. All chemical structures were saved on the sdf format which is compatible to the software for molecular docking.

2.3. Target protein preparation

The sequence of target proteins, including RAS, JAK, and ERK, was retrieved from UniProt database (https://www.uniprot.org/). Then, each database was collected for 3D structure modeling. In this present study, SWISS MODEL (https://swissmodel.expasy.org/) webserver was used to build the 3D structure of target protein. The model with high similarity was chosen for further *in silico* analysis (Hidayatullah et al., 2020; Putra and Rifa'i, 2020).

2.4. Molecular docking and visualization

After ligands and target proteins preparation has done, the molecular docking was performed by using PyRx 0.8 software (https://pyrx.sourceforge.io/). The docking grid was set which cover all the surface of the target proteins. Finally, Discovery Studio software (https://www.3ds.com/) was used to analyze and visualize the molecular docking data (Hidayatullah et al., 2021; Putra, 2018).

2.5. Molecular dynamics simulation

To evaluate the stability of the protein-ligand complex, molecular dynamics simulation was performed. YASARA software (http://www.yasara.org/) was used to evaluate several molecular dynamics simulation, including total energy, Coulomb energy, RMSD, SASA, surface molecule, surface VdW, radius gyration, and H-Bond (Heikal et al., 2024; Putra et al., 2024; Ozvoldik et al., 2023; Hidayatullah et al., 2022).

2.6. Biological activity prediction

Finally, biological activity prediction of *K. galanga* bioactive compounds was performed. The SMILES of each bioactive compound retrieved from PubChem database were used. Way2Drug server (http://www.way2drug.com/passonline/) was occupied to get the biological activity prediction related to the cancer incidence.

3. Results and Discussion

This study assessed the drug-likeness of bioactive compounds from *K. galanga*. Several chemical characteristics such as molecular weight, number of rotatable bonds, number of H-bond acceptors, number of H-bond donors, and molar refractivity were evaluated to assess the drug-likeness of the bioactive compounds (Figure 1A). Five drug-likeness validation parameters, Lipinski, Ghose, Veber, Egan, and Muegge, were employed to assess the number of rule violations exhibited by these bioactive compounds (Figure 1B). The drug-likeness screening of the active compounds revealed varying levels of rule violations; however, all compounds exhibited only minimal deviations from the established parameters. In addition, toxicity prediction indicated that glycidyl stearate, nonoxynol-2, phthalic acid, and sandaracopimaradiene belong to higher toxicity classes, suggesting that these compounds exert relatively low toxic effects on cells (Figure 1C, 1D).

Drug likeness screening plays crucial part in assessing and filtering the bioactive compounds for further test as

drug candidate. Through the assessment from its chemical characters, then it helps to get the reliable and accurate data about the kinetic and dynamic of the compounds (Zhu *et al*., 2020; Wang *et al*., 2019). Similarly, the toxicity prediction also plays pivotal role in drug discovery field. The prediction could help to make accurate decision for dosage related experiment, promote the safety evaluation of chemical, and reduce the use of experimental animals (Füzi *et al*., 2023; Barratt *et al*., 2000). The results indicate that the bioactive compound is a druggable chemical with low toxicity, making it suitable for further analysis.

A

Compounds	Formula	Molecular weight	Num. rotatable bonds	Num. H-bond acceptors	Num. H-bond donors	Molar Refractivity
2-Propenoic acid	C3H4O2	72.06 g/mol	1	2	1	17.83
Glycidyl stearate	C21H40O3	340.54 g/mol	19	3	0	103.32
Hexadecanoic acid	C16H32O2	256.42 g/mol	14	2	1	80.8
Nonoxynol-2	C19H32O3	308.46 g/mol	14	3	1	93.02
Octadecanoic acid	C18H36O2	284.48 g/mol	16	2	1	90.41
Oleic acid	C18H34O2	282.46 g/mol	15	2	1	89.94
Phthalic Acid	C8H6O4	166.13 g/mol	2	4	2	40.36
Sandaracopimaradiene	C20H32	272.47 g/mol	1	0	0	90.18

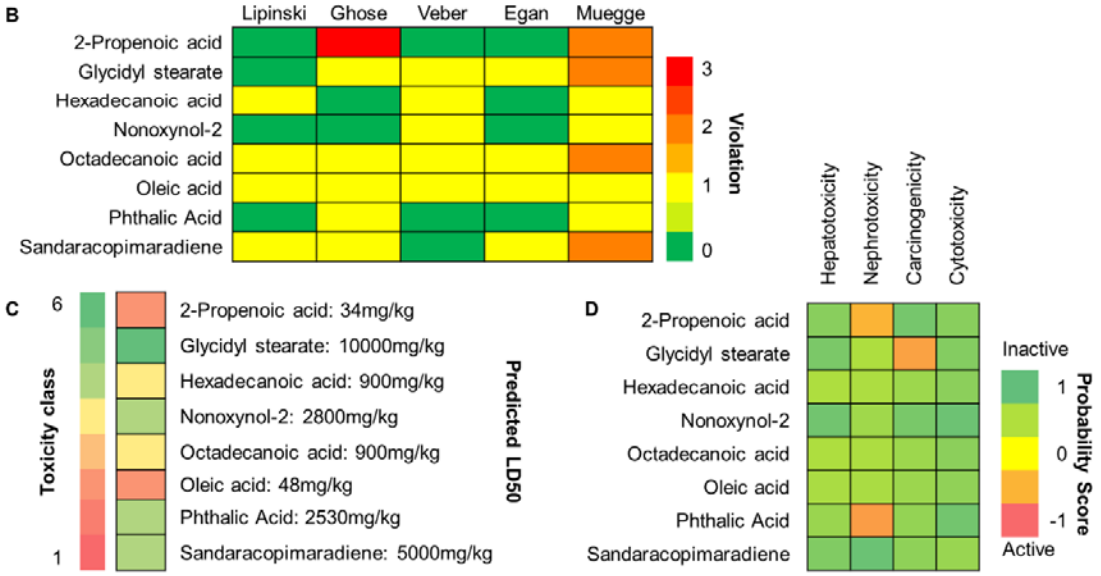

Figure 1. Chemicals characters, drug likeness and toxicity assessment. A). Chemical features of *K. galanga* bioactive compounds. B). Drug likeness evaluation of bioactive compounds. C). Toxicity assessment of bioactive compounds. D). The probability of *K. galanga* bioactive compounds to induce toxicity.

After validating the drug-likeness and evaluating the toxicity profiles of the bioactive compounds, molecular docking simulations were conducted to assess their interactions with target proteins, including RAS, JAK, and ERK (Figure 2). To the greater extent, sandaracopimaradiene have the most favorable binding affinity scores compared to the others. In the interaction with JAK protein, sandaracopimaradiene have better binding affinity compare to the control drug, ruxolitinib. These initial findings suggest that sandaracopimaradiene could be a competitive inhibitor for suppressing the PD-L1 protein by blocking some proteins, especially JAK protein.

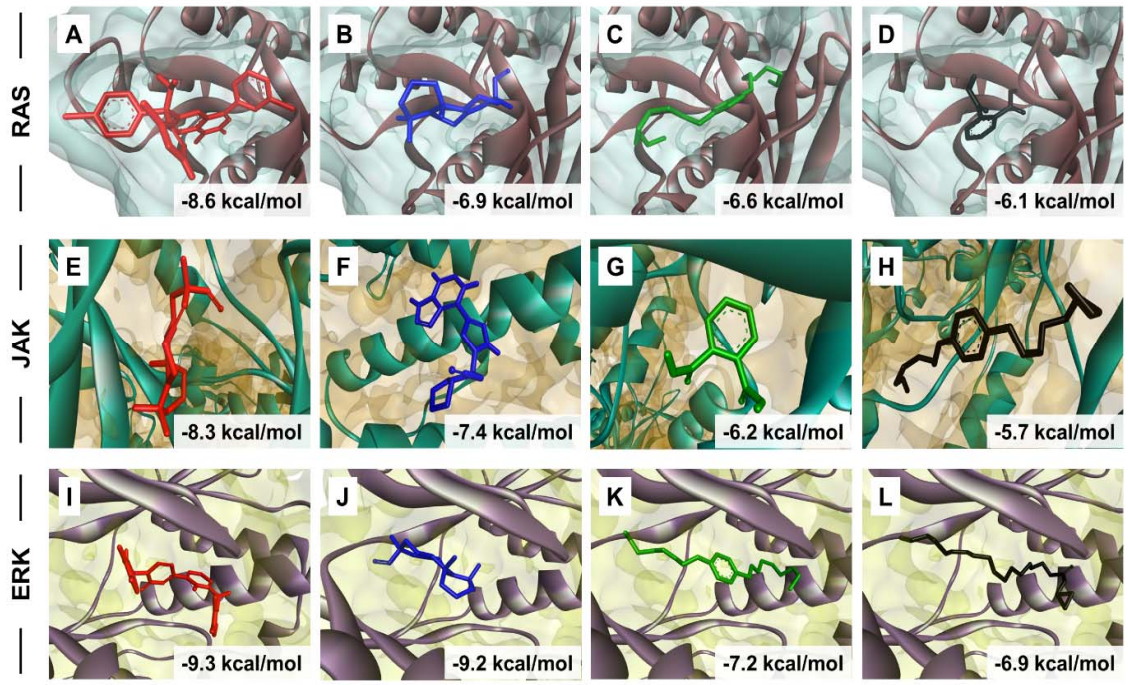

Figure 2. The 3D structure visualization of *K. galanga* bioactive compounds and control drugs toward the RAS, JAK, and ERK proteins. A. Tipifarnib, B. Sandaracopimaradiene, C. Nonoxynol-2, D. Phthalic Acid, E. Sandaracopimaradiene, F. Ruxolitinib, G. Phthalic Acid, H. Nonoxynol-2, I. GDC-0994, J. Sandaracopimaradiene, K. Nonoxynol-2, and L. Glycidyl stearate.

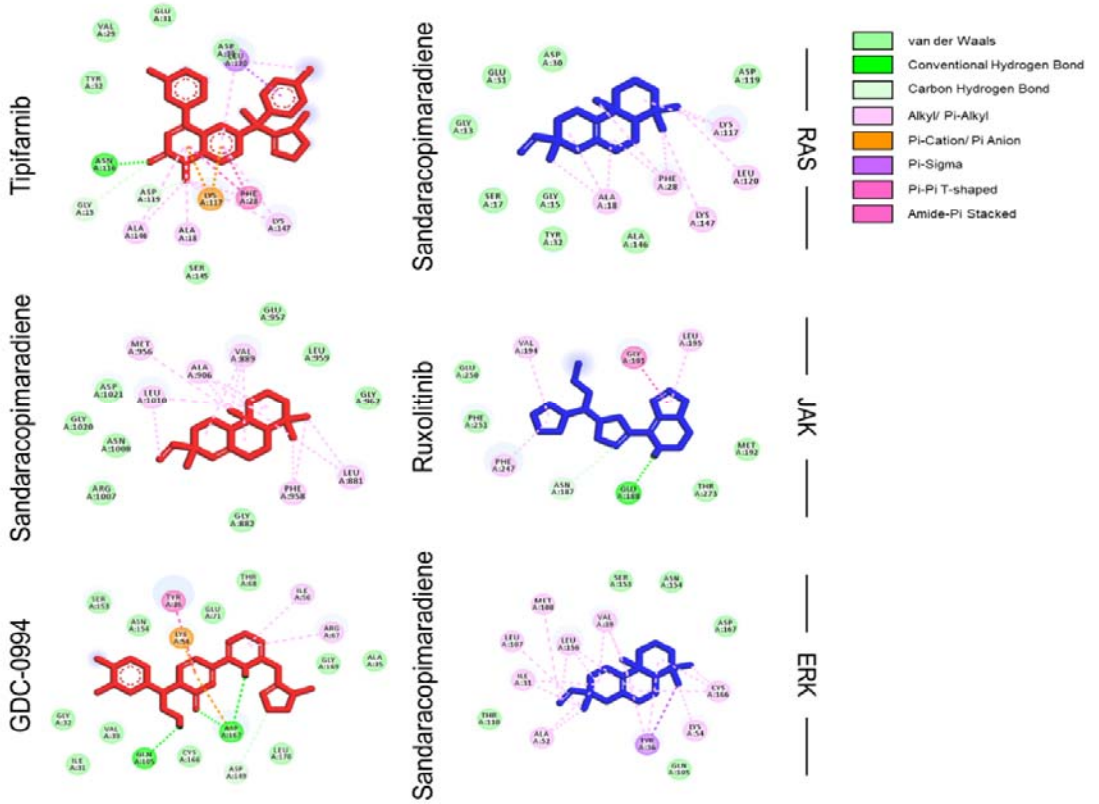

Figure 3. The interaction of *K. galanga* bioactive compound and control drug toward RAS, JAK, and ERK protein.

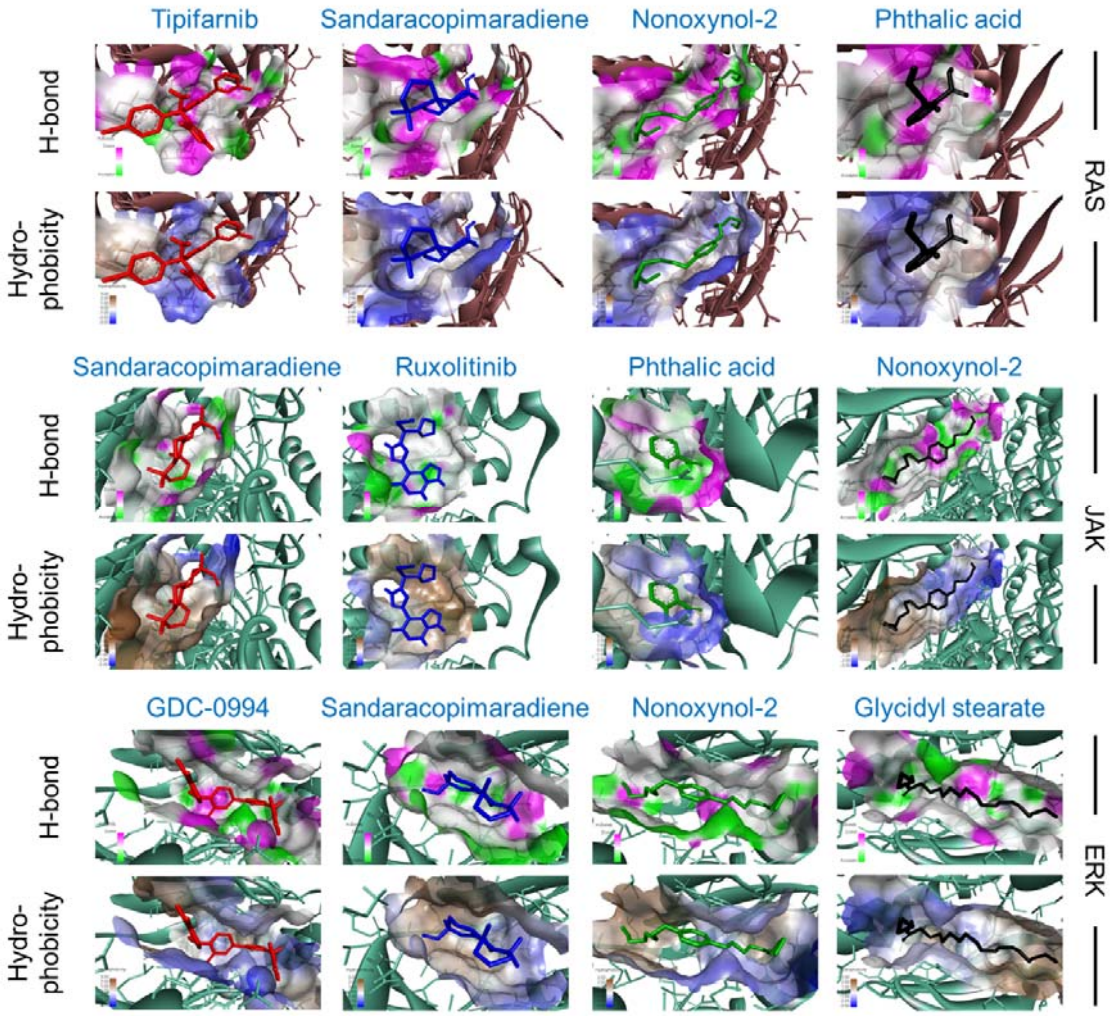

Figure 4. The physicochemical properties of *K. galanga* bioactive compounds and control drugs toward the RAS, JAK, and ERK proteins including H-bonds and hydrophobicity properties.

We examined the chemical interactions formed between sandaracopimaradiene and the RAS, JAK, and ERK proteins. Interestingly, several chemical interactions were observed, including the hydrogen bond and hydrophobic interaction (Figure 3, 4). The hydrogen bond and hydrophobic interaction plays a crucial part in the stability of the protein-ligand interaction (Ruswanto *et al*., 2024). A study has underlined the important function of these interaction in determining the effectiveness and efficacy of the drug (Patil *et al*., 2010).

To ensure the stability of the interaction between the ERK and sandaracopimaradiene, molecular dynamics simulation was performed. The ERK–control drug complex was also evaluated for comparison, to assess the stability of sandaracopimaradiene against the target protein. Several parameters, including total energy, coulomb energy, root mean square deviation (RMSD), solvent accessible surface area (SASA), surface molecule, surface Van der Waals, radius gyration, and H-bond (Figure 5). According to simulation outcomes, even though there are some fluctuations in the beginning of simulation, but almost all parameters including total energy, coulomb energy, RMSD, SASA, surface molecule, surface VdW, radius gyration, and H-bond target protein and sandaracopimaradiene or ruxolitinib were stable and reach the equilibrium in the end of simulation. These results indicate that sandaracopimaradiene exhibits stability comparable to that of the control drug.

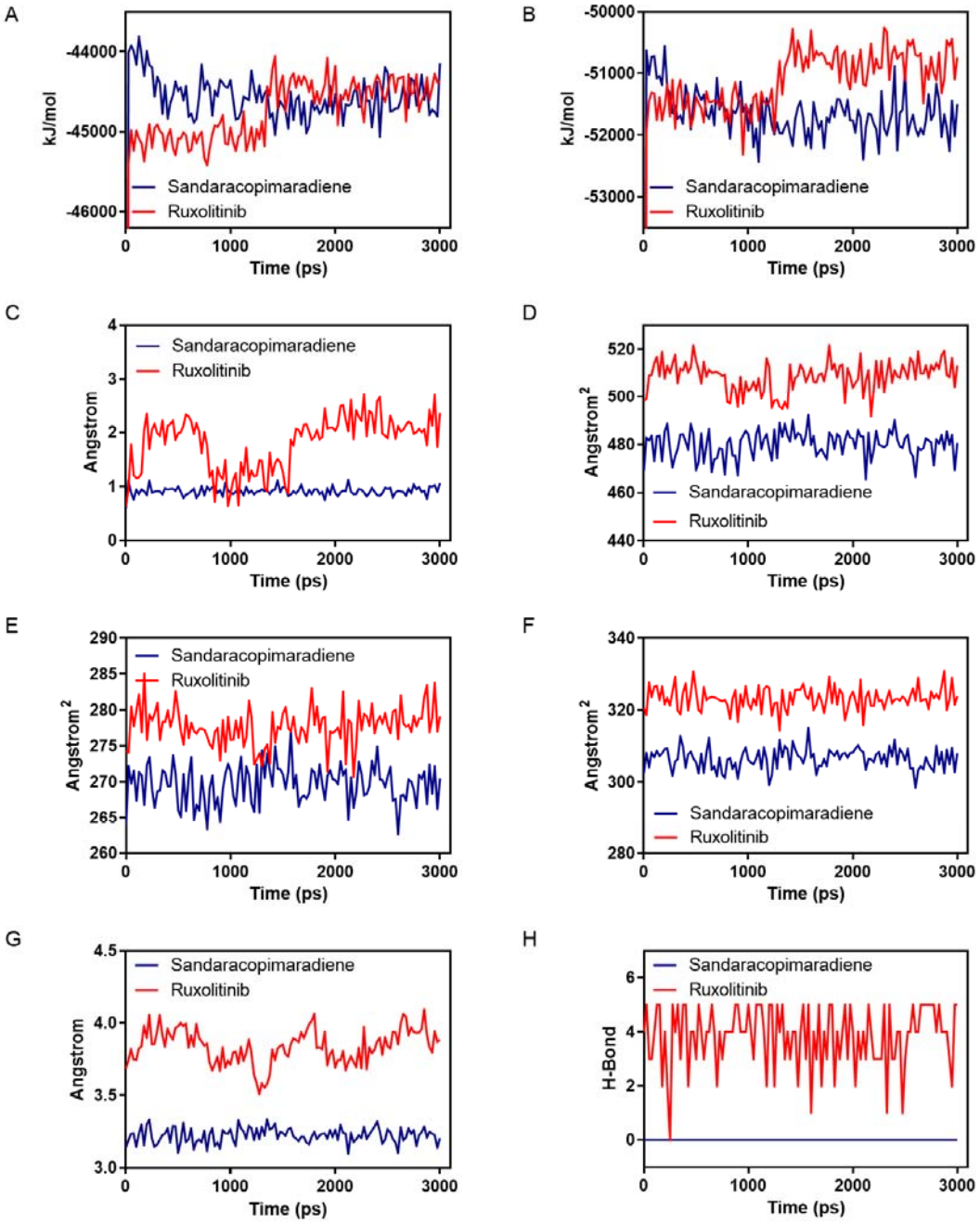

Figure 5. Molecular dynamic simulation of JAK protein - sandaracopimaradiene and JAK protein – Ruxolitinib complex. A). Total energy, B). Coulomb energy, C). RMSD, D). SASA, E). Surface molecule, F). Surface VdW, G). Radius gyration, and H). H-Bond.

Molecular dynamics simulation, a fast growing approach, has become one of the powerful tools in drug discovery study. Molecular dynamics simulation could predict the function and stability of protein, the enzymatic reaction, and also the drug-protein interaction (Son *et al*., 2024; Sinha *et al*., 2022; Hollingsworth and Dror, 2018). Specifically, molecular dynamics simulation could predict the atoms behavior and its change in biological system in time-dependent setting (Badar *et al*., 2022).

Compounds	Pa	Pi	Activity
Sandaracopimaradiene	0.525	0.012	Antineoplastic (lung cancer)
	0.472	0.022	Antineoplastic (breast cancer)
	0.449	0.003	Antineoplastic (thyroid cancer)
	0.425	0.005	Antineoplastic (endocrine cancer)
	0.290	0.020	Antineoplastic (ovarian cancer)
	0.229	0.032	Antineoplastic (glioblastoma multiforme)
	0.234	0.041	Antineoplastic (melanoma)
	0.174	0.076	Antineoplastic (colorectal cancer)
	0.169	0.071	Antineoplastic (colon cancer)
	0.162	0.074	Antineoplastic (glioma)
	0.099	0.083	Antineoplastic (carcinoma)
Nonoxynol-2	0.449	0.066	Antineoplastic (non-Hodgkin's lymphoma)
	0.244	0.146	Antineoplastic (solid tumors)
	0.224	0.208	Antineoplastic (multiple myeloma)
	0.213	0.114	Antineoplastic (bone cancer)
	0.210	0.074	Antineoplastic (liver cancer)
	0.161	0.089	Antineoplastic (lymphoma)
	0.155	0.144	Antineoplastic (sarcoma)
Phthalic Acid	0.291	0.088	Antineoplastic (multiple myeloma)
	0.165	0.115	Antineoplastic (glioblastoma multiforme)
	0.162	0.103	Antineoplastic (bladder cancer)
	0.152	0.109	Antineoplastic (renal cancer)

Figure 6. The predicted biological activities of selected *K. galanga* bioactive compounds related to the cancer.

Finally, based on the biological activity prediction, it has been demonstrated that *K. galanga* bioactive compounds including sandaracopimaradiene, nanoxynol-2, and phthalic acid demonstrate anti-cancer potency in multiple types of cancer. A report summarizes that *K. galanga* extracts exerts anti-cancer properties in several types of cancer. For instance, *K. galanga* active compounds could promote toxicity in HSC-3 and Ca922 lines. On the other hand, *K. galanga* active compounds could induce the apoptosis and influence the cell cycle of HepG2 cell lines. Finally, *K. galanga* active compounds also demonstrate anti-cancer activity in DMH-induce rat colon carcinogenesis model by modulating many pathways including proliferation, invasion, angiogenesis, apoptosis, and inflammation (Wang *et al*., 2021).

4. Conclusion

Inhibiting the expression of PD-L1 through blocking the activation of several target proteins such as RAS, JAK, and ERK could be a promising strategy against cancer. *In silico* study demonstrated that sandaracopimaradiene has favorable binding affinity scores compared to other bioactive compounds against the target proteins. Molecular dynamics simulation also demonstrated the stable pattern of sandaracopimaradiene on some parameters which indicate that this compound is effectively bound to the target proteins. Finally, the biological activity prediction also strengthens the role of sandaracopimaradiene against cancer incidence.

Acknowledgment

Authors thank Universitas Negeri Malang for supporting this study.

Conflict of interests

We declare there is no conflict of interests in this study.

References

Ahlina FN, Nugraheni N, Salsabila IA, Haryanti S, Da'i M and Meiyanto E. 2020. Revealing the Reversal Effect of Galangal (Alpinia galanga L.) Extract Against Oxidative Stress in Metastatic Breast Cancer Cells and Normal Fibroblast Cells Intended as a Co- Chemotherapeutic and Anti-Ageing Agent. *Asian Pac J Cancer Prev.*, **21(1)**: 107-117.

Ali H, Yesmin R, Sstter M, Habib R and Yeasmin T. 2018. Antioxidant and antineoplastic of methanolic extract of Kaempferia galanga Lin. rhizome against Ehrlich ascites carcinoma cells. *J. King Saud Uni. Sci.*, **30**: 386-392.

Andrews LP, Yano H and Vignali DAA. 2019. Inhibitory receptors and ligands beyond PD-1, PD-L1 and CTLA-4: breakthroughs or backups. *Nat Immunol.*, **20(11)**: 1425-1434.

Badar MS, Shamsi S, Ahmed J and Alam MA. 2022. Molecular Dynamics Simulations: Concept, Methods, and Applications. In: Rezaei, N. (eds) Transdisciplinarity. *Integrated Science*, 5. Springer, Cham.

Banerjee P, Kemmler E, Dunkel M and Preissner R. 2024. ProTox 3.0: a webserver for the prediction of toxicity of chemicals. *Nucleic Acids Res.*, **52**: 513-520.

Barratt MD. 2000. Prediction of toxicity from chemical structure. *Cell Biol Toxicol.*, **16(1)**: 1-13.

Bondhopadhyay B, Sisodiya S, Chikara A, Khan A, Tanwar P, Afroze D, Singh N, Agrawal U, Mehrotra R and Hussain S. 2020. Cancer immunotherapy: a promising dawn in cancer research. *Am J Blood Res.*, **10(6)**: 375-385.

Bray F, Laversanne M, Sung H, Ferlay J, Siegel RL, Soerjomataram I and Jemal A. 2024. Global cancer statistics 2022: GLOBOCAN estimates of incidence and mortality worldwide for 36 cancers in 185 countries. *CA Cancer J Clin.*, **74(3)**: 229-263.

Daina A, Michielin O and Zoete V. 2017. SwissADME: a free web tool to evaluate pharmacokinetics, drug-likeness and medicinal chemistry friendliness of small molecules. *Sci Rep.*, **7**: 42717.

Debela DT, Muzazu SG, Heraro KD, Ndalama MT, Mesele BW, Haile DC, Kitui SK and Manyazewal T. 2021. New approaches and procedures for cancer treatment: Current perspectives. *SAGE Open Med.*, **9**: 20503121211034366.

Dunn J. 2023. It Is Time to Close the Gap in Cancer Care. *JCO Glob Oncol.*, **9**: e2200429.

Elshamy AI, Mohamed TA, Essa AF, Abd-ElGawad AM, Alqahtani AS, Shahat AA, Yoneyama T, Farrag ARH, Noji M, El-Seedi HR, Umeyama A, Paré PW and Hegazy MF. 2019. Recent Advances in Kaempferia Phytochemistry and Biological Activity: A Comprehensive Review. *Nutrients.*, **11(10)**: 2396.

Esfahani K, Roudaia L, Buhlaiga N, Del Rincon SV, Papneja N and Miller WH Jr. 2020. A review of cancer immunotherapy: from the past, to the present, to the future. *Curr Oncol.*, **27(2)**: 87-97.

Füzi B, Mathai N, Kirchmair J and Ecker GF. 2023. Toxicity prediction using target, interactome, and pathway profiles as descriptors. *Toxicol Lett.*, **381**: 20-26.

Heikal MF, Putra WE, Sustiprijatno, Hidayatullah A, Widiastuti D and Lelitawati M. 2024. A molecular docking and dynamics simulation study on prevention of merozoite red blood cell invasion by targeting Plasmodium vivax duffy binding protein with Zingiberaceae bioactive compounds. *Uniciencia*, 38(1): 1-15.

Hidayatullah A, Putra WE, Rifa'i M, Sustiprijatno, Widiastuti D, Heikal MF, Susanto H and Salma WO. 2022. Molecular docking and dynamics simulation studies to predict multiple medicinal plants' bioactive compounds interaction and its behavior on the surface of DENV-2 E protein. *KIJOMS*, **8(3)**: 531-542.

Hidayatullah A, Putra WE, Salma WO, Muchtaromah B, Permatasari GW, Susanto H, Widiastuti D and Kismurtono M. 2020. Discovery of drug candidate from various natural products as potential novel dengue virus nonstructural protein 5 (NS5) inhibitor. *CMUJ. Nat. Sci.*, **20(1)**: 1-17.

Hidayatullah A, Putra WE, Sustiprijatno, Permatasari GW, Salma WO, Widiastuti D, Susanto H, Muchtaromah B, Sari DRT, Ningsih FN, Heikal MF, Yusuf AMR and Arizona AS. 2021. In silico targeting DENV2's prefusion envelope protein by several natural products' bioactive compounds. *CMUJ. Nat. Sci.*, **20(3)**: 1-20.

Hollingsworth SA and Dror RO. 2018. Molecular Dynamics Simulation for All. *Neuron*, **99(6)**: 1129-1143.

Koh SA. 2021. An update on immunotherapy with PD-1 and PD-L1 blockade. *Yeungnam Univ J Med.*, **38(4)**: 308-317.

Kumar A. 2020. Phytochemistry, pharmacological activities and uses of traditional medicinal plant Kaempferia galanga L. - An overview. *J Ethnopharmacol.*, **253**: 112667.

Lazarus E and Bays HE. 2022. Cancer and Obesity: An Obesity Medicine Association (OMA) Clinical Practice Statement (CPS) 2022. *Obes Pillars*, **3**: 100026.

Liu J, Chen Z, Li Y, Zhao W, Wu J and Zhang Z. 2021. PD-1/PD-L1 Checkpoint Inhibitors in Tumor Immunotherapy. *Front Pharmacol.*, **12**: 731798.

Łukasiewicz S, Czeczelewski M, Forma A, Baj J, Sitarz R and Stanisławek A. 2021. Breast Cancer-Epidemiology, Risk Factors, Classification, Prognostic Markers, and Current Treatment Strategies-An Updated Review. *Cancers (Basel)*, **13(17)**: 4287.

Marino P, Mininni M, Deiana G, Marino G, Divella R, Bochicchio I, Giuliano A, Lapadula S, Lettini AR and Sanseverino F. 2024. Healthy Lifestyle and Cancer Risk: Modifiable Risk Factors to Prevent Cancer. *Nutrients*, **16(6)**:800.

Ozvoldik K, Stockner T and Krieger E. 2023. YASARA Model-Interactive Molecular Modeling from Two Dimensions to Virtual Realities. *J Chem Inf Model.,* **63(20)**: 6177-6182.

Patil R, Das S, Stanley A, Yadav L, Sudhakar A and Varma AK. 2010. Optimized hydrophobic interactions and hydrogen bonding at the target-ligand interface leads the pathways of drug-designing. *PLoS One*, **5(8)**: e12029.

Putra WE, Agusinta AK, Ashar MSAA, Manullang VA and Rifa'i M. 2023. Immunomodulatory and ameliorative effect of Citrus limon extract on DMBA-induced breast cancer in mouse. *KIJOMS*, **9(2)**: 1-14.

Putra WE and Rifa'i M. 2019. Immunomodulatory activities of Sambucus javanica extracts in DMBA exposed BALB/c mouse. *APB*, **9(4)**: 619-623.

Putra WE and Rifa'i M. 2020. Evaluating the molecular interaction of sambucus plant bioactive compounds toward TNF-R1 and TRAIL-R1/R2 as possible anti-cancer therapy based on traditional medicine: The bioinformatics study. *Sci. Stud. Res., Chem. Chem. Eng. Biotechnol. Food Ind.*, 2020. **21(3)**: 357-365.

Putra WE, Widiastuti D, Hidayatullah A, Heikal MF, Sustiprijatno and Yusuf AMR. 2024. Molecular docking and molecular dynamics simulation study of anti-tuberculosis drug candidates from plant-derived natural products against InhA protein. *Sci. Technol. Asia*, 29(4): 291–301.

Putra WE. 2018. In silico study demonstrates multiple bioactive compounds of sambucus plant promote death cell signaling pathway via FAS receptor. *FTST*, **3(2)**: 682-685.

Reynolds KL, Arora S, Elayavilli RK, Louv WC, Schaller TH, Khandelwal A, Rothenberg M, Khozin S, Guidon AC, Dougan M, Zubiri L, Petrillo L, Sise ME, Villani AC, Johnson DB, Rahma O and Sharon E. 2021. Immune-related adverse events associated with immune checkpoint inhibitors: a call to action for collecting and sharing clinical trial and real-world data. *J Immunother Cancer*, **9(7)**: e002896.

Ruswanto R, Nofianti T, Lestari T, Septian AD, Firmansyah AP and Mardianingrum R. 2024. Potential active compounds of propolis as breast anticancer candidates: In silico study. *Jordan J. Biol. Sci.,* **17(1)**: 153-161.

Shrihastini V, Muthuramalingam P, Adarshan S, Sujitha M, Chen JT, Shin H and Ramesh M. 2021. Plant Derived Bioactive Compounds, Their Anti-Cancer Effects and In Silico Approaches as an Alternative Target Treatment Strategy for Breast Cancer: An Updated Overview. *Cancers (Basel)*, **13(24)**: 6222.

Sinha S, Tam B and Wang SM. 2022. Applications of molecular dynamics simulation in protein study. *Membranes (Basel)*, **12(9)**: 844.

Son A, Kim W, Park J, Lee W, Lee Y, Choi S and Kim H. 2024. Utilizing Molecular Dynamics Simulations, Machine Learning, Cryo-EM, and NMR Spectroscopy to Predict and Validate Protein Dynamics. *Int J Mol Sci.*, **25(17)**: 9725.

Srivastava N, Ranjana, Singh S, Gupta AC, Shanker K, Bawankule DU and Luqman S. 2019. Aromatic ginger (Kaempferia galanga L.) extracts with ameliorative and protective potential as a functional food, beyond its flavor and nutritional benefits. *Toxicol Rep.*, **6**: 521-528.

Sung H, Ferlay J, Siegel RL, Laversanne M, Soerjomataram I, Jemal A and Bray F. 2021. Global Cancer Statistics 2020: GLOBOCAN Estimates of Incidence and Mortality Worldwide for 36 Cancers in 185 Countries. *CA Cancer J Clin.*, **71(3)**:209-249.

Tan S, Li D and Zhu X. 2020. Cancer immunotherapy: Pros, cons and beyond. *Biomed Pharmacother.*, **124**: 109821.

Wang J, Ge Y and Xie XQ. 2019. Development and Testing of Druglike Screening Libraries. *J Chem Inf Model.*, **59(1)**:53-65.

Wang SY, Zhao H, Xu HT, Han XD, Wu YS, Xu FF, Yang XB, Göransson U and Liu B. 2021. Kaempferia galanga L.: Progresses in Phytochemistry, Pharmacology, Toxicology and Ethnomedicinal Uses. *Front Pharmacol.*, **12**: 675350.

Zhu W, Wang Y, Niu Y, Zhang L and Liu Z. 2023. Current Trends and Challenges in Drug-Likeness Prediction: Are They Generalizable and Interpretable? *Health Data Sci.*, **3**: 0098.

JJBS

Volume 18, Number 3,September 2025
ISSN 1995-6673
Pages 411 – 419

Jordan Journal of Biological Sciences

Analysis of EsxH Gene Mutations and Homology Modeling in *Mycobacterium tuberculosis* from Clinical Isolates in South Sulawesi

Ummi Chaera[1], Muhammad Nasrum Massi[2*], Doddy Irawan Setyo Utomo[3], Astutiati Nurhasanah[3], Nihayatul Karimah[3], Israini W. Iskandar[1], Najdah Hidayah[4], Firdaus Hamid[2], Yunialthy D. Pertiwi[2], Fadhilah[2],

[1]*Master Program of Biomedical Science Graduate School, Hasanuddin University, Makassar, 90245, South Sulawesi, Indonesia;* [2]*Department of Microbiology, Faculty of Medicine, Hasanuddin University, Makassar, 90245, South Sulawesi, Indonesia;* [3]*Research Center for Vaccines and Drugs, Health Research Organization, National Research and Innovation Agency (BRIN), Banten 15314, Indonesia;* [4]*Graduate School, Hasanuddin University, Makassar, 90245, South Sulawesi, Indonesia.*

Received: August 3, 2024; Revised: January 13, 2024; Accepted: February 2, 2025

Abstract

Introduction: Tuberculosis (TB) is a significant global public health issue, with Indonesia ranking second worldwide for the highest incidence. Despite the widespread use of the Bacillus Calmette-Guérin (BCG) vaccine, its efficacy remains limited, particularly in preventing the reactivation of latent TB infections in adults. Moreover, *Mycobacterium tuberculosis* (*Mtb*), the causative agent of TB, exhibits considerable genetic diversity, which can influence the virulence, transmissibility, and resistance to treatment. The EsxH gene, part of the ESX-3 secretion system, plays a crucial role in the virulence and immune evasion mechanisms of *Mtb*. Methods and Materials: A total of 40 *Mtb*-positive isolates from South Sulawesi, Indonesia, were used. Samples were analyzed using molecular detection techniques in accordance with the standard procedures. The EsxH gene was amplified using specific primers via polymerase chain reaction (PCR), purified, and Sanger sequencing. Nucleotide variations were identified using Unipro UGENE, and phylogenetic analysis was conducted to explore the evolutionary relationship as well as the uniqueness of mutations. Additionally, the structural impact of the identified mutations was analyzed using the SWISS-MODEL server by comparing the three-dimensional (3D) models of the EsxH protein with and without mutations to assess any significant structural changes.

Results: The study identified unique mutations in the EsxH gene of *Mtb* isolates from South Sulawesi, specifically at nucleotide positions 28 G>A and 29 C>T, leading to amino acid changes at position 10 (alanine to threonine and alanine to valine). Phylogenetic analysis indicated that these mutations were distinct from the region, while 3D homology modeling showed no significant structural changes. Conclusion: This study contributes to the understanding of *M. tuberculosis* genetic diversity in South Sulawesi by identifying region-specific mutations in the EsxH gene. While these mutations did not result in major structural alterations to the EsxH protein, further bioinformatic and in vitro studies are needed to explore their functional implications. These findings underscore the importance of continued surveillance and research to improve TB control strategies, as well as to inform the development of more effective vaccines and treatments.

Keywords: *Mycobacterium tuberculosis*, genetic diversity, mutation, EsxH, Homology modeling

1. Introduction

Tuberculosis (TB) is considered a highly significant global emergency. According to World Health Organization (WHO) data in 2021, an estimated 10.6 million people worldwide suffer from the disease (WHO, 2022). Indonesia ranked second among countries with the highest incidence of tuberculosis in the world after India in 2019. The 2021 Global TB Report also reported 824,000 TB cases (Ministry of Health, 2022). Patients with TB infection have a 5-10% lifetime risk of developing the disease, which increases in various immunodeficiency states to a 16% annual risk (Gill et al, 2022).

The most effective approach to controlling TB in humans entails administering the *Bacillus Calmette-Guérin* (BCG) vaccine. It triggers a strong Th1 immune response and supports the formation of T cells specific to mycobacteria, which are both polyfunctional and cytotoxic. However, BCG vaccine is known to be ineffective in protecting adults and may reactivate latent TB infection (Singh et al., 2022)

The infection process of *Mycobacterium tuberculosis* (*Mtb*) relies on the capacity to interact with the immune system in various ways, including evading the innate immune response, enduring the adaptive immune response without leading to symptomatic illness, and inducing disease. A strong inflammatory reaction leads to significant tissue damage, which facilitates transmission (Chandra et al., 2022)

Mycobacteria use a type VII secretion system (T7S) to transport proteins across intricate cell envelopes, of which

* Corresponding author. e-mail: nasrumm@unhas.ac.id.

there are more than five excretion systems from ESX-1 to ESX-5 known to be associated with *Mtb* host-pathogen interactions. This secreted protein is one of the immunodominant antigens best known to the human immune system. Several antigens that have been identified include the Esx family proteins, including EsxA, EsxB, EsxG, EsxH, EsxG, and EsxN. The ESX family proteins, TB10.4 (EsxH), have been found to possess similar characteristics in terms of immune recognition during infection and protective efficacy in TB vaccines. EsxH is known to disrupt the recognition of infected macrophages by CD4+ T cells. The *EsxH* gene encodes the TB10.4 protein, which elicits CD4 and CD8 T cell responses in both humans and mice. It is part of a vaccine that is currently in clinical trials (Darrah et al., 2019).

Studies on mutational variations in the EsxH protein remain limited. The protective efficacy of EsxH subunit vaccines might be compromised on the global stage. In the research conducted by Davilla et al. (2010), no DNA variations were found in 88 samples tested, meaning the EsxH gene is highly conserved. Therefore, the results suggest that the efficacy of TB10.4 vaccines is unlikely to be affected by the genetic diversity of the *M. tuberculosis* population. However, further research is needed that includes a broader range of *M. tuberculosis* strains to validate this finding.

Building upon this, our research aimed to identify sequence variations in the EsxH antigen coding gene in clinical isolates of *Mtb* from South Sulawesi, Indonesia. The potential ability of these mutations to affect amino acid sequences was also evaluated. In addition, phylogenetic analysis was carried out to determine the evolutionary relationships between *Mtb* strains and genetic diversity in certain populations or species. This study used a simple in silico method with a three-dimensional (3D) structural homology model of the EsxH protein through the SWISS-MODEL server. Information about the 3D structure of proteins can facilitate the development of structure-based studies, including the nature and structure, mechanisms of interaction with other compounds through molecular docking, as well as virtual drug screening related to the EsxH protein.

Information regarding the EsxH gene mutations in the *Mtb* population in Indonesia is important to be further investigated, as it can serve as a foundation for consideration in designing an appropriate TB vaccine. We expected to provide valuable insights into the genetic diversity of *Mycobacterium tuberculosis* (*Mtb*) and identify the potential of EsxH as a key target in the development of innovative TB vaccines, by integrating genomic, structural, and phylogenetic data.

2. Methods and Materials

2.1. Genomic DNA Cultivation and Isolation

This study used 40 clinical samples obtained from TB patients at the HUMR laboratory. The aim of isolating *Mtb* genomic DNA was to obtain the EsxH gene. The *Mtb* culture was then used for genome isolation using the gSYNC DNA extraction kit.

2.2. DNA Purification

After genome extraction, the sample was purified using the Sbeadex Pathogen Nucleic Acid Purification Kit. A 100 µl aliquot was combined with 20 µl of Sbeadex particles and 160 µl of binding buffer, then incubated at room temperature with constant shaking for 5 minutes. A magnet was used for 2 minutes to separate the supernatant. Following this, 400 µl of wash buffer BN1 was added, incubated for 5 minutes with shaking, and separated with the magnet. The sample was further washed with 400 µl each of wash buffers TN1 and TN2. Finally, 100 µl of elution buffer was added, incubated for 10 minutes at 60°C with shaking and placed near the magnet for 3 minutes before transferring the eluate to a new tube.

2.3. Amplification of the EsxH Gene of Mycobacterium tuberculosis using PCR.

Mtb DNA amplification was carried out using a PCR mixture that included 6.25 µl of redmix enzyme, 0.5µl of each forward and reverse primers, 2.75µl of ddH2O, as well as 2.5µl of DNA sample. The negative control used nuclease-free water, while the primers used were EscGH-F-Sukkhu (5' GACCGCAACCAAAGAAC-3') and EscGH-R-Sukkhu (5' CCAGCACCCACGGAAAG-3'), targeting a 951 bp region. The PCR procedure consisted of 35 cycles with initial denaturation at 95°C for 1 minute, followed by denaturation at 95°C for 15 seconds, annealing at 55°C for 15 seconds, extension at 72°C for 20 seconds, and a final extension at 72°C for 2 minutes before cooling to 4°C.

2.4. Electrophoresis

Agarose gel electrophoresis was carried out using a 1% agarose gel, prepared by dissolving 1 g of agarose in 50 ml of 0.5% TBE buffer, heating in the microwave for 1 minute, followed by cooling for 30 minutes. About 4µl of SybrSafe DNA Gel Stain was added, mixed, and poured into a gel mold. The gel was left to solidify before being placed in an electrophoresis chamber with 0.5% TBE buffer. Subsequently, wells were loaded with 4 µl of negative control, 2.5µl of DNA marker, and 4µl of the DNA sample. Electrophoresis was then performed at 80 volts for 60 minutes. The results were analyzed using a 100 bp and 1 kb gene ruler, which confirmed the presence of the expected 951 bp amplified gene fragments for EsxH.

2.5. Sanger Sequencing

Sequencing of PCR results was carried out using the Sanger DNA sequencing method. Sample preparation started with DNA Polymerase, Primer, dNTPs, and ddNTPs which were added to the amplified DNA sample. This was followed by heating to a temperature of 90˚C to trigger DNA denaturation and polymerization. Subsequently, the sample was placed into an electrophoresis machine and the waves captured by the detector were analyzed.

2.6. Phylogenetic analysis

The phylogenetic analysis used Mega Software, running in 500 and 1000 bootstrap to observe the comparison between a mutation in this study and other lineages from NCBI.

2.7. Homology analysis using Swiss Model

Homology modeling is a method used to predict the 3D structure of proteins by comparing and aligning the amino acid sequence with others. This sequence information was used to generate a 3D protein structure model using the SWISS-MODEL server (https://swissmodel.expasy.org/).

Protein sequences were transferred from the Unipro UGENE server to SWISS-MODEL in FASTA format.

3. Results

3.1. Gene Amplification

The results of amplification using Polymerase Chain Reaction (PCR) to detect the presence of EsxH genes were read using agar gel electrophoresis which showed the amplified gene fragment with a target size of 951 bp for 40 samples. As shown in Figure 1, the amplification results showed a clear DNA band in each sample, with a corresponding target size of 951 bp. The results indicate that the sample is ready to proceed to the sequencing stage.

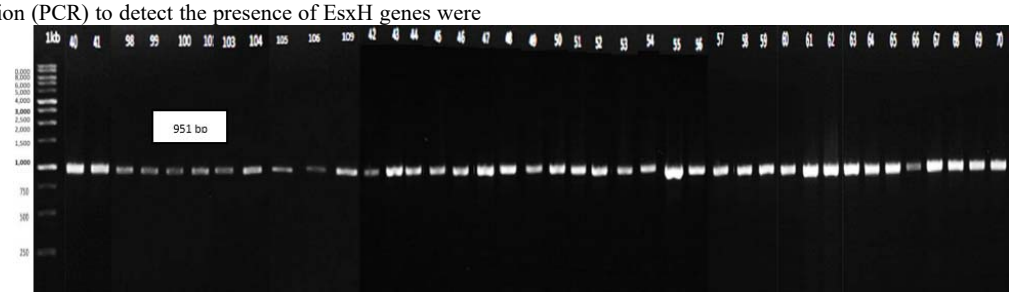

Figure 1. Gene electrophoresis in 40 clinical isolates of *Mtb* EsxH

3.2. Mutation Analysis of Sequencing Sequence Results

After obtaining the amplification results, Sanger sequencing was carried out on 40 samples. The alignment results used the Unipro UGENE application and several DNA variation points were found in the EsxH target gene. As shown in Figure 2, two mutations were found in DNA with sample codes 11X and 30X. These mutations correspond to variations in the EsxH gene with a base change from G to A (Guanine to Adenine) in sample 11X at nucleotide position 28 as well as base C to T (Cytosine to Thymine) in nucleotide position 29 in the 30X sample with a percentage of 2.4% each. The changes in the two samples affected substitutions at the amino acid level, where alterations were found at the 10th amino acid position from Alanine to Threonine in sample code 11X and Alanine to Valine in sample code 30X. (Figure 3)

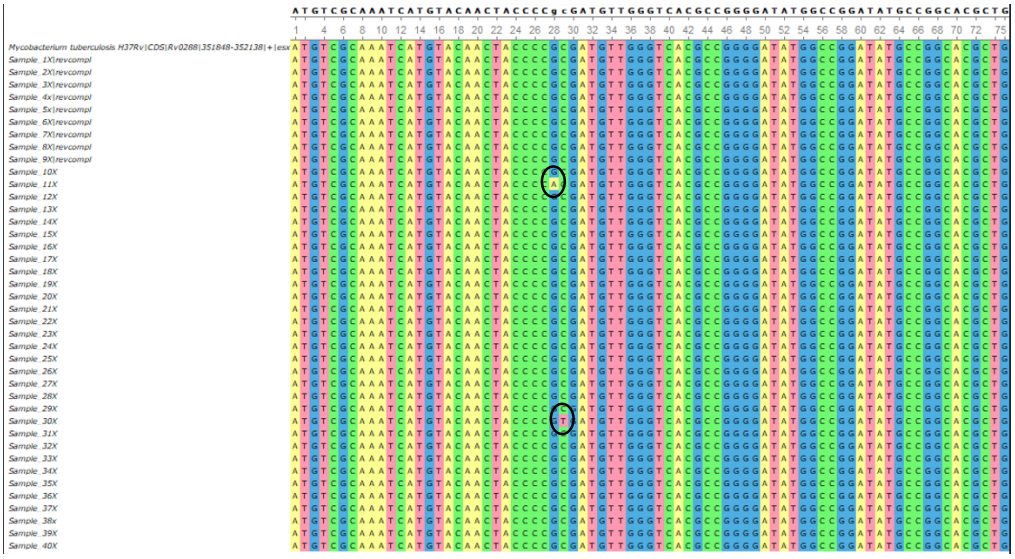

Figure 2. Substitution of nucleotide codon G>A at position 28 and C>T at position 29 of the EsxH gene

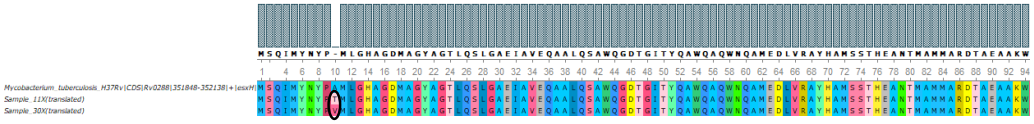

Figure 3. Amino acid substitution at position 10 from Alanine to Threonine with code sample 11X and sample Alanine to Valine sample 30X

The overall variations in the target genes are shown in Table 1. The existence of several variations in these target genes indicates that there are several sequence variations in the *Mtb* clinical isolates.

Table 1. Mutation analysis results of EsxH

Isolate code	H37Rv Nucleotide	Isolate Nucleotide	Mutation sites	Amino acid Change	Percentage
Sample 11X	G	A	28G>A	Ala10Thr	2.4%
Sample 30X	C	Q	29C>T	Ala10Val	2.4%

Ala: Alanine; Thr: Threonine; Val: Valine

3.3. Phylogenetic

In this study, clinical samples of *M. tuberculosis* isolates from around the city of Makassar were screened to obtain genetic information that can be used as reference material for developing TB treatment. A total of 40 samples were obtained for each EsxH gene. The sequencing results showed that the target gene has variations at certain positions, observed phylogenetically to determine the evolutionary relationship. A phylogenetic tree was constructed based on the genetic sequence of the EsxH gene. In this analysis, sequences from clinical samples were compared with reference sequences from strain H37Rv to identify patterns of divergence and evolutionary clusters.

The phylogenetic tree was carried out using the Maximum likelihood (ML) method to ensure consistency of results. The sequences were aligned using the Muscle and ClustalW programs, then a phylogenetic tree was generated with MEGA (Molecular Evolutionary Genetics Analysis) software version 11.0.13. Additionally, bootstrap analysis was performed with 500 and 1000 replications.

Before analyzing the phylogenetic tree, this study first identified the lineage for *Mtb*. Sequences belonging to this lineage were also included in the alignment stage together with samples and reference H37Rv. The data and reference lineage sources for *Mtb* are from the NCBI database.

- L1_1_3→>NZ_CP054014.1 *Mycobacterium tuberculosis* strain FDAARGOS_756 chromosome, complete genome

  (https://www.ncbi.nlm.nih.gov/nuccore/NZ_CP054014.1)
- L1→>NZ_CP040689.1 *Mycobacterium tuberculosis* complex sp. N0072 chromosome, complete genome (https://www.ncbi.nlm.nih.gov/nuccore/NZ_CP040689.1)
- L2→>CP005082.1 *Mycobacterium tuberculosis* str. Beijing/NITR203, complete genome (https://www.ncbi.nlm.nih.gov/nuccore/CP005082.1)
- L3→>NZ_CP028428.1 *Mycobacterium tuberculosis* strain CAS chromosome (https://www.ncbi.nlm.nih.gov/nuccore/NZ_CP028428.1)
- L4→>NC_022350.1 *Mycobacterium tuberculosis* str. Haarlem, complete sequence (https://www.ncbi.nlm.nih.gov/nuccore/NZ_JLDE00000000.1)
- L5→>KK338837.1 Mycobacterium africanum MAL010074 whole genome sequence (https://www.ncbi.nlm.nih.gov/nuccore/KK338837.1)
- L6→>CP010334.1 *Mycobacterium tuberculosis* variant africanum strain 25, complete genome (https://www.ncbi.nlm.nih.gov/nuccore/CP010334.1)

The alignment results for the EsxH gene (Figure 4) showed that, across all lineages, no variation sites were identical to those observed in the 11X and 30X samples at the nucleotide or amino acid level. Furthermore, in the phylogenetic tree (Figure 4.c) with 500 bootstraps, samples "11X" and "30X" were on the same branch as "CP010334.1 africanum strain 25". The bootstrap value for the branch connecting “11X” and “30X” was 37, indicating a relatively low level of confidence in this relationship. In the tree with 1000 bootstraps (Figure 4.d), samples “11X” and “30X” were also on the same branch as “CP010334.1 africanum strain 25”. The bootstrap value for the branch connecting “11X” and “30X” was 58, indicating increased confidence in this relationship compared to a tree with 500 bootstraps.

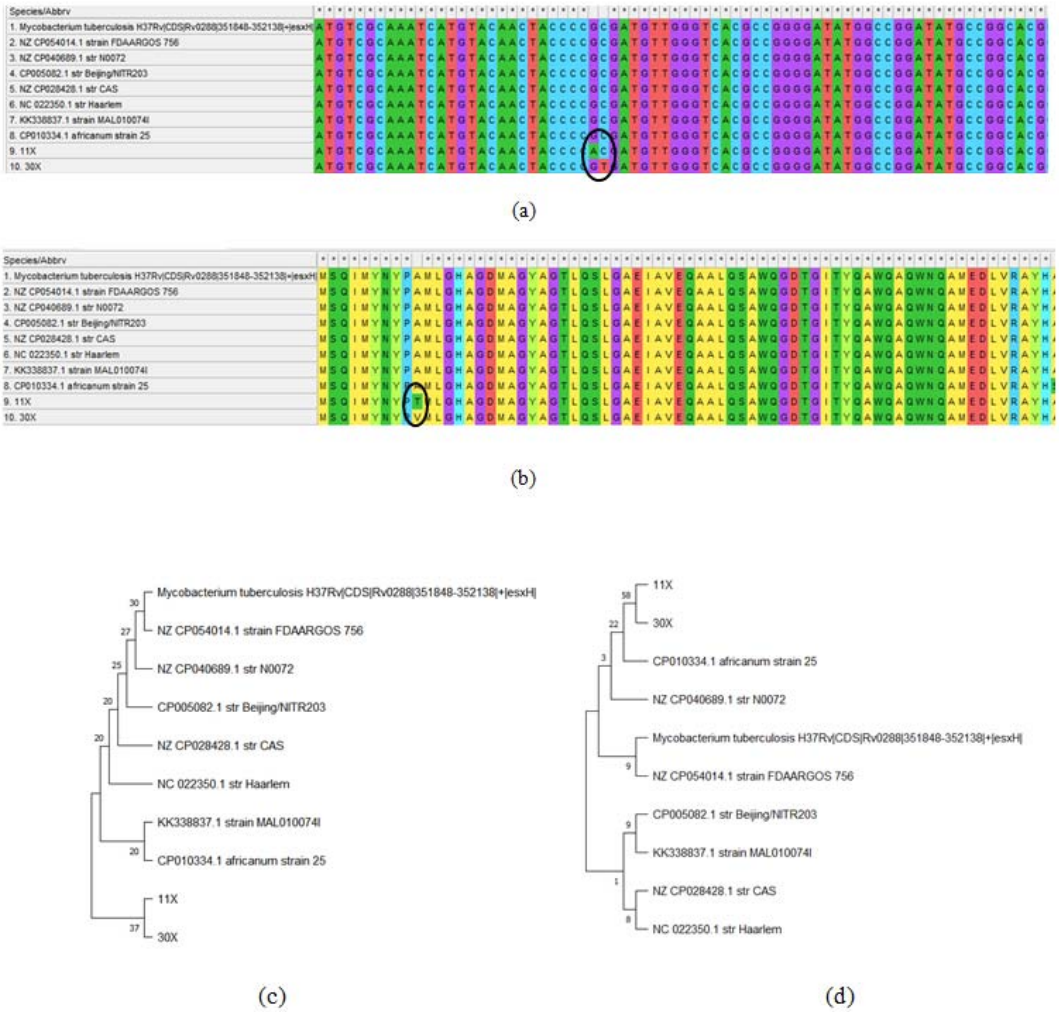

Figure 4. Alignment results of the EsxH gene with the reference gene at the variation point (a) Nucleotide positions 28 and 29 (b) Amino acid position 10 (c) Maximum likelihood phylogenetic tree 500 bootstrap (d) Maximum-likelihood phylogenetic tree 1000 bootstrap.

3.4. Homology Modelling using SWISS-MODEL

The 3D structure of proteins largely determines molecular biochemical properties and functions. In this study, analysis of changes in protein structure was carried out to understand how the mutations identified in the EsxH gene affect the 3D structure. Homology modeling is a technique used to predict the 3D structure of proteins by aligning the amino acid sequence with those of other proteins. Generally, a protein with a recognized 3D structure is called a template. Proteins whose amino acid sequences are related have similar structures. This sequence data was used to create a 3D protein structure model using the SWISS-MODEL server. Copying protein sequences from the Unipro UGENE server to the SWISS-MODEL server was carried out using the FASTA format as in Table 2.

Table 2. Protein target sequence of Esxh

EsxH	MSQIMYNYPAMLGHAGDMAGYAGTLQSLGAEIAVEQAALQSAWQGDTGITYQAWQAQWNQAMEDLVRAYHAMSSTH
Reference	EANTMAMMARDTA EAAKWGGX
11X	MSQIMYNYPTMLGHAGDMAGYAGTLQSLGAEIAVEQAALQSAWQGDTGITYQAWQAQWNQAMEDLVRAYHAMSSTHE ANTMAMMARDTAEAAKWGG
30X	MSQIMYNYPVMLGHAGDMAGYAGTLQSLGAEIAVEQAALQSAWQGDTGITYQAWQAQWNQAMEDLVRAYHAMSSTH EANTMAMMARDTAEAAKWGG

The target protein sequence of EsxH, provided in FASTA format as shown in Figure 1 was submitted to the SWISS-MODEL server (https://swissmodel.expasy.org/). The server then automatically constructed the model using the suitable template. Subsequently, three types of structure models appeared, and the structure with the

coverage value closest to the reference template was selected. In this study, 3D modeling was carried out for samples that had mutations in the EsxH gene. The results showed that model 2 for samples 11X and 30X had the highest coverage among the other two models with the same value, namely 98.96% with the reference template 2kg7.1.BESAT-6-like protein EsxH. (Figure 5)

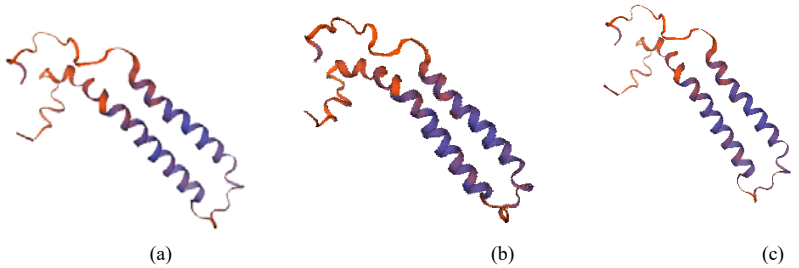

Figure 5. Model structure (a) EsxH reference, (b) 11X (c) 30X

To obtain information regarding the suitability of the model structure that has been obtained, this study also analyzed the protein structure using the Ramachandran Plot to determine the suitability of amino acids position in the protein structure. Figure 6 shows Ramachandran plot results for all EsxH reference protein structures in samples 11X and 30X. The reference structure shows Ramachandran Favored with a value of 89.36% and Ramachandran Outliers. The plot image for each protein structure shows that the amino acids in the protein are in the appropriate area, specifically in the light-dark green zone. The protein structure that has been created in the SWISS-Model has good confidence to be used in the next analysis stage.

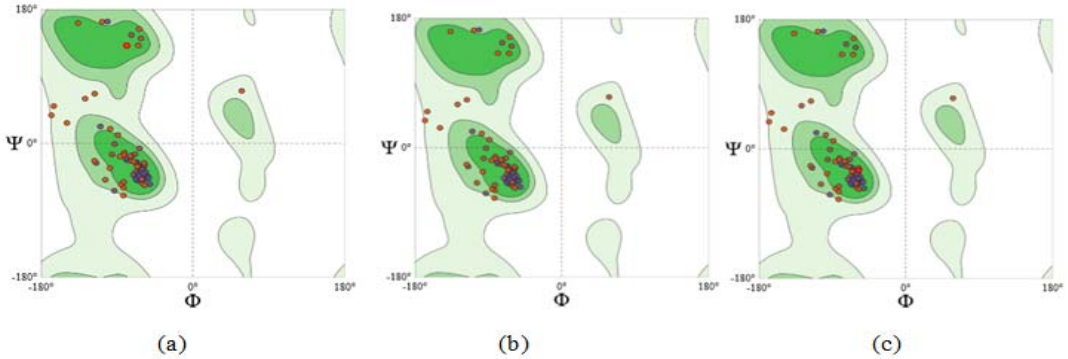

Figure 6. Ramachandran plot on the amino acid protein structure model (a) 11X (b) 30X, (c) Reference EsxH

The variation point in the 10th amino acid sequence did not significantly affect changes in the structure of the protein as a whole when observed from the visualization of the variation position of each amino acid obtained. The first amino acid change of 11X, the reference H37Rv structure is shown in Figure 7.c for the amino acid Alanine (pink).

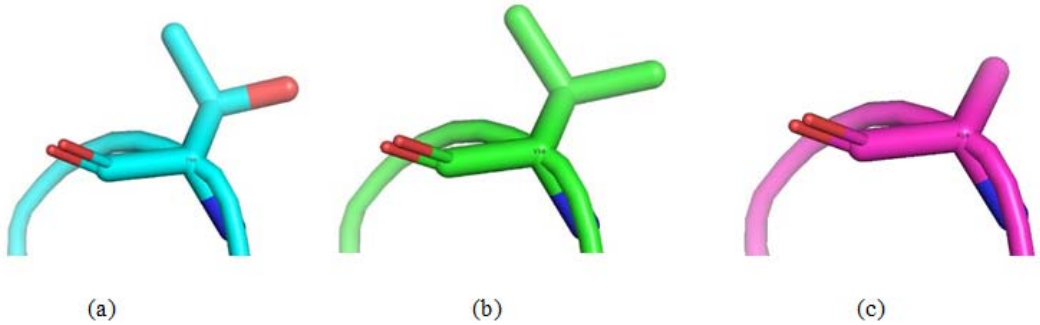

Figure 7. Visualization of the variation position of each amino acid in the protein structure model showing 2 amino acid variation points at (a) 11X (b) 30X, and the reference protein (c) EsxH H37Rv (pink)

4. Discussion

Among the 40 samples isolated, there were nucleotide changes in the EsxH gene with substitutions of G>A (Guanine to Adenine) in the 11X and C>T (Cytosine to Thymine) in the 30X sample with a percentage of 2.4% each. Nucleotide substitution in the two samples was at the amino acid level. The substitution was found at the 10th amino acid position with a change in the amino acid

Alanine to Threonine in the 11X sample and Alanine to Valine in the 30X sample.

Previous studies found that C>T and G>A mutations in clinical isolates of *Mtb* were related to oxidative stress mechanisms. Increased mutation rates were observed in patients with positive smears who showed a higher number of de novo single-nucleotide polymorphisms (SNPs) in *Mtb*, especially C>T mutations, indicating oxidative damage and increased oxidative stress in patients. This study found that increased mutation rate is host-dependent, rather than an inherent characteristic of the *Mtb* strain, linking variation in mutation rates to the host immune response as well as the production and regulation of reactive oxygen species (ROS). Oxidative damage was identified as the main source of mutations, with a significant proportion being C>T transitions. Additionally, *Mtb* samples from HIV-positive hosts had a higher C>T mutation ratio compared to HIV-negative hosts, emphasizing the influence of host immune status on mutation rates(Ly and Liu, 2020)

The balance between ROS and antioxidants may play a significant role in the onset and progression of diseases, particularly those affecting the respiratory system (Crusio and Radeke, 2019). Macrophages are crucial for maintaining tissue homeostasis and responding to pathogenic threats. According to a study, macrophages infected with *Mtb* produce ROS, which might have effects against TB (Shastri et al., 2018). Advancements in antioxidant drug studies could also offer new opportunities to reduce oxidative damage and enhance treatment(Su et al., 2023).

EsxG/EsxH is known to directly interact with host endosomal sorting complexes that are crucial for protein transport, thereby inhibiting phagosome maturation and antigen presentation during *Mtb* infection of macrophages. This gene, secreted through the ESX-3 type VII secretion system, specifically inhibits the endosomal sorting complex required for transport (ESCRT) machinery. Studies on overexpression and loss-of-function show that EsxH impedes the ability of macrophages and dendritic cells to activate CD4+ T cells specific to *Mtb* antigens. The EsxH protein, part of the ESX-3 cluster, plays a critical role in bacteria survival by regulating iron and zinc homeostasis (Portal-Celhay et al., 2016) (Ates et al., 2016)

The exact function of EsxH clusters is not yet completely understood, but studies indicate that EsxG and EsxH may be crucial in mediating interactions with host cells and assisting in nutrient acquisition. The complex is implicated in metal uptake, drug resistance, and evasion of the immune response, making it a promising target for targeted vaccine development (Martinez-Olivares, 2023)

Based on a previous study (Sutiwisesak et al., 2020) *Mtb* natural polymorphism in the EsxH gene disrupts immunodominance by TB10.4-specific CD8 T cell responses. Mice infected with the *Mtb* strain showed changes, where the response of CD8 T cells which normally recognize and fight bacteria was altered. The TB10.44-11 epitope, typically recognized by CD8 T cells, was no longer detected following infection with a strain that has A10T mutation. In contrast, the response to other parts of the bacteria, previously thought to be less strong than the primary response, was increased. This result is quite interesting because although both versions of the TB10.44-11 epitope (A10T and Wild Type versions) tested have the same ability to bind KB proteins and stimulate T cells, the changes affect how the immune response to *Mtb* infection occurs.

Polymorphism A10V in the esxH gene of *Mtb* has been found to play a significant role in immunogenicity. This polymorphism evolved independently three times and was present in one group of four and two unrelated isolates. Although the A10T variant was more abundant, found in 41 isolates, the A10V polymorphism was less. It changes the hierarchy of CD8 T cell responses specific to the antigen, influencing the immune response to *Mtb* infection.

Amino acids are fundamental building blocks in living organisms. Aside from the role in protein synthesis, amino acids are crucial nutrients for host immune cells, aiding in intracellular metabolic processes such as ATP synthesis, nucleotide production, and maintaining redox balance. Amino acids also provide the primary source of nitrogen for *Mtb*, including alanine and valine. Although *Mtb* can absorb all amino acids, it primarily takes up and rapidly metabolizes glutamate (Glu), glutamine (Gln), aspartate (Asp), asparagine (Asn), and alanine (Ala) as the main nitrogen sources (Agapova et al., 2019.) (Amalia et al., 2022).

Alanine dehydrogenase can suppress host immunity, offering valuable insights for the development of effective immunomodulators targeting *Mtb* (Peng et al., 2024). Substitutions from alanine to threonine (A to T), caused by SNPs, occur in various proteins. In some instances, these substitutions lead to the formation of amyloid fibrils or the aggregation of amyloidogenic proteins (Podoly et al., 2010).

Several studies have been conducted on the early functional analysis of EsxH using in silico methods. However, there has been no discussion on the impact of mutations in the EsxH gene on epitope affinity for TB vaccine development. A study by Ramaiah et al. (2019) evaluated the mutation patterns of specific T-cell epitopes in *Mycobacterium tuberculosis* (*Mtb*) accumulated in *Mtb* strains from India. The study identified 64 mutated T-cell epitopes (mTCE) from 79 strains. These mutations involved significant single amino acid changes, most of which affected the binding affinity of the HLA-DR molecule. Mutations that enhanced epitope function exhibited higher HLA-DR binding affinity, while mutations that diminished function resulted in lower affinity. Predictive analysis using IEDB-based tools revealed a strong correlation between changes in binding affinity and the functional impact on immune responses. Functionally, 62% of the tested mTCEs showed significant alterations in IFN-γ and/or IL-2 secretion by CD4 T-cells, with some mutations enhancing the immune response, while others reduced it.

Based on information from identifying variations in genes, a phylogenetic tree was identified to determine the relationship between the variation points found in the sample along with the reference gene H37Rv and several lineages. The phylogenetic tree shows that there were points of variation in the samples tested, but no similar mutations were found in other lineages. Genetic polymorphisms that vary between species and within genomes have important implications for the evolution and conservation of species. According to a previous study, genetic polymorphisms found in a species have been

influenced by demographic history (Ellegren & Galtier, 2016)

Several specific polymorphisms in a species have been studied, such as the substitution of the Ala71Ser amino acid change in EsxH, commonly found in *M. Africanum* strains. The 3D structure of the EsxH complex has been studied using NMR spectroscopy. The contact surface between EsxG and EsxH is essentially hydrophobic (water-repellent), and the Ala71 residue is located at the interface between the molecules in the EsxH complex, near Met72, which, together with Met18, forms the base of the groove. The conservative Ala71Ser substitution in *M. africanum* likely disrupts these hydrophobic interactions (Yruela et al., 2016). However, there has been no further discussion about the mutations occurring in the two isolates, making it a novel finding in vaccine development.

For example, studies on *Mtb*32A, *Mtb*39A, *Mtb*72F, and M72 as vaccine candidates show that these genes have a high degree of identity among different *Mtb* strains. This high identity suggests the genes are relatively stable and do not vary significantly, which is important for vaccine development because the targets tend to persist across strains. The genetic stability suggests vaccines developed from these genes may be effective against multiple *Mtb* variants, reducing the risk of mutations that could cause the vaccine to be less effective. Therefore, genes that show little or no variation between lineage could be promising targets for vaccines (Mortier et al., 2015)

Homology modeling has become a crucial method in structural biology, greatly helping to bridge the gap between known protein sequences and experimentally determined structures. This technique predicts a protein 3D structure by using the amino acid sequence and similarity to other proteins with established structures. SWISS-MODEL is a server used for automatic protein homology modeling (Waterhouse et al., 2018)

The results from the 3D homology modeling visualization showed that structurally, the differences in amino acids in the EsxH gene did not significantly change the overall structure of the protein. The modeling results have also been confirmed regarding the suitability of the position of each amino acid based on Ramachandran calculations. The plot indicates that a protein has high structural quality when there are generally more amino acid residues in the favored regions compared to those in the outlier regions. The results obtained for the EsxH gene have more favorable values than the outlier, suggesting the model can be considered quite good (Park et al., 2023).

5. Conclusion

This study analyzed the genetic diversity of *Mycobacterium tuberculosis* strains from South Sulawesi, Indonesia, focusing on their EsxH gene mutations and implications. The present study showed a unique nucleotide variation at positions 28 G>A and 29 C>T, leading to amino acid substitutions at position 10 (Alanine to Threonine and Alanine to Valine). Phylogenetic analysis of these mutations has shown that this is region-specific and different from previously reported lineages. Structural modelling using SWISS-MODEL server revealed no significant changes in the EsxH protein structure; however the functional implications of these mutations for immune evasion and vaccine design are still to be investigated.

These findings underscore the necessity of further strengthening our efforts in genomic surveillance and molecular studies of diversity in *Mtb* in Indonesia. The comprehensive functional assay and immunological review have yet to be addressed accordingly in these results. Further, bioinformatics analysis and in vitro testing are needed to delineate the effect of these alterations on cell epitopes.

Acknowledgments

The authors are grateful to the National Research and Innovation Agency (Kemenristek/BRIN) and StudiBio for providing computational resources and support during the study.

Source of Funding

This study was funded by the National Research and Innovation Agency (BRIN) under the Research and Innovation for Advanced Indonesia (RIIM) grant, No. 12/II.7/HK/2023, as well as the Health Research Organizations grant for 2023, No. 23/III.9/HK/2023.

Conflict of Interest

The authors declare that there is no conflict of interest or personal relationships.

Ethical Approval

This study protocol adheres to the Declaration of Helsinki and received approval from the Health Research Ethics Committee at the Faculty of Medicine, Hasanuddin University (No. 678/UN4.6.4.5.31/PP36/2023, September 13, 2023). All participants provided written informed consent to take part in the study.

Data Availability

The *Mycobacterium tuberculosis* EsxH gene sequences used in this study have been deposited in the GenBank database and are publicly available at https://www.ncbi.nlm.nih.gov/genbank/ with accession numbers:
BankIt2921642 M.tuberculosis_EsxH_isolate_19x PV074341
BankIt2921642 M.tuberculosis_EsxH_isolate_42x PV074342

References

Agapova, A., Serafini, A., Petridis, M., Hunt, D. M., Garza-Garcia, A., Sohaskey, C. D., & Pedro Só rio de Carvalho, L. 2019. Flexible nitrogen utilization by the metabolic generalist pathogen Mycobacterium tuberculosis. e*life*, **8:**1-22

Amalia, F., Syamsunarno, M. R. A. A., Triatin, R. D., Fatimah, S. N., Chaidir, L., & Achmad, T. H. 2022. The Role of Amino Acids in Tuberculosis Infection: A Literature Review. *Metabolites.,* **12(10)**: 1-13

Ates, L. S., Houben, E. N. G., & Bitter, W. 2016. Type VII Secretion: A Highly Versatile Secretion System. *Microbiol Spectr*. **4(1)**: 1-21

Chandra, P., Grigsby, S. J., & Philips, J. A. 2022. Immune evasion and provocation by Mycobacterium tuberculosis. *Nat Rev Microbiol*. **20(12)**: 750-766.

Crusio, W. E., & Radeke, H. H. 2019. **Advances in Experimental Medicine and Biology** Volume 1304 Series Editors. USA

Darrah, P. A., DiFazio, R. M., Maiello, P., Gideon, H. P., Myers, A. J., Rodgers, M.A., Hackney, J. A., Lindenstrom, T., Evans, T., Scanga, C. A., Prikhodko, V.,Andersen, P., Lin, P. L., Laddy, D., Roederer, M., Seder, R. A., & Flynn, J. A. L.2019. Boosting BCG with proteins or rAd5 does not enhance protection against tuberculosis in rhesus macaques. *NPJ Vaccines*. **4(1)** : 1-13

Davila, J., Zhang, L., Marrs, C. F., Durmaz, R., & Yang, Z. 2010. Assessment of the Genetic Diversity of *Mycobacterium tuberculosis* esxA, esxH, and fbpB Genes among Clinical Isolates and Its Implication for the Future Immunization by New Tuberculosis Subunit Vaccines Ag85B-ESAT-6 and Ag85B-TB10. 4. *Biomed Res Int*. **2010(1)**:1-8.

Ellegren, H., and Galtier, N. 2016. Determinants of genetic diversity. *Nat Rev Genet*. **17(7)**:1-12

Martinez-Olivares, C. E., Hernández-Pando, R., & Mixcoha, E. 2023. In silicoEsxG EsxH rational epitope selection: Candidate epitopes for vaccine designagainst pulmonary tuberculosis. *Plos one*. **18(4)**:1-27

Ly, A., and Liu, J. 2020. Mycobacterial virulence factors: Surface-exposed lipids and secreted proteins. *Int J Mol Sci*. **21(11)**:1-14.

Mortier, M. C., Jongert, E., Mettens, P., & Ruelle, J. L. 2015. Sequence conservation analysis and in silico human leukocyte antigen-peptide binding predictions for the *Mtb*72F and M72 tuberculosis candidate vaccine antigens. *BMC Immunol*. **16(1)**:1-14

Park, S. W., Lee, B. H., Song, S. H., & Kim, M. K. 2023. Revisiting the Ramachandran plot based on statistical analysis of static and dynamic characteristics of protein structures. *J Struct Biol*. **215(1)**:1-10

Peng, C., Cheng, Y., Ma, M., Chen, Q., Duan, Y., Liu, S., Cheng, H., Yang, H.,Huang, J., Bu, W., Shi, C., Wu, X., Chen, J., Zheng, R., Liu, Z., Ji, Z., Wang, J.,Huang, X., Wang, P., Wang, L. 2024. *Mycobacterium tuberculosis* suppresses host antimicrobial peptides by dehydrogenating L-alanine. *Nat Commun*. **15(1)**:1-19

Podoly, E., Hanin, G., & Soreq, H. 2010. Alanine-to-threonine substitutions and amyloid diseases: Butyrylcholinesterase as a case study. *Chem-Biol Interact*. **187(1)**:64–71.

Portal-Celhay, C., Tufariello, J. M., Srivastava, S., Zahra, A., Klevorn, T., Grace, P. S., Mehra, A., Park, H. S., Ernst, J. D., Jacobs, W. R., & Philips, J. A. 2016. *Mycobacterium tuberculosis* EsxH inhibits ESCRT-dependent CD4+ T-cell activation. *Nat Microbiol*. **2(2)**:1-22.

Ramaiah, A., Nayak, S., Rakshit, S., Manson, A. L., Abeel, T., Shanmugam, S., Sahoo, P. N., John, A. J. U. K., Sundaramurthi, J. C., Narayanan, S., D'Souza, G., Von Hoegen, P., Ottenhoff, T. H. M., Swaminathan, S., Earl, A. M., & Vyakarnam, 2019. Evidence for highly variable, region-specific patterns of T-cell epitope mutations accumulating in *Mycobacterium tuberculosis* strains. *Front in immunol*. **10(195)**:1-18

Shastri, M. D., Shukla, S. D., Chong, W. C., Dua, K., Peterson, G. M., Patel, R. P.,Hansbro, P. M., Eri, R., & O'Toole, R. F. 2018. Role of oxidative stress in the pathology and management of human tuberculosis. *Oxid Med Cell Longev.*. **1**:1-10

Singh, S., Saavedra-Avila, N. A., Tiwari, S., & Porcelli, S. A. 2022. A century of BCG vaccination: Immune mechanisms, animal models, non-traditional routes and implications for COVID-19. *Front Immunol*. **13**:1-22

Su, R., Yuan, J., Gao, T., Liu, Y., Shu, W., Wang, Y., Pang, Y., & Li, Q. 2023.Selection and validation of genes related to oxidative stress production and clearance in macrophages infected with Mycobacterium tuberculosis. *Front Cell Infect Microbiol*. **13**:1-13

Sutiwisesak, R., Hicks, N. D., Boyce, S., Murphy, K. C., Papavinasasundaram, K., Carpenter, S. M., Boucau, J., Joshi, N., Le Gall, S., Fortune, S. M., Sassetti, C. M.,and Behar, S. M. 2020. A natural polymorphism of *Mycobacterium tuberculosis* in the esxH gene disrupts immunodomination by the TB10.4-specific CD8 T cell response. *PLoS Pathog*. **16(10)**:1-29

Waterhouse, A., Bertoni, M., Bienert, S., Studer, G., Tauriello, G., Gumienny, R., Heer, F. T., De Beer, T. A. P., Rempfer, C., Bordoli, L., Lepore, R., and Schwede, T. 2018. SWISS-MODEL: Homology modelling of protein structures and complexes. *Nucleic Acids Res*., **46**:1-8

World Health Organization. 2022. **Global Tuberculosis Report 2022**. World Health Organization.

JJBS

Volume 18, Number 3,September 2025
ISSN 1995-6673
Pages 421 – 427

Jordan Journal of Biological Sciences

Characterization and Stress-Responsive Expression of the Lentil Manganese Superoxide Dismutase (LcMn-SOD) Gene in Mitigating Oxidative Stress

Maysa Al-Faris [1], Nidal Odat [2,*], Saeid Abu-Romman [1]

[1] Department of Biotechnology, Faculty of Agricultural Technology, Al-Balqa Applied University, Al-Salt 19117, Jordan;[2] Department of Applied Biological Sciences, Faculty of Science, Al-Balqa Applied University, Al-Salt 19117, Jordan

Received: November 26, 2024; Revised: January 26, 2024; Accepted: February 7, 2025

Abstract

Plants exposed to various stress conditions, such as drought, have developed enzymatic defense mechanisms crucial for mitigating oxidative stress caused by the accumulation of reactive oxygen species (ROS) like superoxide anion (O_2^-) and hydrogen peroxide (H_2O_2). Among these defense mechanisms, superoxide dismutase (SOD) plays an essential role in neutralizing ROS to prevent cellular damage. This study aimed to characterize the LcMn-SOD gene in lentil (*Lens culinaris*) and assess its expression under different stress conditions. The LcMn-SOD gene encodes a protein of 240 amino acids, with a molecular mass of 26.59 kDa and a theoretical isoelectric point of 7.86. The gene's cDNA length is 858 bp, with a 723 bp open reading frame encoding a full-length protein likely localized in the mitochondria. Sequence analysis showed high similarity with mitochondrial Mn-SOD proteins in other legumes, supporting its role in oxidative stress responses across plant species. Quantitative RT-PCR analysis in two-week-old seedlings indicated that LcMn-SOD is a key player in stress response, with notable regulation patterns: hydrogen peroxide significantly upregulated LcMn-SOD expression, while salicylic acid initially downregulated it, followed by a subsequent increase. Abscisic acid treatment led to a 14-fold upregulation after four hours. These findings underscore LcMn-SOD's role in managing oxidative stress, suggesting its potential in enhancing crop resilience to environmental stressors, particularly under changing climate and habitat disturbances. Future research could examine how diverse stresses regulate LcMn-SOD to improve crop resilience.

Keywords: Mn-SOD (Manganese Superoxide Dismutase), Oxidative Stress, Lentil (*Lens culinaris*), Drought Stress, Gene Expression, Phytohormones.

1. Introduction

Plants under biotic and abiotic stresses, such as drought, salinity, extreme temperatures, and heavy metal accumulation, face oxidative stress due to the overproduction of toxic reactive oxygen species, such as (O_2^-) and (H_2O_2), which cause cellular damage that led to impaired plant growth thus productivity and biomass as a consequence of reduction of photosynthetic capacity eventually lead to cell death (Zhang et al., 2021; Hasanuzzaman et al., 2020). As part of their defense mechanisms, plants have developed an enzymatic and non-enzymatic antioxidant network responsible for mitigating the harmful effects of toxic Reactive oxygen species, such as the superoxide radical (O_2^-) and hydrogen peroxide (H_2O_2) (Sharma et al., 2012 Odat, 2018). Manganese superoxide dismutase (Mn-SOD) is one of the important enzymes in plants that play a vital role in mitigating effects of oxidative stress by catalyzing the dismutation of the superoxide radical (O_2^-) into oxygen and hydrogen peroxide (H_2O_2), which is further detoxified by other antioxidant enzymes such as catalase and peroxidase. Under stress conditions, plants increase the expression of ROS especially in mitochondria in order to enhance tolerance to such conditions **(**Wang et al., 2010; Al-Faris et al., 2022). Lentil (Lens culinaris), an important legume crop, is often exposed to abiotic stresses conditions which lead to reduction in crop biomass and productivity **(**Noor et al.,2024; Sachdev et al., 2021**).** Like other plants, lentil relies on its antioxidant defense mechanism that involved the expression of different genes of various enzymes Mn-SOD genes that mitigate the damaging effects of oxidative stress (Odat, 2020). Several studies on SOD genes in plants provided evidence on their dynamic expression level under different stress conditions. For example, Mn-SOD expression is found to upregulated in response to drought and salinity in species such as Arabidopsis, rice, and barley, suggesting a common mechanism across plant. Additionally, abscisic acid (ABA) and jasmonic acid (JA) are shown to modulate SOD expression suggesting the role of the gene in adaptive response to stress (Nguyen &Nambara,2023). Given the increased effect of environmental stresses and habitat perturbation due to increased climate change, studying Mn-SOD gene and its characteristic and expression patterns can provide valuable insight on enhancing stress tolerance of crops. Mn-SOD gene has been studied in several legumes' species, such as soybean and pea, yet in lentil the characteristics and expression level of this gene are less studied, especially

* Corresponding author. nidalodat@bau.edu.jo

under stress conditions. Therefore, studying the role of this gene role in lentil can provide valuable information into its potential applications in breeding programs aimed at enhancing stress tolerance (Al-Tawaha 2022). This study aims to characterize the LcMn-SOD gene in lentil and investigate its expression patterns under various stress conditions. The study utilizes molecular techniques, such as qRT-PCR and bioinformatics tools, to understand how the LcMn-SOD gene contributes to lentil's defense mechanisms and how it can be harnessed to improve crop resilience

2. Materials and Methods

2.1. Experimental setup

Seeds of Lens culinaris Medik cultivar (Jordan 2) were sown in plastic pots (14×14 cm) containing a substrate of peat moss and perlite (1:1) ratio and maintained under greenhouse conditions with regular irrigation using distilled water for a duration of two weeks. The expression of LcMn-SOD was analyzed in lentil seedlings (two-week-old) treated with various stress:

1. Drought: Irrigation was withheld for different durations 3days and 6 days.
2. Hormonal: Seedlings were treated with abscisic acid (100 µM), jasmonic acid (100 µM), or salicylic acid (1 mM) by foliar spraying.
3. Hydrogen peroxide (H_2O_2) treatment: Seedlings were foliar sprayed with 10 mM H_2O_2.

For drought stress experiments, leaf samples were collected at zero, 3 days, and 6 days after the treatment. For hormonal and H_2O_2 treatments, leaf samples were collected at 0, 1, 2, and 4hours post-treatment. Collected leaf samples were immediately frozen in liquid nitrogen and stored at -20°C until RNA extraction.

2.2. RNA isolation and cDNA synthesis:

Frozen lentil leaves were utilized for the extraction of total RNA using the Spectrum™ Plant Total RNA Kit (Sigma), following the manufacturer's protocol. Subsequently, the concentration and purity of RNA were assessed spectrophotometrically at wavelengths of 260 nm and 280 nm (Biochrom, Cambridge). RNA quality was tested by electrophoresis. cDNA was preprepared using two micrograms of lentil leaf RNA and primeScript™MasterMix (Takara, Japan). All cDNA samples were stored at -20°C until further analysis for gene expression.

2.3. Mn-SOD gene cloning:

To identify ORF of the Mn-SOD gene in lentil, a candidate gene approach was employed. Primers (Mn-SOD F: 5'-CATGGCCGCTCGAACCCTA-3', sense; Mn-SOD R: 5'-CGGCCAGATTGCTCAAGTTC-3', antisense) were designed using the known sequence of the pea Mn-SOD gene (GenBank accession No. X60170.1). The PCR reaction was conducted using iNtRON i-MAXTM II (iNtRON, Korea), with the following conditions: initial denaturation at 95ºC for 5 minutes, followed by 35 cycles of denaturation at 95ºC for 30 seconds, annealing at 54ºC for 30 seconds, extension at 72ºC for 2 minutes, and a final extension at 72ºC for 10 minutes. PCR products were resolved on 1% agarose gels. The specific PCR amplicon (855 bp for the Mn-SOD gene) was purified, and the products were cloned into the PGEM®-T Easy Vector (Promega) and subsequently subjected to sequencing analysis.

2.4. Bioinformatics analysis

The ExPASY Translate tool (http://web.expasy.org/translate/) was employed to derive the protein sequences of the Mn-SOD from lentil. Subsequently, the ProtParam tool (http://web.expasy.org/protparam/) was utilized to analyze the physical and chemical parameters of the LcMn-SOD protein. Prediction of the protein targeting of LcMn-SOD was done using ProtComp 9 (Emanuelsson et al., 2000). Similarity analyses were conducted using BLAST, and the conserved domains of protein were predicted by NCBI Conserved Domain Database (Marchler-Bauer et al., 2009). Alignment of multiple sequence analysis was performed using Clustal Omega sofware (Larkin et al., 2007). Protein analysis of predicted proteins was done by neighbor-joining algorithm using MEGA 7 program (Kumar et al., 2016), with 1000 replicates.

2.5. Quantitative RT-PCR:

Gene expression analysis of the LcMn-SOD gene was conducted utilizing quantitative real-time polymerase chain reaction (qRT-PCR). Primers specific to the target gene were designed using Primer 3 software. The qRT-PCR primer pairs for Mn-SOD (sense: 5'-TTGTGCAGAAGAACCCTATCCC-3'; antisense: 5'-GATTTCGCCGCTAATGACAGG -3') yielded an amplicon of 162 base pairs. The genes sequence of Actin was considered as an internal control, with primers (sense: 5'-ATACCCCTGCCATGTATGTAGC-3'; antisense: 5'-AGCCAGATCAAGACGAAGGATG-3') designed accordingly.

Each PCR reaction mixture contained a total volume of 25 µL, comprising 10 µL of KAPA SYBR ®FAST universal qPCR Kit (KAPA, USA), 0.4 µL of each specific primer (10 µM), 120 ng/µL of diluted cDNA as a template, and RNase-free water to adjust the final volume. Amplification was conducted with an initial denaturation step at 95°C for 2 minutes, followed by 45 cycles of denaturation at 95°C for 10 seconds, annealing at 54°C for 25 seconds, and extension at 60°C for 25 seconds, during which fluorescent signals were acquired. A final extension step was performed at 60°C for 2 minutes.

All qRT-PCR were repeated three times for each sample. The level of gene expression was determined by calculating the fold difference using the 2–ΔΔCT method (Livak and Schmittgen, 2001). Differences between treatment times were evaluated by the least significant difference (LSD) at a 5% CI.

3. Results

3.1. Cloning and bioinformatics analyses of Mn-SOD gene in lentil (LcMn-SOD)

To identify the Mn-SOD gene in lentil, a candidate gene approach was used, based on the pea Mn-SOD gene sequence (PsMn-SOD; GenBank accession No. X60170.1). Primers was designed based on the sequence of the gene which used to amplify the lentil Mn-SOD gene from cDNA synthesized. PCR amplification with LcMn-SOD F and LcMn-SOD R primers produced an 858 bp

product, which was purified, cloned into the PGEM®-T Easy Vector, and sequenced.

The full-length LcMn-SOD cDNA is 858 bp, containing both a start and stop codon, indicating the gene is complete. It includes a 723 bp open reading frame (ORF), a 1 bp 5'-untranslated region, and a 134 bp 3'-untranslated region. The ORF encodes a protein of 240 amino acids figure 6, with a predicted molecular mass of 26.59 kDa and a theoretical isoelectric point of 7.86. The nucleotide sequence has been submitted to GeneBank.

Subcellular localization predictions using Target 1.1 and ProtComp 9.0 indicated that LcMn-SOD is likely localized in the mitochondria figure 7, with TargetP 1.1 providing a high confidence prediction. Sequence similarity analysis using BLASTP showed homology between LcMn-SOD and Mn-SOD proteins from other plant species. Multiple sequence alignment using Clustal Omega revealed conserved manganese-binding residues at positions H-64, H-109, H-105, and Asp-101 figure 8, shared with Mn-SOD proteins from pea, common vetch, soybean, chickpea, and barrelclover.

3.2. Gene expression under the stress condition studied

In this study, the involvement of Mn-SOD genes in lentil responses to abiotic stress was explored by analyzing gene expression in seedlings under drought and hydrogen peroxide (H_2O_2). Drought stress was induced by withholding irrigation, and LcMn-SOD gene expression was measured at 3 and 6 days after emergency. The results showed an upregulation of LcMn-SOD, with fold changes of 1.4 and 2.3 at 3 and 6 days, respectively (Fig. 1). Additionally, the plant was treated with 10 mM H_2O_2, and gene expression was monitored at 1, 2, and 4 hours. qRT-PCR analysis revealed that LcMn-SOD was downregulated at 1 hour but showed significant upregulation (3.7-fold) at 4 hours (Fig. 2).

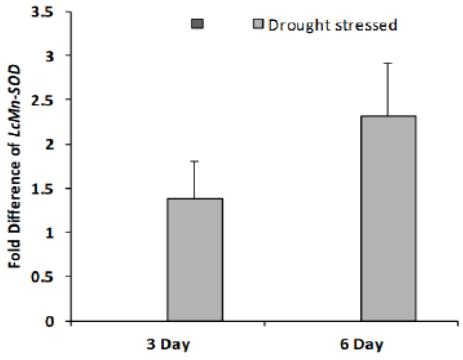

Figure 1. Expression of LcMn-SOD in lentil seedlings subjected to drought stress for 3- and 6-days post emergency (X axis is the days parameter), as measured by qRT-PCR. The LcACT1 was used as reference gene. Data represent the means of three replicates ± SE. Significantly different values are indicated by different letters above the error bars.

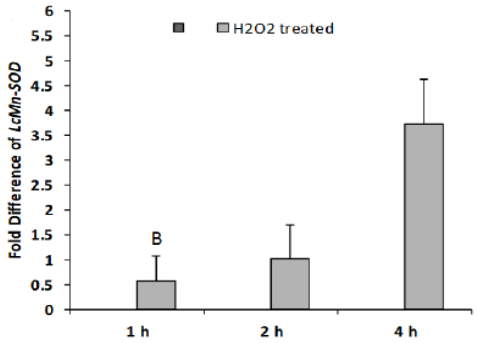

Figure 2. Expression of LcMn-SOD under H_2O_2 for 1, 2, and 4 hours, (X axis is the days parameter), as measured by qRT-PCR. The LcACT1 gene was used as a. Data represent the means of three replicates ± SE. Significantly different values are indicated by different letters above the error bars

3.3. Expression under phytohormonal stressor

The effect of phytohormonal stimuli on LcMn-SOD gene expression was investigated using salicylic acid (SA), abscisic acid (ABA), and jasmonic acid (JA) treatments on two-week-old lentil seedlings. The expression profiles were analyzed via qRT-PCR at 1-, 2-, and 4-hours post-treatment.

Treatment with 1 mM SA led to downregulation of LcMn-SOD at 1 and 2 hours in contrast to the untreated control. However, by 4 hours, gene expression significantly increased, reaching a peak of 1.3-fold (Fig. 3). When the seedlings were treated with 100 µM ABA, LcMn-SOD expression was initially downregulated at 1 hour but began to increase by 2 hours, although the changes were not statistically significant. A dramatic 14-fold upregulation of LcMn-SOD was observed at 4 hours (Fig. 4).

JA treatment (100 µM) also significantly affected LcMn-SOD expression. The gene showed its highest expression at the 1-hour time point with a 1.82-fold increase, followed by a decline at 2 and 4 hours, reaching 30% and 10% of the initial peak, respectively (Fig. 5)

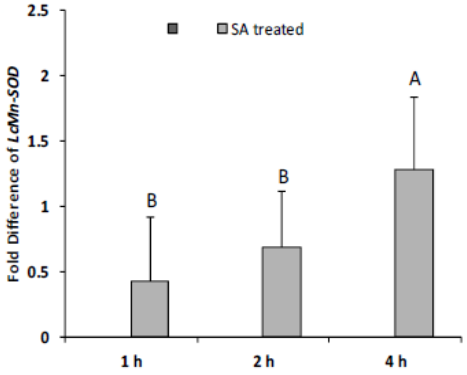

Figur 3. qRT-PCR analysis of LcMn-SOD expression at 1, 2, and 4 hours (X-axis shows time in days). Data represent the mean of three replicates ± SE. Statistically significant differences are denoted by distinct letters above the error bars.

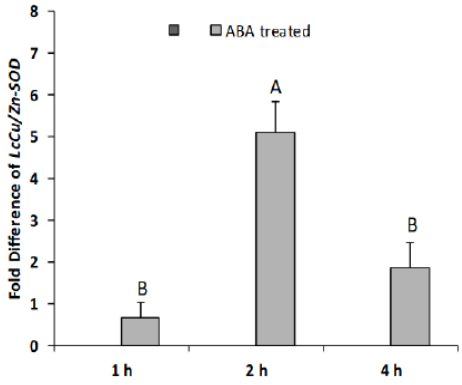

Figure 4. Relative expression of *LcCu/Zn-SOD* (a) and *LcMn-SOD* (b) in lentil seedlings treated with ABA for 1, 2, and 4 h (X axis is the days parameter), as measured by qRT-PCR. The expression of both genes was normalized to *LcACT1* reference gene, and then normalized with their expression in untreated control seedling (set to 1.0) at the corresponding time point. Data Significantly different values are indicated by different letters above the error bars.

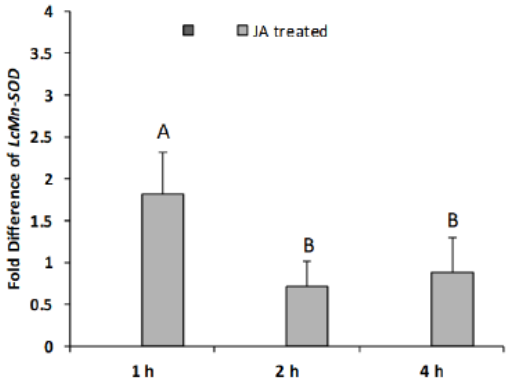

Figure 5. Relative expression of *LcMn-SOD* in lentil seedlings treated with JA for 1, 2, and 4 h (X axis is the days parameter), as measured by qRT-PCR. The expression of gene was normalized to *LcACT1* reference gene, and then was normalized with their expression in untreated control seedling (set to 1.0) at the corresponding time point. Data represent the means of three replicates ± SE. Significantly different values are indicated by different letters above the error bars.

```
                                                                    c
atggccgctcgaaccctattgtgcagaagaaccctatcccctgtcctccgcaacgatgca
 M  A  A  R  T  L  L  C  R  R  T  L  S  P  V  L  R  N  D  A
aaaccaatcggggcagccatagccgccgcatcaactcaatcccgtggtttacatgtcttc
 K  P  I  G  A  A  I  A  A  A  S  T  Q  S  R  G  L  H  V  F
acgctaccggatctcgcttacgactacggagctttggagcctgtcattagcggcgaaatc
 T  L  P  D  L  A  Y  D  Y  G  A  L  E  P  V  I  S  G  E  I
atgcaaatccatcatcagaaacaccaccagacttatattaccaactataacaaagctctc
 M  Q  I  H  H  Q  K  H  H  Q  T  Y  I  T  N  Y  N  K  A  L
gagcagcttcacgatgccgttggtaaagctgatacatctaccactgttaagctccagaat
 E  Q  L  H  D  A  V  G  K  A  D  T  S  T  T  V  K  L  Q  N
gccatcaagttcaacggcggaggtcatattaaccattccattttctggaaaaatctggct
 A  I  K  F  N  G  G  G  H  I  N  H  S  I  F  W  K  N  L  A
cctgttcgggaaggaggtggtgaaccaccaaaggaatccctaggctgggccattgacaca
 P  V  R  E  G  G  G  E  P  P  K  E  S  L  G  W  A  I  D  T
aactttggatctttggaagcattgattcaaaagattaatgccgaaggtgcagctcttcag
 N  F  G  S  L  E  A  L  I  Q  K  I  N  A  E  G  A  A  L  Q
gggtctggatgggtgtggcttggtcttgacaaagatttgaagaggcttgtggttgaaacc
 G  S  G  W  V  W  L  G  L  D  K  D  L  K  R  L  V  V  E  T
actgcaaaccaggacccactggtcactaaaggagcaagtttggttccattgcttggtata
 T  A  N  Q  D  P  L  V  T  K  G  A  S  L  V  P  L  L  G  I
gatgtttgggaacatgcctactacttacagtacaagaatgttagaccagactatttgaag
 D  V  W  E  H  A  Y  Y  L  Q  Y  K  N  V  R  P  D  Y  L  K
aacatttggaaagttattaactggaaacatgccagtgaagtatatgagaaagagagctct
 N  I  W  K  V  I  N  W  K  H  A  S  E  V  Y  E  K  E  S  S
taatctgaagtgctgcttggtatggaacttggataacaggtttgcagcatgtttggcgat

ggaataaaatgatgtgaagtgatagataataccttcctatgatgtacttgtgctttagaa

cttgagcaatctggccg
```

Figure 6. Nucleotide sequence and deduced amino acid sequence of LcMn-SOD. The amino acids are designated with single-letter code below the middle nucleotide of each codon. Start codon is shaded in gray and stop codon is shaded in black.

A

```
### targetp v1.1 prediction results ###################################
Number of query sequences:  1
Cleavage site predictions not included.
Using PLANT networks.

Name                    Len     cTP    mTP     SP   other  Loc  RC
-----------------------------------------------------------------------
LcMn-SOD                240   0.034  0.916  0.041  0.089   M    1
-----------------------------------------------------------------------
cutoff                        0.000  0.000  0.000  0.000
```

B

```
ProtComp Version 9.0. Identifying sub-cellular location (Plant)
Seq name:  test sequence, Length=247
Significant similarity in Location DB - Mitochondrial
Database sequence: AC=P27084 Location:Mitochondrial  DE  Superoxide dismutase [Mn]
Score=99, Sequence length=234, Alignment length=233
Predicted by Neural Nets - Extracellular (Secreted) with score    0.9
Integral Prediction of protein location: Mitochondrial with score    7.8
Location weights:     LocDB / PotLocDB / Neural Nets / Pentamers / Integral
 Nuclear                0.0 /      0.0 /        0.00 /      0.00 /     0.01
 Plasma membrane        0.0 /      0.0 /        0.94 /      0.00 /     0.00
 Extracellular          0.0 /      0.0 /        0.94 /      0.00 /     0.00
 Cytoplasmic            0.0 /      0.0 /        0.00 /      0.00 /     0.00
 Mitochondrial          7.2 /      3.0 /        0.00 /      6.44 /     7.83
 Endoplasm. retic.      0.0 /      0.0 /        0.00 /      0.03 /     0.00
 Peroxisomal            0.0 /      0.0 /        0.93 /      0.13 /     0.01
 Golgi                  0.0 /      0.0 /        0.19 /      0.00 /     0.04
 Chloroplast            2.8 /      0.0 /        0.00 /      0.00 /     2.07
 Vacuolar               0.0 /      0.0 /        0.00 /      0.00 /     0.04
```

Figure 7. Prediction of LcMn-SOD subcellular localization using the online tools TargetP 1.1 (A) and ProtComp 9.0 (B).

```
LcMn-SOD      MAARTLLCRRTLSPVLRNDAKPIGAAIAAASTQSRGLHVFTLPDLAYDYGALEPVISGEI   60
PsMn-SOD      MAARTLLCRKTLSSVLRNDAKPIGAAIAAASTQSRGLHVFTLPDLAYDYGALEPVISGEI   60
VsMn-SOD      MAVRTLLCRKTLSSVLRNDAKPIGAAIAAASTQSRGVHVFTLPDLAYDYGALEPVISGEI   60
GmMn-SOD      MAIRTLFTRKTLTSILRNDPNPIVAGIA-ASTQSRDLHVFTLPDLAYDYGALEPVISGEI   59
CaMn-SOD      MAVRTLLSKKTLTTVLRNDPKPIGAAI----TQSRGLHVFTLPDLAYDYGALEPVISGEI   56
MtMn-SOD      MAARALLTRKTLATVLRNDAKPIIGAGIAAATHSRGLHVYTLPDLDYDYGALEPAISGEI   60
              ** * *    **   ****  **        * **  ** ***** ******** *****

LcMn-SOD      MQIHHQKHHQTYITNYNKALEQLHDAVGKADTSTTVKLQNAIKFNGGGHINHSIFWKNLA   120
PsMn-SOD      MQIHHQKHHQTYITNYNKALEQLHDAVAKADTSTTVKLQNAIKFNGGGHINHSIFWKNLA   120
VsMn-SOD      MQIHHQKHHQTYITNYNKALEQLHDAVGKADASTTVKLQNAIKFNGGGHINHSIFWKNLA   120
GmMn-SOD      MQLHHQKHHQTYVTNYNKALEQLHDAVGKADSSTTVKLQNAIKFNGGGHINHSIFWKNLA   119
CaMn-SOD      MQIHHQKHHQTYITNYNKALEQLHDSVAKADSLTTVKLQNAIKFNGGGHINHSIFWKNLA   116
MtMn-SOD      MQLHHQKHHQTYITNFNKALEQLQDAVAKKDSSAVVKLQGAIKFNGGGHVNHSIFWKNLA   120
              ** ********* ** ******* * * * *    **** ********* **********

LcMn-SOD      PVREGGGEPPKESLGWAIDTNFGSLEALIQKINAEGAALQGSGWVWLGLDKDLKRLVVET   180
PsMn-SOD      PVSEGGGEPPKESLGWAIDTNFGSLEALIQKINAEGAALQASGWVWLGLDKDLKRLVVET   180
VsMn-SOD      PVCEGGGEPPKESLGWAIDTNFGSLEALIQKINAEGAALQGSGWVWLGLDKDLKRLVVET   180
GmMn-SOD      PVREGGGEPPRDSLGWAIDTHFGSLEALIQKINAEGAALQGSGWVWLGLDKELKRLVVET   179
CaMn-SOD      PVREGGGEPPKEALGWAIDTNFGSLEALIQKVNAEGAALQGSGWVWLALDKELKRLVVET   176
MtMn-SOD      PVREGGGEPPKGSLGWAIDTHFGSFEALVQKVNAEGAALQGSGWVWLGLDKELKRLVVET   180
              ** *******   ******* *** *** ** ******** ****** *** ********

LcMn-SOD      TANQDPLVTKGASLVPLLGIDVWEHAYYLQYKNVRPDYLKNIWKVINWKHASEVYEKESS   240
PsMn-SOD      TANQDPLVTKGASLVPLLWIDVWEHAYYLQYKNVRPDYLKNIWKVINWKHASEVYEKESS   240
VsMn-SOD      TANQDPLVTKGASLVPLLWIDVWEHAYYLQYKNVRPDYLKNIWKVINWKHASEVYEKESS   240
GmMn-SOD      TANQDPLVTKGPSLVPLLGIDVWEHAYYLQYKNVRPDYLKNIWKVINWKYASEVYEKESS   239
CaMn-SOD      TANQDPLVTKGTSLVPLLGIDVWEHAYYLQYKNVRPDYLKNIWKVINWKYASEVYENAF-   235
MtMn-SOD      TANQDPLVTKGPNLVPLLGIDVWEHAYYLQYKNVRPDYLKNIWKVINWKYASEVYEKESS   240
              ***********  ***** ******************************** ******
```

Figure 8. Multiple sequence alignment of LcMn-SOD with closely related Mn-SOD proteins from different plant species. Gray boxes represent amino acids coordinating manganese binding. The list from pea (CAA42737), common vetch (AQM49975), soybean (NP_001235066), chickpea (XP_004502849), and barrelclover (XP_013461533).

4. Discussion

4.1. Cloning and Bioinformatics Analysis of the SOD Gene in Lentil

Plants, in their natural environments, are subjected to various stressors that adversely affect their growth, productivity, and development, primarily due to the accumulation of reactive oxygen species (ROS) (Miller et al., 2008). To combat this, plants have evolved sophisticated antioxidative defense systems operating in nearly all cellular compartments (Halliwell et al., 2006, Odat, 2020b). Superoxide dismutases (SODs) are a crucial component of these systems, scavenging superoxide radicals in various organelles to mitigate oxidative stress (Paardekooper et al., 2019; Eraslan et al., 2007). Several SOD genes have been identified across a wide range of species, including Arabidopsis (Kliebenstein et al., 1998), and barley (Abu-Romman & Shatnawi, 2011). This study successfully isolated and characterized the Mn-SOD gene in lentil, designated as LcMn-SOD. Using bioinformatics tools, the LcMn-SOD protein was predicted to localize in the mitochondria, aligning with other studies where Mn-SOD isoenzymes are localized in both mitochondria and peroxisomes (Rio et al., 2003). Sequence similarity analysis revealed significant homology between LcMn-SOD and other legume species, with conserved manganese-binding residues critical for enzymatic activity (Kowalczyk et al.,2021).

4.2. Expression Analysis of LcMn-SOD Genes

Understanding how defense genes like LcMn-SOD are regulated under different environmental stressors provides valuable insight into their functional roles. In this study, drought stress resulted in upregulation of LcMn-SOD, correlating with increased ROS levels in chloroplasts and mitochondria, which disrupt photosynthesis due to stomatal closure (Postiglione & Muday,2023). The upregulation of LcMn-SOD highlights its role in neutralizing ROS, as seen in other plants under abiotic stresses like drought and salinity (Chakrabarty et al., 2016; Kukreja et al., 2005, Al-Tawaha, et al., 2021). H_2O_2, a non-radical ROS, also significantly increased LcMn-SOD expression after 4 hours, suggesting its role as both a damaging agent and a signaling molecule, as observed in other species like maize and Syzygium cumini (Hu et al., 2006; Choudhary et al., 2012).

4.3. Phytohormonal Effects on LcMn-SOD Expression

Phytohormones like salicylic acid (SA), abscisic acid (ABA), and jasmonic acid (JA) play critical roles in plant stress responses by modulating antioxidant enzyme activities. This study demonstrated that SA, ABA, and JA upregulated LcMn-SOD expression at various time points, reflecting the complex signaling interactions these hormones trigger. ABA-induced upregulation aligns with its known role in ROS generation and antioxidant enzyme activation, while JA's early upregulation effect is consistent with the increased ROS levels following its application (Postiglione&Muday,2023).

5. Conclusion and Future Directions:

This study successfully cloned and characterized the full-length Mn-SOD gene from lentil. Bioinformatics analysis confirmed its mitochondrial localization and sequence conservation with Mn-SOD genes from other legumes. Expression analyses showed that LcMn-SOD is responsive to drought, H_2O_2 and phytohormonal treatments, highlighting its key role in lentil's defense against oxidative stress. Future research should focus on generating transgenic lentils overexpressing LcMn-SOD to assess its role in stress tolerance under combined abiotic and biotic stress conditions. Comparative studies across lentil cultivars and wild relatives could further uncover the regulatory mechanisms governing SOD gene expression in diverse environments.

Reference

Abu-Romman, S., and Shatnawi, M. 2011. Isolation and expression analysis of chloroplastic copper/zinc superoxide dismutase gene in barley. *S. Afr. J. Bot.* **77**(2): 328-334.

Abu-Romman, S.2019. Molecular cloning and gene expression analysis of chloroplastic copper/zinc superoxide dismutase gene in Vicia sativa L. *Res. Crops*. **20**(1):215-222.

Al-Faris, M., Abu-Romman, S., and Odat, N.2022. Cloning, sequence analysis and expression profile of a chloroplastic copper/zinc superoxide dismutase gene from lentil. *Int. J. Agric. Biol*. **28**(3):167-174

Al-Tawaha, A. R. M. S., Odat, N. A., Benkeblia, N., Kerkoub, N., Labidi, Z., Boumendjel, M., Nasri, H., & Khalid, S. 2022. Breeding Crops for Tolerance to Salinity, Heat, and Drought. In ***Climate Change and Agriculture: Perspectives, Sustainability and Resilience*** (pp. 95–110). John Wiley & Sons Ltd. DOI: 10.1002/9781119789789.ch5.

Al-Tawaha, A., Awad, A., Odat, N., Abu-Romman, S., and Hasan, M. 2021. Effect of salinity on germination and root growth of Jordanian barley. *J. Ecol. Eng.* **22**(1):41–50.

Bienert, G. P., Schjoerring, J. K., and Jahn, T. P. 2006. Membrane transport of hydrogen peroxide. Biochim. *Biophys. Acta Biomembr*. **1758**(8):994-1003.

Bose, J., Rodrigo-Moreno, A., and Shabala, S. 2014. ROS homeostasis in halophytes in the context of salinity stress tolerance. *J. Exp. Bot*. **65**(5):1241-1257.

Chakrabarty, A., Aditya, M., Dey, N., Banik, N. and Bhattacharjee, S. 2016. Antioxidant signaling and redox regulation in drought-and salinity-stressed plants. In **Drought Stress Tolerance in Plants. Vol 1: Physiology and Biochemistry**. 465-498.

Choudhary, R., Saroha, A. E., and Swarnkar, P. L. 2012. Effect of abscisic acid and hydrogen peroxide on antioxidant enzymes in Syzygium cumini plant. *J. Food Sci. Technol*. **49**:649-652.

Del Río, L. A., Sandalio, L. M., Corpas, F. J., Palma, J. M., and Barroso, J. B. 2006. Reactive oxygen species and reactive nitrogen species in peroxisomes. Production, scavenging, and role in cell signaling. *Plant Physiol*. **141**(2):330-335.

Eraslan, F., Inal, A., Savasturk, O., and Gunes, A. Y. D. I. N.2007. Changes in antioxidative system and membrane damage of lettuce in response to salinity and boron toxicity. *Sci. Hortic.* **114**(1):5-10.

Gill, S. S., and Tuteja, N.2010. Reactive oxygen species and antioxidant machinery in abiotic stress tolerance in crop plants. *Plant Physiol. Biochem*. **48**(12):909-930.

Eyidogan, F., and Öz, M. T. 2007. Effect of salinity on antioxidant responses of chickpea seedlings. *Acta Physiol. Plant*. **29**(5):485-493.

Feng, Z., Wang, L., Pleijel, H., Zhu, J., and Kobayashi, K. 2016. Differential effects of ozone on photosynthesis of winter wheat among cultivars depend on antioxidative enzymes rather than stomatal conductance. *Sci. Total Environ*. **572**:404-411.

Halliwell, B.2006. Reactive species and antioxidants. Redox biology is a fundamental theme of aerobic life. *Plant Physiol*. **141**(2):312-322.

Hernandez, M., Fernandez-Garcia, N., Diaz-Vivancos, P., and Olmos, E.2010. A different role for hydrogen peroxide and the antioxidative system under short and long salt stress in Brassica oleracea roots *J. Exp. Bot*. **61**(2):521-535.

Hasanuzzaman, M., Bhuyan, M.B., Zulfiqar, F., Raza, A., Mohsin, S.M., Mahmud, J.A., Fujita, M. and Fotopoulos, V.2020. Reactive oxygen species and antioxidant defense in plants under abiotic stress: Revisiting the crucial role of a universal defense regulator. *Antioxidants*. **9**(8):681.

Hosseini, S. Z., Ismaili, A., Nazarian-Firouzabadi, F., Fallahi, H., Nejad, A. R., and Sohrabi, S. S. 2021. Dissecting the molecular responses of lentil to individual and combined drought and heat stresses by comparative transcriptomic analysis. *Genomics*. **113**(2):693-705.

Hu, X., Zhang, A., Zhang, J., and Jiang, M. 2006. Abscisic acid is a key inducer of hydrogen peroxide production in leaves of maize plants exposed to water stress. *Plant Cell Physiol*. **47**(11):1484-1495.

Jaleel, C. A., Lakshmanan, G. M. A., Gomathinayagam, M., and Panneerselvam, R.2008. Triadimefon induced salt stress tolerance in Withania somnifera and its relationship to antioxidant defense system. *S. Afr. J. Bot*.**74**(1):126-132.

Janda, T., Szalai, G., Tari, I., and Paldi, E.E.1999. Hydroponic treatment with salicylic acid decreases the effects of chilling injury in maize (Zea mays L.) plants. *Planta*. **208**:175-180.

Kliebenstein, D. J., Monde, R. A., and Last, R. L.1998. Superoxide dismutase in Arabidopsis: an eclectic enzyme family with disparate regulation and protein localization. *Plant Physiol*. **118**(2):637-650.

Kukreja, S., Nandwal, A. S., Kumar, N., Sharma, S. K., Sharma, S. K., Unvi, V., and Sharma, P. K.2005. Plant water status, H 2 O 2 scavenging enzymes, ethylene evolution and membrane integrity of Cicer arietinum roots as affected by salinity. *Biol. Plant*. **49**:305-308.

Kowalczyk, P., Sulejczak, D., Kleczkowska, P., Bukowska-Ośko, I., Kucia, M., Popiel, M., Wietrak, E., Kramkowski, K., Wrzosek, K. and Kaczyńska, K.2021. Mitochondrial oxidative stress—a causative factor and therapeutic target in many diseases. *Int. J. Mol. Sci*. **22**(24):13384.

Kwon, S. I., and An, C. S.2003. Cloning and expression of mitochondrial MnSOD from the small radish (Raphanus sativus L.). *Mol. Cells*. **16**(2):194-200.

Manivannan, P., Jaleel, C. A., Kishorekumar, A., Sankar, B., Somasundaram, R., and Panneerselvam, R.2008. Protection of Vigna unguiculata (L.) Walp. plants from salt stress by paclobutrazol. *Colloids Surf. B Biointerfaces*. **61**(2):315-318.

Miller, G., Shulaev, V., and Mittler, R.2008. Reactive oxygen signaling and abiotic stress. *Physiol. Plant*. **133**(3):481-489.

Nguyen, C.H., Yan, D. and Nambara, E.2023. Persistence of abscisic acid analogs in plants: chemical control of plant growth and physiology. *Genes*. **14**(5):1078.

Noor, M.M.A., Tahjib-Ul-Arif, M., Alim, S.A., Islam, M.M., Hasan, M.T., Babar, M.A., Hossain, M.A., Jewel, Z.A., Murata, Y. and Mostofa, M.G.2024. Lentil adaptation to drought stress: response, tolerance, and breeding approaches. *Front. Plant Sci.* **15**:1403922.

Odat, N. 2020a. Intraspecific genetic variation within and between improved cultivars and landraces of durum wheat in germination and root architectural traits under saline conditions. *Int. J. Plant Biol*. **11**(1-5):4-9.

Odat, N. 2020b. Genotypic variation in germination and some growth parameters of wheat (*Triticum turgidum* spp. *durum*) in response to the toxic effect of aluminum oxide (Al_2O_3) nanoparticles. *Res. Crops*. **21**(3):441–445.

Odat, N. 2018. Differential gene expression of Durum wheat (Triticum turgidum L. var. durum) in relation to Genetic Variation Under NaCl Salinity Stress. *Jordan J. Biol. Sci*. **11** (5):1-6

Paardekooper, L.M., van Vroonhoven, E., Ter Beest, M. and van den Bogaart, G. 2019. Radical stress is more cytotoxic in the nucleus than in other organelles. *Int. J. Mol. Sci*. **20**(17)**:**4147.

Postiglione, A.E. and Muday, G.K.2023. Abscisic acid increases hydrogen peroxide in mitochondria to facilitate stomatal closure. *Plant Physiol*. **192**(1) :469-487.

Ralph, S.G., Chun, H.J.E., Cooper, D., Kirkpatrick, R., Kolosova, N., Gunter, L., Tuskan, G.A., Douglas, C.J., Holt, R.A., Jones, S.J. and Marra, M.A.2008. Analysis of 4,664 high-quality sequence-finished poplar full-length cDNA clones and their utility for the discovery of genes responding to insect feeding. *BMC Genomics*. **9**:1-18.

Sachdev, S., Ansari, S. A., Ansari, M. I., Fujita, M.,and Hasanuzzaman, M.2021. Abiotic stress and reactive oxygen species: Generation, signaling, and defense mechanisms. *Antioxidants*. **10**(2):277.

Scandalios, J. G.2005. Oxidative stress: molecular perception and transduction of signals triggering antioxidant gene defenses. *Braz. J. Med. Biol. Res*. **38**;995-1014.

Sharma, P. and Dubey, R.S.2005. Drought induces oxidative stress and enhances the activities of antioxidant enzymes in growing rice seedlings. *Plant Growth Regul*. **46**:209-221.

Sharma, P., Jha, A. B., Dubey, R. S., and Pessarakli, M. 2012. Reactive oxygen species, oxidative damage, and antioxidative defense mechanism in plants under stressful conditions. *J. Bot*. **2012**:1-26.

Staskawicz, B. J., Mudgett, M. B., Dangl, J. L., and Galan, J. E.2001. Common and contrasting themes of plant and animal diseases. *Science*. **292**(5525):2285-2289.

Touati D.1983. Cloning and mapping of the manganese superoxide dismutase gene (sodA) of Escherichia coli K-12. *J. Bacteriol*. **155**(3):1078-1087.

Wang, W., Zhang, X., Deng, F., Yuan, R., and Shen, F. 2017. Genome-wide characterization and expression analyses of superoxide dismutase (SOD) genes in Gossypium hirsutum. *BMC genomics*. **18**:1-25.

Wang, Y.C., Qu, G.Z., Li, H.Y., Wu, Y.J., Wang, C., Liu, G.F. and Yang, C.P.2010. Enhanced salt tolerance of transgenic poplar plants expressing a manganese superoxide dismutase from Tamarix androssowii. *Mol. Biol. Rep*. **37**:1119-1124.

Wani, S.H., Kumar, V., Shriram, V. and Sah, S.K.2016. Phytohormones and their metabolic engineering for abiotic stress tolerance in crop plants. *Crop J*. **4**(3):162-176.

Zhang, J.D., Li, H.J., Amenyogbe, E., Wang, W.Z., Huang, J.S. and Chen, G.2021. Cloning of Mn-SOD gene and its mRNA expression difference and antioxidant enzyme activities under hypoxia stress of cobia Rachycentron canadum. *Mol. Biol. Rep*. **48**(10):6897-6909.

Zhou, Y., Hu, L., Wu, H., Jiang, L. and Liu, S.2017. Genome-wide identification and transcriptional expression analysis of cucumber superoxide dismutase (SOD) family in response to various abiotic stresses. *Int. J. Genomics*. **2017**: 7243973.

JJBS

Volume 18, Number 3,September 2025
ISSN 1995-6673
Pages 429 – 436

Jordan Journal of Biological Sciences

Identifying Angpt-4 As A Potential Gene in Progression of Hepatocellular Carcinoma Using Bioinformatics Tools and Analysis

Akash K[1], Avinash Sharma[2] and Rupak Nagraik[1,2,*]

[1]Faculty of Applied Sciences and Biotechnology, Shoolini University, Solan, HP, 173229, India; [2*]Department of Biotechnology, Graphic Era (Deemed to be University), 248002, Dehradun, India

Received: November 15, 2024; Revised: February 3, 2024; Accepted: February 13, 2025

Graphical Abstract

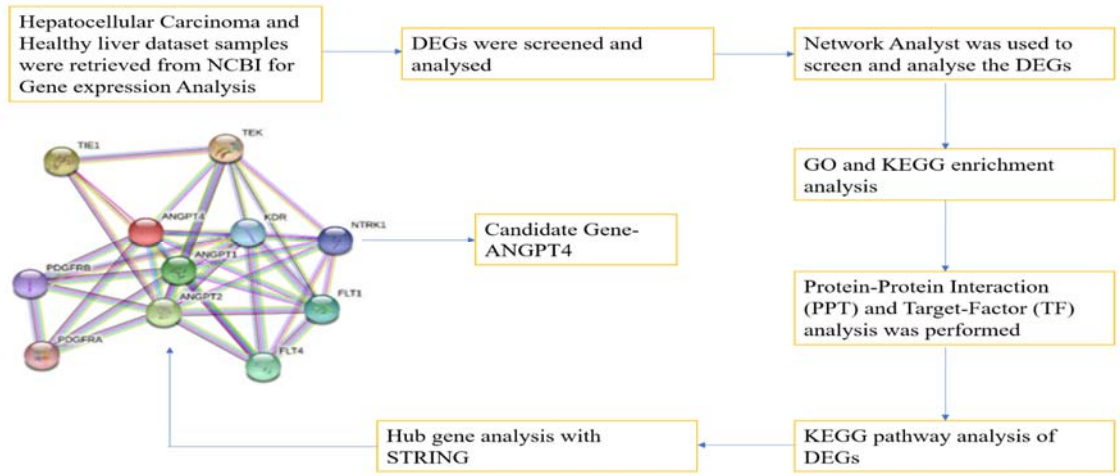

Abstract

Hepatocellular carcinoma (HCC) is a highly lethal malignancy, and the mechanisms underlying its initiation, development, and progression remain poorly understood. To explore differentially expressed genes (DEGs) involved in HCC progression, we utilized the gene expression dataset GSE33006 from the GEO database on NCBI. This dataset includes expression profiles of 3 HCC tumor samples and 3 normal liver samples. To accomplish that, the following bioinformatics tools have been incorporated, and the downloaded data was analyzed with set-parameters Gene Ontology (GO) analysis, Protein-protein Interaction (PPI) network analysis, Target-factor (TF) gene Interactions, and the Kyoto Encyclopedia of Genes and Genomes (KEGG) for pathway analysis; besides, STRING database was also used for enrichment and validation of genes. As a result, a total of 896 genes were seen as Up-regulated genes, and 368 genes were down-regulated. From the analysis among the Up-regulated genes, Angiopoietin 4 (ANGPT-4) was identified as one of the feasible candidate genes. The expression of ANGPT-4 shows results similar to past conducted research proving similarities between both data. This study provides insight into the prognosis of HCC and the possible gene ANGPT-4 along with the HIF-1α signaling pathway that is responsible for the progression of Hepatocellular carcinoma.

Keywords: Hepatocellular Carcinoma, Microarray data analysis, Differently expressed genes, Hub genes, Pathway analysis.

1. Introduction

Cancer is best characterized as an abnormal and uncontrolled growth of living cells that can originate in any organ or tissue of the body. These malignant cells have the potential to invade surrounding tissues and spread to other parts of the body through the bloodstream or lymphatic system, a process known as metastasis. (Mesleh., 2017). Hepatocellular carcinoma (HCC), the most common type of primary liver cancer, is a malignant tumor that develops in the liver. (McGlynn et al., 2021).

* Corresponding author. e-mail: rupak.nagraik@gmail.com.

The deaths related to Liver cancer account for about 830,000 worldwide and it is the third leading cause of death related to cancer, the first being lung and next colon and rectum cancers (Rumgay et al., 2022). The majority of liver cancer is due to the cause of Hepatocellular carcinoma, and minorly due to Cholangiocarcinoma (CAA) or also to the mixture of both CAA and HCC (Affo et al., 2017). Carcinogenic cell development involves, changes to gene expression, and usage of various regulatory pathways, therefore, the distinct etiology of HCC progression is vague (Yang WX et al., 2019). The diagnosis of HCC is strongly influenced by the stage of disease progression. At an early stage, curative therapeutic strategies such as surgical resection or liver transplantation are viable options, with reported 5-year survival rates approaching 70%. In contrast, patients diagnosed at an advanced stage are typically managed with palliative or systemic therapies, which offer limited benefits, with median survival generally less than 12 months (Singal et al., 2014); moreover, the majority of patients with early-stage HCC miss the appropriate treatment period as there are no early clinical symptoms shown by HCC (Zhang C et al., 2017). Normally, all HCCs emanate from chronic diseases such as NAFLD (non-alcoholic fatty liver disease) or hereditary hemochromatosis (HH), Chronic Hepatitis Virus (B & C), increase in corpulence, alcoholic liver disease (Justin Hartke, Matthew Johnson and Marwan Ghabril., 2017). Hepatocellular Carcinoma often originates from genetic mutations that modify the metabolic pathways consequently inducing the proliferation of cells (Chen X et al., 2020). Hepatitis C is a fatal virus as it is symptomless in the majority of patients and is prone to causing HCC and leading to death (Ringelhan et al., 2017). People infected with Hepatitis C have an increased risk of developing liver cirrhosis which is then followed up by fibrosis and thereby developing into HCC meantime (Sebastiani et al., 2014). Angiogenesis can be identified as a process where new leaky vessels develop from pre-existing blood vessels to transport oxygen and nutrients that are crucial and essential for HCC development. Angiogenesis is mainly initiated by various Vascular Endothelial Growth Factors (VEGFs) from cancerous cells (Dai et al., 2019; Jasani et al., 2024). The VEGF growth factor family consists of VEGF-A, VEGF-B, VEGF-C, VEGF-D, and VEGF-E; a majority of cancerous cells secretes VEGF-A and by interaction with tyrosine kinase receptors (RTK) namely VEGFR1 and VEGFR2 promotes angiogenesis, tumor cells over-expresses VEFG thereby promoting angiogenesis (Rafii et al., 2002). Increased VEGF levels in HCC have appeared to be in correspondence with the progression of angiogenesis by cancerous/tumor cells (Morse MA et al., 2018). In recent years, the usage of the bioinformatics-based approach has had a principal role in identifying and studying the expression levels of tumor genes and probing for further tumor key genes (Cao et al., 2023). Microarray technology is a well-advanced technique that has been widely used in the identification of abnormal genes and variations, and using this we have been able to identify the Differentially Expressed Genes (DEGs) and complex multiple pathways that were involved in the proliferation and progression of HCC. In this current study, we establish that HCC-associated DEGs when compared between cancerous and normal samples using the following techniques such as enrichment analysis, PPI and TF network analysis, and KEGG analysis to establish the pathway and genes associated with Hepatocellular carcinoma. As a result, a total of 896 genes were seen as Up-regulated genes, and 368 genes were down-regulated from this pool of genes; and Angiopoietin 4 was found as a significant candidate.

2. Materials and Methods

2.1. Microarray Data Acquisition

Gene Expression Omnibus (GEO) (https://www.ncbi.nlm.nih.gov/geo/) (Edgar et al., 2002) database has a collective dataset of Microarray and Next-generation sequences. The hepatocellular carcinoma-associated microarray dataset with accession number GSE33006 (Huang et al., 2012) was downloaded from NCBI. The GSE33006 dataset altogether consists of 6 datasets, which include 3 normal liver datasets and 3 HCC-affected datasets that were obtained for our study. The dataset GSE33006 was established from GPL570 (Affymetrix Human Genome U133 Plus 2.0 Array) (Chen et al., 2020). We have utilized GSE33006 dataset to analyze the genes.

2.2. Data Set normalization and analysis

The downloaded data were processed and analyzed with the help of the GSE33006 series matrix file, and the downloaded genes were checked for their gene symbol; a total of 45119 genes were obtained after pre-processing the datasets. To screen the DEGs, logFC (Fold change) ≥2 and logFC ≤2 were set as the benchmark criteria to discover desirable genes. After the filtration, a total of 2529 genes were obtained for logFC ≥2 and were termed Up-regulated genes, and for logFC ≤, 2 1087 genes were obtained and termed Down-regulated genes.

2.3. Differentially Expressed Gene's Enrichment Analysis

To identify potential DEGs, Network Analyst was utilized for this process and the gene's significance was analyzed using the Kyoto Encyclopaedia of Genes and Genomes (KEGG), Reactome, Gene Ontology (GO) analysis that includes a biological process (BP), Molecular function (MF) and Cellular component (CC). To be statistically significant for enrichment, the threshold for the genes was adjusted to P-Value(using false discovery rate FDR) < 0.5 and log2 FC was adjusted to <1.0.

2.4. Protein-protein Interaction (PPI) network analysis

PPI Network analysis is an important and key step that helps in the identification of the key genes that were involved in the development of hepatocellular carcinoma. Network analyst integrated STRING interactome (Szklarczyk D et al., 2014) with a cut-off score of 900 was used for the construction and identification of the PPI network of DEGs. We used the Functional Explorer tool in the Network analyst to discover possible modules with DEGs.

2.5. Target-factor (TF) gene Interactions

Gene regulatory networks influenced TF-gene interaction was implemented to recognize DEGs in Network analyst, TF gene database combined with JASPAR (Khan A et al., 2018) was used to discover the Differently expressed genes.

3. Results

3.1. Identification of Differentially expressed genes (DEGs)

We processed our data GSE33006 from NCBI using Network analyst to obtain the required set of DEGs and by applying the cut-off criteria as P-value <0.5 and log2 FC <1.0, a total of 4167 Differentially Expressed Genes were identified, and out of this a total of 896 genes were identified as Up-regulated genes based on parameter logFC ≥2 and 368 genes were identified as Down-regulated genes on the parameter of logFC ≤2 from our bioinformatics analysis.

3.2. Analysis of DEGs

In the due process, we also obtained the significant genes from the Network analyst and we correlated the obtained significant genes with Up-regulated and Down-regulated DEGs that were identified based on the above-mentioned parameters. After the correlation, normal genes were eliminated leaving only the Up-regulated and Down-regulated genes along with their Gene Ontology (GO) terms. The Gene Ontology (GO) annotations encompass a variety of pathways, including key signaling pathways such as MAPK, FOXO, and HIF-1α. Additionally, GO terms cover several cancer types, including colorectal and lung cancers, as well as diseases like Fanconi anemia and chronic myeloid leukemia.

3.3. Gene Ontology Analysis & Enrichment

Gene Ontology analysis was done on the current dataset genes that include Up-regulated and Down-regulated genes, and gene ontology was performed to realize the features and biological implications of the targeted pathways. The gene ontology was categorized into three categories, which include Biological process (BP), Molecular function (MF), and Cellular component (CC). According to Network analysis, Viral reproductive process was significantly enriched in the Biological process, Enzyme binding was highly enriched in the Molecular function, and Cytosol was also highly enriched in the Cellular component. More comprehensive Gene Ontology enrichment analyses are shown in Figures 1 and 2. Further evaluation of HCC prognosis could be enhanced by examining the roles of other notable enriched terms and pathways involving differentially expressed genes

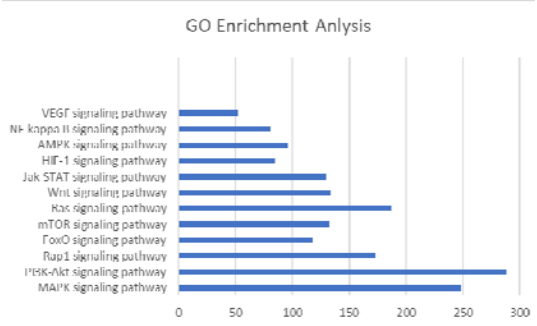

Figure 1. GO Enrichment analysis of top pathways related to our Differently expressed genes with logFC ≥2. It includes both Upregulated and Down-regulated genes.

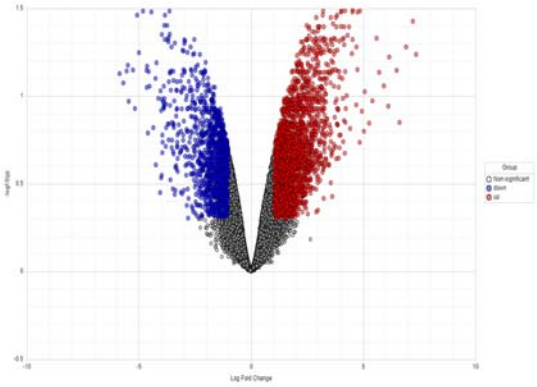

Figure 2. The Volcano plot. The log value fold change of significant genes of logFC ≥2 and logFC ≤2 were used as a parameter, here red colour denotes Up-regulated genes and blue colour denotes Down-regulated genes and the colourless genes are non-significant genes.

3.4. KEGG Pathway Analysis

We used the Kyoto Encyclopedia of Genes and Genomes (KEGG) to analyze the presence of possible DEGs in a pathway, and the enrichment analysis revealed possible pathways related to our desired genes. The analysis revealed 5 possible pathways that show the presence of our shortlisted DEGs; they are the MAPK signaling pathway, Ras signaling pathway, Rap1 signaling pathway, HIF-1 signaling pathway, and PI3-Akt signaling pathway. Various DEGs that include both Up-regulated and Down-regulated genes were found in these pathways for their involvement in the possible regulation of causing Hepatocellular carcinoma. To find the competent pathway, we utilized PANTHER (http://www.pantherdb.org/) a classification system based on the DEGs and pathways as shown in Figures 3 and 4, PANTHER was used to verify the potential competent pathway from our desirable list, and the HIF-1 signaling pathway was found as a feasible candidate.

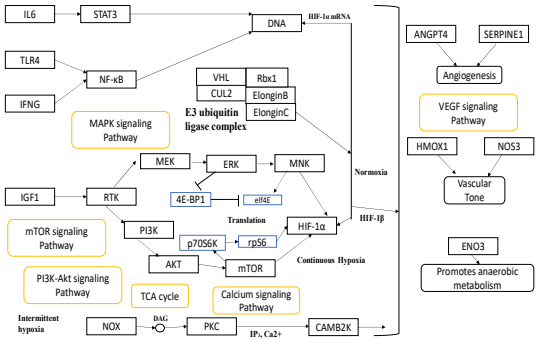

Figure 3. KEGG pathway of the HIF-1 signaling pathway. Note: Only the differently expressed genes are shown here.

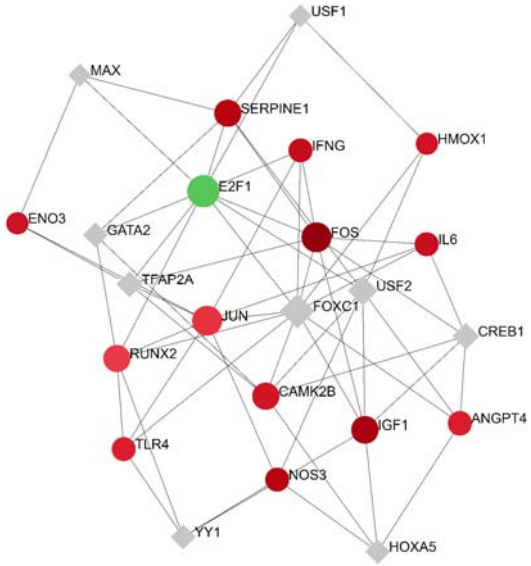

Figure 4. TF-gene interaction analysis of HIF-1 signaling pathway genes, the TF module was constructed using NetworkAnalyst and it consists of differently expressed genes of the HIF-1 signaling pathway.

3.5. PPI Network analysis and Identification of hub gene

To further evaluate the interaction among the identified DEGs and their pathways, a PPI network was analyzed to study the DEGs. The Protein-Protein Interaction (PPI) network for these DEGs consisting of 5548 nodes, 16221 edges, and 1627 seeds was constructed and analyzed by Network analyst based on the STRING database. Among all the Differentially expressed genes based on our research interest and compatibility of the genes concerning the prognosis of hepatocellular carcinoma, a few genes were shortlisted including LDHA, CAMK2B, PGK1, ANGPT4, IL6R, EPO, ENO2, ANGPT2, TEK, INS shown in Figure 5 and 6. Significant genes were shortlisted for further studies and also for their involvement in various pathways.

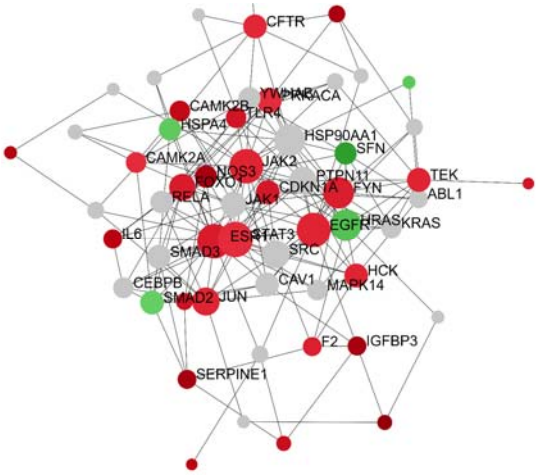

Figure 5. Protein-Protein Interaction analysis of Differently expressed genes at their transcriptional level and red colour denoted down-regulated genes and green colour denoted Up-regulated genes.

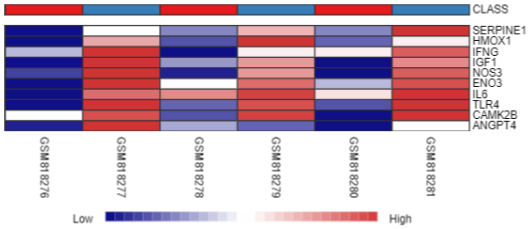

Figure 6. Heatmap of the genes that are differently expressed in the HIF-1 signaling pathway, is shown along with their expression levels in its dataset samples.

3.6. ANGPT4 -A candidate gene

We further studied the expression levels, prognosis, networking pathways, and expression levels of these mentioned genes in shortlisted pathways; we have used GENECARDS (https://www.genecards.org/) a database that provides all the necessary information regarding annotated, human genes and genomic biological data (Rappaport N et al., 2017) to probe the genes to find the suitable gene that directly or indirectly promotes Hepatocellular Carcinoma. We also used the Kyoto Encyclopedia of Genes and Genomes (KEGG) database to study the relevance of the gene and to study on HIF-1 signaling pathway and all the genes that were involved in this pathway. Based on our findings and evaluating it with necessary aspects, we found that the gene ANGPT-4 is a promising candidate here. We have also detected that the expression level of ANGPT-4 from our dataset samples is Up-regulated in Hepatocellular carcinoma according to our findings. To further understand the gene regulation of ANGPT-4, and its receptors, we used the STRING database (https://string-db.org/) to further evaluate the role of ANGPT-4 in its possible progression of Hepatocellular carcinoma. STRING analysis confirmed the expression of the candidate gene in the HIF-1 signaling pathway and also its interaction with Tie receptors, ANGPT-1, ANGPT-2, TEK et., To further validate the expression level of this gene, we used the Human Protein Atlas (https://www.proteinatlas.org/) to authenticate the expression levels in HCC (Liver cancer) and also with all

other cancer types. Therefore, with our findings, we can observe the expression of ANGPT-4 in HCC shown in Figure 7.

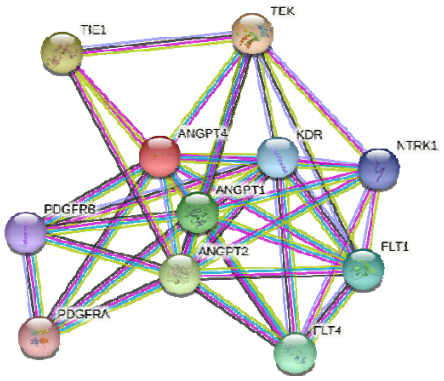

Figure 7. Sub-network analysis of genes and receptors connected with our candidate gene, the genes were analyzed and identified using String tools

4. Discussion

Bioinformatics is an essential tool that plays a critical role as an analyst in Oncogene study including diagnosis, and treatment as it assists in interpretation of the process of carcinogenesis by incorporating data at the genome level with various bioinformatics methods. Identification of prominent genes for HCC diagnosis and treatment is required, but studies related to gene expression levels are inadequate, therefore delaying the treatment process. In this study, Bioinformatics-based microarray analyses were analyzed to screen the desired key genes and their related pathway that directly or indirectly proliferate Hepatocellular Carcinoma. After analysis, 2,529 genes were up-regulated and 1,087 genes were Down-regulated; the Differently Expressed Genes of HCC datasets were screened based on fixed parameters, and this resulted in 896 up-regulated DEGs and 368 down-regulated DEGs were shortlisted along with the respective pathways from NCBI. The Bioinformatics analysis that was utilized to find out the DEGs are Gene Ontology enrichment analysis, KEGG pathway analysis, PPI network analysis, and TF network analysis to find out HCC-related genes and pathways. From Gene ontology enrichment, the desired results with the expected gene and pathway were proven and in KEGG the desirable pathway, the HIF-1 signaling pathway, was analyzed in correspondence with PPI and TF networks interactions, and the following genes were retrieved for further analysis of the following genes, SERPINE1, CAMK2B, HMOX1, ANGPT4, IFNG, IGF1, ENO3, NOS3, IL6, TLR4, ANGPT2, TEK, INS and it is observed from our data that all above-mentioned genes were down-regulated. Downregulation of ENO3 was also observed in HCC by Liu ZK (Liu ZK et al., 2019). SERPINE1 is known to cause carcinogenesis in our liver, and elevated levels of SERPINE1 are reported to be aggressive in tumors, thereby contributing towards angiogenesis stimulation, tumor proliferation, etc. Rosa et al., confirmed the significant increase in SERPINE1 expression promoting cancer progression in HCC, and through KEGG analysis we confirmed the presence of SERPINE1 in HIF-1 signaling pathway (Divella R et al., 2012; Divella R et al., 2001; Itoh T et al., 2000). The expression change of CAMK2B is yet to be found in HCC progression, but Kim JH et al. reported the Down-regulation of CAMK2B, and together with ARFGEF1, they work as biomarkers for the identification of breast cancer (Kim JH et al., 2011), and our data shows the down-regulation of CAMK2B and its presence in the HIF-1 signaling pathway. The downregulation of IGF1 was not only found in our data, but a study performed by Gao X et al. shows the down-regulation of the IGF1 gene and its significant role in HCC initiation and progression that proves our results (Gao X et al., 2018). The genes were co-related and analyzed with relatable pathways from KEGG and ANGPT4, ANGPT2, TEK, and INS were found to be present in the above-mentioned pathways. The analysis from ULCAN DATABASE, STRING DATABASE, HUMAN PROTEIN ATLAS, and GENECARDS DATABASE shows ANGPT4 is predicated to possibly induce HCC. Hepatocellular carcinoma is known to utilize a large number of blood vessels (hypervascularization) using the property of angiogenesis to indulge in an invasion, relapse, and metastasis of the disease (Poon RT et al., 2003); the angiogenic property is controlled based on the balance between anti-angiogenic inhibitors and pro-angiogenic activators and VEGF, FGF2, FGF4, HGF, IL8, Ephrin, CXCL12, ANGPT1, and ANGPT4; it is worth noting that the ligands for TIE family, TIE1 and TIE2 with receptor tyrosine kinases (TEK) are ANGPT1, ANGPT2, and ANGPT4, and they execute the role of HCC progression with interaction with the Tie receptors who are bound by tyrosine kinase receptors (Katoh Y et al., 2006). The angiopoietin/Tie2 system regulates the angiogenesis property, thereby contributing to the progression of HCC; however, the role of the angiopoietin/Tie2 system is ambiguous but recently it was reported that this system plays a crucial role in the initiation and progression of non-small cell lung carcinoma but their precise role in HCC needs further investigation (Zhang ZL et al., 2006). ANGPT4 was identified as a member of the angiopoietin family recently and is orthologous to ANGPT3 identified in mice (Valenzuela DM et al., 1999) but has a dissimilar protein structure, the study of ANGPT4 was derived from blood endothelial stem cells and vascularization properties thereby providing evidence that ANGPT4 expressed via autocrine signaling similar to ANGPT2 and stimulates responses to stimulus such as hypoxia (Lee HJ et al., 2004). ANGPT-4 firmly activates the TIE2 system and downstream signaling (Lund EL et al., 2004) and similar to ANGPT1, ANGPT4 is shown to promote and progress migration, survival, and vessel formation *in vitro,* and it is also reported that ANGPT-4 has initiated and promoted the growth of corneal angiogenesis in mice (Olsen MW., 2006). There is also strong evidence of ANGPT4's impact on breast cancer development and progression and evidence of suggestions for the potential for therapeutic targets (Yang H et al., 2021). ANGPT4 plays a key role in the growth and progression of human glioblastoma as it is up-regulated in it (Brunckhorst MK et al., 2006). The role of the Angpt-tie-2 system and ANGPT4 for initiation, cancer growth, and progression of ovarian cancer is significant from the findings where ANGPT4 is portrayed as a protumor (Brunckhorst MK et al., 2014). ANGPT4 was recorded to have swiftly activated the AKT and ERK-1,2 signaling pathways (Kesler CT et al., 2015). It is

reported that hypoxia-induced factors elevate the ANGPT4 level, thereby inducing angiogenesis in tumor areas (Lee HJ et al., 2004). ANGPT-4 is upregulated by HIF-1 and its pathway, therefore enhancing vessel formation (Andrikopoulou E et al., 2011). An important transcription factor that induces expression levels in ANGPT4 is the HIF-1α which provides an inter-cellular stabilization for growing tumors and it was proved that Hepatitis B virus X-protein on exposure to HIF-1α showed increased transcriptional levels and elevated protein levels thereby inducing angiogenesis (Morse MA et al., 2019). Jiang HY et al. reported higher expression levels of HMOX1 and SERPINE1 in hypoxia condition INHIF-1 signaling pathway that enhances the prognosis of HCC (Jiang HY et al., 2020), and the expression levels of HMOX1 was also reported by Wang Y et al. for its involvement in HCC progression (Wang Y et al., 2020). Freise C et al. reported on the activation of IGF1 that induces VEGF and HIF-1α to critically impart angiogenesis towards HCC growth (Freise C et al., 2011). The HIF-1 functions as a mediator for hypoxic regulation of ANGPT-2 and ANGPT-4 and plays a critical role in the formation of new vessels; under the influence of HIF-1, ANGPT-4 was shown to have improved vessel formation and controlled the permeability of endothelial layers (Yamakawa M et al., 2003). By substituting for ANGPT-1 as a TIE-2 receptor ANGPT-4 assist in angiogenesis in response to hypoxia and it was also confirmed that ANGPT-4 was up-regulated in normoxic conditions due to HIF-1 regulation and the molecular mechanism that is utilized by HIF-1 to upregulate ANFPT-4 levels is yet to be determined (Yamakawa M et al., 2004). By integrating our findings with clinical data from previous research studies and utilizing the KEGG pathway database, we identified similarities between our data and prior observations. This analysis revealed ANGPT-4 within the HIF-1α signaling pathway. Furthermore, our analysis of HCC tissues demonstrated upregulation of ANGPT-4 within the HIF-1 signaling pathway. Based on these findings, we hypothesize that ANGPT-4 may play a crucial role in HCC progression through the HIF-1α signaling pathway.

5. Conclusion

The acquired results from this study present ANGPT-4 as a key associated gene for the progression of Hepatocellular carcinoma, and using bioinformatics tools and various other databases we can detect ANGPT4. The expression levels related to ANGPT1 and ANGPT2 have been studied well for their involvement in HCC initiation, but in contrast the expression levels of ANGPT4 are yet to be explored in-depth for their involvement in cancer progression, including their underlying mechanism in various cancer types and HCC.

Acknowledgments

The authors are thankful to Shoolini University for providing the appropriate facilities and data to complete this work.

Compliance with ethical standards

5.1. Conflict of Interests

The authors declare no conflict of interests.

5.2. Research involving animal/human participants

This article does not contain any studies with animal and human participants.

5.3. Informed Consent/Data Availability Statement

The data supporting the findings for this study are available with the corresponding author upon request.

References

Affo S, Yu LX, Schwabe RF. The Role of Cancer-Associated Fibroblasts and Fibrosis in Liver Cancer. Annu Rev Pathol. 2017 Jan 24;12:153-186.Epub 2016 Dec 5. 10.1146/annurev-pathol-052016-100322

AL-Jasani BM, Sahib HB, Al-Saad HN. The Anti-angiogenic Potential of Thiosemicarbazide Derivative of Captopril (8) in Breast Cancer Cell Lines. Jordan J. Biol. Sci.. 2024 Sep 1;17(3).

Andrikopoulou E, Zhang X, Sebastian R, Marti G, Liu L, Milner SM, Harmon JW. Current Insights into the role of HIF-1 in cutaneous wound healing. Curr Mol Med. 2011 Apr;11(3):218-35 10.2174/156652411795243414

Barrett T, Wilhite SE, Ledoux P, Evangelista C, Kim IF, Tomashevsky M, Marshall KA, Phillippy KH, Sherman PM, Holko M, Yefanov A, Lee H, Zhang N, Robertson CL, Serova N, Davis S, Soboleva A. NCBI GEO: archive for functional genomics data sets--update. Nucleic Acids Res. 2013 Jan;41(Database issue):D991-5.Epub 2012 Nov 27. https://doi.org/10.1093/nar/gks1193

Brunckhorst MK, Wang H, Lu R, Yu Q. Angiopoietin-4 promotes glioblastoma progression by enhancing tumor cell viability and angiogenesis. Cancer Res. 2010 Sep 15;70(18):7283-93 https://doi.org/10.1158/0008-5472.CAN-09-4125

Brunckhorst MK, Xu Y, Lu R, Yu Q. Angiopoietins promote ovarian cancer progression by establishing a procancer microenvironment. Am J Pathol. 2014 Aug;184(8):2285-96. https://doi.org/10.1016/j.ajpath.2014.05.006

Cao T, Wu H, Ji T. Bioinformatics-based construction of prognosis-related methylation prediction model for pancreatic cancer patients and its application value. Front. Pharmacol. 2023 Mar 9;14:1086309.

Chen X, Liao L, Li Y, Huang H, Huang Q, Deng S. Screening and Functional Prediction of Key Candidate Genes in Hepatitis B Virus-Associated Hepatocellular Carcinoma. Biomed Res Int. 2020 Oct 9;2020:7653506. https://doi.org/10.1155/2020/7653506

Dai W, Wang Y, Yang T, Wang J, Wu W, Gu J. Downregulation of exosomal CLEC3B in hepatocellular carcinoma promotes metastasis and angiogenesis via AMPK and VEGF signals. Cell Commun Signal. 2019 Sep 2;17(1):113. https://doi.org/10.1186/s12964-019-0423-6

Divella R, Mazzocca A, Gadaleta C, Simone G, Paradiso A, Quaranta M, Daniele A. Influence of plasminogen activator inhibitor-1 (SERPINE1) 4G/5G polymorphism on circulating SERPINE-1 antigen expression in HCC associated with viral infection. Cancer Genom. Proteom. 2012 Jul-Aug;9(4):193-8. https://cgp.iiarjournals.org/content/9/4/193

Divella R, Taylor M, Grøndahl-Hansen J, Kakolyris S, Gatter KC, Harris AL. Plasminogen activator inhibitor-1 as a measure of vascular remodelling in breast cancer. J Pathol. 2001 Sep;195(2):236-43. https://doi.org/10.1002/path.931

Edgar R, Domrachev M, Lash AE. Gene Expression Omnibus: NCBI gene expression and hybridization array data repository. Nucleic Acids Res. 2002 Jan 1;30(1):207-10. https://doi.org/10.1093/nar/30.1.207

Freise C, Ruehl M, Erben U, Neumann U, Seehofer D, Kim KY, Trowitzsch-Kienast W, Stroh T, Zeitz M, Somasundaram R. A hepatoprotective Lindera obtusiloba extract suppresses growth and attenuates insulin like growth factor-1 receptor signaling and NF-kappaB activity in human liver cancer cell lines. BMC Complement Altern Med. 2011 May 12;11:39. https://doi.org/10.1186/1472-6882-11-39

Gao X, Wang X, Zhang S. Bioinformatics identification of crucial genes and pathways associated with hepatocellular carcinoma. Biosci Rep. 2018 Nov 9;38(6). https://doi.org/10.1042/BSR20181441

Huang Y, Chen HC, Chiang CW, Yeh CT et al. Identification of a two-layer regulatory network of proliferation-related microRNAs in hepatoma cells. *Nucleic Acids Res* 2012 Nov 1;40(20):10478-93. https://doi.org/10.1093/nar/gks789

Itoh T, Hayashi Y, Kanamaru T, Morita Y, Suzuki S, Wang W, Zhou L, Rui JA, Yamamoto M, Kuroda Y, Itoh H. Clinical significance of urokinase-type plasminogen activator activity in hepatocellular carcinoma. J Gastroenterol Hepatol. 2000 Apr;1(4):422-30. https://doi.org/10.1046/j.1440-1746.2000.02150.x

Jiang HY, Ning G, Wang YS, Lv WB. Ahypoxia-related signature enhances the prediction of the prognosis in hepatocellular carcinoma patients and correlates with sorafenib treatment response. Am J Transl Res. 2020 Dec 15;12(12):7762-7781. PMC7791514

Justin Hartke, Matthew Johnson, Marwan Ghabril, The diagnosis and treatment of hepatocellular carcinoma, **Seminars in Diagnostic Pathology**, Volume 34, Issue 2, 2017, Pages 153-159, ISSN 0740-2570mhttps://doi.org/10.1053/j.semdp.2016.12.011

Katoh Y, Katoh M. Comparative integromics on Angiopoietin family members. Int J Mol Med. 2006 Jun;17(6):1145-9.https://doi.org/10.3892/ijmm.17.6.1145

Kesler CT, Pereira ER, Cui CH, Nelson GM, Masuck DJ, Baish JW, Padera TP. Angiopoietin-4 increases permeability of blood vessels and promotes lymphatic dilation. FASEB J. 2015 Sep;29(9):3668-77.Epub 2015 May 14.https://doi.org/10.1096/fj.14-268920

Khan A, Fornes O, Stigliani A, Gheorghe M, Castro-Mondragon JA, van der Lee R, Bessy A, Chèneby J, Kulkarni SR, Tan G, Baranasic D, Arenillas DJ, Sandelin A, Vandepoele K, Lenhard B, Ballester B, Wasserman WW, Parcy F, Mathelier A. JASPAR 2018: update of the open-access database of transcription factor binding profiles and its web framework. Nucleic Acids Res. 2018 Jan 4;46(D1):D260-D266.Erratum in: Nucleic Acids Res. 2018 Jan 4;46(D1):D1284. https://doi.org/10.1186/s12938-017-0359-2

Kim JH, Kim TW, Kim SJ. Downregulation of ARFGEF1 and CAMK2B by promoter hypermethylation in breast cancer cells. BMB Rep. 2011 Aug;44(8):523-8. https://doi.org/10.5483/BMBRep.2011.44.8.523

Lee HJ, Cho CH, Hwang SJ, Choi HH, Kim KT, Ahn SY, Kim JH, Oh JL, Lee GM, Koh GY. Biological characterization of angiopoietin-3 and angiopoietin-4. FASEB J. 2004 Aug;18(11):1200-8. https://doi.org/10.1096/fj.03-1466com

Lee HJ, Cho CH, Hwang SJ, Choi HH, Kim KT, Ahn SY, Kim JH, Oh JL, Lee GM, Koh GY. Biological characterization of angiopoietin-3 and angiopoietin-4. FASEB J. 2004 Aug;18(11):1200-8 https://doi.org/10.1096/fj.03-1466com

Liu ZK, Zhang RY, Yong YL, Zhang ZY, Li C, Chen ZN, Bian H. Identification of crucial genes based on expression profiles of hepatocellular carcinomas by bioinformatics analysis. PeerJ. 2019 Aug 8;7:e7436. 10.7717/peerj.74364 Oct;287(4):F649-57.Epub 2004 Jun 15 https://doi.org/10.1152/ajprenal.00028.2004

Lund EL, Høg A, Olsen MW, Hansen LT, Engelholm SA, Kristjansen PE. Differential regulation of VEGF, HIF1alpha and angiopoietin-1, -2 and -4 by hypoxia and ionizing radiation in human glioblastoma. Int J Cancer. 2004 Mar 1;108(6):833-8. https://doi.org/10.1002/ijc.11662

McGlynn KA, Petrick JL, El-Serag HB. Epidemiology of hepatocellular carcinoma. Hepatology. 2021 Jan;73:4-13.

Mesleh AM. Lung Cancer Detection Using Multi-Layer Neural Networks with Independent Component Analysis: A Comparative Study of Training Algorithms. Jordan J. Biol. Sci.. 2017 Dec 1;10(4).

Morse MA, Sun W, Kim R, He AR, Abada PB, Mynderse M, Finn RS. The Role of Angiogenesis in Hepatocellular Carcinoma. Clin Cancer Res. 2019 Feb 1;25(3):912-920.Epub 2018 Oct 1. https://doi.org/10.1158/1078-0432.CCR-18-1254

Morse MA, Sun W, Kim R, He AR, Abada PB, Mynderse M, Finn RS. The Role of Angiogenesis in Hepatocellular Carcinoma. Clin Cancer Res. 2019 Feb 1;25(3):912-920. https://doi.org/10.1158/1078-0432.CCR-18-1254

Olsen MW, Ley CD, Junker N, Hansen AJ, Lund EL, Kristjansen PE. Angiopoietin-4 inhibits angiogenesis and reduces interstitial fluid pressure. Neoplasia. 2006 May;8(5):364-72. doi: 10.1593/neo.06127. https://doi.org/10.1593/neo.06127

Poon RT, Lau CP, Ho JW, Yu WC, Fan ST, Wong J. Tissue factor expression correlates with tumor angiogenesis and invasiveness in human hepatocellular carcinoma. Clin Cancer Res. 2003 Nov 1;9(14):5339-45.https://clincancerres.aacrjournals.org/content/9/14/5339

Rafii S, Lyden D, Benezra R, Hattori K, Heissig B. Vascular and haematopoietic stem cells: novel targets for anti-angiogenesis therapy? Nat Rev Cancer. 2002 Nov;2(11):826-35. https://doi.org/10.1038/nrc925

Rappaport N, Fishilevich S, Nudel R, Twik M, Belinky F, Plaschkes I, Stein TI, Cohen D, Oz-Levi D, Safran M, Lancet D. Rational confederation of genes and diseases: NGS interpretation via GeneCards, MalaCards and VarElect. Biomed Eng Online. 2017 Aug 18;16(Suppl 1):72. https://doi.org/10.1186/s12938-017-0359-2

Ringelhan M, McKeating JA, Protzer U. Viral hepatitis and liver cancer. Philos Trans R Soc Lond B Biol Sci. 2017 Oct 19;372(1732):20160274. Erratum in: Philos Trans R Soc Lond B Biol Sci. 2018 Jan 5;373(1737) https://doi.org/10.1098/rstb.2016.0274

Rumgay H, Arnold M, Ferlay J, Lesi O, Cabasag CJ, Vignat J, Laversanne M, McGlynn KA, Soerjomataram I. Global burden of primary liver cancer in 2020 and predictions to 2040. J Hepatol. 2022 Dec 1;77(6):1598-606.

Sebastiani G, Gkouvatsos K, Pantopoulos K. Chronic hepatitis C and liver fibrosis. World J Gastroenterol. 2014 Aug 28;20(32):11033-53. https://doi.org/10.3748/wjg.v20.i32.11033

Singal AG, Pillai A, Tiro J. Early detection, curative treatment, and survival rates for hepatocellular carcinoma surveillance in patients with cirrhosis: a meta-analysis. PLoS Med. 2014 Apr 1;11(4):e1001624.https://doi.org/10.1371/journal.pmed.1001624

Szklarczyk D, Franceschini A, Wyder S, Forslund K, Heller D, Huerta-Cepas J, Simonovic M, Roth A, Santos A, Tsafou KP, Kuhn M, Bork P, Jensen LJ, von Mering C. STRING v10: protein-protein interaction networks, integrated over the tree of life. Nucleic Acids Res. 2015 Jan;43(Database issue):D447-52.Epub 2014 Oct 28. https://doi.org/10.1093/nar/gku1003

Valenzuela DM, Griffiths JA, Rojas J, Aldrich TH, Jones PF, Zhou H, McClain J, Copeland NG, Gilbert DJ, Jenkins NA,

Huang T, Papadopoulos N, Maisonpierre PC, Davis S, Yancopoulos GD. Angiopoietins 3 and 4: diverging gene counterparts in mice and humans. Proc Natl Acad Sci U S A. 1999 Mar 2;96(5):1904-9. https://doi.org/10.1073/pnas.96.5.1904

Wang Y, Xie Y, Ma J, Wang Y, Gong R. Development and validation of a prognostic and immunotherapeutically relevant model in hepatocellular carcinoma. Ann Transl Med. 2020 Sep;8(18):1177. https://10.21037/atm-20-6112

Yamakawa M, Liu LX, Belanger AJ, Date T, Kuriyama T, Goldberg MA, Cheng SH, Gregory RJ, Jiang C. Expression of angiopoietins in renal epithelial and clear cell carcinoma cells: regulation by hypoxia and participation in angiogenesis. Am J Physiol Renal Physiol. 200. https://10.1152/ajprenal.00028.2004

Yamakawa M, Liu LX, Date T, Belanger AJ, Vincent KA, Akita GY, Kuriyama T, Cheng SH, Gregory RJ, Jiang C. Hypoxia-inducible factor-1 mediates activation of cultured vascular endothelial cells by inducing multiple angiogenic factors. Circ Res. 2003 Oct 3;93(7):664-73.Epub 2003 Sep 4. https://doi.org/10.1161/01.RES.0000093984.48643.D7

Yang H, Zhang M, Mao XY, Chang H, Perez-Losada J, Mao JH. Distinct Clinical Impact and Biological Function of Angiopoietin and Angiopoietin-like Proteins in Human Breast Cancer. Cells. 2021 Sep 29;10(10):2590 https://doi.org/10.3390/cells10102590

Zhang C, Peng L, Zhang Y, Liu Z, Li W, Chen S, Li G. The identification of key genes and pathways in hepatocellular carcinoma by bioinformatics analysis of high-throughput data. Med Oncol. 2017 Jun;34(6):101.Epub 2017 Apr 21. https://doi.org/10.1007/s12032-017-0963-9

Zhang ZL, Liu ZS, Sun Q. Expression of angiopoietins, Tie2 and vascular endothelial growth factor in angiogenesis and progression of hepatocellular carcinoma. World J Gastroenterol. 2006 Jul 14;12(26):4241-5. https://doi.org/10.3748/wjg.v12.i26.4241

JJBS

Volume 18, Number 3,September 2025
ISSN 1995-6673
Pages 437 – 448

Jordan Journal of Biological Sciences

Composite Fabric Food Packaging with Lactic Acid and Chitosan - Shellac Coating for Preservation of Tomato and Strawberry

Suganthi Ramasamy[1,*], Sanjaivarthan Nallasamy[1], Anujha Sellamuthu[1], Deepa Priya Srinivasan[1], Akileshwaran Kumaravel[1], Sussmitha Kumaresan[1], Shanmugapriya Chidhambaram[1], Antony Berlin Antony Peter[1], Kavinraj Govindaraj[1], Shubashri Nagaraj[1], Aarthi Chinnaswamy Ravi[1], Shyni Mahadevan[1], Sumathy Raj[2],

[1] *Department of Biotechnology, Dr NGP Arts and Science College, Coimbatore, Tamil Nadu, INDIA;* [2] *Department of Biotechnology, Dr G R Damodaran College of Science, Coimbatore, Tamil Nadu, INDIA*

Received: August 16, 2024; Revised: January 27, 2025; Accepted: February 19, 2025

Abstract

The imperative for enhanced food packaging materials that exhibit biodegradability has catalyzed significant progress in the domain of packaging material research. In this inquiry, the application of fibrous structures integrated with lactic acid and chitosan-shellac coatings for food packaging materials is being examined. This system is characterized by multifunctionality, wherein the chitosan-lactic acid layer produced provides a compensatory effect for the antimicrobial and antioxidant properties of the shellac layer, thereby contributing to the mechanical robustness of the coating. Furthermore, the effectiveness of the coated substrates in prolonging preservation was assessed utilizing tomatoes and strawberries as test subjects. Alterations in pH, concentrations of vitamin C, total soluble solids, rates of sensory acceptability, percentage weight loss, total titratable acidity, and activities of polyphenol oxidase (PPO) and peroxidase (POD) were meticulously measured after specified storage durations. The experimental results of 2, 2-diphenyl-1-picrylhydrazyl (DPPH) assay indicated that chitosan displayed the highest antioxidant potency, followed by lactic acid and the combination of chitosan with Lactic acid. This finding was further corroborated by the quality assessments of the tomatoes and strawberries, wherein preserved in chitosan-shellac-lactic acid and chitosan-shellac significantly contributed to quality preservation through the stabilization of pH, ascorbic acid content, and sensory attributes. Moreover, the coatings mitigated weight loss, preserved total titratable acidity levels, and inhibited the activities of PPO and POD during storage, thereby significantly extending the shelf life of the produce. Consequently, the outcomes of this study elucidate the potential application of lactic acid and chitosan-shellac coated composite fabrics as a sustainable and efficacious alternative for food packaging, offering numerous benefits for food preservation and protection.

KeyWords: Composite Fabric, Food Packaging, Lactic Acid, Chitosan-Shellac, Antioxidant Activity, Antimicrobial Properties

1. Introduction

Composite fabric food packaging incorporating lactic acid, chitosan, and shellac coatings presents a promising solution for enhancing food preservation and packaging sustainability. Chitosan, a natural biopolymer, offers antimicrobial properties (Dongkun *et al*., 2024) and when combined with lactic acid, can create biofilms with improved mechanical strength and barrier performance (Baoyimg *et al.,* 2024). Additionally, shellac bio-coatings have been shown to enhance the storage stability of fresh eggs, improving shell strength and reducing breakage rates (Hakan *et al.,* 2024). By incorporating these components into composite fabric packaging, it is possible to develop innovative biofilms that cater to diverse packaging requirements, offer enhanced antimicrobial properties, and contribute to reducing plastic waste in the food industry (Murtaza *et al.,* 2024). This approach holds great potential for sustainable and effective food packaging solutions.

Chitosan-based nanocomposites have emerged as promising materials for enhancing the postharvest quality of agricultural products. These nanocomposites offer unique properties such as biodegradability, antimicrobial activity, and barrier functions, making them suitable for food packaging applications. The postharvest period is critical for agricultural products, where factors like moisture loss, microbial growth, and physical damage can lead to quality deterioration and economic losses. Chitosan, derived from chitin, shows potential for improving food preservation due to its biocompatibility, biodegradability, and non-toxic nature. By incorporating chitosan into nanocomposites, researchers aim to develop innovative coatings and packaging materials that can extend the shelf life of fruits, vegetables, and other perishable goods (Saberi *et al.,* 2023). Furthermore, the fungicidal properties of clay chitosan nanocomposites were assessed both in vitro and in vivo in relation to their efficacy against *Penicillium digitatum*. (Youssef & Hashim, 2020).

* Corresponding author. e-mail: suganthir@drngpasc.ac.in.

Chitosan, a natural biopolymer, possesses intrinsic antimicrobial properties (Dongkun *et al*., 2024). Chitosan is utilized in the food industry for its ability to act as a natural preservative and to improve food quality by reducing microbial contamination (Ismail *et al.,* 2023). When combined with lactic acid in composite fabric food packaging, the resulting material exhibits enhanced antibacterial effects against various pathogens like *Escherichia coli, Staphylococcus aureus, Pseudomonas aeruginosa, and Staphylococcus epidermidis* (Edwin *et al.,*2024). The incorporation of lactic acid not only improves the mechanical and thermal properties of the packaging films but also inhibits the growth of these harmful bacteria, contributing to food safety by preventing contamination and extending the shelf life of meat products (Edwin *et al.,* 2024). This combination of chitosan and lactic acid in composite fabric food packaging showcases promising antimicrobial capabilities that can play a crucial role in maintaining food quality and safety in the industry.

PET (Polyethylene Terephthalate) is a synthetic polymer widely used in food packaging due to its high mechanical strength, thermal stability, and excellent barrier properties for gases and moisture. Hopewell *et al.* (2009) emphasized PET's durability and versatility in packaging applications such as beverage bottles and food containers. PET is non-biodegradable and contributes significantly to global plastic pollution. Geyer *et al.* (2017) reported that most PET waste accumulates in landfills or the natural environment due to limited recycling rates. Even though PET is recyclable, its carbon footprint and the challenges of achieving high recycling efficiency remain barriers to sustainability.

PLA (Polylactic Acid) is a biodegradable polymer derived from renewable resources such as corn starch and sugarcane. Jamshidian *et al.* (2010) noted that PLA exhibits good mechanical strength and optical clarity, making it suitable for disposable packaging and compostable films. PLA has limited moisture and oxygen barrier properties compared to PET, which can restrict its use for long-term food preservation (Lim *et al.,* 2008). Effective biodegradation of PLA requires industrial composting facilities, as natural decomposition is slow under ambient conditions (Emadian *et al.,* 2017). PET and PLA dominate the food packaging industry, each with its unique strengths and limitations. Composite fabric packaging with lactic acid and chitosan-shellac coating emerges as an innovative alternative with enhanced sustainability, biodegradability, and antimicrobial properties, addressing critical gaps in food safety and environmental impact.

Additionally, advancements in nanotechnology are being leveraged to develop bio-based packaging materials with enhanced strength and flexibility, opening up new possibilities for creating eco-friendly packaging options that meet the demands of modern consumers. These cutting-edge developments are not only revolutionizing the packaging industry but also aligning with the growing consumer preference for sustainable and environmentally friendly products, driving a shift towards a more eco-conscious market (Asgher *et al.,* 2020). Moreover, collaborations between researchers and industry experts are accelerating the scale-up and commercialization of these bio-based packaging innovations, bringing us closer to a future where sustainable packaging is the norm rather than the exception (Yuvaraj *et al.,* 2021).

It is an eco-friendly and biodegradable approach where the combination of natural polymers (chitosan and shellac) with lactic acid promotes sustainability. This aligns with global trends toward reducing single-use plastics and offers a new biodegradable alternative. The increasing demand for sustainable and effective food packaging solutions necessitates innovative approaches that extend shelf life, ensure food safety, and reduce environmental impact. The use of this novel composite fabric may enable customizability in food packaging, such as applications in fresh produce, dry goods, or perishable foods, which could distinguish it from conventional films or rigid packaging.

2. Materials and Methods

2.1. Fabric collection

Two different fabrics such as thick cloth, thin cloth and paper were collected from local market, Tiruppur**,** India.

2.2. Preparation of chitosan-shellac solution

Two milliliters of acetic acid were dissolved in one hundred milliliters of distilled water to create an acetic acid solution (2% v/v).To create a 2% (w/v) chitosan solution, 2 g of chitosan (C) was dissolved in 100 mL of a 2% v/v acetic acid solution. Shellac solution (5% w/v) was prepared by dissolving 5g of shellac in 90 ml acetone and the volume is made up to 100ml using distilled water.

2.3. Coating of fabrics and paper

Different extracts (chitosan, chitosan-shellac) were coated on Thin fabric, Thick fabric and Paper**,** and they were left to dry for 2 h and a set of uncoated fabric were kept as standard.

2.4. Antioxidant activity

The radical scavenging activity by chitosan, lactic acid, chitosan + lactic acid *i.e* its antioxidant property was investigated by using 2, 2-diphenyl-1-picrylhydrazyl (DPPH) assay. Stock solution of each sample chitosan, lactic acid, chitosan + lactic acid with a concentration of 10mg/ml was prepared and from the stock solution working standard solution with the concentration of 1mg/ml was prepared. Six boiling test tubes were taken; each was added with 1 ml of distilled water. 1 ml of the working standard solution was added to the first test tube and a serial dilution was performed by taking 1 ml from each test tube and adding it to the next. Then each test tube was added with 0.25 ml of DPPH (stock solution: 0.1 mM DPPH solution was prepared by dissolving 4mg of DPPH in 100ml of methanol) stock solution. The reaction mixture was filled to a 5 ml test tube and incubated for 30 minutes at room temperature in a dark environment. Five milliliters of DPPH was used as a control when the mixture's absorbance was measured at 517 nm after 30 minutes. Butylated hydroxyl toluene (BHT) was the standard.

DPPH inhibition (%) = [Control absorbance – Test absorbance] x 100

2.5. Preparation of packaging material

Twelve 10x10-inch bags made of two distinct fabrics (thin bag = 4, thick bag = 4) and brown paper (paper bag =

4) were made in total. Two milliliters of acetic acid was dissolved in one hundred milliliters of distilled water to create an acetic acid solution (2% v/v). To create a 2% (w/v) chitosan solution, 2 g of chitosan (C) was dissolved in 100 mL of a 2% v/v acetic acid solution. Shellac solution (5% w/v) was prepared by dissolving 5g of shellac in 90 ml acetone and the volume is made up to 100ml using distilled water. A bag from each set was kept as uncoated control. The other set of bags was coated with chitosan, chitosan-shellac and chitosan-shellac-lactic acid. Tomato and strawberry were chosen as vegetable and fruit sample to be stored using the prepared packaging material. The quality characteristics of stored fruit and vegetable were analyzed by following several biochemical assays such as polyphenol oxidase (PPO) and peroxidase (POD), Total soluble solids, Titratable acids, and ascorbic acid estimation for every four days for a total period of 12 days for tomato and for 6 days for strawberry. The sensory quality evaluation, weight loss, pH were also evaluated to determine the enhanced shelf life period of stored fruits and vegetables.

2.6. Quality characteristics of stored fruits and vegetables

2.6.1. 2.6.1 Sensory quality evaluation

With a few adjustments, the sensory quality of food samples was assessed using the methodology outlined by Caleb *et al.* (2013). Scales of taste, look, and color were widely employed to evaluate the quality of strawberries and tomatoes. Thus, five laboratory staff members used hedonic scales to undertake sensory evaluations of changes in taste, appearance, and color: 5, excellent (fully characteristic tomato and strawberry, red and unwrinkled); 4, very good (pleasantly mild tomato and strawberry, red and unwrinkled). 3, good (blandly faint tomato and strawberry, but quite wrinkled; limit of marketability); 2, fair (faint off odor, change in color, wrinkled, limit of unacceptability); and 1, poor (distinct off odor, fully wrinkled and mushy).

2.6.2. Measurement of weight loss

The weight of fruit was compared every 4 days for tomatoes up to 12 days and every 6 days for strawberries in order to determine the gradual weight reduction.

2.6.3. Measurement of pH

Five grams of pulped fruit and vegetables were combined with twenty-five milliliters of distilled water, and then filtered through muslin fabric. To assess pH, a 25 ml aliquot was employed. A pH meter was used to measure the pH.

2.6.4. Measurement of total soluble solids, titratable acid, and ascorbic acid

Using a hand refractometer, the total soluble solids was measured straight from the filtered fruit and vegetable residue and expressed as brix°. 0.1 N NaOH was used to assess the titratable acidity. Using a mortar and pestle, 3g of tomato and strawberry pulp was homogenized. The mixture was then centrifuged at 3500 rpm for 10 minutes. By using the 2, 6-dichlorophenolindophenol titration method, the ascorbic acid content of the supernatant phase was measured and recorded.

2.6.5. Assays of polyphenol oxidase (PPO) and peroxidase (POD)

After homogenizing 5 g of tissue from 3 fruit pulp in 20 ml of 0.05 M phosphate buffer (pH 6.8), the homogenate was filtered through two layers of cotton cloth to eliminate cell debris. Enzyme extracts were obtained by collecting the clear supernatant following centrifugation at 10,000 rpm for 20 minutes at 4°C. PPO activity was measured by measuring the oxidation of 4-methylcatechol, in accordance with Jiang and Fu's (1999) technique. After three minutes, the rise in absorbance at 410 nm was noted. The amount of enzyme activity that changed absorbance by 0.001 per minute was considered to be one unit. POD activity was determined using the MacAdam *et al.,* (1992) method. In a final volume of 3.0 ml, the assay mixture included 0.05 M sodium phosphate buffer (pH 7.0), 0.012M H_2O_2, 0.07 M guaiacol, and 0.1 ml of enzyme solution. For three minutes, the rise in absorbance at 470 nm was noted. The amount of enzyme that changed absorbance by 0.01 per minute was considered to be one unit of enzyme activity.

2.6.6. Data and statistical analysis

All the measurements of antioxidant activity of the samples were conducted in triplicate. The results of antioxidant activity are presented as mean ± standard deviation (SD). Concentrations of each samples are presented as mean ($n = 3$) with the determination of the Least Significant Difference (LSD) for a p value < 0.05. Statistical analysis for stored fruit and vegetable was carried out in two replicates for the control and experimental samples. The data has been analyzed by one-way analysis of variance (ANOVA) followed by Tukey's test, Duncan's multiple range test for the average value of parameter among the treatments and used to compare the mean values between pair of treatments. Difference were calculated to compare significant effect at $p<0.05$ level.

3. Results

3.1. Antioxidant activity

The antioxidant activity such as standard antioxidant assay DPPH done for the samples (Chitosan, Lactic acid and Chitosan + Lactic acid) using BHT as standard. The results (Figure 1) interpreted that the samples showed increase in inhibition with increase in concentration. The standard antioxidant assay for samples chitosan, lactic acid and chitosan- lactic acid was carried out using BHT as standard among which chitosan and chitosan + lactic acid exhibited a good antioxidant activity.

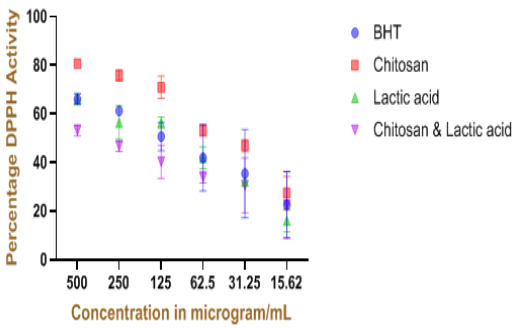

Figure 1. Antioxidant Activity of Chitosan, Lactic acid and Chitosan + Lactic acid

Table 1: EC_{50} values of antioxidant assay of chitosan, Lactic acid and Chitosan + Lactic acid

Samples	EC_{50} values µg/ml
BHT	254.64 ± 3.766^{a}
Chitosan	89.61 ± 1.309^{bc}
Lactic acid	95.505 ± 1.279^{b}
Chitosan + Lactic acid	99.2 ± 0.7778^{b}

EC_{50} values represent the concentration at which 50% of the antioxidant activity is observed, measured in mircrograms per milliliter (µg/ml). BHT- Butylated hydroxytoluene, each values in this table represented as mean± SD (n=3).Values in the same column followed by a different letter (p<0.05) are significantly different.

Chitosan, Lactic acid, and Chitosan combined with Lactic acid demonstrated EC_{50} values of 89.61 ± 1.309^{bc}, 95.505 ± 1.279^{b}, and 99.2 ± 0.7778^{b}, respectively (Table 1). These values indicate the concentration at which each sample exhibits 50% of the antioxidant activity compared to the BHT standard. Among the individual samples, Chitosan displayed the highest antioxidant potency, followed by Lactic acid, and the combination of Chitosan with Lactic acid.

3.2. Quality characteristics of stored Tomato

The tomatoes preserved within the coated fabric exhibited alterations in sensory evaluation (Figure 2, Figure 3, and Figure 4). The vegetable specimens that were subjected to storage within the chitosan-shellac coated fabric demonstrated significantly diminished weight loss in comparison to the other coated materials and uncoated specimens. The samples retained in chitosan-shellac-lactic acid experienced a slight reduction in weight when juxtaposed with the uncoated control and chitosan coated packaging materials (Figure 5, Figure 6 and Figure 7).

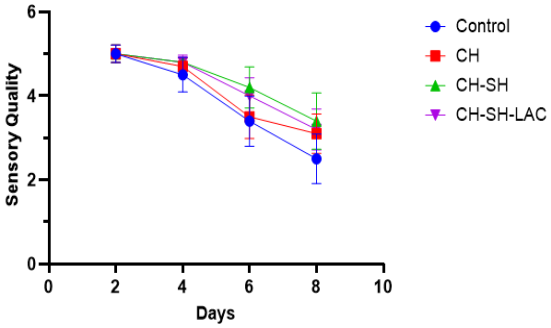

Figure 2. Sensory qualities of tomato stored in paper coated with Chitosan, Chitosan and Shellac, and Chitosan and shellac with lactic acid. [Control - uncoated Paper, CH- Chitosan CH+SH – Chitosan with Shellac, CH+SH+LAC - Chitosan with shellac and lactic acid. Each values represented as ‘mean ± SD (n=2)].

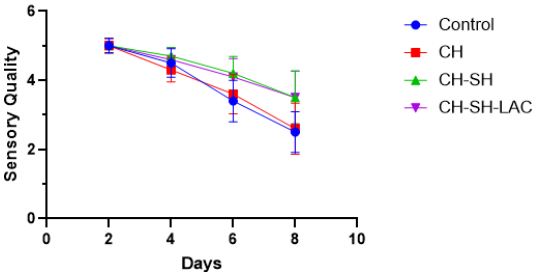

Figure 3. Sensory qualities of tomato stored in thin fabric coated with Chitosan, Chitosan and Shellac, and Chitosan and shellac with lactic acid. [Control - Thin fabric, CH- Chitosan CH+SH – Chitosan with Shellac, CH+SH+LAC - Chitosan with shellac and lactic acid. Each values represented as ‘mean ± SD (n=2)].

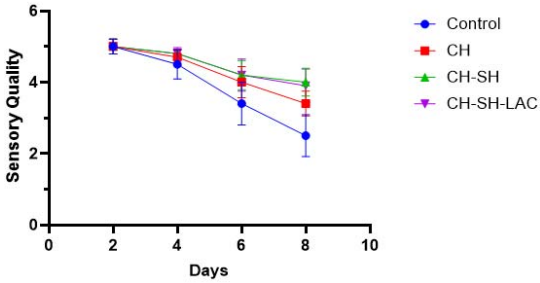

Figure 4. Sensory qualities of tomato stored in thick fabric coated with Chitosan, Chitosan and Shellac, and Chitosan and shellac with lactic acid. [Control - Thick fabric, CH- Chitosan CH+SH – Chitosan with Shellac, CH+SH+LAC - Chitosan with shellac and lactic acid. Each values represented as ‘mean ± SD (n=2)].

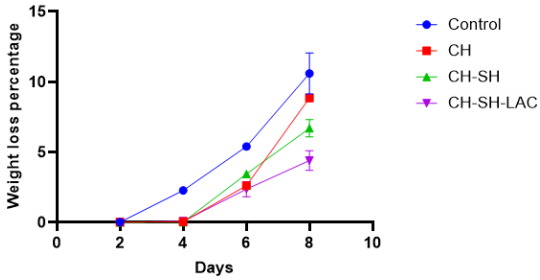

Figure 5. Weight loss % of tomato stored in paper coated with Chitosan, Chitosan and Shellac, and Chitosan and shellac with lactic acid. [Control - uncoated Paper, CH- Chitosan CH+SH – Chitosan with Shellac, CH+SH+LAC - Chitosan with shellac and lactic acid. Each values represented as ‘mean ± SD (n=2)].

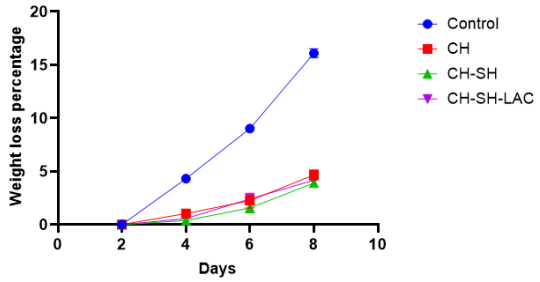

Figure 6. Weight loss % of tomato stored in thin fabric coated with Chitosan, Chitosan and Shellac, and Chitosan and shellac with lactic acid.[Control - Thin fabric, CH- Chitosan CH+SH – Chitosan with Shellac, CH+SH+LAC - Chitosan with shellac and lactic acid. Each values represented as ‘mean ± SD (n=2)].

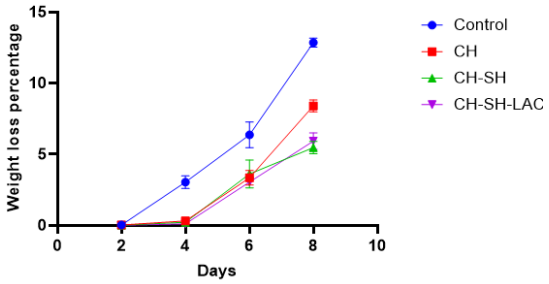

Figure 7. Weight loss % of tomato stored in thick fabric coated with Chitosan, Chitosan and Shellac, and Chitosan and shellac with lactic acid. [Control - Thick fabric, CH- Chitosan CH+SH – Chitosan with Shellac, CH+SH+LAC - Chitosan with shellac and lactic acid. Each values represented as 'mean ± SD (n=2)].

The pH levels of the tomatoes fluctuated in chitosan, chitosan-shellac, and chitosan-shellac-lactic acid when compared to pre-treatment measurements on the 4th, 8th, and 12th days. However, a more pronounced difference was observed when these samples were contrasted with those from uncoated packaging materials on the same days. The specimens that were preserved in chitosan-shellac-lactic acid and chitosan-shellac exhibited minimal variations in pH (Table 2).

Following a storage period of 12 days, the total soluble solids content (Table 2), ascorbic acid levels (Table 3), and titratable acidity (Table 3) of the packed tomatoes exhibited a marked decline in comparison to pre-treatment levels. The disparity observed between the values of samples derived from coated versus uncoated packaging materials suggests that the deterioration rate of tomatoes stored in chitosan-shellac coated and chitosan-shellac-lactic acid coated packaging is relatively less severe than that of tomatoes preserved in chitosan coated and uncoated samples. Tomatoes encapsulated in coated packaging demonstrated elevated levels of total soluble solids and titratable acidity.

Throughout the storage duration, the enzymatic activities of polyphenol oxidase (PPO) and peroxidase (POD) in both packed and unpacked tomatoes exhibited an increase. After 12 days of storage, the packed tomatoes revealed enhanced reduction activities of PPO and POD. This observation implies that the coatings utilized on the paper and fabric effectively inhibited the activities of these two enzymes, as evidenced by the lower reduction activities of PPO (Table 4) and POD (Table 4) in the unwrapped and control groups.

The sensory attributes of stored tomatoes have been effectively maintained by the chitosan-shellac-lactic acid coated and chitosan-shellac coated packaging materials in comparison to the samples derived from chitosan coated and uncoated packaging materials. The color, visual appeal, and flavor of the vegetable samples preserved in the coated packaging material were significantly retained when juxtaposed with the samples from the control group.

Vegetable samples preserved in chitosan-shellac coated fabric demonstrated a markedly lower weight loss relative to those stored in alternative coated materials and uncoated samples. Furthermore, samples stored in chitosan-shellac-lactic acid exhibited a marginal reduction in weight in comparison to both the uncoated control and samples preserved in chitosan-coated packaging material. These observations underscore the effectiveness of the chitosan-shellac coating, particularly in conjunction with lactic acid, in sustaining vegetable freshness and mitigating weight loss during the storage period.

Table 2 pH and Total Soluble Solids (°Brix) of tomato stored in fabric and paper coated with Chitosan, Chitosan and Shellac, and Chitosan and shellac with lactic acid

Sample	**pH**			Total Soluble Solids (°Brix)		
			Before treatment			
	5.8±0.12			4.4±0.17		
			After treatment			
Storage day	4	8	12	4	8	12
			Paper			
Control	5.7±0.04^{a}	5.4±0.04^{a}	5.2±0.09^{a}	4.7±0.09^{b}	4.9±0.09^{b}	5.1±0.04^{a}
CH	5.7±0.09^{a}	5.5±0.09^{a}	5.25±0.04^{a}	5.15±0.04^{a}	5.1±0.09^{a}	4.9±0.04^{b}
CH- SH	5.6±0.09^{b}	5.1±0.09^{b}	5.05±0.04^{a}	5.05±0.14^{a}	5.1±0.09^{a}	4.7±0.04^{c}
CH-SH-LAC	5.4±0.04^{c}	4.9±0.04^{c}	4.7±0.09^{b}	4.65±0.14^{b}	4.75±0.04^{b}	4.9±0.04^{b}
			Thin fabric			
Control	5.55±0.04^{b}	5.3±0.14^{a}	4.8±0.04^{b}	4.45±0.04^{a}	4.6±0.09^{a}	5.1±0.09^{a}
CH	5.75±0.04^{a}	5.5±0.19^{a}	4.8±0.04^{b}	4.4±0.09^{b}	4.6±0.09^{a}	4.6±0.09^{b}
CH-SH	5.65±0.14^{a}	5.1±0.04^{b}	5.5±0.09^{a}	4.15±0.04^{b}	4.4±0.09^{b}	4.5±0.04^{b}
CH-SH-LAC	5.55±0.04^{b}	5.3±0.09^{a}	4.8±0.04^{b}	4.45±0.04^{a}	4.65±0.04^{a}	4.0±0.14^{c}
			Thick fabric			
Control	5.45±0.14^{a}	5.25±0.04^{b}	4.9±0.09^{b}	4.6±0.09^{a}	4.85±0.04^{a}	5.15±0.14^{a}
CH	5.65±0.04^{a}	6.3±0.09^{a}	4.85±0.04^{c}	4.75±0.04^{a}	4.8±0.09^{a}	5.1±0.09^{a}
CH-SH	5.5±0.12^{a}	5.25±0.04^{b}	5.5±0.09^{a}	4.35±0.14^{b}	4.4±0.09^{c}	4.65±0.14^{b}
CH-SH-LAC	5.4±0.1^{b}	4.9±0.09^{c}	4.85±0.04^{c}	4.55±0.04^{a}	4.65±0.14^{b}	4.75±0.047^{b}

Control - uncoated Paper, thin fabric and Thick fabric, CH- Chitosan CH+SH – Chitosan with Shellac, CH+SH+LAC - Chitosan with shellac and lactic acid. Each values in this table represented as 'mean ± SD (n=2).Values in the same column followed by a different letter ($P<0.05$) are significantly different'.

The pH levels of tomatoes subjected to treatment with chitosan, chitosan-shellac, and chitosan-shellac-lactic acid were noted to diminish in comparison to their baseline levels over a duration of 12 days. Nevertheless, when juxtaposed with tomatoes maintained in uncoated packaging materials over the same timeframe, the fluctuations in pH were markedly more pronounced. Specifically, tomatoes preserved in chitosan-shellac-lactic acid and chitosan-shellac displayed relatively minimal alterations in pH, indicating the efficacy of these coating combinations in sustaining pH stability throughout the storage period.

The findings suggest that the total soluble solids content demonstrated a significant reduction in packed tomatoes following a 12-day storage period relative to pre-treatment levels. Conversely, tomatoes stored in coated packaging exhibited a lower total soluble solids content than those maintained in uncoated packaging. This observation implies that the implementation of chitosan-shellac and chitosan-shellac-lactic acid coatings effectively alleviated the decline in TSS content during storage, underscoring their potential role in preserving the quality of tomatoes.

Table 3 Total Titratable Acid (%) and Ascorbic acid (mg/ml) of tomato stored in fabric and paper coated with Chitosan, Chitosan and Shellac, and Chitosan and shellac with lactic acid

Sample	**Total Titratable Acid (TA) (%)**			**Ascorbic acid (mg/ml)**		
			Before treatment			
	57.12±3.5			34.87±2.06		
			After treatment			
Storage day	4	8	12	4	8	12
			Paper			
Control	49.1±1.20^{c}	45.36±2.4^{b}	39.06±1.78^{b}	33.9±1.38^{a}	31.4±0.93^{a}	17.6±1.10^{c}
CH	52.9±2.41^{b}	44.1±1.2^{b}	39.07±1.76^{b}	31.5±0.95^{b}	31.5±0.95^{a}	22.07±0.40^{a}
CH- SH	51.6±1.20^{b}	44.1±1.2^{b}	46.62±1.78^{a}	27±1.43^{d}	22.8±0.60^{c}	17.8±0.90^{c}
CH-SH-LAC	59.2±1.20^{a}	51.66±1.2^{a}	39.3±4.94^{b}	29.5±0.95^{c}	25.1±0.59^{b}	19.6±1.14^{b}
			Thin fabric			
Control	51.6±1.20^{c}	46.6±1.78^{b}	39.0±1.20^{c}	29.5±1.14^{b}	24.6±0.94^{c}	19.9±0.31^{b}
CH	51.6±1.78^{c}	50.4±7.12^{a}	41.5±1.20^{b}	27.3±1.14^{c}	24.8±4.33^{c}	21.3±1.07^{a}
CH-SH	61.7±1.78^{a}	51.6±1.78^{a}	49.1±1.20^{a}	33.6±1.14^{a}	31.9±3.33^{a}	21.6±0.81^{a}
CH-SH-LAC	56.7±1.78^{b}	50.4±3.56^{a}	44.08±1.22^{b}	29.4±1.14^{b}	26.6±0.87^{b}	19.6±1.10^{b}
			Thick fabric			
Control	56.7±1.78^{a}	49.1±1.20^{b}	39.0±1.20^{b}	29.5±0.95^{a}	24.6±1.07^{b}	19.1±0.40^{c}
CH	54.1±1.78^{b}	51.6±3.61^{a}	46.5±1.16^{a}	31.3±1.07^{a}	26.6±0.83^{a}	19.8±0.38^{c}
CH-SH	55.4±3.56^{a}	49.1±1.20^{b}	44.0±1.22^{a}	27.8±0.62^{c}	24.5±0.95^{b}	21.6±0.81^{a}
CH-SH-LAC	49.1±1.78^{c}	45.3±2.4^{c}	38.0±2.16^{b}	28.8±1.57^{b}	26.4±0.98^{a}	20.8±1.33^{b}

Control - uncoated Paper, thin fabric and Thick fabric, CH- Chitosan CH+SH – Chitosan with Shellac, CH+SH+LAC - Chitosan with shellac and lactic acid. Each values in this table represented as 'mean ± SD (n=2).Values in the same column followed by a different letter ($P<0.05$) are significantly different'.

The results indicate a significant reduction in titratable acidity (TA) of packaged tomatoes after a 12-day storage period when compared to the initial measurements. Nonetheless, tomatoes preserved in coated packaging demonstrated elevated TA levels in contrast to those in uncoated packaging. This highlights the efficacy of chitosan-shellac and chitosan-shellac-lactic acid coatings in alleviating the reduction of TA during the storage process, suggesting their potential role in sustaining the acidity and overall quality of tomatoes over time.

The content of ascorbic acid in packaged tomatoes, as illustrated in Table 3, significantly diminished following a 12-day storage interval relative to pre-treatment levels. Conversely, tomatoes housed in coated packaging exhibited diminished levels of total ascorbic acid. The variation in these measurements between samples derived from coated and uncoated packaging materials implies that the degradation rate in tomatoes stored in chitosan-shellac coated and chitosan-shellac-lactic acid coated packaging is relatively lower than that observed in tomatoes stored in chitosan-coated and uncoated samples.

Table 4 PPO Activity ($\times 10^2$ units/g) and POD Activity ($\times 10^2$ units/g) of tomato stored in fabric and paper coated with Chitosan, Chitosan and Shellac, and Chitosan and shellac with lactic acid

Sample	PPO Activity ($\times 10^2$ units/g)			POD Activity ($\times 10^2$ units/g)		
	Before treatment					
	14.77±0.72			1.83±0.26		
	After treatment					
Storage day	4	8	12	4	8	12
	Paper					
Control	12±1.91^{c}	11±0.95^{c}	12±1.9^{c}	2±0.3^{a}	2.8±0.7^{a}	3.3±0.3^{a}
CH	12±1.91^{c}	13.6±0.32^{a}	14.7±0.6^{a}	2.17±0.1^{a}	2.67±0.3^{b}	2.8±0.1^{c}
CH- SH	14.7±0.69^{a}	13.6±0.32^{a}	13.6±03^{b}	1.8±0.1^{b}	2.8±0.1^{a}	3.6±0.03^{a}
CH-SH-LAC	13.6±0.32^{b}	12±1.91^{b}	10.6±1.5^{d}	1.8±0.1^{b}	2.1±0.1^{c}	3±0.6^{b}
	Thin fabric					
Control	12±1.91^{b}	11.6±1.5^{c}	12±1.9^{b}	2.07±0.1^{b}	3.15±0.4^{a}	3.3±0.3^{a}
CH	14.72±0.6^{a}	13.6±0.3^{b}	12±1.9^{b}	2±0.3^{c}	2.49±0.1^{b}	3.1±0.4^{b}
CH-SH	14.72±0.6^{a}	14.7±0.6^{a}	11.6±1.5^{c}	2.49±0.1^{a}	3.15±0.4^{a}	2.8±0.1^{c}
CH-SH-LAC	14.72±0.6^{a}	11.6±1.5^{c}	13.6±0.3^{a}	2.07±0.1^{b}	2.49±0.1^{b}	3.3±0.3^{a}
	Thick fabric					
Control	12±1.91^{c}	13.6±0.3^{b}	12±1.9^{b}	2.17±0.1^{a}	2.9±0.6^{a}	3.0±0.54^{b}
CH	12±1.91^{c}	13.6±0.3^{b}	13.6±0.3^{a}	2±0.3^{b}	2.4±0.1^{b}	3.0±0.6^{b}
CH-SH	13.6±0.32^{b}	15.2±0.2^{a}	14.2±0.6^{a}	1.8±0.1^{c}	2.4±0.1^{b}	3.1±0.4^{a}
CH-SH-LAC	14.3±1.01^{a}	13.6±0.3^{b}	11.6±1.5^{c}	2.06±0.1^{a}	2±0.3^{c}	3.3±0.2^{a}

Control - uncoated Paper, thin fabric and Thick fabric, CH- Chitosan CH+SH – Chitosan with Shellac, CH+SH+LAC - Chitosan with shellac and lactic acid. Each values in this table represented as 'mean ± SD (n=2).Values in the same column followed by a different letter ($P<0.05$) are significantly different'.

The enzymatic activities of polyphenol oxidase (PPO) in both tomatoes subjected to packaging and those left unpackaged exhibited a temporal increase. Nevertheless, following a 12 day storage period, the tomatoes that were packed demonstrated a more pronounced reduction in PPO activities relative to their unpackaged counterparts. This observation implies that the coatings utilized in the fabric and paper packaging effectively mitigated the enzymatic activity, as indicated by the diminished PPO reduction activities observed in the unwrapped control samples.

Similarly, the activities of peroxidase (POD) in both packed and unpacked tomatoes manifested an increase over the duration of the study. However, after 12 days of storage, the packed tomatoes revealed a more substantial reduction in POD activities in comparison to their unpacked counterparts. This finding suggests that the coatings employed in the fabric and paper packaging served to inhibit the enzymatic activities, as evidenced by the reduced POD activities in the unwrapped control samples.

3.3. Quality characteristics of stored strawberry

The sensory attributes of preserved strawberries have been effectively maintained by the chitosan-shellac-lactic acid coated and chitosan-shellac coated packaging materials when contrasted with samples derived from chitosan coated and uncoated packaging materials (Figure 10). Following a storage duration of six days, the strawberries underwent complete deterioration.

The fruit samples that were retained within the chitosan-shellac coated material demonstrated significantly reduced weight loss in comparison to the other samples from both coated and uncoated materials. The samples preserved in chitosan shellac lactic acid exhibited a reduction in weight relative to the uncoated control and chitosan coated packaging materials (Figure 8). The pH levels of the strawberries varied among those stored in chitosan, chitosan-shellac, and chitosan-shellac-lactic acid when assessed against pre-treatment values on the sixth day. However, a more pronounced difference was observed when these were compared to samples housed in uncoated packaging material on the same days. The samples maintained in chitosan-shellac-lactic acid and chitosan-shellac exhibited minimal alteration in pH (Figure 9).

The concentration of total soluble solids, titratable acidity, and ascorbic acid in packaged strawberries exhibited a significant decline following a storage period of six days (Table 5). Strawberries encased in coated packaging demonstrated elevated levels of total soluble solids, titratable acidity, and ascorbic acid content, and the disparity between these parameters in samples derived from coated versus uncoated packaging materials suggests that the degradation rate of strawberries preserved within chitosan-shellac-coated and chitosan-shellac-lactic acid-coated packaging is relatively lower than that observed in strawberries stored in chitosan-coated and uncoated configurations.

The enzymatic activities of both polyphenol oxidase (PPO) and peroxidase (POD) in both packaged and unpackaged strawberries showed an upward trend throughout the storage duration. The strawberries that were packaged exhibited a greater reduction in the activities of PPO and POD after six days of storage, demonstrating that the coatings applied to the fabric and paper effectively inhibited the activity of these two enzymes, as evidenced by the reduced activities of PPO and POD in the unwrapped and control samples (Table 6).

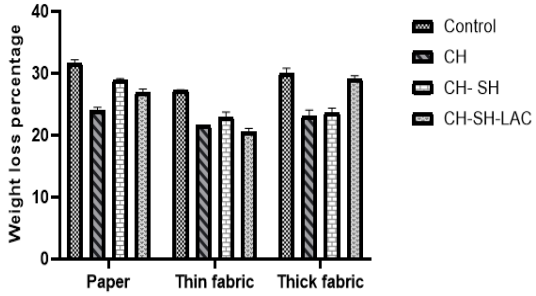

Figure 8. Weight Loss (%) of strawberry stored in fabric and paper coated with Chitosan, Chitosan and Shellac, and Chitosan and shellac with lactic acid [Control - uncoated Paper, thin fabric and Thick fabric, CH- Chitosan CH+SH – Chitosan with Shellac, CH+SH+LAC - Chitosan with shellac and lactic acid. Each values represented as 'mean ± SD (n=2)].

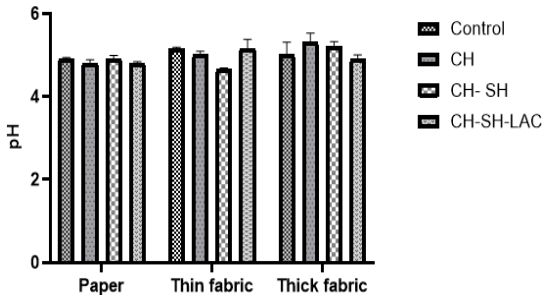

Figure 9. pH of strawberry stored in fabric and paper coated with Chitosan, Chitosan and Shellac, and Chitosan and shellac with lactic acid [Control - uncoated Paper, thin fabric and Thick fabric, CH- Chitosan CH+SH – Chitosan with Shellac, CH+SH+LAC- Chitosan with shellac and lactic acid. Each values represented as 'mean ± SD (n=2)].

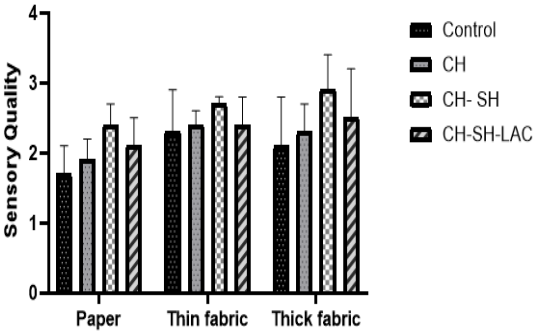

Figure 10. Sensory quality of strawberry stored in fabric and paper coated with Chitosan, Chitosan and Shellac, and Chitosan and shellac with lactic acid [Control - uncoated Paper, thin fabric and Thick fabric, CH- Chitosan CH+SH – Chitosan with Shellac, CH+SH+LAC - Chitosan with shellac and lactic acid. Each values represented as 'mean ± SD (n=2)].

The sensory attributes of strawberries were significantly retained by both chitosan-shellac-lactic acid coated and chitosan-shellac coated packaging materials when juxtaposed with chitosan-coated and uncoated samples. Nonetheless, subsequent to a storage period of 6 days, all strawberries commenced to exhibit signs of deterioration. Among the coated materials, strawberries preserved within chitosan-shellac-coated fabric demonstrated a markedly reduced weight loss, whereas those encapsulated in chitosan-shellac-lactic acid experienced a reduction in weight in comparison to both the uncoated control and the chitosan-coated packaging. Fluctuations in pH levels were detected in strawberries subjected to various coatings, with chitosan-shellac-lactic acid and chitosan-shellac exhibiting minimal alteration relative to uncoated samples throughout the equivalent time frame.

Table 5 Soluble solids (°Brix), Total Titratable Acid (%) and Ascorbic acid (mg/ml) of strawberry stored in fabric and paper coated with Chitosan, Chitosan and Shellac, and Chitosan and shellac with lactic acid

Sample	Total soluble solids (°Brix)	Total Titratable Acid (%)	Ascorbic acid (mg/ml)
Before Treatment			
	7.18±0.64	57.3±1.82	41.67±1.97
After Treatment			
Storage day	6		
	Paper		
Control	7.65±0.14^{b}	50.9±2.97^{a}	34.07±1.3^{c}
CH	7.1±0.09^{c}	44.5±0.75^{c}	35.95±0.4^{b}
CH- SH	8.3±0.09^{a}	47.09±3.16^{b}	35.95±0.4^{b}
CH-SH-LAC	6.1±0.09^{d}	48.4±5.38^{b}	39.95±0.5^{a}
	Thin Fabric		
Control	7.65±0.14^{b}	57.45±0.75^{a}	37.5±1.07^{b}
CH	8.45±0.04^{a}	47.65±1.23^{c}	33.4±1.0^{c}
CH-SH	7.55±0.04^{b}	50.96±0.53^{b}	41±0.47^{a}
CH-SH-LAC	6.25±0.23^{c}	57.31±0.61^{a}	38.02±1.31^{a}
	Thick Fabric		
Control	6.9±0.09^{b}	50.9±0.53^{b}	37.9±1.41^{b}
CH	6.45±0.04^{b}	53.5±0.54^{b}	35.4±0.90^{c}
CH-SH	8.1±0.09^{a}	57.3±1.81^{a}	34.05±1.3^{c}
CH-SH-LAC	5.2±0.19^{c}	47.0±3.16^{c}	39.95±0.52^{a}

Control - uncoated Paper, thin fabric and Thick fabric, CH- Chitosan CH+SH – Chitosan with Shellac, CH+SH+LAC - Chitosan with shellac and lactic acid. Each values in this table represented as 'mean ± SD (n=2).Values in the same column followed by a different letter (P<0.05) are significantly different'.

The findings obtained indicate a notable reduction in total soluble solids, titratable acidity, and ascorbic acid concentration in packed strawberries subsequent to merely six days of storage. Conversely, strawberries encased in coated packaging exhibited diminished levels of these parameters when juxtaposed with those housed in uncoated packaging. This disparity highlights the potential efficacy of chitosan-shellac and chitosan-shellac-lactic acid coatings in alleviating the deterioration of strawberries throughout the storage period, thereby suggesting their effectiveness in maintaining the quality of the fruit over an extended duration.

Table 6 Polyphenol oxidase (PPO) and peroxidase (POD) activity of strawberry stored in fabric and paper coated with Chitosan, Chitosan and Shellac, and Chitosan and shellac with lactic acid

Sample	PPO Activity ($\times 10^2$ units/g)	POD Activity ($\times 10^2$ units/g)
	Before Treatment	
	15.67.±0.25	1.45±0.18
	After Treatment	
Storage day	6	6
	Paper	
Control	13.6±0.32^{a}	1.9±0.6^{c}
CH	8.33±1.59^{c}	2.5±0.1^{b}
CH- SH	11.6±1.59^{b}	2.8±0.1^{a}
CH-SH-LAC	8.33±1.59^{c}	2.0±0.3^{c}
	Thin Fabric	
Control	8.33±1.5^{c}	2.5±0.1^{b}
CH	8.33±1.5^{c}	2.8±0.1^{a}
CH-SH	11.6±1.5^{a}	2.1±0.4^{c}
CH-SH-LAC	9.33±1.5^{b}	2.0±0.6^{c}
	Thick Fabric	
Control	8.33±1.5^{c}	2.3±0.6^{b}
CH	11.6±1.5^{b}	2.5±0.1^{a}
CH-SH	13.6±03^{a}	2.1±0.4^{c}
CH-SH-LAC	8.33±1.5^{c}	2.1±0.4^{c}

Control - uncoated Paper, thin fabric and Thick fabric, CH-Chitosan CH+SH – Chitosan with Shellac, CH+SH+LAC - Chitosan with shellac and lactic acid. Each values in this table represented as 'mean ± SD (n=2).Values in the same column followed by a different letter ($P<0.05$) are significantly different'.

During the process of storage, the enzymatic activities of both polyphenol oxidase (PPO) and peroxidase (POD) in strawberries, irrespective of packaging conditions, exhibited a progressive increase over time. On the sixth day of storage, strawberries housed within coated packaging materials demonstrated a more pronounced reduction in the activities of PPO and POD in contrast to those that remained unpackaged. This observation implies that the coatings utilized in the fabric and paper packaging effectively mitigated the enzymatic activity of these biocatalysts, as corroborated by the diminished reduction activities of PPO and POD observed in the unwrapped control samples.

4. Discussion

The research on composite fabric food packaging with lactic acid and chitosan-shellac coating demonstrates the effectiveness of these coatings in preserving the quality and extending the shelf life of both tomatoes and strawberries.

The antioxidant activity assays revealed that both chitosan and chitosan-lactic acid exhibited strong antioxidant properties, with chitosan showing the highest antioxidant potency. This suggests that the incorporation of chitosan in food packaging can effectively enhance the oxidative stability of the packaged produce. The EC_{50} values for chitosan, lactic acid, and their combination were 89.61 ± 1.309^{bc}, 95.505 ± 1.279^{b}, and 99.2 ± 0.7778^{b}, respectively, highlighting the superior antioxidant potential of chitosan over lactic acid, either alone or in combination. These results align with other studies that have reported the strong antioxidant properties of chitosan, which contribute to its ability to protect food products from oxidative damage during storage. Relevant studies on the antioxidant properties of chitosan have demonstrated its efficacy in enhancing oxidative stability in food products. According to Sun *et al.* (2022), chitosan blended with ginseng residue polysaccharides acts as an antioxidant in food packaging, delaying deterioration in fresh-cut melon by enhancing oxidative stability through a proposed antioxidant mechanism. Similarly, Han *et al.* (2018) reported that chitosan enhances oxidative stability in food products by reducing lipid oxidation products through altering microstructure, entrapping fat droplets, and impacting water mobility in the meat-based matrix. Chitosan enhances oxidative stability in food products by incorporating natural extracts, essential oils, and plant extracts, which provide antioxidant properties, thus extending shelf-life and preserving quality (Muñoz-Tebar *et al.,* 2023).

Tomatoes stored in chitosan-shellac coated fabric experienced significantly lower weight loss compared to those stored in other coatings or uncoated materials. This reduction in weight loss can be attributed to the barrier properties of the chitosan-shellac coating, which effectively reduces moisture loss and delays dehydration, a common issue in the storage of fresh produce. Additionally, the chitosan-shellac-lactic acid coating further minimized weight loss, although the effect was slightly less pronounced than that of the chitosan-shellac combination. The pH stability, total soluble solids, titratable acidity, and ascorbic acid content were better preserved in tomatoes stored in chitosan-shellac and chitosan-shellac-lactic acid coated packaging, indicating the coatings' ability to maintain the quality of the tomatoes over a 12-day storage period. The inhibition of PPO and POD activities in coated tomatoes further supports the coatings' role in delaying enzymatic browning and spoilage, consistent with findings from other studies that have highlighted the effectiveness of chitosan-based coatings in reducing enzymatic activities in stored fruits. This result ties well with previous studies by Zhelyazkov *et al.* (2023), wherein Chitosan-lactic acid coatings positively impact sensory qualities by reducing water loss, enhancing taste, and increasing soluble solids and acidity, thus preserving quality and extending shelf life of food products. A similar conclusion was reached by Riseh *et al.* (2023) in the research, where Chitosan-based nanocomposites, including chitosan-lactic acid coatings, enhance postharvest quality of agricultural products without significant sensory or nutritional property alterations. Other results were broadly in line with the work carried out by Esin & Özlem (2019), and the insights are chitosan-lactic acid-based coatings inhibit *Escherichia coli* and *Salmonella enteritidis*, enhancing food safety without affecting sensory or nutritional properties of chicken and quail eggs. In addition, Pagno *et al.* (2018) reported that Chitosan-lactic acid coatings maintain firmness, reduce weight loss, lower ethylene emission, and slow down nutraceutical loss in fruits like tomatoes, preserving their sensory and nutritional qualities during storage.

In the quality characteristics of stored strawberries, similar trends were observed in strawberries, although the storage duration was shorter, with significant deterioration occurring after 6 days. The chitosan-shellac and chitosan-shellac-lactic acid coatings were effective in reducing

weight loss, maintaining pH stability, and preserving total soluble solids, titratable acidity, and ascorbic acid content. The reduced PPO and POD activities in coated strawberries further demonstrate the coatings' ability to inhibit enzymatic reactions that lead to spoilage, consistent with previous research on the preservation of strawberries using chitosan-based coatings. The rapid deterioration of strawberries compared to tomatoes may be due to their higher metabolic activity and sensitivity to storage conditions, underscoring the need for effective preservation techniques in the storage of delicate fruits like strawberries. In a similar research, chitosan-based edible coatings, enriched with lactic acid bacteria, have shown significant potential in reducing strawberry spoilage during refrigerated storage. Studies have demonstrated that coatings incorporating chitosan, lactic acid bacteria, and other natural compounds like putrescine can effectively extend the shelf life of strawberries by reducing decay, weight loss, and microbial growth (Bahmani *et al*., 2024). Additionally, the application of chitosan and beeswax coatings has been found to enhance the physicochemical properties of strawberries, such as hardness, total soluble solids, and ascorbic acid content, thereby improving their overall quality and longevity at room temperature (Lalengmawii & Topno, 2024). Furthermore, the integration of phytochemical-encapsulated nanoparticles in chitosan-based coatings has been shown to inhibit microbial growth, prevent nutrient loss, and preserve the quality of strawberries during storage at both room and refrigerated temperatures (Benavides & Franco, 2023; Fan & Aimo, 2023). These findings collectively highlight the efficacy of chitosan-based edible coatings in mitigating spoilage and enhancing the storage quality of strawberries.

The integration of lactic acid and chitosan in composite fabric food packaging, particularly with shellac coating, presents a novel approach to preserving tomatoes and strawberries. This method not only enhances the shelf life of these fruits but also aligns with the growing demand for sustainable and biodegradable packaging solutions. Novel contributions to food preservation is the enhanced mechanical properties, which is evident by the incorporation of lactic acid that improves the mechanical strength of the packaging, making it more durable compared to existing chitosan-based films (He *et al.,* 2024). Studies indicate that the proposed composite can extend the shelf life of strawberries by over 15 days, surpassing many current packaging solutions (Yaowen *et al.,* 2016). This approach utilizes renewable resources, contributing to a more sustainable food packaging industry, as highlighted in recent advancements in edible coatings (Juric *et al.,* 2024).

The cost-effectiveness of composite fabric food packaging with lactic acid and chitosan, particularly when compared to traditional waxed paper, is supported by several studies. Chitosan-based coatings have demonstrated significant effectiveness in extending the shelf life of fruits like strawberries and tomatoes. For instance, coatings can reduce weight loss and inhibit microbial growth, prolonging freshness by several days (He *et al.,* 2024; Lai *et al*., 2024). Chitosan is biodegradable and non-toxic, making it a more environmentally friendly option compared to traditional waxed papers, which often contain synthetic materials (Priyadarshi *et al.,* 2024; Suresh *et al.,* 2024). The development of chitosan-based coatings aligns with the growing demand for sustainable packaging solutions, potentially reducing waste and environmental impact (Zou *et al.,* 2024). Although initial costs may be higher, the extended shelf life and reduced spoilage rates can lead to lower overall costs for producers and retailers (Suresh *et al.,* 2024). The ability to maintain product quality can enhance consumer satisfaction and reduce losses due to spoilage, ultimately benefiting the supply chain economically (Lai *et al.,* 2024).

This approach leverages the biodegradable properties of chitosan and lactic acid, enhancing food preservation while addressing environmental concerns associated with synthetic coatings. Chitosan exhibits excellent film-forming, mechanical strength, and antimicrobial properties, making it effective for extending the shelf life of strawberries (Priyadarshi *et al.,* 2024). Polylactic acid (PLA) reinforced with antibacterial fillers shows improved barrier properties and moisture resistance, effectively preserving fruits (Pradhan *et al.,* 2024). Chitosan-essential oil films enhance antimicrobial activity and antioxidant effects, providing a natural preservation method (Liu *et al.,* 2024). While synthetic coatings like polyethylene offer superior barrier properties, they are non-biodegradable and contribute to environmental pollution (Cheng *et al*., 2024). The migration of microplastics from synthetic films into food raises health concerns, prompting a shift towards biodegradable alternatives (Liu *et al*., 2024). In contrast, while biodegradable coatings like chitosan and PLA composites offer environmental benefits, they may face challenges such as inferior mechanical strength and higher costs compared to synthetic options (Cheng *et al.,* 2024). The use of composite fabric food packaging incorporating lactic acid and chitosan with shellac coating presents a promising alternative for preserving fruits like tomatoes and strawberries.

5. Conclusion

In conclusion, the application of chitosan, shellac, and lactic acid coatings on composite fabric food packaging materials demonstrated significant potential in enhancing the preservation of both tomatoes and strawberries during storage. The antioxidant activity, particularly in chitosan and the chitosan-lactic acid combination, was effective, as evidenced by their superior EC_{50} values, indicating strong antioxidant potency. The quality characteristics of the stored tomatoes and strawberries, including weight loss, pH stability, total soluble solids, titratable acidity, and ascorbic acid content were better preserved in the chitosan-shellac and chitosan-shellac-lactic acid coated packaging compared to uncoated or solely chitosan-coated samples.

Furthermore, the inhibition of polyphenol oxidase (PPO) and peroxidase (POD) activities in both tomatoes and strawberries suggests that these coatings effectively slow down enzymatic reactions that contribute to the deterioration of the fruits. The coatings also maintained the sensory qualities, such as color, appearance, and taste, of the fruits more effectively than the other tested materials.

Overall, the findings highlight the efficacy of chitosan-shellac and chitosan-shellac-lactic acid coatings in extending the shelf life and preserving the quality of fruits during storage. These results suggest that such coatings have significant potential for use in food packaging applications, offering a promising approach to reducing food spoilage and waste.

Acknowledgments

We are thankful to DBT STAR College Scheme for Strengthening of Science Education and Training at Undergraduate Level and DST FIST for their continuous support.

The authors thank the Management of Dr NGP Arts and Science College, Coimbatore, Tamil Nadu, India for the equipments provided for the research.

Disclosure

The authors report no conflicts of interest in this work.

References

Asgher M, Qamar SA, Bilal M, Iqbal HMN. 2020. Bio-based active food packaging materials: Sustainable alternative to conventional petrochemical-based packaging materials. *Food Res Int*., **137**:109625.

Baoying Shi Zhanhua Hao, Yuchen Du, Mengke Jia and Siqi Xie. 2024. Mechanical and barrier properties of chitosan-based composite film as food packaging: A review. *Bioresources*, **19(2)**:4001-4014.

Benavides S and Franco W. 2023. Innovative Integration of Arrayan (*Luma apiculata*) extracts in chitosan coating for fresh strawberry preservation. *Int. J. Mol. Sci.,* **24(19)**:14681.

Carlos Henrique Pagno, Antonella Castagna, Alice Trivellini, Anna Mensuali-Sodi, Annamaria Ranieri, Ester Alice Ferreira, Alessandro de Oliveira Rios and Simone Hickmann Flôres. 2018. The nutraceutical quality of tomato fruit during domestic storage is affected by chitosan coating. *J. Food Process. Preserv*., **42**:e13326.

Caleb OJ, Mahajan PV, Al-Said FA and Opara UL. 2013. Modified atmosphere packaging technology of fresh and fresh-cut produce and the microbial consequences - a review. *Food Bioproc. Tech,* **6(2)**: 303-329.

Changyuan He Liubo Yuan, Siwei Bi, Chaomei Zhou, Qin Yang, Jun Gu, Bin Yan and Jin He. 2024. Modified Chitosan-based coating/packaging composites with enhanced antibacterial, antioxidant, and UV-resistant properties for fresh food preservation. *ACS Appl. Mater. Interfaces*., **16(36)**:48352-48362.

Dongkun Yu, Indra Bhusan Basumatary, You Li, Xingyan Zhang, Santosh Kumar, Fei Ye and Joydeep Dutta. 2024. Chitosan-photocatalyst nanocomposite on polyethylene films as antimicrobial coating for food packaging. *Prog. Org. Coat*., **186**:108069-108069.

Edwin Shigwenya Madivoli, Jacqueline Kisato J, Gichuki CM, Wangui P, Kimani and Patrick Gachoki Kareru. 2024. Antimicrobial and food barrier properties of polyvinyl alcohol - lactic acid food packaging films. *Food sci. nutr.,* **12(1)**: 1-10.

Emadian SM, Onay TT and Demirel B. 2017. Biodegradation of bioplastics in natural environments. *J Waste Manag.,* **59**: 526-536.

Esin Derelioğlu and Özlem Turgay. 2019. Effect of chitosan combined coating on chicken and quail eggs for controlling *Escherichia coli* and *Salmonella enteritidis*. *Innov. Food Sci. Emerg. Technol.,* **2(6):**170-178.

Geyer R, Jambeck JR and Law KL. 2017. Production, use, and fate of all plastics ever made. *Sci Adv.,* **3(7):**e1700782.

Hakan Şahansoy, Cengiz Caner and Muhammed Yüceer. 2024. The shellac and shellac nanocomposite coatings on enhanced the storage stability of fresh eggs for sustainable packaging. *Int. J. Biol. Macromol.,* **261**:129817-129817.

Hopewell J, Dvorak R and Kosior E. 2009. Plastics recycling: Challenges and Opportunities. *Philos Trans R Soc B.,* **364(1526):** 2115-2126.

Ismail Siham, Shaimaa, Hassan Mohamed, Abosereh Nivien, Khattab Om, Abo-Elnasr Amany, Helal Mohamed and Hashem, Amal. 2023. Optimization, characterization of newly immobilized Mannanase on activated Chitosan beads and its applications. *Jordan J. Biol. Sci*., **6**:73 – 84.

Jamshidian M, Tehrany EA, Imran M, Jacquot M and Desobry S. 2010. Poly-lactic acid: Production, applications, nanocomposites, and release studies. *Compr Rev Food Sci.,* **9(5):** 552-571.

Jiang YM and Fu JR. 1999. Postharvest browning of litchi fruit by water loss and its prevention by controlled atmosphere storage at high relative humidity. *Food Sci. Technol.*, **32(5)**: 278-283.

Juan Cheng, Rui Gao, Yong Zhu and Qinbao Lin. 2024. Applications of biodegradable materials in food packaging: A review. *Alex. Eng. J.,* **(91)**:70-83.

Lalengmawii and Samir Ebson Topno. 2024. Effect of different level of chitosan and beeswax edible coating on storage life and physio-chemical properties of strawberry (Fragaria × Ananassa) Cv Winter Dawn. *J. appl. biol. Biotechnol.,* **27(6)**:657-64.

Li N, Cheng Y, Li Z, Yue T and Yuan Y. 2024. An alginate-based edible coating containing lactic acid bacteria extends the shelf life of fresh strawberry (Fragaria × ananassa Duch.). *Int J Biol Macromol*., **274(1)**:133273.

Lim LT, Auras R and Rubino M. 2008. Processing technologies for poly (lactic acid). *Prog Polym Sci.,* **33(8)**: 820-852.

Liu Yaowen, Liang Xue, Wang Shuyao, Qin Wen, Feng Chaohui, Zhang Qing, Chen Hong, Lin, Derong and Hu Ke. 2016. Strawberry preserving composite packaging film and preparation method thereof. *JoFPSTT.,* **6(4)**: 45-52.

Macadam JW, Nelson CJ and Sharp RE. 1992. Peroxidase activity in the leaf elongation zone of tall fescue: I. Spatial distribution of ionically bound peroxidase activity in genotypes differing in length of the elongation zone. *Plant Physiol*., **99(3)**:872-8.

Marina Jurić, Luna Maslov Bandić, Daniele Carullo and Slaven Jurić. 2024. Technological advancements in edible coatings: Emerging trends and applications in sustainable food preservation. *Food Biosci*., **58**:103835.

Minyi Han, Mathias P Clausen, Morten Christensen, Els Vossen, Thomas Van Hecke and Hanne Christine Bertram. 2018. Enhancing the health potential of processed meat: the effect of chitosan or carboxymethyl cellulose enrichment on inherent microstructure, water mobility and oxidation in a meat-based food matrix. *Food & Function*, **9**: 4017-4027.

Muñoz-Tebar N, Pérez-Álvarez JA, Fernández-López J and Viuda-Martos M. 2023. Chitosan edible films and coatings with added bioactive compounds: Antibacterial and antioxidant properties and their application to food products: A Review. *Polymers*, **15(2)**:396.

Syed MH, Khan MMR, Zahari MAKM, Beg MDH and Abdullah N. 2024. Developing of nanocellulose loaded chitosan-polylactic acid biofilms for green food packaging. *Green Materials*, 1-11.

Reza Bahmani, Farhang Razavi, Seyed Najmmaddin Mortazavi, Antonio Juárez-Maldonado and Gholamreza Gohari. 2024. Chitosan - putrescine nanoparticle coating attenuates postharvest decay and maintains ROS scavenging system activity of strawberry cv. 'Camarosa' during cold storage. *Folia Hort*., **36(1)**: Article 36.

Roohallah Saberi Riseh, Masoumeh Vatankhah, Mohadeseh Hassanisaadi, John F. Kennedy. 2023. Chitosan-based nanocomposites as coatings and packaging materials for the postharvest improvement of agricultural product. A review. *Carbohydr. Polym.,* **309**:120666.

Priyadarshi R, El-Araby A and Rhim JW. 2024. Chitosan-based sustainable packaging and coating technologies for strawberry preservation: A review. *Int J Biol Macromol*., **278(2)**:134859.

Saberi R Riseh, Masoumeh Vatankhah, Mohadeseh Hassanisaadi and John F Kennedy. 2023. Chitosan-based nanocomposites as coatings and packaging materials for the postharvest improvement of agricultural product. A review. *Carbohydr. Polym.*, **309:** 120666-120666.

Siva Nandhini Suresh, Ramesh Subramani, Charumathi Pushparaj, Prakash Kumar Sarangi, Viduthalai R Regina and Ramesh Subramani. 2024. Almond gum-chitosan nanocomposite as edible formulation for advancing postharvest longevity of fruits and vegetables. *Polym advan technol.,* **35(6)**: e6453.

Smitirupa Pradhan, Aswathy NR, Sudha GS, Alaka Samal, Aswini Kumar Mohapatra, Payoja Praharaj and Sony Pandey. 2024. Augmented barrier properties of poly (lactic acid) composite packaging film reinforced by antibacterial hybrid bio-filler: Extending the shelf life of fruits. *Polym. Compos*., Wiley.

Sun J, Li Y, Cao X, Yao F, Shi L, Liu Y. 2022. A film of chitosan blended with ginseng residue polysaccharides as an antioxidant packaging for prolonging the shelf life of fresh - cut melon. *Coatings*, **12(4)**:468.

Wenqin Lai, Lin Wang, Yu Pang, Meihua Xin, Mingchun Li, Libao Shi, and Yaping Mao. 2024. Preparation of citric acid cross-linked chitosan quaternary phosphonium/polyvinyl alcohol composite film and its application in strawberry preservation. *Food Chem*., **455**: 139908-139908.

Yang Zou, Yanfen Zhang, Hui Zhang, Bin Cao, Zixin Luo and Huawei Duan. 2024. Facile preparation of chitosan/carnauba wax emulsion-based coatings for hydrophobic and oleophobic cellulose-based food packaging. *Packag. Tech. Sci.,* **37(10)**: 965-974.

Youssef Khamis and Aya Hashim. 2020. Inhibitory effect of Clay/Chitosan Nanocomposite against *Penicillium digitatum* on citrus and its possible mode of action. *Jordan J. Biol. Sci.,* **13(3)**:349-355.

Yuvaraj D, Iyyappan J, Gnanasekaran R, Ishwarya G, Harshini RP, Dhithya V, Chandran M, Kanishka V and Gomathi K. 2021.Advances in bio food packaging - An overview. *Heliyon*, **7 (9)**:e07998.

Zhaoyang Fan and Alberto Aimo. 2023. Development of Multifunctional Nanoencapsulated trans - Resveratrol/Chitosan nutraceutical edible coating for strawberry preservation. *ACS Nano.*, **17(9)**:8586-8597.

Zhelyazkov Stoil, Zsivanovits Gabor, Marudova-Zsivanovits and Maria. 2023. Investigation of edible coatings on the physical, chemical and microbiological characteristics of processed melons during storage. *BIO Web of Conferences*. **58**.

Zhiqing Liu, Siting Wang, Hui Liang, Jintao Zhou, Min-Hua Zong, Yufei Cao and Wen-Yong Lou. 2024. A review of advancements in chitosan-essential oil composite films: Better and sustainable food preservation with biodegradable packaging. *Int. J. Biol. Macromol.,* **274 (2)**:133242-133242.

JJBS

Volume 18, Number 3,September 2025
ISSN 1995-6673
Pages 449 – 455

Jordan Journal of Biological Sciences

Evaluating the Cytotoxic Impact of 5FU and Green-Synthesized Silver Chloride Nanoparticles on Gastric Cancer Cells

Erfaneh Dalghi[1], Rahim Ahmadi[2,*], Atefeh Dehghani[3], Atefeh Hasanli [4]

[1] Department of Biology, Faculty of Life Science and Biotechnology, Shahid Beheshti University, Tehran, Iran; [2] Department of Biology, Avicenna International College, Budapest, Hungary; [3] Department of Biology, Sanandaj Branch, Islamic Azad University, Kurdistan, Iran, Member of Young Researchers and Elite Club, Islamic Azad University, Sanandaj, Iran; [4] Department of Nanobiotechnology, Faculty of Biological Science, Tarbiat Modares University, Tehran, Iran

Received: August 18, 2024; Revised: February 7, 2025; Accepted: February 20, 2025

Abstract

Aim: This study aims to comprehensively evaluate the cytotoxic effects of silver chloride nanoparticles and 5-fluorouracil (5FU) on gastric cancer cells, comparing them to non-cancerous HEK293 cells and investigating the potential synergistic effects of their combined treatment.

Background and Objective: Nanoparticles and chemotherapeutic agents have demonstrated potential in inducing cytotoxic effects in cancer cells. However, the synergistic effects of silver chloride nanoparticles and 5FU on gastric cancer cells remain insufficiently understood.

Methods and Analysis: In this experimental study, gastric cancer cells were allocated into four groups: control (untreated), groups treated exclusively with silver chloride nanoparticles, groups treated exclusively with 5FU, and groups receiving a combination of silver chloride nanoparticles and 5FU. Cell viability was assessed using the MTT assay 24 hours post-treatment. Data were analyzed using one-way analysis of variance (ANOVA) to identify statistically significant differences among the treatment groups.

Results: The cytotoxic effects of 5FU on AGS cells were comparable to its effects on non-cancerous HEK293 cells. Silver chloride nanoparticles exhibited cytotoxic effects at concentrations exceeding 12 μg/mL in HEK293 cells and concentrations exceeding 3.1 μg/mL in gastric cancer cells. While individual treatments with 5FU or silver chloride nanoparticles induced dose-dependent cytotoxic effects on gastric cancer cells, the combined treatment exhibited enhanced cytotoxicity compared to either agent alone. Notably, the combination of 5FU and silver chloride nanoparticles at specific concentrations led to a significant reduction in cell viability, suggesting synergistic effects.

Conclusion: The findings of this study indicate that the co-administration of silver chloride nanoparticles and 5FU exerts greater cytotoxic effects on gastric cancer cells compared to 5FU monotherapy.

Keywords: Silver chloride nanoparticles, 5FU, Gastric cancer

1. Introduction

Gastric cancer, characterized by the uncontrolled proliferation of malignant cells in the stomach lining, remains a significant global health challenge, contributing substantially to morbidity and mortality. The disease exhibits a notably higher incidence in men, who are twice as likely to develop gastric cancer as women, making it the fourth most common cancer worldwide (Mamun et al., 2024). The primary etiological factor for gastric cancer is Helicobacter pylori infection, which accounts for over 60% of reported cases (Dunan et al., 2025). Other major risk factors include smoking, dietary habits (e.g., high consumption of pickled vegetables), obesity, and genetic predisposition (Vahid & Davoodi, 2021). Early symptoms often include heartburn, upper abdominal discomfort, nausea, loss of appetite, weight loss, jaundice, vomiting, and hematochezia (Nagaich & Sharma, 2018).

Nanoparticles, particularly silver nanoparticles, have demonstrated significant anticancer properties across various cancer cell lines, making them a promising area of study in cancer research. Their unique physicochemical properties have driven interest in their potential therapeutic applications in oncology (Huy et al., 2020; Faridi et al., 2023). The emergence of nanoparticle-based therapies represents a new frontier in precision medicine, offering innovative strategies for improving cancer treatment outcomes.

Chemotherapy remains the cornerstone of gastric cancer treatment, with 5-fluorouracil (5FU) being one of the most extensively studied and widely used chemotherapeutic agents. 5FU, commonly marketed under the trade name Adrucil, is a cytotoxic drug known for its efficacy against various malignancies, particularly gastrointestinal cancers (Yuan et al., 2021). Its role in gastric cancer therapy is well-established, whether used as a monotherapy or in combination with other agents (Na et al., 2021; Yamashita et al., 2021; Wolpin et al., 2007).

* Corresponding author. e-mail: drrhmahmadi@gmail.com.

Recent studies suggest that combining 5FU with other compounds, including nanoparticles, may improve therapeutic efficacy and enhance postoperative survival rates in gastric cancer patients (Hong and Feng, 2021). This growing body of research underscores the potential of combination therapies, particularly those incorporating nanoparticles, as a promising avenue for optimizing treatment strategies (Guo et al., 2025; Meng et al., 2025).

Nanoparticles hold immense potential as novel therapeutic agents for gastrointestinal cancers (Mittal et al., 2018). Studies have investigated their cytotoxic effects on gastrointestinal cancer cell lines, as well as their influence on apoptotic gene expression. The cytotoxicity of nanoparticles against gastric cancer cells has been shown to be dose- and time-dependent (Miethling-Graff et al., 2014). Additionally, research examining the cytotoxic effects of nanoparticles on human gastric cancer cells has highlighted their significant impact on cell viability (Li et al., 2017). A growing number of studies has also explored the green synthesis of silver chloride nanoparticles using plant extracts, revealing their potent anticancer properties (Rani et al., 2022). The eco-friendly, cost-effective green synthesis method has gained traction due to its simplicity and its demonstrated cytotoxic effects against AGS cells (gastric adenocarcinoma) (Aslany et al., 2020).

Given the substantial global burden of gastric cancer and its profound clinical, social, and economic impact, there is a critical need for novel and more effective treatment strategies. While previous research has largely focused on the individual effects of nanoparticles on cancer cells, there remains a notable gap in understanding their combined effects with conventional chemotherapeutic agents. Therefore, this study aims to investigate the synergistic effects of 5FU and silver chloride nanoparticles on gastric cancer cells. The findings from this research could provide valuable insights into optimizing treatment approaches and improving therapeutic outcomes for gastric cancer patients.

2. Material and Methods

In this experimental study, we obtained cancer cell lines HEK293 and AGS from the molecular cell bank of the Pasteur Institute of Iran and maintained them under strictly sterile and standardized conditions within liquid nitrogen tanks. We categorized gastric cancer cells into specific groups for analysis, including control (untreated), groups treated solely with silver chloride nanoparticles, groups treated solely with 5-fluorouracil (5FU), and groups exposed to a combination of silver chloride nanoparticles and 5FU. The determination of all concentrations, both individual and combined, was carefully carried out based on the collective expertise of the researchers and preliminary pilot studies conducted in the laboratory.

For drug preparation, 5FU powder was obtained from Aburaihan Pharmaceutical Company. 5FU was then dissolved in phosphate-buffered saline (PBS), sterilized, and prepared at various concentrations. Silver chloride nanoparticles were synthesized through an environmentally friendly and green method using a plant extract, as described in previous studies. Fresh leaves of the cotton thistle plant (Onopordum acanthium) were harvested, thoroughly washed, and homogenized to obtain a uniform aqueous extract. The extract was then mixed with a silver chloride solution, and the resulting mixture was incubated at room temperature. The reduction of silver ions to AgCl nanoparticles was facilitated by the bioactive compounds in the plant extract. The change in color observed in the reaction mixture served as an indicator of nanoparticle formation.

The identity, size, morphology, and crystalline structure of the green-synthesized AgCl nanoparticles were characterized using scanning electron microscopy (SEM) and X-ray diffraction (XRD). SEM was employed to analyze the surface morphology and particle size distribution, providing high-resolution images to confirm the structural integrity and shape of the nanoparticles. XRD analysis was conducted to determine the crystalline phase and purity of the nanoparticles, identifying characteristic diffraction peaks corresponding to silver chloride. These techniques collectively ensured the precise characterization of the synthesized nanoparticles, confirming their successful formation and structural properties.

HEK293 and AGS cells were treated with varying doses of 5FU and AgCl nanoparticles, both independently and in combination. Control groups without any treatment were included for baseline comparison. Following treatment initiation, the cells were incubated for 24 hours to assess their responses to the administered treatments. Subsequently, the viability of HEK293 and AGS cells was evaluated using the MTT colorimetric assay method, allowing for a comprehensive analysis of cellular viability across different concentration gradients.

After the incubation period, the cell culture medium was carefully aspirated, and an MTT solution with a concentration of 5.0 mg/ml was added to each well. The cells were then incubated for an additional 4 hours at 37°C, enabling viable cells to convert the yellow tetrazolium salt into formazan crystals. At the end of this incubation period, the MTT solution was removed, and the formazan crystals were dissolved using dimethyl sulfoxide (DMSO). The absorbance of the resulting solution at a wavelength of 570 nanometers was then measured using a microplate reader. The data obtained from the MTT assay were used to construct dose-response curves, facilitating the determination of IC50 values, which represent the concentrations of 5FU and AgCl nanoparticles required to inhibit cell viability by 50%.

For statistical analysis, we employed SPSS 20 software, with the normal distribution of data confirmed using the Kolmogorov-Smirnov test. Group comparisons were conducted using one-way analysis of variance (ANOVA) among the subjects, followed by Tukey's post hoc test for further analysis. Significance levels were set at $P < 0.05$ to determine differences between groups.

3. Results

The morphology of the synthesized AgNPs was analyzed using SEM to assess their shape, size, and surface characteristics. Figure 1 presents a high-resolution microscopic image of the AgNPs, providing detailed insight into their structural properties. A point-to-point analysis conducted through SEM confirmed that the nanoparticles exhibit a size distribution ranging between 50 and 70 nm. The observed variations in nanoparticle size

may be attributed to factors such as synthesis conditions, plant extract composition, and reaction kinetics. Additionally, the SEM images indicate that the nanoparticles possess a relatively uniform spherical or quasi-spherical morphology with minimal aggregation, further supporting the successful formation of AgNPs through the green synthesis method.

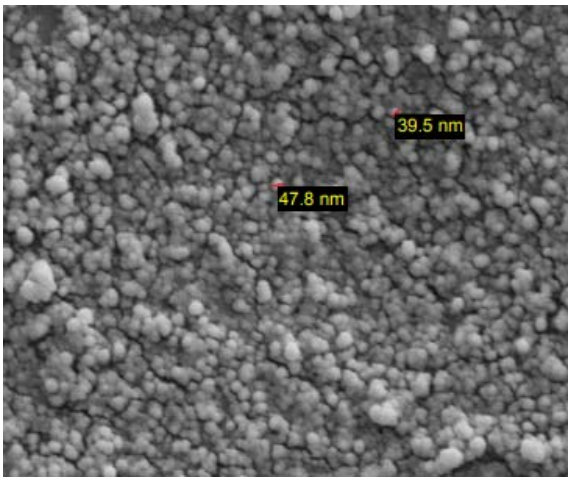

Figure 1. SEM Image of green-synthesized AgNPs showing size distribution and morphology.

Silver chloride nanoparticles (AgNPs) were characterized using X-ray diffraction (XRD) analysis to investigate their composition and purity. Figure 2 presents the XRD patterns of AgNPs synthesized using plant leaf extract. The characteristic diffraction peaks observed in the XRD pattern appeared at 2θ values of 38.4°, 44.5°, and 64.8°, corresponding to the (111), (200), and (220) crystallographic planes of the face-centered cubic (FCC) structure of silver, respectively, as per the Joint Committee on Powder Diffraction Standards (JCPDS) file No. 04-0783. The absence of any additional diffraction peaks indicates that no impurities were present, confirming the high purity and successful synthesis of AgNPs.

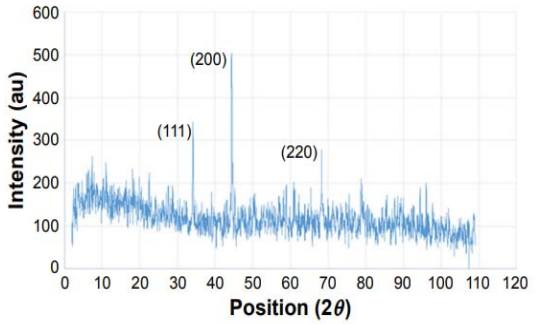

Figure 2: XRD pattern of green-synthesized AgNPs

The MTT assay results showed no significant difference in the cell viability of HEK cells treated with 3.9, 7.8, and 15.6 µg/mL of 5FU compared to the control group. However, significant reductions in cell viability were observed at higher concentrations of 5FU (31.2, 62.5, 125, 250, and 500 µg/mL) relative to the control group ($p < 0.05$, $p < 0.01$, and $p < 0.001$, respectively) (Figure 3). The IC50 value for 5FU in HEK cells was determined to be 174 µg/mL (Figure 4).

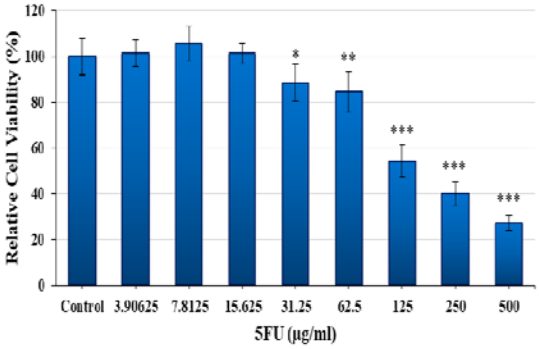

Figure 3. Cell viability of HEK293 cells at various concentrations of 5FU (µg/ml). The * symbol indicates a significant difference compared to the control group (**: $p < 0.01$, ***: $p < 0.001$).

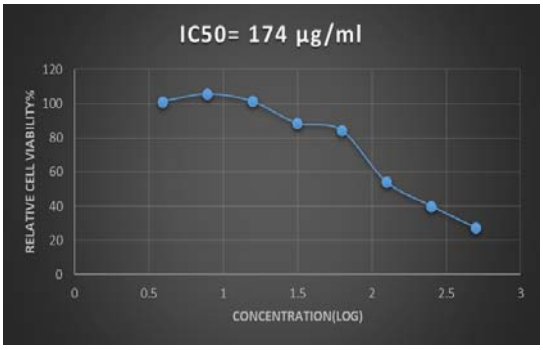

Figure 4. Plot illustrating the calculation of IC50 corresponding to the cytotoxic effects of 5FU on HEK293 cells.

Similarly, in the AGS cell line, no significant difference in viability was observed at 3.9, 7.8, and 15.6 µg/mL of 5FU compared to the control. However, cell viability significantly decreased at concentrations of 31.2, 62.5, 125, 250, and 500 µg/mL ($p < 0.001$) (Figure 5). The IC50 value for 5FU in AGS cells was found to be 92 µg/mL (Figure 6).

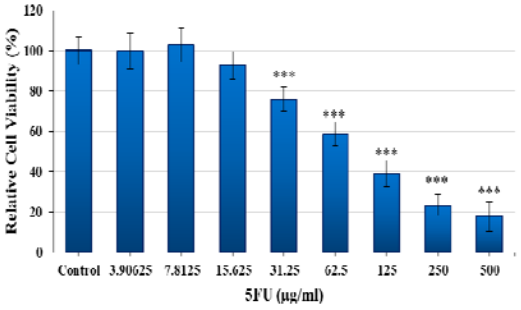

Figure 5. Cell viability of AGS cells exposed to different doses of 5FU (µg/ml). The * symbol indicates a significant difference compared to the control group (***:$p<0.001$).

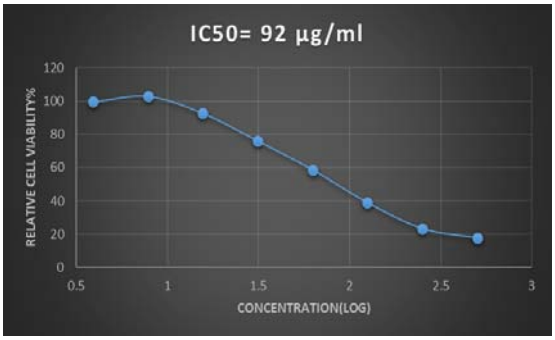

Figure 6. The graph illustrates the calculation of IC50 corresponding to the cytotoxic effects of 5FU on AGS cells.

For AgCl, the viability of HEK293 cells showed no significant difference at concentrations of 1.5, 3.1, and 6.2 µg/mL compared to the control group. However, significant reductions in viability were observed at concentrations of 12.5, 25, and 50 µg/mL ($p < 0.001$) (Figure 7). The IC50 value for AgCl in HEK293 cells was calculated to be 16.2 µg/mL (Figure 8).

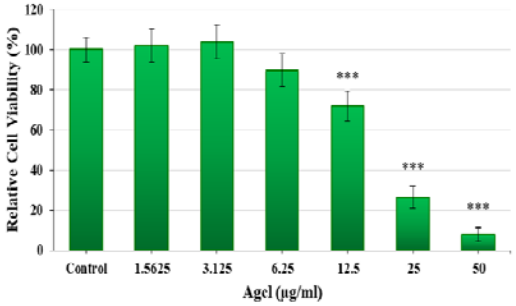

Figure 7. Viability of HEK293 cells exposed to different doses of green-synthesized silver chloride nanoparticles (µg/ml). The * symbol indicates a significant difference compared to the control group (***: $p<0.001$).

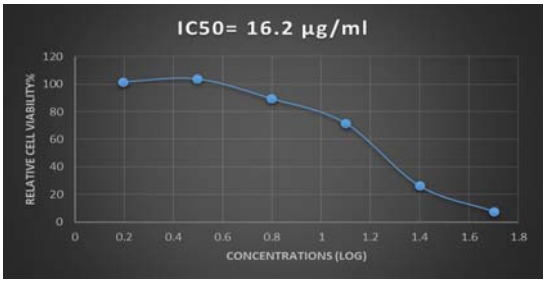

Figure 8. Graph depicting the calculation of IC50 for the cytotoxic effects of silver chloride nanoparticles on HEK293 cells.

For AgCl, the viability of HEK293 cells showed no significant difference at concentrations of 1.5, 3.1, and 6.2 µg/mL compared to the control group. However, significant reductions in viability were observed at concentrations of 12.5, 25, and 50 µg/mL ($p < 0.001$) (Figure 9). The IC50 value for AgCl in HEK293 cells was calculated to be 16.2 µg/mL (Figure 10).

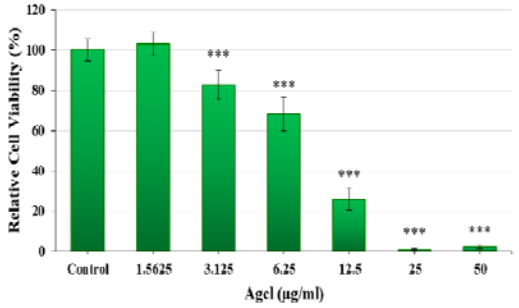

Figure 9. Cell viability of AGS cells exposed to various doses of green-synthesized silver chloride nanoparticles (µg/ml). The * symbol indicates a significant difference compared to the control group (***: $p<0.001$).

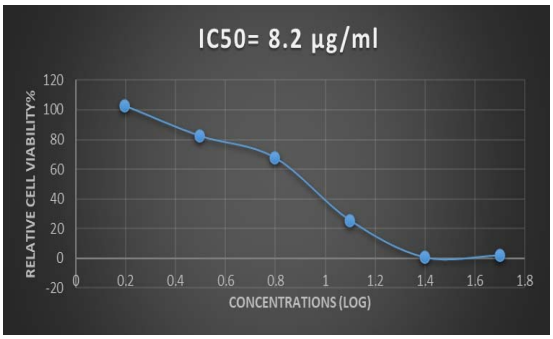

Figure 10. Graph depicting the calculation of IC50 related to the cytotoxic effects of silver chloride nanoparticles on AGS cancer cells.

For the combination of 5FU and AgCl, HEK293 cell viability was not significantly affected at concentrations of 3.9, 7.8, 15.6, and 31.2 µg/mL compared to the control. However, significant reductions in viability were observed at concentrations of 62.5, 125, 250, and 500 µg/mL ($p < 0.01$, $p < 0.001$, respectively) (Figure 11). The IC50 value for the 5FU + AgCl combination in HEK293 cells was 181 µg/mL (Figure 12).

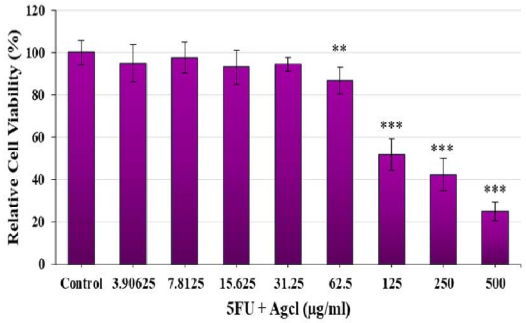

Figure 11. Viability of HEK293 cells exposed to different doses of 5FU+AgCl (µg/ml). The * symbol indicates a significant difference compared to the control group(**: $p<0.01$, ***: $p<0.001$).

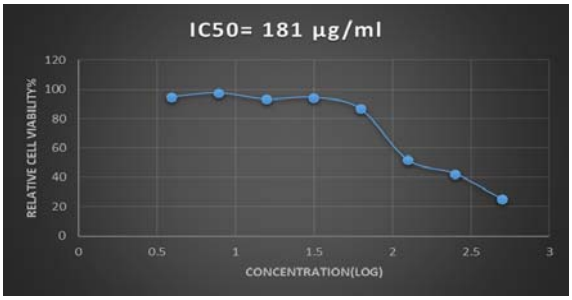

Figure 12. IC50 plot related to the synergistic cytotoxic effects of silver chloride nanoparticles and 5FU on HEK293 cells.

In AGS cells, the 5FU+AgCl combination at 3.9 µg/mL had no significant effect on viability compared to the control. However, concentrations of 7.8, 15.6, 31.2, 62.5, 125, 250, and 500 µg/mL caused significant reductions in viability ($p < 0.001$) (Figure 13). The IC50 for the combination in AGS cells was 43 µg/mL (Figure 14).

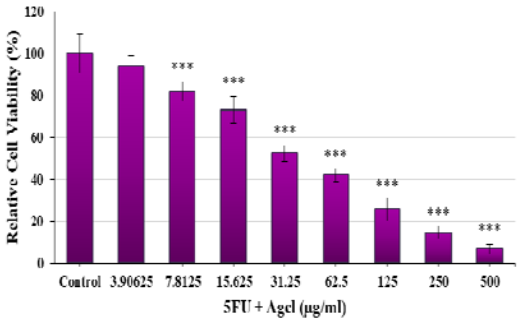

Figure13. Viability of AGS cells exposed to various doses of 5FU+AgCl (µg/ml). The * symbol indicates a significant difference compared to the control group (***: p<0.001).

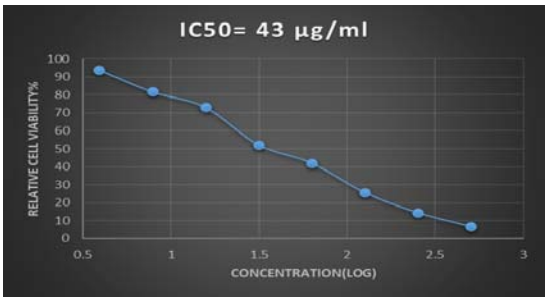

Figure 14. IC50 plot related to the synergistic cytotoxic effects of silver chloride nanoparticles and 5FU on AGS cells.

4. Discussion

The experimental results of this study provide valuable insights into the dose-dependent reduction in the viability of gastric cancer cells (AGS) and human non-cancerous cells (HEK293) following exposure to varying concentrations of 5-fluorouracil (5FU), silver chloride (AgCl) nanoparticles, and their combination. The data reveal a proportional decrease in cell survival as drug and nanoparticle concentrations increase, highlighting the cytotoxic effects of both agents on gastric cancer cells and their potential as therapeutic candidates.

The anti-cancer effects of 5FU are attributed to its inhibition of thymidylate synthase and disruption of DNA synthesis, while silver chloride nanoparticles contribute cytotoxic properties that enhance overall treatment efficacy (Dongsar et al., 2023; Rojas-Cessa et al., 2024). Notably, concentrations of 5FU below 31 µg/mL did not significantly impact cell survival compared to controls. However, above this threshold, a distinct and statistically significant reduction in viability was observed. The combination of 5FU and AgCl nanoparticles exhibited a more pronounced cytotoxic effect on AGS cells than 5FU alone, suggesting a synergistic therapeutic interaction.

The IC50 values further illustrate differential cellular responses to treatment. In HEK293 cells, the IC50 for 5FU was 174 µg/mL, while AGS cells exhibited a lower IC50 of 92 µg/mL, indicating higher sensitivity in cancer cells. Similarly, AGS cells demonstrated greater susceptibility to silver chloride nanoparticles compared to HEK293 cells. The combination therapy resulted in IC50 values of 181 µg/mL for HEK293 cells and 43 µg/mL for AGS cells, reinforcing the enhanced cytotoxicity in gastric cancer cells.

Extensive research has explored the anti-proliferative and apoptosis-inducing effects of nanoparticles, particularly their potential in cancer treatment (Do et al., 2025; Sepand et al., 2020). Nanoparticles such as zinc oxide, nickel, and magnesium oxide have demonstrated efficacy against gastric cancer cells (Hosseinkhah et al., 2022; Mittag et al., 2019; Tang et al., 2020), while silver nanoparticles exhibit notable anticancer activity due to their antimicrobial and pro-apoptotic properties (Hashemi et al., 2020; Rojas-Cessa et al., 2024). Recent clinical studies also report the synergistic effects of chemotherapeutic agents with flavonoids (Abd El Latif et al., 2024) and nanoparticles, suggesting that nanoparticles enhance drug permeability while simultaneously inducing apoptosis through multiple pathways (Karimbaevna et al., 2024; Shrestha et al., 2019).

In alignment with these findings, this study demonstrates a significant anticancer effect when green-synthesized silver chloride nanoparticles are combined with 5FU in gastric cancer cells. The proposed mechanism involves enhanced cellular uptake of 5FU facilitated by AgCl nanoparticles, alongside concurrent apoptosis induction through multiple pathways (Cai et al., 2024).

However, the cytotoxic effects of 5FU and AgCl nanoparticles were not limited to gastric cancer cells, as HEK293 cells also exhibited dose-dependent toxicity. While this highlights the broad-spectrum activity of these agents, it underscores the necessity for optimized treatment protocols to minimize potential off-target effects on healthy cells. The combination of 5FU and AgCl nanoparticles presents a promising therapeutic approach for gastric cancer, leveraging synergistic effects to enhance treatment efficacy while potentially reducing individual drug dosages and associated side effects.

Nevertheless, this study is limited by its reliance on in vitro cell culture models. Further in vivo investigations and clinical trials are essential to validate these findings and assess the safety and efficacy of this combination therapy in a physiologically relevant setting. Additionally, elucidating the molecular mechanisms underlying the observed synergy would provide critical insights for the development of targeted therapeutic strategies tailored to individual patient needs.

5. Conclusion

This study demonstrates the dose-dependent cytotoxic effects of 5-fluorouracil (5FU) and silver chloride (AgCl) nanoparticles on gastric cancer (AGS) and human non-cancerous (HEK293) cells. The findings highlight a significant reduction in cancer cell viability, particularly with the combined treatment, suggesting a potential synergistic therapeutic effect. The lower IC50 values observed in AGS cells compared to HEK293 cells further indicate the selective efficacy of this approach against gastric cancer. Given the enhanced cytotoxicity observed with the combination therapy, AgCl nanoparticles may serve as effective drug carriers, improving 5FU's cellular uptake and amplifying its anticancer effects. However, the observed toxicity in non-cancerous cells underscores the need for careful dose optimization to minimize off-target effects. While these in vitro findings are promising, further in vivo and clinical studies are required to validate the safety and therapeutic efficacy of this combination. Understanding the molecular mechanisms underlying their interaction will be crucial in optimizing treatment strategies. Overall, the combination of 5FU and AgCl nanoparticles presents a compelling avenue for enhancing gastric cancer treatment and warrants further investigation.

Acknowledgment

This research was conducted with the financial support of the Global Research, Education, and Events Network (GREEN) and received approval from the Ethics Committee of the International Association of Scientists (IAS). The authors of this article express their gratitude and appreciation to all colleagues who assisted us in implementing this research project.

Conflict of Interests

There is no conflict of interests.

References

Abd El Latif HM, El-Morsy AM, Ibrahim HM, Morsi DS. Synergistic Antineoplastic and Immunomodulatory Effects of Hesperidin in Ehrlich Ascites Carcinoma Tumor Model Treated with Cisplatin. *JJBS*. 2024;**17(1).**

Aslany S, Tafvizi F, Naseh V. Characterization and evaluation of cytotoxic and apoptotic effects of green synthesis of silver nanoparticles using Artemisia Ciniformis on human gastric adenocarcinoma. *Mater. Today Commun*. 2020;**24**:101011.

Cai J, Tan X, Hu Q, Pan H, Zhao M, Guo C, Zeng J, Ma X, Zhao Y. Flavonoids and gastric cancer therapy: from signaling pathway to therapeutic significance. *Drug Des. Devel. Ther*. 2024:3233-53.

Carvalho-Silva JM, dos Reis AC. Exploring the anti-tumor effect of silver nanoparticles in oral and skin cancer in vivo: Systematic review and meta-analysis. *Res., Soc. Dev.* 2024;**13(4):**e5913445505.

Dongsar TT, Dongsar TS, Gupta N, Almalki WH, Sahebkar A, Kesharwani P. Emerging potential of 5-Fluorouracil-loaded chitosan nanoparticles in cancer therapy. *J Drug Deliv Sci Technol.* 2023;**82**:104371.

Do HT, Nguyen NP, Saeed SI, Dang NT, Doan L, Nguyen TT. Advances in silver nanoparticles: unraveling biological activities, mechanisms of action, and toxicity. *Appl. Nanosci.* 2025;**15(1):**1.

Duan Y, Xu Y, Dou Y, Xu D. Helicobacter pylori and gastric cancer: mechanisms and new perspectives. *J. Hematol. Oncol.* 2025;**18(1):**10.

Faridi UA, Zidan NS, Almutairi FM, Alalawy AI, Atteia HH, Al-Awthan YS, Akhtar MQ, Sakran MI. The Antioxidative, Anticancer and Hepatoprotective of Quercetin Nanoparticles In-vitro and In-vivo. *Biological.* 2023;**16(1):**1117.

Guo LJ, Wu J, Lu W, Li J, Wang Y, Yang H, Wang TZ. Nanoparticles Modulating the Immune Microenvironment in Breast Cancer Treatment. *Int. J. Nanomed.* 2025:1367-82.

Hashemi SF, Tasharrofi N, Saber MM. Green synthesis of silver nanoparticles using Teucrium polium leaf extract and assessment of their antitumor effects against MNK45 human gastric cancer cell line. *J. Mol. Struct.* 2020;**1208**:127889.

Hong J, Feng Z. Synergic fabrication of combination therapy of irinotecan and 5-fluorouracil encapsulated polymeric nanoparticles for the treatment of gastric cancer therapy. *Process Biochem.* 2021;**106**:191-8.

Hosseinkhah M, Ghasemian R, Shokrollahi F, Mojdehi SR, Noveiri MJ, Hedayati M, Rezaei M, Salehzadeh A. Cytotoxic potential of nickel oxide nanoparticles functionalized with glutamic acid and conjugated with thiosemicarbazide (NiO@ Glu/TSC) against human gastric cancer cells. *J. Clust. Sci*. 2022;**33(5)**:2045-53.

Huy TQ, Huyen P, Le AT, Tonezzer M. Recent advances of silver nanoparticles in cancer diagnosis and treatment. *Anti-Cancer Agents Med. Chem.* 2020;20(11):1276-87.

Karimbaevna TM, Burkhanovich AO, Sokhiba Z, Mirza Ali GA, Xasanovna YD, Ibragimovna MZ, Karimberdievich ES, Mukhidinovich JO, Shafkarov B, Khudayberganovna JL, Abdullayevna SM. Synergistic effects of Paclitaxel and Doxorubicin with liposomes nanoparticles in Cancer therapy: A review. *J. Nanostruct.* 2024;**14(2):**578-87.

Li R, Liu B, Gao J. The application of nanoparticles in diagnosis and theranostics of gastric cancer. *Cancer Lett.* 2017;**386**:123-30.

Mamun TI, Younus S, Rahman MH. Gastric cancer-Epidemiology, modifiable and non-modifiable risk factors, challenges and opportunities: An updated review. *Cancer Treat Res Commun.* 2024;**41**:100845.

Meng X. Therapeutic Efficacy of Platinum Based Medicines Combined with Various Nanoparticles in the Treatment of Colorectal Cancer: A Comprehensive Review. *J. Cancer Biomol. Ther.* 2025;**2(1):**57-72.

Miethling-Graff R, Rumpker R, Richter M, Verano-Braga T, Kjeldsen F, Brewer J, Hoyland J, Rubahn HG, Erdmann H. Exposure to silver nanoparticles induces size-and dose-dependent oxidative stress and cytotoxicity in human colon carcinoma cells. *Toxicol. In Vitro*. 2014;**28(7):**1280-9.

Mittag A, Schneider T, Westermann M, Glei M. Toxicological assessment of magnesium oxide nanoparticles in HT29 intestinal cells. *Arch. Toxicol.* 2019;**93**:1491-500.

Mittal R, Patel AP, Jhaveri VM, Kay SI, Debs LH, Parrish JM, Pan DR, Nguyen D, Mittal J, Jayant RD. Recent advancements in nanoparticle based drug delivery for gastrointestinal disorders. *Expert Opin. Drug Deliv.* 2018;**15(3)**:301-18.

Na D, Chae J, Cho SY, Kang W, Lee A, Min S, Kang J, Kim MJ, Choi J, Lee W, Shin D. Predictive biomarkers for 5-fluorouracil and oxaliplatin-based chemotherapy in gastric cancers via profiling of patient-derived xenografts. *Nat. Commun.* 2021;**12(1):**4840.

Nagaich N, Sharma R. Gastric cancer–an update. *J Tumor Med Prev.* 2018;**2(5):**1-8.

Rani N, Singla RK, Redhu R, Narwal S, Sonia, Bhatt A. A review on green synthesis of silver nanoparticles and its role against cancer. *Curr. Top. Med. Chem.* 2022;**22(18):**1460-71.

Rojas-Cessa MA. Recent plant-synthesized gold nanoparticle advancements for gastric cancer therapy. *Nano TransMed.* 2024; **3**:100050.

Sepand MR, Ranjbar S, Kempson IM, Akbariani M, Muganda WC, Müller M, Ghahremani MH, Raoufi M. Targeting non-apoptotic cell death in cancer treatment by nanomaterials: recent advances and future outlook. *Nanomed.: Nanotechnol. Biol. Med.* 2020;**29**:102243.

Singh U, Kokkanti RR, Patnaik S. Beyond Chemotherapy: Exploring 5-FU Resistance and Stemness in Colorectal Cancer. *Eur. J. Pharmacol.* 2025:177294.

Tang Q, Xia H, Liang W, Huo X, Wei X. Synthesis and characterization of zinc oxide nanoparticles from Morus nigra and its anticancer activity of AGS gastric cancer cells. *J. Photochem. Photobiol. B: Biol.* 2020;**202**:111698.

Vahid F, Davoodi SH. Nutritional factors involved in the etiology of gastric cancer: a systematic review. *Nutr. Cancer.* 2021;**73(3)**:376-90.

Wolpin BM, Meyerhardt JA, Mamon HJ, Mayer RJ. Adjuvant treatment of colorectal cancer. *CA Cancer J Clin.* 2007;**57(3):**168-85.

Yamashita K, Hosoda K, Niihara M, Hiki N. History and emerging trends in chemotherapy for gastric cancer. *Ann. Gastroenterol. Surg.* 2021;**5(4):**446-56.

Yuan X, Xue J, Tan Y, Yang Q, Qin Z, Bao X, Li S, Pan L, Jiang Z, Wang Y, Lou Y. Albuca bracteate polysaccharides synergistically enhance the anti-tumor efficacy of 5-fluorouracil against colorectal cancer by modulating β-catenin signaling and intestinal flora. *Front. Pharmacol.* 2021;**12**:736627.

JJBS

Volume 18, Number 3,September 2025
ISSN 1995-6673
Pages 457 – 467

Jordan Journal of Biological Sciences

Kinetic Studies in Shake Flask and Impact of Impeller Speed on Amoxicillin Biodegradation by *Aspergillus tamarii*

Muhammad Zafri Zamri[1], Muhammad Naziz Saat[1], Muhammad Asyraf Mohamad Kamil[2], Zaidah Zainal Ariffin[1,*]

[1]*Faculty of Applied Sciences, Universiti Teknologi MARA. 40450 Shah Alam, Selangor, Malaysia;* [2]*Bacteriology Unit, Infectious Disease Research Centre, National Institute of Health, 40170 Shah Alam, Selangor, Malaysia*

Received: December 21, 2024; Revised: February 17, 2025; Accepted: February 30, 2025

Abstract

Amoxicillin is a β-lactam antibiotic widely used to treat against bacterial infections, including pneumonia, sinusitis, diarrhoea and many more. Due to poor digestion by humans and animals, AMX residues are excreted into wastewater and pollute the environment. AMX can be degraded by microorganisms like fungi. Therefore, this study evaluates the fermentation profiles of *Aspergillus tamarii* with the presence and absence of AMX in shake flasks. Results showed that AMX presence had minimal impact on *A. tamarii*'s growth, glucose consumption and protein production. Kinetic models demonstrated strong agreement between simulated and experimental data. Further experiments were conducted in a stirred tank reactor (STR) at 250, 500 and 770 rpm impeller speeds. Among the tested speeds, 770 rpm showed the highest efficiency, yielding the lowest residual glucose concentration (3.94 g/L) and the highest protein production (0.071 g/L). AMX degradation data fitted well with the second-order polynomial regression model, with high R^2 values at 250 rpm (0.98) and 770 rpm (0.94). *A. tamarii* may exhibit potential degradation abilities against pollutants like AMX. Stringent control of operational parameters is required to ensure efficient and predictable biodegradation.

Keywords: biodegradation kinetics, stirred-tank bioreactor, amoxicillin, biodegradation, *Aspergillus tamarii*

1. Introduction

Amoxicillin (AMX) is one of the most consumed antibiotics, categorized under the β-lactam antibiotics with a chemical formula $C_{16}H_{19}N_3O_5S$. It is often used to treat bacterial infections such as skin infections, pneumonia, sinusitis, acute infectious diarrhoea, bone and joint infection and urinary tract infections (Huttner *et al.*, 2020). Its pollution is found worldwide, which includes European countries, Australia, China, India, and many more (Elizalde-Velázquez *et al.*, 2016; Jia *et al.*, 2018; Velpandian *et al.*, 2018; Rodriguez-Mozaz *et al.*, 2020). AMX has a low metabolic degradation rate; therefore, large portions of the drug end up in aquatic ecosystems, promoting antibiotic resistance to bacteria in the environment. Consequently, antibiotic resistance in bacteria poses risks to both the ecosystem and human health (Verma & Haritash, 2020). According to Chowdhury *et al.* (2020), AMX residues can harm organisms like zebrafish by causing DNA damage, which impacts embryo development. These findings underscore the need for effective and sustainable methods to degrade AMX residues in the environment.

Other existing methods, such as advanced oxidation process, coagulation, and membrane separation, are high cost, may have fouling problems, are too complex in actual field operations, and have high energy consumption (Oulebsir *et al.*, 2020; Carvalho & Moraes, 2021; Liang *et al.*, 2023). In addition, technology may not be easily accessible to developing countries. On the other hand, biodegradation is a degradation method that is low-risk, low-cost, environmentally friendly, and easy to control.

Biodegradation is a highly effective approach to mitigate environmental pollutants such as AMX. Biological methods utilize their diverse metabolic pathways to break down and transform target compounds by adapting to their environment (Murshid & Dhakshinamoorthy, 2019; Firoozeh *et al.*, 2022; Abdullahi Taiwo *et al.*, 2024). However, the need to characterize and comprehend microorganisms' behavior under different physical and chemical conditions, such as temperature, pH, and water activity, is crucial. Mathematical models are commonly used to describe the growth curve, product formation, and biodegradation rate by microorganisms (Zhang *et al.*, 2016; Osadolor *et al.*, 2017; Pan *et al.*, 2019; Uba *et al.*, 2020). These predictive models help in assessing microbial safety, estimating product shelf life, identifying critical control points in production and distribution, and optimizing processes within the production and supply chain (Stavropoulou & Bezirtzoglou, 2019).

A white rot fungus, *Aspergillus tamarii*, is used to biodegrade AMX in the present study. Previous literature has proven its ability to biodegrade the antibiotic by 49.0% using suboptimal parameters (Abd Hamid *et al.*, 2023).

* Corresponding author. e-mail: drzaidah@uitm.edu.my.

Despite that, there is a lack of studies regarding the kinetics of *A. tamarii* to biodegrade pollutants, especially β-lactam antibiotics. This study emphasizes the kinetics of fungal biomass growth, glucose consumption and protein production by *A. tamarii* in shake flasks for both the presence and absence of AMX in a biodegradation medium. This study could provide essential insights into fungal metabolism when exposed to AMX. Furthermore, the process was also investigated using a stirred-tank bioreactor at three different impeller speeds to provide data for potential upscaling and an industrial large-scale cultivation protocol.

2. Materials and methods

2.1. Preparation of Fungal Spore Suspension

A. tamarii strain was obtained from the Institute for Medical Research (IMR) in Shah Alam, Selangor. Following the method outlined by Abd Hamid *et al.* (2023), the fungus was prepared and diluted to a concentration of $1x10^6$ CFU/mL to be used in the biodegradation experiments.

2.2. Biodegradation Assay in Shake Flask

Biodegradation experiment followed the submerged fermentation method as conducted by Abd Hamid *et al.* (2023). Two different cultures were carried out, in which one was spiked with AMX while the other had no AMX. The *A. tamarii* spore suspension is inoculated into 100 mL sterile potato dextrose broth (PDB) medium (Merck, Germany) in a 250 mL Erlenmeyer flask under aseptic conditions. Biodegradation parameters were controlled at an initial pH of 4.0, agitation speed of 120 rpm, 168 hours of incubation time and 1000 µL of inoculum size. After an initial 72-hour incubation, AMX solution is spiked into the culture broth to achieve a final concentration of 100 ppm. The cultures were then incubated further until 168 hours and subjected to analysis. Fermentation flasks were prepared for each 24-hour interval in triplicate.

2.3. Analytical Methods

2.3.1. Determination of Fungal Biomass Concentration

The fungal biomass concentration was measured via the gravimetric method as utilized by Saat *et al.* (2014). The entire fermentation medium (100 mL) was filtered through a pre-weighed Whatman No. 44 filter paper. To ensure purity, the biomass on the filter was rinsed with sterile distilled water. The filter paper with the biomass was then dried in an oven at 60ºC until reaching a consistent weight. Once dried, it was cooled to room temperature in a desiccator and weighed to obtain the final biomass measurement. The filtered biodegradation medium was further used for glucose and protein determination.

2.3.2. Determination of Glucose Residual Concentration

The 3,5-Dinitrosalicylic acid (DNS) method was conducted to determine the biodegradation medium's residual glucose. The standard calibration curve was plotted using a series of known glucose concentrations by diluting a glucose stock solution. In each test, 3.0 mL of DNS reagent was added to a test tube, followed by 3.0 mL of the prepared glucose solution. The tubes were covered with aluminium foil and placed in a 95ºC water bath for 10 minutes. Once removed, 1.0 mL of 40% Rochelle salt solution was added to stabilize the colour. Absorbance was measured at 575 nm, with distilled water as a blank. This procedure was repeated for each known concentration, allowing for the creation of a glucose standard calibration curve, and a linear regression equation was used to determine the sample's glucose concentration accurately. The samples were run using the same procedure, and the concentration of residual glucose was measured using the standard curve.

2.3.3. Determination of Protein Concentration

The Bradford assay was employed to measure residual protein concentration. The Bradford reagent was filtered beforehand. To prepare the standard calibration curve, a series of nine dilutions of bovine serum albumin (BSA) was prepared, with 3 mL of Bradford reagent added to each of nine test tubes. Subsequently, 0.06 mL of each diluted protein solution was mixed into its respective test tube containing the reagent. After 5 minutes of incubation at room temperature, the absorbance for each protein standard was measured at 595 nm with a spectrophotometer and the standard curve was generated. The same procedure was applied for biodegradation samples and the concentration of protein was determined using the standard curve.

2.4. Kinetic Modelling

The batch fermentation profiles for glucose concentration (S), biomass concentration (X), and protein concentration (P) were simulated using unstructured kinetic models. Measurements were taken over time (t). Kinetic parameters were calculated with the mathematical software Polymath 6.0, employing non-linear regression to determine each kinetic variable.

2.4.1. Kinetic of Fungal Growth

To describe the kinetic of fungal growth, the integrated form of Verhulst-Pearl logistic model was utilized as in Equation 1 below:

$$X = \frac{X_0\left(e^{\mu max t}\right)}{1-\left(\frac{X_0}{X_{max}}\right)\left(1-e^{\mu max t}\right)} \quad \text{Eq. 1}$$

where X is the biomass concentration (g L^{-1}), μ_{max} is the maximum specific growth rate (h^{-1}), and X_{max} is the maximum attainable biomass concentration (g L^{-1}).

2.4.2. Kinetic of Glucose Utilization

The kinetic analysis of glucose consumption was performed using a hybrid model based on Leudeking-Piret logistic approach. The modified and integrated Leudeking-Piret (MLP) model (Eq. 2) incorporates additional variables, m_s and Y_G is expressed as follows:

$$S - S_0 = -\frac{1}{Y_G}\left[\frac{X_0\left(e^{\mu max t}\right)}{1-\left(\frac{X_0}{X_{max}}\right)\left(1-e^{\mu max t}\right)} - X_0\right] - m_s\left[\ln\left(1-\left(\frac{X_0}{X_{max}}\right)\left(1-e^{\mu max t}\right)\right)\left(\frac{X_{max}}{\mu_{max}}\right)\right] \quad \text{Eq.2}$$

where Y_G is the yield coefficient of biomass on glucose (g g^{-1}) and m_s is the biomass maintenance coefficient (g g^{-1} h^{-1}).

2.4.3. Kinetic of Protein Production

The Leudeking-Piret model is also applied to analyze protein production kinetics. This model's equation

includes specific coefficients that account for growth-associated and non-growth-associated product formation. The integrated form (Eq. 3) of the Leudeking-Piret equation can be expressed as:

$$P - P_0 = \alpha\left[\frac{X_0(e^{\mu max t})}{1-(\frac{X_0}{X_{max}})(1-(e^{\mu max t}))} - X_0\right] + \beta\left[\left(\frac{X_{max}}{\mu_{max}}\right)\ln\left(1-\left(\frac{X_0}{X_{max}}\right)(1-e^{\mu_{max}t})\right)\right] \quad \text{Eq.3}$$

where α represents the coefficient for growth-associated product formation (g g^{-1}) while β denotes the coefficient for product formation that is non-growth associated (g g^{-1} day^{-1}).

2.5. Biodegradation in Stirred Tank Reactor (STR)

The amoxicillin biodegradation experiment was conducted in a 3.6-litre double-walled vessel with a working volume of 2.0 litres, as shown in Figure 1. The cylindrical borosilicate reactor is 37 cm in height and 11.5 cm in diameter, including two Rushton impellers (4.6 cm diameter each) to ensure proper agitation. Equipped with a control system to manage pH, aeration, temperature and antifoam, the reactor maintained optimal conditions at 30ºC, monitored by a Pt100 sensor. The initial pH was set to 4.3, monitored but not adjusted throughout the 7-day fermentation period.

Following 24 hours of preliminary growth in a 250 mL Erlenmeyer flask, 100 mL of *A. tamarii* culture medium was transferred into the reactor. The study explored three agitation speeds, 250, 500, and 770 rpm. Each was performed in duplicate for a total of 168 hours. AMX was introduced after 72 hours to reach a concentration of 100 ppm, with subsequent sampling at 24-hour intervals for HPLC analysis of residual AMX. Additionally, glucose residual concentration and protein concentrations were measured using the DNS assay and Bradford reagent, respectively.

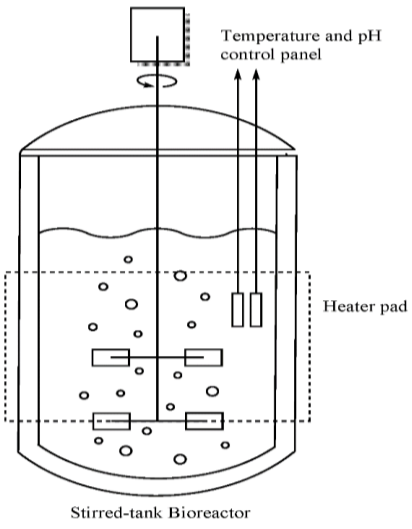

Figure 1. A schematic diagram of the stirred-tank bioreactor (STR) used for AMX biodegradation experiments.

2.6. Partial purification and Extraction of AMX residues

The AMX residues were first processed using a modified liquid-liquid extraction adapted from Abd Hamid *et al.* (2023) and Seifollahi *et al.* (2019). In this procedure, 25 mL each of HPLC-grade water and HPLC-grade ethyl acetate, along with 6 mL of biotransformation products, were added to a separating funnel. The mixture was agitated and settled down for 10 minutes. After two layers of solvents are formed, the layers will be collected individually and concentrated with a rotary evaporator. Concentrated AMX was subsequently dissolved in 3.0 mL of dimethyl sulfoxide (DMSO).

Afterwards, the residues underwent solid-phase extraction using a C18 Hypersep SPE (CHROMABOND) cartridge. The method was based on Zhang *et al.* (2020) with slight modifications. The SPE cartridge was pre-conditioned with methanol and water. The sample with a volume of 3.0 mL was loaded, passed by gravity, and then washed with 2.0 mL of HPLC-grade water and eluted with 3.0 mL of acetonitrile. This extraction method yielded an efficiency of 97.31%. The percentage recovery of AMX (AMX_{rec}) was determined using Equation 4.

$$AMX_{rec} = \frac{a}{b}X100 \quad \text{Eq. 4}$$

where AMX_{rec} is the percentage recovery of AMX, a represents the concentration of AMX post-separation while b represents the concentration of AMX without separation.

2.7. AMX Standard Calibration Curve Preparation

The AMX stock was diluted to create a standard concentration from 100 to 700 ppm, measured at five points, each in triplicate. The results were recorded, and a standard curve was created by plotting the average area under the curve (mAU*s) against AMX concentration. The curve's fit was evaluated using the coefficient of determination (R^2).

2.8. High-Performance Liquid Chromatography with Diode-Array Detection (HPLC-DAD)

This procedure followed the method from Heaton *et al.* (2019) with modifications. The extraction used a C18 Agilent analysis reverse phase column (ZOBRAX SB-C18, 5 µm, 4.6 x 250 mm). Prior to separation, any contaminants were removed from the column by washing and eluting with using mobile phase, HPLC-grade acetonitrile and 0.1 M phosphate buffer (KH_2PO_4, pH 3.5) (60:40) for 10 minutes. The Agilent 1200 system analyzed AMX residues post-biodegradation with a detection wavelength of 215nm.

3. Results and Discussion

3.1. Fermentation Profiles of A. tamarii in Shake Flasks

3.1.1. Fungal Growth Profiles with and without the presence of AMX

The influence of AMX on *A. tamarii* growth during submerged fermentation was assessed, showing similar growth rates for both AMX-present and AMX-absent conditions until the 72-hour mark as shown in Figure 2. After 72 hours, *A. tamarii* biomass increased more with AMX, achieving a peak of 8.35 g/L at 168 hours, whereas without AMX, it reached a maximum of 7.7 g/L at 240 hours. These results suggest that *A. tamarii* not only exhibits high tolerance to AMX but may also benefit in terms of growth from its presence. Similarly, studies have shown minimal impact of β-lactam antibiotic *Verticillium leptobactrum* growth (Kumar *et al.*, 2013) and *Aspergillus*

species often degrade substrates to utilize them as nutrients, adapting their enzyme production to optimize available carbon sources for growth (Kowalczyk *et al.*, 2014).

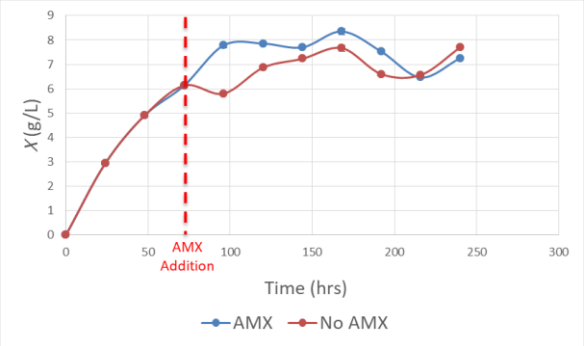

Figure 2. Fungal growth profile of *A. tamarii* in the presence and absence of AMX.

3.1.2. Glucose Consumption Profiles with and without the presence of AMX

Consumption of glucose by *A. tamarii* in the presence and absence of AMX were analyzed. As the main carbon source, glucose supports growth by providing cellular energy. A study by Chen *et al.* (2023) indicates that β-lactam antibiotic degradation is enhanced when glucose is utilized as a substrate by undergoing phosphorylation and enters the glycolytic or pentose phosphate pathways (Khosravi *et al.*, 2015). According to Figure 3, a similar amount of glucose was consumed until 72 hours, but post-AMX addition, glucose was used more slowly in AMX culture up to 120 hours. With extended incubation, however, glucose consumption slightly increased, possibly due to AMX biodegradation. This is consistent with studies showing antibiotic breakdown rates in activated sludge are influenced by the decrease in available carbon sources like glucose (Nguyen *et al.*, 2018). Similarly, Peng *et al.* (2020) found that glucose combined with antibiotics, like tetracycline, can improve microbial abundance compared to sole glucose. Other studies have noted maximal antibiotic degradation in organic environments like swine manure, where glucose supports degradation by anaerobes (Xu *et al.*, 2011; Wang *et al.*, 2021). These findings underline that the degradation of antibiotics by microbial cultures is affected by glucose consumption.

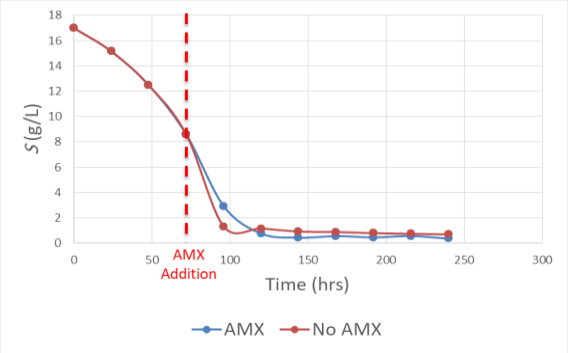

Figure 3. Glucose utilization profile of *A. tamarii* in the presence and absence of AMX.

3.1.3. Protein Production Profiles with and without the presence of AMX

The protein production, as plotted in Figure 4, followed a similar pattern in cultures with and without AMX, peaking at 96 hours. This suggests that optimal protein synthesis for *A. tamarii* occurs at this point, corresponding with the exponential phase as indicated by glucose consumption (Figure 3) and fungal biomass growth (Figure 2). During this phase, primary metabolic processes yield essential metabolites such as amino acids, enzymes, and organic acids that support growth (Walker & White, 2017; Gupta & Gupta, 2021). Although the protein yield was slightly higher in cultures without AMX from 72 hours to 120 hours, suggesting a mild inhibitory effect, the overall difference was minimal. This may indicate that AMX has a negligible impact on protein production. After 192 hours, protein levels declined, likely due to a reduction in glucose levels, pushing cells into a stationary or death phase with decreased metabolic activity. These results imply that AMX presence has little effect on peak protein synthesis yield, as both conditions reached maximum production simultaneously.

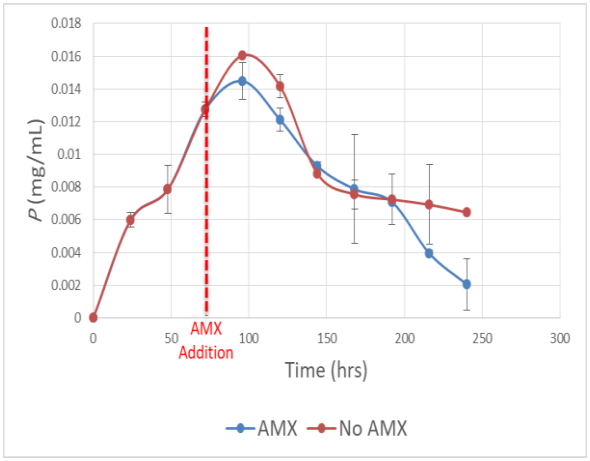

Figure 4. Protein production profile of *A. tamarii* in the presence and absence of AMX.

3.2. Kinetic Parameters Estimation

Batch fermentation experiments were conducted to analyze the kinetics of amoxicillin (AMX) biodegradation by *A. tamarii* both with and without AMX. Key kinetic parameters, including the rates of biomass formation (d*X*/d*t*), glucose utilization (d*S*/d*t*), and protein production (d*P*/d*t*), were calculated by solving the corresponding differential equations through non-linear regression analysis as shown in Table 1. The software Polymath 6.0 was used for solving these non-linear equations and determining the kinetic parameters.

Table 1: Kinetic parameters of fungal growth, glucose consumption and protein production in the presence and absence of AMX

Kinetic Model	Parameters	Presence of AMX	Absence of AMX
Fungal Growth	X_0 (g L^{-1})	0.76 (± 0.67)	0.81 (± 0.97)
	X_{max} (g L^{-1})	7.54 (± 0.56)	6.95 (± 0.58)
	μ_{max} (day^{-1})	1.42 (± 0.58)	1.44 (± 0.87)
Glucose Consumption	Y_G (g g^{-1})	0.62 (± 0.19)	0.56 (± 0.20)
	m_s (g g^{-1} day^{-1})	0.11 (± 0.08)	0.12 (± 0.10)
Protein Production	α (g g^{-1})	0.003 (± 0.0003)	0.003 (± 0.0006)
	β (g g^{-1} day^{-1})	-2.507×10^{-4} ($\pm 5.33 \times 10^{-5}$)	-2.026×10^{-4} ($\pm 8.97 \times 10^{-5}$)

3.2.1. Kinetics of Fungal Growth

This study investigated the kinetic parameters of fungal growth, specifically the maximum specific growth rate (μ_{max}) and maximum cell growth (X_{max}) for *A. tamarii*, both the presence and absence of AMX in fermentation flasks, using Verhulst-Pearl logistic growth model as presented in Table 1. The logistic growth model is widely used for microbial growth due to its ease of fitting (Goveas & Sajankila, 2020). The X_{max} values for both cultures were similar, 7.54 g L^{-1} with AMX and 6.95 g L^{-1} without AMX. Similar X_{max} values were found as well by Abd Rahim and Saari (2018) when fermenting *A. oryzae* NSK in glucose. Likewise, μ_{max} was 1.42 day^{-1} for AMX present and 1.44 day^{-1} for AMX absent suggesting similar values. The results indicate that AMX did not inhibit the growth of *A. tamarii*. Contrastingly, a study by Mohamad *et al.* (2024) showed significant growth reduction in *A. tamarii* when exposed to Nitrofurazone (0.529 g L-1), indicating that *A. tamarii* may specifically resist β-lactam antibiotics but not Nitrofurazone. In line with this, previous research on *A. flavus* found that AMX did not hinder fungal growth below concentrations of 4000 µg/mL (Day *et al.*, 2009). The *A. tamarii* culture in this study had an AMX concentration of 100 µg/mL, likely below the inhibition threshold. Additionally, *A. tamarii* may produce enzymes that degrade AMX at low levels. Ji *et al.* (2021) found that *A. niger* exhibits minimal β-lactamase activity (0.02 ± 0.01 U/g). Further studies are needed to confirm *A. tamarii's* enzyme synthesis or resistance mechanisms against AMX.

3.2.2. Kinetics of Glucose Utilization

The kinetic model for glucose consumption was developed using the Verhulst-Pearl logistic growth model as shown in Table 1 which describes growth dynamics in a confined environment (Gatto *et al.*, 1988). For fermentation with AMX, the biomass yield coefficient on glucose, Y_G, was 0.62 g g-1, and the maintenance coefficient, m_s, was 0.11 g g^{-1} day^{-1}. Without AMX, the Y_G and m_s values were slightly different at 0.56 g g^{-1} and 0.12 g g^{-1} day^{-1}, respectively. The slight increase in Y_G values in the AMX environment may suggest that the fungus is slightly more efficient when consuming glucose for biomass growth. Meanwhile, similar m_s values may indicate that the energy demand for cell maintenance functions is not affected by AMX, implying the antibiotic at this concentration does not induce stress. Another study by Pusztahelyi *et al.* (2011) found that *A. nidulans* produces a wide variety of enzymes for carbon metabolism, such as glycolysis, gluconeogenesis, and pentose phosphate under stress conditions as a defence mechanism. In contrast, when *A. tamarii* culture was exposed to nitrofurazone, Y_G (0.139 g g^{-1}) dropped. In comparison, m_s increased (0.239 g g^{-1} day^{-1}) (Mohamad *et al.*, 2024), showing that energy was diverted more toward maintenance than growth due to antibiotic inhibition (Emri *et al.*, 2015). This demonstrates how the type and severity of stress impact fungal growth and maintenance. The μ_{max} and X_{max} values observed align with the YG and ms, supporting that AMX may not significantly influence the consumption of glucose by *A. tamarii*.

3.2.3. Kinetics of Protein Production

The kinetics of protein synthesis were analyzed using the Leudeking-Piret equation, widely applied for modelling product formation as demonstrated in Table 1. Through nonlinear regression analysis, the kinetic parameters for growth-associated α and non-growth-associated β for culture are 0.003 g g^{-1} and -2.507 x 10^{-4} g g^{-1} day^{-1}, respectively, for AMX present culture. Similar values were calculated for AMX absent culture (α = 0.003 g g^{-1} and β = -2.026×10^{-4} g g^{-1} day^{-1}) respectively. The product formation can be unrelated to growth, hence the value of non-growth-associated β can be positive, negative or zero (Singh & Srivastava, 2014). The findings indicate that protein production is growth-associated as the α value is higher than the non-growth-associated coefficient β. Under a stressful environment, fungi may produce various enzymes such as catalases, superperoxidase dimutases and mitogen-activated protein kinase to overcome harsh environments, increasing overall protein production (Abdel-Hadi *et al.*, 2012). A previous study has shown that nitrofurazone can induce *A. tamarii*'s protein production, both growth and non-growth-associated proteins (Mohamad *et al.*, 2024). The results suggest that AMX degradation is likely due to primary metabolites produced by *A. tamarii*. Further research is required to identify the enzymes and mechanisms involved in this biodegradation.

3.2.4. Simulations of Kinetic Model

Kinetic models were simulated to represent the rate of fungal growth (d*X*/d*t*), rate of glucose utilization (d*S*/d*t*) and the rate of protein production (d*P*/d*t*) generated using Polymath 6.0 software. These parameters displayed in Table 1 solved the differential equations and fitted the curve for fermentations in both the presence and absence of AMX, as shown in Figure 5. The simulations and experimental data have shown a considerable agreement by the coefficient correlation (R^2) for each kinetic model used in culture flasks in both the presence and absence of AMX, detailed in Table 2.

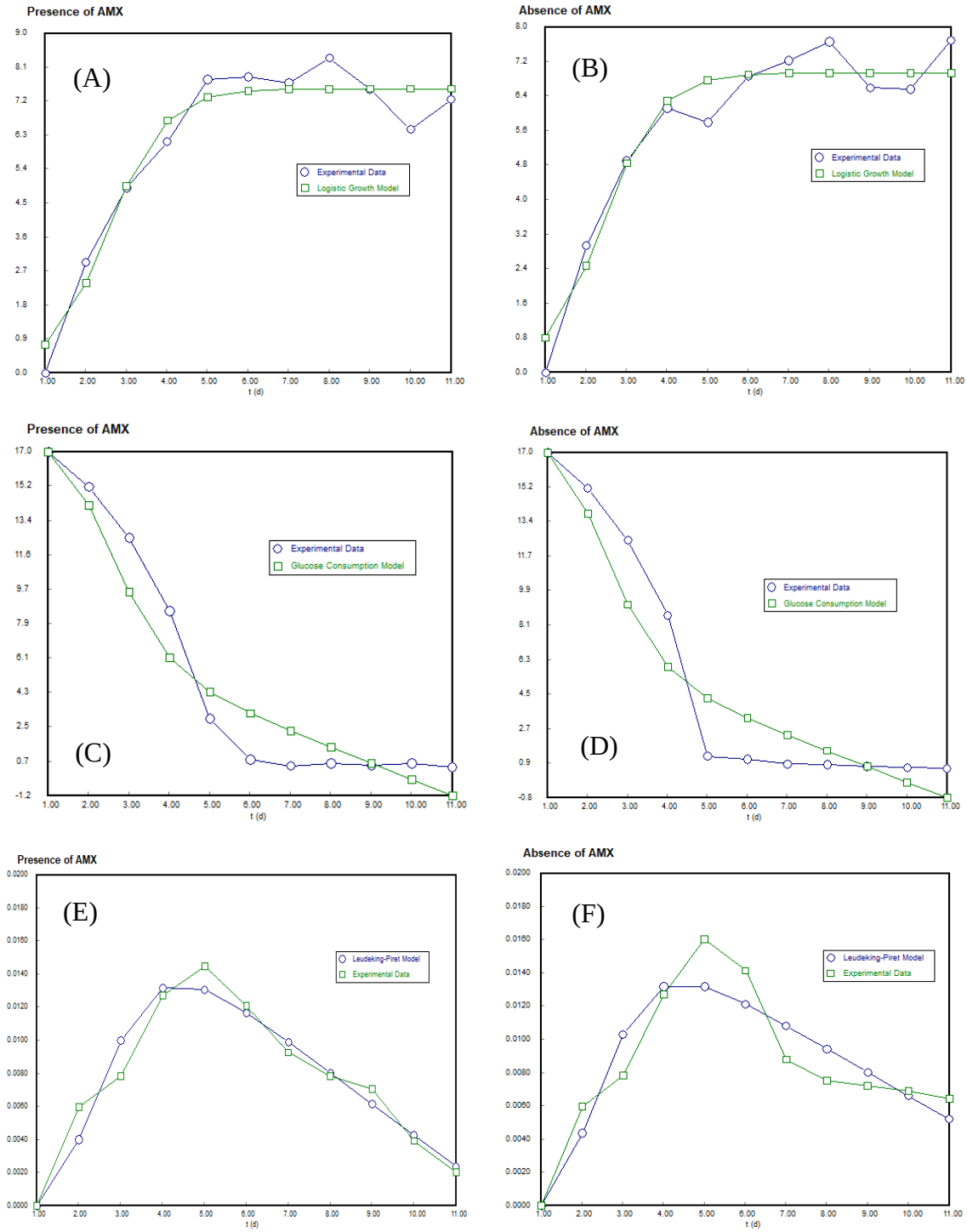

Figure 5. Kinetic model simulation for *A. tamarii* fermentation in the presence and absence of AMX: Logistic growth model (A, B), glucose consumption model (C, D) and Leudeking-Piret model (E, F).

Table 2. Correlation coefficient (R^2) for the simulation of experimental data in shake flasks for presence and absence of AMX

Model Simulation	R^2	
	Presence of AMX	Absence of AMX
Fungal growth $\frac{dX}{dt} = \mu_{max}(X)\left(1 - \frac{X}{X_{max}}\right)$	0.9469	0.9388
Glucose Utilization $-\frac{dS}{dt} = \frac{1}{Y_G}\left(\frac{dX}{dt}\right) + m_s(X)$	0.9309	0.9089
Protein Production $\frac{dP}{dt} = \alpha\left(\frac{dX}{dt}\right)$	0.9395	0.8419

Table 2 describes the R^2 of three kinetic models used in this study. All three models have a good fit between simulated and experimental data. The logistic model for fungal growth has an R^2 of 0.9469 in the presence of AMX and 0.9388 in the absence of AMX. The glucose utilisation model in the presence and absence of AMX resulted in a R^2 of 0.9309 and 0.9089, respectively. The Leudeking-Piret model for protein production in the presence of AMX exhibited a good fit as well, with an R^2 of 0.9395. Comparatively, in the absence of AMX, it showed decent R^2 values of 0.8419.

3.3. Fermentation of A. tamarii in Stirred-tank reactor (STR)

3.3.1. Glucose Utilization profile with AMX in STR

Glucose utilization was analyzed and graphed at three different impeller speeds (250, 500 and 770 rpm) during fermentation, starting with similar initial glucose concentrations. The results as shown in Figure 6, indicate steady glucose reduction across all three speeds. At 250 rpm, final glucose residual concentration was 6.8 g/L, while at 500 rpm, it was 14.34 g/L. Lastly, at 770 rpm, the concentration of residual glucose was 3.94 g/L. This suggests that glucose consumption was highest at 770 rpm and the lowest in 500 rpm. The findings align with studies showing that higher impeller rates improve substrate mixing and oxygen transfer which enhances the cell growth and substrate uptake (Mitrović *et al.*, 2017). Table 3 highlights glucose consumption rates at two time points: 72 hours (when AMX was added) and 168 hours. The glucose depletion rates were 0.105 g/L/hr at 250 rpm, 0.137 g/L/hr at 500 rpm, and 0.092 g/L/hr at 770 rpm. The faster glucose depletion at 500 rpm compared to 770 rpm may be due to higher residual glucose availability at 500 rpm. At 770 rpm, residual glucose levels at 72 hours were low (12.90 g/L), potentially limiting fungal growth and metabolic activity. For future research, introducing AMX earlier in the fermentation process, when glucose levels are high, may enhance *A. tamarii*'s capacity for AMX degradation.

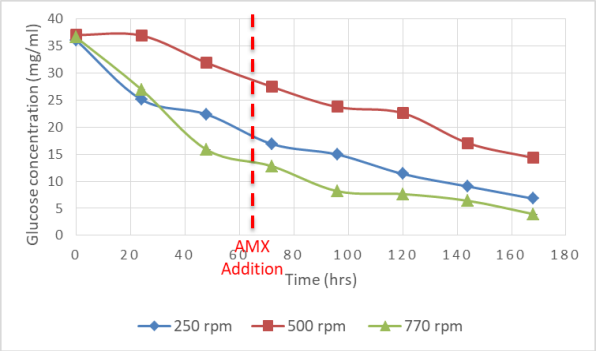

Figure 6. Glucose consumption profile by *A. tamarii* spiked with AMX in STR

Table 3. Glucose concentration decrease rate for 96 hrs (from 72 hrs to 168 hrs)

Agitation Speed (rpm)	Residual glucose concentration (72 hours, g/L)	Residual glucose concentration (168 hours, g/L)	Decrease in residual glucose concentration (g/L)	Rate of glucose consumption (g/L/hrs)
250	16.89	6.80	10.09	0.105
500	27.48	14.34	13.14	0.137
770	12.80	3.95	8.85	0.092

Studying fungal fermentation in bioreactors poses challenges, particularly in maintaining consistency when tracking fermentation profiles. Issues may arise from uncontrolled mycelium growth, which can disrupt reactor operations. For example, fungal growth on reactor walls has been shown to reduce the efficiency of producing exopolysaccharides, bioactive compounds with medicinal properties (Supramani *et al.*, 2023). To overcome this, strict optimization and continuous monitoring of parameters is required (Espinosa-Ortiz *et al.*, 2016; Svobodová & Novotný, 2018; Petre *et al.*, 2021). In extreme cases, mycelium can grow over reactor probes, causing them to malfunction and further complicating the operations.

3.3.2. Protein production profile with AMX in STR

The protein production profile in Figure 7 shows that *A. tamarii* cultured at 250, 500 and 770 rpm followed a similar hyperbolic pattern. Peak protein concentrations occurred at 72 hours for 250 rpm (0.069 g/L) and 500 rpm (0.047 g/L), while the maximum protein level at 770 rpm was 0.071 g/L and was reached 24 hours later at 96 hours. Fermentation at 500 rpm resulted in the lowest protein production overall. Cultures at 250 rpm and 770 rpm, displayed similar protein levels, although 770 rpm showed a sharper decline after peaking. These results align with glucose utilization patterns by *A. tamarii* where higher glucose consumption correlated with higher protein production. Table 4 shows protein production rates at two time points: 72 hours (AMX addition) and 168 hours. The most significant reduction in protein production occurred at 250 rpm (-0.0110 g/L/hr), followed by 500 rpm (-0.0103 g/L/hr). The least reduction was observed at 770 rpm (-0.0049 g/L/hr), indicating greater stability in protein production under higher agitation speeds.

The differences in impeller speed influenced the protein production of *A. tamarii*. The highest protein yield

occurred at 770 rpm, likely due to better substrate mixing and oxygen transfer at this speed. However, Fenice *et al.* (2012) found in their study that reduced protein production yielded at 500 rpm by *Lecanicillium muscariuum* compared to lower agitation speed. It is likely due to less efficient oxygen transfer, as higher viscosity at moderate agitation speeds can hinder fluid flow and microbial activity (Garcia-Ochoa & Gomez, 2009; Maiorano *et al.*, 2020).

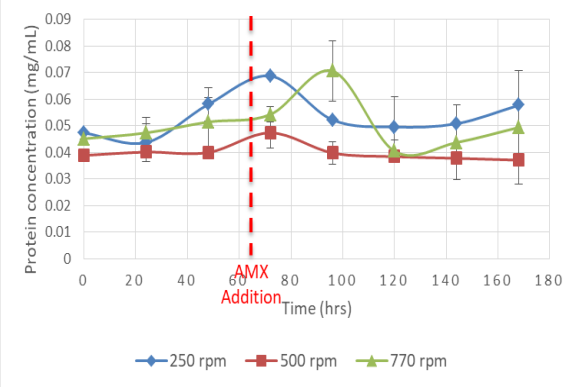

Figure 7. Protein production profile by *A. tamarii* spiked with AMX in STR.

Table 4. Protein production rate for 96 hrs (from 72 hrs to 168 hrs)

Agitation Speed (rpm)	Protein concentration (72 hours, g/L)	Protein concentration (168 hours, g/L)	Rate of Protein production (g/L/hrs)
250	0.0688	0.0578	-0.0110
500	0.0474	0.0371	-0.0103
770	0.0543	0.0494	-0.0049

3.3.3. AMX degradation profile in STR

The biodegradation percentage of AMX in a stirred-tank reactor (STR) was analyzed after 168 hours, with AMX spiked at the 72nd hour. The patterns of AMX degradation at impeller speeds of 250, 500, and 770 rpm were modelled using second-order polynomial regression. Each speed exhibited distinct trends in degradation efficiency, as indicated by the regression model's R^2 values and coefficients. At 250 rpm, the model demonstrated a strong fit with an R^2 value of 0.98, reflecting a predictable degradation pattern. The negative x^2 coefficient (-0.0012) suggested a declining degradation rate over time, a common observation in biological processes where substrate depletion slows reactions (Huang *et al.*, 2016; Yang *et al.*, 2016; Chinaglia *et al.*, 2018). The high linear coefficient (0.436) indicated rapid degradation during the early stages, supported by concurrent glucose consumption and protein production. In contrast, the results for 500 rpm showed the least consistent pattern, with an R^2 value of 0.86. A positive x^2 coefficient (0.0008) implies a slight acceleration in degradation, though the smaller linear coefficient (0.268) suggested slower initial rates. This variability might result from reactor hydrodynamics at this speed, which provided intermediate mixing and oxygen transfer but did not fully optimize the fungus's ability to utilize substrate for AMX degradation. For 770 rpm, the regression model again fit well, with an R^2 value of 0.94. The higher positive x^2 coefficient (0.0012) indicated a faster acceleration in degradation rates, though the smaller linear coefficient (0.132) reflected a gradual start. Higher impeller speed may offer better substrate mixing and oxygen transfer but may destroy the cells and enzymes due to shear stress (Mitrović *et al.*, 2017; Shu *et al.*, 2019; Deniz *et al.*, 2021). The rapid depletion of glucose by the 72nd hour likely created a substrate-limited environment, potentially restricting further metabolic degradation. However, biosorption by fungal cell walls containing glycoproteins and chitin may have contributed to AMX removal through chemical interactions (Legorreta-Castañeda *et al.*, 2020). ANOVA was carried out to test the significance between the three impeller speeds, and no difference was found between the groups as the p-value was higher than the significance level (0.05). To confirm further, Tukey Pairwise Comparisons were used, and no significant differences were found between the three impeller speeds. In contrast to other studies, Mohd Hanafiah *et al.* (2024) found that *Ganoderma lucidum* degraded pharmaceutical compounds effectively at 50 rpm. Cytostatic drugs bleomycin and vincristine were removed effectively by white-rot fungi using 100 rpm (Jureczko *et al.*, 2024). The *A. tamarii's* poor AMX degradation may have been caused by mechanical damage to the fungal mycelium. This indicates that a lower agitation speed may be needed. These findings emphasize the importance of optimizing impeller speed to enhance substrate mixing and oxygen transfer while minimizing shear stress. Such optimization can significantly improve AMX biodegradation and removal of other pharmaceutical pollutants in STR systems.

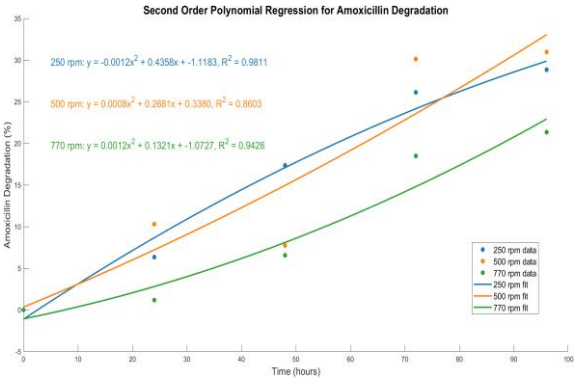

Figure 8. Second order polynomial regression for amoxicillin degradation by *A. tamarii* in STR.

4. Conclusions

The fermentation profiles of *A. tamarii* were studied in shake flasks, both with and without AMX, focusing on fungal growth, glucose consumption, and protein production. Results indicated that AMX had minimal impact on fungal growth, glucose uptake, or protein synthesis. Simulated kinetics models closely matched the experimental data, demonstrating a strong correlation. AMX degradation experiments were conducted in a stirred tank reactor (STR) at different impeller speeds. While fermentation profiles were analyzed, fungal biomass measurement was excluded due to time and cost constraints. Among the tested speeds, *A. tamarii* exhibited

the highest efficiency at 770 rpm, where residual glucose concentration was the lowest (3.94 g/L) and protein production yield peaked at 0.071 g/L, outperforming results at 250 and 500 rpm. The AMX degradation data followed a second-order polynomial regression model, with high R^2 values for 250 rpm (0.98) and 770 rpm (0.94), indicating a well-fitted model.

These findings suggest that *A. tamarii* holds significant promise for wastewater treatment by degrading pharmaceutical pollutants like AMX. However, scaling up the process to bioreactors requires strict control of operational parameters to ensure effective and reliable degradation.

Acknowledgements

This work was supported and funded by a grant 600-RMC/GIP 5/3 (013/2023).

Conflict of Interest

The authors have declared that no conflict of interest exists.

Funding

None.

Ethics Statement

Not applicable.

Reference

Abd Hamid, A. H. H., Zulkifle, N. T., Mahat, M. M., Safian, M. F., & Ariffin, Z. Z. (2023). *Aspergillus tamarii* isolate 58 and *Lichtheimia ramosa* strain R: A potential amoxicillin biodegrader. *J. Appl. Pharm. Sci.*, *13*(10), 149-156. https://doi.org/https://doi.org/10.7324/JAPS.2023.118866

Abd Rahim, M. H., & Saari, N. (2018). Evaluation of a Malaysian soy sauce koji strain *Aspergillus oryzae* NSK for c-aminobutyric acid (GABA) production using different native sugars.

Abdel-Hadi, A., Schmidt-Heydt, M., Parra, R., Geisen, R., & Magan, N. (2012). A systems approach to model the relationship between aflatoxin gene cluster expression, environmental factors, growth and toxin production by *Aspergillus flavus*. *J. R. Soc. Interface*, *9*(69), 757-767.

Abdullahi Taiwo, J.-H., Oluwabukola Kudirat, A., Wakili, T., & Jimoh, F. A. (2024). Evaluation of the Potential of Immobilized Cyanide-Degrading Bacteria for the Bioremediation of Cassava Mill Effluent. *Jordan J. Biol. Sci.*, *17*(3).

Carvalho, J. F. d., & Moraes, J. E. F. d. (2021). Treatment of simulated industrial pharmaceutical wastewater containing amoxicillin antibiotic via advanced oxidation processes. *Environ. Technol.*, *42*(26), 4145-4157.

Chen, H., Wang, Z., Huang, Y., Wei, J., Guo, G., & Miao, L. (2023). Anaerobic co-metabolic degradation of ceftriaxone sodium: Performance and mechanism. *J. Clean. Prod.*, *394*, 136388. https://doi.org/https://doi.org/10.1016/j.jclepro.2023.136388

Chinaglia, S., Tosin, M., & Degli-Innocenti, F. (2018). Biodegradation rate of biodegradable plastics at molecular level. *POLYM DEGRAD STABIL*, *147*, 237-244. https://doi.org/https://doi.org/10.1016/j.polymdegradstab.2017.12.011

Chowdhury, J., Mandal, T. K., & Mondal, S. (2020). Genotoxic impact of emerging contaminant amoxicillin residue on zebra fish (*Danio rerio*) embryos. *Heliyon*, *6*(11), e05379. https://doi.org/https://doi.org/10.1016/j.heliyon.2020.e05379

Day, S., Lalitha, P., Haug, S., Fothergill, A. W., Cevallos, V., Vijayakumar, R., Prajna, N. V., Acharya, N. R., McLeod, S. D., & Lietman, T. M. (2009). Activity of antibiotics against *Fusarium* and *Aspergillus*. *Br J Ophthalmol.*, *93*(1), 116-119.

Deniz, I., Demir, T., Oncel, S. S., Hames, E. E., & Vardar-Sukan, F. (2021). Effect of agitation and aeration on keratinase production in bioreactors using bioprocess engineering aspects. *Protein J.*, *40*, 388-395.

Elizalde-Velázquez, A., Gómez-Oliván, L. M., Galar-Martínez, M., Islas-Flores, H., Dublán-García, O., & SanJuan-Reyes, N. (2016). Amoxicillin in the aquatic environment, its fate and environmental risk. ***Environmental Health Risk-Hazardous Factors To Living Species***, *1*, 247-267.

Emri, T., Szarvas, V., Orosz, E., Antal, K., Park, H., Han, K.-H., Yu, J.-H., & Pócsi, I. (2015). Core oxidative stress response in *Aspergillus nidulans*. *BMC Genomics*, *16*, 1-19.

Espinosa-Ortiz, E. J., Rene, E. R., Pakshirajan, K., van Hullebusch, E. D., & Lens, P. N. L. (2016). Fungal pelleted reactors in wastewater treatment: Applications and perspectives. *Chem. Eng. J.*, *283*, 553-571. https://doi.org/https://doi.org/10.1016/j.cej.2015.07.068

Fenice, M., Barghini, P., Selbmann, L., & Federici, F. (2012). Combined effects of agitation and aeration on the chitinolytic enzymes production by the Antarctic fungus *Lecanicillium muscarium* CCFEE 5003. *Microb. Cell Fact.*, *11*, 1-11.

Firoozeh, F., Shahamat, Y. D., Rodríguez-Couto, S., Kouhsari, E., & Niknejad, F. (2022). Bioremediation for the Decolorization of Textile Dyes by Bacterial Strains Isolated from Dyeing Wastewater. *JJBS*, *15*(2).

Garcia-Ochoa, F., & Gomez, E. (2009). Bioreactor scale-up and oxygen transfer rate in microbial processes: An overview. *Biotechnol. Adv.*, *27*(2), 153-176. https://doi.org/https://doi.org/10.1016/j.biotechadv.2008.10.006

Gatto, M., Muratori, S., & Rinaldi, S. (1988). A functional interpretation of the logistic equation. *ECOL MODEL*, *42*(2), 155-159. https://doi.org/https://doi.org/10.1016/0304-3800(88)90113-5

Goveas, L. C., & Sajankila, S. P. (2020). Effect of yeast extract supplementation on halotolerant biosurfactant production kinetics coupled with degradation of petroleum crude oil by *Acinetobacter baumannii* OCB1 in marine environment. *Bioresour. Technol. Rep.*, *11*, 100447. https://doi.org/https://doi.org/10.1016/j.biteb.2020.100447

Gupta, R., & Gupta, N. (2021). ***Fundamentals of Bacterial Physiology and Metabolism***. Springer.

Heaton, J. C., Smith, N. W., & McCalley, D. V. (2019). Retention characteristics of some antibiotic and anti-retroviral compounds in hydrophilic interaction chromatography using isocratic elution, and gradient elution with repeatable partial equilibration. *Anal. Chim. Acta.*, *1045*, 141-151. https://doi.org/https://doi.org/10.1016/j.aca.2018.08.051

Huang, X., Zhang, X., Feng, F., & Xu, X. (2016). Biodegradation of tetracycline by the yeast strain *Trichosporon mycotoxinivorans* XPY-10. *Prep. Biochem. Biotechnol.*, *46*(1), 15-22.

Huttner, A., Bielicki, J., Clements, M. N., Frimodt-Møller, N., Muller, A. E., Paccaud, J. P., & Mouton, J. W. (2020). Oral amoxicillin and amoxicillin–clavulanic acid: properties, indications and usage. *Clin Microbiol Infect.* , *26*(7), 871-879. https://doi.org/https://doi.org/10.1016/j.cmi.2019.11.028

Ji, J., Gao, T., Salama, E.-S., El-Dalatony, M. M., Peng, L., Gong, Y., Liu, P., & Li, X. (2021). Using *Aspergillus niger* whole-cell biocatalyst mycelial aerobic granular sludge to treat pharmaceutical wastewater containing β-lactam antibiotics. *Chem. Eng. J.*, *412*, 128665. https://doi.org/https://doi.org/10.1016/j.cej.2021.128665

Jia, J., Guan, Y., Cheng, M., Chen, H., He, J., Wang, S., & Wang, Z. (2018). Occurrence and distribution of antibiotics and antibiotic resistance genes in Ba River, China. *Sci. Total Environ.*, *642*, 1136-1144. https://doi.org/https://doi.org/10.1016/j.scitotenv.2018.06.149

Jureczko, M., Krawczyk, T., López de Alda, M., Garcia-Vara, M., Banach-Wiśniewska, A., & Przystaś, W. (2024). Removal of the cytostatic drugs bleomycin and vincristine by white-rot fungi under various conditions, and determination of enzymes involved, degradation by-products, and toxicity. *Sci. Total Environ. 954*, 176420. https://doi.org/https://doi.org/10.1016/j.scitotenv.2024.176420

Khosravi, C., Benocci, T., Battaglia, E., Benoit, I., & de Vries, R. P. (2015). Chapter One - Sugar Catabolism in *Aspergillus* and Other Fungi Related to the Utilization of Plant Biomass. In S. Sariaslani & G. M. Gadd (Eds.), ***Advances in Applied Microbiology*** (Vol. 90, pp. 1-28). Academic Press. https://doi.org/https://doi.org/10.1016/bs.aambs.2014.09.005

Kowalczyk, J. E., Benoit, I., & de Vries, R. P. (2014). Chapter Two - Regulation of Plant Biomass Utilization in *Aspergillus*. In S. Sariaslani & G. M. Gadd (Eds.), ***Advances in Applied Microbiology*** (Vol. 88, pp. 31-56). Academic Press. https://doi.org/https://doi.org/10.1016/B978-0-12-800260-5.00002-4

Kumar, R. R., Park, B. J., Jeong, H. R., Lee, J. T., & Cho, J. Y. (2013). Biodegradation of B-lactam antibiotic ampicillin by white rot fungi from aqueous solutions. *J PURE APPL MICROBIO.*, *7*(4), 3163-3169.

Legorreta-Castañeda, A. J., Lucho-Constantino, C. A., Beltrán-Hernández, R. I., Coronel-Olivares, C., & Vázquez-Rodríguez, G. A. (2020). Biosorption of water pollutants by fungal pellets. *Water*, *12*(4), 1155.

Liang, J., Wang, W., & Zeng, F. (2023). The purification and concentration of amoxicillin by novel alkali-sensitive polypiperazine amide/polysulfate composite nanofiltration membranes. *SEP PURIF TECHNOL.*, *326*, 124824. https://doi.org/https://doi.org/10.1016/j.seppur.2023.124824

Maiorano, A. E., da Silva, E. S., Perna, R. F., Ottoni, C. A., Piccoli, R. A. M., Fernandez, R. C., Maresma, B. G., & de Andrade Rodrigues, M. F. (2020). Effect of agitation speed and aeration rate on fructosyltransferase production of *Aspergillus oryzae* IPT-301 in stirred tank bioreactor. *Biotechnol. Lett.*, *42*(12), 2619-2629.

Mitrović, I. Ž., Grahovac, J. A., Dodić, J. M., Grahovac, M. S., Dodić, S. N., Vučurović, D. G., & Vlajkov, V. R. (2017). Effect of agitation rate on the production of antifungal metabolites by *Streptomyces hygroscopicus* in a lab-scale bioreactor. *Acta Period. Technol.* (48), 231-244.

Mohamad, N. A., Zamri, M. Z., Saat, M. N., & Ariffin, Z. Z. (2024). Nitrofurazone biodegradation kinetics by batch fermentation of *Aspergillus tamarii*. *APJMBB*, *32*, 98-109.

Mohd Hanafiah, Z., Wan Mohtar, W. H. M., Wan-Mohtar, W. A. A. Q. I., Bithi, A. S., Rohani, R., Indarto, A., Yaseen, Z. M., Sharil, S., & Binti Abdul Manan, T. S. (2024). Removal of pharmaceutical compounds and toxicology study in wastewater using Malaysian fungal *Ganoderma lucidum*. *Chemosphere*, *358*, 142209. https://doi.org/https://doi.org/10.1016/j.chemosphere.2024.142209

Murshid, S., & Dhakshinamoorthy, G. P. (2019). Biodegradation of Sodium Diclofenac and Mefenamic Acid: Kinetic studies, identification of metabolites and analysis of enzyme activity. *Int Biodeter Biodegrad.*, *144*, 104756. https://doi.org/https://doi.org/10.1016/j.ibiod.2019.104756

Nguyen, L. N., Nghiem, L. D., & Oh, S. (2018). Aerobic biotransformation of the antibiotic ciprofloxacin by *Bradyrhizobium sp*. isolated from activated sludge. *Chemosphere*, *211*, 600-607. https://doi.org/https://doi.org/10.1016/j.chemosphere.2018.08.004

Osadolor, O. A., Nair, R. B., Lennartsson, P. R., & Taherzadeh, M. J. (2017). Empirical and experimental determination of the kinetics of pellet growth in filamentous fungi: A case study using Neurospora intermedia. *Biochem. Eng. J. , 124*, 115-121. https://doi.org/https://doi.org/10.1016/j.bej.2017.05.012

Oulebsir, A., Chaabane, T., Tounsi, H., Omine, K., Sivasankar, V., Flilissa, A., & Darchen, A. (2020). Treatment of artificial pharmaceutical wastewater containing amoxicillin by a sequential electrocoagulation with calcium salt followed by nanofiltration. *J. Environ. Chem. Eng.*, *8*(6), 104597.

Pan, S., Chen, G., Zeng, J., Cao, X., Zheng, X., Zeng, W., & Liang, Z. (2019). Fibrinolytic enzyme production from low-cost substrates by marine Bacillus subtilis: Process optimization and kinetic modeling. *Biochem. Eng. J. , 141*, 268-277. https://doi.org/https://doi.org/10.1016/j.bej.2018.11.002

Peng, X., Cao, J., Xie, B., Duan, M., & Zhao, J. (2020). Evaluation of degradation behavior over tetracycline hydrochloride by microbial electrochemical technology: Performance, kinetics, and microbial communities. *Ecotoxicol Environ Saf.*, *188*, 109869. https://doi.org/https://doi.org/10.1016/j.ecoenv.2019.109869

Petre, A., Ene, M., & Vamanu, E. (2021). Submerged Cultivation of Inonotus obliquus Mycelium Using Statistical Design of Experiments and Mathematical Modeling to Increase Biomass Yield. *Appl. Sci.*, *11*(9), 4104. https://www.mdpi.com/2076-3417/11/9/4104

Pusztahelyi, T., Klement, É., Szajli, E., Klem, J., Miskei, M., Karányi, Z., Emri, T., Kovács, S., Orosz, G., Kovács, K. L., Medzihradszky, K. F., Prade, R. A., & Pócsi, I. (2011). Comparison of transcriptional and translational changes caused by long-term menadione exposure in *Aspergillus nidulans*. *Fungal Genet. Biol.*, *48*(2), 92-103. https://doi.org/https://doi.org/10.1016/j.fgb.2010.08.006

Rodriguez-Mozaz, S., Vaz-Moreira, I., Varela Della Giustina, S., Llorca, M., Barceló, D., Schubert, S., Berendonk, T. U., Michael-Kordatou, I., Fatta-Kassinos, D., Martinez, J. L., Elpers, C., Henriques, I., Jaeger, T., Schwartz, T., Paulshus, E., O'Sullivan, K., Pärnänen, K. M. M., Virta, M., Do, T. T., Walsh, F., & Manaia, C. M. (2020). Antibiotic residues in final effluents of European wastewater treatment plants and their impact on the aquatic environment. *Environ. Int.*, *140*, 105733. https://doi.org/https://doi.org/10.1016/j.envint.2020.105733

Saat, M. N., Annuar, M. S. M., Alias, Z., Chuan, L. T., & Chisti, Y. (2014). Modeling of growth and laccase production by Pycnoporus sanguineus. *Bioprocess Biosyst Eng*, *37*, 765-775.

Seifollahi, Z., Abbasi, A., & Rahbar-Kelishami, A. (2019). Application of solvent extraction for the removal of amoxicillin drug residues in environmental waters. *Iran. J. Pharm. Sci.*, *15*(4), 41-52. https://doi.org/https://doi.org/10.22037/ijps.v15.40453

Shu, L., Yang, M., Zhao, H., Li, T., Yang, L., Zou, X., & Li, Y. (2019). Process optimization in a stirred tank bioreactor based on CFD-Taguchi method: A case study. *J. Clean. Prod.*, *230*, 1074-1084. https://doi.org/https://doi.org/10.1016/j.jclepro.2019.05.083

Singh, Y., & Srivastava, S. (2014). Performance improvement of *Bacillus aryabhattai* ITBHU02 for high-throughput production of a tumor-inhibitory L-asparaginase using a kinetic model based approach. *J. Chem. Technol. Biotechnol.*, *89*(1), 117-127.

Stavropoulou, E., & Bezirtzoglou, E. (2019). Predictive modeling of microbial behavior in food. *Foods*, *8*(12), 654.

Supramani, S., Rejab, N. A., Ilham, Z., Ahmad, R., Show, P.-L., Ibrahim, M. F., & Wan-Mohtar, W. A. A. Q. I. (2023). Performance of Biomass and Exopolysaccharide Production from the Medicinal Mushroom *Ganoderma lucidum* in a New Fabricated Air-L-Shaped Bioreactor (ALSB). *Processes*, *11*(3), 670. https://www.mdpi.com/2227-9717/11/3/670

Svobodová, K., & Novotný, Č. (2018). Bioreactors based on immobilized fungi: bioremediation under non-sterile conditions. *Appl. Microbiol. Biotechnol.*, *102*, 39-46.

Uba, G., Yakasai, H. M., & Abubakar, A. (2020). Mathematical modeling of the biodegradation of phenol from industrial effluents using immobilized *Pseudomonas putida*. *JOBIMB*, *8*(1), 15-18.

Velpandian, T., Halder, N., Nath, M., Das, U., Moksha, L., Gowtham, L., & Batta, S. P. (2018). Un-segregated waste disposal: an alarming threat of antimicrobials in surface and ground water sources in Delhi. *Environ. Sci. Pollut. Res.*, *25*, 29518-29528.

Verma, M., & Haritash, A. K. (2020). Photocatalytic degradation of Amoxicillin in pharmaceutical wastewater: A potential tool to manage residual antibiotics. *Environ. Technol. Innov.*, *20*, 101072. https://doi.org/https://doi.org/10.1016/j.eti.2020.101072

Walker, G. M., & White, N. A. (2017). Introduction to fungal physiology. ***Fungi: biology and applications***, 1-35.

Wang, S., Yuan, R., Chen, H., Wang, F., & Zhou, B. (2021). Anaerobic biodegradation of four sulfanilamide antibiotics: Kinetics, pathways and microbiological studies. *J. Hazard. Mater.* , *416*, 125840. https://doi.org/https://doi.org/10.1016/j.jhazmat.2021.125840

Xu, B., Mao, D., Luo, Y., & Xu, L. (2011). Sulfamethoxazole biodegradation and biotransformation in the water–sediment system of a natural river. *Bioresour. Technol.*, *102*(14), 7069-7076. https://doi.org/https://doi.org/10.1016/j.biortech.2011.04.086

Yang, C.-W., Hsiao, W.-C., & Chang, B.-V. (2016). Biodegradation of sulfonamide antibiotics in sludge. *Chemosphere*, *150*, 559-565. https://doi.org/https://doi.org/10.1016/j.chemosphere.2016.02.064

Zhang, C., Zeng, J., Xiong, W., & Zeng, Z. (2020). Rapid determination of amoxicillin in porcine tissues by UPLC-MS/MS with internal standard. *J. Food Compos. Anal.*, *92*, 103578. https://doi.org/https://doi.org/10.1016/j.jfca.2020.103578

Zhang, W., Li, Y., Wang, C., Wang, P., Hou, J., Yu, Z., Niu, L., Wang, L., & Wang, J. (2016). Modeling the biodegradation of bacterial community assembly linked antibiotics in river sediment using a deterministic–stochastic combined model. *Environ. Sci. Technol.*, *50*(16), 8788-8798.

JJBS

Volume 18, Number 3,September 2025
ISSN 1995-6673
Pages 469 – 478

Jordan Journal of Biological Sciences

Genotyping of Methicillin-Resistant *Staphylococcus epidermidis* in Healthcare Workers in a Jordanian Hospital Using Molecular Tools

Saqr Abushattal [1*]; Sulaiman M Alnaimat [1]; Saif M Dmour [1]; Nehaya Saidat [2]; Esraa H. Al-Nsour [3]

[1] Department of Medical Analysis, Princess Aisha Bint Al-Hussein College of Nursing and Medical Sciences, Al-Hussein Bin Talal University, Ma'an 71111, JORDAN; [2] Al-Tafilah Hospital, Ministry of Health, Jordan; [3] Department of Basic Pharmaceutical Sciences, Faculty of Pharmacy, Isra University, Amman, Jordan.

Received: October 22, 2024; Revised: February 2, 2025; Accepted: March 10, 2025

Abstract

Methicillin-resistant *Staphylococcus epidermidis* (MRSE) represents a significant challenge in healthcare-associated infections, contributing to increased infection rates, medical complications, and mortality. Originating from human skin, nasal passages, and healthcare environments, MRSE exploits skin breaches and hospital surfaces to spread, complicating treatment due to its antibiotic resistance, particularly conferred by the *mecA* gene. Effective isolation and control of MRSE in healthcare settings require stringent hygiene practices, infection control measures, and continuous education for healthcare workers and patients. Addressing these challenges necessitates a multifaceted approach, including research into new therapeutic strategies and responsible antibiotic usage.

In our study, *mecA* gene analysis was conducted on 24 MRSE isolates using PCR and gel electrophoresis. Results confirmed the prevalence of the *mecA* gene in 95.8% (23/24) of the isolates, highlighting its significant role in methicillin resistance. Additionally, we identified 13 MRSE haplotypes across diverse sources, with Hap_2 being the most prevalent (67%, 26/39 isolates), widely distributed across nasal (53.8%) and skin (34.6%) samples. Phylogenetic analysis of 39 MRSE isolates, including 15 from GenBank, revealed significant genetic diversity. Hap_2 exhibited extensive variation, whereas the isolates designated as IHN (nasal samples) and IHS (skin samples) formed a distinct monophyletic cluster, characterized by high genetic relatedness and a common evolutionary origin. This pattern contrasted with the separate clustering observed for the GenBank strains. These findings emphasize the need for targeted infection control measures, particularly in healthcare settings, to address the prevalence of MRSE and its genetic diversity. Practical applications include the development of screening programs for healthcare workers, improving decontamination protocols, and fostering research into novel therapeutic strategies to mitigate antibiotic resistance.

Keywords: Methicillin-Resistant *Staphylococcus epidermidis* (MRSE), *mecA* gene, Antibiotic resistance, Healthcare workers, Genotyping, Jordanian hospital, *16S rRNA* gene.

1. Introduction

Isolates of methicillin-resistant *Staphylococcus epidermidis* (MRSE) are among the formidable foes in the realm of healthcare-associated infections, contributing significantly to the burden on healthcare systems and public health at large (Mirzaei et al., 2022; Sharma & Kalawat, 2023). These resilient bacteria, resistant to conventional antibiotics like methicillin, present a daunting challenge for treatment, complicating medical interventions and heightening the risk of infection transmission (Sun et al., 2023; Becker et al., 2023). Originating from various sources, including human skin, nasal passages, and the ambient environment within healthcare facilities, MRSE finds ample opportunities to colonize and proliferate (Lee et al., 2023; Guo et al., 2022). Skin breaches, such as wounds and fissures, serve as entry points for these bacteria, while the nasal cavity can harbor them stealthily, devoid of overt symptoms (Liang et al., 2022). It can facilitate the spread of antibiotic-resistant strains to patients, increase the likelihood of hospital-acquired infections, and complicate treatment outcomes. Therefore, identifying and managing MRSE carriers, particularly in healthcare settings, is crucial for infection control and preventing the transmission of resistant bacteria. Furthermore, the hospital environment itself, with its multitude of surfaces and medical apparatus, acts as a reservoir for these resilient microbes, facilitating their spread among patients and healthcare workers (Dai et al., 2023).

The ramifications of MRSE isolates extend beyond individual health concerns to encompass broader public health risks. Increased infection rates, complications in medical treatments, and elevated mortality rates all underscore the urgent need to address this menace (Leung

* Corresponding author. e-mail: Saqr.S.abushattal@ahu.edu.jo.

et al., 2022; Brown & Smith, 2023). MRSE strains, in particular, serve as a significant reservoir of antibiotic resistance genes, notably the *mecA* gene, which confers methicillin resistance. This genetic trait not only allows MRSE to resist treatment with beta-lactam antibiotics like methicillin, but it can also be transferred to other bacterial species through horizontal gene transfer. Moreover, the emergence of antibiotic resistance compounds the issue, rendering conventional treatment modalities increasingly ineffective (Wang et al., 2023; Yao et al., 2023).

Effectively managing MRSE within healthcare facilities requires a comprehensive approach, combining strict infection control measures, rigorous hygiene practices, and ongoing staff training initiatives. This includes both the careful collection of MRSE isolates for study and the implementation of strategies to limit the bacteria's spread among patients and healthcare workers (Di Russo Case et al., 2023; Fisher et al., 2023). From environmental decontamination to promoting personal hygiene among patients and staff, every aspect of infection prevention must be rigorously implemented and continually reinforced. However, the challenges of isolation extend beyond the realm of technical procedures to encompass human factors and systemic issues within healthcare settings. Time constraints, competing priorities, and the relentless pace of medical practice all contribute to the complexity of ensuring strict adherence to isolation protocols (Hill et al., 2023). Addressing these challenges necessitates a multifaceted approach that goes beyond mere procedural compliance. Continuous education and awareness campaigns targeting both healthcare workers and patients are essential to foster a culture of vigilance and responsibility (Naylor et al., 2023). Additionally, efforts to curb inappropriate antibiotic usage and support research into novel therapeutic approaches are crucial for combating the escalating threat of antibiotic resistance (López-López et al., 2022).

In confronting the menace of methicillin-resistant *S. epidermidis* and its ilk, the imperative for collective action and unwavering commitment to infection control has never been more urgent. Only through concerted efforts, grounded in sound scientific principles and bolstered by a shared sense of responsibility, can we hope to stem the tide of healthcare-associated infections and safeguard public health for generations to come. Our study specifically aims to identify and genotype MRSE isolates from healthcare workers in a Jordanian hospital, focusing on the presence of the *mecA* gene and its impact on antibiotic resistance. We hypothesize that MRSE strains from healthcare workers harboring the *mecA* gene will exhibit higher levels of resistance to methicillin and other antibiotics. The findings could provide crucial insights into the role of healthcare workers in the transmission and evolution of MRSE, offering a pathway for improved infection control measures.

2. Materials and Methods:

2.1. Bacterial Isolation and Identification:

At the selected Jordanian hospital, stringent protocols are implemented to efficiently isolate bacterial groups, particularly when dealing with large healthcare workers. In previous study, a total of 175 bacterial isolates were obtained, with 25 isolates identified as *S. epidermidis* through a series of biochemical tests (Al-Nsour et al., 2024). The isolates from healthcare workers (carriers) and the environment were randomly isolated in roughly equal numbers to ensure a representative selection from both sources. While the exact number of samples from each source varied slightly, this was expected. A substantial number of samples were successfully isolated, identified, genotyped, and characterized. These isolates were sourced from various origins, including the skin and nasal passages of hospital workers, predominantly doctors and nurses, as well as environmental surfaces within the hospital premises. After isolation, the bacterial isolates were preserved and subsequently subjected to molecular analyses focusing on specific genetic structures.

2.2. DNA Extraction for Staphylococcus epidermidis Isolates:

Our study commenced by isolating *S. epidermidis* strains, with a focus on identifying those potentially exhibiting Methicillin-resistant properties. Recognizing the critical significance of employing robust protocols, we prioritized established methods to ensure the extraction of genomic DNA of the highest quality. To achieve this, we utilized a combination of techniques including enzymatic lysis and column-based purification. These methods were meticulously executed to yield pure DNA samples, thereby reducing the risk of contaminants that could compromise subsequent analyses. Importantly, all procedures were conducted in strict adherence to manufacturer instructions to guarantee optimal outcomes (Al-Nsour et al., 2024).

2.3. PCR Amplification for 16S rRNA Identification:

After DNA extraction, Polymerase Chain Reaction (PCR) was utilized to amplify the *16S rRNA* gene. Selecting universal primers like the forward primer 27F (5'-AGAGTTTGATCMTGGCTCAG-3') and reverse primer 1492R (5'-TACGGYTACCTTGTTACGACTT-3') was crucial to ensure broad applicability across bacterial taxa (Stahl, 1991; Ludwig, 1999). These primers were specifically designed to target highly conserved regions of the *16S rRNA* gene, ensuring accurate amplification of the target gene. PCR amplification was performed using LILIF 2x Master Mix (Korea) in a 50 µL reaction volume. The PCR reaction mixtures were initially incubated at 94°C for 5 minutes for denaturation, followed by 40 cycles of denaturation at 94°C for 30 seconds, annealing at 58°C for 25 seconds, and elongation at 72°C for 1.20 minutes. A final extension step was performed at 72°C for 5 minutes. The conditions were optimized to ensure efficient amplification of the target gene.

To assess methicillin resistance, PCR amplification targeted the *mecA* gene, a key determinant of resistance in *S. epidermidis*. The primer sequences used for amplification were P2 (5'-ATCGATGGTAAAGGTTGGC-3' and P3 (5'-AGTTCTGCAGTACCGGATTTGC-3' which generated an amplicon of 530 base pairs in size. These primers were carefully designed to specifically target the *mecA* gene, ensuring accurate detection of methicillin resistance in the MRSE isolates. For the amplification of the *mecA* gene, the PCR reaction mixtures were initially incubated at 94°C for 5 minutes for denaturation. This was followed by 40 cycles of denaturation at 94°C for 30 seconds, annealing at 57°C for 25 seconds, and elongation at 72°C for 1.20

minutes. A final extension was carried out at 72°C for 5 minutes.

2.4. Sequence Editing, NCBI Submission, and Bioinformatic Analysis:

The purified PCR products were sequenced using a commercial service provided by MACROGEN, Korea, and the obtained sequences underwent meticulous editing using the EditBio program to remove any artifacts or low-quality regions (Hall, 1999). Edited sequences were then subjected to BlastN analysis to confirm their identity and assess their similarity to known sequences (https://www.ncbi.nlm.nih.gov) (Sayers et al., 2020). Subsequently, the edited sequences were submitted to the National Center for Biotechnology Information (NCBI) database, providing a publicly accessible repository for the genetic information of the MRSE isolates. Accession numbers corresponding to each sequence were acquired, associating them with distinct identifiers within the NCBI database. These accession numbers are listed in Table 1.

Table 1. Accession numbers corresponding to each sequence, linked with distinct identifiers in the NCBI database

	Isolate code	Accession number	Source	Isolation Date	Location
1	IHN1B	OQ568718	Human Nasal	2022	Jordan
2	IHN2B	OQ568719	Human Nasal	2022	Jordan
3	IHN3B	OQ568720	Human Nasal	2022	Jordan
4	IHN4B	OQ568721	Human Nasal	2022	Jordan
5	IHN5B	OQ568722	Human Nasal	2022	Jordan
6	IHN6B	OQ568723	Human Nasal	2022	Jordan
7	IHN7B	OQ568724	Human Nasal	2022	Jordan
8	IHN8B	OQ568725	Human Nasal	2022	Jordan
9	IHN9B	OQ568726	Human Nasal	2022	Jordan
10	IHN10B	OQ568727	Human Nasal	2022	Jordan
11	IHN11B	OQ568728	Human Nasal	2022	Jordan
12	IHN12B	OQ568729	Human Nasal	2022	Jordan
13	IHN13B	OQ568730	Human Nasal	2022	Jordan
14	IHN14B	OQ568731	Human Nasal	2022	Jordan
15	IHS1B	OQ568732	Human Skin	2022	Jordan
16	IHS2B	OQ568733	Human Skin	2022	Jordan
17	IHS3B	OQ568734	Human Skin	2022	Jordan
18	IHS4B	OQ568735	Human Skin	2022	Jordan
19	IHS5B	OQ568736	Human Skin	2022	Jordan
20	IHS6B	OQ568737	Human Skin	2022	Jordan
21	IHS7B	OQ568738	Human Skin	2022	Jordan
22	IHS8B	OQ568739	Human Skin	2022	Jordan
23	IHS9B	OQ568740	Human Skin	2022	Jordan
24	IHE1B	OQ568741	Environment	2022	Jordan

2.5. Phylogenetic Tree Construction with MEGA11:

MEGA11 software was employed for constructing phylogenetic trees based on the edited 16S rRNA sequences (Tamura et al., 2021). This facilitated the visualization of evolutionary relationships among MRSE isolates. Parameters such as tree-building methods and bootstrap values were carefully considered to ensure the robustness of the phylogenetic analysis. For the analysis, some *Staphylococcus epidermidis* isolates were retrieved from NCBI and included alongside our experimental data. The evolutionary history of these isolates was inferred using the Maximum Likelihood method and the Tamura-Nei model. The tree with the highest log-likelihood value of -1249.25 is presented. The percentage of trees in which the associated taxa clustered together is indicated next to the branches. Initial trees for the heuristic search were generated automatically using the Maximum Parsimony method. This analysis involved 39 nucleotide sequences, and all positions containing gaps or missing data were excluded (complete deletion option). The final dataset consisted of 676 positions. Evolutionary analyses were performed using MEGA11 software.

2.6. Haplotype Analysis:

A previous phylogenetic tree, constructed using 16S rRNA sequences, was utilized to explore haplotype diversity among the *S. epidermidis* and MRSE isolates. This analysis provided insights into the relatedness and evolutionary history of the isolates, offering a nuanced perspective on their genetic diversity within the population. To further elucidate the genetic variation and population structure, additional analyses were conducted using DnaSP6 (Rozas et al., 2017) and PopArt (Leigh and

Bryant, 2015) programs. In DnaSP6, parameters such as haplotype diversity, nucleotide diversity (π), and the number of polymorphic sites were calculated to assess the genetic variability. For PopArt, haplotype networks were visualized using the Median-Joining method to explore the relationships between different haplotypes. These software tools enabled the examination of haplotype frequencies, nucleotide diversity, and the visualization of haplotype networks, enhancing our understanding of the *S. epidermidis* and MRSE population dynamics and evolutionary patterns.

2.7. Identity and Similarity Percentage Calculation:

Specialized bioinformatics programs were employed to calculate identity and similarity percentages among the *S. epidermidis* and MRSE isolates. This comparative analysis delved into the molecular similarities and differences, contributing to a deeper understanding of the relatedness and divergence within the population at a genomic level. The Sequence Demarcation Tool (SDT), version 1.2, was utilized to facilitate this analysis, providing robust metrics for assessing genetic identity and similarity among the isolates (Muhire et al., 2014); in addition, the TBtools-I software was used to obtain the phylogenetic relatedness between all of isolates (Chen et al., 2023).

3. Results

In this study, we conducted a phylogenetic analysis involving 39 *S. epidermidis* strains. This included one isolate of *S. epidermidis* that does not harbor the *mecA* gene and 23 MRSE isolates from various sources (skin, nasal, and environmental) and 15 additional strains selected from GenBank based on their genetic identity to our isolates. The phylogenetic tree clearly demonstrates the evolutionary relationships between the IHS and IHN isolates (red squares) and various *S.epidermidis* strains from GenBank (green circles). The IHS and IHN isolates form a distinct monophyletic cluster, indicating their close genetic relatedness, with examples such as IHS9B, IHS6B, IHS3B, IHS2B, and IHS1B grouped together with high bootstrap support, suggesting a common or closely related source. Conversely, the GenBank sequences like MN022539.1, LC648284.1, and OU548756.1 also form a monophyletic group, reflecting their tight evolutionary relationship. Despite the clear separation between the IHS/IHN isolates and the GenBank strains, the tree shows they share a distant common ancestor, underscoring a more remote evolutionary connection. This relationship, supported by moderate to high bootstrap values, highlights that while the IHS and IHN isolates are genetically distinct from the GenBank strains, they still belong to the broader phylogenetic context of *S. epidermidis*.

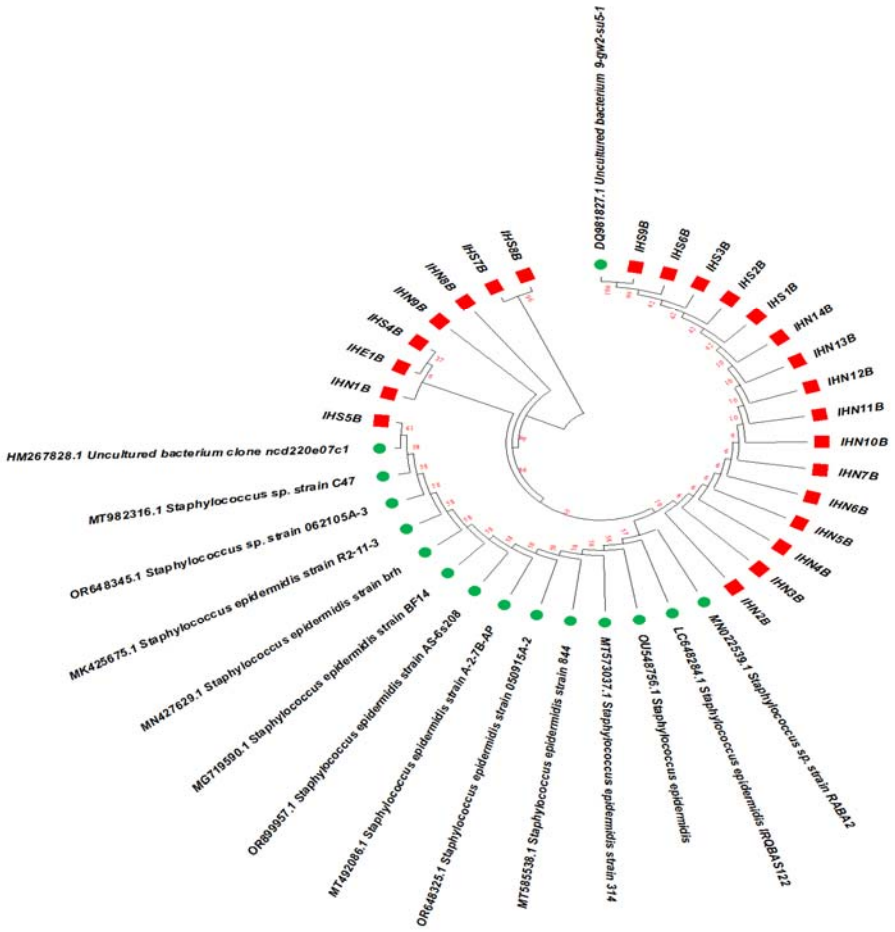

Figure 1. Evolutionary analysis of 16S rRNA sequences by the Maximum Likelihood method

The evolutionary history was inferred by using the Maximum Likelihood method and Tamura-Nei model (Tamura and Nei, 1993). The tree with the highest log likelihood (-1249.25) is shown. The percentage of trees in which the associated taxa clustered together is shown next to the branches. Initial tree(s) for the heuristic search were obtained automatically by applying the Maximum Parsimony method. This analysis involved 39 nucleotide sequences. All positions containing gaps and missing data were eliminated (complete deletion option). There were a total of 676 positions in the final dataset. Evolutionary analyses were conducted in MEGA11 (Tamura et al., 2021). The phylogenetic tree depicts the genetic relationships among *S. epidermidis* isolates. The green circles ● represent strains from the GenBank database, while the red squares ■ indicate isolates from the current study.

The clustering within the IHS and IHN isolates can aid in understanding their diversity and potential functional or pathogenic differences. A monophyletic group (or clade) includes an ancestor and all of its descendants. The cluster of S. epidermidis strains from GenBank (green circles) is a monophyletic group, including sequences such as MN022539.1, LC648284.1, and OU548756.1, all sharing a common ancestor with IHS5B, distinct from other groups in the tree. rue except for IHS5B that is clustered with the GenBank isolates and DQ981827.1 that is clustering with the red squares. Similarly, the IHS and IHN isolates (red squares) form a monophyletic group, which includes sequences such as IHS9B, IHS6B, IHS3B, IHS2B, IHS1B, and their related isolates, all descending from a common ancestor unique to them. However, IHS5B deviates from this pattern, as it clusters with the GenBank isolates, while DQ981827.1 clusters with the red square isolates, indicating some level of genetic diversity within the group. A paraphyletic group includes an ancestor and some, but not all, of its descendants. If we consider the entire group of *S. epidermidis* strains along with the IHS/IHN isolates, excluding certain sequences like DQ981827.1 and HM267828.1, the group could be classified as paraphyletic. This is because it includes their common ancestor and several, but not all, of the descendants. Specifically, HM267828.1 clusters with the other GenBank isolates, while DQ981827.1 is an outlier, sharing a common ancestor with the rest of the group but not fully fitting within it. A polyphyletic group includes members from different ancestral lines and does not include the most recent common ancestor of the group. If we were to group some of the IHS/IHN isolates with certain unrelated GenBank sequences based on some arbitrary similarity, ignoring their actual common ancestors, this would form a polyphyletic group. The phylogenetic tree indicates that IHS9B and DQ981827 are closely related and share a recent common ancestor. The IHS isolates (such as IHS9B, IHS6B) are more closely related to each other, forming a tight cluster. Similarly, the IHN isolates (such as IHN14B,

IHN13B) are more closely related to each other. The GenBank strains of *S. epidermidis* are more closely related to each other than to the IHS/IHN isolates. The overall tree shows that while both the IHS/IHN isolates and the GenBank strains of *S. epidermidis* share a distant common ancestor, they form distinct clades, indicating separate evolutionary paths.

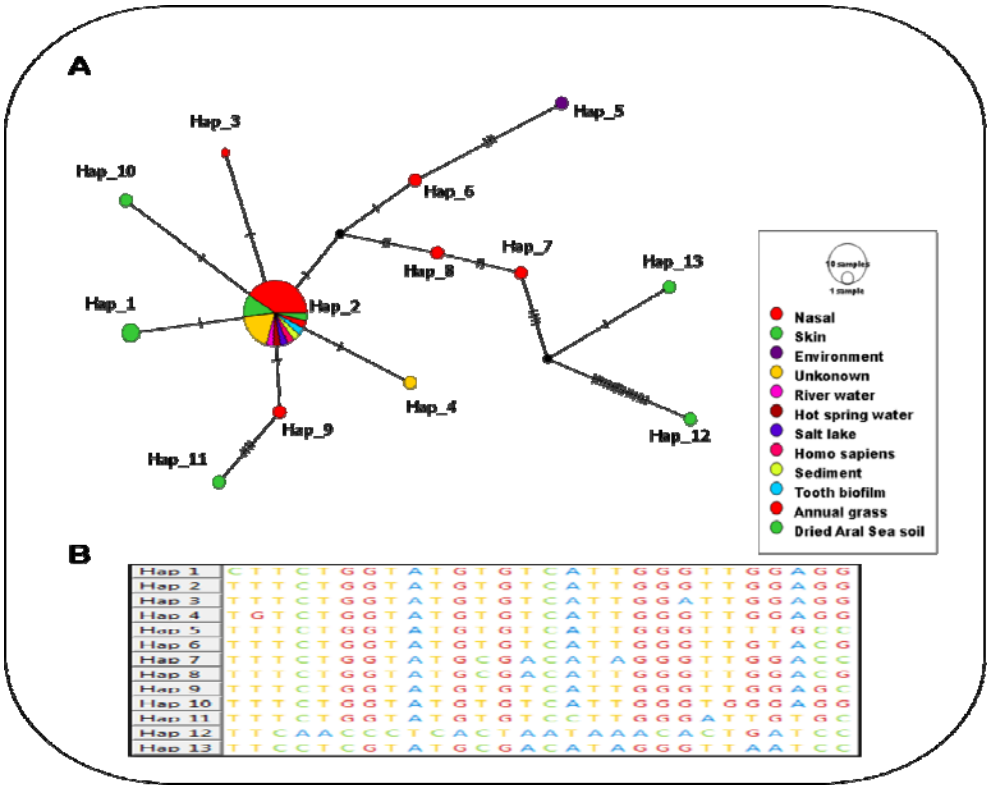

Figure 2 A) This analysis illustrates the mutation count between each pair of haplotypes, indicated by the number of dashed lines between them. Each mutation represents a variation in nucleotides at specific positions within the sequence. **B)** The analysis reveals the distinct positions of targeted sequences needed to derive the haplotypes, based on the discrepancies among the sequences. Each mutation signifies a variation in nucleotides at specific positions within the sequence.

The dataset in figure 2A comprises 13 unique haplotypes (Hap_1 to Hap_13) derived from 39 MRSE isolates, including 15 from NCBI. In figure 2A, the size of the circles represents the number of isolates within each haplotype, with larger circles indicating haplotypes that contain a greater number of isolates. This visual representation helps to illustrate the relative abundance of each haplotype in the dataset. The dominant haplotype, Hap_2, is represented by 26 isolates and encompasses a diverse array of sequences. These sequences include isolates with the following codes: DQ981827.1, OR648345.1, MK425675.1, MN427629.1, MG719590.1, OR899957.1, MT492086.1, OR648325.1, MT573037.1, OU548756.1, LC648284.1, MN022539.1, IHN2B, IHN3B, IHN4B, IHN5B, IHN6B, IHN7B, IHN10B, IHN11B, IHN12B, IHN14B, IHS1B, IHS2B, IHS6B, and IHS9B. These diverse isolates collectively contribute to the extensive variation observed within Hap_2, highlighting the genetic heterogeneity present within the MRSE population, while the rest of haplotypes are singleton haplotypes. By single genotype, we refer to isolates each possessing a unique genetic sequence, with no more than one isolate sharing the same pattern. In contrast, haplotypes represented by more than one isolate, such as Hap_2, indicate genetic clusters where multiple isolates share the same sequence. This distinction highlights the genetic diversity within the MRSE group. The sequence comparison in Figure 2B shows the 16S rRNA sequence exclusively. It demonstrates that all isolates within haplotype 2 share the same sequence, which differs from other haplotypes by one or more nucleotide variations. The haplotypes exhibit notable diversity, as seen in their sequence variations across 28 nucleotide sites. Hap_2 is particularly diverse, represented by sequences with variations at multiple sites. Hap_1, although occurring twice (HM267828.1 and IHS5B), differs from the predominant Hap_2 by a single nucleotide, highlighting its distinct sequence variation. The overall shape of the haplotype distribution suggests a predominant central haplotype (Hap_2) surrounded by several peripheral haplotypes, indicating a core-periphery structure in the MRSE population. These findings underscore the genetic relatedness and variation within the MRSE isolates, providing insights into their evolutionary dynamics and population structure.

Hap_2 emerges as the most prevalent haplotype, with occurrences across multiple sources, including nasal, skin, unknown, river water, hot spring water, salt lake, *Homo sapiens*, sediment, tooth biofilm, annual grass, and dried Aral Sea soil. This suggests a widespread distribution and adaptability of Hap_2 across various environments.

Several other haplotypes, such as Hap_6, Hap_7, Hap_8, and Hap_9, are predominantly isolated from specific sources, indicating potential specialization or niche adaptation. In contrast, haplotypes such as Hap_3, Hap_4, and Hap_5 exhibit a more limited presence, as they tend to originate from a single source, unlike Hap_2, which shows broader distribution across multiple sources. This suggests that these haplotypes may be rare or specifically associated with particular environments, as evidenced by the clustering patterns in Figure 2A. We identified 13 MRSE haplotypes, with Hap_2 emerging as the most prevalent, representing 67% (26/39) of the total isolates. Hap_2 was significantly more common in nasal samples (53.8%, 14/26) compared to skin samples (34.6%, 9/26) ($p < 0.05$, Chi-square test), emphasizing the role of nasal colonization in MRSE dissemination. Other haplotypes, such as Hap_1, Hap_3, Hap_4, and Hap_5, were less common, with 3 or fewer isolates each. Haplotypes Hap_8 to Hap_13 were not detected in either nasal or skin samples. Phylogenetic analysis revealed clustering patterns with bootstrap values >70%, confirming the evolutionary relationships and genetic reliability of the observed haplotype distributions. Overall, the data provides insights into the distribution patterns of MRSE haplotypes across diverse isolation sources, highlighting potential ecological niches and sources of transmission for these bacterial strains.

Continuing with the analysis (Figure 3), each sequence listed, including HM267828.1, DQ981827.1, MT982316.1, OR648345.1, MK425675.1, MN427629.1, MG719590.1, OR899957.1, MT492086.1, OR648325.1, MT585538.1, MT573037.1, OU548756.1, LC648284.1, and MN022539.1, displays varying degrees of identity with other sequences. For instance, HM267828.1 exhibits 100% identity with itself and various percentages of identity with other sequences. Similarly, DQ981827.1 shows 99.89% identity with HM267828.1 and 100% identity with itself, along with varying degrees of identity with other sequences. This pattern persists for the remaining sequences, each demonstrating different levels of identity with others in the dataset. Moving on to the isolates coded with IHN and IHS, each of these isolates, from IHN1B to IHN14B and IHS1B to IHS9B, also demonstrates varied percentages of identity with other sequences, including those with IHN and IHS codes. These identity percentages provide insights into genetic resemblance or divergence among the sequences, aiding in the understanding of evolutionary relationships, genetic variation, and potential functional similarities or differences.

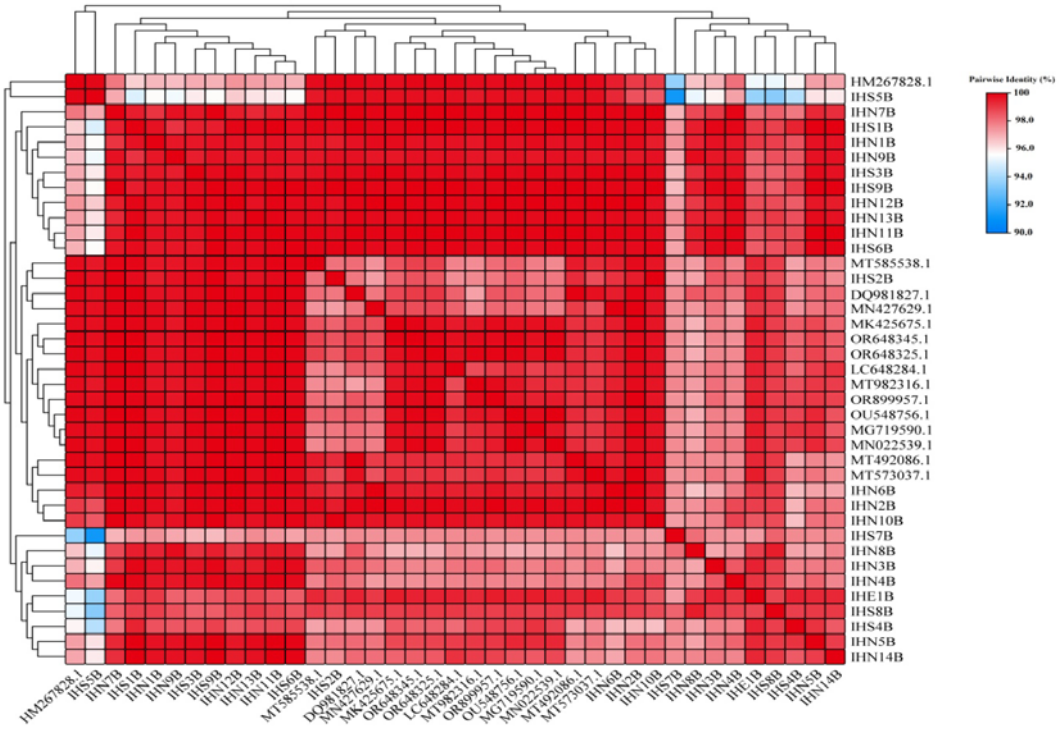

Figure 3 Colour-coded pairwise identity matrix generated from the 16S rRNA sequences of 39 *S. epidermidis* isolates sequences. Each coloured cell represents a percentage identity score between two sequences (one indicated horizontally to the left and the other vertically at the bottom). A coloured key indicates the correspondence between pairwise identities and the colours displayed in the matrix. Per cent nucleotide identity based heat map was created using TBtools-I (Chen et al., 2023).

In our exploration of the *mecA* gene, Figure 4 presents the findings from gel electrophoresis, revealing a noteworthy and consistent revelation across all 25 *S. epidermidis* isolates: the presence of the *mecA* gene within their genetic makeup. The distinct visualization of PCR amplification products corresponding to the *mecA* gene unequivocally confirms its widespread prevalence among these MRSE strains. This significant observation establishes a robust genetic basis for methicillin resistance within the sampled strains, emphasizing the pivotal role of the *mecA* gene in transmitting resistance to beta-lactam antibiotics. Moreover, within the same investigative

framework, among the 24 isolates scrutinized, only one exhibited negative outcomes in PCR amplification targeting the *mecA* gene. Specifically, this isolate is identified as isolate IHN12B, while the remaining 23 isolates demonstrated positive PCR outcomes.

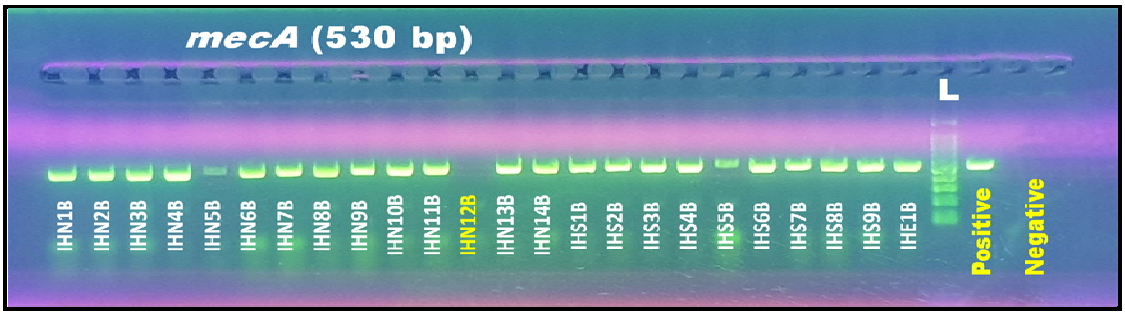

Figure 4. illustrates a compelling finding: amplification of the *mecA* gene was exclusively detected in 23 *S. epidermidis* isolates, signalling their resistance to methicillin. Notably, amidst 24 isolates, only one (**IHN12B**) exhibited a negative result for PCR amplification. The gel electrophoresis image showcases the (L) lane, symbolizing the ladder (DNA marker) with a size of 100 bp. The presence of both negative and positive controls is clearly delineated within the gel image, ensuring the validity and reliability of the experimental results.

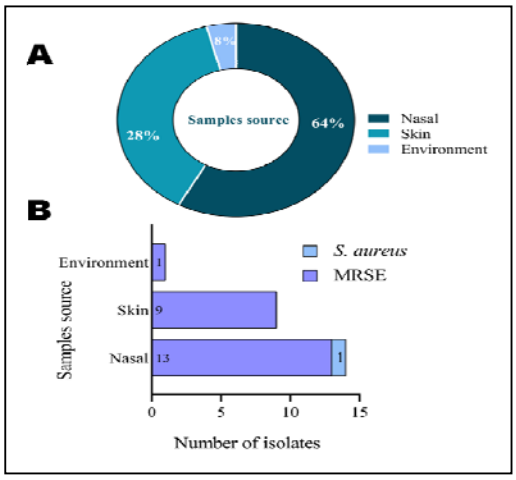

Figure 5. Representation of the distribution frequency of *S.epidermidis* isolates from various sources and the presence of MRSE isolates among the total isolates. **A:** Pie chart illustrates the total number of isolation sources and the distribution of isolates among these sources. **B:** Bar chart displays the total number of isolates of MRSE and *S. epidermidis* from selected sources.

The Pie chart in Figure 5A illustrates the distribution of *S. epidermidis* isolates across different isolation sources. It clearly shows that the nasal cavity is the most significant reservoir for *S. epidermidis*, with 14 isolates, followed by the skin with 9 isolates, and the environment with only 1 isolate. This visualization highlights the predominance of *S. epidermidis* in nasal and skin habitats, reflecting its role as a common commensal organism in these areas. The minimal environmental presence suggests either limited sampling or lower environmental colonization by *S. epidermidis* in the sampled settings. The bar chart data in Figure 5B indicates a significant presence of Methicillin-Resistant *Staphylococcus epidermidis* (MRSE) in skin and nasal passages, with 9 and 13 isolates respectively, and a minimal presence in the environment with just one isolate. In contrast, *S. epidermidis* (that does not contain the *mecA* gene) was only found in one nasal isolate and was absent from skin and environmental samples. This highlights the nasal cavity as a critical reservoir for both MRSE and *S. epidermidis*, although MRSE is more predominant. The findings emphasize the importance of targeted infection control measures, particularly in clinical settings, and suggest the need for increased environmental sampling to better understand the presence of these bacteria. Further research is recommended to explore factors contributing to the higher prevalence of MRSE in the nasal cavity, aiding in the development of effective prevention and treatment strategies.

4. Discussion

The battle against antibiotic-resistant bacteria has intensified and will continue to escalate (O'Neill, 2016). The pace of bacterial resistance to antibiotics is accelerating, making control efforts increasingly challenging (Aslam et al., 2018). Antibiotic-resistant bacteria, especially those exhibiting genetic mechanisms underlying antimicrobial resistance, require ongoing monitoring to address the sources and causes of this increasing resistance (CDC, 2019). In this study, we tracked methicillin-resistant *S. epidermidis* isolates in a teaching hospital in Jordan as part of a surveillance program aimed at monitoring genetic developments in these isolates. We focused on the genetic relatedness and proximity of isolates from various sources, including skin, nose, and the hospital environment, using ribosomal gene analysis. The evolutionary tree in Figure 1 illustrates the relatedness of isolates from different sources and their clustering with those in the gene bank (Kumar et al., 2016). The evolutionary tree revealed three clusters: the first cluster contains IHS8B, IHS7B, IHN8B, IHN9B, IHS4B, IHE1B, and IHN1B; the second cluster includes the GenBank isolates (except for DQ981827.1), along with IHS5B; and the third cluster comprises the remaining isolates. This relatedness indicates a connection between isolates from diverse geographical regions and sources. Our analysis aimed to determine the number of individual haplotypes and their similarities through ribosomal gene sequences. Using the DnaSP software, Hap_2 is the dominant haplotype, found in 26 out of 39 sequences, suggesting it may represent a common ancestral lineage or possess a selective advantage (Rozas et al., 2017). The remaining 12 haplotypes (Hap_1 and Hap_3 to Hap_13) are each found in only one or two sequences, indicating their rarity and possibly reflecting recent mutations, genetic drift, or specific selective pressures (Nei & Kumar,

2000). This distribution points to a diverse genetic population with several rare variants, incorporating sequences from both NCBI and specific isolates from our study. The data in figure 2A provides valuable insights into genetic diversity, evolutionary relationships, and population structure, which can be applied in various fields such as population genetics, conservation biology, and medical research (Hohenlohe et al., 2018). The arrangement and position differences among the haplotypes across all positions provide insights into the evolutionary pressures and genetic drift occurring within bacterial populations. By analyzing these sequence variations, we can infer the evolutionary pathways and selective pressures that have led to the emergence of resistant strains (Didelot & Maiden, 2010). The clustering of haplotypes, as shown in the evolutionary tree, indicates shared evolutionary histories and possible horizontal gene transfer events (Data not shown here), which are common mechanisms for the spread of resistance genes among bacteria (Arnold et al., 2018). In Figure 2B, we noted the different sequences for 13 haplotypes, highlighting the variations in arrangement and the positions of difference among all haplotypes across 1086 positions, which correspond to the length of the sequenced region within the *16S rRNA* gene. The use of software tools to analyze ribosomal gene sequences and identify haplotypes underscores the importance of bioinformatics in modern molecular biology (Gauthier & Singh, 2018). These tools allow for the rapid analysis of large datasets, facilitating the identification of genetic variations that would be challenging to detect through traditional methods. Such comparisons enable us to determine the geographical spread and epidemiological linkages of antibiotic-resistant strains (Benson et al., 2018). If our study isolates show high similarity to strains from different regions or environments deposited in GenBank, it suggests possible transmission routes and sources of infection, aiding in the development of targeted public health interventions (Benson et al., 2018).

The observed genetic relatedness between our isolates and those in GenBank prompted further investigation into the identity and connections between our study isolates and those previously deposited in the Genbank. Using the TBtools-I software, we accessed and analyzed this information, as depicted in Figure 3. The values in this figure demonstrated the identity between bacterial isolate sequences and their closer origins based on ribosomal gene analysis. The investigation into the genetic similarities and connections between study isolates and GenBank sequences, as facilitated by the TBtools-I software and depicted in Figure 3, is a powerful approach in molecular microbiology. It enhances our understanding of the genetic underpinnings of antibiotic resistance, informs clinical practices, and supports public health initiatives. This integrative approach underscores the importance of comparative genomics and bioinformatics in addressing the global challenge of antibiotic resistance (Gauthier & Singh, 2018; Benson et al., 2018). To investigate the presence of the *mecA* gene among our study isolates, we found that all of the isolates, except one (IHN12B), contained the *mecA* gene. The *mecA* gene is a critical determinant of methicillin resistance in *S. epidermidis* and other staphylococcal species. It encodes an alternative penicillin-binding protein (PBP2a) that has a low affinity for beta-lactam antibiotics, including methicillin (Becker et al., 2014). The finding that all but one isolate (IHN12B) possess the *mecA* gene is significant, indicating a high prevalence of methicillin resistance within this bacterial population, which is concerning for treatment options. Moreover, the widespread presence of the *mecA* gene suggests that this resistance mechanism is likely disseminated through horizontal gene transfer or clonal expansion of resistant strains (Howden et al., 2013). Therefore, this highlights the urgent need for effective strategies to combat antibiotic resistance. Significantly, the only exception, IHN12B, may offer insights into potential vulnerabilities in the bacterial population.

5. Conclusion

Methicillin-resistant *S. epidermidis* (MRSE) poses a significant healthcare challenge due to its high infection rates, complications, and resistance, primarily driven by the *mecA* gene. This study confirmed the widespread presence of the *mecA* gene in MRSE isolates and highlighted the genetic diversity and evolutionary dynamics of these bacteria. The nasal cavity and skin were identified as primary reservoirs for MRSE, emphasizing the need for stringent infection control practices. Phylogenetic analyses revealed significant genetic relatedness among isolates, underscoring the necessity for continuous monitoring and research into new therapeutic strategies. The findings underscore the importance of comprehensive infection control measures and the role of bioinformatics in addressing antibiotic resistance, aiding in the development of targeted public health interventions. Our findings highlight the genetic diversity and dominance of Hap_2 among MRSE isolates, underscoring the importance of nasal colonization in the dissemination of MRSE. These results emphasize the need for routine screening programs targeting healthcare workers, particularly nasal carriers, to prevent MRSE transmission.

Acknowledgements

We extend our heartfelt gratitude to Al-Balqa' Applied University, Isra University, and Jordan University Hospital for their invaluable support and assistance in completing this project. Their contributions were crucial to the success of our research, and we deeply appreciate their efforts.

References:

Al-Nsour EH, AL-Hadithi T, Al-Groom RM., Abushattal S., Naser AY, Al Nsour AH, Sallam RA, Kollab LM, Alswalha L, Khan MSA. 2024. Increased incidence of methicillin resistant *Staphylococcus aureus* and methicillin resistant *Staphylococcus epidermidis* in the skin and nasal carriage among healthcare workers and inanimate hospital surfaces after the COVID-19 pandemic. *Iran J of Microbiol* **16**:584.

Arnold, BJ, Huang, IT, Hanage, WP. 2018. Horizontal gene transfer and adaptive evolution in bacteria. *Nat Rev Microbiol*, **16(8)**: 471-483.

Aslam B, Wang W, Arshad MI, Khurshid M, Muzammil S, Rasool MH, Baloch Z. 2018. Antibiotic resistance: a rundown of a global crisis. *Infect Drug Resist*, **11**: 1645-1658.

Becker K, et al. 2023. Methicillin-resistant *Staphylococcus epidermidis*: recent trends in molecular diagnostics and

therapeutic strategies. *Infect Drug Resist,* **16**: 1271-1285. DOI: 10.2147/IDR.S351134

Becker K, Heilmann C, & Peters G. 2014. Coagulase-negative *staphylococci. Clin Microbiol Rev*, **27**(**4**): 870-926.

Benson DA, Cavanaugh M, Clark K, Karsch-Mizrachi I, Lipman DJ, Ostell J, Sayers, EW. 2018. GenBank. *Nucleic Acids Res*, **46**(D1): D41-D47.

Brown M, Smith R. 2023. The role of biofilm formation in the pathogenicity of methicillin-resistant *Staphylococcus epidermidis*. *Journal of Med Microbiol,* ***72*****(4)**: 570-578. DOI: 10.1099/jmm.0.001291

Centers for Disease Control and Prevention (CDC). 2019. *Antibiotic resistance threats in the United States, 2019*. Retrieved from https://www.cdc.gov/drugresistance/biggest-threats.html

Chen C, Wu Y, Li J, Wang X, Zeng Z, Xu J, Liu Y, Feng J, Chen H, He Y. 2023. TBtools-II: A "one for all, all for one" bioinformatics platform for biological big-data mining. *Mol Plant* **16**:1733-1742.

Dai M, et al. 2023. Adherence to infection control protocols and the impact on MRSE containment in healthcare facilities. *BMC Infect Dis,* **23(1)**: 102. DOI: 10.1186/s12879-023-08072-4

Di Russo Case E, et al. 2023. Infection control practices and the reduction of MRSE prevalence in a hospital setting. *Am J Infect Control,* **51(3)**: 285-290. DOI: 10.1016/j.ajic.2022.11.019

Didelot X, Maiden MC. 2010. Impact of recombination on bacterial evolution. *Trends in Microbiol*, **18(7)**: 315-322.

Fisher J, et al. 2023. Environmental contamination and the risk of methicillin-resistant *Staphylococcus epidermidis* transmission in hospitals. *J Hosp Infect,* **125**: 43-49. DOI: 10.1016/j.jhin.2023.02.014

Gauthier J, Singh M. 2018. In silico regulatory genomics: Bioinformatics comes of age. *Brief in Bioinform*, **19(1)**: 3-5.

Guo LJ, et al. 2022. Strategies for controlling methicillin-resistant *Staphylococcus epidermidis* in healthcare settings: A review. *Journal of Hosp Infect,* **119**: 20-27. DOI: 10.1016/j.jhin.2022.07.013

Hall TA. 1999. BioEdit: a user-friendly biological sequence alignment editor and analysis program for Windows 95/98/NT. *In Nucleic acids symp ser*, **41**(**41**): pp. 95-98).

Hill S, et al. 2023. Time management and its impact on infection control compliance in healthcare facilities. *BMC Health Serv Res,* **23(1)**: 200. DOI: 10.1186/s12913-023-09123-7

Hohenlohe PA, Phillips PC, Cresko WA. 2018. Population genomics provides key insights into ecological and evolutionary processes. *Evol Appl*, **11(11)**: 1951-1968.

Howden BP,Davies JK, Johnson PDR, Stinear TP, Grayson ML. 2013. Genomic insights to control the emergence of vancomycin-resistant enterococci. *mBio*, **4(4)**: e00412-13.

Kumar S, Stecher G, Tamura K. 2016. MEGA7: Molecular Evolutionary Genetics Analysis version 7.0 for bigger datasets. *Mol Biol Evol*, **33(7)**: 1870-1874.

Lee J, et al. 2023. Epidemiology and characteristics of methicillin-resistant *Staphylococcus epidermidis* isolates from various clinical samples. *J Clin Microbiol,* **61(2)**: e01123-22. DOI: 10.1128/jcm.01123-22

Leigh JW, Bryant D. 2015. POPART: full-feature software for haplotype network construction. *Methods ecol evol* **6**:1110-1116.

Leung V, et al. 2022. The impact of methicillin-resistant *Staphylococcus epidermidis* on healthcare-associated infections and patient outcomes. *Infect Control Hosp Epidemiol,* **43(1)**: 56-63. DOI: 10.1017/ice.2021.203

Liang X, et al. 2022. Prevalence and characteristics of methicillin-resistant *Staphylococcus epidermidis* in healthcare workers. *Antimicrob Resist Infect Control,* **11**: 40. DOI: 10.1186/s13756-022-01099-4

López-López R, et al. 2022. Novel therapeutic approaches against methicillin-resistant *Staphylococcus epidermidis*. *Curr Opin Pharmacol,* **67**: 102278. DOI: 10.1016/j.coph.2022.102278

Ludwig W, Schleifer KH. 1999. Phylogeny of bacteria beyond the 16S rRNA standard. *ASM News*, **65(12)**: 752-757.

Mirzaei R, Alikhani MY, Arciola CR, Sedighi I, Yousefimashouf R, Bagheri KP. 2022. Prevention, inhibition, and degradation effects of melittin alone and in combination with vancomycin and rifampin against strong biofilm producer strains of methicillin-resistant *Staphylococcus epidermidis*. *Biomed Pharmacother,* **147**: 1-15. DOI: 10.1016/j.biopha.2022.112670

Muhire BM, Varsani A, Martin DP. 2014. SDT: a virus classification tool based on pairwise sequence alignment and identity calculation. *PloS one* **9**:e108277.

Naylor NR, et al. 2023. Addressing human factors in the implementation of infection prevention and control measures: A systematic review. *BMJ Qual Saf,* **32(3)**: 223-230. DOI: 10.1136/bmjqs-2022-014632

Nei M, Kumar S. 2000. **Molecular evolution and phylogenetics**. Oxford university press.

O'Neill, J. 2016. *Tackling drug-resistant infections globally: Final report and recommendations*. The Review on Antimicrobial Resistance. Retrieved from https://amr-review.org/Publications.html

Rozas J, Ferrer-Mata A, Sánchez-DelBarrio JC, Guirao-Rico S, Librado P, Ramos-Onsins SE, Sánchez-Gracia A. 2017. DnaSP 6: DNA sequence polymorphism analysis of large data sets. *Mol biol evol* **34**:3299-3302.

Sayers EW, Cavanaugh M, Clark K, Ostell J, Pruitt KD, Karsch-Mizrachi, I. 2020. GenBank. *Nucleic Acids Res*, **48**(**D1**): D84-D86.

Sharma M, Kalawat U. 2023. Epidemiology and Molecular Characteristics of Methicillin-Resistant *Staphylococcus epidermidis* in a Tertiary Care Hospital. *J Clin Microbiol,* **61**(**3**): e01123-22. DOI: 10.1128/jcm.01123-22

Stahl DA. 1991. Nucleic acid techniques in bacterial systematics. *Development and application of nucleic acid probes*, **205-248**.

Sun FH, et al. 2023. Molecular Characteristics of Methicillin-Resistant *Staphylococcus epidermidis* on the Abdominal Skin of Females before Laparotomy. *Int J of Mol Sci,* **24**(**1**): 1032. DOI: 10.3390/ijms24031032

Tamura K, Nei M. 1993. Estimation of the number of nucleotide substitutions in the control region of mitochondrial DNA in humans and chimpanzees. *Mole biol evol* **10**:512-526.

Tamura K, Stecher G, Kumar S. 2021. MEGA11: molecular evolutionary genetics analysis version 11. *Mol biol evol* **38**:3022-3027.

Wang X, et al. 2023. Comparative genomics of methicillin-resistant *Staphylococcus epidermidis* isolated from different environments. *Front Microbiol,* **14**: 815. DOI: 10.3389/fmicb.2023.1230121

Yao Y, et al. 2023. Genome sequencing reveals the evolution and spread of methicillin-resistant *Staphylococcus epidermidis* in clinical settings. *Antimicrob Agents Chemother,* **67**(**1**): e01234-22. DOI: 10.1128/aac.01234-22

JJBS

Volume 18, Number 3,September 2025
ISSN 1995-6673
Pages 479 – 485

Jordan Journal of Biological Sciences

Effect of orally administered *Fusobacterium nucleatum*, *Bifidobacterium animalis*, and *Lactobacillus bulgaricus* on skin cancer development in a mouse model

Muhamad Ali K. Shakhatreh[1,*], Nadeen M. Alotaiby[1] , Diala Alshiyab[2] , Zaid Shakhatreh[3], Jacob H. Jacob[4], Mo'ath M. Alrjoub[5]

[1] *Department of Medical Laboratory Sciences, Faculty of Applied Medical Sciences, Irbid, Jordan;* [2]*Department of Dermatology, King Abdullah University Hospital, Faculty of Medicine, Jordan University of Science and Technology, Irbid, Jordan;* [3]*Faculty of Medicine, Jordan University of Science and Technology, Irbid, Jordan;* [4]*Department of Biological Sciences, Faculty of Science, Al al-Bayt University, Al-Mafraq, Jordan;* [5] *Department of Pathology and Microbiology, Faculty of Medicine, Jordan University of Science and Technology, Irbid, Jordan*

Received: December 28, 2024; Revised: February 15, 2025; Accepted: March 10, 2025

Abstract

Skin cancer is one of the most common cancers worldwide. While ultraviolet radiation is the main causative agent of skin cancer, there is some evidence that the microbiome, both of the skin and gastrointestinal tract, may negatively or positively influence its development depending on the abundance of certain bacterial species. The influence of administrating three bacterial species on the early development of skin cancer in mouse two-factor skin carcinogenesis model was evaluated in this study. The bacterial species include *Fusobacterium nucleatum*, which is associated with multiple cancers and skin conditions, *Bifidobacterium animalis*, which has beneficial properties as a probiotic, and *Lactobacillus bulgaricus*, one of the main bacteria used in yogurt production. Mice treated with *B. animalis* had mildly decreased signs of early carcinogenesis, while the mice treated with *L. bulgaricus* had a more severe outcome along with a significant change in cancer promoting cytokines in serum. Finally, administration of *F. nucleatum* significantly increased blood IL-10 concentration but did not significantly affect early cancer development in mice in the short term (12 weeks).

Keywords: microbiome, skin cancer, carcinogenesis, mice model.

1. Introduction

The bacteria of the human gut have been known to influence many diseases of the gastrointestinal tract (Glassner *et al*., 2020) and other body systems ((Helmink *et al*., 2019, Cenit *et al*., 2017). One of those effects is their modulation of the body's immune system through antigen presentation and the release of molecules such as cytokines (Wang *et al*., 2021, Polkowska-Pruszyńska *et al*., 2020). One of the biggest factors in skin cancer development and progression is decreased immunity; immunosuppression is associated with more aggressive and invasive cutaneous tumors. UVB radiation has a large immunosuppressive role in exposed skin. It can induce natural killer cells (Moodycliffe *et al*., 2000), T-regulatory cells, keratinocytes, and macrophages, all of which suppress anti-tumor immunity such as cytotoxic T-cells and helper T-cells by the secretion of cytokines such as interleukin-10. Some studies have shown that the oral administration of bacteria can affect the development of skin conditions such as eczema (Kim *et al*., 2010a) and atopic dermatitis (Sheikhi *et al*., 2017, Rusu *et al*., 2019), and protect against UV damage (Guéniche *et al*., 2006).

Some probiotics, which are beneficial bacteria used to enhance health, have shown anti-cancer activities (Kumar *et al*., 2010), mainly through immune modulation (Sao *et al*., 2017) and the release of anti-tumor compounds (Nakatsuji *et al*., 2018). Two of the most commonly used probiotic genera are *Lactobacillus* and *Bifidobacterium* (Sharma *et al*., 2021), which are key bacteria in the healthy gut microbiome (Turroni *et al*., 2014).

Lactobacillus delbrueckii subsp. *bulgaricus* (*L. bulgaricus*) is a Gram-positive pleomorphic bacterium. *L. bulgaricus* and *Streptococcus thermophilus* are the main fermenters responsible for fermenting milk into yogurt. *L. bulgaricus* has been used to treat constipation and other gastrointestinal disorders since the early 20th century. A study found *L. bulgaricus* may be able to modulate immunity in atopic dermatitis (Sheikhi *et al*., 2017). Another study showed that a probiotic mix containing *L. bulgaricus* and *Streptococcus thermophilus* may inhibit tumor growth (Guha *et al*., 2019, Neish 2017).

Bifidobacterium animalis subsp. *lactis* (*B. animalis*) is a Gram-positive anaerobic pleomorphic bacterium that is one of the most commonly used probiotic species. Studies found that healthy individuals tend to have a higher amount of *Bifidobacterium* in their guts than individuals with gastrointestinal diseases (Uusitupa *et al*., 2020). Some

* Corresponding author. e-mail: mkshakhatreh@just.edu.jo.

strains of *B. animalis* have shown several benefits as a probiotic; studies have found that it enhances NK cell and neutrophil function in elderly subjects (Miller *et al*., 2017), improves cholesterol and LDL-C concentration in type 2 diabetics when combined with *L. acidophilus* (Ejtahed *et al*., 2011), and reduces the incidence of atopic dermatitis in infants when given to mothers with *B. bifidum* and *L. acidophilus* during pregnancy and breastfeeding (Kim *et al*., 2010a). *B. animalis* also suppressed NF-κB activity in intestinal epithelial cells and suppressed the development of acute colitis and colitis-associated carcinogenesis (Kim *et al*., 2010b).

Fusobacterium nucleatum is part of the oral flora (Verma *et al*., 2018) and can be found in other microbial environments of the human body, particularly in tumor microenvironments. It is associated with colorectal (Shang and Liu, 2018), oral (McIlvanna *et al*., 2021), and other cancers. There is some evidence it may also act as an oncogenic bacteria in skin cancer (Mrázek *et al*., 2021).

In the current study, we studied the effects of oral administration of *Fusobacterium nucleatum* and the probiotics *Lactobacillus delbrueckii* subsp. *bulgaricus* and *Bifidobacterium animalis* subsp. *lactis* on skin cancer development in an *in vivo* mouse carcinogenesis model.

2. Materials and Methods

2.1. Mouse model

Five groups of female Swiss albino mice were used to examine the effects of orally administered bacteria on skin cancer development *in vivo* (Table3). Experiments included two control groups: no-treatment control (NTC), which was only treated with vehicles to establish the healthy baseline for the mice (n=5), and cancer control (CC) that was not given any bacteria (n=5), *L. bulgaricus* group (n=8), *B. animalis* group (n=8), and *F. nucleatum* group (n=8). Four mice were excluded due to sudden death during the isolation period of the treatment. The final group counts were NTC=5, CC=4, *L. bulgaricus* =8, *B. animalis* =7, and *F. nucleatum* =6. All mice weighed 18 grams and were 10 weeks old at the beginning of the experiment. The dorsal area of the mice was shaved before treatment and once every 2 weeks to ensure direct application of the treatment to the skin.

2.2. Bacterial strains

Three types of bacteria were administered to the mouse subjects: Fusobacterium nucleatum subsp. nucleatum knorr ATCC 23726 (F. nucleatum), Bifidobacterium animalis subsp. lactis ATCC 27536 (B. animalis), and Lactobacillus delbruekii subsp. bulgaricus (L. bulgaricus) strain isolated from a commercially available yogurt mixture of lyophilized L. bulgaricus and Streptococcus thermophilus used in industrial yogurt production. The ATCC strains were revived according to the manufacturer's instructions. The yogurt mixture was revived by suspending the lyophilized powder in skim milk and incubating at 37°C for 2 hours, followed by culturing on blood agar for 24 hours. L. bulgaricus was isolated by subculturing an isolated L. bulgaricus colony.

Bacterial stocks of the strains were preserved at -80 °C, and a fresh subculture was grown from this stock weekly for use in treatment by suspending a loopful of stock in thioglycollate broth and incubating it at 37°C for 24 hours. The bacteria were suspended in normal saline to produce a 0.5 optical density (OD_{600nm}) suspension, approximately equal to 1.5 x 10^8 CFU/ml. Each mouse was given 0.2 ml of the suspension, except the no-treatment and cancer control groups which were given normal saline. The suspension was given via oral gavage using a 20-gauge curved gavage needle twice weekly.

2.3. Cancer induction

Pre-cancerous changes were induced using two-stage carcinogenesis as shown in (Tables 1 and 2, Figure 1). The initiation stage was done once using 50 µg of 7,12-dimethylbenz[a]-anthracene (DMBA; a mutagen that damages DNA) in 200 µL of acetone, and the promotion stage was done twice weekly for 12 weeks using 5 µg of 12-O-tetradecanoyl phorbol-13-acetate (TPA; promotes tumor growth) in 200 µL of acetone (Vähätupa *et al*., 2019). The no treatment control group was only given 200 µL of the vehicle (acetone) at the same time. Physical changes (hair loss and skin texture) were noted and rated using the rating system in (Table 3). The animals were weighed in the last week of treatment following the last dose of TPA and bacteria.

Table 1. Mouse carcinogenesis treatment schedule. DMBA (a carcinogen) was administered once, and TPA (a pro-inflammatory chemical) was administered twice each week.

Week 1	Week 2-13
50 µg DMBA once	5 µg TPA twice weekly

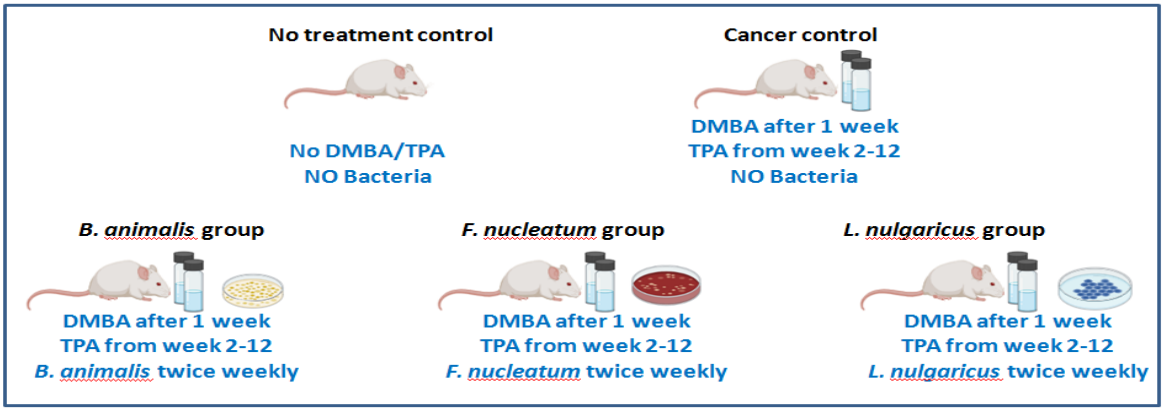

Figure 1. Explanation of the different treatments groups.

Table 2. Mouse treatment groups.

	No treatment control	Cancer control	*B. animalis*	*L. bulgaricus*	*F. nucleatum*
DMBA/TPA treatments	no	yes	yes	Yes	Yes
Bacterial strain administered	none	none	*Bifidobacterium animalis* subsp. *lactis* ATCC 27536	*Lactobacillus delbruekii* subsp. *bulgaricus*	*Fusobacterium nucleatum* subsp. *nucleatum* knorr ATCC 23726

Table 3. Physical grading of mouse skin changes guidelines.

	Degree of hair loss	Skin texture
0	0%	Smooth skin
1	<25%	Isolated areas of changed texture
2	25%-75%	Large areas of changed texture not visibly apparent
3	>75%	Visibly rough skin covering most of the treatment area
Physical score= hair loss score + skin texture score		

2.4. Sample collection and storage

Animals were euthanized a week after the last TPA administration. Blood was collected into silica gel blood tubes with no additives and centrifuged after clot formation. The serum was stored at -80 °C until analysis. The dorsal skin was cut and stored in Bouin's solution then washed with cold phosphate-buffered saline and placed in 70% alcohol at 4 °C until histological analysis.

2.5. Cytokine analysis

As the systemic effects of bacteria are often mediated through immune modulation, the concentrations of interleukin 6 (IL-6), interleukin 10 (IL-10), and tumor necrosis factor-alpha (TNFα) were measured in mouse serum using Mouse IL-6 ELISA Kit (ab222503), Mouse IL-10 ELISA Kit (ab255729), and Mouse TNF alpha ELISA Kit (ab46105) (Abcam PLC, UK) according to the manufacturer's instructions.

2.6. Histology

To examine the microscopic effect the carcinogenesis and bacterial treatment had on mouse skin, mouse tissue was formalin-fixed and embedded in paraffin wax blocks. The tissue was cut using a microtome and placed on slides and the slides were then stained with hematoxylin and eosin. The stained slides were examined by a pathologist for any pathological changes including mast cell numbers, keratinocytes layer thickness, and dysplastic changes.

2.7. Statistical analysis

IBM's SPSS statistics software was used to analyze the results and a P value lower than 0.05 using Mann–Whitney U test was considered significant. Mann-Whitney U test was used as the data was not normally distributed and the medians were calculated using only the positive samples.

3. Results

3.1. Physical changes of mouse groups

To study the *in vivo* effects of orally administered bacteria on skin cancer, five groups of mice were given a two-factor carcinogenesis treatment as well as each group was treated with *F. nucleatum*, one of two probiotics (*L. bulgaricus* or *B. animalis*), or no bacteria. Mice were ranked on a scale of 0-6 for both hair loss and skin texture changes (Figure 2). There was no significant difference in physical score between the bacteria groups and the cancer control group (Figure 3). There were also no significant weight changes between the groups (not shown).

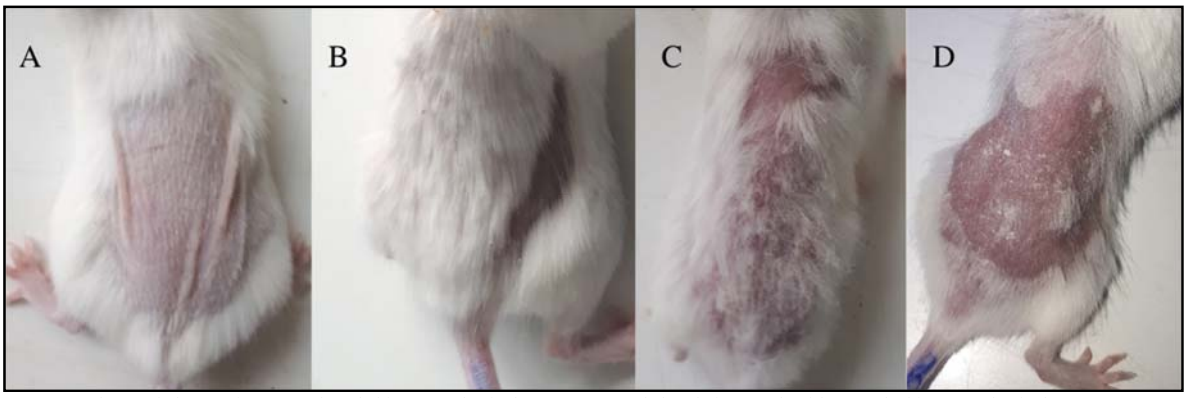

Figure 2. Observed changes in mouse dorsal skin. A: 0 physical score, even and slow hair growth with smooth skin. B: 2 physical score, with slightly irritated skin and a single area of complete hair loss. C: 4 physical score with several areas of hair loss and slightly rough skin. D: 6 physical score, near complete hair loss with rough, irritated skin.

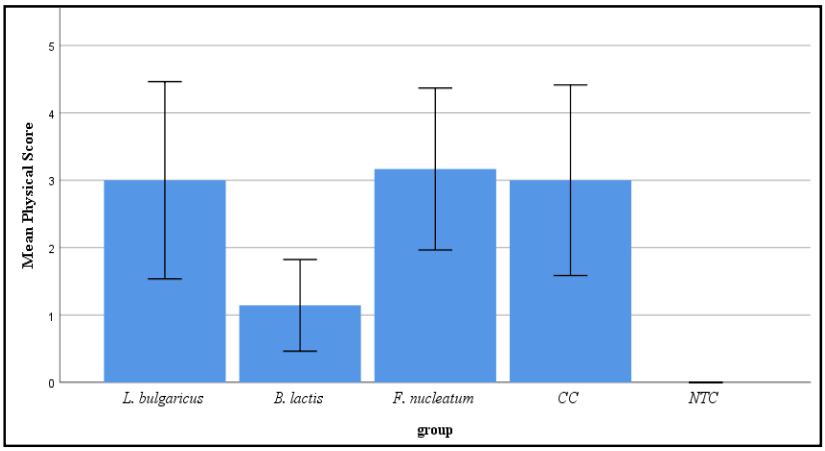

Figure 3. Mean physical score for mice. Mice were given a physical score of 0-6 depending on physical characteristics of treated skin (skin texture and hair loss) and showed no significant difference. Data represents Mean +/- SEM.CC: cancer control group. NTC: no treatment control.

3.2. L. bulgaricus and B. animalis groups had an increase in keratinocyte layer thickness

Following carcinogenesis treatment, mice were sacrificed and skin biopsies were taken from the treated skin and examined microscopically by a pathologist for changes between treatment groups. Keratinocytes layer thickness (as shown in Figure 4) was not significantly different *in L. bulgaricus*, *B. animalis*, or *F. nucleatum* groups in comparison with CC. *L. bulgaricus* and *B. animalis* groups had significantly higher keratinocytes layer thickness than the no treatment control group (p= 0.036, 0.009) (Figure 5).

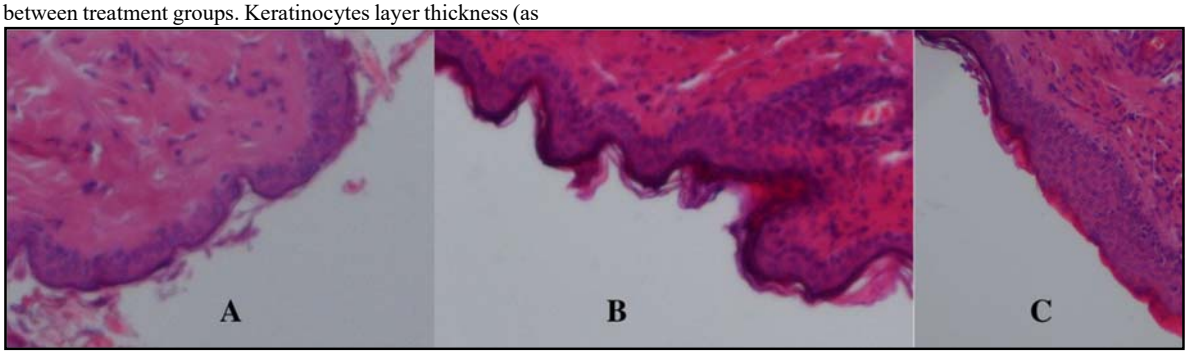

Figure 4. Microscopic examination of mouse skin. Mouse skin biopsies were examined at 100x magnification to determine characteristics such as keratinocyte layer thickness and mast cell invasion. A: 2-3 cell layers. B: 3-4 cell layers. C: focal keratinocytes proliferation.

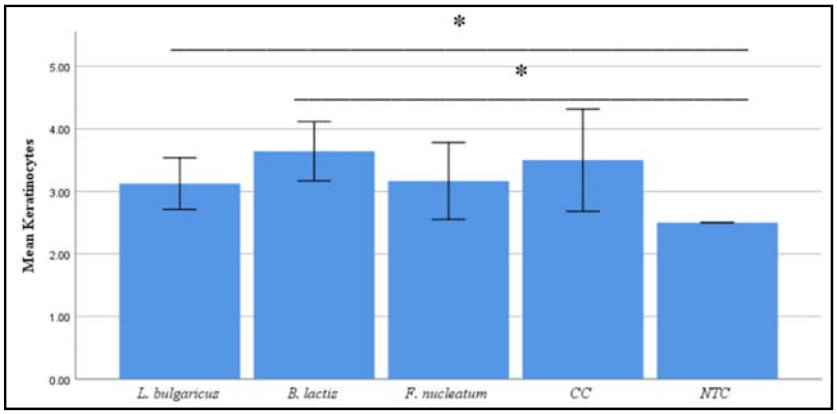

Figure 5. Mean number of keratinocyte layers in mouse skin. Microscopic examination of mouse skin biopsies showed no significant changes between groups given bacteria and the cancer control group. Data represents Mean +/- SEM. CC: cancer control group. NTC: no treatment control. *: p <0.05.

3.3. Mice treated with L. bulgaricus had more severe signs of dysplasia

Microscopic examination of mouse skin biopsies showed that, as detailed in (Table 4), mice treated with *B. animalis* had fewer focal papillomas than other groups. The *L. bulgaricus* group had the highest amount of mast cell invasion. One cancer control and two *L. bulgaricus* treated animals developed dysplasia.

Table 4: Mice subjects' results for the presence of focal apilloma, mast invasion, and dysplasia.

Subject	Focal papilloma	Degree of mast cell invasion	Dysplastic changes
NTC1	-	NONE	-
NTC2	-	RARE	-
NTC3	-	NONE	-
NTC4	-	RARE	-
NTC5	-	NONE	-
CC1	+	MILD	-
CC2	+	MILD	-
CC3	+	MILD	+
CC4	+	MILD	-
L1	+	MODERATE	+
L2	+	MILD	-
L3	-	MILD	-
L4	+	MODERATE	+
L5	+	MODERATE	-
L6	+	MODERATE	-
L7	+	MILD	-
L8	+	MILD	-
B1	-	MILD	-
B2	-	RARE	-
B3	-	MILD	-
B4	-	MILD	-
B5	-	MILD	-
B6	+	MILD	-
B7	+	MILD	-
F1	-	MILD	-
F2	-	MILD	-
F3	+	MILD	-
F4	+	MILD	-
F5	+	MILD	-
F6	+	MILD	-

NTC: no treatment control group, CC: cancer control group, L: *L. bulgaricus* group, B: *B. animalis* group, F: *F. nucleatum* gro

3.4. Mice treated with L. bulgaricus had significantly changed cytokine levels

Cancer-associated cytokines were examined by ELISA to study the systemic effects the bacterial treatment had on the mouse subjects. As shown in (Figure 6), the *F. nucleatum* group had significantly higher IL-10 serum levels than CC (p= 0.033) and no treatment control (p=0.008). The *L. bulgaricus* group had significantly higher IL-10 levels than no treatment control (p=0.026), significantly higher IL-6 levels (p= 0.017), and significantly lower TNFα levels (p=0.027) than cancer control.

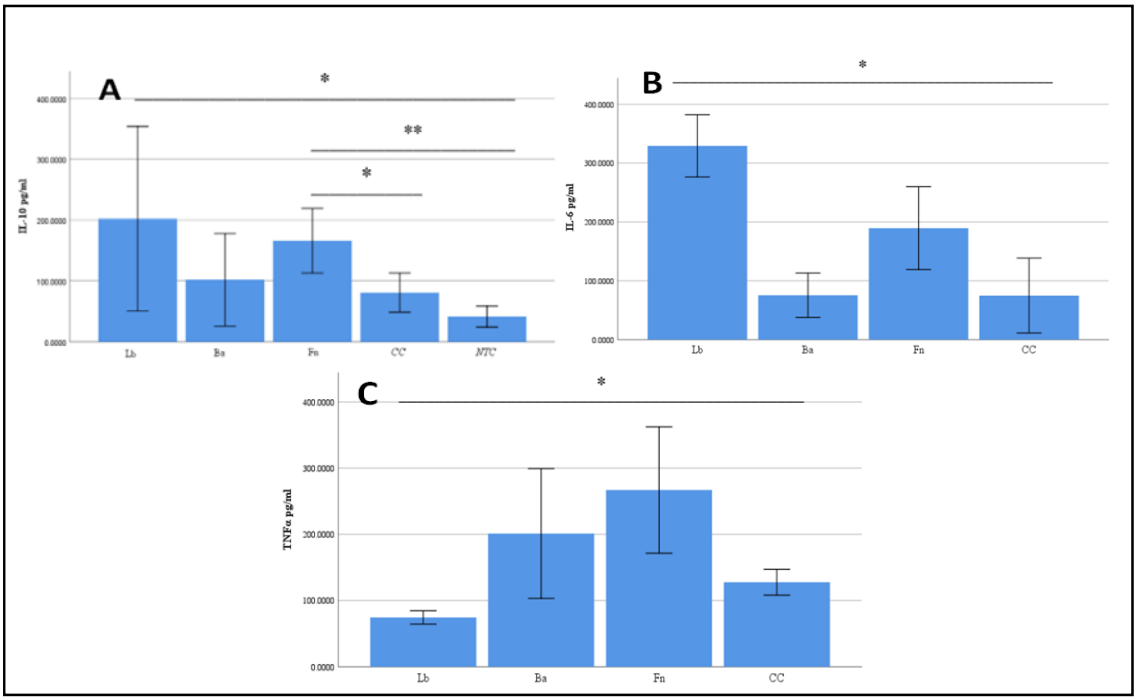

Figure 6. ELISA results for IL-10 (A) , IL-6 (B) , and TNFα (C). Cancer-associated cytokines were examined in mouse subjects' serum to determine the systemic effects of the bacteria administered. Data represents Mean +/- SEM. Lb*: L. bulgaricus* group. Ba: *B. animalis* group. Fn: *F. nucleatum* group. CC: cancer control group. NTC: no treatment control group. *: $p < 0.05$. **: $p < 0.01$.

4. Discussion

In the current study, mice were divided into 5 groups: the first is the No Treatment Control, which was only treated with vehicle (acetone) and no carcinogens or bacteria. This group was used to establish the healthy characteristics of the mice and determine if the changes observed were pathological or physiological. The second group was the Cancer Control (CC), where the cancer was induced but no bacteria were given. CC was used as a baseline to determine how carcinogenesis affected the mice. The 3 groups of interest were the ones treated with *F. nucleatum*, *B. animalis*, and *L. bulgaricus*. We focused on the effects the bacteria had on cancer initiation and not progression, and as such no macroscopic tumors were observed. Regarding the ELISA studies, the *F. nucleatum* group did not show significant changes from the CC group except for IL-10 levels in mouse serum. IL-10 is an anti-inflammatory cytokine that inhibits the activity of anti-tumor immunity.

It is possible in the long term that systematic effects of *F. nucleatum* would aid the progression of skin cancer. However, we observed no meaningful influence on initiation. Both probiotic groups, *B. animalis* and *L. bulgaricus*, had significantly higher non-papilloma keratinocytes thickness compared to the no treatment control group. Other probiotics, *L. rhamnosus* GG and *L. reuteri*, have been shown to stimulate keratinocyte proliferation in a wound-healing model (Mohammedsaeed *et al*., 2015). This suggests a possible beneficial effect for *B. animalis* and *L. bulgaricus* in wound healing. While *B. animalis* did not significantly change the levels of the 3 cytokines studied, it inhibited cancer initiation. This was evident on a microscopic scale with the *B. animalis* treated group showing much less mast cell invasion than other bacteria-treated groups. Furthermore, only 2 of the 7 mice in the *B. animalis* treated group developed papillomas which was less than that of the other bacteria-treated groups. A different strain of *B. animalis* was shown to inhibit NF-κB activity in intestinal epithelial cells (Kim *et al*., 2010b). This inhibition may be associated with cancer initiation.

Interestingly, the *L. bulgaricus* group had the worst outcome of all groups, with 2 mice showing dysplastic changes and a higher degree of mast cell invasion, as well significantly higher IL-6 levels and significantly lower TNFα serum levels. This result is consistent with a study of the effects of an *S. thermophilus* and *L. bulgaricus* yogurt culture on dextran sodium sulfate (DSS)-induced colitis. In this study, they observed that the culture increased IL-6 in the spleen. There was also an increase in T-regulatory cells in mesenchymal lymph nodes and peripheral blood in the yogurt culture treatment group (Wasilewska *et al*., 2019). As cancer prevention includes measures that can decrease the threat of developing cancer (Khabour *et al*., 2023), *L. bulgaricus* was proposed to be beneficial to the hosts with colitis and other diseases (Mahasneh *et al*., 2015). However, it was found in our study that later species may promote skin carcinogenesis.

5. Conclusions

Mice treated with *B. animalis* had mildly decreased signs of early carcinogenesis, while the mice treated with *L. bulgaricus* had a more severe outcome along with a significant change in cancer-promoting cytokines in serum. Administration of *F. nucleatum* significantly increased blood IL-10 concentration but did not show any significant effect on early cancer development in mice in the short term. However, we recommend exploring of the use of such probiotic bacteria in the presence of cancer-treatment drugs to evaluate their effect on cancer therapy.

References:

Cenit MC, Sanz Y, and Codoñer-Franch P. 2017. Influence of gut microbiota on neuropsychiatric disorders. *World J Gastroenterol.*, **23(30):** 5486–98.

Ejtahed HS, Mohtadi-Nia J, Homayouni-Rad A, Niafar M, Asghari-Jafarabadi M, and Mofid V. 2011. Effect of probiotic yogurt containing *Lactobacillus acidophilus* and Bifidobacterium lactis on lipid profile in individuals with type 2 diabetes mellitus. *J Dairy Sci*., **94(7):** 3288–94.

Glassner KL, Abraham BP, and Quigley EMM. 2020. The microbiome and inflammatory bowel disease. *J Allergy Clin Immunol*., **145(1)**:16–27.

Guéniche A, Benyacoub J, Buetler TM, Smola H, and Blum S. 2006. Supplementation with oral probiotic bacteria maintains cutaneous immune homeostasis after UV exposure. *Eur J Dermatol*., **16(5):** 511–7.

Guha D, Banerjee A, Mukherjee R, Pradhan B, Peneva M, and Aleksandrov G. 2019. A probiotic formulation containing *Lactobacillus bulgaricus* DWT1 inhibits tumor growth by activating pro-inflammatory responses in macrophages. *J Funct Foods*., **56:**232–45.

Helmink BA, Khan MAW, Hermann A, Gopalakrishnan V, and Wargo JA. 2019. The microbiome, cancer, and cancer therapy. *Nat Med*., **25(3):** 377–88.

Khabour O, Alzoubi K, Alkofahi A, and Al-Awad R. 2023. Skin-Cancer Protective Effect of Ziziphus Spina-christi Leaf Extract: In vitro and in Vivo Models. *Jordan J Biol Sci*., **16(2)**: 243 – 248.

Kim JY, Kwon JH, Ahn SH, Lee S Il, Han YS, and Choi YO. 2010a. Effect of probiotic mix (Bifidobacterium bifidum, Bifidobacterium lactis, Lactobacillus acidophilus) in the primary prevention of eczema: A double-blind, randomized, placebo-controlled trial. *Pediatr Allergy Immunol*., **21**(2 PART 2).

Kim SW, Kim HM, Yang KM, Kim SA, Kim SK, and An MJ. 2010b. Bifidobacterium lactis inhibits NF-κB in intestinal epithelial cells and prevents acute colitis and colitis-associated colon cancer in mice. *Inflamm Bowel Dis*., **16(9):** 1514–25.

Kumar M, Kumar A, Nagpal R, Mohania D, Behare P, and Verma V. 2010. Cancer-preventing attributes of probiotics: An update. *Int J Food Sci Nutr*., **61(5):** 473–96.

Mahasneh A, Hamdan S, and Mahasneh S. 2015. Probiotic Properties of *Lactobacillus* Species Isolated from Local Traditional Fermented Products. *Jordan J Biol Sci*., **8(2)**: 81- 87.

Miller LE, Lehtoranta L, and Lehtinen MJ. 2017. The effect of bifidobacterium animalis ssp. lactis HN019 on cellular immune function in healthy elderly subjects: Systematic review and meta-analysis. *Nutrients*., **9(3)**.

Mohammedsaeed W, Cruickshank S, McBain AJ, and O'Neill CA. 2015. *Lactobacillus rhamnosus* GG Lysate Increases Re-Epithelialization of Keratinocyte Scratch Assays by Promoting Migration. *Sci Rep.*, **5**:1–11.

Moodycliffe AM, Nghiem D, Clydesdale G, and Ullrich SE. 2000. Immune suppression and skin cancer development: Regulation by NKT cells. *Nat Immunol*., **1(6)**:521–5.

Mrázek J, Mekadim C, Kučerová P, Švejstil R, Salmonová H, and Vlasáková J. 2018. Melanoma-related changes in skin microbiome. *Folia Microbiol (Praha)*., **64(3):** 435–42.

Nakatsuji T, Chen TH, Butcher AM, Trzoss LL, Nam SJ, and Shirakawa KT. 2018. A commensal strain of *Staphylococcus epidermidis* protects against skin neoplasia. *Sci Adv.*, **4(2)**.

Neish AS. 2017. Probiotics of the Acidophilus Group: *Lactobacillus acidophilus*, delbrueckii subsp. bulgaricus and johnsonii. The Microbiota in Gastrointestinal Pathophysiology. Elsevier Inc.

Polkowska-Pruszyńska B, Gerkowicz A, and Krasowska D. 2020. The gut microbiome alterations in allergic and inflammatory skin diseases – an update. *J Eur Acad Dermatology Venereol.*, **34(3):** 455–64.

Rusu E, Enache G, Cursaru R, Alexescu A, Radu R, and Onila O. 2019. Prebiotics and probiotics in atopic dermatitis (Review). *Exp Ther Med*., **2019:** 926–31.

Shang FM and Liu HL. 2018. Fusobacterium nucleatum and colorectal cancer: A review. *World J Gastrointest Oncol*., **10(3):** 71–81.

Sharma M, Wasan A, and Sharma RK. 2021. Recent developments in probiotics: An emphasis on Bifidobacterium. *Food Biosci*., **41(February):**100993.

Sheikhi A, Giti H, Heibor MR, Jafarzadeh A, Shakerian M, and Baharifar N. *Lactobacilus Delbrueckii* subsp. 2017. Bulgaricus Modulates the Secretion of Th1/Th2 and Treg Cell-Related Cytokines by PBMCs from Patients with Atopic Dermatitis. *Drug Res* (Stuttg)., **67(12):** 724–9.

Soa SSY, Wana MLY, and El-Nezami H. 2017. Probiotics-mediated suppression of cancer. *Curr Opin Oncol.*, **29(1):** 62–72.

Turroni F, Ventura M, Buttó LF, Duranti S, O'Toole PW, and Motherway MOC. 2014. Molecular dialogue between the human gut microbiota and the host: A Lactobacillus and Bifidobacterium perspective. *Cell Mol Life Sci*., **71(2):**183–203.

Uusitupa HM, Rasinkangas P, Lehtinen MJ, Mäkelä SM, Airaksinen K, Anglenius H, Ouwehand AC, and Maukonen J. 2020. Bifidobacterium animalis subsp. lactis 420 for Metabolic Health: Review of the Research. *Nutrients*., **12(4):**892.

Vähätupa M, Pemmari T, Junttila I, Pesu M, and Järvinen T.A. 2019. Chemical-Induced Skin Carcinogenesis Model Using Dimethylbenz[a]Anthracene and 12-O-Tetradecanoyl Phorbol-13-Acetate (DMBA-TPA). *J. Vis. Exp.*, **154**: e60445, doi:10.3791/60445.

Verma D, Garg PK, and Dubey AK. 2018. Insights into the human oral microbiome. *Arch Microbiol*., **200(4):** 525–40.

Wang Z, Zhong J, Meng X, Gao J, Li H, and Sun J. 2021. The gut microbiome-immune axis as a target for nutrition-mediated modulation of food allergy. *Trends Food Sci Technol*., **114**:116–32.

Wasilewska E, Zlotkowska D, and Wroblewska B. 2019. Yogurt starter cultures of *Streptococcus thermophilus* and *Lactobacillus bulgaricus* ameliorate symptoms and modulate the immune response in a mouse model of dextran sulfate sodium-induced colitis. *J Dairy Sci*., **102(1)**: 37–53.

JJBS

Volume 18, Number 3,September 2025
ISSN 1995-6673
Pages 487 – 502

Jordan Journal of Biological Sciences

Bio-Fertilizers and Bacterial Bio-Control for Root-Knot Nematode Management and Tomato Yield Enhancement

Sameh M. El-Sawy[1] . Wafaa M.A. El-Nagdi[2] . Shereen A. H. Mohamed[3,*] . Bigad E. Khalil[3] · Gaziea M. Soliman[2]

[1]*Vegetable Research Department, National Research Centre, Dokki 12622, Egypt;* [2]*Department of Plant Pathology, Nematology Unit, National Research Centre, Dokki 12622, Egypt;* [3]*Microbial Genetics Department, National Research Centre, Dokki, 12622, Egypt*

Received: August 24, 2024; Revised: March 16, 2025; Accepted: March 25, 2025

Abstract

Agriculture faces growing population pressure for food security and sustainability. Controlling root-knot nematodes and reducing fertilizer use is crucial for environmental resources preservation. In Egypt, tomato production faces pollution and human health risks by using chemical nematicides for control nematode, so rhizobacteria can be used for controlling parasitic nematodes and bio-fertilization for reduce chemical fertilizers. This experiment was established to study the role of modified bacterial to control *Meloidogyne incognita* and improve using nitrogen fertilizer to increase tomato crop productivity. The tomatoes were cultivated in a greenhouse, 100 ml of different bacterial strains (fusant (F7), *Bacillus thuringiensis* (Bt), *Bacillus cereus* (Bc), and *Achromobacter xylosoxidans* (Ax)) were compared to a chemical nematicide (Oxamyl) applied as foliar spraying and as soil drenching at two doses after 3 and 30 days from the transplanting, where, using two levels of nitrogen fertilization (250 and 500 N/ha). Results showed that all treatments effectively reduced root-knot nematode reproduction, with F7 being more effective in reducing nematode all parameters like J2, galls, and egg masses. Soil drench achieved the best reduction compared to spraying foliage. Our result, the detection and amplification of the alkaline serine protease gene, which has the ability to improve nematode control for F7, and their parental strains (Bc and Bt), produced 1100 base pair fragments. Results clearly reported that bio-fertilizer treatments significantly improved all vegetative growth. The nitrogen treatments had improvements in yield parameters and tomato fruit quality characteristics grown under deficit nitrogen treatment. Tomato plants that received the minimum quantity of nitrogen fertilizers (250 N/ha) and were treated by F7 as a soil drench produced the highest vegetative growth, flowering, fruit yield, and fruit quality. Where, harmony yield parameters and tomato fruit quality characteristics are compared with SDS-PAGE protein banding patterns for eleven treatments leaf tomato plant treatment varieties for leaf water-soluble proteins. The plant exposed to F7 as a soil drench showed the highest number of bands (17 bands) in comparison to the lesser number of bands in the control when applied the minimum quantity of nitrogen fertilizers.

Keywords: Tomato plant, Root-knot nematode -Bio-control, Bacterial strains, Fusant F7, Deficit nitrogen, Bio-fertilizer.

1. Introduction

An increasing population is placing pressure on agriculture to provide food security. The search for natural and safe alternatives for controlling root-knot nematodes that attack crops and reduce fertilizer use is a necessity for preserving environmental resources and ensuring their sustainability. The tomato, or *Solanum lycopersicum* L., is one of the most significant vegetable crops and a favorite vegetable in Egypt, especially for local consumption and export, according to the Food and Agriculture Organization (FAO 2018; Godfray *et al.*, 2010).

To increase agricultural production, it must control the diseases and pests that reduce crop output and use chemical fertilizers as a crucial source of plant nourishment. Due to this, farmers began to believe that expanding their usage of chemical nematicides and fertilizers would result in higher crop yields, and this is regarded as an excess expense on agricultural inputs and a source of increased pollution and hazard to humans.

One of the most serious pests affecting tomato production and other vegetable crops is root-knot nematodes. *M. incognita* is one of the world's most destructive agricultural pests and one of the most economically significant nematode species (Sasanelli *et al.*, 2018). Chemical nematicides have detrimental effects on human health and the environment (Mohamed *et al*., 2021a; Mohammad *et al.*, 2022). This negative effect pushes the search for non-chemical alternatives to chemical nematicides that are more effective, eco-friendly, and safe (Forghani *et al.*, 2020; Mohammad *et al.*, 2022).

New production tools for controlling plant pathogens and improving plant growth are needed to advance sustainable agriculture practices. Many Plant Growth-Promoting Rhizobacteria (PGPRs), such as *Bacillus* spp., constitute an environmentally acceptable method of enhancing crop productivity. They have the potential to stimulate and enhance crop output through

* Corresponding author. e-mail: shereen_asba@yahoo.com.

biocontrol of plant parasitic nematodes and biofertilization for plants (Borriss 2011; Ramezani *et al.,* 2014; Yao *et al.,* 2006). Many bacteria, such as *Bacillus* spp., can boost plant growth and yield while reducing the need for chemical fertilizers by fixing nitrogen (Al-Hawamdeh *et al*., 2024; Mohamed *et al*., 2021b; Sivasakthi *et al.,* 2014).

In agricultural production, bio-fertilizers have several advantages, including the replacement of chemicals nitrogen (N) and phosphorus (P), stimulation of plant growth through increased root formation, raising plant dry matter and plant biomass, carotenoids, chlorophyll, and antioxidant enzymes (İİlbaş 2009).

Protoplast fusion is regarded as a crucial tool for genetic recombination. By combining genes from different microorganisms to create strains with desired characteristics, the improved strains are used to increase the efficiency of plant nematode control and reduce chemical fertilizer use (Mohamed *et al.,* 2021; Soliman *et al.,* 2020). Mohamed *et al.* (2021) found that protoplast fusion of *B. cereus* (Bc) and *B. thuringiensis* (Bt) produced ten stable bacterial fusants with stronger nematicidal activity than parental strains. In vitro, bacterial F7 achieved the highest juvenile mortality (J2) of 98.3%. F7 showed the greatest reduction in the galls and egg masses by 77.18 and 72.35%, respectively, in vivo. Also, in pot trials, F7 had the largest significant increase in eggplant parameters. F7 was found to be more capable of fixing atmospheric nitrogen than its bacterial parents. Soliman *et al*. (2023) found that Mutant No. 1 of *B. cereus*, developed through UV-induced mutation, significantly increased the mortality rate of *M. incognita* juveniles. This mutant had the strongest impact in reducing nematode infection and promoting tomato plant growth. These results align with the observation that plants treated with Mutant No. 1 showed the highest number of protein bands in soluble-protein electrophoretic

patterns, both at the end of the application and one month later. Geng *et al*. (2016) discovered that the serine protease produced by *B. firmus* is a novel biocontrol agent against root-knot nematodes. This enzyme was shown to degrade multiple intestinal and cuticle-associated proteins, effectively breaking down the nematode's physical defenses and contributing to its control.

This study aimed to replace chemical fertilizers, which pose risks to human health and the environment, with more effective, eco-friendly, and safe bio-fertilizers. Additionally, it explored the potential of bio-control strategies against *M. incognita*, focusing on bacterial strains carrying the alkaline serine protease gene, known for inducing plant resistance. The study also examined the impact of bio-fertilizers on tomato leaf protein profiles using SDS-Protein Electrophoresis, highlighting their influence on plant growth and yield. These findings will enhance our understanding of the mechanisms by which bacteria combat plant-parasitic nematodes.

2. Materials and Methods

2.1. Bacterial strain source and growth conditions

The bacterial bio-agents *B. thuringiensis* subsp *tenebrionis* (Bt) strain (El-Kawokgy *et al*., 2004), *B. cereus* NRC12 (Bc) under accession number MW548408 in the GeneBank (USA), F7 fusant between Bc:Bt were obtained from previous studies (Mohamed *et al*., 2021) and *Achromobacter xylosoxidans* under accession number LC214968.1 obtained from (Soliman *et al*., 2019). Luria-Bertani (LB) medium (Sigma-Aldrich company) was used to cultivate different bacterial strains (Davis *et al.,* 1980).

2.2. PCR amplification of protease genes

Primers were developed utilizing the protein sequence of a serine protease found in the Uniprot database (https://www.uniprot.org/uniprotkb/A0A316Y3T2/entry) and the gene sequence corresponding to the alkaline serine protease, which was imported into GenBank under the entry PWN77930.1 (https://www.ncbi.nlm.nih.gov/protein/PWN77930.1). The design of the primers was conducted using Primer3 Plus software (https://www.bioinformatics.nl/cgibin/primer3plus/primer3plus.cgi). The forward primer, F, possesses the nucleotide sequence 5'-CATAAAGTTAATATTGTTCTGATGTCACTG -3'. The reverse primer, R, consists of the nucleotide sequence 5'-ATATGAAATTGTATTGCCATCTTTATAGC -3 .'

To initiate the experiment, a single colony of *B. cereus* strain NRC12 was cultivated in LB broth media at 37 °C with 180 rpm shaking for 18 hours using a shaking incubator (Thermoscientific, USA). Genomic DNA was isolated using the GeneJET Genomic DNA Purification Kit (Thermoscientific, USA) following the manufacturer's instructions.

2.3. PCR amplification and agrose gel electrophoresis

For PCR-based amplification of the alkaline serine protease gene, a DNA thermal cycler (Perkin Elmer GeneAmp PCR System 9600, Waltham, MA, USA), was employed according to the provided protocol. The PCR reaction was set up using a 25 µL reaction mixture containing 1X Taq buffer (with $MgCl_2$), 0.2 mM dNTPs, 0.5 µM of each primer, 1.25 U Taq DNA polymerase (Thermo Fisher Scientific, USA), and 50 ng of template DNA, following the standard PCR protocol. The annealing temperature used for the PCR reaction was set at 62 °C, based on the calculated melting temperature (Tm) of the primer pairs using the nearest-neighbor thermodynamic model. For agarose gel electrophoresis, a 1.5% (w/v) agarose gel was prepared in 1X TAE buffer, and electrophoresis was carried out at 100V for 45 minutes. The PCR products were visualized under UV light after staining with ethidium bromide/sybr safe.

GenBank submission

The alkaline protease sequences were submitted to GenBank under the accession number OR030044 https://www.ncbi.nlm.nih.gov/nuccore/OR030044.1/

2.4. Multiple sequence alignment and phylogenetic analysis

Molecular Evolutionary Genetics Analysis (MEGA) software version MEGA 11 was used for multiple sequence alignment analysis. ClustalW was employed for sequence alignment with default gap opening and extension penalties. A neighbor-joining (NJ) phylogenetic tree was constructed using the p-distance model with pairwise deletion for gaps/missing data. The statistical reliability of the phylogenetic tree was assessed using a bootstrap analysis with 100 replicates (Mahmoud *et al.,*

2021). The tree was midpoint-rooted, and branch lengths were measured in the number of substitutions per site.

2.5. Field experiment

Site description

A field experiment was conducted during the winter season on the 1st of October 2020 in the National Research Centre farm, El-Noubaria region, Beheira Governorate, north of Egypt. The experimental site was located at latitude: 30°15"N, longitude: 30°47"E (Figure 1). The experimental soil was analyzed to test the physical and chemical properties. The soil texture was 90.5% sand, 6.22% clay and 3.28% silt; the soil pH and EC were 7.95 and 2.18 dS m^{-1} respectively. The soluble cations in the soil (Ca^{++}, Mg^{++}, Na^{+} and K^{+}) were 6.02, 3.97, 9.44 and 2.37 mmol L^{-1}, respectively. The soil soluble anions (CO_3^{--}, HCO_3^{-}, Cl^{-} and SO_4^{--}) were 0, 0.64, 12.9 and 8.26 mmol L^{-1}, respectively (Sims, 1996).

Figure 1. Experimental site (Google map, Satellite) at which the field experiment was conducted

Tomato seeds (*S. lycopersicum* Mill. cv. CH7) were transplanted into a greenhouse with sandy soil in the October 1st 2020. A 10.5 m^2 (3 x 3.5m) plot with five rows was used in this experiment. Tomato seedlings were cultivated 0.5 m apart on one side of the irrigation line (21 plants per plot). Two doses of all treatments were applied after 3 and 30 days from the transplant date. One hundred milliliter of bacteria was applied as foliar spraying and as soil drenching around the plant root (10^{9} CFU/ml). According to Ali and El-Ashry's (2021), vydate was used at the recommended rates of 0.2 ml/plant and 12.5 kg/fed in Egypt. Horticulture techniques for growing tomato plants and the fertilizers were applied according to the Egyptian Ministry of Agriculture and Land Reclamation (150 units of P_2O_5 and 200 units of K_2O/ha), while nitrogen fertilizer was given in accordance with the experimental treatments.

2.6. Experimental treatments

Tomato seedlings (35 days of age) were exposed to foliar spraying and soil drench of bacterial suspension treatments, for controlling nematode diseases and improving tomato growth and productivity. In this study, the experiment included two fertilization groups (250 and 500 N/hectare), each group contained two sub-groups of bacterial suspension addition, whether (foliar spraying or soil drenching). Each sub-group underwent six treatments

Fusant (F7), *Bacillus thuringiensis* (Bt), *Bacillus cereus* (Bc), *Achromobacter xylosoxidans* (Ax), xamyl as a chemical nematicide marketed as "Vydate", and a control).

All nitrogen treatments (and other mentioned fertilizers P and K) were applied with a drip irrigation system during the season, while bacteria treatments were applied as foliar spraying and soil drenching at two times (after two days and one month of cultivation date). Nitrogen fertilizer was applied in the form of ammonium nitrate (NH_4NO_3) (33.5 N).

2.7. Measurements and Data analysis

After 65 days from cultivation (flowering stage), three tomato plants were randomly selected from each plot to assess the following characteristics: plant height (cm), number of branches and leaves, fresh and dry leaf weight (g), flowering and fruit yield, and the number of clusters per plant.

Tomato yield was evaluated by harvesting fully red-ripe fruits over five collection periods, beginning three months after planting. The total marketable yield, fruit count, fruit yield per plant (g), and overall fruit yield (tons/ha) were recorded.

For fruit quality analysis, tomato samples were randomly selected from each experimental plot during the middle of the harvest period. Measurements included average fruit weight (g), fruit diameter (cm), and total soluble solids (TSS), determined using a hand refractometer (Atago, U.S.A.).

2.8. Determination of nitrogen, phosphorus, and potassium percentages in tomato leaves:

The percentage of nitrogen was determined using the Kjeldahl method (A.O.A.C., 1990). Phosphorus content was assessed colorimetrically using the NH4-Metavanadate method, as described by Motsara and Roy (2008). Potassium percentage was measured using a flame photometer, following A.O.A.C. (1990) guidelines. Additionally, soil-accessible nitrogen (mg/kg) was analyzed according to the method outlined by Wolf and Beegle (2011).

2.9. SDS-Protein Electrophoresis

To evaluate the induction of systemic resistance (ISR) in tomatoes against nematode infection and assess the role of nitrogen fixation in improving plant yields, 1 g of tomato leaf samples from different treatments (at a rate of 250 N/ha) was used for protein analysis. Protein profiling was conducted using sodium dodecyl sulfate-polyacrylamide gel electrophoresis (SDS-PAGE), following the method of Laemmli (1970). Sample preparation and water-soluble protein extraction were performed according to Stegmann (1979). Gel images were captured and analyzed using Gel-Pro Analyzer V.3 with the Gel Doc Bio-Rad System.

2.10. Cluster analysis to protein profiles of treated plants using NTSYS methods

The SDS-PAGE results were compiled and encoded in binary form for analysis. The data were then processed using the NTSYSpc v2.10e statistical software. Statistical analysis was performed following the method of El-Kawokgy *et al.* (2015), with a 5% probability level used to determine the least significant difference (LSD) values.

2.11. Initial soil sample collection

Soil samples were randomly collected from the experimental plots to determine the initial population of second-stage juveniles (J2s). One week before planting,

five sub-samples were taken from each plot at a depth of 15–30 cm. These sub-samples were thoroughly mixed, and a 250 g aliquot of the composite soil sample was used for nematode extraction. The nematodes were identified as *Meloidogyne incognita* based on the perennial pattern morphology of mature females in tomato roots, observed under a light microscope (Eisenback, 1985).

To assess nematode damage, J2s were extracted from 250 g of soil using the sieving and Baermann technique (Barker, 1985). The extracted juveniles were then counted using a Hawksley slide under a light microscope, and the J2 population in soil was calculated according to Puntener (1981).

For root analysis, tomato root systems were gently washed with tap water. The reduction percentages in root galls and egg masses (5 g of root sample) were calculated and indexed on a 1–10 scale, following the method of Sharma *et al*. (1994).

2.12. Experimental design and statistical analysis

The experiment was conducted with three replicates using a split-plot design. The major plots received nitrogen treatments, while the sub-plots were subjected to bacteria treatments. A total of 24 treatments were included in each replicate. All data collected were directly analyzed using the Mstatic (M.S.) software, and analysis of variance (ANOVA) was performed. Significant differences between means were determined using Duncan's Multiple Range Test (DMRT) at the $P < 0.05$ level. The comparison between means of different treatments was based on the methodology described by Snedecor and Cochran (1982). Means followed by the same alphabetical letter were considered not statistically different at the 5% significance level according to Duncan (1955).

3. Results

The *alkaline protease* gene ASP16 from strains Bc and Bt, as well as its F7, were utilized for the amplification process. The amplification resulted in fragments with a length of 1100 base pairs, which were visualized on an agarose gel (Figure 2).

The resulting amino acid sequence of the alkaline protease gene comprised 359 amino acids. Further analysis using BLASTp and phylogenetic methods revealed a strong association between our alkaline protease ASP16 and the S8 family peptidases of *B. cereus* (Figure 3).

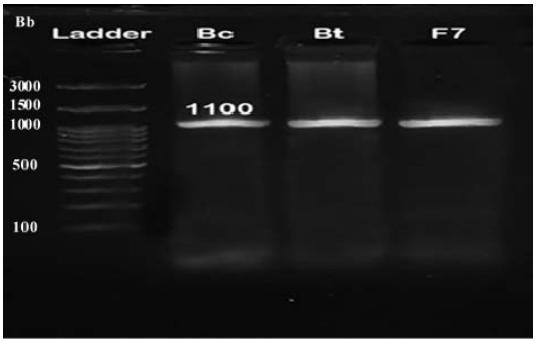

Figure 2. Agarose gel of the amplified protease gene. Line 1, DNA ladder (GeneRuler100 Bp, Thermo Fisher Scientific Inc., US), line 2,3 and 4 1100 bp band of the protease gene in Bc, Bt and F7 respectively.

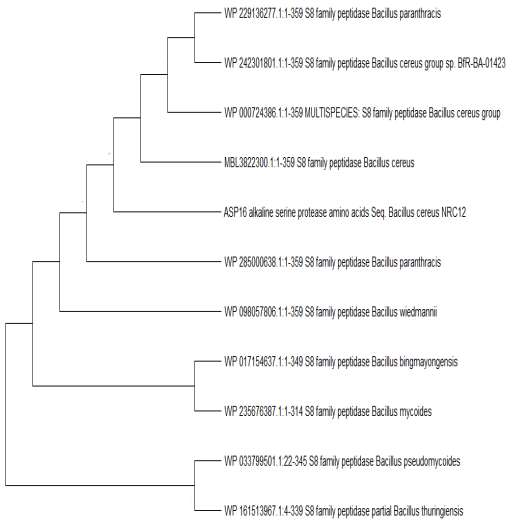

Figure 3. Neighbor-Joining phylogenetic analysis of ASP16 alkaline protease and those of *Bacillus*.

3.1. Protein band expression in tomato leaves following foliar spray and soil drench treatments

According to the results of SDS-PAGE protein banding patterns for leaf water-soluble proteins from eleven tomato plant treatment varieties (Table 1), the majority of the extracted proteins migrated in the range from 24 to 191 kDa, with 18 bands; seven of these bands were monomorphic at M.W. 134, 110, 98, 74, 60, 47, and 37 kDa, while eleven of the bands were polymorphic.

Overall, the soil drench treatment resulted in the highest number of protein bands across all treatments, compared to both the foliar spray and the control. For instance, the control plants expressed 7 bands, while plants treated with F7 via foliar spray and soil drench expressed up to 17 bands. The number of protein bands in tomato plants ranged from a low of 8 bands in the control to a high of 18 bands in plants treated with F7. The protein bands were ranked as follows, from highest to lowest: soil drench treatments produced 12 bands in Bt and Bc, 15 bands in Bt, 11 bands in Bc and Ax, and 10 bands in Oxamyl, while foliar spray treatments resulted in 10 bands in Ax and Oxamyl.

Table 1. The electrophoretic water-soluble protein patterns for tomato plant leaves when spraying foliage and drenching the soil

No	MW	Spraying foliage					Soil drench					
	KD	F7	Bt	Bc	Ax	Oxamyl	F7	Bt	Bc	Ax	Oxamyl	Control
1	191	+	-	-	-	-	+	-	-	-	-	-
2	170	+	+	+	+	+	+	+	+	+	+	-
3	152	+	-	+	-	-	+	+	-	+	-	-
4	134	+	+	+	+	+	+	+	+	+	+	+
5	124	+	-	-	-	-	+	-	-	-	-	-

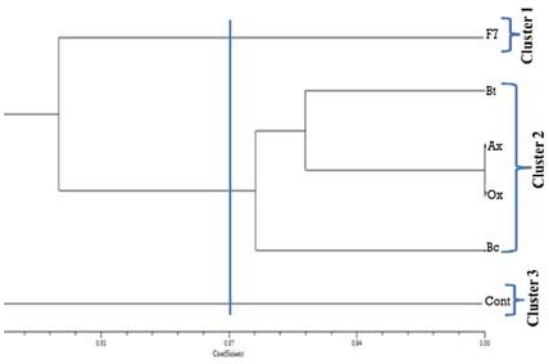

6	110	+	+	+	+	+		+	+	+	+	+	+
7	98	+	+	+	+	+		+	+	+	+	+	+
8	80	+	+	+	+	+		+	+	+	+	+	-
9	74	+	+	+	+	+		+	+	+	+	+	+
10	68	+	+	-	-	-		+	+	-	-	-	-
11	60	+	+	+	+	+		+	+	+	+	+	+
12	47	+	+	+	+	+		+	+	+	+	+	+
13	43	+	-	-	-	-		+	-	-	-	-	-
14	42	-	-	-	-	-		-	+	+	-	-	-
15	37	+	+	+	+	+		+	+	+	+	+	+
16	33	+	-	+	-	-		+	+	-	-	-	-
17	28	+	+	+	+	+		+	+	+	+	+	-
18	24	+	+	-	-	-		+	+	-	-	-	-
Total Bands		17	12	12	10	10		17	15	11	11	10	7

3.2. Cluster analysis of protein profiles of treated plants using NTSYS

The findings of a numerical analysis of the whole-cell protein profiles of treated plants using an arithmetic averages algorithm and an unweighted pair group approach are displayed in (Figures 4 and 5). Figure 4 reveals the presence of three clusters: the first includes the protein profile of plants treated with cell suspension of F7; the second includes plants treated with Bt in its own subcluster separated from the subcluster that includes plants treated with Ax (*A. xylosoxidans*) and Ox (Oxamyl), where they have the same protein profile with a similarity of 100%; and the third cluster includes the protein profile of the control treatment. However, in case spraying foliage trial protein profiles in treated plants displayed different similarity compared to that in trial of soil drainage (Figure 5) revealed three clusters. Interestingly, the protein profile in plants treated with Ox was the same as in those treated with Ax and different from those treated with Bc and Bt. Our findings implied that the expressed proteins in plants were different as a response to different external factors and this behavior is logical and that depends on the interaction between plant biological system and external environmental factors.

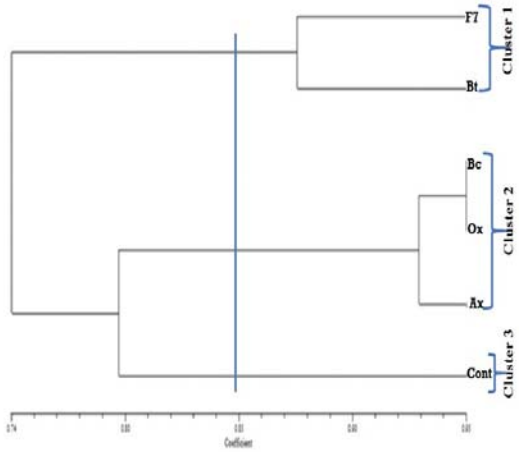

Figure 4. Dendrogram of the SDS-PAGE profiles of the total proteins of the treated plants in the case of the soil drench trial. The dendogram was created using the unweighted pair group approach and an arithmetic averages algorithm.

Figure 5. Dendrogram of the SDS-PAGE profiles of the total proteins of the treated plants in the spraying foliage trial. The dendogram was created using the unweighted pair group approach and an arithmetic averages algorithm.

3.3. The effect of bacterial strains on the reduction of nematode parameters on tomato plants

The data presented in Table 3 highlight the evaluation of modified F7 and its parental strains (Bt::Bc) in comparison with *A. xylosoxidans* (a nitrogen-fixing bacterium) and Oxamyl (a nematicide) for controlling *M. incognita* using foliar spray and/or soil drench application methods. Overall, the results demonstrate that all treatments, when compared to the controls, effectively reduced root-knot nematode reproduction.

Among the treatments, the nematicidal effects of F7 were more pronounced, showing greater effectiveness than the parental strains and control in reducing all nematode parameters, including the number of J2 juveniles in soil, galls, and egg masses (untreated plants). The highest percentage reduction in J2s in soil was observed with F7 (95.45%), followed by Oxamyl (87.98%) and Bc (87.79%) under foliar spray application. For soil drench application, the reductions were even higher with F7 (96.24%), followed by Oxamyl (89.37%), Ax (89.03%), Bc, and Bt.

Oxamyl showed greater reduction in all nematode parameters compared to *B. cereus*, as compared to the untreated control (Table 3). Specifically, galls in 5g of root were significantly reduced by F7, Bt, Bc, Ax, and Oxamyl by 66.75%, 29.90%, 41.39%, 40.91%, and 52.39%, respectively, when applied as a foliar spray. The reduction for the soil drench application was 75.60%, 38.04%, 46.17%, 47.39%, and 55.26%, respectively.

The trend for egg mass reduction followed a similar pattern, with a few exceptions. In general, F7 was the most effective in reducing all nematode-related parameters compared to the other treatments, and soil drench application was found to provide the best reduction in nematode infestations compared to foliar spray.

Table 2. The nematicidal effect of bacterial strains on the percentage reduction of *M. incognita* parameters on tomato plants

Treatments	Applications	Nematode parameters							
		No. J2 in soil	% Reduction	No. galls / roots	% Reduction	GI**	No. egg-masses / root	% Reduction	EI**
F7	Spraying foliage	92[b]	95.45	25.50 [g]	66.75	5	6.75 [h]	88.41	3
Bt		268[b]	86.80	64.75 [c]	29.90	7	17.25 [cd]	81.50	4
Bc		248[b]	87.79	56.25 [d]	41.39	7	13.75[ef]	84.15	4
Ax		262[b]	86.99	55.00 [d]	40.91	7	13.25[fg]	86.99	4
Oxamyl		242[b]	87.98	46.75 [e]	52.39	6	11.75 [g]	83.94	4
F7	Soil drench	76[b]	96.24	34.75 [f]	75.60	6	14.25[f]	95.51	4
Bt		248[b]	87.84	73.25 [b]	38.04	8	22.75 [b]	85.98	5
Bc		234[b]	88.56	61.25 [c]	46.17	7	19.50[bc]	88.82	5
Ax		224[b]	89.03	61.75 [c]	47.39	7	16.00 [de]	89.23	5
Oxamyl		217[b]	89.37	49.75 [e]	55.26	6	19.75[bc]	90.45	5
Control		2079[a]		104.50 [a]		9	123.00 [a]		9

The values represent the mean of five replicates. According to Duncan's Multiple Range Test, means that are followed by the same letter (s) are not statistically different.

** Gall index –GI, Egg masses index =EI, R % = % Reduction.* Bt: *B. thuringiensis* Bc: *B. cereus* Ax: *A. xylosoxidans*

3.4. Vegetative growth

The effect of nitrogen treatments (250 and 500 N/ha) and bacterial treatments (F7, *B. thuringiensis* (Bt), *B. cereus* (Bc), *A. xylosoxidans* (Ax), Oxamyl, and control) on vegetative growth characteristics (plant length (cm), the branch number, leaf number, fresh weights of leaves (g), and dry weights of leaves (g) of tomato plants are shown in Table (3). Tomato plants treated with 250 and 500 N/ha with fusant, F7, as a soil drench produced the highest plant length (174.70 cm and 171.30 cm, respectively), had no statistically significant differences between them, while the control treatment produced the shortest plant lengths (110.30 cm). While the maximum significant branch number values for tomato plants were noticed with 500 N/ha with fusant and F7 as a soil drench treatment (6.67) and the lowest values were observed with the control treatment (1.6), as for the effect of the interaction between nitrogen and bacteria treatments on leaf number, fresh and dry weights of leaves per plant were in the same

Table 3. Effect of the interaction of nitrogen deficiency and bacterial treatments on vegetative growth of tomato plants

Nitrogen dose	Treatments	Application	Plant length (cm)	Number of branches / plant	Number of leaves/ plant	Fresh weights of leaves/ plant (g)	Dry weights of leaves/ plant (g)
250 N/ha	Fusant F7	Foliar spraying	155.30^{fg}	4.00^{def}	80.00^{gh}	639.30^{gh}	39.05^{cd}
	Bt		151.00^{ghi}	3.00^{ghi}	70.67^{i}	541.60^{i}	36.50^{fg}
	Bc		142.30^{kl}	3.00^{ghi}	57.33^{lm}	390.70^{kl}	34.37^{hi}
	Ax		151.00^{ghi}	3.00^{ghi}	71.66i	543.00^{i}	36.55^{fg}
	Oxamyl		140.00^{l}	2.00^{ikl}	54.67^{m}	355.90^{lm}	33.39^{i}
	Control		102.70^{o}	1.33^{l}	30.68^{o}	194.10^{p}	30.33^{j}
	Fusant F7	Soil drench	171.30^{ab}	5.33^{bc}	144.70^{b}	1204.00^{b}	41.29^{b}
	Bt		159.30^{def}	4.00^{def}	86.67^{f}	706.00^{fg}	35.87^{g}
	Bc		164.30^{cd}	4.33^{de}	105.71^{d}	988.90^{d}	37.65^{ef}
	Ax		159.00^{ef}	4.00^{def}	86.33^{f}	703.30^{fgh}	35.83^{g}
	Oxamyl		147.70^{hij}	3.00^{ghi}	61.00^{kl}	447.90^{jk}	35.41^{gh}
	Control		110.30^{mn}	1.67^{kl}	33.00^{o}	219.00^{op}	31.04^{j}
500 N/ha	F7	Foliar spraying	158.30^{ef}	4.67^{cd}	85.00^{fg}	725.10^{ef}	39.67^{c}
	Bt		154.80^{fg}	4.33^{de}	77.33^{h}	632.30^{h}	38.14^{de}
	Bc		146.00^{ijk}	4.00^{def}	64.33^{jk}	475.10^{ij}	35.73^{g}
	Ax		155.00^{fg}	4.33^{de}	77.67^{h}	634.70^{gh}	38.50^{cde}
	Oxamyl		143.70^{jkl}	3.33^{fgh}	61.66^{kl}	445.40^{jk}	34.13^{i}
	Control		106.30^{no}	2.67^{hij}	35.68^{no}	280.60^{no}	31.52^{j}
	F7	Soil drench	174.70^{a}	6.67^{a}	153.0^{a}	1284.00^{a}	42.47^{a}
	Bt		163.00^{cde}	5.67^{b}	94.00^{e}	792.30^{e}	37.65^{ef}
	Bc		167.20^{bc}	5.33^{bc}	111.3^{c}	1074.00^{c}	39.44^{c}
	Ax		163.30^{cde}	5.66^{b}	93.00^{e}	792.70^{e}	37.99^{de}
	Oxamyl		151.70^{gh}	3.66^{efg}	67.66^{ij}	531.60^{i}	36.35^{g}
	Control		113.20^{m}	2.34^{ijk}	40.00^{n}	307.30^{mn}	33.54^{i}

Means with the same letter(s) are not statistically ($P < 0.05$) different from each other. F7: fusant, Bt: *B. thuringiensis,*Bc: *B. cereus,* Ax: *A. xylosoxidans* trend., where the highest significant values were achieved with 500 N/ha with, F7 as a soil drench treatment (153.0, 1284.00 g, and 42.47 g, respectively), followed by 250 N/ha with, F7 as a soil drench, while the lowest values were observed with 250 N/ha with control plants as foliar spraying (30.00, 194.10 g, and 30.33 g).

As for the effect of nitrogen treatments (250 and 500 N/ha) on the vegetative growth parameters of tomato plants was clear in (Fig. 6 A-E.) Tomato plants which received the minimum quantity of nitrogen fertilizers (250 N/ha) produced the highest significant plant length values, and the other above mentioned vegetative growth characteristics. While tomato plants treated by, F7, as a soil drench achieved the most significant plant length values, branch numbers, leaf numbers, fresh and dry weights of leaves (g), and followed by Bc as a soil drench treatment. While tomato plants grown in control treatments had the lowest values of vegetative growth characteristics (Fig. 7A-E.).

3.5. Flowering and fruit yield

The data presented in Table 4 illustrate the effects of nitrogen treatments (250 N/ha and 500 N/ha) and bacterial treatments (F7, Bt, Bc, Ax, Oxamyl, and the control) on flowering and fruit yield characteristics of tomato plants, including cluster number, fruit number per plant, fruit yield (g/plant), and fruit yield (ton/ha).

The results show that tomato plants treated with 500 N/ha and F7 as a soil drench produced the highest significant values for number of clusters per plant (36.00), followed by 250 N/ha with F7 as a soil drench. The lowest values for clusters per plant were observed in the control treatment (6.00).

In terms of fruit number per plant and fruit yield (ton/ha), the maximum significant values were achieved with 500 N/ha and F7 as a soil drench (60.67 fruits per plant and 43.61 ton/ha). This was followed by 500 N/ha with Bc as a soil drench (58.33 fruits per plant and 41.29 ton/ha) and 250 N/ha with F7 as a soil drench (57.50 fruits per plant and 41.02 ton/ha), with no significant differences between these treatments. The control treatment produced the lowest values for fruit number per plant and fruit yield (ton/ha) (36.67 fruits per plant and 30.88 ton/ha).

For fruit yield per plant (g/plant), tomato plants treated with 250 N/ha and 500 N/ha with Fusant F7 as a soil drench produced the highest significant values (2821.00 g and 2734.00 g), followed by 500 N/ha with Bc as a soil drench (2655.00 g). The minimum values were found with 250 N/ha and the control treatment (2059.00 g).

Regarding the effect of nitrogen treatments on flowering and fruit yield characteristics, data shown in Figures 8A–D indicate that these characteristics were negatively affected by higher nitrogen fertilizer rates. The 250 N/ha treatment showed significant superiority in all the mentioned characteristics compared to the 500 N/ha treatment.

As for the effect of bacteria treatments on flowering and fruit yield characteristics, Figures 9A–D show that all bacteria treatments positively influenced these characteristics in both soil drench and foliar application methods when compared to the control. The highest significant values for cluster number, fruit number per plant, fruit yield (g/plant), and fruit yield (ton/ha) were achieved with F7 as a soil drench, followed by Bc as a soil drench treatment.

Table 4. Effect of the interaction of nitrogen deficiency and bacterial treatments on flowering and fruit yield of tomato plants

Nitrogen dose	Treatments	Application	Number of clusters/ plant	Number of fruits/ plant	Fruit yield (g/plant)	Fruit yield (ton/ha)
250 N/ha	F7	Foliar spraying	17.33^{fg}	45.83^{fg}	2498.00^{de}	89.18^{ef}
	Bt		16.00^{gh}	45.00^{gh}	2491.00^{de}	88.94^{ef}
	Bc		12.00^{j}	40.83^{jk}	2290.00^{g}	81.75^{g}
	Ax		16.00^{gh}	45.00^{gh}	2489.00^{de}	89.49^{ef}
	Oxamyl		10.00^{k}	40.00^{jk}	2275.00^{g}	81.23^{g}
	Control		5.83^{l}	36.00^{l}	2016.00^{h}	71.30^{i}
	F7	Soil drench	34.00^{b}	57.50^{b}	2734.00^{ab}	97.63^{bc}
	Bt		20.00^{e}	47.50^{ef}	2500.00^{de}	89.23^{ef}
	Bc		27.67^{c}	54.17^{c}	2580.00^{cd}	92.11^{de}
	Ax		20.00^{e}	47.50^{ef}	2503.00^{de}	89.73^{ef}
	Oxamyl		13.00^{ij}	41.67^{ij}	2302.00^{fg}	82.18^{g}
	Control		6.00^{l}	36.67^{l}	2059.00^{h}	73.49^{i}
500 N/ha	F7	Foliar spraying	18.67^{ef}	48.33^{e}	2591.00^{cd}	94.51^{cd}
	Bt		17.67^{fg}	48.33^{e}	2585.00^{cd}	94.80^{cd}
	Bc		14.33^{hi}	44.00^{gh}	2378.00^{fg}	87.66^{f}
	Ax		18.00^{f}	48.67^{e}	2584.00^{cd}	95.53^{bcd}
	Oxamyl		11.33^{jk}	43.33^{hi}	2403.00^{ef}	87.20^{f}
	Control		7.667^{l}	39.67^{jk}	2074.00^{h}	77.23^{h}
	F7	Soil drench	36.00^{a}	60.67^{a}	2821.00^{a}	103.79^{a}
	Bt		22.33^{d}	51.00^{d}	2564.00^{cd}	94.65^{cd}
	Bc		29.33^{c}	58.33^{b}	2655.00^{bc}	98.27^{b}
	Ax		22.67^{d}	51.00^{d}	2560.00^{cd}	95.25^{bcd}
	Oxamyl		14.33^{hi}	44.33^{gh}	2375.00^{fg}	88.27^{f}
	Control		7.00^{l}	39.33^{k}	2113.00^{h}	79.21^{gh}

Means with the same letter(s) are not statistically ($P < 0.05$) different from each other. F7: fusant, Bt: *B. thuringiensis*, Bc: *B. cereus,* Ax: *A. xylosoxidans*

3.6. Fruit quality of tomatoes

The effect of nitrogen treatments (250 N/ha and 500 N/ha) and bacterial treatments (F7, Bt, Bc, *A.* Ax, Ox, and the control) on tomato fruit quality characteristics (average fruit weight (g), fruit diameter (cm), and TSS%) are presented in Table 5. Tomato plants treated with 500 N/ha and F7 as a soil drench produced the highest average fruit weight (138.80 g), followed by 500 N/ha with Bc as a soil drench. The highest fruit diameter values were achieved with 500 N/ha treatments using F7 and Bc as soil drench, with no significant differences between them (6.10 cm and 5.95 cm, respectively). Conversely, the lowest values for both average fruit weight (64.83 g) and fruit diameter (4.42 cm) were observed in plants treated with 250 N/ha and the control. Regarding the effect of the interaction between nitrogen and bacteria treatments on TSS%, no clear trend was observed.

Table 5. Effect of the interaction of nitrogen deficiency and bacterial treatments on average fruit weight, fruit diameter and TSS % of tomato plants

Nitrogen dose	Treatments	Application	Average fruit weight (g)	Fruit diameter (cm)	TSS %
250 N/ha	F7	Foliar spraying	103.50^{gh}	5.50^{efg}	4.93^{abc}
	Bt		102.10^{h}	5.43^{fgh}	4.72^{abc}
	Bc		90.77$_{i}$	5.27^{ghi}	4.50^{cd}
	Ax		102.00^{h}	5.43^{fgh}	4.78^{abc}
	Oxamyl		89.03^{j}	5.23^{hi}	4.17^{de}
	Control		64.83^{l}	4.42^{k}	3.55^{f}
	F7	Soil drench	125.40^{c}	5.70^{b-e}	5.00^{ab}
	Bt		106.60^{f}	5.53^{ef}	5.00^{ab}
	Bc		119.30^{d}	5.63^{c-f}	5.00^{ab}
	Ax		106.90^{f}	5.50^{efg}	5.17^{a}
	Oxamyl		91.77^{i}	5.26^{ghi}	4.50^{cd}
	Control		65.22^{l}	4.83^{j}	3.65^{f}
500 N/ha	F7	Foliar spraying	116.70^{e}	5.81^{bc}	5.05^{ab}
	Bt		115.20^{e}	5.73^{b-e}	4.85^{abc}
	Bc		104.00^{g}	5.56^{c-f}	4.58^{bcd}
	Ax		115.50^{e}	5.71^{b-e}	4.88^{abc}
	Oxamyl		102.10^{h}	5.55^{def}	4.23^{d}
	Control		78.07^{k}	4.86^{j}	3.67^{f}
	F7	Soil drench	138.80^{a}	6.10^{a}	5.10^{a}
	Bt		119.90^{d}	5.80^{bcd}	5.03^{ab}
	Bc		132.50^{b}	5.95^{ab}	5.03^{ab}
	Ax		120.00^{d}	5.82^{bc}	5.08^{a}
	Oxamyl		105.00^{g}	5.52^{efg}	4.60^{bcd}
	Control		78.45^{k}	5.15^{i}	3.77^{ef}

Means with the same letter(s) are not statistically ($P < 0.05$) different from each other, F7: fusant, Bt: *B. thuringiensis*, Bc: *B. cereus*,Ax: *A. xylosoxidans*

The data presented in Figures 10 A-C show the impact of nitrogen treatments (250 N/ha and 500 N/ha) on various fruit quality characteristics of tomatoes. Plants treated with 250 N/ha produced the highest values for fruit weight (g), fruit diameter (cm), and average fruit weight (g), with no significant differences found between the 250 N/ha and 500 N/ha treatments for total soluble solids (TSS%).

The effects of bacteria treatments including F7, Bt, Bc, Ax, Oxamyl, and the control applied as either foliar sprays or soil drenches on tomato fruit quality characteristics are shown in Figures 11 A-C. The results indicate that plants treated with F7 as a soil drench produced the highest values for fruit weight (g), fruit diameter (cm), and average fruit weight (g), followed by Bc as a soil drench treatment. However, no distinct trend in TSS% was observed across the bacteria treatments.

3.7. Tomato plant chemical composition and soil available nitrogen

Data in Table 6 reveal the effect of nitrogen treatments (250 N/ha and 500 N/ha) and bacterial treatments (F7, Bt, Bc, Ax, Ox, and the control) on the chemical composition of tomato plants and soil available nitrogen characteristics (leaf N%, P%, K%, and soil available nitrogen in mg/kg). The results show that tomato plants treated with 250 N/ha and F7 as a soil drench produced the highest significant values for leaf N% and leaf K% (4.27% and 5.20%, respectively), followed by 250 N/ha with F7 as a soil drench (4.14% and 4.98%). The lowest values for leaf N% and leaf K% were observed in the 250 N/ha control treatment (2.43% and 1.88%, respectively). For leaf P% and soil available nitrogen (mg/kg), tomato plants treated with 250 and 500 N/ha with F7 as a soil drench had the highest significant values (0.654% and 0.639% for P%; 254.40 mg/kg and 252.00 mg/kg for soil nitrogen), followed by 500 N/ha with F7 applied as a foliar spray. The lowest values for P% and soil available nitrogen were found with the 250 N/ha control treatment (0.0707% for P% and 145.10 mg/kg for soil nitrogen).

Table 6. Effect of the interaction of nitrogen deficiency and bacterial treatments on leaf N, P and K percentage and soil available nitrogen of tomato plants

Nitrogen dose	Treatments	Application	N %	P %	K %	Soil available nitrogen mg kg-1
250 N/ha	F7	Foliar spraying	3.80^{cd}	0.539^{bc}	4.68^{d}	242.30^{cd}
	Bt		3.65^{fg}	0.467^{de}	4.14^{f}	226.60^{gh}
	Bc		3.13^{j}	0.252^{f}	3.06^{i}	183.80^{k}
	Ax		3.54^{h}	0.467^{de}	4.11^{f}	224.00^{h}
	Oxamyl		2.64^{l}	0.115^{gh}	2.52^{k}	164.30^{l}
	Control		2.43^{n}	0.0707^{h}	1.88^{m}	145.10^{n}
	F7	Soil drench	4.14^{b}	0.639^{a}	4.98^{b}	252.00^{ab}
	Bt		3.57^{gh}	0.436^{e}	3.84^{g}	226.40^{gh}
	Bc		3.74^{def}	0.517^{bcd}	4.38^{e}	234.80ef
	Ax		3.57^{gh}	0.432^{e}	3.85^{g}	227.10^{fgh}
	Oxamyl		3.22^{j}	0.285^{f}	3.12^{i}	192.40^{ij}
	Control		2.48^{mn}	0.113^{gh}	1.90^{m}	152.50^{m}
500 N/ha	F7	Foliar spraying	3.82^{cd}	0.551^{b}	4.84^{c}	246.00^{bc}
	Bt		3.78^{de}	0.484^{cde}	4.35^{e}	230.30^{fgh}
	Bc		3.19^{j}	0.266^{f}	3.29^{h}	187.40^{jk}
	Ax		3.76^{de}	0.489^{cde}	4.368^{e}	232.20^{efg}
	Oxamyl		2.76^{k}	0.130^{g}	2.74^{j}	168.00^{l}
	Control		2.57^{lm}	0.0817^{gh}	2.13^{l}	149.70^{mn}
	F7	Soil drench	4.27^{a}	0.654^{a}	5.20^{a}	254.40^{a}
	Bt		3.69^{ef}	0.450^{e}	4.05^{f}	229.50^{fgh}
	Bc		3.88^{c}	0.533^{bc}	4.62^{d}	238.10^{de}
	Ax		3.70^{ef}	0.450^{e}	4.07^{f}	230.40^{fgh}
	Oxamyl		3.35^{i}	0.298^{f}	3.35^{h}	194.60^{i}
	Control		2.64^{l}	0.128^{gh}	2.16^{l}	152.80^{m}

Means with the same letter(s) are not statistically ($P < 0.05$) different from each other. F7: fusant, Bt: *B. thuringiensis*, Bc: *B. cereus,* Ax: *A. xylosoxidans*

Regarding the effect of nitrogen treatments on the chemical composition of tomato plants and soil available nitrogen characteristics, data presented in Figures 12 A-D show that leaf N%, leaf K%, and soil available nitrogen (mg/kg) were negatively affected by increasing nitrogen fertilizer levels. The 250 N/ha treatment produced the highest significant values compared to the 500 N/ha treatment. There were no significant differences between 250 N/ha and 500 N/ha for leaf P%.

For the effect of bacteria treatments on the chemical composition of tomato plants and soil available nitrogen, results showed that all bacteria treatments positively influenced both the chemical composition of the plants and the soil available nitrogen characteristics, regardless of the application method (foliar or soil drench), when compared to Oxamyl and the control treatments (Figures 13 A-D). The highest significant values for leaf N%, leaf P%, leaf K%, and soil available nitrogen (mg/kg) were achieved with F7 applied as a soil drench, followed by F7 applied as a foliar spray.

4. Discussion

In Egypt, root-knot nematodes (RKNs) are among the most significant agricultural pests, causing substantial crop losses. The use of synthetic nematicides poses risks to both human health and the environment, emphasizing the need for sustainable agricultural practices such as biological control. However, controlling RKNs is challenging since they are obligatory root parasites that spend most of their life cycle inside host roots (Tian *et al*., 2007). One of the most effective biological control methods is breaking the nematode life cycle. The eggshell, which is the most resilient component of nematode eggs, plays a key role in their resistance to chemical and biological pesticides (Wharton, 1980). The inner protein layer is the most common eggshell structure (Bird and McClure, 1976). Lytic bacterial activity has been associated with biocontrol mechanisms for years (Kassab *et al*., 2017).

Many plant growth-promoting rhizobacteria (PGPRs), including *Bacillus* species, contribute significantly to agroecosystem sustainability by promoting plant growth and productivity while reducing the need for chemical fertilizers through nitrogen fixation (Albdaiwi *et al*., 2019, Sivasakthi *et al*., 2014). Biological control methods, biofertilization, and biostimulation techniques using Bacillus spp. can decrease disease prevalence and enhance agricultural productivity (Borriss, 2011; Yao *et al*., 2006).

Lytic enzymes, particularly proteases, play a crucial role in breaking down structural components of nematodes. There is a positive correlation between bacterial nematode-killing efficiency and alkaline protease production, supporting findings by Kassab *et al.* (2017). The amplification of the alkaline protease gene ASP16 from Bc) and Bt) strains, as well as their F7, successfully generated 1100-base pair fragments, confirming the presence of the targeted gene. Visualization on an agarose gel (Figure. 2) validated this amplification process.

Analysis of the amino acid sequence of ASP16 showed a strong relationship with the S8 family peptidases of *B. cereus* (Figure. 3), classifying ASP16 as a serine protease, in line with findings by Mahmoud *et al.* (2021) and Ariyaei *et al*. (2019). Identifying ASP16 as a serine protease is significant as it provides insights into its enzymatic activity and functional properties. Further studies can focus on characterizing ASP16 and its role in biological processes.

The serine protease from *Paecilomyces lilacinus* strain 251 was found to significantly alter the eggshell structure of *M. javanica*. Protease-treated eggs exhibited a thinner chitin layer and loss of the lipid layer compared to the control (Khan *et al*., 2004). In this study, the protease gene was detected in F7 and its parental strains (Bt, and Bc).

Soil drenching was the most effective treatment, showing the highest number of protein bands in soluble protein electrophoresis compared to foliar spraying and control. The highest number of bands (18) appeared in plants exposed to F7 via foliar spraying and soil drenching, while the control exhibited only 8 bands. This finding aligns with Ramadan and Soliman (2020), who reported that biotic stress from nematode infection induced increased protein bands in plants treated with bio-agents such as *A. xylosoxidans*. Protein synthesis and enzymatic alterations occur due to biotic stress, as evidenced by SDS-PAGE. Soil drenching with *A. xylosoxidans* at the time of planting was more effective in protecting against *M. incognita* and promoting tomato growth than foliar spraying.

Induction of resistance genes is associated with an increase in protein bands, correlating with improved tomato growth (Vyomesh *et al*., 2018). Similar findings were reported by Sharaf *et al*. (2016), who suggested that these proteins inhibit nematode infections. Resistance genes influence plant growth, with changes reflected in shoot length, fresh weight, and dry weight (Ramadan and Soliman, 2020). An increase in protein band density was observed when *B. subtilis* strains were applied against *M. incognita* in tomatoes (Sharaf *et al*., 2016).

Our findings demonstrate that all treatments reduced RKN proliferation compared to the control. F7 exhibited the highest nematicidal efficiency, reducing J2 populations in soil, gall numbers, and egg masses more effectively than its parental strains or the control. Several factors contribute to nematode suppression, including:

1. Biocontrol agents produce lytic enzymes, bioactive compounds, iron siderophores, antioxidant enzymes, antibiotics, and compete for nutrients (Beneduzi et al., 2012).
2. PGPRs activate plant defense mechanisms, inducing systemic resistance (ISR) against phytopathogens via signaling pathways such as *B. cereus* AR156 (Chowdappa *et al.,* 2013). ISR is frequently induced in the rhizosphere by Pseudomonas and Bacillus species (Choudhary and Johri, 2009).
3. PGPRs employ eco-friendly biocontrol strategies, including exopolysaccharides (EPSs), salicylic acid, biosurfactants, N-acyl-homoserine lactones (AHLs), and antibiotics (Wang *et al*., 2015; Zou *et al*., 2018).
4. PGPRs produce plant hormones such as indole-3-acetic acid (IAA), gibberellins (GAs), and cytokinins, promoting root and shoot growth, chlorophyll content, hydration, and nutrient uptake (Arora *et al*., 2013; Bhutani *et al*., 2018).

Soil drenching proved to be the most effective application method, corroborating Ramadan and Soliman's (2020) findings that soil drenching enhances bacterial efficiency as a bio-agent in plant nematode biocontrol, plant growth induction, and protein band augmentation.

In our previous study, F7 and its parental strains (Bc and Bt) were assessed for nitrogen fixation ability using glucose nitrogen-free mineral media. Parental strains exhibited a blue color, while F7 displayed a dark blue color (Mohammed *et al*., 2021). Recent data indicate that fertilizers lead to significant losses of nitrogen (40–70%), phosphorus (80–90%), and potassium (50–90%) (Verma and Sandeep, 2023). Consequently, biofertilizers are being

explored as alternatives to chemical fertilizers to improve plant growth and yield.

Tomato plants receiving minimal nitrogen (250 N/ha) exhibited the highest plant length, branch numbers, leaf numbers, and leaf fresh and dry weights. F7 soil drenching at 500 or 250 N/ha yielded the tallest plants, while 500 N/ha F7 treatment produced the highest branch numbers. These findings align with Rascio and La Rocca (2013), who highlighted bacteria's role in sustainable agriculture through biological nitrogen fixation (BNF). Bacteria facilitate BNF by converting atmospheric nitrogen into plant-accessible compounds using nitrogenase (Udvardi and Poole, 2013).

Higher nitrogen levels negatively impacted cluster numbers, fruit numbers, and yield, with 250 N/ha treatments yielding the best results. F7 soil drenching significantly improved fruit yield over foliar application. Increased biological nitrogen fixation during flowering correlates with plant nitrate demands and yield enhancement (Kapulnik *et al*., 1985). PGPRs improve plant growth through hormone production, phosphate solubilization, and antimicrobial activity (Günsu *et al*., 2015; Bhutani *et al*., 2018; Liu *et al*., 2019; Reis *et al*., 2022). These phytohormones stimulate root growth, enhancing water and nutrient uptake (Arora *et al*., 2013). Our results confirm that nitrogen application, F7 treatment, and soil drenching influence tomato chemical composition and soil nitrogen availability.

5. Conclusion

Fusant F7 enhances biocontrol activity against *Meloidogyne incognita*, significantly reducing J2 nematode populations in soil, as well as the number of galls and egg masses in tomato roots. The reduction in nematode infestation, coupled with its bio-fertilization effects, positively influences tomato growth parameters and protein band expression in leaves. Overall, F7 exhibited the most significant impact when applied as a soil drench, achieving the greatest reduction in nematode-related parameters, enhancing nitrogen fixation, and improving plant growth and yield. Notably, soil drenching proved to be more effective than foliar spraying in all measured outcomes.

References

Albdaiwi R N, Khyami-Horani H, Ayad J Y, Alananbeh K M and Al-Sayaydeh R. 2019. Isolation and characterization of halotolerant plant growth promoting rhizobacteria from durum wheat (Triticum turgidum subsp. durum) cultivated in saline areas of the dead sea region. *Frontiers in Microb,* **10**, 1639.

Al-Hawamdeh F, Jamal Y A, Kholoud M A and Muhanad W A. 2024. Bacterial Endophytes and Their Contributions to Alleviating Drought and Salinity Stresses in Wheat: A Systematic Review of Physiological Mechanisms. *Agriculture* **14** (5): 769.

AOAC 1990. In K. Helrich (Ed.), Official Methods of Analysis (15th ed.). Arlington, VA, USA: Association of Official Analytical Chemists, Inc.

Arora N K, Tewari S and Singh R. 2013. Multifaceted plant-associated microbes and their mechanisms diminish the concept of direct and indirect PGPRs. In: Arora NK (ed) Plant microbe symbiosis: fundamentals and advances. Springer New Delhi 411–449.

Barker T R .1985. Nematode extraction and bioassays. In An Advanced Treatise on *Meloidogyne* Vol **2** (eds Barker, T. R. et al.) 19–35 (North Carolina University, 1985).

Beneduzi A, Ambrosini A and Passaglia LMP. 2012. Plant growth-promoting rhizobacteria (PGPR): Their potential as antagonists and biocontrol agents. *Genet Mol Biol* **4:**1044–1051.

Bhutani N, Maheshwari R, Negi M and Suneja P. 2018. Optimization of IAA production by endophytic *Bacillus* spp. from Vigna radiata for their potential use as plant growth promoters. *Isr J Plant Sci* **65**:83–96.

Borriss R. 2011. Use of plant-associated *Bacillus* strains as bio-fertilizers and biocontrol agents, in Bacteria in Agrobiology. In: Maheshwari DK, pp. 41-76 (ed.), Plant Growth Responses. Heidelberg, Springer.

Choudhary D K and Johri B N. 2009. Interactions of *Bacillus* spp. and plants-with special reference to induced systemic resistance (ISR). *Microbiol Res* **164**:493–513.

Chowdappa P, Kumar SM, Lakshmi MJ, Mohan SP, Upreti KK. 2013. Growth stimulation and induction of systemic resistance in tomato against early and late blight by *Bacillus subtilis* OTPB1 or *Trichoderma harzianum* OTPB3. *Biol Control* **65**:109–117.

Davis RW, Botstein D Rotho JR. 1980. Transfection of DNA. in Bacterial Genetics: A Manual for Genetic Engineering Advanced Bacterial Genetic. *Cold Spring Harbor laboratory New York* **67**:134-137.

Dubey D C and Maheshwari D K. 2011. Role of PGPR in integrated nutrient management of oil seed crops. In: Maheshwari DK (ed) Bacteria in agrobiology: plant nutrient management. Springer- Verlag Heidelberg 1–17.

Duncan DB. 1955. Multiple ranges and multiple F test. *Biometrics* **11:**11-24.

Eisenback JD. 1985. Detailed morphology and anatomy of second-stage juveniles, males, and females of the genus *Meloidogyne* (root-knot nematodes). In: Sasser, J.N. & Carter, C.C. (Eds.) – An advanced treatise on *Meloidogyne* Volume I (pp. 47-77) Raleigh, USA, North Carolina State University Graphics.

El-Kawokgy T, Zowail MA, Hegazy MEM, Wafaa K and Salem H. 2004. Genetic improvement of *Bacillus thuringiensis* as a biocontrol agent against *Biomphalaria alexandrina* snail. *J Agr Sci* **29**:5317–5334.

FAO. 2018 Statistical Database. Food and agricultural organization of the united nations. Available at http:\\www.faostat.fao.org.

Forghani F, Hajihassani A. 2010. Recent Advances in the Development of Environmentally Benign Treatments to Control Root-Knot Nematodes. *Front Plant Sci* **11**:1125.

Geng C, Xiangtao N, Zhichao T, Zhang Y, Lin J, Ming S and Donghai P. 2016. A novel serine protease, Sep1, from *Bacillus firmus* DS-1 has nematicidal activity and degrades multiple intestinal-associated nematode proteins. *Sci. Rep* **6:**25012.

Godfray HCJ, Beddington JR, Crute IR, Haddad L, Lawrence D and Muir JF. 2010. Food security: the challenge of feeding 9 billion people. S*cience* **327**:812-818.

Günsu B K, Sencer Ö, Hasan FA, Ekin UK, Vahap K, Murat AT. 2015. Effect of *Bacillus subtilis* Ch-13, Nitrogen and Phosphorus on Yield, Protein and Gluten Content of Wheat (*Triticum aestivum* L.) *J of Agri.al Faculty of Uludag Univ* **29 (1):** 19-28.

İlbaş İA. 2009. Organik Tarım (İlkeler ve Ulusal Mevzuat). Eflatun Yayınevi. Ankara

Kapulnik Y, Okon Y and Henis Y. 1985. Changes in root morphology of wheat caused by *Azospirillum inoculation*. *Can J Microbiol* **31:**881–887.

Kassab SA, Eissa MF, Bader UM, Ismail AE, Abdel Razik BA, Soliman GM. 2017. The nematocidial effect of a wild type of *Serratia marcescens* and their mutants against *Meloidogyne incognita* juveniles. *Egypt J Agronematol* **16 (2):**95-114.

Khan A, Williams K, Helena KM and Nevalainen H. 2004. Effect of *Paecilomyces lilacinus* protease and chitanase on the eggshell structures and hatching of *Meloidogyne javanica* juveniles. *Biol Con* **31**:346-352.

Laemmli UK. 1970. Cleavage of structural proteins during assembly of the head of bacteriophage T4. *Nature* **227**:680-685

Liu X, Li Q, Li Y, Guan G and Chen S. 2019. *Paenibacillus* strains with nitrogen fixation and multiple beneficial properties for promoting plant growth. *Peer J* **7:** e7445.

Mohamed SAH, Ameen HH, Elkelany US, El Wakeel MA, Hammam MMA and Soliman GM. 2021. Genetic improvement of *Pseudomonas aeruginosa* and *Bacillus cereus* for controlling root knot nematode and two weeds under laboratory conditions. *J J of Biol Sci* 14 (4):859-865.

Mohamed SAH, El-Sayed GM, Elkelany US, Youssef MMA, El-Nagdi WMA, Soliman GM. 2021 A local *Bacillus* spp.: isolation, genetic improvement, nematode biocontrol, and nitrogen fixation. *Egypt Pharma J* **20(4):**352-363.

Mohammad AA, Amer HM, El-Sawy SM, Youssef DA, Nour SA, Soliman GM. 2022. Nematicidal activity of sweet annie and garden cress nano-formulations and their impact on the vegetative growth and fruit quality of tomato plants. *Scientific Reports* **12(1):** 22302.

Motsara MR and Roy RN. 2008. Guide to laboratory establishment for plant nutrient analysis. Food and agricultural organisation of the United Nations FAO Fertilizer and Plant Nutrition Bulletin. *Rome* **219**.

Puntener W. 1981. Manual for field trials in plant protection-Basle, Switzerland: Agric Division, Ciba Geigy Limited, 205.

Ramadan WA and Soliman GM. 2020. Effect of different applications of bio-agent *Achromobacter xylosoxidans* against *Meloidogyne incognita* and gene expression in infected eggplant. *J J of Biol Sci* **13(3):**363–370.

Ramezani MM, Mahdikhani ME, Baghaee RS and Rouhani H. 2014.The nematicidal potential of local *Bacillus* species against the root-knot nematode infecting greenhouse tomatoes. *Biocontrol Sci Technol* **24:**279–290.

Rascio N, La Rocca N. 2013. Biological Nitrogen Fixation. In *Encyclopedia of Ecology*; Fath, B., Ed.; Elsevier: Amsterdam, Netherlands 264–279.

Reis MNO, Vitorino L C, Lourenço LL and Bessa LA. 2022. Microbial Inoculation Improves Growth, Nutritional and Physiological Aspects of Glycine max (L.) *Merr Microorganisms* **10:**1386. https://doi.org/10.3390/ microorganisms10071386.

Sasanelli N, Toderas I, Iurcu-Straistaru E, Rusu S, Migunova V and Konrat A. 2018. Yield losses caused by plant parasitic nematodes graphical estimation. In Book of International Symposium "Functional Ecology of Animals"; National Book Chamber of R. Moldova, Ed.; Institute of Zoology: *Chisinau Moldova* 319–329.

Sharaf AMA, Kailla AM, Mohamed S, Attia MS, Mohamed M and Nofa MM. 2016. Induced resistance in tomato plants against root knot nematode using biotic and abiotic inducers. *Int. J Adv Re. Biol Sci* **3(11):**31-46.

Sims JT. 1996. Methods of Soil Analysis, Part 3, Chemical Methods. Soil Science Society of America, Madison, WI, USA.

Sivasakthi S, Usharan, G and Saranraj P. 2014. Biocontrol potentiality of plant growth promoting bacteria (PGPR)—*Pseudomonas fluorescens* and *Bacillus subtilis*: a review. *Afr J Agric Res* **9(16):**1265–1277.

Snedecor GW and Cochran WG. 1982. Statistical methods. 7th ed. Iowa State Univ. Press, Iowa

Soliman GM, Ameen HH, Abdel-Aziz M, E-lsayed GM. 2019. In vitro evaluation of some isolated bacteria against the plant parasite nematode *Meloidogyne incognita*. *Bull NRC* **43:**171.

Soliman GM, El-Sawy SM, Rasha G, Salim RG, El-Sayed GM and Ramadan WA. 2023. Bioefficacy of *Bacillus cereus* and its three mutants by UV irradiation against *Meloidogyne incognita* and gene expression in infected tomato plants. *J J of Biol Sci* **16** (2):233 – 242.

Soliman GM, Mohamed SAH, Haggag LF, El-Hady ES. 2020. Efficiency of biological control of root-knot nematodes in infected grapevines seedling by genetic improved bacteria. *Plant Archives* **20 (1):**951-961.

Stegmann H. 1979. Electrophoresis and focusing in slabs using the Pantaphor apparatus for analytical and preparative separations in gel (Polyacrylamide, Agarose, Starch, Sephadex). Messeweg 11, D-3300, Braunschweig Institute of Biochemistry, West-Germany 1-29.

Tian B, Yang J and Zhang KQ. 2007. Bacteria used in the biological control of plant-parasitic nematodes: populations, mechanisms of action, and future prospects, *FEMS Microbial Ecol* **61 (2):**197–213.

Udvardi M and Poole PS. 2013. Transport and metabolism in legume-rhizobia symbioses. *Annu Rev Plant Biol* **64**:781–805.

Verma A and Sandeep KV. 2023. Use of Nano-Fertilizers to Improve Crop Production and Nutrient Use Efficiency of Crops. *The Agriculture magazine* **2 (4):**136-139.

Vyomesh SP and Shukla YM. 2018. Proteomics study during root knot nematode (*Meloidogyne incognita*) infection in tomato (*Solanum lycopersicum* L.). *J of Pharmacog Phytochem* **7** (3):1740-1747.

Wang T, Liang Y, Wu M, Chen Z, Lin J and Yang L. 2015. Natural products from *Bacillus subtilis* with antimicrobial properties. *Chin J Chem Eng* **23**:744–754.

Wharton DA. 1980. Nematode egg shells. *Parasitology* **81**:447-463.

Wolf AM and Beegle DB. 2011. Recommended soil tests for macronutrients. p. 39-47. In J.T. Sims and A. Wolf (eds.) Recommended Soil Testing Procedures for the Northeastern United States. Northeast Regional Bulletin, 493. 3rd edition. Agricultural Experiment Station, University of Delaware, Newark, DE.

Yao A, Dr HB, Karimov S, Boturov U, Sanginboy S and Sharipov A K. 2006. Effect of FZB 24® *Bacillus subtilis* as a biofertilizer on cotton yields in field tests. *Arch Phyto Plant Protect* **39:**323-328.

Zou J, Jiang H, Cheng, H, Fang J and Huang G. 2018. Strategies for screening, purification and characterization of bacteriocins. *Int J Biol Macromol* **11**7:781–789.

Appendices

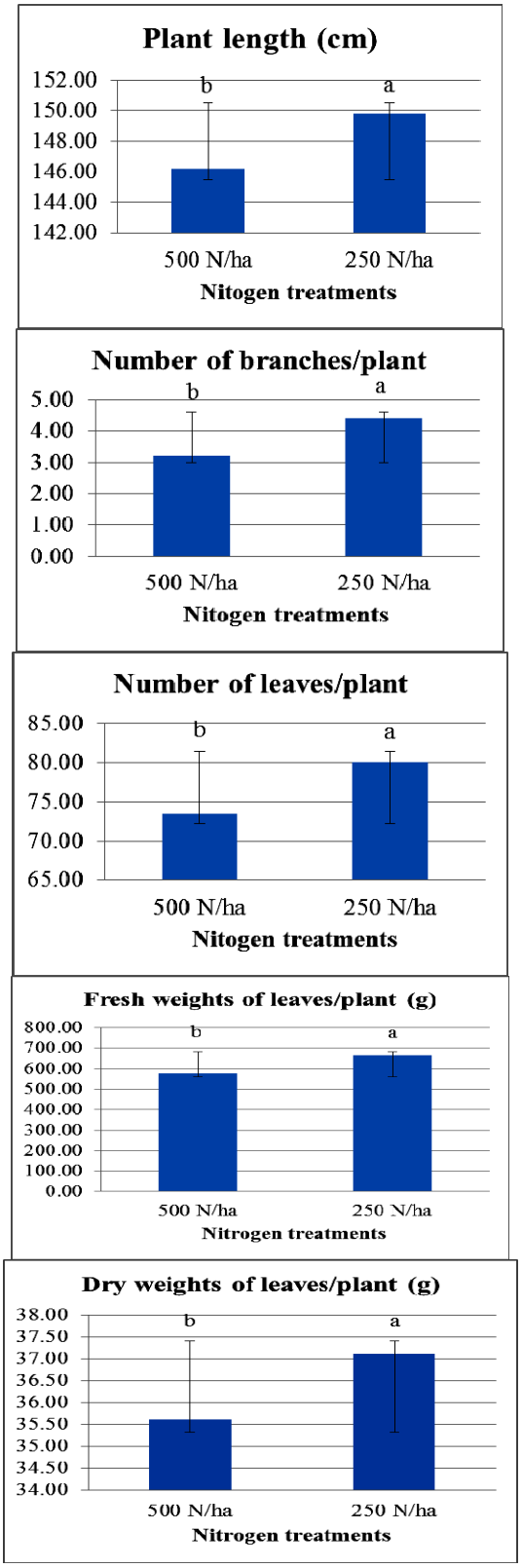

Figure 6A-E. Effect of nitrogen treatments only on vegetative growth of tomato plants

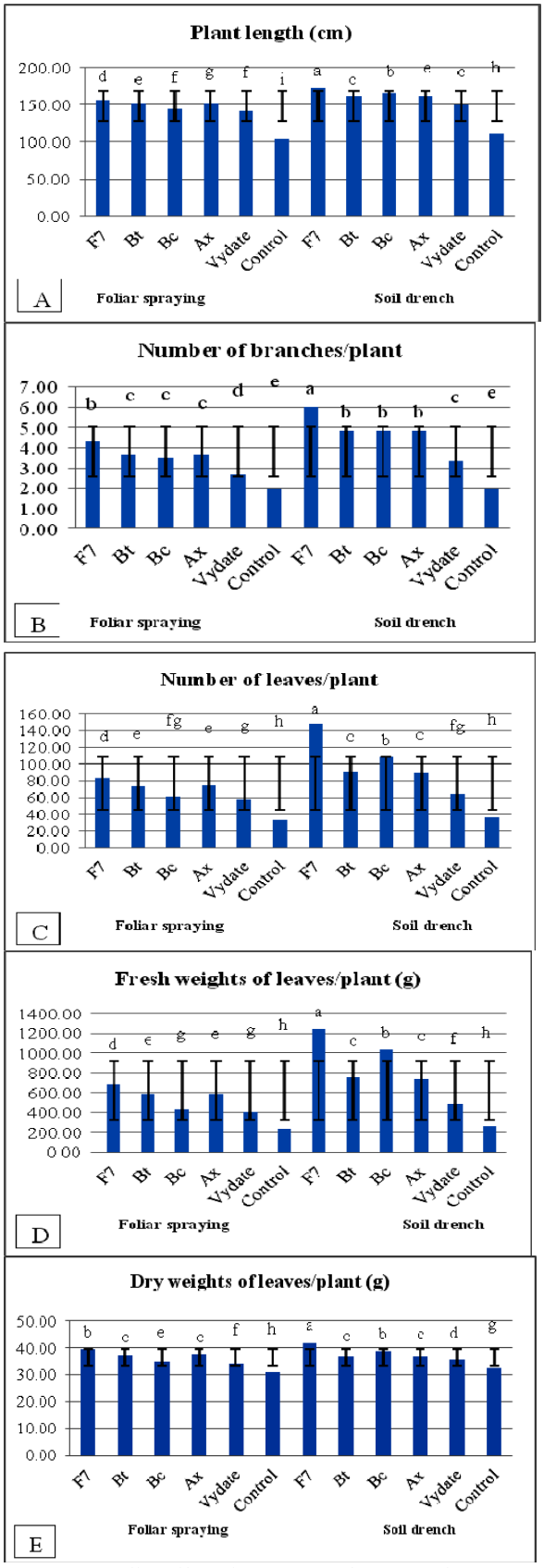

Figure 7A-E. Effect of bacteria treatments only on vegetative growth of tomato plants

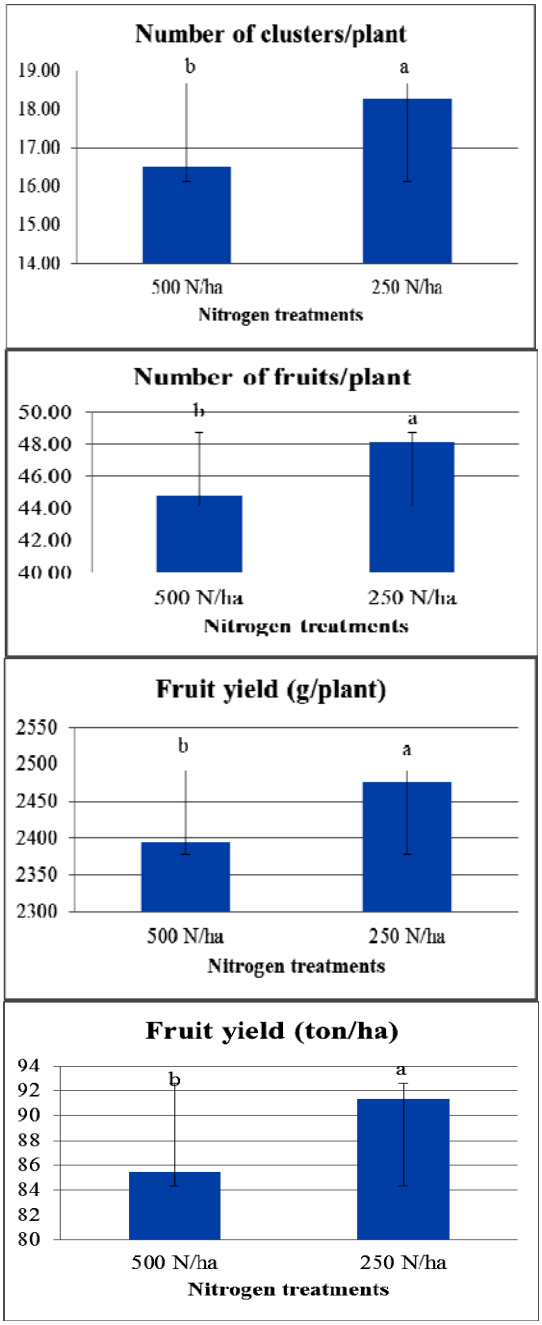

Figures 8A-D. Effect of nitrogen treatments on flowering and fruit yield of tomato plants

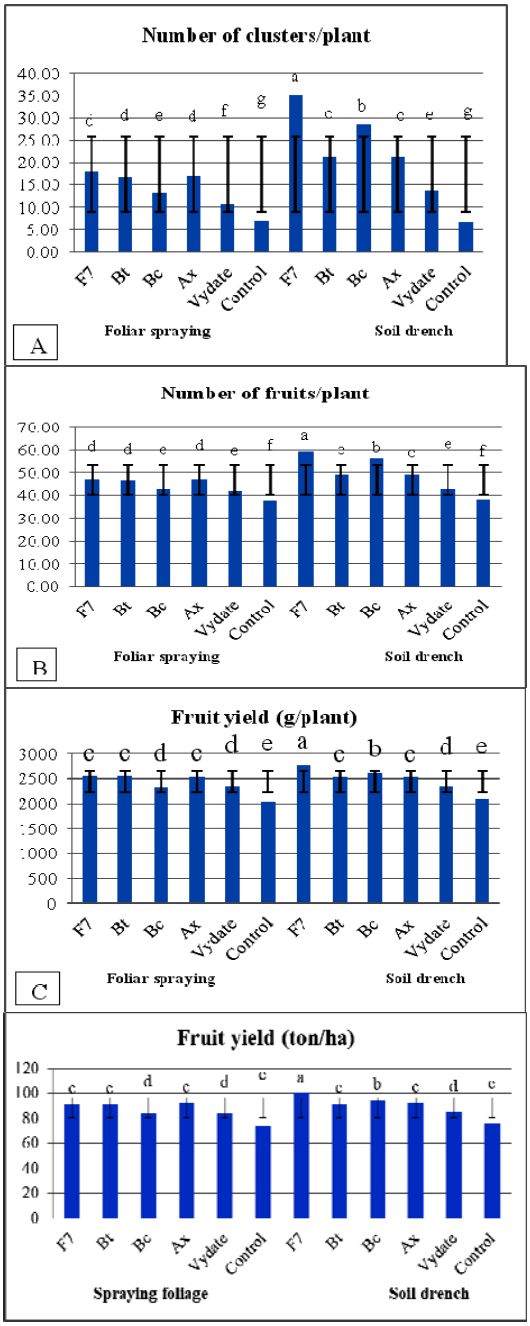

Figures 9A-D. Effect of bacteria treatments on flowering and fruit yield of tomato plants

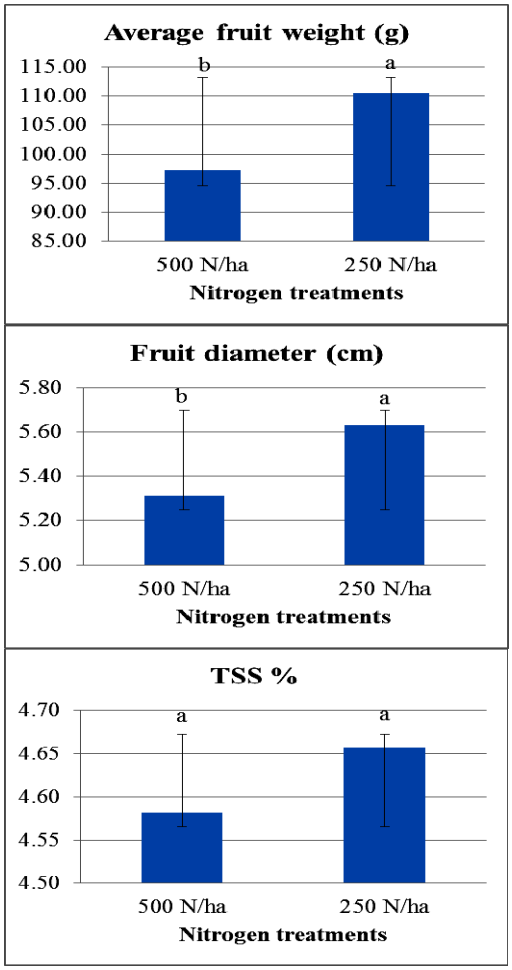

Figures 10A-C. Effect of nitrogen treatments on average fruit weight, fruit diameter and TSS % of tomato plants

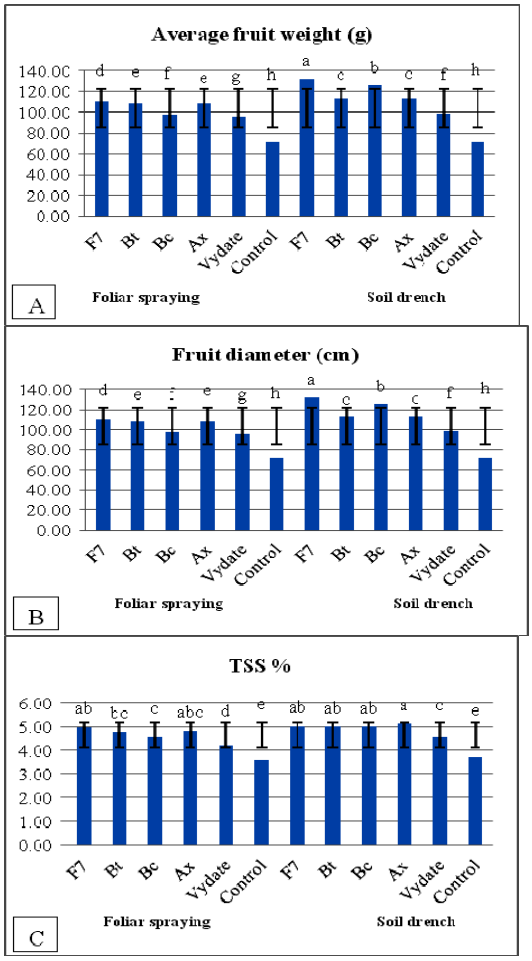

Figures 11A-C. Effect of bacteria treatments on average fruit weight, fruit diameter and TSS % of tomato plants

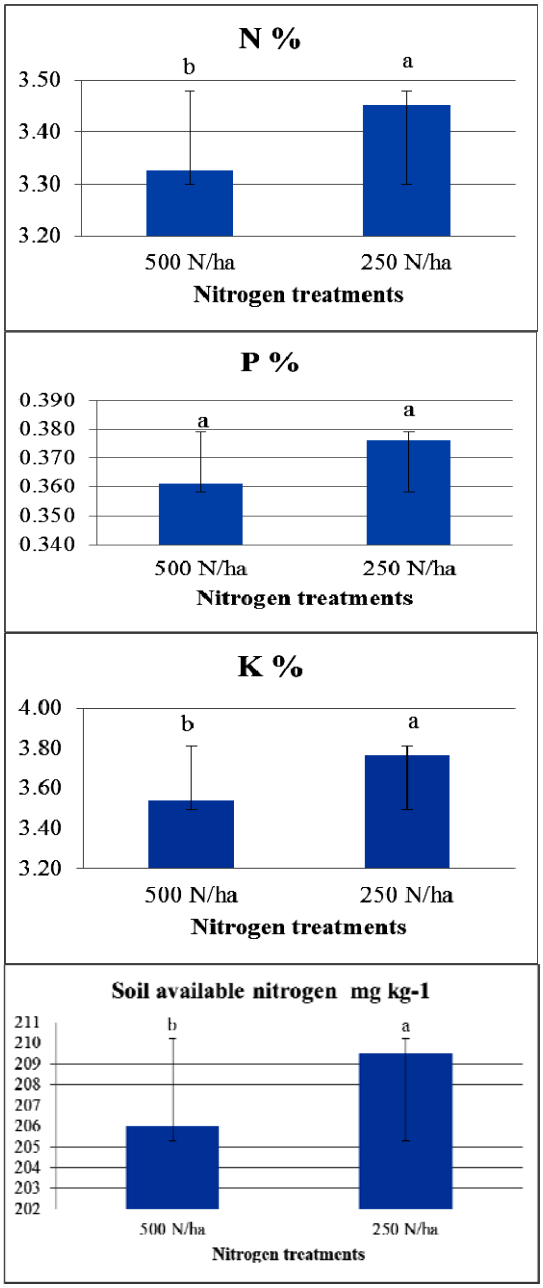

Figures 12A-D. Effect of nitrogen treatments on leaf N, P and K percentage of tomato plants and soil available nitrogen

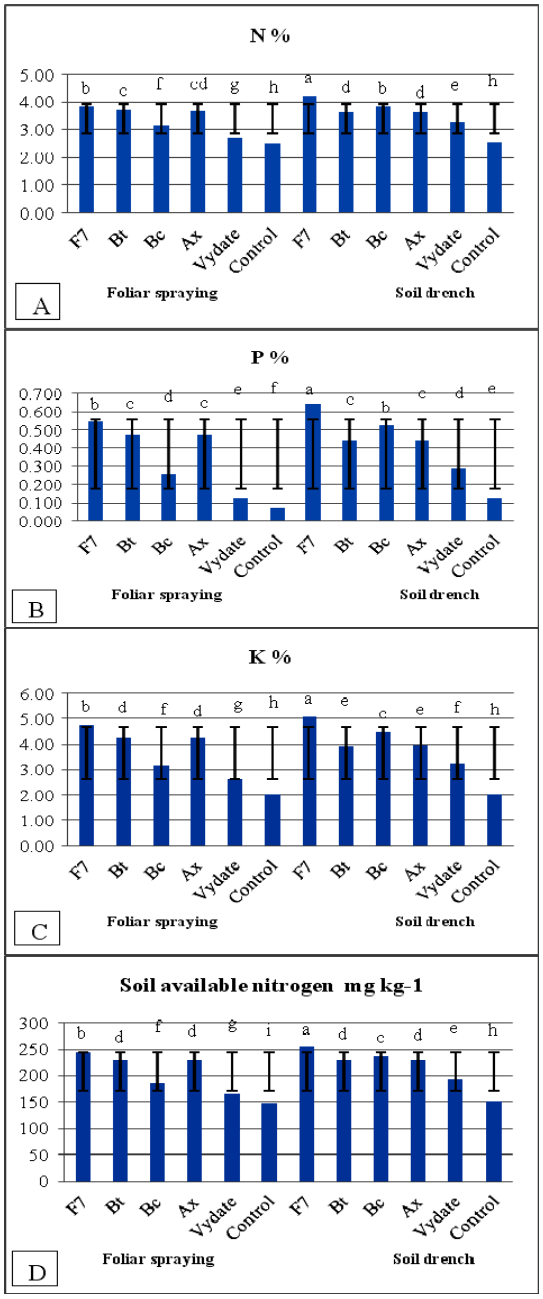

Figures 13A-D. Effect of bacteria treatments on leaf N, P and K percentage of tomato plants and soil available nitrogen

JJBS

Volume 18, Number 3,September 2025
ISSN 1995-6673
Pages 503 – 508

Jordan Journal of Biological Sciences

Synthesis and Characterization of Liposomes Derived from Oleaginous Yeast, *Candida tropicalis*

Chellapandian Balachandran[1,2,*], Appasamy Surendran[3], Ravichandran Yaamini[1], Natarajan Arun Nagendran[4,5] and Kathirvelu Baskar[6,**]

[1]*Department of Biotechnology, Thiagarajar College, Madurai, Tamil Nadu, India;* [2]*PG and Research Department of Zoology, Pachaiyappa's College, Chennai - 600 030, Tamil Nadu, India;* [3]*Department of Biochemistry, The American College, Tallakkulam, Madurai – 625002, Tamil Nadu, India;* [4]*Department of Zoology, Thiagarajar College, Madurai, Tamil Nadu, India;* [5]*NCoE (MHRD), Thiagarajar College, Madurai, Tamil Nadu, India;* [6]*Department of Ecotoxicology, Ross Lifescience Limited, Bhosari, Pune, Maharastra-411026, India.*

Received: December 28, 2024; Revised: March 17, 2025; Accepted: March 25, 2025

Abstract

Liposomes are nano or microvesicles used as carrier molecules for the transport of hydrophilic and hydrophobic substances. Oleaginous yeast is one of the potential source for the production of liposomes and hence an attempt has been made to produce liposomes from the lipids of oleaginous yeast, isolated from cultivation soil. The candidate species of oleaginous yeast producing elevated quantity of lipid (3.9U/ml in 96 hrs) was identified by 18s rRNA sequencing as *Candida tropicalis*. The lipids and phospholipids extracted were confirmed using FTIR spectroscopy and were used for the synthesis of liposomes by solvent injection method. The size of the liposome (78.7nm) was determined by AFM analysis. The HPLC analysis revealed the presence of phosphatidylcholine (0.44%) and ethanolamine (0.15%). The encapsulation efficiency was between 30 – 50% as determined by UV-visible spectroscopy. Further research will throw light on the scope and applications of liposomes synthesized using *Candida tropicalis* in the biomedical and food industries.

Keywords: *Candida tropicalis*, Encapsulation, Liposome, Phospholipids, HPLC

1. Introduction

Yeasts are well-known diverse clusters of microorganisms exhibiting a high level of genetic variations within the same species. They have more biotechnological importance and finds a larger applications in various industries and a greater number of yeast species were identified and explored for their biotechnological potentials (Kieliszek *et al.,* 2017). The morphology of yeast cells facilitates single cell development and hence are better candidate for easy cultivation than fungi since the latter produces pellets or mycelia. Several species, such as *Lipomycesstarkeyi*, *Rhodosporidium toruloides*, *Candida curvata*or, *Rhodotorula* spp., *Trichosporon fermentans* and *Yarrowia lipolytica* were exploited for liposome production with cheese-whey, glucose, glucose syrups, xylose, hemicellulose hydrolysates, molasses, waste glycerol deriving from bio-diesel production, organic acids, etc. as substrata (Morata and Loira, 2017).

Oleaginous yeast is one of the suitable agent, which can produce and accrue high amount of lipid, for example selective strains under optimal conditions may accumulate about 20% to 76% lipid (Lamers *et al.,* 2016). Within cells, the lipids are found as granular forms and its content and fatty acid profile differs between species. The oleaginous yeast commonly produces myristic (C14:0), palmitic (C16:0), stearic (C18:0), palmitoleic (C16:1), oleic (C18:1), and linoleic (C18:2) acids (Chen and Wang, 2007; Carsanba *et al*., 2018). The microbial lipids are involved in the production of biodiesel (Sundarsingh *et al*., 2024), dietary supplements and infant nutrition (Beligon *et al*., 2016; Rodrigues *et al*., 2024). The oleo chemical production involves in the production of two classes of value added oleo chemicals, alkanes and fatty alcohol through free fatty acids derived pathways (Zhou *et al*., 2016). The liposomes produced from the lipids released by microorganisms (Bacteria, Archeae and Yeast) can be used for drug delivery in treating cancer and targeting biofilms (Makhlouf *et al*., 2023; Ameri *et al*., 2016). The phospholipids are the major components of liposomes among various lipid forms produced by yeasts. They are microscopic spherical structures with one or more phospholipid membranes that entraps aqueous component. Generally, liposome composition includes natural and/or synthetic phospholipids like Phosphatidylethanolamine, Phosphatidylglycerol, Phosphatidylcholline, Phosphatidylserine, Phosphatidylinositol. Among them Phosphatidylcholine and phosphatidylethanolamine constitute two major structural components of most biological membranes (Alavi *et al*., 2017).

Liposomes possess versatile properties such as target specificity, regulated release, biocompatibility and biodegradability, which makes them an efficient candidate for pharmaceutical applications (Liu *et al.,* 2022) and potential applications in various industries such as pharmaceutical, food and cosmetic industries. Liposomes serve as significant carrier of drugs and enhance the

* Corresponding author. e-mail: bchandruji@gmail.com; suribaskar@hotmail.com

solidity and solubility of the drugs and aids in targeted drug delivery. Due to high encapsulation ability, they prevent degradation of encapsulated drugs due to pH, light and reduce tissue irritation (Alavi *et al*., 2017; Li *et al.,* 2015). Studies on the synthesis of liposomes from different sources of lipids and the characterization of liposomes have much focus in recent days due to their vast applications and biological importance. In this context, the present study aims to synthesize and characterize liposomes from the lipids derived from the oleaginous yeast isolated from soil samples under different vegetation.

2. Materials and methods

2.1. Isolation of yeast from soil samples

The top soil were collected from carrots, beans, coffee plantation areas and coffee processing areas in Kodaikanal, Tamil Nadu, India. These samples were kept in a pre-sterilized zip-lock cover and stored in a refrigerator. One gm soil sample was added to 50ml of Glycerol Enriched Medium (GEM) and incubated in shaker incubator 30ºC for 24 hrs at 120 rpm for enrichment of oleaginous yeast (Pan *et al*., 2009). 1 ml of enriched yeast culture was serially diluted from 10^{-1} to 10^{-5}, 0.1 ml of the diluted samples were inoculated in GYEP medium by spread plate method. The plates were then incubated for 48 hrs at 30º C (Atlas, 2010).

2.2. Screening of yeast

The morphology of the isolated yeast was studied by the wet mount technique. The Sudan red III (2 g in 100 ml of isopropanol) staining was done to qualitatively analyze the presence of lipids in the isolated yeast colonies. The yellow intracellular inclusions confirm the presence of lipids in the isolates (Jiru *et al*., 2016). Those isolates of yeasts which were confirmed for the presence of lipids were selected for further process. The selected yeast isolates were sub-cultured using GYEP for further use. The pre-culture of the yeast isolates was prepared by adding one loop of culture to 50 ml of GYEP broth and incubated for 48 hrs at 30ºC. 1 ml of pre-culture was transferred to 50 ml inoculation medium containing GYEP broth and incubated at 30ºC for 5 days in an incubator shaker.

2.3. Extraction of lipid from yeast sample

Modified Bligh and Dyer method was adopted for extracting lipid from the yeast culture. In this method, centrifugation of 50 ml of yeast sample was carried out for 5 min at 5000 rpm. The pellet was washed two times with 50 ml of distilled water and to the washed pellet 10 ml of 4 M HCl was added. The mixture was incubated at 60ºC for 1-2 hrs for acid hydrolysis. After hydrolysis, the content was incubated at room temperature for 2-3 hrs with the addition of 20 ml of chloroform/methanol mixture (1:1). Then, the aqueous upper phase and organic lower phase of the mixture was separated by centrifugation at 2000 rpm for 5 min and the lipid in the lower phase was stored for further analysis (CastanhaI *et al*., 2013).

2.4. Estimation of wet biomass, glucose utilized and lipid from yeast

The wet biomass of yeast was estimated at the various time periods of 24, 48, 72, 96 and 120 hrs. 5ml of culture was centrifuged at 5000 rpm for 5 min and the pellet obtained was weighed to know the wet biomass. The supernatant was used for estimation of concentration of glucose utilized by the biomass by Dinitro Salicylic Acid (DNS) method. In the estimation of lipid, 2 ml of concentrated sulfuric acid was added to the known volume of the sample and heated at 100ºC for 10min. The sample was allowed to cool for 5min in an ice bath and incubated for 15min at 37ºC with the addition of 5 ml of freshly prepared phospho-vanillin reagent was added to it and was incubated for 15min at 37ºC. The absorbance was read at 540nm in a UV spectrophotometer (Cheng *et al.,* 2011).

2.5. Molecular identification of yeast

The potentially important yeast strain was selected and the culture was inoculated on PD broth and incubated at 30ºC for 24 hrs. Twenty-four hours old yeast culture was used for DNA extraction by silica column-based method (Santos *et al*., 2010). The intergenic spacer regions (ITS) of DNA was amplified using the primers ITS1 (5'TCCGTAGGTGAACCTGCGG'3) and ITS4 (5'TCCTCCGCTTATTGATATGC'3) adopting the procedure described by Williams *et al.,* (1995). The optimum PCR cycle conditions, a reaction volume of 25 µL containing 12 µL of 2X Master mix1.5 µL of Forward prime (ITS1) and Reverse primer (ITS2), 5µL of deionized water and 5µL of isolated DNA as template were used. The reaction mixtures were subjected to 30 cycles performed in a thermocycler (Eppendorf, USA) of the following incubation: Denaturation at 94ºC for 5 min, initial denaturation at 94 ºC for 30 sec, annealing 50 ºC for 60 sec, and extension for 72 ºC for 1 min and final extension at 72 ºC for 10 min (Ali and Latif, 2016). The PCR products were purified and sequenced using an ABI 3730xl sequencer (Applied Biosystems). The sequence was analyzed with the NCBI BLAST online tool used to confirm the organism, for getting accession number, the sequence was sent to GenBank. The query sequences and 19 related sequences from the GenBank (NCBI) database were aligned and phylogenetic analyses were done using MEGA 11 version. The phylogenetic relationship of the Oleaginous Yeast strain is displayed in a distance based Neighbor-Joining tree.

2.6. Separation of phospholipid

The extracted lipids were dissolved in 30ml of hexane, the flask was kept in an ice bath, and to this 60ml of cold acetone was added with continuous stirring. The phospholipids get precipitated, and the supernatant was discarded. Following precipitation of phospholipid, the supernatant was discarded. Further, ice cold acetone was used to wash the precipitate (Gladkowsi *et al.,* 2012)

2.7. FTIR conformation of lipid and phospholipids

The sample was subjected to FTIR spectroscopic analysis (IR-Affinity 1S, Shimadzu). The lipid and phospholipids samples were dissolved in methanol for analysis. Then the sample was subjected to FTIR analysis in the range of 4,000–400 cm^{-1} in FTIR spectroscopy with 1 cm^{-1} resolution of (Ami *et al.,* 2014).

2.8. Synthesis of liposome

Solvent injection method involves injection of methanol-lipid solutions into warmed aqueous phases (1M Tris buffer or water). The methanol vaporizes upon contacting the aqueous phase, and the dispersed lipid forms liposomes (Laouini, 2012).

2.9. Liposome characterization

2.9.1. Size analysis

Atomic force microscopy (AFM) was used to measure the size of newly synthesized liposomes. This sample was mounted as a thin film on a coverslip to analyse its size according to Laouini, 2011. The topography analysis was done at 50µm.

2.9.2. Phospholipids analysis

Phospholipids separations were carried out using a HPLC system (Agilent- infinity 1260, Agilent Technologies, India). Spherical silica particles of 5 µm bearing 80 Å pores packed in stainless-steel Beckman Ultra sphere SI 250 mm × 4.6 mm ID analytical column was used for the separation of phospholipids. Acetonitrile methanol 85% phosphoric acid (100:10:1.8, v/v/v) was applied for the isocratic separation of phospholipids, with 1.5ml/min, 75ba and 25°C as flow rate, pressure and temperature of the mobile phase respectively. The detector wavelength was fixed as 205 nm for getting the eluting peaks with greater sensitivity. Prior to pumping, the mobile solvent was subjected to ultrasonic bath for degassing. The phospholipid sample in the chloroform-methanol mixture was dried under a stream of nitrogen gas. The residue obtained was dissolved in n-hexane and 2-propanol (3:1, v/v) solvent mixture for analysis at 205nm with retention time of 20 mins.

2.9.3. Efficiency of entrapment

The liposomal formulations were centrifuged at 11000rpm for 30 min to segregate entrapped and free drugs. The supernatant after appropriate dilution was analyzed by UV-visible spectrophotometer (UV-1800, Shimadzu) to determine the quantity of free drugs. The entrapped drugs in the liposome was also determined by UV-visible spectrophotometer after redispersal of the pellet in chloroform. The procedure described by Srilatha *et al*. (2021) was adopted to calculate the encapsulation efficiency.

3. Results and Discussion

3.1. Isolation of Oleaginous yeasts and its screening

The collected soil samples were enriched with glycerol enriched medium and grown GYEP medium, which facilitates the oleaginous yeast to accumulate lipids as it is the sole carbon source and a lipid analogue, (Papanikolaou and Aggelis, 2011); and four oleaginous yeast isolates, named as OY1, OY2, OY3 and OY4, were obtained. Similar to the present isolation, Pan *et al*., 2009, Amaretti *et al*., 2010 have obtained oleaginous yeasts from different natural ecosystems like soil, water and flower surfaces. Many studies reported that the carbon excess and nitrogen-limited medium are suitable for the isolation of oleaginous yeasts (Schulze *et al*., 2014). The use of GYEP medium in the present experiment as a carbon excess and nitrogen-limited medium, resulted in the isolation of oleaginous yeasts. Glucose, as simple sugar, can be readily utilized by the yeast isolates than other sugars such as xylose. The xylose will not be completely utilized by the isolates, as reported by Pan *et al.* (2009). The morphologically different isolates OY1, OY2, OY3 and OY4 were identified as spherical, round, elongated rods and disc-shaped cells by wet mount technique. The isolates OY1, OY2, OY3 and OY4 were screened for the presence of lipids using the Sudan red III dye. The yellow intracellular inclusions were observed in the isolates. The Sudan red III dye stains the lipid yellow (Jiru *et al*., 2016). The yellow intracellular inclusions confirmed the presence of lipids in the yeast isolates. All four isolates OY1, OY2, OY3 and OY4 showed a positive result and they were selected for the estimation process.

3.2. Estimation of biomass, utilization of glucose and production of lipid

The biomass, glucose utilization and lipid production by the isolates were estimated at different time intervals viz., 24, 48, 72, 96 and 120 hrs (Table 1). The strain OY3 showed increased glucose utilization increase in biomass. After the exhaustion of nutrients, the biomass decreased and the lipid accumulation increased up to 3.9 U/ml at 96 hrs of incubation, whereas the other isolates OY1, OY2, OY4 have not utilized glucose completely, which lead to poor lipid accumulation. Hu *et al.* (2011) reported that the oleaginous yeast utilized glucose and xylose and yielded 0.17g and 0.15g of lipid/g of glucose and of xylose, respectively.

Table 1. Estimation of biomass, glucose and lipid

Incubation time (hrs)	Isolate No.	Biomass (U/ml)	Glucose (U/ml)	Lipid (U/ml)
24	OY-1	0.11	4.3	0.31
	OY-2	0.18	1.7	0.62
	OY-3	0.06	13.01	0.2
	OY-4	0.1	13.02	0.06
48	OY-1	0.12	1.8	0.02
	OY-2	0.14	1.6	0.21
	OY-3	0.13	3.21	0.21
	OY-4	0.11	3.14	0.1
72	OY-1	0.41	1.93	0.59
	OY-2	0.49	1.92	0.56
	OY-3	0.58	1.87	0.96
	OY-4	0.53	2.44	1.06
96	OY-1	0.46	2.91	1.33
	OY-2	0.43	4.27	2.36
	OY-3	0.52	1.57	3.9
	OY-4	0.53	2.7	3.2
120	OY-1	0.41	2.94	0.75
	OY-2	0.36	2.11	1.06
	OY-3	0.43	2.86	2.97
	OY-4	0.37	2.85	3.07

*Glucose standard, Y= 4.061x-0.094, R^2= 0.957
*Lipid standard, Y=3.58x-0.019, R^2= 0.954

3.3. Molecular identification by 18s rRNA sequencing:

The NCBI BLAST similarity search results showed 98% of identity and the sequence was submitted in GenBank (Accession number: MH424455). The OY3 was identified as *Candida tropicalis* by 18s rRNA sequencing using the ITS1 and ITS4 primers. Further, the sequences obtained from this study and that of closely related sequences from GenBank are displayed in Figure 1.

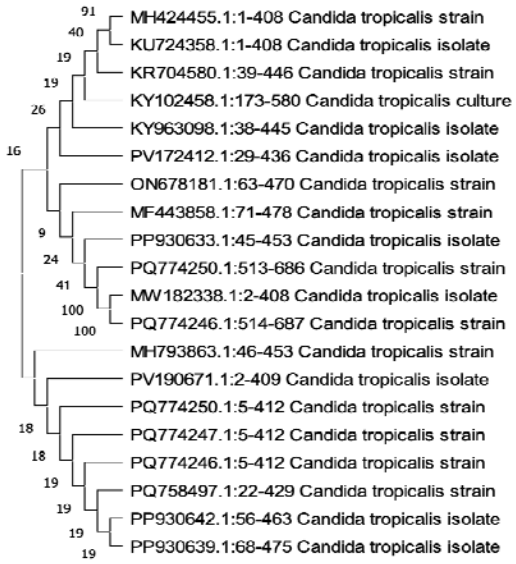

Figure 1. Phylogenetic tree of the isolate OY-3 (MH424455 *Candida tropicalis)*

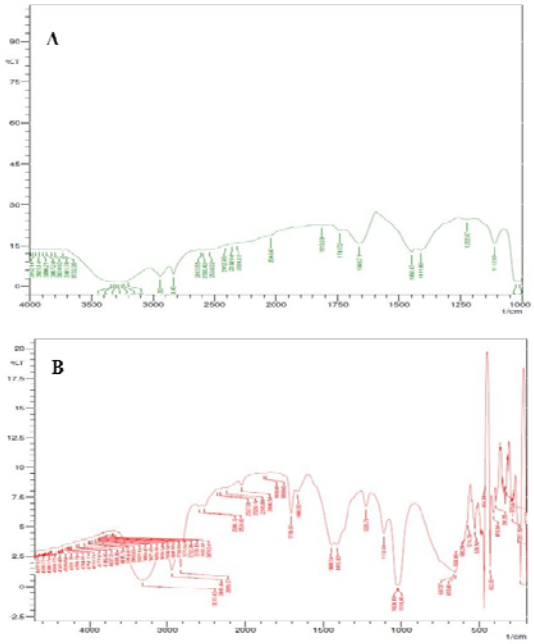

Figure 2. FTIR spectra of lipids (A) and phospholipids (B).

3.4. Liposome characterization:

3.4.1. .Size analysis

The size of the liposome of *Candida tropicalis* at 50µm topography was about 78.7nm (Figure 3). The liposomes synthesized by solvent injection method had an encapsulation efficiency of 20-40%, with the vesicles measuring up to 50-100nm. The encapsulation efficiency of the liposomes is based on their size, which makes them more suitable for pharmaceutical applications (Nsairat *et al*., 2022).

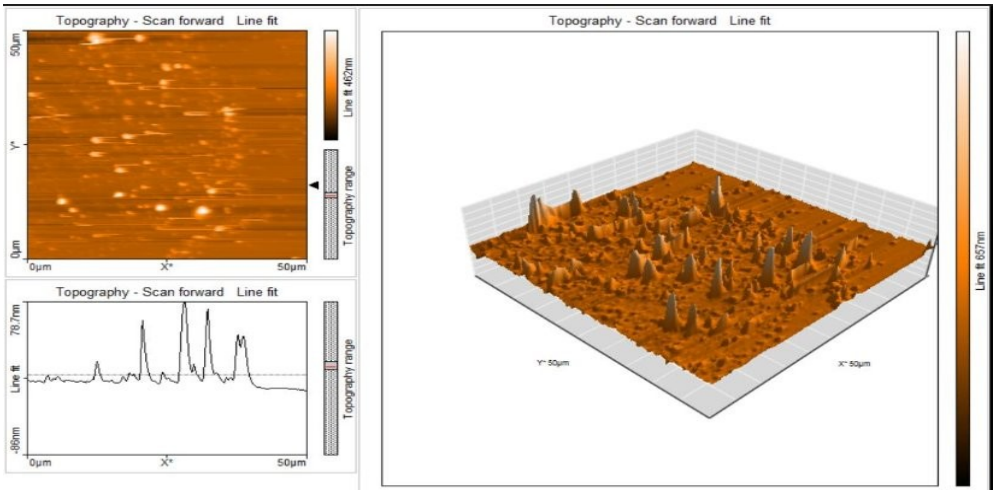

Figure 3. Liposome topography of *Candida tropicalis*

3.4.2. Phospholipids analysis

The peaks obtained at a retention time of 20 min indicated the presence of phospholipids. The phosphatidylcholine and phosphatidylethanolamine present in the samples were 0.44% and 0.15% indicated by the area of the peak obtained. The chromatogram developed by HPLC analysis indicates the presence of phosphatidylcholine (0.44%) and ethanolamine (0.15%) through the presence of peak at the retention time of 10.720 and 11.847 minutes. The traces of other lipids such as phosphatidylguanine (Rt 9.187 mins), phosphatidylinositol (Rt14.493 mins), phosphatidic acid (Rt 17.147 mins) were also found (Figure 4). The traces of other lipids may be due to improper temperature

conditions maintained during precipitation procedures (Aisha *et al*., 2014).

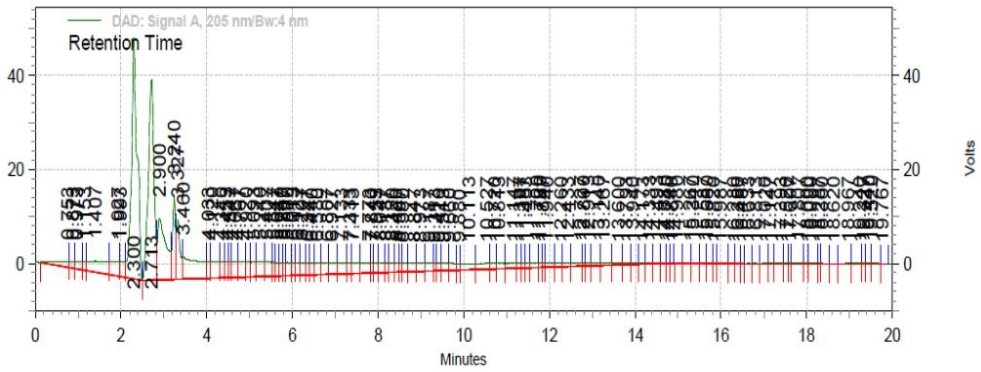

Figure 4. HPLC chromatogram of phospholipids

3.4.3. Encapsulation Efficiency

The PDE for the yeast liposome was determined by UV-visible spectroscopy using the drug ciprofloxacin at 600nm and the results are given in Table 2. The PDE for the liposome was 40.9% for ciprofloxacin. The encapsulation efficiency of liposomes synthesized by solvent injection method ranges up to 30-50%. The use of solvents like ethanol may increase the efficiency up to 49% (Ong *et al*., 2016). The study by Fan *et al.* (2008) reveals that the encapsulation efficiency of liposomes ranges from 20-40% when synthesized by ethanol injection method which is in corroboration with our results.

Table 2. Determination of PDE using UV-Vis spectroscopy

CONTENT	OD VALUE (nm)	CONCENTRATION (U/ml)
Pellet	0.009	0.000153
Supernatant	0.013	0.000221

*Ciprofloxacine standard, Y=0.017*0.000, R^2=0.964

3.4.4. Lipid and phospholipids confirmation by FTIR

The lipid and phospholipids were confirmed by the presence of functional groups using FTIR. The lipid and phospholipids extracted were confirmed by the appearance of peaks at the wave numbers of 1200-1000cm^{-1} and 1740cm^{-1} respectively (Figure 2). The peaks related to C-H stretching vibrations, C = O and C-O-C stretching in esters, CH_2, C-O-C bending and CH_2 rocking (Fan *et al*., 2008) were used to identify lipid content of the fungal biomass.

4. Conclusion

Liposomes are amphibilic carriers with high biocompatibility, degradability and low immunogenicity and allow modifications with diverse functional properties. These properties authorize them as potential agent for various clinical and pharmaceutical applications especially in drug delivery. The present study emphasizes *Candida tropicalis* as a prospective candidate for the production of liposomes.

References

Aisha AF, Majid AM and Ismail Z. 2014. Preparation and characterization of nanoliposomes of *Orthosiphon stamens* ethanolic extract in soybean phospholipids. *BMC Biotechnol.,* **14(23):** 1-11. https://doi.org/10.1186/1472-6750-14-23

Alavi M, Karimi N and Safaei M. 2017. Application of various types of liposomes in drug delivery systems. *Adv Pharm Bull.* **7:** 3-9.

Ali MS and Latif Z. 2016. Molecular characterization of yeast strains isolated from different sources by Restriction Fragment Length Polymorphism. *Pak J Bot.,* **48(1)**: 363-370.

Amaretti A, Raimondi S, Sala M, Roncaglia L, de Lucia M, Leonardi A and Rossi M. 2010. Single cell oils of the cold-adapted oleaginous yeast *Rhodotorula glacialis* DBVPG 4785. *Microb Cell Factories.* 9.

Ameri M, Moghimipour E, Ramezani Z, Kargar M, Hashemitabar M, Saremy S and Handali S. 2016. Formulation of a New Generation of Liposomes from Bacterial and Archeal Lipids. *Trop J Pharm Res.,* **15 (2):** 215-220.

Ami D, Posteri R, Merghetti P, Porro D, Doglia SM and Branduardi P. 2014. FTIR spectroscopy as a method to study lipid accumulation in oleaginous yeasts. *Biotechnol Biofuels.*, **7(12):**1-14.

Atlas RM. 2010. **Handbook of microbiological media**, 4th edition, CRC press, USA, 1923-1943

Beligon V, Christophe G, Fontanille P and Larroche C. 2016. Microbial lipids as potential source to food supplements. *Curr Opin Food Sci.*, **7:** 35-42.

Carsanba E, Papanikolaou S and Erten H. 2018. Production of oils and fats by oleaginous microorganisms with an emphasis given to the potential of the nonconventional yeast *Yarrowia lipolytica*, *Crit Rev Biotechnol.*, **38(8)**:1230-1243. https://doi.org/10.1080/07388551.2018.1472065

Castanhal RF, de Morais LAS, Moriano AP and Monteiro RTR. 2013. Comparison of two lipid extraction methods produced by yeast in cheese whey. *Braz Arch Biol Technol.,* **56(4)**: 629-636.

Chen C and Wang JL. 2007. Characteristics of Zn^{2+} biosorption by *Saccharomyces cerevisiae*. *Biomed Environ Sci.,* **20**: 478-482.

Cheng YS, Zheng Y and Vandergheynst JS. 2011. Rapid quantitative analysis of lipids using a colorimetric method in a microplate format. *Lipids* **46**: 95-103.

Dua JS, Rana AC and Bhandari AK. 2012. Liposome: methods of preparation and applications. *Int J Pharm Stud Res.,* **3(2)**: 14-20.

Fan M, Xu S, Xia S and Zhang X. 2008. Preparation of salidroside nano-liposomes by ethanol injection method and in vitro release

study. *Eur. Food. Res. Technol.* **227:** 167–174. https://doi.org/10.1007/s00217-007-0706-9

Forfang K, Zimmermann B, Kosa G, Kohler A and Shapaval V. 2017. FTIR spectroscopy for evaluation and monitoring of lipid extraction efficiency for oleaginous fungi. *Plos one* **12(1)**: 1-17.

Gładkowski W, Chojnacka A, Kiełbowicz G, Trziszka T and Wawrzenczyk C. 2012. Isolation of Pure Phospholipid Fraction from Egg Yolk. J Am Oil Chem Soc., **89**: 179-182.

Hu C, Wu S, Wang Q, Jin G, Shen H and Zhao ZK. 2011. Simultaneous utilization of glucose and xylose for lipid production by *Trichosporon cutaneum*. *Biotechnol Biofuels.,* **4(25)**: 25. https://doi.org/10.1186/1754–6834–4-25

Jiru TM, Abate D, Kiggundu N. Phil G and Groenewald M.. 2016. Oleaginous yeasts from Ethiopia. *AMB Expr*., **6**: 78. https://doi.org/10.1186/s13568-016-0242-8

Lamers, D., van Biezen, N., Martens, D. et al. 2016. Selection of oleaginous yeasts for fatty acid production. BMC Biotechnol., **16**:45. https://doi.org/10.1186/s12896-016-0276-7

Laouini A, Jaafar-Maalej C, Limayem-Blouza I, Sfar S, Charcosset C and Fessi H. 2012. Preparation, characterization and applications of liposomes: State. *Art J Colloid Sci.,* **1**: 147–168.

Li J, Wang X, Zhang T, Wang C, Huang Z, Luo X and Deng Y. 2015. A review on phospholipids and their main applications in drug delivery systems. *Asian J Pharm Sci* **10 (2)**: 81–98.

Liu P, Chen G, Zhang J. 2022. A Review of Liposomes as a Drug Delivery System: Current Status of Approved Products, Regulatory Environments, and Future Perspectives. Molecules. **27(4)**:1372. https://doi.org/10.3390/molecules27041372 PMID: 35209162.

Makhlouf Z, Ali AA and Al-Sayah MH. 2023. Liposomes-Based Drug Delivery Systems of Anti-Biofilm Agents to Combat Bacterial Biofilm Formation. *Antibiotics*. **12(5)**: 875.

Marek Kieliszek, AnnaM. Kot, Anna BzduchaWróbel, Stanisław BŁażejak, Iwona Gientka, Agnieszka Kurcz, 2017. Biotechnological use of Candida yeasts in the food industry: A review, *Fungal Biology Reviews*. **31(4)**: 185-198.

Morata A and Loira I. 2017. **Yeast – Industrial Applications.** InTech Pub., Croatia.

Nsairat H, Khater D, Sayed U, Odeh F, Al Bawab A and Alshaer W. 2022. Liposomes: structure, composition, types, and clinical applications. *Heliyon* **8(5)**: e09394. https://doi.org/10.1016/j.heliyon.2022.e09394.

Ong SGM, Ming LC, Lee KS and Yuen KH. 2016. Influence of the Encapsulation Efficiency and Size of Liposome on the Oral Bioavailability of Griseofulvin-Loaded Liposomes. *Pharmaceutics* **8(3)**: 25. https://doi.org/10.3390/pharmaceutics8030025

Pan L, Yang D, Shao L, Li W, Chen G and Liang Z. 2009. Isolation of the oleaginous yeasts from the soil and studies of their lipid-producing capacities. *Food Techn Biotech*., **47 (2)**: 215-220.

Papanikolaou S and Aggelis G. 2011. Lipids of Oleaginous Yeasts. Part I: Biochemistry of Single Cell Oil Production. *Eur J Lipid Sci Technol.* **113**: 1031-1051.

Rodrigues M, Rosa A, Almeida A, Rui Martins, Ribeiro T, Pintado M, Gonçalves RFS, Pinheiro AC, Fonseca AJM, Maia MRG, Cabrita ARJ, Barros L and Caleja C. 2024. Omega-3 fatty acids from fish by-products: Innovative extraction and application in food and feed. *Food Bioprod Proces.,* **145**: 32-41.

Santos MS, Souza ES, Junior RMS, Talhari S and Souza JVB. 2010. Identification of fungemia agents using the polymerase chain reaction and restriction fragment length polymorphism analysis. *Braz J Med Biol Res* **43:** 712-716.

Schulze I, Hansen S, Großhans S, Rudszuck T, Ochsenreither K, Syldatk C and Neumann A. 2014. Characterization of newly isolated oleaginous yeasts - *Cryptococcus podzolicus*, *Trichosporon porosum* and *Pichia segobiensis*. *AMB Expr.,* **4**- 24. https://doi.org/10.1186/s13568-014-0024-0

Srilatha T, Umashankar K, Reddy PJ and Srikar N. 2012. Synthesis, screening and nanotechnology based in vivo drug delivery of curcumin and its analogues. *Asian J Pharm Sci Technol.,* **2(2)**: 62-87.

Sundarsingh TJA, Ameen F, Ranjitha J, Raghavan S, Vijayalakshmi S. 2024. Engineering microbes for sustainable biofuel production and extraction of lipids-Current research and future perspectives. *Fuel* **355**: 129532, https://doi.org/10.1016/j.fuel.2023.129532

Zhou YJ, Buijs NA, Zhu Z, Qin J, Siewers V and Nielsen J. 2016. Production of fatty acid-derived oleochemicals and biofuels by synthetic yeast cell factories. *Nat Commun.,* **25:** 7:11709.

JJBS

Volume 18, Number 3,September 2025
ISSN 1995-6673
Pages 509 – 520

Jordan Journal of Biological Sciences

Comparative Metabolomics Studies Related to Lipid Biosynthesis Indicate Metabolic Pathways Regulation Differences in Mature and Young Seeds (MYS) of *Jatropha curcas*

Eko Setiawan[1], Miftahul Huda Fendiyanto[2, *], Ifan Rizky Kurniyanto[3], Mentari Putri Pratami[4, 2]

[1]*Natural Resource Management, Faculty of Agriculture, Universitas Trunojoyo Madura (UTM), Bangkalan Regency 69162, East Java, Indonesia;* [2]*Department of Biology, Faculty of Military Mathematics and Natural Sciences, Indonesia Defense University (Universitas Pertahanan RI), Komplek Indonesia Peace and Security Center (IPSC) Sentul, Bogor 16810, Indonesia;* [3]*Department of Agribusiness, Faculty of Agriculture, Universitas Trunojoyo Madura(UTM), Bangkalan Regency 69162, East Java, Indonesia;* [4]*National Research and Innovation Agency of Indonesia (BRIN), KST. Soekarno, Jalan Raya Jakarta-Bogor Km. 46, Cibinong 16911, Indonesia*

Received: October 22, 2024; Revised: March 11, 2025; Accepted: April 6, 2025

Abstract

Jatropha curcas is an alternative bioenergy source that can be developed as a solution to the global energy crisis. This plant represents a promising new alternative energy source. This study aims to conduct a comparative study of the characteristics of metabolites in mature (MS) and young (YS) seeds in *Jatropha* plants through metabolomic studies. Six samples of *Jatropha curcas* seeds (accessions) were used, grown by the cutting method using a completely randomized block design (CRBD) using three replications, and the seed harvesting process was carried out according to the type of development (MS and YS). Seed extraction was tested using the GC-MS method. A total of 25 different metabolites, 19 which of metabolites were highly expressed in mature seeds of *Jatropha curcas*. In contrast, there were only 6 metabolites that were highly expressed in young seeds. In general, the four metabolites that have the highest correlation (strong positive intercorrelation) are the intercorrelation of the metabolites Eicosadienoic acid, Tetracosahexane, Sitosterol, and Aminoethanethiol. Based on the PLS-DA study, the metabolites showed that three MS accessions grouped and were separated from three YS accessions with a total PC value of 91.1%. 24 compounds had the highest impact value on the galactose metabolism pathway. The detected metabolic pathways included the pentose phosphate pathway, pentose and glucuronate interconversions, and amino sugar or nucleotide metabolism. Other relatively significant metabolite pathways that could distinguish between the two types of MS and YS seeds were sesquiterpenoid and triterpenoid biosynthesis and steroid biosynthesis. Thus, mature and young seeds showed differences in the expression of metabolite content and these differences globally occurred in the galactose metabolism, triterpenoid, and steroid biosynthesis pathways. This research is expected to contribute to the study of the selection of the best seeds for lipid synthesis as a raw material for biofuel in *Jatropha curcas.*

Keywords: *Jatropha curcas*, metabolomics, pathway, mature seed (MS), young seed (YS)

1. Introduction

Jatropha curcas is a plant species classified under the class Magnoliopsida or dicotyledons, belonging to the order Malpighiales. This plant is part of the Euphorbiaceae family, a group of plants known for containing various bioactive chemical compounds (Makkar et al., 2008). Taxonomically, Jatropha curcas falls under the genus Jatropha, which includes multiple species with similar characteristics. Jatropha curcas is a perennial shrub or small tree that retains some of its foliage year-round and can grow beyond 6 meters in height (Janick and Paull, 2008; Fendiyanto et al., 2024).

Its remarkable ability to withstand extreme arid conditions allows it to thrive in desert environments. However, the plant contains phorbol esters, which are known to be toxic. Despite this, non-toxic, edible varieties native to Mexico exist and are locally referred to by names such as piñón manso, xuta, chuta, and aishte (Gunjan et al., 2016; Martínez-Herrera et al., 2010). Additionally, J. curcas contains other bioactive compounds, including trypsin inhibitors, phytate, saponins, and a specific type of lectin called curcin (Valdes-Rodríguez et al., 2013). Its seeds have an oil content ranging from 27% to 40% (average 34.4%) (Martínez-Herrera et al., 2012), which can be refined into high-quality biodiesel suitable for use in standard diesel engines (Lin et al., 2010). As a plant capable of withstanding dry conditions, Jatropha curcas is widely utilized for various purposes, including as a source of biodiesel (Fendiyanto et al., 2024).

The utilization of oil-producing plants such as Jatropha curcas to produce alternative energy sources and promote environmental sustainability, as well as to create an energy-independent region, is one of the objectives of developing new energy materials, especially liquid fuels.

* Corresponding author. e-mail: miftahul.fendiyanto@idu.ac.id.

Jatropha is one of the plants that can be utilized by major non-edible oil producers (Openshaw, 2000; Sato et al., 2011). The potential of Jatropha can replace other crops. In addition to having a high level of adaptation to the environment, this plant has many advantages over other edible oil-producing plants such as being resistant to pests, relatively fast growth, and being able to be planted on marginal land that has little soil nutrition (Openshaw 2000; Maes et al., 2009; Mishra, 2009).

Jatropha plants start producing seeds within their first year, but it usually takes about 2 to 3 years for them to reach substantial yields. In the beginning, farmers can expect around 0.4 tons of seeds per hectare, but as the plant matures, this can increase to over 5 tons per hectare by the third year. On average, under moderate soil conditions, jatropha produces about 3.5 tons of seeds per hectare. This translates to roughly 1,590 kilograms of oil per hectare annually, or about 1,892 liters of oil per hectare, making it a promising option for biodiesel production (Valdes-Rodríguez et al., 2013). High adaptability to less fertile environments makes J. curcas an alternative solution to overcome the problem of land shortages due to agricultural land conversion in Indonesia. Based on the category of land suitability of J. curcas, from the total land area of 49.53 million ha, there are 29.72 million ha, or 60% of marginal land that is suitable but has not been utilized efficiently (Fendiyanto et al., 2024). An environmentally friendly fuel called biofuel can be a solution to frequent environmental problems (Fendiyanto et al., 2024). Compared to fossil fuels, biofuels have relatively lower levels of gas emissions in the form of CO and unburned hydrocarbons (CH)n, and can be a solution to global problems as a result of the use of fossil fuels. Unlike non-renewable fossil fuels, J.curcas can be categorized as an alternative renewable bioenergy resource, i.e., edible oil, non-edible oil, and lignocellulosic biomass (Maes et al., 2009). The development of bioenergy resources can be an alternative solution to the problem of the energy crisis in the world, so it is very important to conduct a study of its development.

Although Jatropha curcas has been widely studied as a biodiesel source, there are still many unanswered questions regarding the biochemical and metabolic differences between its young and mature seeds (Fendiyanto et al., 2024). One key area that needs further investigation is how lipid biosynthesis changes throughout seed development. While mature seeds are known to have a high oil content (27–40%), the metabolic processes responsible for this accumulation are not yet fully understood, especially in comparison to young seeds. Exploring these differences could provide valuable insights into the regulatory mechanisms that drive lipid production, potentially leading to improved oil yields through genetic advancements or better farming practices.

Metabolomics provides a powerful tool for unraveling the biochemical pathways involved in lipid biosynthesis in Jatropha curcas. By analyzing the metabolites present in both young and mature seeds, scientists can identify key compounds and regulatory factors that influence fatty acid and triacylglycerol (TAG) production (Fendiyanto et al., 2024). For example, shifts in carbohydrate metabolism, amino acid composition, and hormone activity could indicate how metabolic priorities change as the seed matures, transitioning from early growth to oil storage (Fendiyanto et al., 2024). Moreover, combining metabolomics with transcriptomics and proteomics could create a more detailed picture of how genes, enzymes, and metabolites interact to regulate lipid production.

A deeper understanding of how lipid metabolism differs between young and mature Jatropha curcas seeds could pave the way for strategies to boost oil production, enhance biodiesel quality, and refine cultivation techniques. Addressing these knowledge gaps would help researchers identify key metabolic limitations and develop Jatropha varieties with higher oil content and better adaptability to diverse environmental conditions. Thus, this study aimed to conduct a comprehensive study to characterize the potential of the oil plant (Jatropha curcas) as a renewable bioenergy source through a metabolomic approach.

2. Materials and Methods

2.1. Plant materials

Plant materials used in this research were the young and mature seeds of Jatropha curcas. Comparative study of J. curcas that was at least 2 years old, cuttings in polybags with 12 experimental units and grouped into two types of treatments, namely mature seed type (MS) and young seed type (YS) using a completely randomized block design (RCBD). We conducted the study three times a year, across three different periods. In addition, J. curcas from existing land or gardens were also used in this study, especially for metabolomic testing. The growth and development of J. curcas potential were performed by the following Fendiyanto et al., (2024). In addition, J. curcas harvesting in this study was carried out when the fruit was ripe and the fruit turned yellow for mature seed (MS) samples, which were 5-6 months old, while the fruit was green for young seeds (YS), which were 1-2 months old after flowering. Seed collection was carried out by cutting and then the sample was soaked in liquid nitrogen.

2.2. Metabolites extraction and identification

GC-MS study of J. curcas seeds was carried out to identify chemical components using a modified method from Fendiyanto et al., (2024). In the initial stage, 10 grams of seeds were extracted using ethyl acetate solvent at a temperature of 25°C for 1 hour, where the solution was continuously stirred with a shaker at a speed of 50 rpm. The mixture obtained was then evaporated for 60 mins with an evaporator (Caliper-Life-Science, USA), and then injected into the GC-MS instrument. The GC-MS system used includes a main unit (Agilent Tech-Palo Alto-USA), an auto-sampler (Agilent Tech-Palo Alto-USA), and a mass selective detector (inert MSD Detector, Agilent Tech-Palo Alto-USA) (Fendiyanto et al., 2021).

We performed GC-MS Column Specifications, particularly column Type Capillary column (Agilent HP-5MS), Column Dimensions in 30 m × 0.25 mm ID × 0.25 µm film thickness, Stationary Phase in 5% Phenyl / 95% Dimethylpolysiloxane. In addition, we used temperature gradient (oven program), i.e. initial temperature in 50°C, hold for 1–2 min, Ramp in 10–15°C/min to 250–300°C, and Final temperature in hold for 5–10 min. We conducted Ionization Parameters (MS Conditions) particularly Ionization Mode in Electron Ionization (EI), Ionization Energy in 70 eV, Mass Scan Range in 50–600 m/z,

Detector Voltage in Optimized based on instrument specifications, Source Temperature in 230–250°C, and Quadrupole Temperature in ~150°C. The final stage of this analysis includes mass spectrum detection and metabolite identification, which is performed by referring to the operational procedures of Fendiyanto et al., (2020). Thus, this method is expected to optimize the detection of chemical compounds in J. curcas seed samples.

2.3. Comparative Fold Change Study and Data Analysis

Metabolomics data were analyzed using MetaboAnalyst.R (Xia and Wishart, 2016) with a fold change approach. The settings used in the analysis included the analysis type 'unpaired', the fold change threshold '2', the comparison type 'Mature/Young', and the significance threshold of '85%'. Furthermore, the correlation between metabolites was analyzed using the 'feature' dimension setting with the 'Spearman rank correlation' distance measure. The display mode was set as 'overview', with red/green color contrast, without fixed color distribution, and without clustering. For heatmap analysis, the distance was measured using the 'Euclidean' method, the 'single' clustering algorithm, and standardization using the autoscale feature, with normalized data sources. The selected display mode was 'overview with T-test/ANOVA' without additional display options. Then, all metabolites were compared with the KEGG, HMDB (Wishart et al., 2018), and PubChem databases based on the adapted guidelines from Fendiyanto et al., (2020). Further analysis was carried out using univariate and multivariate data (Fendiyanto et al., 2019a; Fendiyanto et al., 2019b; Satrio et al., 2019) with R (Lander, 2014) and MetaboAnalystR (Chong et al., 2018; Chong and Xia, 2018; Chong et al., 2019; Pang et al., 2020). In addition, morphological identification (Sunil et al., 2013) of potential J. curcas was done by direct observation following Fendiyanto et al., (2024).

3. Results

3.1. Comparative study of metabolites in mature and young seeds of Jatropha curcas

Metabolite content in mature and young seeds showed differences in metabolite content expression. Twenty-five metabolites were detected, with 19 showing high expression in mature J. curcas seeds. In contrast, there were only 6 metabolites that were highly expressed in young seeds (Figure 1, Table 1). The compounds that were highly expressed in mature seeds included butanoic acid, benzene acetaldehyde, hexahydro, germa-cyclo pentane, benzodioxane, 3 oxobutyric acid, pyrazol, galactose, and others. The compounds that were highly expressed in young seeds included hexadecenoic acid, eicosadienoic acid, tetracohexane, sitosterol, amino ethathiol, and octadecadiene (Figure 1). The tissue in mature seeds that had the highest significant metabolite expression was MS01 followed by MS02 and MS03. The highest metabolite expression in young seeds was YS01 followed by YS02, while accession YS03 had relatively low global lipid metabolite expression (Figure 1).

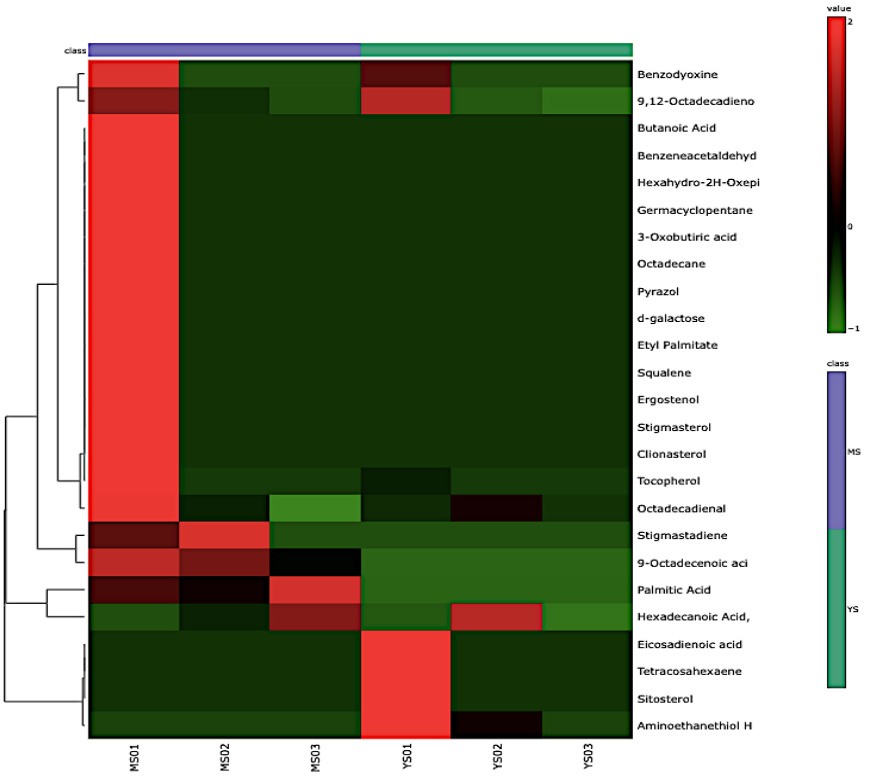

Figure 1. Differences in metabolite content in young and mature seeds of *Jatropha curcas*. There were 25 compounds detected significantly different by the gas chromatography-mass spectrophotometry (GC-MS) test. The heatmap comparison difference value ranged from -1 to 2. The class groups used were mature seed (MS, purple) and young seed (YS, green). MS01: mature seed repeat 1, MS02: mature seed repeat 2, MS03: mature seed repeat 3, YS01: young seed repeat 1, YS02: young seed repeat 2, YS03: young seed repeat 3.

Table 1. List of significant metabolite differences between mature seeds (MS) and young seeds (MS) of *Jatropha curcas*

Compound	HMDB	PubChem	KEGG
Benzeneacetaldehyde	HMDB0006236	998	C00601
Butanoic Acid	HMDB0000039	264	C00246
Hexahydro-2H-Oxepino	NA	NA	NA
Germacyclopentane	HMDB0031407	8452	C00557
Hexadecanoic Acid, Methyl hexanoate	HMDB0035238	7824	NA
3-Oxobutiric acid	HMDB0000005	58	C00109
Octadecane	HMDB0033721	11635	NA
Pyrazol	NA	NA	NA
d-galactose	HMDB0000143	439357	C00124
Ethyl Palmitate	HMDB0061709	164860	NA
Palmitic Acid	HMDB0000220	985	C00249
9,12-Octadecadienoic Acid (9z)	NA	NA	NA
Octadecadienal	HMDB0005047	5282796	C04056
Squalene	HMDB0000256	638072	C00751
9-Octadecenoic acid	HMDB0000207	445639	C00712
Tocopherol	HMDB0001492	92729	C02483
Benzodyoxine	HMDB0040528	4685450	NA
Ergosterol/Phytosterol	HMDB0000878	444679	C01694
Stigmasterol	HMDB0000937	5280794	C05442
Clionasterol	HMDB0000649	457801	C19654
Stigmastadiene	HMDB0000937	5280794	C05442
Aminoethanethiol Hydrogene Sulphate	NA	NA	NA
Tetracosahexaene	HMDB0000256	638072	C00751
Eicosadienoic acid	HMDB0005060	6439848	C16525
Sitosterol	HMDB0000649	457801	C19654

3.2. Correlation study between metabolites in two types of Jatropha curcas seeds

The content of metabolite compounds obtained from two types of J. curcas seeds showed three types of groups, namely: groups of compounds that have strong positive correlation values, compounds that have strong negative correlations, and compounds that have low correlations (Figure 2). In general, the four metabolites that have the highest correlation (strong positive intercorrelation) are the intercorrelation of the metabolites Eicosadienoic acid, Tetracosahexane, Sitosterol, and Aminoethathiol. The four compounds included in the strong negative correlation type group and have the most negative values are Aminoethanethiol-Octadecanoic acid, Benzodioxane-Hexadeconoic Acid, Aminoethanethiol-Palmitic acid, and Octadecenoic acid-Hexadeconoic Acid (Figure 2).

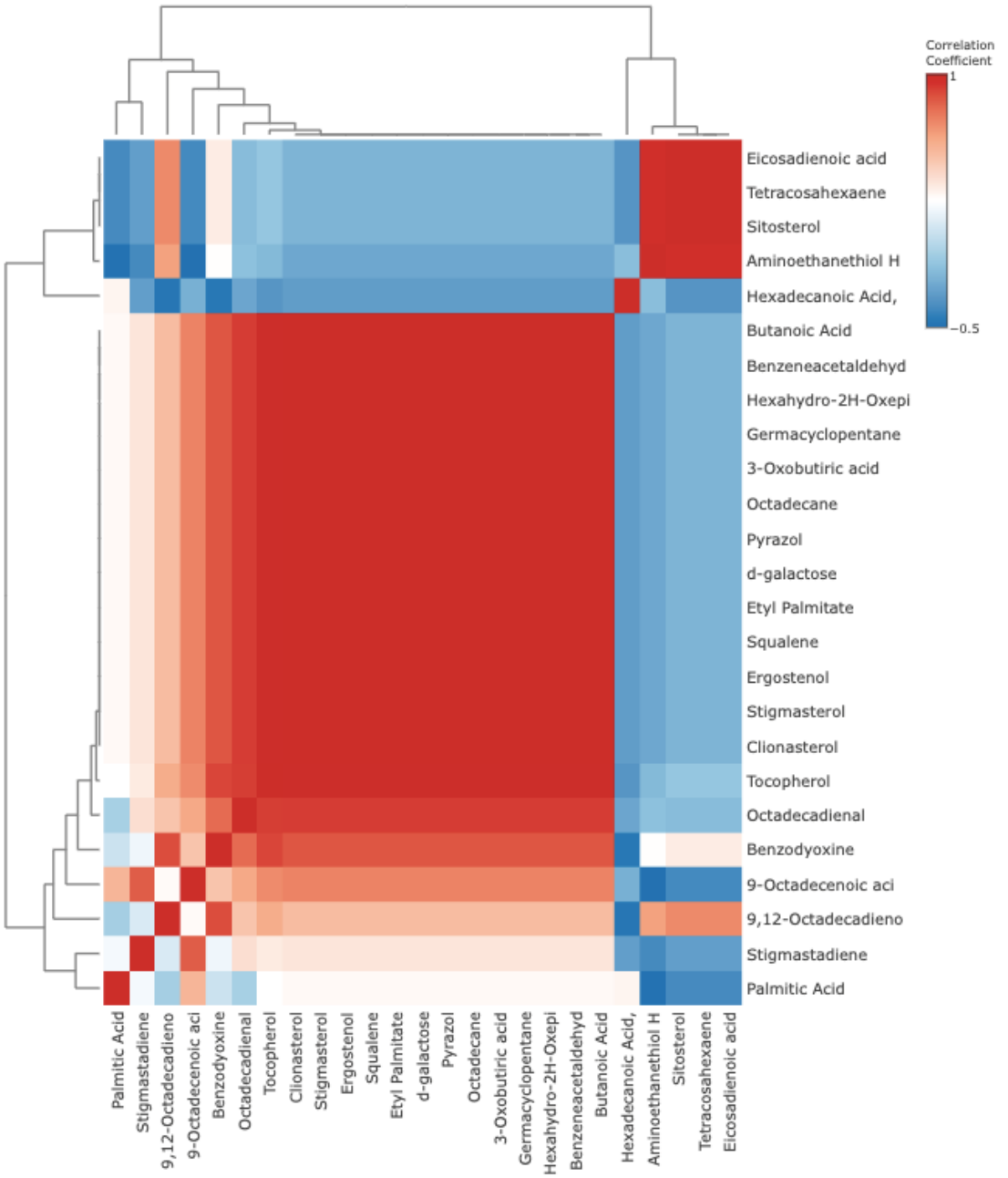

Figure 2. Correlation between metabolites in young and mature seeds of *Jatropha curcas*. Testing was done using correlation heatmap and statistical testing. Correlation values range from -1 to +1 with threshold values of (-0.5 and 1). The red color indicates a strong positive correlation value. The blue color indicates a strong negative correlation value. The white color indicates no correlation.

3.3. Metabolite profiles in two types of Jatropha curcas seeds

The metabolite profiles showed normal distribution based on a comparative study using multi boxplot (Figure 2A). The metabolite that showed a wide distribution was the compound 9,12-Octadecanoic acid, while the narrowest distribution was Eicosadinoic acid and Benzeneacetaldehyde (Figure 3A). Globally, the metabolite profiles in *Jatropha curcas* seeds showed a division into three clusters, namely types 1, 2, and 3. Based on a comparative study of the concentration between mature (MS) and young (YS) seeds, Cluster type 1 had a relatively moderate fluctuation value, cluster type 2 showed a relatively low value, while cluster type 3 showed a high value (Figure 3B). Based on the sensitivity study of the metabolite profile, the metabolites in both types of *J. curcas* seeds showed differences in Var.AUC and CI value groups were different and grouped into 6 types with specificity values from 0 to 1 (Figure 3C).

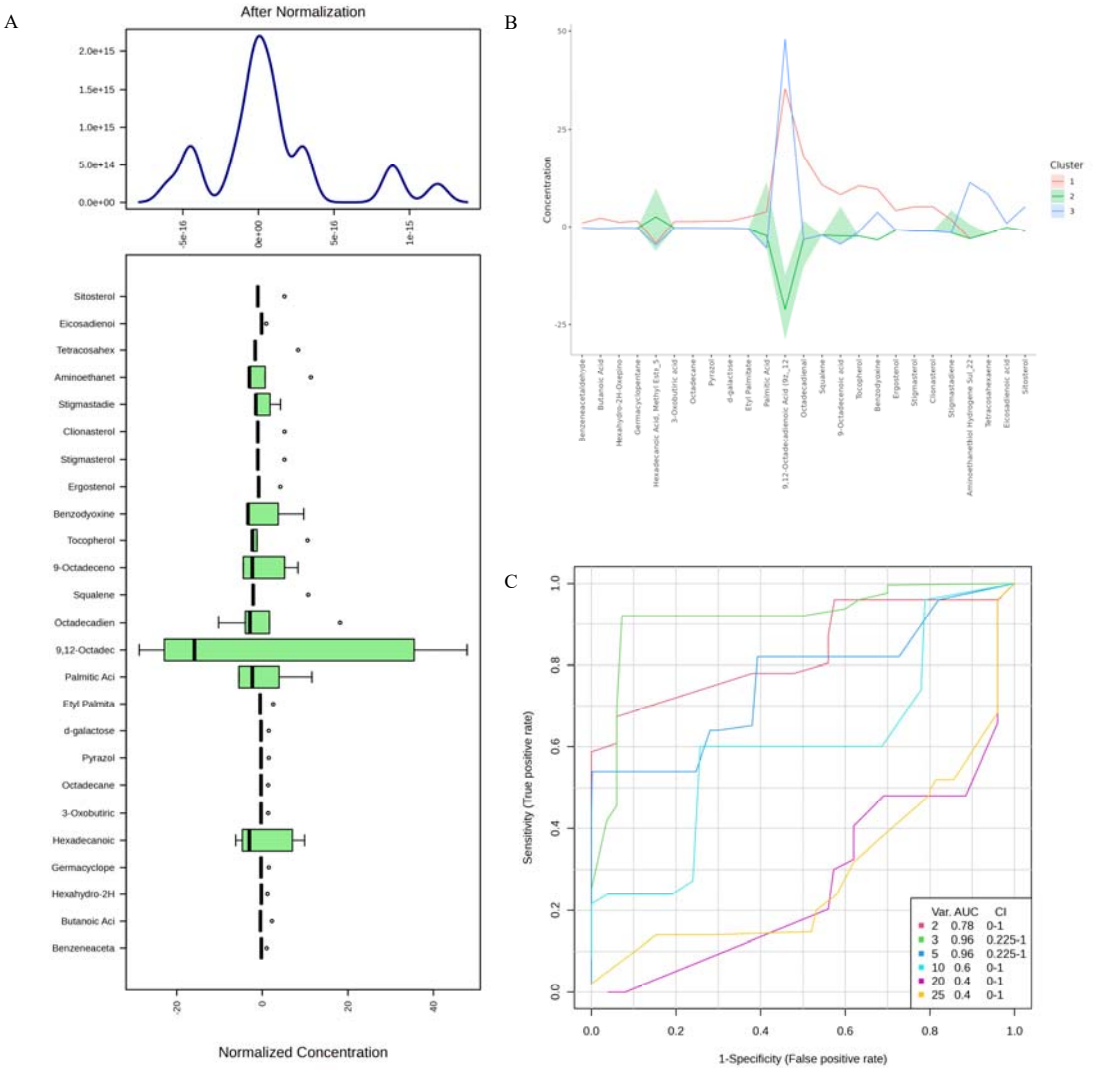

Figure 3. Comparison of the concentration of compounds in the lipid metabolism pathway in mature and young seeds of *Jatropha curcas*. The normality value of each metabolite compound detected based on the boxplot in each compound (A). The difference in concentration of 25 metabolites is divided into 3 clusters, namely clusters 1, 2, and 3 (B). The sensitivity rate value of each metabolite in *J. curcas*, especially in the difference in seed development stages (C).

3.4. etabolite profile clustering and network analysis test

Mature seeds (MS) tend to have high loading and frequency values, while young seeds (YS) have low values. The differences that occur are due to the frequency of expression of compounds 9 Octadecanoic acid, palmitic acid, Hexadecanoic acid, Stigmastadiene, 9.12 Octadecadienoic acid, and Octadecadienal. The expression value of 9 Octadecanoic acid shows a relatively high-frequency value, which is close to 1 (Figure 4A). The predictive accuracy value of *J. curcas* seed metabolites shows as much as 93% at the number of features 3, while the lowest value is 32% at the number of features 20 (Figure 4B). Based on the PLS-DA study, metabolites show three MS accessions grouped into one and separated from three YS accessions with a total PC value of 91.1% (Figure 4C). The network analysis test showed that 25 metabolites were closely related to each other and centered on Oxobutyric acid (Figure 4D).

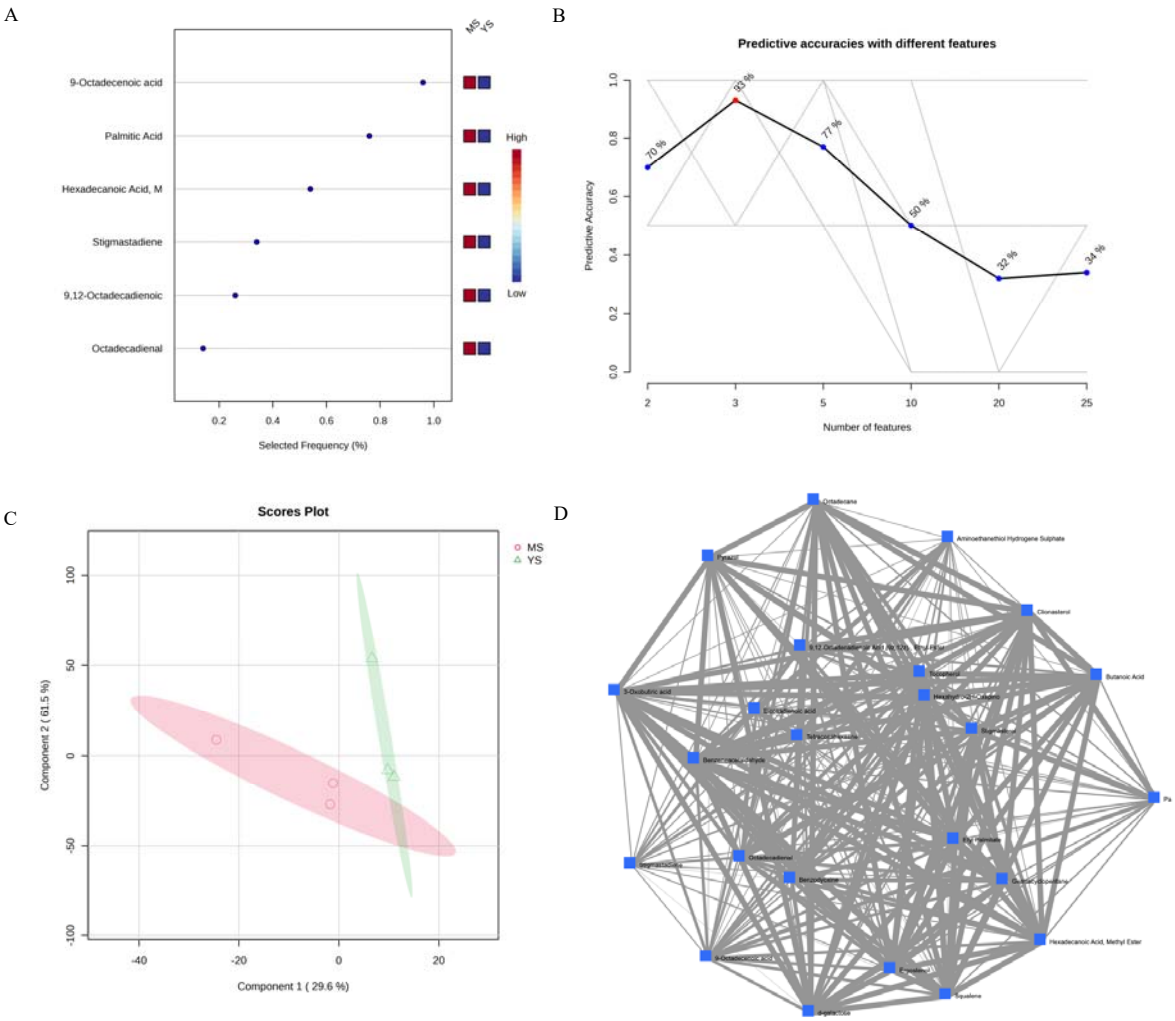

Figure 4. Frequency loading plot (A), Predictive accuracy (B), PLS-DA clustering (C), and network analysis (D) of 25 metabolites in young and mature seeds of *Jatropha curcas.*

3.5. Metabolite set enrichment studies

Metabolite set enrichment showed that the metabolites detected in the two types of seeds were found in the Benzo 1.4 dioxanes, Phenylacetaldehyde, and keto acid and its derivatives groups. The highest enrichment ratio value was shown in Benzo 1.4 dioxanes, while the lowest was found in fatty acid esters (Figure 5A). If the -log10 ratio value is tested, the highest value is fatty acids and conjugates, followed by stigmastanes and Benzo 1.4 dioxanes (Figure 5B). Globally, these metabolites are also included in the fatty acids and conjugates compound set group along with stigmastanes and derivatives. Other groups include alkanes, benzo 1.4-dyoxans, carbohydrates, carbonyl compounds, ergostane steroids, fatty acid esters, linolenic acid, phenylacetaldehyde, quinone & hydroxyquinone lipids, keto acids and derivatives, and triterpenoids (Figure 5C). The highest pathway impact pathway value reached a value of 0.30 while the highest hold value reached a value of 2.6 (Figure 5D). The highest pathway value that has the highest hits value is fatty acids & conjugates, and the lowest is fatty acid ester (Figure 5E).

A

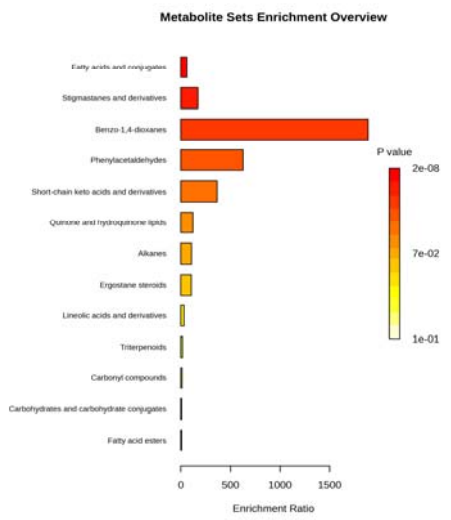

B

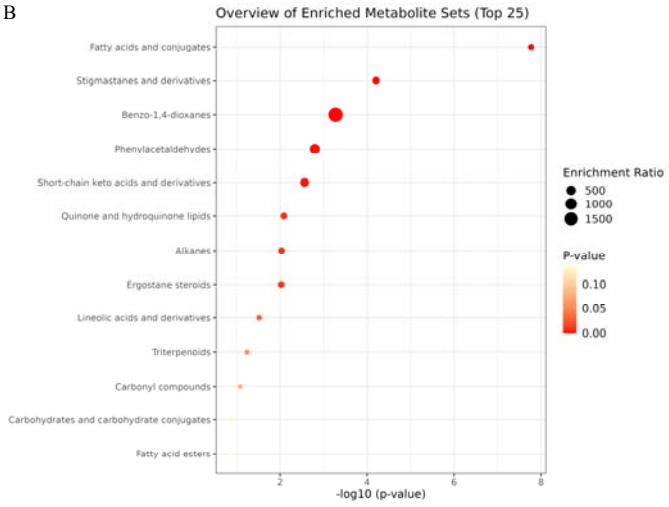

C

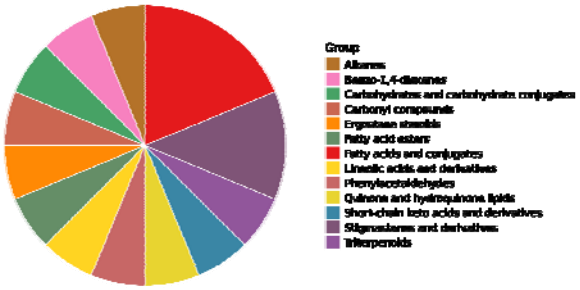

D

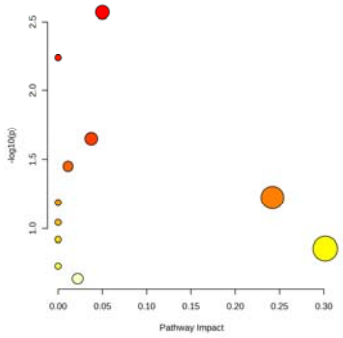

E

	Metabolite Set	Total	Hits	Expect	P value	Holm P	FDR
	Fatty acids and conjugates	941	5	0.0831	1.69E-8	1.51E-5	1.51E-5
	Stigmastanes and derivatives	131	2	0.0116	6.23E-5	0.0554	0.0277
	Benzo-1,4-dioxanes	6	1	5.3E-4	5.3E-4	0.471	0.157
	Phenylacetaldehydes	18	1	0.00159	0.00159	1.0	0.354
	Short-chain keto acids and derivatives	31	1	0.00274	0.00274	1.0	0.487
	Quinone and hydroquinone lipids	93	1	0.00822	0.00818	1.0	1.0
	Alkanes	105	1	0.00928	0.00924	1.0	1.0
	Ergostane steroids	107	1	0.00945	0.00941	1.0	1.0
	Lineolic acids and derivatives	348	1	0.0307	0.0303	1.0	1.0
	Triterpenoids	672	1	0.0594	0.0577	1.0	1.0
	Carbonyl compounds	975	1	0.0861	0.0827	1.0	1.0
	Carbohydrates and carbohydrate conjugates	1600	1	0.141	0.132	1.0	1.0
	Fatty acid esters	1650	1	0.146	0.136	1.0	1.0

Figure 5. Set of metabolite enrichment (A), enrichment ratio (B), grouping of compound types (C), pathway impact (D), and pathway analysis group (E) in young and mature seeds of *Jatropha curcas.*

3.6. KEGG Pathway

The metabolite pathway in galactose metabolism showed significant compounds detected in two types of seeds relatively high. 24 compounds had the highest impact value on the galactose metabolism pathway. The detected metabolic pathways included the pentose phosphate pathway, pentose and glucuronate interconversions, and amino sugar or nucleotide metabolism (Figure 6). Significant metabolites included the farnesol, germacrene, lupeol, squalene, and farnesyl-PP groups (Figure 7). A total of 41 metabolites played a role in the steroid biosynthesis pathway. This pathway is also related to the biosynthesis pathways of brassinosteroids, phytosterols, bile acid biosynthesis, steroid hormone biosynthesis, and phytosterols biosynthesis (Figure 8).

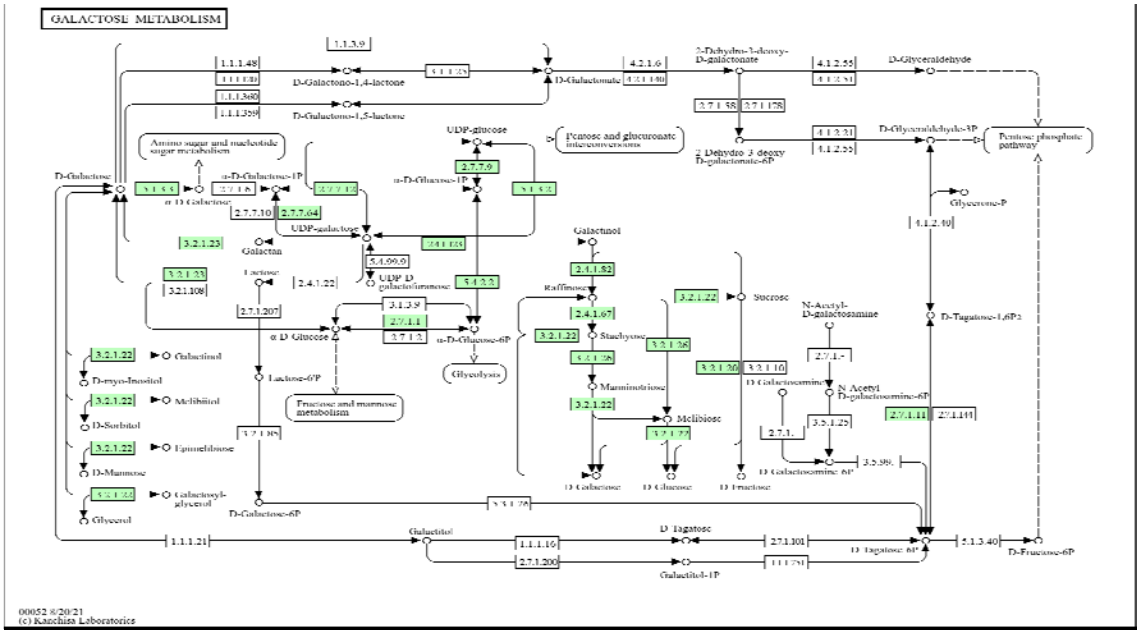

Figure 6. Metabolite pathway of galactose metabolism in *Jatropha curcas* seeds. Green marks indicate the significance of metabolites that affect galactose metabolism.

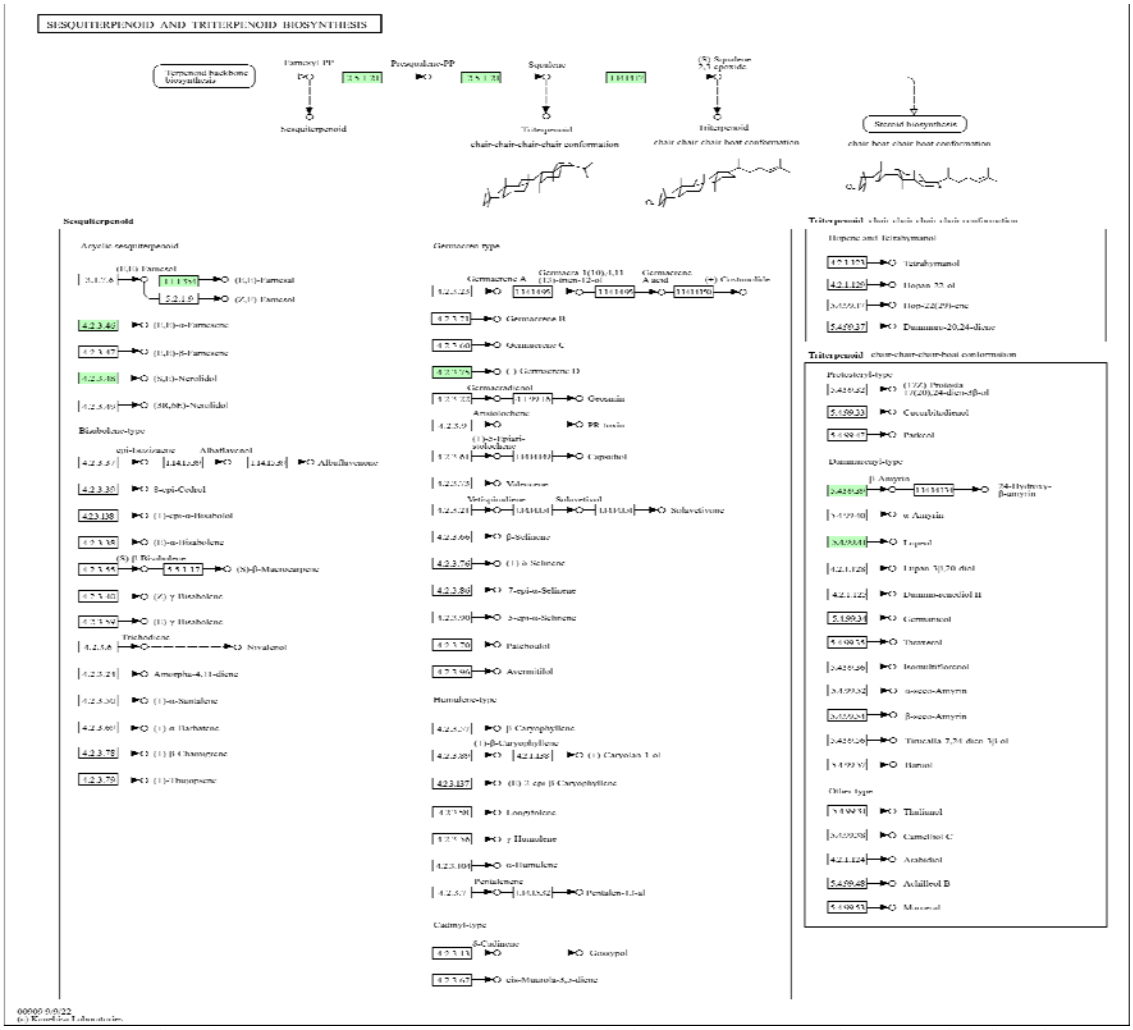

Figure 7. Metabolite pathway of sesquiterpenoid and triterpenoid biosynthesis in *Jatropha curcas* seeds. Green marks indicate the significance of metabolites that affect sesquiterpenoid and triterpenoid biosynthesis.

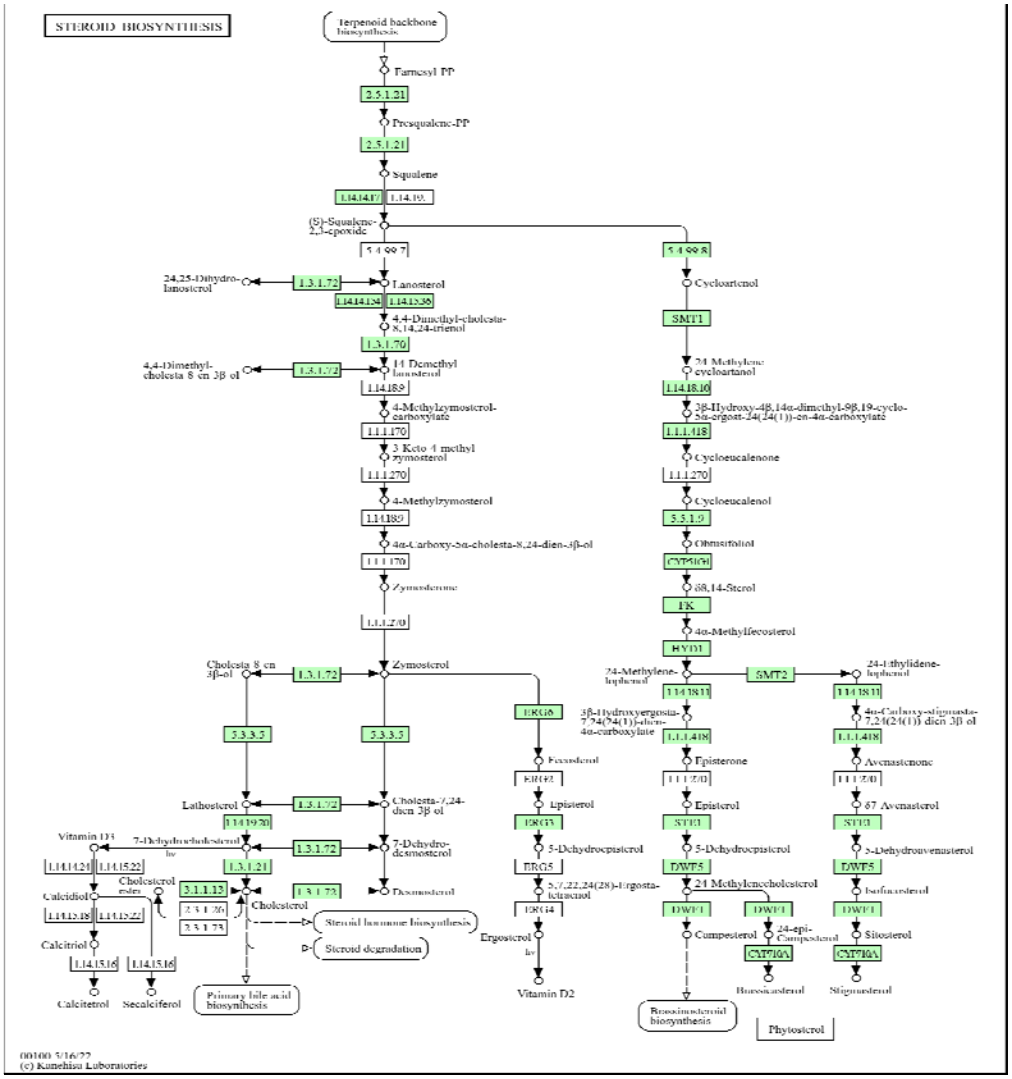

Figure 8. Metabolite pathway of steroid biosynthesis in *Jatropha curcas* seeds. Green marks indicate the significance of metabolites that affect steroid biosynthesis.

4. Discussion

Metabolomics in plants like *Jatropha* aims to characterize organ-specific metabolite profiles under defined conditions (Debnath *et al.,* 2011). The target of metabolomics research is low molecular weight compounds that are synthesized by an organism at a certain time and condition (Mastrangelo *et al.,* 2015). Plants are estimated to have more than 200 thousand types of metabolites (Valdes-Rodríguez *et al.,* 2013). Metabolomics, especially in plants, investigates compound identification strategies with statistical approaches to measure metabolite profiles found in cells and tissues, i.e. in *Pistia stratiotes* (Tyagi and Agarwal, 2017). Compared to transcriptomics analysis, metabolomics is an easier method to study comparative analysis in plant abiotic stress (Amaral *et al.,* 2016). Metabolomics studies consist of metabolites profiling, which is a quantitative estimate of a certain group of metabolites, metabolic fingerprinting, and isotope-based analysis which is intended to analyze specific compounds from intermediate metabolites from a metabolic pathway (Kibazohi and Sangwan, 2011).

Compared to Nuclear Magnetic Resonance (NMR), metabolomics studies using GC-MS or LC-MS are considered relatively easy because the methods do not require isotopes in their use. The application of metabolomics research has been used in studying plant responses to abiotic stress particularly stress to waterlogging conditions, drought, and other stresses. Gas chromatography (GC), liquid chromatography (LC), and capillary electrophoresis (CE) are types of Mass Spectrometry (MS) analytical tools that can be used to estimate quantitatively the mass-to-charge ratio of one or more molecules in a sample used for the study. GC-MS is a sophisticated omics study in metabolite investigation with high chromatographic resolution. However, GC-MS cannot be used to detect polar compounds. Therefore, to cover this weakness, HPLC-MS is used which has a wide range in analyzing compounds including with lower chromatographic resolution. Integrated omics studies like genomic (Satrio *et al.,* 2021; Halim *et al.,* 2021; Pratami *et al.,* 2022), transcriptomic and gene expression (Wang *et al.,* 2013; Satrio *et al.,* 2019; Ratnadewi *et al.,* 2021), and metabolomic (Bates *et al.,* 2007) can combine each other

to understand comprehensive studies of oil producing pathway, particularly in *J. curcas*.

Jatropha curcas plants do not require special growing conditions (Abdelgadir *et al.,* 2012). This plant is widely planted in tropical areas as a hedge around fields and villages. *Jatropha curcas* easily adapts to the environment including critical and marginal environmental conditions, this plant can also be planted for reforestation of eroded areas. *Jatropha curcas* can live at an altitude of 0-2000 m above sea level, rainfall of 300-1200 mm per year, and temperatures ranging from 18-30ºC. In areas with low temperatures (< 18ºC) it can inhibit growth, while at high temperatures (>35ºC) it can cause leaves and flowers to fall, and the fruit becomes dry so that the production of this plant decreases. *Jatropha curcas* can grow in less fertile areas but must have good drainage, not be flooded, and a soil pH of 5.0-6.5 (Prihandana and Hendroko, 2006). Such growing habits can be used as a preference for obtaining oil metabolites in *J. curcas*. *Jatropha curcas* can produce 15-20 times more lipids than lipid-producing plants (oil palm) in its best condition, 1000 per year (Valdes-Rodríguez *et al.,* 2013). *Jatropha curcas* has the greatest potential as a producer of biodiesel raw materials compared to other plants. Unlike other plants, *J. curcas* can produce very high lipids for biodiesel raw materials with a fast harvest time. This research is expected to contribute to the study of the selection of the best seeds for lipid synthesis as a raw material for biofuel in *J. curcas.*

5. Conclusion

Mature (MS) and young (YS) seeds showed differences in metabolite content expression and these differences globally occurred in the galactose metabolism, triterpenoid, and steroid biosynthesis pathways. A total of 25 different metabolites, 19 which of metabolites were highly expressed in mature seeds of *Jatropha curcas*. In contrast, there were only 6 metabolites that were highly expressed in young seeds. In general, the four metabolites that have the highest correlation (strong positive intercorrelation) are the intercorrelation of the metabolites Eicosadienoic acid, Tetracosahexane, Sitosterol, and Aminoethanethiol. This funding showed that mature seeds (MS) have significantly higher metabolite expression than young seeds (YS) in *Jatropha curcas*. Therefore, the best seed selection synthesis as a raw material for biofuel in *J. curcas* is mature seed (MS). This funding has practical implications for harvesting seeds from *J. curcas* at a mature age seeds (MS) to produce high lipid production as biofuel which is characterized by high expression of metabolites related to lipid biosynthesis.

Acknowledgments

This research was fully supported by Trunojoyo Madura University (UTM) through the Mandiri Research (Risman) scheme (PI: E.S). We thank the Biology Laboratory, Indonesia Defense University for metabolites extraction. We thank the Health Laboratory of DKI Jakarta for supporting the metabolite identification of *J. curcas.*

References

Abdelgadir HA, Johnson SD, and Van Staden J. 2012. Pollen viability, pollen germination, and pollen tube growth in the biofuel seed crop *Jatropha curcas* (Euphorbiaceae). *South Afr J Bot.,* **79**:132-139. https://doi.org/10.1016/j.sajb.2011.10.005.

Bates PD, Ohlrogge JB, and Pollard M. 2007. The incorporation of newly synthesized fatty acids into cytosolic glycerolipids in pea leaves occurs via acyl editing. *J Biol Chem.,* **282**:31206–31216. https://doi.org/10.1074/jbc.M705447200.

Chong J, Soufan O, Li C, Caraus I, Li S, Bourque G, Wishart DS, and Xia J. 2018. MetaboAnalyst 4.0: towards more transparent and integrative metabolomics analysis. *Nucleic Acids Res.,* **46**: 486-494, https://doi.org/10.1093/nar/gky310.

Chong J, and Xia J. 2018. MetaboAnalystR: an R package for flexible and reproducible analysis of metabolomics data. *Bioinformatics.,* **34**:4313–4314. https://doi.org/10.1093/bioinformatics/bty528.

Chong J, Wishart DS, and Xia J. 2019. Using metaboAnalyst 4.0 for comprehensive and integrative metabolomics data analysis. *Curr Protoc Bioinformatics.,* **68**:e86.

Debnath M, Pandey M, and Bisen PS. 2011. An omics approach to understand the plant abiotic stress. OMICS A J. Integr. Biol. **15**:739-762, https://doi.org/10.1089/omi.2010.0146.

do Amaral MN, Arge LWP, Benitez LC, Danielowski R, da Silveira SF, Farias DR, de Oliveira AC, da Maia LC, and Braga EJB. 2016. Comparative transcriptomics of rice plants under cold, iron, and salt stresses. *Funct Integr Genomics.,* **16**: 567–579. https://doi.org/10.1007/s10142-016-0507-y.

Fendiyanto MH, Satrio RD, Suharsono, Tjahjoleksono A and Miftahudin. 2019a. Correlation among Snpb11 markers, root growth, and physiological characters of upland rice under aluminum stress. *Biodiversitas.*, **20(5)**: 1243-1254. https://doi.org/10.13057/biodiv/d200514.

Fendiyanto MH, Satrio RD, Suharsono, Tjahjoleksono A, Hanarida I and Miftahudin. 2019b. QTL for aluminum tolerance on rice chromosome 3 based on root length characters. *SABRAO J Breed Genet.,* **51(4)**: 451-469.

Fendiyanto MH, Satrio RD and Darmadi D. 2020. Metabolic profiling and pathway analysis in red arillus of Salacca sumatrana demonstrate significant pyruvate, sulfur, and fatty acid metabolisms. *Biodiversitas.,* **21(9)**: 4361-4368. https://doi.org/10.13057/biodiv/d210955.

Fendiyanto MH, Satrio RD, Widana IDKK, Pratami MP, Nikmah IA and Darmadi D. 2021. Differential hierarchical metabolites expression of red/white Salacca sumatrana arillus and its molecular docking studies. *Biodiversitas.*, **22(2)**: 1014-1024. https://doi.org/10.13057/biodiv/d220258.

Fendiyanto MH, Pratami MP, Satrio RD , Nikmah IA, Sari NIP, Awwanah M, Farah N, Nurhadiyanta N. 2021. Analysis of *Superoxide Dismutase (OsSOD)* Gene Expression Using qRT-PCR, Its Morphophysiological Characters, and Path Analysis in Rice Variety IR64 Under Aluminum Stress. *Inter J Agric Biol.*, **26(4)**: 546-554. https://doi.org/10.17957/IJAB/15.1866.

Fendiyanto MH, Pratami MP, Satrio RD , Nikmah IA, Sari NIP, Awwanah M, Farah N, Nurhadiyanta N. 2023. Species diversity of freshwater Microalgae in dramaga, bogor based on morpho-ecological identification between low and high light intensity environment. *Jordan J Biol Sci.*, 16 (1): 27-34. https://doi.org/10.54319/jjbs/160105.

Fendiyanto MH, Hastilestari BR, Maysha DJ. 2023. *LCYB* Gene Expression and Morphophysiological Traits of Musa acuminata Cultivars. *SABRAO J Breed Genet.,* **55(6)**: 1984-1993.

Fendiyanto MH, Anshori MF, Pratami MP, Wasonga DO, Seleiman MF. 2024. Metabolite comparative variation related lipid metabolisms among fruit, leaf, and stem of *Jatropha curcas*. *Heliyon.,* **10(15)**: e35861.

Gunjan G, Makkar HPS, Francis G, and Becker K. 2016. Phorbol Esters: Structure, Biological Activity, and Toxicity in Animals. *Int J Toxicol.,* **26(4)**: 279–288. https://doi.org/10.1080/10915810701464641.

Halim I, Fendiyanto MH, and Miftahudin M. 2021. SgRNA design for *DLT* gene editing using CRISPR-Cas9 and in-silico mutation prediction in Rice cv. Hawara Bunar. *IOP Conf Ser Earth Environ Sci.,* **1088**:e1315. https://doi.org/10.1088/1755-1315/948/1/012083.

Janick J, and Paull RE. 2008. **The Encyclopedia of Fruit and Nuts, first ed**. CABI, Cambridge. pp. 371–372.

Kibazohi O, and Sangwan RS. 2011. Vegetable oil production potential from Jatropha curcas, Croton megalocarpus, *Aleurites moluccana*, *Moringa oleifera* and *Pachira glabra*: Assessment of renewable energy resources for bio-energy production in Africa. *Biomass & Bioen*., 35(3):1352-1356. https://doi.org/10.1016/j.biombioe.2010.12.048.

Lander JP. **R for Everyone, Advanced Analytics and Graphics**. Addison-Wesley, USA, Boston, 2014.

Lin J, Zhou X, Wang J, Jiang P, and Tang K. 2010. Purification and characterization of curcin, a toxic lectin from the seed of *Jatropha curcas. Preparative Biochem & Biotech*., **40(2)**: 107-118. https://doi.org/10.1080/10826060903558588.

Maes WH, Achten WMJ, Reubens B, Raes D, Samson R, and Muys B. 2009. Plant-water relationships and growth strategies of *Jatropha curcas* L. seedlings under different levels of drought stress. *J Arid Environ.,* **73**:877–884. https://doi.org/10.1016/j.jaridenv.2009.04.013.

Makkar HPS, Francis G, and Becker K. 2008. Protein concentrate from *Jatropha curcas* screw-pressed seed cake and toxic and antinutritional factors in protein concentrate. *J Sci Food Agric*., **88**: 1542-1548.

Martínez-Herrera J, Martínez-Ayala A, Makkar HPS, Francis G, and Becker K. 2010. Agroclimatic conditions, chemical and nutritional characterization of different provenances of *Jatropha curcas* L. from Mexico. *J Food Qual*., **35**:152-158.

Martínez-Herrera J, Jiménez-Martínez C, Martínez AA, Garduño-Siciliano L, Mora-Escobedo R, Dávila-Ortiz G, Chamorro-Cevallos G, Makkar HPS, Francis G, and Becker K. 2012. Evaluation of the nutritional quality of non-toxic kernel flour from *Jatropha curcas* L. in rats. *J Food Qual*., **35**:152-158.

Mastrangelo A, Ferrarini A, Rey-Stolle F, García A, and Barbas C. 2015. From sample treatment to biomarker discovery: a tutorial for untargeted metabolomics based on GC-(EI)-Q-MS. *Anal Chim Acta*., **900**:21–35.

Mishra DK. 2009. Selection of candidate plus phenotypes of *Jatropha curcas* L. using method of paired comparisons. *Biomass Bioenergy.,* **33**:542–545.

Openshaw K. 2000. A review of *Jatropha curcas*: an oil plant of unfulfilled promise. *Biomass Bioenergy.,* **19**:1-15.

Pang Z, Chong J, Li S, and Xia J. 2020. Metaboanalystr 3.0: toward an optimized workflow for global metabolomics. *Metabolites.,* **10**:1-15. https://doi.org/10.3390/metabo10050186.

Pratami MP, Fendiyanto MH, Satrio RD , Nikmah IA, Awwanah M, Farah N, Sari NIP, Nurhadiyanta N. 2022. In-silico Genome Editing Identification and Functional Protein Change of *Chlamydomonas reinhardtii* Acetyl-CoA Carboxylase (CrACCase). *Jordan J Biol Sci*., **15 (3):** 431-440. https://doi.org/10.54319/jjbs/150312.

Prihandana R and Hendroko R. 2006. **Petunjuk Budidaya Jarak Pagar**, first ed. Agro Media Pustaka, Jakarta.

Ratnadewi D, Fendiyanto MH, Satrio RD, Miftahudin M, and Laily AN. 2021. Strictosidine synthase coding gene expression towards quinine biosynthesis and accumulation: inconsistency in cultured cells and fresh tissues of *Cinchona ledgeriana*. *Int J Agric Biol.,* **26**:131–138. https://doi.org/10.17957/IJAB/15.1817.

Sato S, Hirakawa H, Isobe S, Fukai E, Watanabe A, Kato M, Kawashima K, Minami C, Muraki A, Nakazaki N, Takahashi C, Nakayama S, Kishida Y, Kohara M, Yamada M, Tsuruoka H, Sasamoto S, Tabata S, Aizu T, Toyoda A, Shin T, Minakuchi Y, Kohara Y, Fujiyama A, Tsuchimoto S, Kajiyama S, Makigano E, Ohmido N, Shibagaki N, Cartagena JA, Wada N, Kohinata T, Atefeh A, Yuasa S, Matsunaga S, and Fukui K. 2011. Sequence analysis of the genome of an oil-bearing tree, *Jatropha curcas* L. DNA Res., **18**: 65–76. https://doi.org/10.1093/dnares/dsq030.

Satrio RD, Fendiyanto MH, Suharsono, Supena EDJ and Miftahudin. 2019. Identification of drought-responsive regulatory genes by hierarchical selection of expressed sequence tags and their expression under drought stress in rice. *Intl J Agric Biol.,* **22(6)**: 1524-1532. https://doi.org/10.17957/IJAB/15.1230.

Satrio RD, Fendiyanto MH, Supena EDJ, Suharsono S, and Miftahudin M. 2021. Genome-wide SNP discovery, linkage mapping, and analysis of QTL for morphophysiological traits in rice during vegetative stage under drought stress. *Physiol Mol Biol Plants.*, **27**:2635–2650. https://doi.org/10.1007/s12298-021-01095-y.

Sunil N, Kumar V, Sujatha M, Rajeswara G, and Varaprasad KS. 2013. Minimal descriptors for characterization and evaluation of *Jatropha curcas* L. germplasm for utilization in crop improvement. *Biomass Bioenergy*., **48**:239-249. https://doi.org/10.1016/j.biombioe.2012.11.008.

Tyagi T, and Agarwal M. 2017. Phytochemical screening and GC-MS analysis of bioactive constituents in the ethanolic extract of *Pistia stratiotes* L. and *Eichhornia crassipes* (Mart.). *Pharmacogn Phytochemistry*., **6**:195–206.

Valdes-Rodríguez OA, Sánchez-Sánchez O, Pérez-Vazquez A, and Caplan J. 2013. The Mexican non-toxic *Jatropha curcas* L., food resource or biofuel?. *Ethnobot Res & Appl.,* **11**: 001-007.

Wang H, Zou Z, Wang S, and Gong M. 2013, Global analysis of transcriptome responses and gene expression profiles to cold stress of *Jatropha curcas* L. *PLoS One.*, **8**:e1371. https://doi.org/10.1371/journal.pone.0082817.

Wishart DS, Feunang YD, Marcu A, Guo AC, Liang K, V´azquez-Fresno R, Sajed T, Johnson D, Li C, Karu N, Sayeeda Z, Lo E, Assempour N, Berjanskii M, Singhal S, Arndt D, Liang Y, Badran H, Grant J, Serra-Cayuela A, Liu Y, Mandal R, Neveu V, Pon A, Knox C, Wilson M, Manach C, and Scalbert A. 2018. Hmdb 4.0: the human metabolome database for 2018. *Nucleic Acids Res.,* **46**:D608–D617. https://doi.org/10.1093/nar/gkx1089.

Xia J, and Wishart DS. 2016. Using MetaboAnalyst 3.0 for comprehensive metabolomics data analysis current protocols in bioinformatics. *Bioinformatics.,* **55**: 81–91.

JJBS

Volume 18, Number 3,September 2025
ISSN 1995-6673
Pages 521 – 529

Jordan Journal of Biological Sciences

Exploring antibacterial activity of diclofenac sodium and determining the phenotypic and genotypic analysis of some efflux pump genes in methicillin-resistant *Staphylococcus aureus*

Shahad N. Abdullah and Zina H. Shehab*

Department of Biology , College of Science for Women , University of Baghdad , Iraq

Received: December 30, 2024; Revised: March 31, 2025; Accepted: April 7, 2025

Abstract

Multidrug-resistant (MDR) *Staphylococcus aureus* is becoming a remarkable crisis because of the potential of this bacterium to develop resistance to many groups of antibiotics. This study investigated the antibacterial effect of diclofenac sodium (Olfen) and the phenotypic and genotypic detection of two classes of efflux pumps among (MDR) *Staphylococcus aureus*. Methecillin-resistant *Staphylococcus aureus* (MRSA) can be identified via culture and biochemical examinations and confirmed via the use of the specific primers *16SrRNA* and the *mecA* gene. Antibiotic susceptibility tests were performed via the disc diffusion method against ten antibiotics. The results revealed the highest resistance of the *S. aureus* isolates to cefoxitin (55.55%), and the resistance of the isolates gradually decreased with erythromycin (38.88%), doxycycline (30.55%), norofloxacin (25%), ciprofloxacin (19.44%), clindamycin (16.66%), rifampin and trimethoprim-sulfamethoxazole (11.11%), and chloramphenicol (8.33%). Diclofenac sodium, a non-steroidal anti-inflammatory drug (NSAID), showed distinct antibacterial activity against some MRSA isolates at 125 µg/ml. The efflux pump phenotype was identified via the Ethidium Bromide - Cart Wheel (EtBr-CW) method. The results indicated that 10 isolates (27%) had efflux pumps, and polymerase chain reaction was used to look at the genotypic efflux pump genes. The findings revealed that 34 (94%) MRSA strains presented the *mdeA* and *mepA* genes, whereas 28 (77%) *norB* genes were found.

Keywords: Antibiotic resistance, Efflux pump, EtBr-CW method, diclofenac sodium, MRSA.

1. Introduction

Staphylococcus aureus is an important infectious pathogen in the health sector and communities. It causes various infections ranging from simple to life-threatening ones (Rasheed and Hussein, 2021). Typically, this bacterium is found in the body's regular flora. It is present in the upper respiratory system and on the skin (Sabbar *etal*.,2023). Opportunistic bacteria are responsible for a variety of infectious diseases, including infections contracted in hospitals and communities. Methicillin-resistant *S. aureus* (MRSA) can cause skin infections, urinary tract infections (UTIs), bloodstream infections, food poisoning, and respiratory disorders by generating enterotoxins and alpha pore-forming toxins that kill host cells and tissues. The virulence of *S. aureus* infections is influenced by several factors (Scudiero *et al.*, 2020). *Staphylococcus aureus* exhibits a variety of antibiotic resistance mechanisms, such as target site mutation, antibiotic efflux systems, enzymatic drug inactivation, and changes in antibiotic permeability (Foster, 2017). Penicillin-binding protein 2a (PBP2a), which is encoded by *mecA* and has a poor affinity for methicillin and other β-lactams, is the cause of methicillin and oxacillin resistance. Moreover, staphylococcal cassette chromosome element (*SCCmec*) horizontal gene transfer and chromosomal alterations that change drug binding sites might result in methicillin-resistant *S. aureus* (Jang, 2016). Many commonly used antibiotics, including β-lactamases, fluoroquinolones, aminoglycosides, macrolides, and lincosamides, frequently cause resistance in MRSA (El-Baz *et al.*, 2021 and Youssef *et al.*, 2021). One of the main mechanisms of antibiotic resistance is efflux pumps (Saber *et al.*, 2019). Following their attachment to substrates often antibiotics these membrane proteins aggressively catalyze the outward translocation of the substrates, lowering their intracellular concentrations and, hence, the efficacy of the therapy (Pu, *et al*.,2017). The efflux systems are divided into two groups according to the energy-obtaining method used. While secondary efflux pumps obtain energy from chemical gradients created by protons or ions, primary efflux pumps obtain energy from the hydrolysis of ATP molecules (Li *et al*.,2015). Certain bacterial efflux systems can only extrude one class of antibiotics; however, multidrug-resistant (MDR) bacterial efflux systems can extrude multiple classes (Sharma *et al.*, 2016 and Hassanzadeh *et al.*,2017). The ATP binding cassette (ABC) family, the major facilitator superfamily (MFS), the resistance nodulation cell division (RND) family, the small multidrug resistance (SMR) family, and the multidrug and toxin extrusion (MATE) family are the five primary families of efflux pumps found in prokaryotes (Blair *et al.*, 2014). According to recent studies, both *S.aureus* infection

* Corresponding author. e-mail: zinahs_bio@csw.uobaghdad.edu.iq.

and influenza virus infection increase the risk of pneumonia and death (Jia *et al*., 2019 and Al- Mayahi, 2021). Diclofenac sodium is a non-steroidal anti-inflammatory medication (NSAID) that has FDA approval. It was used to treat *S. aureus* osteomyelitis as an ant virulence agent in conjunction with antibiotics (Abdel-Karim *et al.* 2022). The aim of the current study, we determined the presence of several chromosomal efflux pump genes (*mdeA* , *mepA* and *norB*) by phenotypic and genotypic methods and their relationship with antibiotic resistance in methicillin-resistant *S. aureus* and explored the impact of diclofenac sodium (Olfen) as a synergistic antibacterial agent at a first attempt in Iraq.

2. Materials and Methods

2.1. Bacterial isolates and identification of Staphylococcus aureus

One hundred and twenty-five samples were collected from various sources from patients who visited some Baghdad hospitals. These samples were Wound 37 (29,6%), Urine 55 (44%), Burn 8 (6,4%), Sputum 9 (7.2%), Nasal swap 6 (4,8%), Throat swap 7 (5.6%) and Cerebro-Spinal Fluid (CSF) 3 (2,4%), which were selected between the ages of 15 and 60 and represented both genders. Each sample was immediately inoculated in blood agar and incubated for 24 hours at 37°C. Gram stain and biochemical tests were used, and growth on mannitol salt agar (MSA) was used as a selective medium (Nuaimi *et al*., 2023). Next, the PCR technique for genotypic detection via *the 16S rRNA* gene was used.

2.2. Antibiotic susceptibility test.

To assess the antibiotic susceptibility of *S. aureus* isolates on Mueller Hinton agar (Hi-media), the Kirby–Bauer method was employed for eleven antibiotic discs (Mehrotra et al., 2000). The plates were incubated at 37°C for eighteen hours. The diameter of the inhibitory zone was evaluated following the incubation period at the Clinical and Laboratory Standards Institute (CLSI 2024). The following antibiotics were examined in this study: cefoxitin (FOX: 30 µg), ciprofloxacin (CIP:5µg), erythromycin (ERY:15µg) and norfloxacin (NOR: 10µg). Clindamycin (CD:10µg), doxycycline (DOX: 30µg), nitrofurantion (F:30µg), chloramphenicol(C:30µg), rifampin (RIF: 5µg), and trimethoprim-sulfamethoxazole (SXT: 1.25/23.75 µg).

2.3. Phenotypic methicillin resistance detection

All identified *S. aureus* isolates were screened for methicillin resistance phenotypically via the cefoxitin disk diffusion test, which is alternative to a 30 µg disk on Mueller Hinton agar for methicillin. Cefoxitin (methicillin) was found to be resistant to inhibition zones < 21 mm in size but susceptible to those > 21 mm in size (CLSI 2024).

2.4. The antibacterial activity of diclofenac sodium was evaluated according to the MIC via the microtiter plate method (MTP)

The assay was designed to test the minimum inhibitory concentrations (MICs) of diclofenac sodium in the range of concentrations (1000,500,250,125,26.5,31.25) tested against several multidrug-resistant isolates of MRSA, according to the guidelines recommended by the CLSI (2024) document and (Elshikh *et al*., 2016). A 96-well microtiter plate supplemented with resazurin dye in Mueller Hinton broth (MHB).

2.5. Ethidium bromide qualitative efflux detection via the cart-wheel method.

The efflux of ethidium bromide was measured via the cartwheel(EtBr-CW) method. After the bacterial isolates were cultured overnight at 37°C, the cell concentration was increased the next day to 0.5 of the McFarland standard. A cartwheel-shaped pattern was created by dividing Tryptone soy agar with varying concentrations of ethidium bromide (0, 1, 2 and 4) mg/L via radial lines. After the bacterial isolates were swabbed with a sterile cotton swab, they were incubated for 16 hours at 37°C. A UV transilluminator was used to evaluate the colonies on tryptone soy agar plates. Martins *et al.*, 2013). Positive efflux activity was defined as the isolates' response to ethidium bromide exceeding 2 mg/mL, whereas moderate efflux activity was defined as the isolates' response to ethidium bromide equal to 2 mg/mL. Furthermore, isolates with ethidium bromide concentrations of 1 µg/mL or lower were regarded as negative.

2.6. Molecular identification by polymerase chain reaction (PCR)

A commercial genomic DNA purification kit (Promega, USA) was used to extract the genomic DNA of the *S. aureus* isolates. DNA samples from *S. aureus* isolates were used for this investigation to identify and identify efflux pump genes. By comparing their molecular weight on a DNA ladder and analyzing the bands via gel electrophoresis, the PCR results were verified. The primers used are listed in Table 1 of our previous study (Hamel *et al*., 2021).

Table 1. Primers used in this study

Primers name	Primer's sequence 5´ 3´	Product size (bp)	Reference
16S rRNA	AACCTACCTATAAGACTGGG CATTTCACCGCTACACATGG	578	(Kumar *et al*., 2020)
mecA	ACTGCTATCCACCCTCAAAC CTGGTGAAGTTGTAATCTGG	163	(Mehrotra *et al*., 2000)
norB	TCGCCTTCAACACCATCAAC GGCGTAGGAGATGATGGTCA	236	Shamkhi *et al*., 2019)
mdeA	TATGGCGATTGTTGTTTTTACTAC AACCGTGTGCATTCATTTCTGG	173	(Ahmed and Al-Daraghi, 2022)
mepA	GCAGTTATCATGTCTATCGGCG TGCACCTTGTAAAATGGCCA	240	(Patel *et al.*, 2010)

The PCR components of 25 µl of master mix, 4µl of extracted template DNA, 11 µl forward and 11µl reverse primers, and 6.5 µl of nuclease-free water. In a PCR thermal cycler, the mixture was amplified by first denaturing at 94°C for five minutes, and then amplifying it 35 times (denaturing it for 20 seconds at 94°C, annealing it for 45 seconds at 55, 57,54,55 and 55) °C respectively for genes in Table (1), and elongating it for 1 minute at 72°C.

Following a final extension at 72°C for 5 minutes, the PCR products were run on a 1.5% agarose gel at 70 volts for 80 minutes. For the *16S rRNA* gene, ethidium bromide dye was used, which was then observed under an ultraviolet transilluminator and photographed. For the *mecA* gene, the mixture was amplified by first denaturing at 94°C for five minutes, after with the amplification process involved 35 cycles: denaturation at 94°C for 2 minutes, annealing at 57°C for 2 minutes, and elongation at 72°C for 1 minute. The final extension was conducted for 7 minutes at 72°C , and 90 minutes at 70 volts were used to run the PCR products on a 1.5% agarose gel via an ultraviolet transilluminator, ethidium bromide dye, and photography.

2.7. Statistical analysis

The Statistical Packages of Social Sciences-SPSS (2019) program was used to detect the effects of different groups and factors on the study parameters. The chi-square test was used to compare significant differences between percentages (0.05 and 0.01 probability) in this study (SPSS, 2019).

3. Results and Discussion

3.1. Isolation and identification of Staphylococcus aureus

A total of 125 clinical samples were collected from Baghdad hospitals. The presence of beta-hemolytic colonies on blood agar and yellow (golden) colonies resulting from the fermentation of mannitol sugar, which turns phenol red golden, are indicators of samples produced directly on mannitol salt agar and blood agar. As a selective medium, these samples also exhibit tolerance to elevated salt concentrations of MSA, and the isolates were examined through typical biochemical examinations. Both the coagulase and catalase responses in these samples were positive. However, the results of oxidase testing were negative. In addition, culture, morphology and biochemistry revealed that these isolates *S. aureus* (Tille, 2017). The results revealed that only 36 (24%) samples had typical biochemical testing and morphological characteristics peculiar to *Staphylococcus aureus*. The isolates proportions were as follows: burn 2 (5,5%), sputum 3 (8,3%), nasal swab 2 (5,5%), throat swab 2 (5,5%), wound 8 (22.2%), urine 18 (50%), and CSF 1 (2,7%). Our findings concur with those of Ahmed and Al-Daraghi (2022), who reported that fifteen *S. aureus* isolates were isolated from UTIs and nine from wounds. The variation in the prevalence rates of isolates is due to several factors, including differences in sample collection methods and sample sizes. Likewise, differences in isolation and diagnosis methods and the purpose of the study.

3.2. Molecular identification of MRSA

An effective method for identifying and detecting bacteria is the amplification of DNA from phylogenetically distinct bacteria by focusing on specific regions of the *16S rRNA* gene. (Vestergaard *et al.,* 2019). This gene's bacterial DNA was amplified via the PCR technique in a monoplex pattern via certain primers under ideal conditions. The results of the PCR via agarose gel electrophoresis revealed that 36 (100%) *S. aureus* isolates were 100% positive for the *16SrRNA* gene (578 bp), as shown in Figure (1). Our findings agree with those of (Shamkhi *et al*., 2019), who also reported that 100% of clinical *S. aureus* isolates were positive for the *16S rRNA* gene.

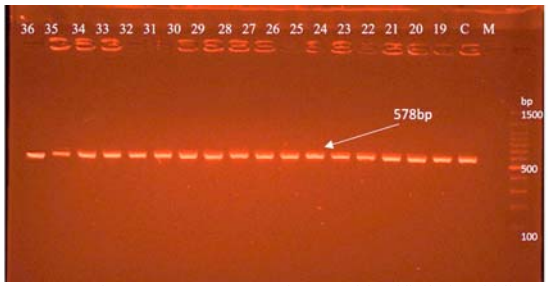

Figure 1: The *16SrRNA* gene (578bp) was identified via ethidium bromide-stained agarose gel electrophoresis of the amplified PCR product in lanes 19–36 on 1.5% agarose (80 min at 70 volts); M: marker DNA ladder (1500 bp); and C: negative control.

3.3. Investigation of the mecA gene

Methicillin-resistant *S. aureus* (MRSA) was detected via the *mecA* gene, a proprietary genetic marker. (Kadhum and Abood, 2022). PCR was used to amplify the bacterial DNA of this gene in a monoplex pattern under certain primer conditions. Figure (2) shows the 163 bp result of *mecA* gene amplification, which was confirmed by agarose gel electrophoresis and recorded on a camera with an ultraviolet transilluminator of clinical *S. aureus* isolates had positive *mecA* gene tests (97.22%). These results disagree with research by Kadhum and Abood, (2022) who identified the *mecA* gene in 100% of clinical *S. aureus* isolates.

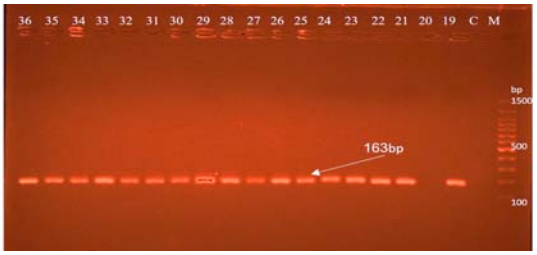

Figure 2: Identification of the *mecA* gene (163 bp), the amplified PCR product was electrophoresed on 1.5% agarose for 90 minutes at 70 volts in lanes 19–36 of the ethidium bromide-stained agarose gel; M: marker DNA ladder (1500 bp); and C: negative control.

3.4. Antibiotic resistance profiles in Staphylococcus aureus isolates

Antibiotic resistance summaries were studied for *S. aureus* isolates. Thirty-six *S. aureus* isolates, only 11 (30.55%), were determined to be MDR. The results revealed the greatest resistance of the *S. aureus* isolates to cefoxitin (FOX) 20 (55.55%). The resistance of the isolates gradually decreased, followed by erythromycin (ERY) 14(38.88%), doxycycline (DOX) 11(30.55%), norofloxacin (NOR) 9(25%), ciprofloxacin (CIP) 8(22.22%). Most of the isolates were highly sensitive to nitrofurantoin (F) 0(100%), chloramphenicol(C) (91.66%), rifampicin(RIF)(88.88%), and trimethoprim-sulfamethoxazole(STX) (86.11%), and clindamycin(CD) (75%), and the sensitivity of the isolates gradually decreased to other antibiotics. A high proportion of resistance levels to the various antibiotic classes found in the majority of *S. aureus* isolates is depicted in Figure (3).

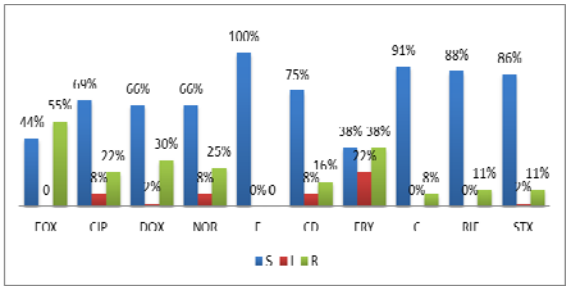

Figure (3) Percentages of antibiotic susceptibility rates of 36 *S.aureus* isolates to ten antibiotic agents.

The results agreed with of Jabur and Kandala (2022) who reached (6%) resistance to chloramphenicol and no resistance to nitrofurantion; however, they disagreed with those of Doxycyclin (10%) and cefoxitin (87%). However, the results agreed with those of Maharjan *et al.* (2021), who reached (60.8%) resistance to cefoxitin; however, they disagreed with those of chloramphenicol (56.8%). The results disagreed with Hantoosh, (2022), who reached 25% resistance to rifampin and 26% resistance to nitrofurantion, and disagreed with Hamad, (2023), who reached 40.6% resistance to clindamycin while agreeing with norfloxacin (25%), while he reached 21.9% resistance to trimethoprim-sulfamethoxazole. In addition, the results agreed with Belbase *et al.*, who reported that 27.8% of the strains were resistant to erythromycin. In addition to the previously mentioned outcome of Hamad (2023), who reported that isolates of *S. aureus* are sensitive to trimethoprim(78.1%), the results do not agree with those of clindamycin (59.4%), while the results agreed with those of Awayid and Mohammad (2022), who reached 94.2% sensitivity to rifampin but disagreed with those of cefoxitin (0), which also disagreed with Hantoosh (2022) , who reached 75% sensitivity to rifampin and 74% sensitivity to nitrofurantion, while the results of Aniba *et al.*(2024), erythromycin (28%), also agreed with those of Saud *et al.* (2023).The prevalence of methicillin-resistant *Staphylococcus aureus* (MRSA) drug resistance is due to numerous factors, including inappropriate prescription of antibiotics and self-medication by the use of antibiotics without a prescription. Additionally, hospital infections can spread between patients and staff via a breeding ground for MRSA, and poor hygiene through failure to adhere to proper hygiene practices in hospitals can facilitate the transmission of infection. In addition, genetic mutations lead to the development of antibiotic resistance mechanisms. Finally, the failure to treat with antibiotics before the end of treatment can lead to the persistence of resistant bacteria and a weakened immune system in individuals (Alghamdi *et al.*, 2023., Marciniak *et al.*, 2024).

3.5. Phenotypic detection of efflux pumps

As shown in Figure (4) and Table (2), EtBr-CW method is utilized to phenotypically detect efflux pumps in 36 isolates of *S. aureus* as an easy way to evaluate MDR bacteria for overexpressed efflux pumps by expelling ethidium bromide(EtBr) dye. Fluorescent growth indicates no efflux, whereas isolates with active efflux pumps do not exhibit fluorescent growth. Our work revealed that 10 of the 36 isolates, or approximately 27%, do not show fluorescence at a concentration of 2 mg/L EtBr, which indicates intermediate results for efflux pumps. This finding is consistent with the findings of Baiomy *et al.* (2020), who reported a value of 30%, whereas the results of Silva *et al.* (2021) , who reported a value of 34.7%; however, 6 of the 36 isolates that were positive (16%) did not show fluorescence at a concentration of 4 mg/L EtBr, which indicates positive results for the phenotypic detection of efflux pumps, as shown in Figure (3). We considered the 1 mg/L concentration a negative control compared with the positive results of the presence of efflux pumps in *S. aureus.* Similarly, another study revealed that the ratios between average EtBr intermediate and positive EtBr were similar (Costa *et al.*, 2013).

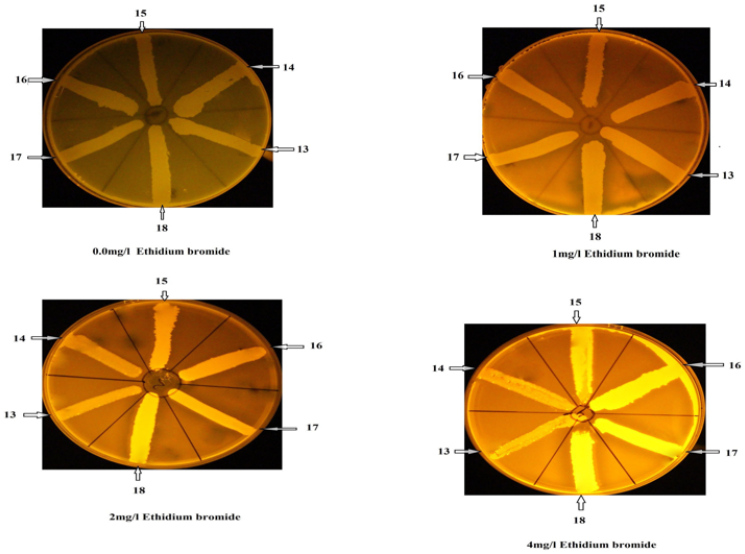

Figure (4): Tryptone soy agar plates containing different concentrations of EtBr were swabbed with *S. aureus* isolates.

In summary, the EtBr-CW approach is simple to implement, takes less time, and can screen a large number of bacterial strains, making it easier to identify isolates with an MDR phenotype quickly. It can be utilized to identify MDR strains caused by efflux in both gram-

positive and gram-negative clinical isolates. (Martins *et al.*, 2011).

Table (2): Phenotypic detection of *Staphylococcus aureus* pump efflux at varying ethidium bromide dye concentrations in a tryptone soy agar plate.

Isolates code	No.	EtBr_dye concentration		
		1 mg/l	2 mg/l	4 mg/l
St1,St4,St8,St9, St10,St11,St13, St14,St16,St17, St23,St25,St29, St30,St33,St34, St35,St36	17	-	-	-
St3,St6,St31,St18 St24	5	+	+	+
St12,St15,St20, St29	4	+	+	-
St55,St7,St21, St22,St26, St27, St28	7	+	-	-
St32	1	-	+	-
St19	1	-	-	+

A positive result is no florescence (+), and a negative result is florescence (-)

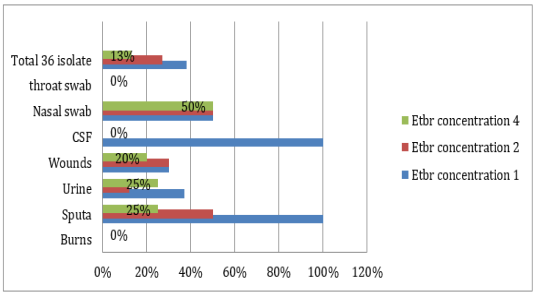

Figure (5): Efflux pump gene prevalence in clinical isolates from different *S. aureus* sources.

Figure (5) shows the relationship between the ability of the isolates to expel ethidium bromide dye and the source of the isolates, where the highest percentage of efflux pumps appeared in 50% of the nasal swab isolates at a concentration of 4 mg/L, followed by 25% of the urine and sputum isolates, 20% of the wound isolates and 15% of the throat swabs; however, these pumps did not appear in the burn or cerebrospinal fluid isolates. This finding reinforces the role of efflux pumps in resistance to antibiotics, disinfectants, and detergents, as well as the importance of this method for detecting efflux pumps in methicillin-resistant isolates. (Costa *et al.*, 2013).

3.6. Detection of some efflux pump genes via PCR

One of the highly distributed chromosomally encoded traits of resistance is the efflux pump. In our study, a PCR amplification approach was used for several efflux pump genes, *norB*, *mdeA* and *mepA,* which were examined in the 36 MDR isolates to further identify the efflux pump as a resistance mechanism of the tested MDR *S. aureus*. In our study, 28 isolates (77%) were positive for the *norA* gene, 34 (94%) were positive for the *mpeA* gene, and 34 (94%) were positive for the *mdeA* gene. In light of the results we obtained above, the genes encoding efflux pumps that are most abundant in the isolates of *S. aureus* were *mdeA* and *mepA*, whereas the result for the *norB* gene was the lowest among these two genes. The authors reported that 60.9% of the isolates produced from clinical samples from Korean patients were *norB* to be the most often overexpressed MDR efflux pump gene, and in another study, the presence of the *mdeA* gene in their isolates was the equivalent of 61.7%, which disagrees with our results, whereas in the search results of Suma *et al.* (2023), the *mdeA* gene percentage agreed with them, who reached 93.33%, and the *mepA* gene was present in their isolates (93.33%), which is in agreement with the results mentioned above. The *mepA* gene disagreed with the results of Antiabong *et al.*, (2017), who reached 97.9%. The *norB* gene was the lowest percentage that appeared between the *mepA* gene and the *mdeA* gene, which agreed with the findings of Shamkhi *et al.* (2019), who reached 56.25%, which is the lowest percentage of the two genes mentioned.

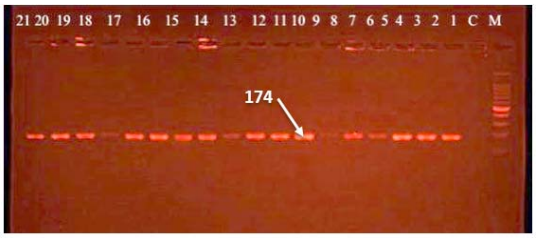

Figure 6: Identification of the *mdeA* gene (174 bp), the amplified PCR product was electrophoresed on 1.5% agarose for 90 minutes at 70 volts in lanes 1–21 of the ethidium bromide-stained in agarose gel; M: marker DNA ladder (100 bp); and C: negative control.

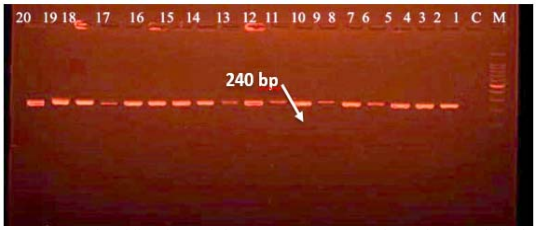

Figure 7: Identification of the *mepA* gene (240 bp), the amplified PCR product was electrophoresed on 1.5% agarose for 90 minutes at 70 volts in lanes 1–20 of the ethidium bromide-stained in agarose gel; M: marker DNA ladder (100 bp); and C: negative control.

Figure 8: Identification of the *norB* gene (236 bp), the amplified PCR product was electrophoresed in lanes 1–21 of an ethidium bromide-stained agarose gel on 1.5% agarose for 90 minutes at 70 volts; M: marker DNA ladder (100 bp); and C: negative control.

3.7. Antibiotic resistance profile associated with efflux pump genes in MRSA

This study examined the profiles of antibiotic resistance genes in 35 clinical MRSA isolates. The three genes identified in those clinical isolates of *S. aureus* (*norB, mdeA and mepA*) have been associated primarily with resistance to several drugs encode efflux pumps. The isolates were resistant to nine different antibiotics, namely, cefoxitin (FOX), ciprofloxacin (CIP), erythromycin

(ERY), norfloxacin (NOR), doxycycline (DOX), chloramphenicol (C), rifampin (RIF), clindamycin (CD), and trimethoprim-sulfamethoxazole (STX).

Table (3): The percentages of total genes related to resistance to nine different antibiotics.

Genes	Isolates no. 36	Antibiotic susceptibility									P- value
		FOX	CIP	ERY	NOR	DOX	C	CD	RIF	SXT	
norB	28 (77%)	15 (53%)	6(21%)	13 (46%)	6 (21%)	11 (39%)	2(7%)	4(14%)	3(10%)	2(7%)	0.0001 **
mepA	34 (94%)	20 (58%)	7 (20%)	15 (44%)	7 (20%)	12 (35%)	3(8%)	5(14%)	4(11%)	2(5%)	0.0001 **
mdeA	34 (94%)	19 (55%	8 (23%)	16(47%)	8 (23%)	11 (32%)	2(5%)	4(11%)	4(11%)	2(5%)	0.0001 **
P value	0.681 NS	0.237 NS	0.794 NS	0.547 NS	0.732 NS	0.904 NS	0.866NS	0.902 NS	0.894 NS	1.00 NS	---

** (P≤0.01), NS: Non-Significant.

Table (3) shows the relationships between the presence of resistance genes (*norB, mepA, and mdeA*) and the extent of their sensitivity or resistance to nine different antibiotics. The *norB* gene is relatively highly resistant to the following antibiotics: FOX: 53%, ERY: 46%, and DOX: 39%, whereas it has low resistance to other antibiotics, such as C (7%) and SXT (7%). The *mepA* gene has greater resistance: FOX: 58%. ERY: 44%. DOX: 35%. However, its resistance to some antibiotics, such as SXT (5%), is also low. Finally, the resistance pattern of the *mdeA* gene is similar to that of *mepA*, with greater resistance to the following antibiotics: FOX: 55%. ERY: 47%. DOX: 32% and low resistance to antibiotics such as C (5%) and SXT (5%). As an explanation for this, the most prevalent genes are *mepA* and *mdeA* (94%), which indicates that these two genes play major roles in the resistance of isolates to antibiotics. The three genes show significant resistance to FOX and ERY, which means that these antibiotics may be less effective against these isolates. Low resistance to antibiotics such as C and SXT indicates the possibility of using these antibodies as therapeutic options.

Table (4): The percentages of total MDSs and MDRs according to gene distribution.

Isolate sources	Total no. 35	Genes			EtBr Agar concentration			P value
		norB	*mepA*	*mdeA*	1 mg\L	2 mg\L	4 mg\L	
Multidrug sensitive (MDS) isolates	24 (68%)	21 (87%)	24(100%)	24 (100%)	13 (54%)	9 (37%)	6 (25%)	0.037 *
Multidrug resistance (MDR) isolates	11 (23%)	7 (63%)	10 (90%)	10 (90%)	3 (27%)	2 (18%)	1 (9%)	0.816 NS
P value	0.0087 **	0.0074 **	0.0082 **	0.0082**	---	0.0367 *	0.078 NS	---

* (P≤0.05), ** (P≤0.01), NS: Non-Significant.

Table (4) shows the distinctions between multidrug-susceptible (MDS) and multidrug-resistant (MDR) isolates. The percentages of each type of isolate from a total of 35 MRSA isolates are indicated. Gene distribution and percentages of *norB, mepA*, and *mdeA* genes in the isolates. All drug-susceptible (MDS) isolates contained the *mepA* and *mdeA* genes (100%), while the *norB* gene was present in 87% of them. For resistant (MDR) isolates, the norB gene is present in 63%, and the *mepA* and *mdeA* genes are present in 90%. The table displays the response of the isolates to different concentrations of ethedium bromide (1, 2, and 4 mg/L). The percentage of susceptible isolates (MDS) gradually decreased with increasing concentration (54% at 1 mg/L to 25% at 4 mg/L). Resistant (MDR) isolates showed a similar reduction but were less susceptible (27% at 1 mg/L to 9% at 4 mg/L). The results revealed that resistant isolates (MDR) carry a greater percentage of resistance genes than susceptible isolates (MDS). Increasing the concentration of ethedium bromide led to reduced growth of both types of isolates, but resistant isolates were more resistant to high concentrations than were susceptible isolates.

3.8. The minimal inhibitory concentration (MIC) of diclofenac sodium

The inhibitory effects of diclofenac sodium at various concentrations (1000-500-250-125- 62.5 -32.25) tested against eight MDR strains that were methicillin-resistant encoded *mecA* gene and also encoded three efflux pump genes after PCR amplification. The isolates code no. (3,7,8,15,20,30,32,36) were examined via a resazurin based microplate broth dilution assay. The color of resazurin an indicator dye can be altered in response to the metabolic activity of living cells, which is the basis for the assay. Resazurin turns pink when bacterial growth occurs because the metabolic activity of the bacteria reduces the hue of the dye (Belbase *et al.*, 2017). As one of the most standardized techniques for testing antibiotics, it does not require a spectrophotometer because, unlike the conventional assay, the color change may be observed visually(Teh *etal.*,2017). Several studies have shown that several non-steroidal anti-inflammatory drugs(NSAIDs) have strong antibacterial qualities. Diclofenac sodium, in particular, has strong antibacterial activity against both gram positive and gram negative bacteria (Chan *et al.*,2017). The results of this investigation revealed that the lowest inhibitory concentration of olfen varied between 250 and 125µg/ml. Olfen, which has analgesic, antipyretic, and anti-inflammatory qualities, has demonstrated antibacterial activity. With MICs ranging from 50 µg/ml to 200 µg/ml for gram negative bacteria and even lower for some gram-positive bacteria, this non-steroidal anti-inflammatory medication has demonstrated antimicrobial action against a variety of gram positive and gram negative bacteria in recent years (Dutta *et al.*, 2007). These variations in the MICs of this drug may be caused by the

different strain types used in different studies or by methodological factors such as the culture media used, the research methods, and the minimum inhibitory concentrations (MICs) of olfen against all tested gram positive bacteria (Chan *et al*., 2017), which disagrees with the results we obtained. This may be attributed to the fact that the isolates are more resistant and to other reasons, such as the incorrect use of this type of analgesic drug when suffering from bacterial infections. This clearly reveals antibacterial metabolic activity. The effect of diclofenac sodium on the inhibition of bacteria, specifically *S. aureus*, affects many virulence factors in bacteria and this has been confirmed by many studies (Silva *et al.*, 2021). The purpose of this comparison was to clarify the extent of the inhibitory effect of this drug on virulence factors. In particular, for the bacteria *Staphylococcus aureus.* The exact mechanism of antibacterial activity of diclofenac remains to be elucidated. Studies have proposed different mechanism of action like inhibition of bacterial DNA synthesis, impairment of membrane activity, anti-plasmid activity, DNA synthesis and cell envelope, down-regulation of efflux pumps (Dastidar *et al.*, 2000).

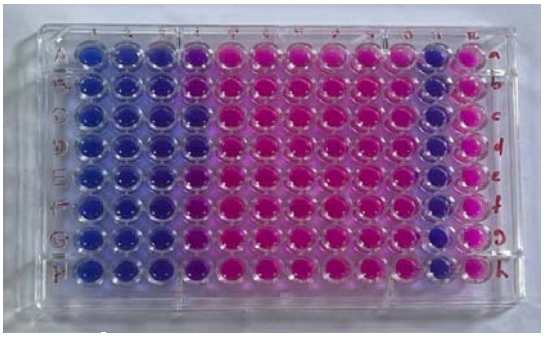

Figure (9): Diclofenac sodium minimum inhibitory concentration of eight MDR *S. aureus* strains determined via the resazurin-based method. Row (11) represents the negative control, which shows the natural color of resazurin (blue/purple). Row 12 represents a positive control, was changed to a reduced form (pink). Wells A-F of each raw isolate contained diclofenac sodium at 1000 –31.25 µg/ml, respectively.

4. Conclusion

Application of NSAIDs, such as diclofenac sodium, could serve as adjunctive agents in combating antibiotic resistance as the first study in Iraq against MRSA isolates. Diclofenc sodium might be considered as antibacterial and anti-efflux pump inhibitors agent for the growth inhibition of MRSA isolates harboring for some efflux pump genes. This points to the need for further researches into adjunctive therapies like another NSAIDs or efflux pump inhibitors.

Funding

There is no funding.

Conflicts of Competing Interest

The authors declare that they have no potential conflicts of interest.

References

Abdel-Karim SA, El-Ganiny AM, El-Sayed MA and Abbas, HA. 2022. Promising FDA-approved drugs with efflux pump inhibitory activities against clinical isolates of *Staphylococcus aureus. Plos One*, **17(7)**: 1-27.

Ahmed ZF and Al-Daraghi WA. 2022. Molecular detection of *medA* virulence gene in *Staphylococcus aureus* isolated from Iraqi patients. *Iraqi J. Biotech.*,**21(1)**:8-18.

Alghamdi, BA, Al-Johani I, Al-Shamrani JM, Alshamrani HM, Al-Otaibi BG, Almazmomi K and Yusof NY. 2023.Antimicrobial resistance in methicillin-resistant *Staphylococcus aureus*. *Saudi J. Biol. Sci.*, **30(4)**:103604.

Al-Mayahi FSA. 2021.A preliminary study of Aminoglycoside Modifying Enzymes (AMEs) of Multiple Antibiotic Resistance of Methicillin-resistant *Staphylococcus aureus* (MRSA) isolated from clinical specimens in Al-Diwaniya/Iraq. *Jordan J. Biol. Sci.*, **4:** 733-741.

Aniba R, Dihmane A, Raqraq H, Ressmi A, Nayme K, Timinouni M, Hicham B, Khalil A and Barguigua A. 2024. Characterization of biofilm formation in uropathogenic *Staphylococcus aureus* and their association with antibiotic resistance. *The Microbe*,**2**: 1-3.

Antiabong JF, Kock MM, Mbelle NM and Ehlers MM. 2017. Diversity of multidrug efflux genes and phenotypic evaluation of the in vitro resistance dynamics of clinical *Staphylococcus aureus* isolates using methicillin; a model β-lactam. *Open Microbiol. J.*, **11**:132.

Awayid SH and Mohammad QS. 2022. Prevalence and antibiotic resistance pattern of methicillin-resistant *Staphylococcus aureus* isolated from Iraqi hospitals. *Arch. Razi Inst.*, **77(3)**:1147-1156.

Baiomy AA, Shaker GH and Abbas HA. 2020. Sensitizing multi-drug resistant *Staphylococcus aureus* isolated from surgical site infections to antimicrobials by efflux pump inhibitors. *Afr. Health Sci.*, **20(4)**,:1632.

Belbase A, Pant ND, Nepal K, Neupane B, Baidhya R, Baidya R and Lekhak B. 2017. Antibiotic resistance and biofilm production among the strains of *Staphylococcus aureus* isolated from pus/wound swab samples in a tertiary care hospital in Nepal. *Ann. Clin. Microbiol. Antimicrob.*,**16**:1-5.

Blair JM, Richmond GE and Piddock LJ. 2014. Multidrug efflux pumps in gram-negative bacteria and their role in antibiotic resistance. *Future Microbiol.*, **9(10)**:1165-1177.

Chan EW, Yee ZY, Raja I and Yap JK.2017. Synergistic effect of nonsteroidal anti-inflammatory drugs (NSAIDs) on antibacterial activity of cefuroxime and chloramphenicol against methicillin-resistant *Staphylococcus aureus*. *J. Glob. Antimicrob. Resist.*,**10**:70-74.

Clinical and Laboratory Standards (CLSI).2024. **Performance Standards for Antimicrobial Susceptibility Testing**. M100 Thirty fourth ed. CLSI Supplement M100 Clinical and Laboratory Standard Institute, USA.

Costa SS, Junqueira E, Palma C, Viveiros M, Melo-Cristino J, Amaral L and Couto I. 2013. Resistance to antimicrobials mediated by efflux pumps in *Staphylococcus aureus*. *Antibiotics*, **2(1)**:83-99.

Couto I, Costa SS, Viveiros M, Martins M and Amaral L. 2008. Efflux-mediated response of *Staphylococcus aureus* exposed to ethidium bromide. *J. Antimicrob. Chemother.*, **62(3)**:504-513.

Dastidar SG, Ganguly K, Chaudhuri K and Chakrabarty AN.2000. The antibacterial action of diclofenac shown by inhibition of DNA synthesis. *Int. J. Antimicrob. Agents*, **14(3)**:249-251.

Dutta NK, Annadurai S, Mazumdar K, Dastidar SG, Kristiansen JE, Molnar J, Martins M and Amaral L. 2007. Potential management of resistant microbial infections with a novel nonantibiotic: the anti-inflammatory drug diclofenac sodium. *Int. J. Antimicrob. Agents*, **30(3):**242-249.

El-Baz AM, Yahya G, Mansour B, El-Sokkary MM, Alshaman R, Alattar A and El-Ganiny AM. 2021.The link between occurrences of class I integron and acquired aminoglycoside resistance in clinical MRSA isolates. *Antibiotics*,**10(5)**:488.

Elshikh M, Ahmed S, Funston S, Dunlop P, McGaw M, Marchant R and Banat IM. 2016. Resazurin-based 96-well plate microdilution method for the determination of minimum inhibitory concentration of biosurfactants. *Biotechnol. Lett.*, **38** :1015-1019.

Foster TJ. 2017. Antibiotic resistance in *Staphylococcus aureus:* current status and future prospects. *FEMS Microbiol. Rev.*, **41(3)**:430-449.

Gaurav A, Bakht P, Saini M, Pandey S and Pathania R.2023. Role of bacterial efflux pumps in antibiotic resistance, virulence, and strategies to discover novel efflux pump inhibitors. *Microbiol.* (Reading, England),**169(5)**:001333.

Hamad PA. 2023. Phenotypic and molecular detection of biofilm formation in methicillin-resistant *Staphylococcus aureus* isolated from different clinical sources in Erbil city. *Mediterr. J. Hematol. Infect. Dis.*, **15(1)**: e2023016.

Hamel MS, Hussain AM, Shehab ZH, Al-Mayyahi AW and Abdulhassan AA.2021. Effect of ultraviolet light on the expression of *icaD* gene in *Staphylococcus aureus* local isolates in Iraq. *Arch. Razi Inst.*,**76(5)**:1221-1227.

Hantoosh SM. 2022. Nasal carriage of vancomycin- and methicillin-*resistant Staphylococcus aureus* among intermediate students of urban and rural schools of Muthanna Province in Iraq. *Iraqi J. Pharm. Sci.*, **31(1)**:102-108.

Hassanzadeh S, Mashhadi R, Yousefi M, Askari E, Saniei M and Pourmand MR. 2017. Frequency of efflux pump genes mediating ciprofloxacin and antiseptic resistance in methicillin-resistant *Staphylococcus aureus* isolates. *Microb. Pathog.*, **111** :71-74.

Jabur EQ and Kandala N. 2022.The production of biofilm from methicillin-resistant *Staphylococcus aureus* isolated from post-surgical operation inflammation. *Iraqi J. Sci.*, **63(9)**:3688-3702.

Jang S. 2016. Multidrug efflux pumps in *Staphylococcus aureus* and their clinical implications. *J. Microbiol.*, **54**: 1-8.

Jia L, Zhao J, Yang C, Liang Y, Long P, Liu X, Qiu S, Wang L, Xie J, Li H and Liu H. 2019. Severe pneumonia caused by coinfection with influenza virus followed by methicillin-resistant *Staphylococcus aureus* induces higher mortality in mice. *Front. Immunol.*, **9**:3189.

Kadhum, HH and Abood ZH. 2022. *Staphylococcus aureus* incidence in some patients with atopic dermatitis in Baghdad City. *Iraqi J. Biotech.*, **21(2)**:13-20.

Kumar MK, Tyagi C, Sahu A, Desai N, Manjhi J, Mohan KC, *et al.*2020. Identification and characterization of *Staphylococcus aureus 16S rRNA* gene isolated from different food specimens from South Indian region. *J. Drug Deliv. Ther.*, **10(5)**:24-32.

Li XZ, Plésiat P and Nikaido H.2015. The challenge of efflux-mediated antibiotic resistance in Gram-negative bacteria. *Clin. Microbiol. Rev.*, **28(2)**:337-418.

Maharjan M, Sah AK, Pyakurel S, Thapa S, Maharjan S, Adhikari N, Rijal KR, Ghimire P. and Thapa Shrestha, U.2021. Molecular confirmation of vancomycin-resistant *Staphylococcus aureus* with *vanA* gene from a hospital in Kathmandu. *Int. J. Microbiol.*, **1:**3847347.

Marciniak K, Tyczewska A and Grzywacz K. 2024. Genetics of antibiotic resistance in methicillin-resistant *Staphylococcus aureus* (MRSA). *BioTechnologia*, **105(2)**:169-177.

Martins M, McCusker MP, Viveiros M, Couto I, Fanning S, Pagès JM and Amaral L. 2013. A simple method for assessment of MDR bacteria for overexpressed efflux pumps. *Open Microbiol. J.*, **7** :72-82.

Martins M, Viveiros M, Couto I, Costa SS, Pacheco T, Fanning S, Pagès JM and Amaral L. 2011. Identification of efflux pump-mediated multidrug-resistant bacteria by the ethidium bromide-agar cartwheel method. *In Vivo (Athens, Greece)*, **25(2)**:171-178.

Mehrotra M, Wang G and Johnson WM. 2000. Multiplex PCR for detection of genes for *Staphylococcus aureus* enterotoxins, exfoliative toxins, toxic shock syndrome toxin 1, and methicillin resistance. *J. Clin. Microbiol.*, **38(3)**:1032-1035.

Nuaimi IS , Al Joubori B. and Kanan, S.2023. Activity of lactic acid-producing Streptomyces strain CSK1 against *Staphylococcus aureus*. *Jordan J. Biol. Sci.*, **2 :**353-361.

Patel D, Kosmidis C, Seo SM and Kaatz GW.2010. Ethidium bromide MIC screening for enhanced efflux pump gene expression or efflux activity in *Staphylococcus aureus*. *Antimicrob. Agents Chemother.*, **54** :5070-5073.

Pu Y, Ke Y and Bai F. 2017. Active efflux in dormant bacterial cells–new insights into antibiotic persistence. Drug Resist. *Updates*, **30** :7-14.

Rasheed, NA and Hussein NR. 2021. *Staphylococcus aureus*: an overview of discovery, characteristics, epidemiology, virulence factors and antimicrobial sensitivity. *Eur. J. Mol. Clin. Med.*, **8(3)**:1160-1183.

Sabbar SR, Talib AH and Fakhry SS. 2023. Antibiotic resistance of *Staphylococcus sp.* isolated from air, surface, food and clinical samples collected from Baghdad Hospital. *Baghdad Sci. J.*, **20(5)**, pp.1858-1865.

Saber N, Kandala NJ and Mohammed HA. 2019. Detection of a new antiseptic-resistant variant of qac gene in some multi-drug resistant *Staphylococcus aureus* isolated from different clinical sources. *Baghdad Sci. J.*, **16(3)**:571-579.

Saud B, Khatri G, Amatya N, Paudel G and ShresthaV. 2023. Methicillin-resistant and biofilm-producing *Staphylococcus aureus* in nasal carriage among healthcare workers and medical students. *Can. J. Infect. Dis. Med. Microbiol.*, **2023**:1-6.

Scudiero O, Brancaccio M , Mennitti C, Laneri S, Lombardo B, De Biasi MG, De Gregorio E, Pagliuca C, Colicchio R, Salvatore P and Pero R.2020. Human defensins: A novel approach in the fight against skin colonizing *Staphylococcus aureus*. *Antibiotics*, **9(4):**198.

Shamkhi GJ, Saadedin SM and Jassim KA. 2019. Detection of the prevalence of some chromosomal efflux pump genes in methicillin-resistant *Staphylococcus aureus* isolated from Iraqi patients. *Iraqi J. Biotech.*,**18(3)**:33-42.

Sharma A, Sharma R, Bhattacharyya T, Bhando T and Pathania R. 2016. Fosfomycin resistance in *Acinetobacter baumannii* is mediated by efflux through a major facilitator superfamily (MFS) transporter AbaF. *J. Antimicrob. Chemother.*, **72(1)**:68-74.

Silva AL, Viana AS, Silva PM, de Matos Nogueira E, Salgado LT, Tomazetto de Carvalho R, Geraldo da Silva Filho R. 2021. Diclofenac may induce PIA-independent biofilm formation in *Staphylococcus aureus* strains. *Int. J. Microbiol.*, **2021**:1-11.

Smith J, Brown P and Johnson R. 2021. Diclofenac as an antivirulence agent in *Staphylococcus aureus* osteomyelitis: Enhancing antibiotic efficacy. *Front. Microbiol.*, **12** :1-10.

SPSS. 2019. **Statistical Packages of Social Sciences-SPSS-IBM Statistics 26 step by step**. Sixteenth ed.,New York.

Suma TA, Alam N, Raihan SZ, Zahid MA, Mandal SC, Suchana FJ, Kundu R, Hossain A, Muhit MA.2023. Association of antibacterial susceptibility profile with the prevalence of genes encoding efflux proteins in the Bangladeshi clinical isolates of *Staphylococcus aureus*. *Antibiotics*, **12(2)**:305.

Teh CH, Nazni WA, Nurulhusna AH, Norazah A. and Lee HL. 2017. Determination of antibacterial activity and minimum inhibitory concentration of larval extract of fly via resazurin-based turbidometric assay. *BMC Microbiol.*, **17**:1-8.

Tille PM. 2017. **Bailey & Scott's Diagnostic Microbiology**, Fourteenth ed. Elsevier.

Vestergaard M, Frees D. and Ingmer H. 2019. Antibiotic resistance and the MRSA problem. *Microbiol. Spectrum*, **7(2)**:10-128.

Woodford, N., 2003. Novel agents for the treatment of resistant gram-positive infections. *Expert Opin. Investig. Drugs*, **12(2)**:117-137.

Youssef CR, Kadry AA, Shaker GH and El-Ganiny AM. 2021.The alarming association between antibiotic resistance and reduced susceptibility to biocides in nosocomial MRSA isolates from two regional hospitals in Egypt. *Arch. Microbiol.*, **203**:3295-3303.

JJBS

Volume 18, Number 3,September 2025
ISSN 1995-6673
Pages 531 – 537

Jordan Journal of Biological Sciences

Highlighting Protease-Producing Bacteria from The Shrimp Wastewater Treatment Plant as Potential Bioremediation Agents

Devi Oktavia Anjani[1,2], Wilis Ari Setyati[1*], Delianis Pringgenies[1]

[1]Department of Marine Science, Faculty of Fisheries and Marine Science, Universitas Diponegoro, Jl. Prof. H. Soedarto, S.H, Semarang, Central Java, 50275, Indonesia; [2]Department of Aquatic Resources Management, Faculty of Fisheries and Marine Science, Universitas Diponegoro, Jl. Prof. H. Soedarto, S.H, Semarang, Central Java, 50275, Indonesia

Received: January 12, 2024; Revised: May 8, 2025; Accepted: May 22, 2025

Abstract

Shrimp cultivation waste comprises uneaten feed, residual material from digestion, exoskeletons, and metabolic byproducts. This waste is considered a potential source of bioremediation agents due to the abundance of decomposing bacteria. This study aimed to evaluate the growth kinetics and proteolytic enzyme activity of bacteria isolated from shrimp pond waste for their potential use in bioremediation. Water samples were collected from the wastewater treatment plant of a shrimp cultivation facility at the Diponegoro Science Techno Park, Jepara, Indonesia. The methods used in this study included bacterial isolation and purification, screening for protease-producing bacteria, observation of bacterial growth kinetics, measurement of protein content and total protease activity, and molecular identification using 16S rRNA gene sequencing. The results showed that 6 out of 37 bacterial isolates exhibited proteolytic activity. Two isolates, namely IT.2 and IC.1, were selected as the most promising candidates based on their high proteolytic index values (PI > 5). Growth kinetics analysis revealed that both IT.2 and IC.1 underwent logarithmic, stationary, and death phases within a 48-hour cultivation period. Isolate IT.2 exhibited the highest protease activity at 40.92 U/mL, while IC.1 reached 39.65 U/mL. Molecular identification indicated that IT.2 and IC.1 have the closest similarity to *Vibrio fluvialis* and *Pseudoalteromonas piscicida*, respectively. These findings demonstrate that bacteria isolated from shrimp pond waste have significant potential as bioremediation agents to mitigate pollution in aquaculture environments.

Keywords: Bacteria, bioremediation agent, growth kinetics, protease enzyme

1. Introduction

The high market demand for shrimp has driven a significant increase in shrimp farming operations in Indonesia (KKP, 2020). This expansion in aquaculture has led to greater volumes of waste being discharged into surrounding environments. Waste generated during the cultivation process includes undigested feed, shrimp excreta, exoskeletons, and various metabolic byproducts. The amount of waste produced is closely linked to the shrimp stocking density. According to Tampangallo et al. (2020), at a stocking density of 500 individuals/m², waste levels can reach 50.12 g of total nitrogen (TN), 15.73 g of total phosphorus (TP), and 126.85 g of carbon (C) per kilogram of feed.

Feed serves as the primary nutritional source for cultured shrimp; however, only about 22% of the total feed provided is effectively absorbed and converted into shrimp biomass. The remainder is lost in various forms: 57% dissolves in water, 14% settles at the pond bottom, and 7% is consumed by microorganisms (Jackson et al., 2003).

Protein, the most significant component of waste in shrimp ponds, undergoes degradation through aerobic and anaerobic pathways (Sanjaya et al., 2023). Under aerobic conditions, nitrogen-rich proteins are broken down into carbon dioxide (CO_2), water, and ammonium (NH_4^+), a process that increases the biological oxygen demand (BOD) in the pond. When oxygen becomes depleted, degradation proceeds anaerobically, producing ammonia (NH_3), which is highly toxic to aquatic organisms and poses a serious threat to coastal ecosystems (Xu et al., 2021).

Aerobic biodegradation agents are crucial for breaking down proteins into simpler compounds, thereby minimizing the accumulation of harmful anaerobic byproducts. Gichana et al. (2018) reported that microorganisms are effective agents for organic waste degradation and are widely used in aquaculture waste management. The addition of such microorganisms facilitates the transformation of organic matter into less harmful compounds that can be further processed by the natural environment.

Protease enzymes play a vital role in protein degradation by hydrolyzing complex peptide bonds into simpler peptides or free amino acids (Thanoon et al., 2018). This enzymatic process enhances the functional, biological, and nutritional properties of the resulting compounds. Proteases are extensively used across various industries, including pharmaceuticals, leather production, detergents, food processing, and waste treatment (Sharma et al., 2019). These enzymes can be sourced from animals,

* Corresponding author. e-mail: wilisarisetyati@yahoo.com.

plants, or microorganisms, with bacteria being the most commonly used due to their rapid growth, ease of cultivation, consistent enzyme yields, and suitability for large-scale production (Song et al., 2023). Microbial sources contribute to approximately 66% of global protease production, accounting for nearly 40% of optimized compounds used in industrial processes (Sharma et al., 2019).

Shrimp pond waste, rich in protein and other nutrients, provides a favorable environment for bacterial growth. Ariaeenejad et al. (2022) reported that bacteria isolated from various liquid and solid waste sources can degrade protein-rich materials, dissolve proteins, and survive extreme environmental conditions. Leiva-Portilla et al. (2023) further demonstrated the potential of shrimp pond-associated bacteria to produce bioactive compounds, such as antioxidants, through enzymatic hydrolysis.

Given this context, further investigation is warranted to explore the protease-producing capabilities of bacteria isolated from shrimp pond waste. Hence, the present study evaluated the enzymatic activity and growth kinetics of these bacteria in degrading proteins, thereby assessing their potential as bioremediation agents.

2. Method

2.1. Sampling

Water samples were obtained from the tanks of a wastewater treatment plant (WWTP) at a shrimp cultivation facility located at Diponegoro Science Techno Park, Jepara, Indonesia (6°37'8.18"S, 110°38'25.58"E). *Litopenaeus vannamei* was the species cultivated at the facility. Two bottle samples were collected from two different wastewater tanks, each containing 45 mL of wastewater, and stored securely in Falcon tubes. The samples were kept in a cool box and transported to the laboratory for further bacterial isolation.

2.2. Bacterial Isolation

The wastewater samples were serially diluted up to a dilution factor of 10^{-5} (Al-Zereini, 2014). Bacteria were isolated using the pour plate method, where 1 mL of the 10^{-5} dilution was added to a sterile Petri dish. Sterile Zobell Marine Agar (ZMA) medium was then poured into the dish. The inoculated Petri dishes were incubated at 37°C for 2-3 days.

2.3. Purification and Characterization of Bacterial Isolates

Bacterial isolates were purified and characterized. The isolates that appeared were streaked onto fresh media using the four-quadrant streaking method. Morphological characterization was performed by observing colony size, shape, margin, elevation, and color on the culture media (Zebua et al., 2020).

2.4. Proteolytic Activity Screening

Proteolytic activity was screened following the method described by Setyati et al. (2023). The screening medium was prepared by adding 1% skim milk to Zobell Marine Agar. Previously cultured bacterial isolates were inoculated onto sterile blank paper discs, which were then placed on top of the prepared medium. The Petri dishes were incubated for 48 hours, with observations made every 24 hours. Proteolytic activity was indicated by the formation of a clear zone surrounding the paper disc and bacterial colony.

2.5. Bacterial Growth Kinetics

The growth kinetics of protease-producing bacterial isolates were evaluated using time-course optical density measurements in liquid culture. Isolates exhibiting the highest proteolytic activity were selected and cultured in Zobell Broth. A single colony from each isolate was inoculated into 10 mL of Zobell Broth and incubated at 30°C with constant shaking at 110 rpm for 18-24 hours to obtain a preculture. A 1% (v/v) inoculum from the preculture was transferred into 250 mL of sterile Zobell Broth in a 500 mL Erlenmeyer flask. The cultures were incubated at 30°C in a shaker incubator at 110 rpm for 48 hours.

Bacterial growth was monitored by measuring optical density at 600 nm (OD_{600}) using a UV-Vis spectrophotometer at predetermined time intervals: 0, 2, 4, 6, 12, 18, 24, 30, 36, 42, and 48 hours. At each time point, 4 mL of the culture was aseptically withdrawn into a sterile Falcon tube and centrifuged at 3000 rpm for 10 minutes. The supernatant was discarded, and the remaining biomass was resuspended in 4 mL of sterile phosphate-buffered saline (PBS). The mixture was homogenized thoroughly, and OD_{600} readings were recorded to assess bacterial growth (Nguyen-Sy et al., 2020).

2.6. Measurement of Protease Enzyme Activity

Protease enzyme activity was measured using the casein assay method, following the protocols described by Anh et al. (2021) and Sher et al. (2011), with slight modifications. Bacterial cultures were prepared as described in the bacterial growth kinetics section. Enzyme activity was evaluated at intervals of 0, 2, 4, 6, 12, 18, 24, 30, 36, 42, and 48 hours. At each time point, 4 mL of culture was aseptically withdrawn into a sterile Falcon tube and centrifuged at 3000 revolutions per minute (rpm) for 10 minutes. The resulting supernatant was collected and used as the crude enzyme extract.

To perform the assay, 0.2 mL of the crude enzyme extract was transferred into a clean test tube. Afterward, 1 mL of Tris(hydroxymethyl)aminomethane-hydrochloride (Tris-HCl) buffer and 0.5 mL of a 1% (w/v) casein substrate were added. The mixture was vortexed and incubated at 37°C for 10 minutes to allow the enzymatic reaction to proceed. The reaction was stopped by adding 1 mL of 10% trichloroacetic acid (TCA) solution. The mixture was then centrifuged at 10,000 rpm for 10 minutes. From the resulting solution, 0.5 mL of the supernatant was transferred to a new test tube and mixed with 2.5 mL of 0.5 M sodium carbonate (Na_2CO_3) solution. This mixture was incubated at 37°C for 10 minutes.

After incubation, 1 mL of Folin-Ciocalteu reagent was added, and the solution was mixed thoroughly. The reaction mixture was incubated in the dark for 30 minutes. Absorbance was measured at 660 nanometers (nm) using a UV-Vis spectrophotometer. A blank control was prepared using the same procedure, substituting distilled water for the enzyme extract. Absorbance values were converted to micromoles of tyrosine using a tyrosine standard curve.

Protease activity was calculated using the following formula (Bhavikatti et al., 2020):

$$AP = \frac{mM}{(T \times V)}$$

(Source: Bhavikatti et al., 2020)

Notes:

AP = Protease enzyme activity (Units per milliliter, U/mL)

mM = Micromoles of tyrosine released (equivalent to µmol/mL)

T = Incubation time (minutes)

V = Volume of enzyme used (mL)

2.7. Protein Content Measurement

Protein content was determined using the Bradford assay method, originally developed by Bradford (1976) and later modified by Kruger (2009). This colorimetric method relies on the binding of Coomassie Brilliant Blue G-250 dye to proteins. A total of 400 µL of the crude enzyme extract (i.e. the supernatant from the centrifuged bacterial culture) was transferred into a clean reaction tube. Then, 4 mL of diluted Bradford reagent was added, and the mixture was vortexed to ensure uniform mixing. The solution was incubated at room temperature for 10 minutes to allow color development. After incubation, the absorbance was measured at 595 nm using a UV-Vis spectrophotometer. Protein concentrations were calculated based on a standard curve generated using Bovine Serum Albumin (BSA), and results were expressed in milligrams per milliliter (mg/mL).

2.8. DNA Extraction

DNA extraction from bacterial isolates obtained from shrimp pond wastewater was performed using the Presto™ Mini gDNA Bacteria Kit (Geneaid Ltd., Taiwan), following the manufacturer's protocol.

2.9. Polymerase Chain Reaction (PCR)

PCR amplification was conducted using universal bacterial primers 27F (5′-AGAGTTTGATCCTGGCTCAG-3′) and 1492R (5′-TACGGCTACCTTGTTACGACTT-3′). Each 25 µL PCR reaction mixture contained 1 µL of 27F primer (10 µM), 1 µL of 1492R primer (10 µM), 12.5 µL of MyTaq Green Mix, 9.5 µL of DDH_2O, and 1 µL of DNA template. Thermal cycling was performed with the following conditions: initial denaturation at 95°C for 1 minute, followed by 35 cycles of denaturation at 95°C for 15 seconds, annealing at 55°C for 30 seconds, and extension at 72°C for 45 seconds, with a final extension step at 72°C for 3 minutes. Amplification products were verified through electrophoresis on a 1% agarose gel, run at 100 V for 30 minutes.

2.10. Sequencing

DNA sequencing was performed using the Sanger sequencing method. The sequencing data were analyzed using MEGA 11 Software. Bacterial species were identified by comparing the obtained nucleotide sequences against the NCBI GenBank database (https://www.ncbi.nlm.nih.gov) using the BLAST (Basic Local Alignment Search Tool) algorithm.

3. Results

3.1. Bacterial Isolation

A total of 37 isolates were obtained from the isolation and purification of two wastewater samples. Of these, 21 isolates were obtained from water samples taken from Tank A of the WWTP and were assigned the isolate code "IT." Similarly, 16 isolates were obtained from Tank C of the WWTP and were assigned the code "IC."

3.2. Proteolytic Enzyme Activity

The screening results showed that six isolates exhibited proteolytic activity after 48 hours of observation. The isolate with the highest proteolytic index (PI) at the end of the observation period was IT.2 (5.83), followed by IC.1 (5.51), IC.5 (4.11), IT.9 (3.95), IT.1 (3.00), and IC.8 (2.82), which had the lowest PI. The clear zone diameter and the proteolytic index for each isolate are presented in Table 1.

Table 1. Clear Zone Diameter and Proteolytic Index of Bacterial Isolates from Shrimp Pond Wastewater

Isolate Code	Proteolytic Activity Assay			
	Clear Zone Diameter		Proteolytic Index (PI)	
	24h	48h	24h	48h
IT.1	14.7±0.084	17.975±0.7	2.45	3.00
IT.2	34.9±0.42	35±0.28	5.82	5.83
IT.9	13.95±0.63	23.7±0.42	2.33	3.95
IC.1	21.5±0.42	33.05±0.49	3.58	5.51
IC.5	11.35±0.63	24.65±0.49	1.89	4.11
IC.8	13.18±0.48	16.895±0.27	2.20	2.82

3.3. Bacterial Growth Kinetics

Growth kinetics were observed for isolates IT.2 and IC.1, demonstrating the highest proteolytic activity. The results of the bacterial growth measurements are shown in Figure 1 and Table 2. Both isolates underwent logarithmic, stationary, and death phases over the 48-hour observation period.

Table 2. Growth Rate and Generation Time of Isolate IT.2 and Isolate IC.1

Isolate Code	Growth Rate (hr^{-1})	Generation Time (hours)
IT.2	0.24	2.83
IC.1	0.26	2.68

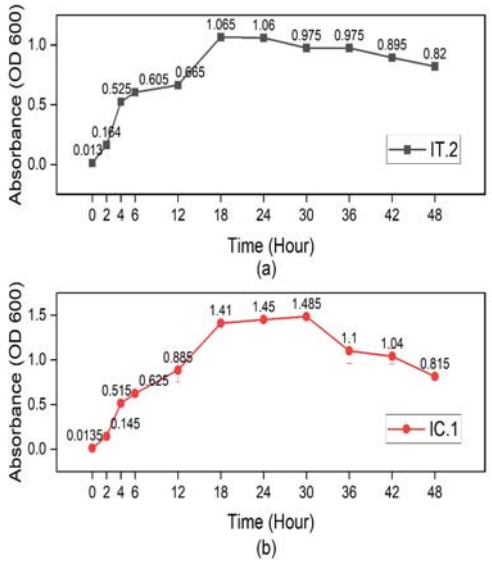

Figure 1. Growth Kinetics Curve of Isolate IT.2 (a) and Isolate IC.1 (b)

Isolate IT.2 exhibited a slower growth rate (0.24 h^{-1}) and longer generation time (2.83 hours) compared to isolate IC.1, which had a growth rate of 0.26 h^{-1} and a generation time of 2.68 hours. The cell density of IT.2 increased until the 24th hour, after which it gradually declined. As shown in Figure 1, isolate IT.2 reached its peak density at 24 hours (1.06±0.02). In contrast, isolate IC.1 followed a similar growth trend but peaked at 30 hours (1.485±0.007) before declining.

3.4. Protease Enzyme Activity

Isolate IT.2 showed increasing protease enzyme production, reaching a peak of 40.92 U/mL at the 30th hour. However, enzyme activity significantly declined afterward, reaching 17.67 U/mL by the 48th hour. Conversely, isolate IC.1 exhibited a continued increase in enzyme activity, peaking at 39.65 U/mL at the 42nd hour, with a slight decrease to 35.91 U/mL by the 48th hour. The protease enzyme production profiles of both isolates are illustrated in Figure 2.

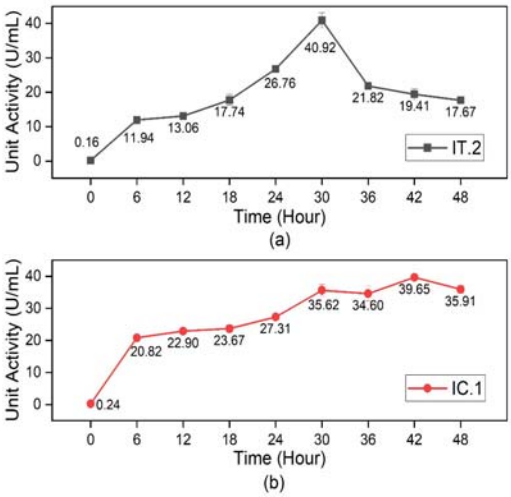

Figure 2. Protease Enzyme Production by Isolate IT.2 (a) and Isolate IC.1 (b)

3.5. Protein Content

The protein content in the growth medium was measured throughout the observation period, and the results are shown in Figure 3. Both isolates exhibited a reduction in protein concentration from the beginning to the end of the experiment. For isolate IT.2, the protein content decreased from 0.258 mg/mL at 0 hours to 0.122 mg/mL at 48 hours. Similarly, the protein content in the medium for isolate IC.1 declined from 0.317 mg/mL at 0 hours to 0.123 mg/mL after 48 hours.

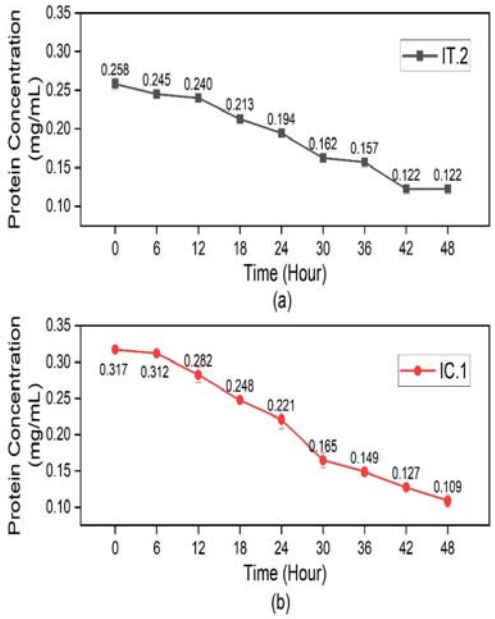

Figure 3. Protein Hydrolysis by Isolate IT.2 (a) and isolate IC.1 (b)

3.6. Bacterial Identification

Based on BLAST analysis, isolate IT.2 was identified as *Vibrio fluvialis* with a 99.65% similarity. Meanwhile, isolate IC.1 showed the closest match to *Pseudoalteromonas piscicida*, with a similarity of 99.76%. The detailed BLAST results of the bacterial sequences are presented in Table 4.

Table 4. BLAST Identification Results for Isolates IT.2 and IC.1

Isolate Code	Closest Similarity	Percent Identification	Query Coverage	Accession Number
IT.2	*Vibrio fluvialis*	99.65%	100%	PQ326252.1
IC.1	*Pseudoalteromonas piscicida*	99.76%	100%	PQ326253.1

4. Discussion

Out of the 37 bacterial isolates obtained, six demonstrated proteolytic enzyme activity, as presented in Table 1. The proteolytic index (PI) and the average diameter of the proteolytic zone for these six isolates increased between the 24-hour and 48-hour observations. Bacterial colonies produced protease enzymes that hydrolyzed proteins in skim milk into simpler peptides and amino acids. This process involved the insertion of water

molecules into the CO-NH peptide bonds, leading to their cleavage and the transformation of solid casein into a liquid or hydrolyzed form (Razzaq et al., 2019). Although all bacteria contain intracellular protease enzymes, not all are capable of producing extracellular proteases. These extracellular enzymes are secreted by bacteria to degrade complex polymers such as proteins, polysaccharides, and lipids present in their external environment. This enzymatic activity allows bacteria to access nutrients from surrounding organic materials (Rosazza et al., 2023).

Among the tested isolates, IT.2 and IC.1 displayed the highest proteolytic index values at the end of the observation period (PI > 5), signifying strong proteolytic activity. A PI value above 3.5 is generally considered high. This classification is supported by Ayuningrum et al. (2022), who defined PI values less than 1.5 as low, between 1.5 and less than 3.5 as moderate, and 3.5 or higher as high. High PI values suggest potential for further development as a protein source. Based on these classifications, except for isolates IC.8 and IT.1, four isolates demonstrated high proteolytic activity by the end of the study.

No lag phase was observed in the growth curves of either isolate, as illustrated in Figure 1. This could be due to their ability to rapidly adapt to the growth medium. Madigan et al. (2012) noted that microbes transferred to fresh media during their logarithmic phase, or those previously cultured in similar media, often adapt quickly without an adaptation period.

The logarithmic phase for isolate IC.1 was observed from hour 0 (OD_{600} = 0.0135) to hour 18 (OD_{600} = 1.41), during which absorbance increased significantly. The stationary phase occurred from hour 18 (OD_{600} = 1.41) to hour 30 (OD_{600} = 1.485), where absorbance values plateaued. A sharp decline in absorbance from hour 30 (OD_{600} = 1.485) to hour 48 (OD_{600} = 0.815) indicated the onset of the death phase. The growth pattern of isolate IT.2 closely mirrored that of IC.1, though IT.2 exhibited slightly lower absorbance values. IT.2 entered the logarithmic phase between hour 0 (OD_{600} = 0.013) and hour 18 (OD_{600} = 1.065), followed by a stationary phase until hour 36 (OD_{600} = 0.975), and finally a death phase from hour 36 to hour 48 (OD_{600} = 0.82). These growth dynamics are presented in Figure 1.

The bacterial growth cycle consists of several distinct phases: the lag phase (adaptation phase), the exponential (logarithmic) phase, the stationary phase, and the death phase (Allen & Maclaw, 2018). During the lag phase, bacteria adjust their cellular metabolism to adapt to the new environmental conditions. The duration of this phase varies depending on the bacterial species, environmental stressors, and the physiological state of cells from the previous culture medium. Interestingly, Ilmiah et al. (2018) also reported bacterial growth that bypassed the lag phase, where the logarithmic phase began immediately at hour 0 and continued until maximum growth was achieved.

The logarithmic phase is characterized by exponential cell division and heightened metabolic activity. In this phase, the bacterial culture consumes more energy and synthesizes metabolites required for cell growth. The specific growth rate remains constant, but the medium undergoes chemical changes due to substrate consumption and metabolic by-product accumulation (Allen & Maclaw, 2018). The stationary phase follows when the growth rate slows and the number of viable cells stabilizes. This stagnation is primarily due to the depletion of essential nutrients and the build-up of toxic metabolic by-products. Jaishankar and Srivastava (2017) support this condition, stating that the transition to the stationary phase typically occurs when nutrients become limiting. During the death phase, viable bacterial cells decrease as cell lysis occurs, leading to a drop in turbidity. This phase marks the end of the growth cycle and reflects unfavorable conditions for cell survival.

Based on growth analysis, isolate IT.2 exhibited a growth rate of 0.24 h^{-1} with a generation time of 2.83 hours, while isolate IC.1 demonstrated a slightly higher growth rate of 0.26 h^{-1} and a shorter generation time of 2.68 hours, as summarized in Table 2. These results indicate that the IT.2 isolate increased by approximately 24% per hour, while IC.1 grew by 26% per hour. The bacterial growth rate is defined as the rate at which a bacterial population increases over time and is typically expressed as the logarithmic change in cell count per unit of time (Allen & Maclaw, 2018). Generation time, or doubling time, refers to the duration required for a bacterial population to double in size. These two parameters are inversely related; faster growth rates correspond to shorter generation times.

The enzyme activity of isolate IT.2 increased progressively from hour 0 (0.16 U/mL), peaking at hour 30 with 40.92 U/mL. By the 36th hour, enzyme activity began to decline, reaching 17.67 U/mL at hour 48. These results indicate that the highest protease production by isolate IT.2 occurred during the stationary phase of its growth (between the 18th and 36th hours). This observation aligns with the findings by Ilmiah et al. (2018), who reported peak protease production by *Bacillus licheniformis* during the stationary phase or at the end of the logarithmic phase. Suleiman et al. (2020) further support this, suggesting that enzyme synthesis typically correlates with active cell growth and reaches maximum levels during the late exponential or early stationary phase due to the accumulation of cellular metabolites. The subsequent decline in protease activity after the 36th hour might be attributed to substrate limitation. Ramadhan et al. (2023) noted that enzyme activity declines when substrate availability decreases because it lacks sufficient substrate to interact with, preventing it from reaching its full catalytic potential.

For isolate IC.1, protease activity began at 0.24 U/mL at hour 0 and steadily increased, peaking at 39.65 U/mL at hour 42. A decrease was observed at hour 48, with activity dropping to 35.91 U/mL. Unlike isolate IT.2, which exhibited a decline in enzyme activity at the onset of the death phase, isolate IC.1 maintained increasing enzyme production even as the cell population began to decline after hour 36. This suggests that enzyme synthesis continued despite a reduction in biomass. The total protein content in the culture media of both isolates showed a declining trend from the start to the end of the observation period (see Figure 3), indicating substrate depletion over time.

A study by Ramin and Allison (2019) found that high enzyme activity can still occur when bacterial growth rates

are near zero. In such conditions, bacteria may continue to produce enzymes even when no degradable substrate is present in the medium. This phenomenon is attributed to the production of constitutive enzymes that are continuously synthesized and secreted regardless of substrate presence. The persistence of protease activity in isolate IC.1 during the death phase could thus be explained by this constitutive enzyme production mechanism. As nutrients in the environment become limited, bacterial cells may have reallocated internal resources to prioritize secondary metabolic activities, including enzyme secretion. However, since extracellular enzyme synthesis requires energy and substrates for processes such as transcription, translation, and protein secretion, the eventual decline in biomass and nutrient depletion led to reduced enzyme activity observed at hour 48 (35.91 U/mL).

Several key factors affect enzyme activity, including pH, temperature, carbon source, incubation time, and salinity. Anh et al. (2021) reported that protease activity produced by halophilic bacteria is significantly affected by variations in temperature, pH, salinity, and incubation duration. A study by Sun et al. (2023) observed that under optimized fermentation conditions, protease production by *Bacillus subtilis* increased by up to 300.72% compared to baseline levels. Similarly, Osesusi et al. (2021) found that *Bacillus ruris* produced stable alkaline proteases at pH 9 and 55°C, demonstrating that specific environmental conditions can enhance enzyme stability and activity. These findings highlight the significant effect of environmental parameters on protease expression and underscore the need for further research to optimize these conditions. Given these insights, it is essential to conduct additional studies focused on the purification, optimization, and characterization of the protease enzyme produced by isolate IC.1. Such investigations would provide a more comprehensive understanding of its catalytic properties and potential industrial applications.

Protein concentrations in the culture media for IT.2 and IC.1 isolates steadily declined throughout the study (see Figure 3). For isolate IT.2, the protein content decreased from 0.258 mg/mL at hour 0 to 0.122 mg/mL at hour 48. Similarly, for isolate IC.1, the protein concentration dropped from 0.317 mg/mL to 0.109 mg/mL over the same time period. This reduction is attributed to the proteolytic activity of the secreted enzymes, which hydrolyze proteins into smaller peptides and amino acids. Bhavikatti et al. (2020) similarly reported an inverse correlation between protease enzyme production and the remaining protein content in the growth medium. In essence, higher enzyme activity levels correlate with greater protein degradation in the surrounding medium.

Molecular identification revealed that isolate IT.2 shared the closest genetic similarity with *Vibrio fluvialis*, while isolate IC.1 was closely related to *Pseudoalteromonas piscicida*. *V. fluvialis* is a well-known marine bacterium frequently isolated from seawater and marine environments. Previous studies have shown that this species is capable of protease production. For instance, Wang et al. (2007) reported that crude extracts from *V. fluvialis* strain TKU005 exhibited protease activity totaling 34 U, with optimal activity at pH 8 and 60°C. Additionally, research by Venugopal and Saramma (2006) showed that crude proteases from *V. fluvialis* achieved a specific activity of 8.199 U/mg, which increased to 10.212 U/mg following purification via ammonium sulfate precipitation.

P. piscicida is a marine bacterium classified within the class *Gammaproteobacteria*. It is heterotrophic, rod-shaped, motile via long flagella, sporeless, and Gram-negative (Eze et al., 2023). Commonly found in marine habitats and mangrove ecosystems, *P. piscicida* is recognized for its ability to produce a wide range of biologically active compounds, including antimicrobial, antifouling, algicidal, and therapeutic agents. According to Eze et al. (2023), these bioactive properties make the bacterium of considerable biotechnological interest. Richard et al. (2017) further reported that genomic analysis of three *P. piscicida* strains revealed the presence of 13 genes encoding extracellular proteases. Detailed characterization showed that the bacterium could secrete various classes of proteases, including cysteine proteases, serine proteases, and metalloproteases.

5. Conclusion

Bacterial isolates from the wastewater treatment plant of a shrimp cultivation facility exhibited proteolytic activity. The results showed that out of 37 isolates, six of them (IT.2, IC.1, IT.1, IT.9, IC.8, and IC.5) demonstrated proteolytic activity, ranging from moderate ($1.5 < PI \leq 3.5$) to high ($PI > 3.5$) protease index levels. Growth kinetics observations of the two most potent protease-producing isolates, IT.2 and IC.1, revealed that both underwent logarithmic, stationary, and death phases within a 48-hour period. The IT.2 isolate showed the highest similarity to *Vibrio fluvialis*, producing protease enzymes with a peak activity of 40.92 U/mL. Meanwhile, the IC.1 isolate exhibited the closest similarity to *Pseudoalteromonas piscicida*, with a maximum protease activity of 39.65 U/mL.

References

Allen RJ and Waclaw B. 2018. Bacterial growth: A statistical physicist's guide. *Rep Prog Phys.*, **82(1):** 1-55.

Al-Zereini WA. 2014. Bioactive crude extracts from four bacterial isolates of marine sediments from Red Sea, Gulf of Aqaba, Jordan. *Jordan J Biol Sci.*, **7(2):** 133-137.

Anh HTH, Shahsavari E, Bott NJ and Ball AS. 2021. Application of co-culture technology to enhance protease production by two halophilic bacteria, *Marinirhabdus* sp. and *Marinobacter hydrocarbonoclasticus*. *Molecules.*, **26(11):** 1-10.

Ariaeenejad S, Kavousi K, Mamaghani ASA, Ghasemitabesh R and Salekdeh GH. 2022. Simultaneous hydrolysis of various protein-rich industrial wastes by a naturally evolved protease from tannery wastewater microbiota. *Sci Total Environ.*, **815(152796):** 1-10.

Ayuningrum D, Sabdaningsih A and Jati OE. 2022. The potential of phylogenetically diverse culturable Actinobacteria from *Litopenaeus vannamei* pond sediment as extracellular proteolytic and lipolytic enzyme producers. *Trop Life Sci Res.*, **33(3):** 165.

Bhavikatti JS, Bodducharl SM, Kamagond RS, Desai SV and Shet AR. 2020. Statistical optimisation of protease production using a freshwater bacterium *Chryseobacterium cucumeris* SARJS-2 for multiple industrial applications. *Biotechnol.*, **10(279):** 1-17.

Eze OC, Berebon DP, Emencheta SC, Evurani SA, Okorie CN, Balcão VM and Vila MM. 2023. Therapeutic potential of marine probiotics: A survey on the anticancer and antibacterial effects of *Pseudoalteromonas* spp. *Pharmaceuticals.*, **16(8):** 1-35.

Gichana ZM, Liti D, Waidbacher H, Zollitsch W, Drexler S and Waikibia J. 2018. Waste management in recirculating aquaculture system through bacteria dissimilation and plant assimilation. *Aquac Int.*, **26:** 1541-1572.

Ilmiah SN, Mubarik NR and Wahyuntari B. 2018. Characterization of protease from *Bacillus licheniformis* F11.1 as a bio-detergent agent. *Makara J Sci.*, **22(3):** 105-112.

Jackson C, Preston N, Thompson PJ and Burford M. 2003. Nitrogen budget and effluent nitrogen components at an intensive shrimp farm. *Aquaculture.*, **218:** 397-411.

Jaishankar J and Srivastava P. 2017. Molecular basis of stationary phase survival and applications. *Front Microbiol.*, **8:** 2000.

KKP. 2022. Produksi Budidaya Udang di Indonesia. https://kkp.go.id/brsdm/sosek/artikel/39265-produksi-budi-daya-udang-di-indonesia (accessed on 12nd October 2023).

Kruger NJ. 2009. The Bradford method for protein quantitation. In: Walker JM (Ed.), **The Protein Protocols Handbook**. Humana Press, New York, pp. 17–24.

Leiva-Portilla D, Martínez R and Bernal C. 2023. Valorization of shrimp (*Heterocarpus reedi*) processing waste via enzymatic hydrolysis: protein extractions, hydrolysates and antioxidant peptide fractions. *Biocatal Agric Biotechnol.*, **48:** 102625.

Madigan DP, Martinko MT, Stahl JM and Clark D. 2012. **Brock Biology of Microorganisms,** 13th ed. Pearson, New York.

Nguyen-Sy T, Yew GY, Chew KW, Nguyen TDP, Tran TNT, Le TDH, ... and Show PL. 2020. Potential cultivation of *Lactobacillus pentosus* from human breastmilk with rapid monitoring through the spectrophotometer method. *Processes.*, **8(8):** 902.

Osesusi AO, Oyetayo VO and Arotupin DJ. 2021. Purification and characterization of a detergent compatible alkaline protease produced by *Bacillus ruris* isolated from vegetable oil factory effluent in Owo, Ondo State, Nigeria. *Jordan J Biol Sci.*, **14(4):** 629-635.

Ramadhan AMF, Ardyati T and Jatmiko YD. 2023. Halophilic bacteria producing protease from salted fish in Ponrang, Luwu Regency, South Sulawesi. *J Exp Life Sci.*, **13(1):** 35-42.

Ramin KI and Allison SD. 2019. Bacterial tradeoffs in growth rate and extracellular enzymes. *Front Microbiol.*, **10:** 2956.

Razzaq A, Shamsi S, Ali A, Ali Q, Sajjad M, Malik A and Ashraf M. 2019. Microbial proteases applications. *Front Bioeng Biotechnol.*, **7:** 110.

Richards GP, Watson MA, Needleman DS, Uknalis J, Boyd EF and Fay JP. 2017. Mechanisms for *Pseudoalteromonas piscicida*-induced killing of vibrios and other bacterial pathogens. *Appl Environ Microbiol.*, **83(11):** 1-17.

Rosazza T, Eigentler L, Earl C, Davidson FA and Stanley-Wall NR. 2023. *Bacillus subtilis* extracellular protease production incurs a context-dependent cost. *Mol Microbiol.*, **120(2):** 105-121.

Sanjaya EH, Amara A, Pamungkas YH, Wijaya AR, Santoso A, Yulistyorini A, ... and Fadhil M. 2023. The effectiveness of aerobic and anaerobic methods during start-up in biological shrimp pond wastewater treatment. *J Pure Appl Chem Res.*, **12(3).**

Sembiring A and Sumanto NL. 2022. Identification of potential isolat phosphate solubilizing bacteria used 16S rRNA gene. *Bioscientist J Ilm Biol.*, **10(2):** 941-949.

Setyati WA, Martani E and Zainuddin M. 2015. Growth kinetics and protease activity of isolate 36k from mangrove ecosystem sediments, Karimunjawa, Jepara. *Indones J Mar Sci.*, **20(3):** 163-169.

Setyati WA, Pringgenies D, Soenardjo N and Pramesti R. 2023. Enzyme-producing symbiotic bacteria in gastropods and bivalves molluscs: Candidates for bioindustry materials. *Biodiversitas J Biol Divers.*, **24(1).**

Sharma M, Gat Y, Arya S, Kumar V, Panghal A and Kumar A. 2019. A review on microbial alkaline protease: An essential tool for various industrial approaches. *Ind Biotechnol.*, **15(2):** 69-78.

Sher MG, Nadeem M, Syed Q, Abass S and Hassan A. 2011. Study on protease from barley tempeh and in vitro protein digestibility. *Jordan J Biol Sci.*, **4(4):** 257-264.

Song P, Zhang X, Wang S, Xu W, Wang F, Fu R and Wei F. 2023. Microbial proteases and their applications. *Front Microbiol.*, **14:** 1236368.

Suleiman AD, Abdul Rahman NA, Mohd Yusof H, Mohd Shariff F and Yasid NA. 2020. Effect of cultural conditions on protease production by a thermophilic *Geobacillus thermoglucosidasius* SKF4 isolated from Sungai Klah hot spring park, Malaysia. *Molecules.*, **25(11).**

Sun B, Zou K, Zhao Y, Tang Y, Zhang F, Chen W and Zheng Y. 2023. The fermentation optimization for alkaline protease production by *Bacillus subtilis* BS-QR-052. *Front Microbiol.*, **14:** 1301065.

Thanoon RD, Subramaniam RS, Makky EA and Yusoff MM. 2018. Utilization of extracted protein from fish fin and chicken feather waste for alkaline protease production by indigenous bacteria. *Jordan J Biol Sci.*, **11(1):** 17-22.

Venugopal M and Saramma AV. 2006. Characterization of alkaline protease from *Vibrio fluvialis* strain VM10 isolated from a mangrove sediment sample and its application as a laundry detergent additive. *Process Biochem.*, **41(6):** 1239-1243.

Wang SL, Chio YH, Yen YH and Wang CL. 2007. Two novel surfactant-stable alkaline proteases from *Vibrio fluvialis* TKU005 and their applications. *Enzyme Microb Technol.*, **40(5):** 1213-1220.

Xu Z, Cao J, Qin X, Qiu W, Mei J and Xie J. 2021. Toxic effects on bioaccumulation, hematological parameters, oxidative stress, immune responses and tissue structure in fish exposed to ammonia nitrogen: A review. *Animals.*, **11(11):** 3304.

Zebua AHP, Nursyirwani N and Feliatra F. 2020. Molecular identification of proteolytic bacteria from mangrove sediment in Dumai marine station. *Asian J Aquat Sci.*, **3(2):** 179-188.

JJBS

Volume 18, Number 3,September 2025
ISSN 1995-6673
Pages 539 – 547

Jordan Journal of Biological Sciences

Optimizing the Extraction of Total Phenolic, Flavonoid Content, and Antiradical activity from *Salvia tingitana* Using Mixture Design and Triangular Surfaces

Amine Azzane[1], HouriaNekhla[2], and Mohamed Eddouks[1,*]

[1]*Team of Ethnopharmacology and Pharmacognosy, Faculty of Sciences and Techniques Errachidia, Moulay Ismail University of Meknes, BP 509, Boutalamine, Errachidia, 52000, Morocco;* [2] *Higher Institute of Nursing Professions and Health Techniques (ISPITS), Errachidia,Morocco;*

Received: December 6, 2024; Revised: March 29, 2025; Accepted: April 17, 2025

Abstract

Background: Salvia tingitana is a medicinal and aromatic plant with several medicinal properties. Pharmacological investigation revealed the antihyperglycemic and antihyperlipidemic proprieties of this herb. In addition, phytochemical screening of Salvia tingitana demonstrated the presence of polyphenols, flavonoids, and tannins.
Aims: The study aimed to evaluate the effect of different solvents on the yield of polyphenols and flavonoids, and molecules endowed with antiradical activity derived from Salvia tingitana.
Material and Methods: Ten solvents were used to determine their efficacy in extracting total flavonoid and total phenolic content, as well as other antioxidant molecules. 2,2- diphenyl-1-picrylhydrazyl (DPPH) scavenging was used to evaluate the antiradical activity. We used a simplex axial mixture design to optimize the extraction of polyphenols, flavonoids, and molecules with antiradical activity by using response surface methodology.
Results: The results indicated that extraction was influenced by the solvent nature. The most effective solvents for achieving good polyphenol and flavonoid yields were water, ethanol, and methanol concerning the part of solvent screening. The second part of the solvent mixture extraction revealed that pure water was the most appropriate solvent for extracting the highest amounts of total polyphenolic content (3.344±0.03 GAE/g). Concerning total flavonoid content, the equi-proportional solvent mixture "water-methanol" revealed the highest quantity (3.213±0.06 QE/g). In addition to the extraction solvent's nature, the mixture's nature had a significant impact on the anti-radical activity of Salvia tingitana. The percentage of inhibition of DPPH was higher in the extract obtained with the ternary mixture (103.15±4.20 %) the following proportions: ethanol 66.66%; methanol 16.66%; water 16.66%. Generally, the percentage of inhibition of DPPH was also influenced significantly and positively by the methanol proportion.
Conclusion: In conclusion, the study demonstrates that water, ethanol, and methanol act synergistically to improve the bioactive recovery. Thus, solvent combination methods may result in better yields of flavonoids and antiradical molecules compared to single extraction methods. Moreover, the use of solvents can help to reduce the amount of time and energy required to extract the desired compounds.

Keywords: *Salvia tingitana*; solvent extraction; polyphenols; flavonoids; antioxidant activity; surface design methodology.

1. Introduction

Plants belonging to the *Salvia* genus are increasingly recognized as a rich reservoir of biologically active phytochemicals, like polyphenolic, flavonoid, and phenolic acids compounds, well-known for their biological properties (Lu and Foo, 2022). The chemical composition of essential oils obtained from the aerial parts of Salvia plants has been determined and dominant components are 1,8-cineole, camphor, limonene, α-pinene, β-pinene, 3-carene, campene, p-cymene, sabinene, β-caryophyllene, and α-gurjunene (Lu and Foo, 2022; Kelen and Tepe, 2008). The bioactive compounds present in *Salvia* species exhibit a considerable antioxidant potential, rendering them well-suited for maintaining various physiological functions (Martino *et al.,* 2010; Asadollahi *et al.,* 2019; Khiyari *et al.,* 2014; Bisio *et al.,* 1998). Several studies have demonstrated that many Salvia species exhibit hypoglycemic, hypolipidemic, anticancer, antioxidant, antihypertensive, antimicrobial, and anti-inflammatory effects (Sharifi-Rad *et al.,* 2018; Li *et al.,* 2013; Azzane *et al.,* 2022). For this reason, some plants of this genus have been cultivated worldwide for their applications in traditional medicine and culinary practices (Askun *et al.,* 2010).

Salvia tingitana (ST) is known to contain a diverse range of phytochemical compounds, such as polyphenols, flavonoids, tannins, saponins, sterols, terpenoids, alkaloids, and carbohydrates (Azzane and Eddouks, 2022). These Compounds have garnered substantial attention due to their antioxidant and antibacterial properties (Bouaziz *et al*., 2009). In addition, Pharmacological investigation revealed the antihyperglycemic and antihyperlipidemic

* Corresponding author. e-mail: mohamededdouks2017@gmail.com; mohamed.eddouks@laposte.net.

proprieties of *Salvia tingitana* (Azzane and Eddouks, 2022).

The extraction yield is linked to various factors, including variety, fruit maturity, pedoclimatic conditions, extraction process, and polarity of the solvent used for extraction (Oliveira *et al*., 2001). The composition of the obtained extract, which influences its biological properties, is affected by the efficacy of the extraction method and the appropriateness of the extractor solvents. In addition, a successful extraction technique involves combining solvents in appropriate proportions. Choosing an extraction method requires evaluating factors such as accuracy, stability of extracted substances, resource availability, and processing costs, all contributing to the eventual biological application of the extract (Oliveira *et al.*, 2001). Bioactive compounds are generally extracted from plant material with alcohols, acetone, and water, but the selection depends on the compound of interest and the plant material (Zhang *et al.*, 2018). In the objective to determine bioactive compounds and antioxidant ability, optimization of the extraction proves to be an effective method for examining the impact of a single variable, particularly the solvent (Aazza, 2021). Utilizing response surface methodology (RSM) stands as a precise approach to enhance the extraction process (Saravana *et al.*, 2023).

According to our knowledge, no reported investigation has employed solvents or solvent mixtures to extract active compounds from ST. In addition, some studies have been conducted on ST, but its full potential has not been fully explored. For this reason, the present study was undertaken to determine the optimal appropriate solvent mixture for extracting a higher quantity of total flavonoid content (TFC), total phenolic content (TPC), and molecules with antioxidant activity. The objective was to establish an efficient and reproducible model with the desired properties. It is important to develop a model with desirable properties that is efficient and reproducible.

2. Materiel and Methods

2.1. Plant Material

Fresh plant material of ST was purchased in March 2022 from a local market in the Tafilalet region (semi-arid area) of Morocco. This herb was air-dried in the shade at 40°C for one week in the laboratory. Taxonomic identification and authentication of the plant were conducted, and a voucher specimen (ST 25/35) was deposited in the herbarium of the Faculty of Sciences and Techniques, Errachidia.

2.2. Extraction Methodology

The extraction procedure was prepared as previously described (Tawaha *et al.*, 2007; El Baakili *et al.,* 2021). Briefly, 50 mg of the arterial part of ST was subjected to a 20-minute sonication with 1 ml of the selected solvents (water, acetonitrile, methanol, acetone, ethyl acetate, ethanol, chloroform, dichloromethane, toluene, and hexane). Following this, the mixture underwent centrifugation at 6000 rpm for 15 minutes, and the recovered supernatant was stored at 4 °C.

2.3. Estimation of total Polyphenol Content

TPC using Folin Ciocalteu method, polyphenol contents were measured according to the method described previously (Chansriniyom *et al.*, 2021; Azzane *et al*., 2023).

2.4. Estimation of Flavonoid Content.

As described by Kim et *al.* total flavonoid content (TFC) was measured (Kim *et al.*, 2003; Azzane *et al.*, 2022a).

2.5. Determination of DPPH Radical Scavenging Activity

In accordance with previous studies, anti-DPPH radical activity was measured (Louli *et al.*, 2024).

2.6. Optimizing Solvent Mixtures with Simplex Axial Design (SAD)

To illustrate the behavior of solvent mixtures used for extracting active ingredients from herbs, mixing models has proven effective (Garcia *et al.*, 2010). Due to its advantageous properties in exploring the experimental space, the simplex axial plane (SAP) was selected for optimizing the extraction process, particularly its vertices at (2/3, 1/6, 1/6), (1/6, 2/3, 1/6) and (1/6, 1/6, 2). It is interesting to note that the top point represents pure solvent (1 : 0 : 0;0 : 1 : 0;0 : 0 : 1); each intermediate point represents a permutation of binary mixtures (1/2: 1/2 : 0;1/2:0:1/2; 0:1/2:1/2), while the center point represents a ternary mixture (1 : 1 : 1).

To determine the TPC, TFC, and antiradical activity of ST this design of extraction, (DOE) allows greater precision in determining the proportion of solvents, such as water (X1), ethanol (X2), and methanol (X3), in the solvent mixture shown in Figure 1. Experimental data were fitted using a polynomial equation:

$$Y = \beta 1X1 + \beta 2X2 + \beta 3X3 + \beta 12X1X2 + \beta 13X1X3 + \beta 23X2X3 + \beta 123X1X2X3,$$

where $\beta 1$, $\beta 2$, $\beta 3$, $\beta 12$, $\beta 13$, and $\beta 23$ are interaction coefficients of linear, and nonlinear terms and Y is the response or predicted value.

2.7. Confirmation of the Model

With the surface response model (SRM), the extraction conditions for ST were optimized for maximum TPC concentration, TFC concentration, and antioxidant activity. To validate the model, the predicted values based on standard errors were compared with the experimental data obtained.

2.8. Statistical Analysis

Three independent experiments were conducted to determine the solvent proportions and each of TPC content, TFC content, and antiradical activity, and the results were summarized as mean + standard deviation. Using the analysis of variance (ANOVA), in objective to validated the multiple regression model ($p < 0.05$) and evaluated the significant effects of the variables and their interactions. Concerning the regression coefficients, the contour graphs and the model's response surface were produced. Tukey test was used to define the significant differences, with $p < 0.05$ as the significance criterion. STATISTICA (data analysis software system), version 10 (StatSoft, 2011) was used for the design and analysis of mixture design experiments.

3. Results and Discussion

3.1. Solvent Screening

Ultrasound assisted extraction (sonication) improves extraction efficiency because it accelerates dissolution, diffusion, and heat transfer. In addition to reducing extraction temperature and extraction time, this extraction method requires little solvent and energy consumption (Saravana *et al.*, 2023). As a result, sonication is used in this study to extract different compounds.

Ten solvents with various polarities ranging between 0.1 and 10.2 were systematically evaluated for their efficacy in extracting a great quantity of TPC and TFC. The data are detailed in Table **1**. Indeed, the results showed that water, ethanol, and methanol proved their ability for extracting highest amounts of TPC and TFC. In contrast, toluene and hexane showed the lowest TPC extraction, and hexane and acetonitrile presented the lowest TFC extraction. Interestingly, the findings demonstrate a substantial impact of solvent extraction capabilities on the yield of TPC and TFC. Polyphenolic compounds generally possess polar proprieties, and the pronounced polarity of water as a solvent enhances its efficiency in extracting these polar compounds often conjugated with multiple carbohydrates. Several studies demonstrated the effectiveness of employing a combination of solvents with differing polarities to extract substantial amounts of bioactive compounds (Pan *et al.,* 2015). In addition, a study has shown that extracting phenolic compounds from plants is best done by using aqueous organic solvent mixtures (Venkatesan *et al.*, 2019). Thus, a mixture design optimization was conducted using water, methanol, and ethanol.

Table 1. Influence of selected solvents on TPC and TFC contents.

Solvant	Polarity index	TPC mg GAE/g	TFC mg QE/g
Water	10.2	3.344±0.03	0.592±0.03
Acetonitrile	5.8	0.184±0.030	0.049±0.08
Methanol	5.1	1.47±0.039	0.66±0.16
Acetone	5.1	0.395±0.084	0.320±0.02
Ethyl Acetate	4.4	0.23±0.079	0.17±0.06
Ethanol	4.3	2.108±0.14	0.63±0.16
Chloroform	4.1	0.47±0.08	0.124±0.15
Dichloromethane	3.1	0.39±0.058	0.072±0.02
Toluene	2.4	0.10±0.031	0.32±0.02
Hexane	0.1	0.079±0.005	0.044±0.02

3.2. Solvent Mixture Extraction

Surface response methodology coupled with axial simplex design provides a powerful approach to optimize solvent mixtures for maximizing TPC contents, TFC contents, and other molecules with antiradical activity. Besides, analytical methods such as food and herbal medicine are often optimized using response surface methodology (RSM) (Plaza *et al,* 2018). Strati *et al*. effectively employed this approach to enhance the extraction of phenolics from *Allium ampeloprasum* (Strati *et al.,* 2018).

The findings of the effects of the solvent mixture on the antiradical activity and the contents of TPC and TFC are illustrated in Table **2**. The results revealed that pure water proved its ability for extracting high amounts of TPC, followed by the water-ethanol binary mixture in a 1:1 ratio. Concerning TFC, the equi-proportional solvent mixture "water-methanol" revealed the highest extraction, followed by the equi-proportional solvent mixture "water-ethanol". These findings could be explained by the synergistic effect between water and methanol as well as methanol. Selectivity, solubility, cost, and safety are key considerations in the selection of solvents. In this context, water emerges as a potentially green solvent due to its non-toxicity to both health and the environment. Additionally, it stands out as the safest and most cost-effective solvent (Mansouri *et al.,* 2020; Nicetin *et al.,* 2021).

According to Table **2**, the antiradical activity of ST based on the solvent mixtures used was assessed by DPPH free radical scavenging. Identically, the findings revealed that the anti-radical activity of ST extracts was importantly affected by the nature of solvent and the composition of the mixture. Indeed, among all extracts, the one obtained with the ternary mixture (16.66 water / 16.66 methanol /16.66 ethanol) showed the strongest ability to inhibit DPPH radicals flowed by pure methanol and ternary mixture (33.33 water / 33.33 methanol /33.33 ethanol). In contrast, the binary mixture “water-ethanol” produced the lowest activity. According to many studies, phenolic compounds play an important role in antioxidant activity (Mansouri *et al.,* 2020). Herb's antioxidant activity was mainly derived from phenolic compounds (Han *et al.,* 2010). In addition, polyphenols compounds can be used to enhance the economic and nutritional value of functional foods, as well as enhance their full utilization (Chater *et al.,* 2023).

Table 2. Findings of mixture tested of TPC, TFC, and DPPH and simplex axial design.

Run	Water	Methanol	Ethanol	TPC mg GAE/g	TFC mg QE/g	DPPH (%)
1	100	0	0	3.334±0.03	0.592±0.03	65.23±0.09
2	0	100	0	1.471±0.039	0.664±0.16	63.39±3.64
3	0	0	100	2.108±0.14	0.635±0.16	93.80±3.65
4	50	50	0	2.83±0.03	3.213±0.06	49.18±2.41
5	0	50	50	2.175±0.17	0.685±0.06	83.57±2.77
6	50	0	50	3.313±0.04	3.158±0.25	48.26±0.418
7	33.33	33.33	33.33	3.050±0.10	0.456±0.06	91.09±3.75
8	16.66	16.66	66.66	3.179±0.04	0.311±0.33	103.15±4.20
9	16.66	66.66	16.66	2.819±0.14	0.748±0.07	79.50±3.64
10	66.66	16.66	16.66	3.081±0.14	0.798±0.08	71.52±1.04

3.3. Analysis of Variance Test (ANOVA).

ANOVA was performed to test significance and fit the model. To determine the significance of the corresponding coefficient, p-values are used, and the smaller the p-value < 0.05, the more significant the difference (Nekhla *et al.*, 2023). F-tests were used to examine model significance. Coefficients of determination (R2) and the adjusted correlation coefficient (AdjR2) were used to determine model robustness. Analysis of linear, quadratic and special cubic models was performed for independent and response variables. Table 3 shows the TPC, TFC and free radical

scavenging activity measured for the aerial part of the plant studied. Among the models considered, the cubic model was satisfactorily reproduced for TPC (p = 0.001992), TFC (p = 0.0000) and DPPH (p = 0.0000).

Table 3. Statistical evaluation of mixture model effects using ANOVA.

		SS	df	MS	F	P	R^2	R^2-Adjustd
TPC	Linear	76.58	2	38.29	14.48	0.000053	0.5176	0.4819
	Quadratic	40.49	3	13.49	10.49	0.000134	0.7913	0.7479
	Special Cubic	10.67	1	10.67	12.15	0.001992	0.8635	0.8279
	Total Adjusted	147.93	29	5.10				
TFC	Linear	9.033	2	4.51	4.8177	0.0162	0.2630	0.2084
	Quadratic	6.4408	3	2.1469	2.7304	0.0661	0.4505	0.3360
	Special Cubic	15.6871	1	15.687	113.306	0.0000	0.9072	0.8831
	Cubic	1.4409	2	0.7204	8.6789	0.00179	0.9492	0.9299
	Total Adjusted	34.34	29	1.1843				
DPPH (%)	Linear	3951.924	2	1975.962	9.549	0.00073	0.4143	0.3709
	Quadratic	1660.183	3	553.394	3.3824	0.0346	0.5883	0.5025
	Special Cubic	3281.918	1	3281.918	117.0827	0.0000	0.9324	0.91478
	Cubic	257.23	2	128.616	6.9706	0.004767	0.959	0.943904
	Total Adjusted	9538.732	29	328.922				

A global fit was applied to study the special cubic model. The degree of model fit was verified by the R2 coefficient. This coefficient expresses the proportion of total response variation predicted by the model. The closer the R2 value is to 1, the better the model fits the real data. The R2 results for the special cubic models were 0.863, 0.907 and 0.932 respectively for TPC, TFC and DPPH. This indicates that the model adequately represents the true relationship between the selected parameters. Indeed, a high R2 value indicates that the statistical model can explain a large proportion of the observed data variability, improving its reliability and predictive ability. When R2 is close to 1, the model is well suited to the experimental data, reducing prediction uncertainty (Nekhla *et al.,* 2023).

According to Table 4, all special cubic models were highly significant, as indicated by low p-values of 0.000000 and high F-values: 24.2529; 24.2529 and 61.99643 for TPC, TFC and DPPH respectively. Given the calculated F-values and probability values, the models below do not suffer from a lack of fit and are very reasonable and significant.

The model presented p-values for TPC, TFC and DPPH that are highly significant (p=0.00000), confirming the validity of the model and indicating that the model developed is reliable and accurate in predicting relevant responses.

Relationships between responses are described by polynomial models

TPC = 5.795*ethanol + 5.133*water +1.531*methanol + 10.362*ethanol*water + 16.610*ethanol*methanol – 3.762*water*methanol – 60.505*ethanol*water*methanol +0

TFC = +1.499*ethanol + 0.774*water + 0.060*methanol + 7.927*ethanol*water + 9.136*ethanol*methanol + 0.694*water*methanol - 73.359*ethanol*water* -7.174*ethanol* water*(ethanol - water) – 3.929 *ethanol*ethanol*(ethanol - methanol) + 0

% Inhibition = +65.830*ethanol + 63.991*water + 94.396*methanol - 58.156*ethanol *water - 122.68*ethanol*methanol +22.255 * water * methanol + 1061.077 * ethanol * water * methanol + 1 1.992 * ethanol * water * (ethanol-water)-146.785 * ethanol * methanol * (ethanol-methanol) +0

3.4. Contour plots analysis

Three dimensional (3D) interaction contour plots are presented in Figures 1, 2, and 3 (A and B) based on interactions between water, ethanol, and methanol. Correspondingly, hydromethanolic (1/2methanol and 1/2 water) and hydroethanolic (1/2 ethanol and 1/2water) combinations are the most efficient binary interactions for removing both the highest amounts of TPC and TFC. In contrast, the lowest TPC and TFC extraction was observed in methanol. In the same vein, the results are in accord with previous studies, showing that methanol-water binary combination is the most efficient for the extraction of polyphenols (El ksibi *et al.,* 2015). TPC and TFC amounts were found to be influenced by the solvent system. Numerous factors have been shown to influence TPC, such as geographical and climatic factors genetic factors, plant maturity, and storage time (Generalić *et al.,* 2012; Benhouda *et al.,* 2014).

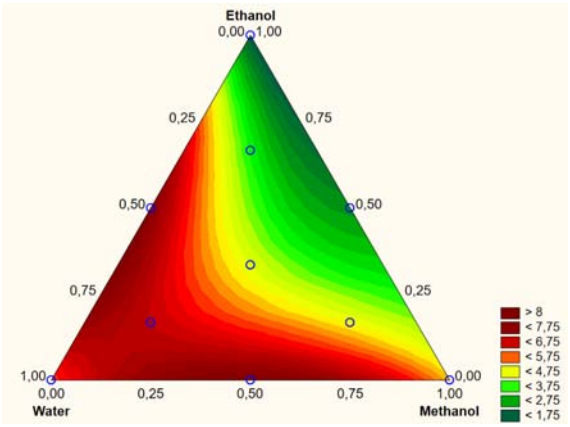

Figure 1A. The Special Cubic Model predicts TAC using water, ethanol, and methanol mixture (2D).

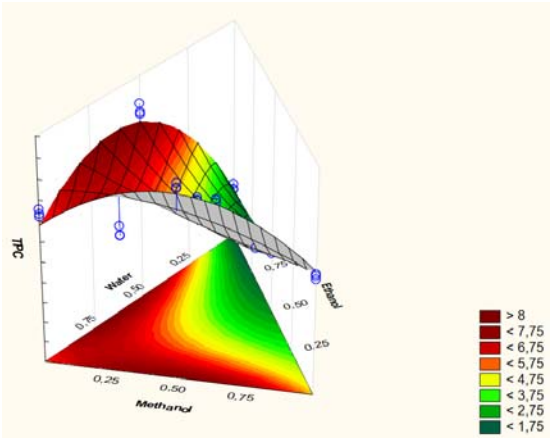

Figure 1B. The Special Cubic Model predicts TAC using water, ethanol, and methanol mixture (2D).

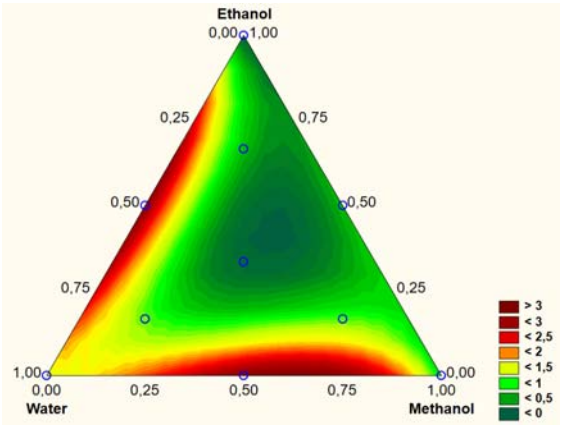

Figure 2A. The Special Cubic Model predicts TFC using water, ethanol, and methanol mixture (2D).

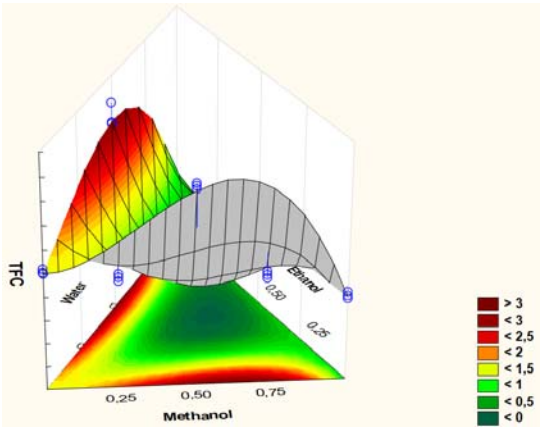

Figure 2B. The Special Cubic Model predicts TFC using water, ethanol, and methanol mixture (2D).

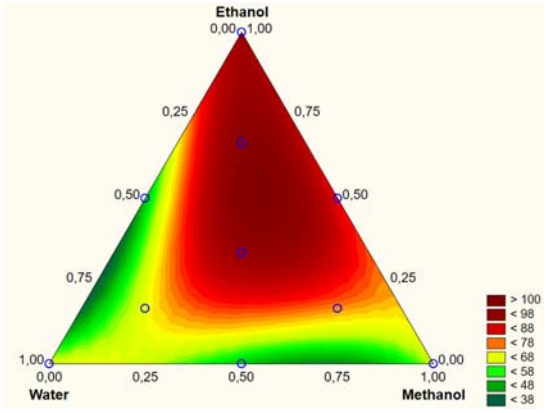

Figure 3A. The Special Cubic Model predicts DPPH using water, ethanol, and methanol mixture (2D).

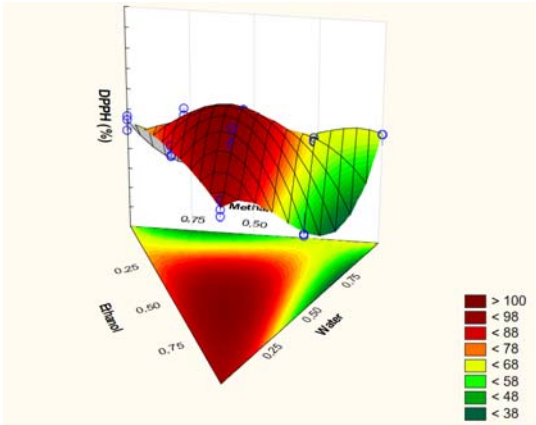

Figure 3B. The Special Cubic Model predicts DPPH using water, ethanol, and methanol mixture (2D).

The optimum solvent system was determined to have a significant effect on the TPC. The solvent system was found to have a significant impact on TPC extraction efficiency. Furthermore, the solvent system was also shown to have a significant effect on the antioxidant capacity of the extract. According to the contour graph, the high level of antioxidant activity was produced by pure ethanol, while a low level was produced by pure water and methanol. In the same vein, the highest antioxidant capacities occur between the positions: ethanol (100%), methanol; ethanol (50%; 50%), water; and ethanol (50%; 50%).

Based on the results of the desirability analysis (as presented in Fig 4A and 4B), the best solvent combination to extract both TPC and TFC is a binary interaction of water and methanol (50%; 50%). The best solvent combination to extract both TPC and TFC is a binary interaction of water and methanol (50%; 50%). The great solvent interactions to extract secondary metabolites with efficiencies of antioxidants are tertiary combination of water-ethanol-methanol with 18.75 % of water, 25 % of methanol, and 56.25 % of ethanol.

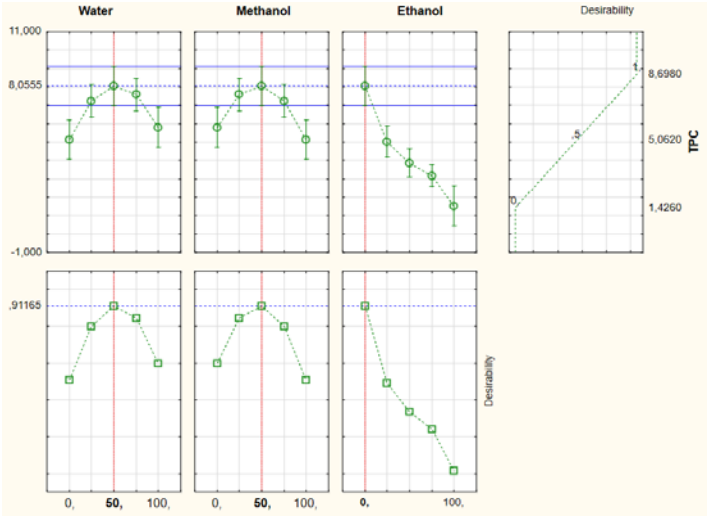

Figure 4A. Desirability results of TPC

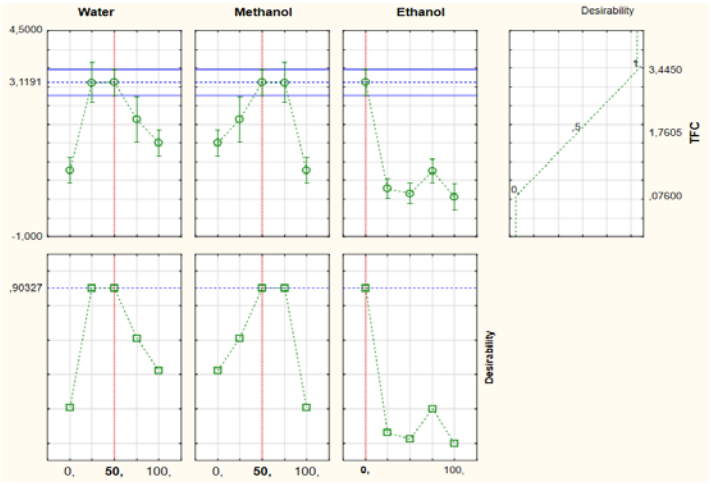

Figure 4B. Desirability results of TFC

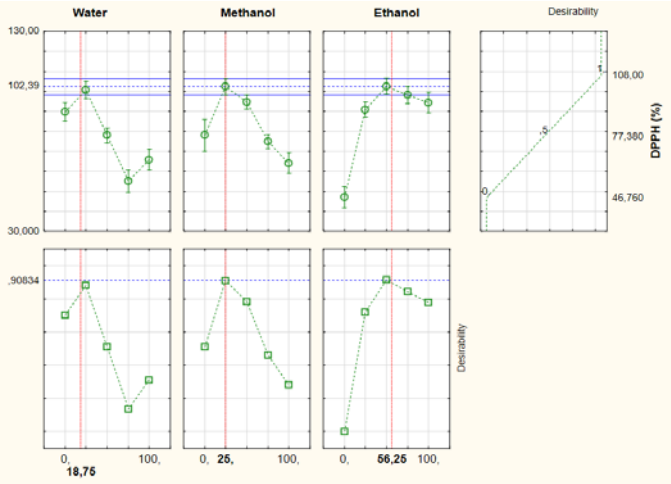

Figure 4C. Desirability results of DPPH

3.5. Pareto Chart Analysis

A standardized Pareto chart was used to assess the relative relevance of main effects and their interactions with statistical significance (p 0.05). Figure 5 shows the effect of independent variables (solvent mixtures) and their interactions on TPC, TFC recovery and TS antioxidant activity. At the 0.05 level, which extends beyond the reference line, the effect is significant. According to Figure 5A, water (A) and methanol (B) are the most influential factors on TPC extraction from TS, and the following solvents: (AC) water∗ ethanol > (AB) water ∗ methanol > (ABC) water ∗ methanol ∗ ethanol showed the most significant effect. According to Figure 5B, the parameters with a greater normalized effect on the extraction of TFC from TS were classified as follows: (ABC) water ∗ methanol ∗ ethanol > (AC) water ∗ ethanol > (AB) water ∗ methanol > (A) water > (B) methanol. Whereas in the case of antioxidant activity (DPPH) evaluation (Figure 5C), methanol (C), water (A) and ethanol (B) showed the most significant effect, followed by the following ternary interaction: (ABC) water∗ ethanol ∗ methanol and finally the binary interactions: (AC) water ∗ ethanol > AB) water ∗ methanol.

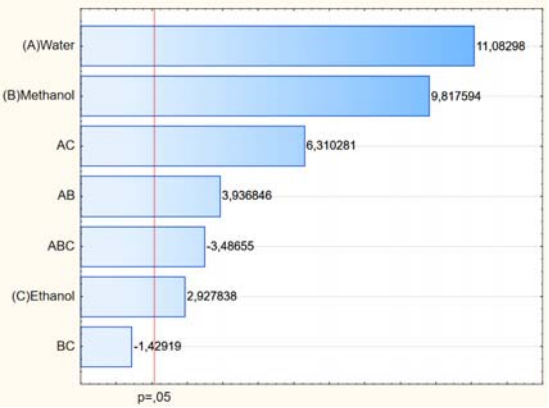

Figure 5A. TPC standardized effects Pareto chart analysis.

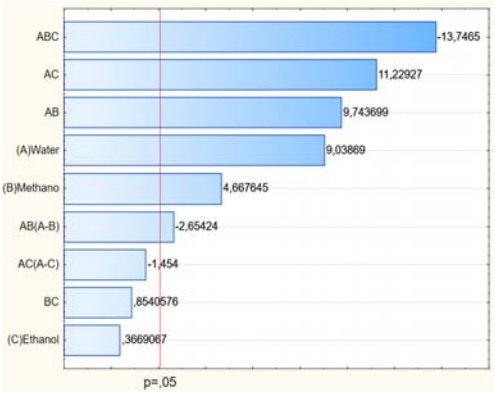

Figure 5B. TFC standardized effects Pareto chart analysis.

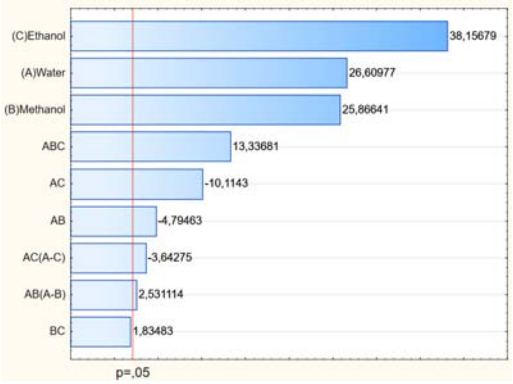

Figure 5C. DPPH standardized effects Pareto chart analysis.

The results found showed that the type of solvent could have an effect on the amount of TPC (Figure 6). Several studies have revealed that different parameters can influence TPC, namely geographical and climatic conditions (Skroza *et al.,* 2012), genetic factors, plant maturity stage and storage period (Benhouda *et al.*, 2014),

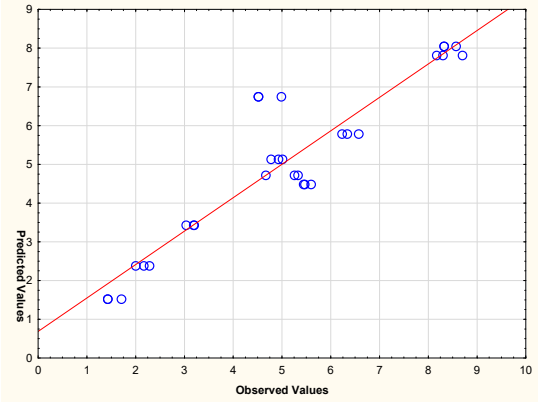

Figure 6A. Actual values (from experiments) compared to predicted values (from the model) (TPC)

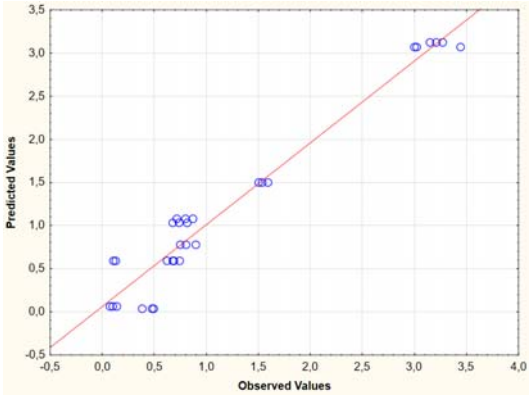

Figure 6B. Actual values (from experiments) compared to predicted values (from the model) (TFC)

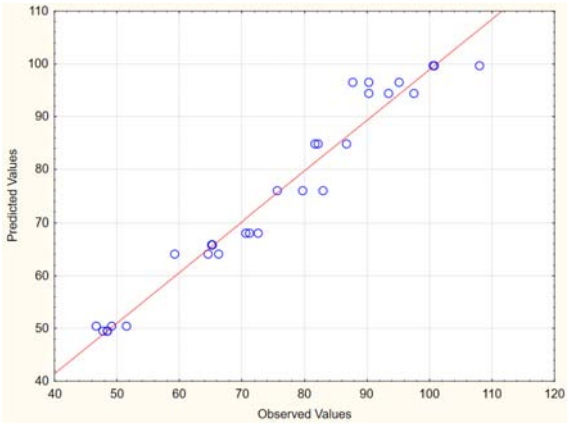

Figure 6C. Actual values (from experiments) compared to predicted values (from the model) (DPPH)

3.6. Principal Components Analysis

Principal components analysis (ACP) can be used to summarize variability in complex data sets that are difficult to interpret (Nićetin *et al.,* 2021). The degree of correlation between two vectors is determined by the angle at which they subtend to each other in this analysis. To assess the correlation between the different variables, principal component analysis was performed. The first factor (factor 1) explained 55.20% of the total variability, while the second factor (factor 2) explained 25.50%. As a result, the first two factors were able to explain 80.7% of the total variability. Figure 7 shows the correlations between the PCA components and the initial variables. Water correlates with total polyphenol and flavonoid content, while ethanol correlates with antioxidant activity (DPPH). This explains why increasing the amount of water in the extraction system enhances its ability to extract phenolic compounds and flavonoids. Similarly, the presence of ethanol favors the extraction of molecules with antioxidant capacity. The same conclusion was reached using Pareto analysis.

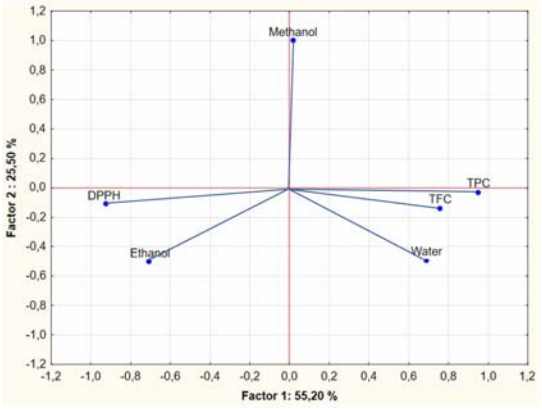

Figure 7: Principal components analysis (ACP).

4. Conclusion

This is the first study to optimize phenolic contents and other molecules with ST's antiradical activity, showing that this waste has the potential to be a useful source of bioactive compounds. Pure water dissolves polyphenols in the plant studied more effectively than other and/or mixture solvents, which is a function of their polar properties. Combined with their ability to cover a wider range of polarity and their synergistic interactions, water and methanol create an ideal solvent environment for flavonoid extraction. As a result of the synergistic interactions between ethanol (66.66%), methanol (16.66%) and water (16.66%), the ternary mixture is found to optimize the extraction of antioxidant compounds from a wide range of molecules. Due to the richness of its metabolites, *Salvia tingitana* can be utilized in a variety of fields, particularly pharmaceuticals. Interestingly, STs' bioactive potential could be further explored through future studies exploring the sustainability and scalability of extraction methods, as well as testing their bioactivity in in vivo and in vitro models

Availability of Data and Materials

Not applicable.

Funding

This study was supported by CNRST under grant number PPR/2015/35.

Conflict of Interest

The authors declare no conflict of interests, financial or otherwise.

References

Aazza S. 2021. Application of multivariate optimization for phenolic compounds and antioxidants extraction from Moroccan Cannabis sativa waste. *J Chem*., **2021**: 1-11.

Asadollahi M, Firuzi O, Jamebozorgi F H, Alizadeh M and Jassbi AR. 2019. Ethnopharmacological studies, chemical composition, antibacterial and cytotoxic activities of essential oils of eleven Salvia in Iran. *J HerbMed*., **17**: 100250.

Aşkun T, BAŞER K, Tümen G and Kürkcüoğlu M. 2010. Characterization of essential oils of some Salvia species and their antimycobacterial activities. *Turk J Biol.*, **34(1)**: 89-95.

Azzane A, Amssayef A and Eddouks, M. 2022. Salvia aucheri Exhibits Antihypertensive Activity in Hypertensive Rats. *Cardiovasc Hematol* Agents *Med Chem.*, **21**: 167-176.

Azzane A and Eddouks M. 2022. Antihyperglycemic, Antihyperlipidemic, and Antioxidant Effects of *Salvia Tingitana* in Streptozotocin-Induced Diabetic Rats. *Cardiovasc Hematol Disord Drug Targets*., **22 (2):** 118–127.

Azzane A, Farid O and Eddouks M. 2023. Antihyperglycemic and Antidyslipidemic Effects of *Artemisia arborescens* Aqueous Extract on Streptozotocin-induced Diabetic Rats. *Cardiovasc Hematol* Agents *Med Chem.*, **21(2):** 120-138.

Benhouda A and Yahia M. 2014. Toxicity, analgesic and anti-pyretic activities of methanolic extract from Hyoscyamus albus' leaves in albinos rats. *Int J Pharm PharmSci*, **6(3):** 121-127.

Bisio A, Ciarallo G, Romussi G, Fontana N, Mascolo N, Capasso R and Biscardi D. 1998. Chemical composition of essential oils from some Salvia species. *Phytother Res*., **12:** 117-S120.

Bouaziz M, Dhouib A, Loukil S, Boukhris M and Sayadi S. 2009. Polyphenols content, antioxidant and antimicrobial activities of extracts of some wild plants collected from the south of Tunisia. *Afr J Biotechnol.*, **8(24).**

Chansriniyom C, Nooin R, Nuengchamnong N, Wongwanakul R, Petpiroon N, Srinuanchai W, Chantarasuwan B, Pitchakarn P, Temviriyanukul P, Nuchuchua O. 2021. Tandem mass spectrometry of aqueous extract from *Ficusdubia*sap and its cell-based assessments for use as a skin antioxidant. *Sci Rep.,* **11(1):** 16899.

Chater O, El ghadraoui L, Harrach A and Aazza S. 2023. Extractive optimization of antioxidants and phenolic compounds from Anacyclus pyrethrum. *Not Sci Biol*., **15(4)**: 11616-11616.

El Baakili A, Fadil M and Es-Safi NE. 2023. Ultrasonic-assisted extraction for phenolic compounds and antioxidant activity of Moroccan Retama sphaerocarpa L. leaves: Simultaneous optimization by response surface methodology and characterization by HPLC/ESI-MS analysis. *Heliyon*., **9(6).**

El Ksibi I, Slama RB, Faidi K, Ticha MB and M'henni MF. 2015. Mixture approach for optimizing the recovery of colored phenolics from red pepper (Capsicum annum L.) by-products as potential source of natural dye and assessment of its antimicrobial activity. *Ind Crop Prod*., **70**: 34-40.

Garcia LMZ. Oliveira TF, Soares PK, Bruns RE and Scarminio IS. 2010. Statistical mixture design—Principal component determination of synergic solvent interactions for natural product extractions. *Chemometr Intel Lab Sysi.*, **103(1):** 1-7.

Generalić I, Skroza D, Šurjak J, Možina S, Ljubenkov I, Katalinić A, Šimat V and Katalinić V. 2012. Seasonal variations of phenolic compounds and biological properties in sage (Salvia officinalis L.). *Chem Biodivers*., **9(2)**: 441-457.

Han L, Gao X, Xia T, Zhang X, Li X and Gao W. 2019. Effect of digestion on the phenolic content and antioxidant activity of celery leaf and the antioxidant mechanism via Nrf2/HO-1 signaling pathways against Dexamethasone. *J Food Biochem*., **43(7)**:12875.

Kelen M and Tepe B. 2008. Chemical composition, antioxidant and antimicrobial properties of the essential oils of three Salvia species from Turkish flora. *BioresourTechnol*., **99(10)**: 4096-4104.

Khiyari MEA, Kasrati A, Jamali CA, Zeroual S, Markouk M, Bekkouche K, Wohlmuth H, Leach D and Abbad A. 2014. Chemical composition, antioxidant and insecticidal properties of essential oils from wild and cultivated Salvia aucheri subsp. blancoana (Webb. &Helder)), an endemic, threatened medicinal plant in Morocco. *Ind Crop Prod*., **57**:106-109.

Li M, Li Q, Zhang C, Zhang N, Cui Z, Huang L and Xiao P. 2013. An Ethnopharmacological Investigation of Medicinal Salvia Plants (Lamiaceae) in China. *Acta Pharm Sin. B*., **3 (4):** 273–280.

Louli V, Ragoussis N, Magoulas K. 2024. Recovery of phenolic antioxidants from wine industry by-products. 2004. *Bioresour. Technol.,* **92(2):** 201-208.

Lu Y. and Foo LY. 2022. Polyphenolics of Salvia—a review. *Phytochem*., **59(2)**: 117-140.

Mansouri I, Laaroussi H, El Ghouizi A, Lyoussi B and El Arabi, I. 2020. Phytochemical content and antioxidant activity of flesh fruits Rosa canina extracts collected from AitAyachMidelt. *Indian J Agric Res*., **54(3)**: 373-377.

Martino LD, Roscigno G, Mancini E, Falco ED and Feo VD. 2010. Chemical composition and antigerminative activity of the essential oils from five Salvia species. *Molecules*., **15(2)**: 735-746.

Nekhla H, Aazza S, Tarmoun K, El Hanafi L, Lahrizi L, Squalli W, Ahmed Harrach A and El Ghadraoui L. 2023. Optimization of Polyphenol Extraction from Three Parts of Chamaeropshumilis L.(Leaves, Fruit And Pulp) Through Response Surface Methodology. *Chem Afr.*, **6(3)**:1191-1200.

Nićetin M, Pezo L, Filipović V, Lončar B, Filipović JS, Šuput D and Knežević V. 2021. The effects of solution type temperature and time on antioxidant capacity of osmotically dried celery leaves. *Therm Sci*., **25(3):** 1759-1770.

Oliveira A, Padilha C, Gonzales Ortega G, and Petrovick P. 2001. Achyrocline satureioides (Lam.) DC. (marcela), Asteraceae, avaliaçãocomparativa da drogavegetal e estudospreliminares de otimização da extração. *Caderno de Farmácia. Porto Alegre.,* **17**: 33-38.

Pan Y, Zhang J, Shen T, Zuo ZT, Jin H, Wang YZ and Li WY. 2015. Optimization of ultrasonic extraction by response surface methodology combined with ultrafast liquid chromatography–ultraviolet method for determination of four iridoids in Gentianarigescens. *J Food Drug Anal*., **23(3)**: 529-537.

Plaza M and Marina ML. 2023. Pressurized hot water extraction of bioactives. *TrAC Trends Anal Chem*., **166**: 117201.

Saravana Pandian P, Sindhanaiselvan S, Subathira A and Saravanan SA. 2023. correlative algorithmic optimization study for an integrated soft computing technique in aqueous two-phase protein extraction from Litopena eusvannamei waste. *Biomass Convers Biorefin*., **13(18):** 16819-16833.

Sharifi-Rad M, Ozcelik B, Altın G, Daşkaya-Dikmen C, Martorell M, Ramírez-Alarcón K, Alarcón-Zapata P, Morais-Braga MFB, Carneiro JNP, Alves Borges Leal Al. 2018. Salvia Spp. Plants-from Farm to Food Applications and Phytopharmacotherapy. *Trends Food Sci Technol*., **80**: 242–263.

Skroza D, Surjaka J, Mozinab SS. 2012. Seasonal variations of phenolic compounds and biological properties in sage (*Salvia officinalis* L.). *Chem Biodivers* **9(2):** 441–57

StatSoft I. 2011. Statistica (data analysis software system).

Strati IF, Kostomitsopoulos G, Lytras F, Zoumpoulakis P, Proestos C and Sinanoglou V. 2018. Optimization of polyphenol extraction from Allium ampeloprasum var. porrum through response surface methodology. *Foods*., **7(10)**: 162.

Tawaha K, Alali FQ, Gharaibeh M, Mohammad M and El-Elimat T. 2007. Antiradical activity and total phenolic content of selected Jordanian plant species. *Food Chem*., **104(4)**: 1372–1378

Venkatesan T, Choi Y. W and Kim YK. 2019. Impact of different extraction solvents on phenolic content and antioxidant potential of Pinusdensiflora bark extract. *BioMed Res Int.*, **2019 (1)**: 3520675.

Zhang QW, Lin LG and Ye WC. 2018. Techniques for extraction and isolation of natural products: A comprehensive review. *Chin med.,* **13**: 1-26.

JJBS

Volume 18, Number 3,September 2025
ISSN 1995-6673
Pages 549 – 561

Jordan Journal of Biological Sciences

Maximizing Phytochemical Content for Some Medicinal Plants along with Nile tilapia (*Oreochromis niloticus*) Yield under Two Different RAS Aquaponic Models

Sara E. Gomaa[1,*] and Hadir A. Aly[2]

[1] *Medicinal and Aramatic Plants Research Dept., Horticulture research Institute. Agriculture Research Center (ARC), Giza, Egypt;* [2] *National Institute of oceanography and Fisheries, Cairo, Egypt*

Received: October 11, 2024; Revised: March 20, 2025; Accepted: April 7, 2025

Abstract

Aquaponics is a promising system for producing high-quality medicinal plants with more pharmacological content along with enhanced fish yield. The aim of the study was to examine two recirculating aquaculture system (RAS) hydroponic models using two medicinal plants (*Salvia officinalis* and *Origanum majorana*) plant characters parallel with Nile Tilapia (*Oreochromis niloticus*) performance. Results revealed that using nitrate as nitrogen source (model B) showed superiority over model A (using ammonia as nitrogen source) in all plant characters in both tested plants under study. Gas Chromatography (GC) results showed a huge number of phytochemicals variety from monoterpene, sesquiterpene, diterpene, phenolic diterpene, fatty acid alkyne, fatty acid, Alkaloid and steroid. Also, Nile tilapia production indicators were significantly better in model B compared to model A. Furthermore, the average net yield and gross yield were increased. Gross yield values ranged from 6.72 to 8.30 kg/m^3 over 63 days. One of the major factors that could enhance fish performance in this study was the bioactive compounds that may be released into the water due to the cultivated plants. GC-Mass analysis indicated that both plants contained antioxidant compounds. Regarding plant type, it was obvious that the production was slightly higher in common sage treatments than in marjoram regardless of the models. Meanwhile, fish differently performed according to assorted models, where production indicators were better in model B (nitrate) than in model A (ammonia).

Keywords: Sage, Marjoram, Nile Tilapia, GS-MS, ammonia, nitrate, aquaponic.

1. Introduction

Aquaponic is a cutting-edge high lighting technology helping crops to adapt to climate change challenges (Aslanidou *et al.,* 2023). Unlike conventional agricultural resource management, an aquaponic model saves water and reduces waste, costs, and helps enhancing environmental contamination (Ibrahim *et al.,* 2023). Aquaponics, a mix of aquaculture and hydroponics, offers a sustainable and environmentally sound way to crop growing, particularly for medicinal plants. The fish tank's nutrient-rich water serves as a natural fertilizer for the plants, while the plants help filter the water, establishing a symbiotic connection to satisfy the United Nations' planned sustainable development objectives (Ibrahim *et al* 2023)). Researchers have investigated the physiological and chemical changes noticed in medicinal plants growing at RAS aquaponic systems, with encouraging results (Dadras *et al.,* 2023). Researchers have investigated chemical changes at medicinal plants grown under RAS aquaponic systems, revealing promising outcomes (Liao *et al*., 2022). RAS aquaponic systems help medicinal plants to enhance aquaponics to produce high-quality medicinal plants with enhanced nutritional content and pharmacological activity (Patloková and Pokluda 2024). Aquaponic systems can be achieved by using medicinal plants with a consistent and ideal growing environment (Flores-Aguilar *et al.,* 2023). The nutrient-rich water from the fish tank provides plants with a steady supply of important elements including nitrogen, phosphate, and potassium. The nutrient-rich water from the fish tank can raise secondary metabolites level in plants, which are plant chemicals that are not required for plant development which may have pharmacological effect (Roslan *et al.,* 2021 and Mielcarek *et al*., 2024). Aquaponic systems can boost the concentrations of antioxidants, anti-inflammatory substances, and other useful phytochemicals in medicinal plants. These chemicals can provide a number of health advantages, including lowering risks of cancer, heart disease, and stroke (Cuevas-Cianca *et al*., 2023). This can lead to increased plant growth and biomass production (Trimble, 2022). Aquaponic systems can also help to reduce stress in plants, thus the constant flow of water through the system helps to regulate plant temperature and humidity as well as protecting plants from pests and diseases (Akpenpuun *et al.,* 2023). Aquaponics has proved to be successful and efficient for small and big scale outputs of lettuce, tomatoes, and other green salads (Ibrahim *et al.,* 2023). However, not all plant species can

* Corresponding author. e-mail: sara_gomaa@hotmail.com.

live and flourish under aquaponic systems; therefore, it is necessary to identify plant species that can be grown and produced under these systems, since biomass production is a function of survival and growth (Carlos Valdez *et al.*, 2020).

Aquaponics provides a distinct benefit in semi-intensive systems with moderate input levels by increasing the overall efficiency of fish production, especially for species like the Nile tilapia (*Oreochromis niloticus*), a crucial species in aquaculture worldwide because of its high growth rates and adaptability. Studies have indicated that aquaponic systems may significantly increase tilapia productivity and improve production efficiency (Barbosa *et al.*, 2020) by maintaining optimal water quality parameters, which are crucial for fish health and growth. Aquaponics is a highly effective and profitable method in semi-intensive settings since it incorporates hydroponic plants into these systems, which not only helps to purify the water, but also generates an additive value (Krastanova *et al* 2022).

The current study aimed to:-

- Examine the impact of two different aquaponic models on the growth and chemical compositions of two medicinal plants, common sage (*Salvia officinalis*) and marjoram (*Origanum majorana*).
- Evaluate the influence of the growing plants and models on the **performance of** Nile tilapia (*Oreochromis niloticus*) fish.
- Optimize the use of water and feed unit to achieve maximum efficiency.

2. Materials and Methods

The experimental design took place at El-Max Station for Applied Research, National Institute of Oceanography and Fisheries, Alexandria Branch, with collaboration of El-Sabaheya Horticulture Research station (SHRS), Horticulture Research institute (HRI), Agriculture Research Center (ARC), Egypt.

2.1. Plant Material

Plants under study were Common Sage (*Salvia officinalis*) and Marjoram seedlings (*Origanum majorana*) supplied by Elqanater Aromatic and Medicinal Plants Research Dept., HRI, ARC, at the age of 3 weeks. Control was planted in pots while plant seedlings were transferred to the hydroponics unit in the floating raft technique and planted at a density of 10 plants per tray. The hydroponic system was supplied with two different nitrogen sources, model A (before the biological filter): Ammonia and model B (after the biological filter): Nitrate. Plant vegetative characters were recorded. They include shoot and root length (cm), number of leaves, number of branches, fresh and dry weight for shoot and root (g).

2.2. Fish Material

Monosex Nile Tilapia (*Oreochromis niloticus*) fingerlings were obtained from a commercial fish hatchery in Kafr Elshikh, Egypt, and were transported to the experimental site through the aeration plastic tanks. The fish were stocked for acclimatization to the experimental conditions for 15 days in circular 300-liter freshwater tanks with continuous aeration, then transported to the aquaponics unit. Acclimatization period took 14 days in fresh water; about 30% of the water volume was regularly exchanged to remove the faecal matter and leftover feed. After acclimatization in the aquaponic system, Nile tilapia fingerlings were kept in 300-liter rearing tanks at a total biomass of about 1 kg/L. The mean weight of stocked fish was 28.22 g. It was given a commercial diet, to satiation, in the morning (8 am and 2 pm) that included 25% protein and 4% crude fat. Fish weight and other growth evaluation metrics were measured every 15 days using a digital balance (Generic, SF- 400A).

Four aquaponic units were investigated in this study; each consists of three circular fibreglass fish tanks of 500 L capacity (water volume 300 L) and three hydroponic plants grow beds of 0.52 m^2 (0.93 m ×0.56 m) area, fixed on a wooden table (Figure 1). The flood and drain system with gravity and pumps was used to regulate the water flow in the system sub-units. A submersible pump (SH-25l, 25 W power) was used to pump water from the sediment /or biological filter to the hydroponic bed and from the sump to the fish tank. Throughout the experiment, a flow rate of 180 L hour−1 was maintained, and the frequency of pumping was controlled by an automated timer (220v, time switch).

Continuous aeration was provided to each unit in the aquaponic system except the sediment tanks. The experiment followed a completely randomized design with four treatments allotted with different water flow orders as shown in Fig. (1) with two different plants. The same water unit was used along the whole experiment with no exchange rate except for a few amounts to compensate for normal evaporation losses.

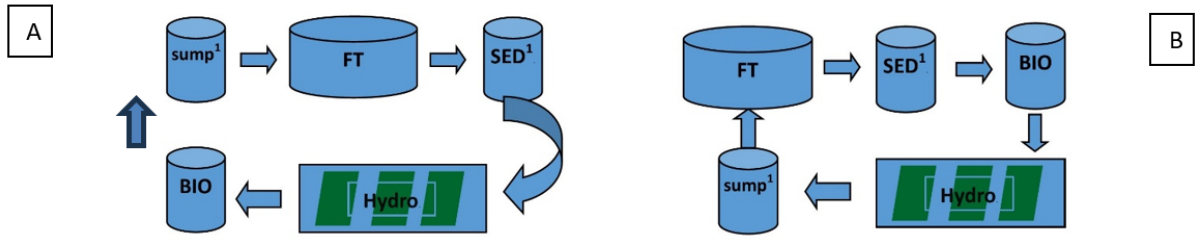

Figure 1. Two sequences used in the aquaponic models according to water flow direction; Model A: (Ammonia): Fish tank (FT), Sediment tank (SED.), Hydroponic unit (Hydro), Biological filter (BIO.) and sump tank (sump) then to the fish tank again. Model B: (Nitrate): Fish tank (FT), Sediment tank (SED.), Biological filter (BIO.) Hydroponic unit (Hydro) and sump tank (Sump) then to the fish tank again. [1] submerged pump.

2.3. Essential oil extraction and GC-MS analysis:

Preparing plant samples for Gas Chromatography-Mass Spectrometry (GC-MS) involves sample collection and preparation choose healthy plant material representative of the study. Thoroughly wash the plant material to remove any surface contaminants (soil, dust, etc.). Dry the material

to remove excess moisture. Reduce the plant material to a fine powder using a grinder, mortar and pestle, or liquid nitrogen which is very important increases the surface area for efficient extraction. Ethanol solvent was selected based on the polarity of the target compounds.

"Sage and Marjoram's chemical profiles were analyzed using GC-MS. Extracted oils were dried and then injected (1 µL, split mode) into a Trace GC-ISQ system equipped with a TG-5MS column. Helium (1 mL/min) was the carrier gas. A temperature gradient (50°C to 300°C) was applied to separate compounds, with a 4-minute solvent delay. Mass spectra (m/z 50-650, 70 eV) were acquired and compared to the NIST 05 database for identification as recommended by Mohamed et al. (2020). Following extraction, oil was dried with anhydrous sodium sulfate; the same was prepared for GC-MS analysis (Abd El-Kareem et al., 2016 and Farouk et al., 2018).

2.4. Water quality analysis

The water quality parameters: temperature, pH and dissolved oxygen (DO) were weekly analyzed in situ using a portable multi-parameter (Lovibond, SensoDirect 150, Germany). Ammonia was analyzed by colorimetry after sample fixation for 8 hours and then measured by spectrophotometer according to Grasshoff *et al.* (2009) at wavelengths 550.

2.5. Plant growth characteristics:

The following parameters were undertaken at 63 days after planting for the two studied species of medical plants, common sage (*Salvia officinalis*) and marjoram (*Origanum majorana*): plant length (cm), root length (cm), number of leaves per plant, number of branches per plant, fresh and dry plant weight (g), shoot fresh and dry weight (g), and root fresh and dry weight (g).

2.6. Fish production calculation:

Fish production indicators were calculated according to the following equations:

Net fish yield (NFY) = Total fish harvested (kg) − Total fish stocked (kg)

Net annualized Production (NAP) = NFY x 365/Pond surface area m^2 x Growth period in days

Net Biomass Gain (NBG) = Final Biomass− Initial Biomass

Net Fish Production = Final Biomass− Initial Biomass/Area of Pond×Time Period Gross Yield (GY) = Final Biomass/Area of Pond

Net Annual Production (NAP) = Final Biomass−Initial Biomass /Area of Pond

Biomass increase% = (final biomass-initial biomass/initial biomass)*100

2.7. System Purification Efficiency and Ammonia Removal Amount:

Purification Efficiency percentage (PE%) was calculated according to the following equation:

PE%= [(ammonia in the production tank-ammonia after biofilter)/ammonia in the production tank] *100

Amount of TAN removed (VTR/m^3/day) = [((NH4-N_{in}-NH4-N_{out})*Q)/V_{media}]

When: NH4-N in and out: the concentration of TAN in and out of the hydroponic system (g/m^3),

TAN: total ammonia nitrogen, VTR: volume of TAN removed.

Q: flow rate (m^3/day),

V_{media} is the volume of filter media (m^3).

2.8. Statistical analysis

The study was designed as a Randomized Complete Design (RCD) and statistically analyzed using Costat version (6.4). Statistical package SPSS 24 was used to analyze fish performance data to compare the means of different parameters. Two-way ANOVA tests were used, and Tuckey's test was applied to define the significant difference ($p \leq 0.05$) between the treatments for different parameters.

3. Results

This study was conducted to assess the effects of two different aquaponic models, referred to as Model A and Model B, on the growth performance of two medicinal plants, common sage (*Salvia officinalis*) and marjoram (*Origanum majorana*). The study focused on a numerous of plant growth parameters, including plant length, root length, number of leaves per plant, number of branches per plant, fresh and dry plant weight, shoot fresh and dry weight, and root fresh and dry weight. Additionally, the study examined the productivity and overall performance of Nile tilapia (Oreochromis niloticus) reared within these two aquaponic systems.

he data presented in Table (1) show that the majority of the studied growth characteristics of the common saga plants were significantly influenced by the varying hydroponic models, with the exceptions of root length and root fresh and dry weight characters. Among the models, Model (B) was found to produce significantly higher mean values for plant length (cm), number of leaves per plant, plant fresh weight (g), plant dry weight (g), shoot fresh weight (g) and shoot dry weight (g).

Table 1. Mean performance for common sage plants under two different hydroponic models:

Treat.	Plant length (cm)	Root length (cm)	No. of leaves/plant	No. of branches/plant	Plant fresh weight (g)	plant dry weight (g)	Shoot fresh weight (g)	Shoot dry weight (g)	Root fresh weight (g)	Root dry weight (g)
Control	23.83±2.57b	24.87±1.63a	54.00±4.44b	5.33±0.58b	15.33±3.31b	3.99±0.67b	12.28±2.29b	2.66±0.43b	3.05±1.43a	1.33±0.25a
Model (A)	23.99±2.36b	25.56±3.08a	55.58±1.69ab	6.67±0.33a	13.98±1.65b	5.30±1.60ab	11.10±1.55b	3.53±1.15ab	2.87±1.15a	1.76±0.45a
Model (B)	29.39±2.55a	29.31±3.88a	62.18±4.01a	7.32±0.34a	22.87±2.78a	6.31±0.40a	17.44±1.23a	4.73±0.25a	5.43±2.94a	1.58±0.21a

Means having letter in common do not significantly differ, using Duncan's multiple range test at p= 0.05 level of significance.

The data of Table (2) indicate that the numbers of the studied characters of marjoram plants were significantly affected by the different hydroponic models. These include plant length (cm), root length (cm), fresh plant weight (g)

and shoot fresh weight (g). Among the tested models; Model (B) appeared to be the most promising, as it is possessed the highest mean values for these characters followed by model (A), meanwhile the control treatment gave the lower means. Each of the following character; number of branches per plant, plant dry weight (g), shoot dry weight (g) and root fresh and dry weight (g) characters were not significantly affect by the two hydroponic models examined.

Table 2. Mean performance for marjoram plants under two different hydroponic models.

Treat.	Plant length (cm)	Root length (cm)	No, of Branches/plant	Plant fresh weight (g)	plant dry weight (g)	Shoot fresh weight (g)	Shoot dry weight (g)	Root fresh weight (g)	Root dry weight (g)
Control	20.76±1.85b	12.13±0.76c	10.07±1.81a	6.09±0.87b	3.00±0.63a	3.93±0.77b	2.17±0.48a	2.17±0.17a	0.83±0.17a
Model (A)	22.72±1.07ab	15.05±0.79b	12.89±1.35a	6.83±0.74b	3.87±0.51a	4.51±0.61b	2.77±0.34a	2.31±0.20a	1.09±0.18a
Model (B)	25.24±1.13a	17.58±1.04a	14.55±3.75a	9.19±0.48a	3.84±0.50a	6.71±0.19a	2.80±0.37a	2.49±0.47a	1.03±0.14a

Means having letter in common do not significantly differ, using Duncan's multiple range test at p= 0.05 level of significance.

Figure 2 shows GC-MS spectrum of common sage and marjoram with x- axis and y-axis showing the retention time (min) and the relative abundance area, respectively. Common sage *(S. officinalis)* GC-MS analysis results revealed 50 bioactive phytochemical compounds identified from different growing models (Table 3). Here, we will focus on the primary bioactive compounds that serve as the basis for cultivating Common sage and evaluate the extent to which their concentrations are influenced by various hydroponic and conventional agricultural systems. The key compounds of interest include Eucalyptol, Podocarpa-1,8,11,13-tetraen-3-one, 14-isopropyl-1,13-dimethoxy, and Carnosol. The findings presented in Table 3 indicate that the control treatment exhibited the highest concentrations of both eucalyptol and carnosol. These values were followed by those observed in hydroponic model B, whereas hydroponic model A displayed the lowest concentrations for these two compounds. Moreover, the control treatment and hydroponic model A produced comparable concentrations of the compound Podocarpa-1,8,11,13-tetraen-3-one, 14-isopropyl-1,13-dimethoxy. In contrast, this particular compound was completely absent in hydroponic model B.

Marjoram (*O. majorana*) GC-MS analysis results revealed 38 bioactive phytochemical compounds identified from different growing model designs (Table 3). Different filter arrangements of each model design revealed different metabolite as there were unique compounds for each, as well as common compounds among them as illustrated in fig (4). Marjoram cultivation primarily focuses on three active compounds: Sabinene, 4-Thujanol-CIS, and Z-Sabinene hydrate. Regarding the compound Sabinene, the data presented in Table (4) indicate that its concentration was highest under the control treatment, followed by the Model A system. The Model B system demonstrated the lowest concentration of this particular compound. The estimates for the 4-Thujanol, CIS compound, analyzed in three separate parts, showed variability without any clear trend in the data to assess the impact of the three treatments on the compound's concentration. Regarding the Z-Sabinene hydrate compound, the data presented in Table (4) indicated that its highest concentration was achieved under the control treatment, with a significant margin compared to hydroponic systems A and B.

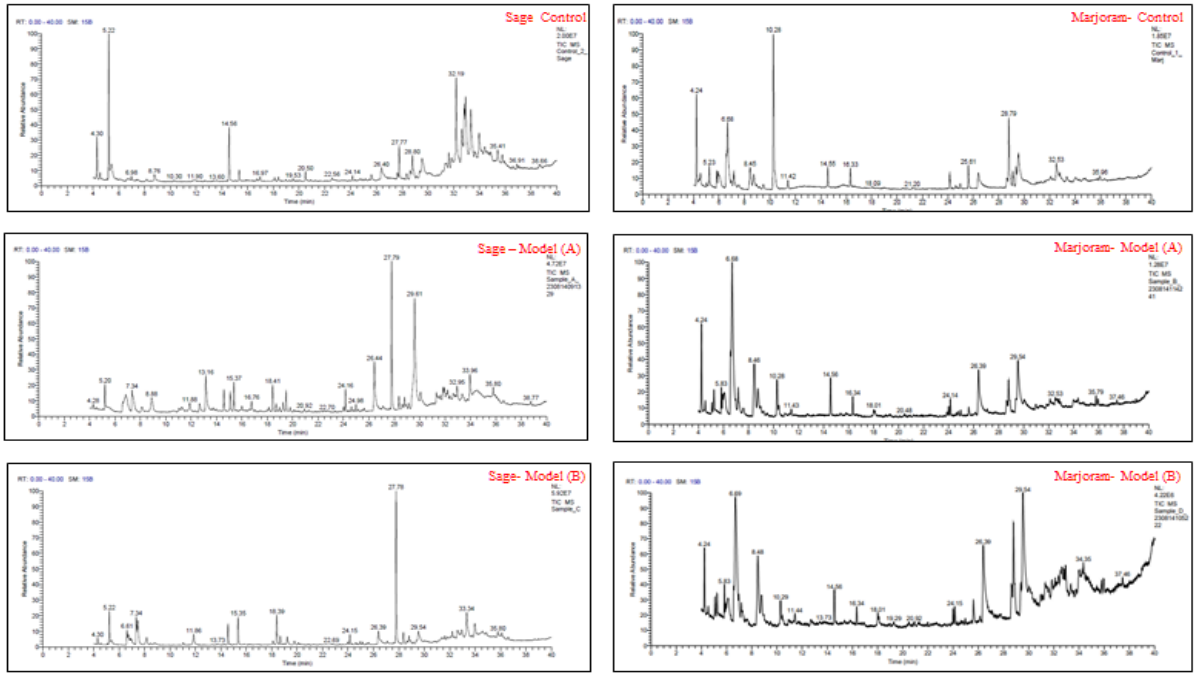

Figure 2. GC-MS spectrum of common sage and marjoram.

Table 3. Chemical Composition (%) of sage and their treatments under study as inspected by (GC-MS).

Compound name	RT	Cas number	Library*	Terpene type	Control	Model A	Model B
a Pinene	4.3	127-91 -3	M	Mono	4.48	0.47	1.31
β-Pinene	4.54	18172-6 7-3	R	Mono	0.84	0	0
Eucalyptol	5.22	470-82 -6	M	Mono	16.54	2.51	6.59
3-Isothujone	6.61	471-15 -8	R	Mono	0	0	2.42
3-Thujanol	6.84	513-23 -5	W	Mono	0	1.13	0
Camphore	7.34	464-48 -2	W	Mono	0	2.31	4.5
(+)-2-Bornanone	7.45	464-49 -3	R	Mono	0	2.41	5.64
endo-Borneol	8.16	507-70 -0	R	Mono	0	2.15	2.11
α-Terpineol	8.76	98-55-5	W	Mono	1.12	0	0
Estragol	8.88	140-67 -0	R	Mono	0	2.14	0
(1R)-(+)-pulegone	11.86	54345-6 1-8	M	Mono	0	1.21	2.36
trans-Isoeugenol	12.66	97-54-1	M	Mono	0	1.16	0
Methyl cis-cinnamate	13.15	103-26 -4	M	Mono	0	4.71	0
Caryophyllene	14.56	87-44-5	M	Sesqui	6.9	2.46	3.72
cis-α-Bergamotene	15.08	17699-0 5-7	R	Sesqui	0	2.36	0
a-Humulene	15.35	6753-9 8-6	C	Sesqui	1.39	3.27	4.9
6-epi-β-Cubebene	16	13744-1 5-5	R	Sesqui	0	0.57	0
cis-γ-cadinene	16.76	39029-4 1-9	R	Sesqui	0	1.13	0
Epiglobulol	18.39	552-02 -3	W	Sesqui	0	3.11	5.58
Humulene epoxide I	18.67	19888-3 4-7	M	Sesqui	0	0.87	1.57
Caryophyllene oxide	19.22	1139-3 0-6	W	Sesqui	0	1.39	1.96
τ-Cadinol	19.48	5937-1 1-1	R	Sesqui	0	2.38	0
Epiglobulo	20.5	NA	M	Sesqui	1.21	0	0
6,10,14-pentadecanone	24.01	502-69 -2	R	Sesqui	0	0.56	0
Ethanol, 2-(9-octadecenyloxy)-, (Z)-	24.14	5353-2 5-3	M	Fatty acid	0.66	0	0
Neophytadiene	24.15	504-96 -1	M	Diter	0	2.35	2.02
17-Octadecynoic acid	24.63	34450-1 8-5	M	Fatty acid alkyne	0	0.52	0

*Library: R = Replib, W = WileyRegi, M = Mainlib, C= CaymanSp.

Table 3. Continued

Compound name	RT	Cas number	Library*	Terpene type	Control	Model A	Model B
cis-Phytol	24.98	102608 -53-7	M	Diter	0	0.76	0
Hexadecanoic acid	26.39	57-10-3	W	Fatty acid	2.54	6.11	3.75
Epimanool; 1-Naphthalenepropanol	27.78	1438-6 2-6	R	Diter	4.17	17.26	28.14
Aromadendrene	28.36	489-39 -4	W	Sesqui	0.88	1.6	2.16
Methyl 10-octadecenoate	28.8	13481-9 5-3	W	Fatty acid methyl ester.	3.96	1.4	1.51
Isohiapin B	29.13	NA	W	Sesquit	0	0.72	0
Oliec acid	29.54	03-Jul	R	Fatty acid	2.73	13.94	5.04
1H-Pyrido[3,4-Bjindole-1-Bu Tanol ç-Sec-Butyl-2,3,4,9-Tetrahy	31.32	14358-6 0-2	W	NA	0	1.36	0
3,4,7,8-Tetraazatricyclo[4.2.2.0(1,5)] dec-9-ene-3,4:7,8-bis(N-methyldicarboximide), 2,2-diphenyl-	31.34	NA	W	NA	0	0	2.37
Cortisone Acetate	31.63	50-04-4	R	Steroid hormone	2.25	0	0
Podocarpa-1,8,11,13-tetraen-3-one, 14-isopropyl-1,13-dimethoxy	31.84	18326-2 0-0	W	Diter	1.55	1.45	0
Isoboldine	31.95	5140-28-3	C	Alkaloid	0	1.4	0
Naphtho[2,3-Cjfuran-1,3-Dio Ne, 6,7-Bis (Trimethylsilyl)-	32.61	80964-2 4-5	W	NA	4.8	2.48	0
Podocarpa-1,8,11,13-tetraen-3-one, 14-isopropyl-1,13-dimethoxy	32.64	18326-2 0-0	M	Diter	9.28	0.95	0
Pregnenolone	32.83	145-13 -1	W	Steroid	6.07	0	0
Trimethylsilylestrone	32.94	1839-5 4-9	R	NA	0	1.75	1.62
Carnosol	33.34	92519-8 2-9	W	Phenolic diterpene	7.18	1.66	2.17
Ferruginol	33.35	514-62 -5	W	Diter	3.87	3.35	0
9-Antheracenol, 1,4,8-Trimethoxy-2-Methyl	33.95	70946-2 6-8	W	NA	0	3.27	3.57
17α-Hydroxypregnenolone	35.41	387-79 -1		Steroid	1.94	0	0
Benzenamine, 2-(6,7-Dimethoxy-2-Quinonlin)-4,5-Dimethoxy	35.79	76798-5 0-0	W	NA	1.32	0	1.72
1-Linolenoylglycerol, 2TMS derivative	35.8	55521-2 2-7	W	NA	0	1.15	0
Total percentage of monoterpene					22.98	20.2	24.93
Total percentage of sesquiterpene					10.38	20.42	19.89
Total percentage of diterpene					31.12	27.32	31.62
Total percentage of phenolic diterpene					7.18	1.66	2.17
Total percentage of fatty acid alkyne					0	0.52	0
Total percentage of fatty acid					5.27	20.05	8.79
Total percentage of Alkaloid					0	1.4	0
Total percentage of steroid					1.94	0	0

*Library: R = Replib, W = WileyRegi, M = Mainlib, C= CaymanSp

Table 4. Chemical Composition (%) of marjoram and their treatments under study as inspected by (GC-MS).

compound name	RT	Cas number	Library*	Terpene type	Control	Model A	Model B
(+)-Sabinene	4.24	3387-41-5	R	Mono	10.1	9.12	5.73
β-Pinene	4.54	18172-6 7-3	R	Mono	1.19	1.51	0
1,3,6-Octatriene, 3,7-dimethyl-	5.01	18172-67-3	W	Mono	2.56	0.57	1.06
α-Terpinolene	5.08	586-62-9	M	Mono	0	0.89	1.07
4-Thujanol,	5.23	17699-16-0	W	Mono	2.56	0	0
(+)-3-Carene	5.24	3387-41-5	W	Mono	0	2.72	2.13
ç-Terpinene	5.83	99-85-4	R	Mono	1.53	2.22	2.35
ç-Terpinene	5.93	99-85-4	R	Mono	3.05	1.59	0
Trans-4-Thujanol	6.04	15537-55-0	M	Mono	0	3.16	0
4-Thujanol, CIS-(.+-.)-	6.56	15826-82-1	W	Mono	2.98	5.59	2.15
4-Thujanol, CIS-(.+-.)-	6.68	15826-82-1	W	Mono	10.55	19.28	19.09
4-Thujanol, CIS-(.+-.)-	6.98	513-23 -5	W	Mono	0.42	0	1.07
Trans-4-methoxy thujane	7.17	1100111-06-5	M	Mono	1.76	1.4	0
Terpinen-4-ol	8.44	562-74-3	M	Mono	4.09	7.6	7.7
L-à-Terpineol	8.74	98-55-5	W	Mono	2.11	2.89	0
Sabinene hydrate isomer	9.48	15537-55-0	R	Mono	0.77	0	0
Z- Sabinene hydrate	10.28	15537-55-1	R	Mono	21.6	9.88	5.62
(1R)-(+)-Pulegone	11.86	54345-6 1-8	M	Mono	1.31	0	0
Caryophyllene	14.56	87-44-5	M	sesqui	2.51	4.03	3.43
ç-Elemene	16.33	100762-46-7	W	Sesqui	2.32	2.62	3.34
Neophytadiene	24.15	504-96 -1	M	Diter	2	1.44	0
cis-Phytol	24.98	102608 -53-7	M	Diter	0.67	0	0
Palmetic acid	25.06	112-39-0	W	Fatty acid	2.99	1.25	2.34
Hexadecanoic acid	26.39	57-10-3	W	Fatty acid	2.38	1.25	6.1
Linoleic acid ethyl ester	28.62	544-35-4	R	Fatty acid	1.29	1.71	3.54
10-Octadecenoic acid, methyl ester	28.8	13481-9 5-3	W	Fatty acid methyl ester.	9.93	4.04	8.72
Methyl 10-octadecenoate	28.91	56554-49-5	M	Fatty acid methyl ester.	0	1.12	1.68
Isopropyl palmitate	29.36	56051-5	M	isopropyl alcohol	1.62	0.86	0
Oliec acid	29.54	03-Jul	R	fatty acid	3.53	4.25	5.99
Phenanthrene methanol	32.35	24035-43-6	M	Sesqui	3.53	4.25	0
Naphtho 3-Cjfuran-1,3-Dio Ne, 6,7-Bis (Trimethylsilyl)-	32.61	80964-2 4-5	W	NA	0	2.01	6.21
1-Phenanthrenemethanol, 1,2,3,4,4a,9,10,10a-octahydro-1,4a-dimethyl-7-(1-methylethyl)-, [1S-(1à,4aà,10aá)]-	32.5	24035-43-6	M	NA	2.71	0	0

*Library: (R = Replib, W = WileyRegi, M = Mainlib).

Subscription

Jordan Journal of Biological Sciences

An International Peer – Reviewed Research Journal

Published by the Deanship of Scientific Research, The Hashemite University, Zarqa, Jordan

Name: ..... الاسم:

Specialty: ..... التخصص:

Address: ..... العنوان:

P.O. Box: ..... صندوق البريد:

City &Postal Code:..... المدينة: الرمز البريدي:

Country: ..... الدولة:

Phone: ..... رقم الهاتف

Fax No.: ..... رقم الفاكس:

E-mail: ..... البريد الإلكتروني:

Method of payment: ..... طريقة الدفع:

Amount Enclosed: ..... المبلغ المرفق:

Signature: ..... التوقيع:

Cheque should be paid to Deanship of Research and Graduate Studies – The Hashemite University.

I would like to subscribe to the Journal

For

- ☐ One year
- ☐ Two years
- ☐ Three years

One Year Subscription Rates

	Inside Jordan	Outside Jordan
Individuals	JD10	$70
Students	JD5	$35
Institutions	JD 20	$90

Correspondence

Subscriptions and sales:

The Hashemite University
P.O. Box 330127-Zarqa 13115 – Jordan
Telephone: 00 962 5 3903333
Fax no. : 0096253903349
E. mail: jjbs@hu.edu.jo

المجلة الأردنية للعلوم الحياتية
Jordan Journal of Biological Sciences (JJBS)

http://jjbs.hu.edu.jo

المجلة الأردنية للعلوم الحياتية: مجلة علمية عالمية محكمة ومفهرسة ومصنفة، تصدرعن الجامعة الهاشمية وبدعم من صندوق دعم البحث العلمي والإبتكار – وزراة التعليم العالي والبحث العلمي.

ترسل البحوث الى العنوان التالي:

رئيس تحرير المجلة الأردنية للعلوم الحياتية
الجامعة الهاشمية
ص.ب , 330127 , الزرقاء, 13115 , الأردن
هاتف: 0096253903333
E-mail: jjbs@hu.edu.jo, Website: www.jjbs.hu.edu.jo

المملكة الأردنية الهاشمية

المجلة الأردنية

للعلوم الحياتية

مجلة علمية عالمية محكمة

تصدر بدعم من صندوق دعم البحث العلمي و الابتكار

http://jjbs.hu.edu.jo/